ISSN 2434-9488

KURNS Progress Report 2022

Institute for Integrated Radiation and Nuclear Science,
Kyoto University

KURNS Progress Report 2022

APRIL 2022 – MARCH 2023

Published by
Institute for Integrated Radiation and Nuclear Science,
Kyoto University,
Kumatori-cho, Sennan-gun, Osaka 590-0494, Japan

Preface for the KURNS Progress Report 2022

It is our pleasure to announce that the KURNS Progress Report 2022 has been published. This report contains all of the accomplishments of research and related activities at the Institute for Integrated Radiation and Nuclear Science, Kyoto University (KURNS) during the fiscal year 2022 (hereafter called as FY2022). A large number of research subjects have been enrolled also in FY2022, which covers various fields of nuclear science and technology, material science, radiation life science and radiation medical science. It means that our institute continues to play a distinctive role as a Joint Usage/Research Center, promoting an extensive range of studies from fundamental to applied research with research reactors and accelerators.

FY2022 was a period of gradual settling down of the COVID-19 pandemic. As a result, research activities, which had been greatly restricted for the past two years, have largely returned to their pre-pandemic status. Note that even during the circumstances of the COVID-19 situation, activities related to safety management still continued. In FY 2022, KUR was operated for 516 hours and KUCA was for 0 hours. In total, we accepted 2640 man-day researchers and students for using research facilities and for attending scientific meetings.

We strive for safe and stable operations for nationwide use, making it our primary mission to provide scientists the opportunity to conduct research and education. We are happy to dedicate our support to enable users conduct significant interdisciplinary research at KURNS.

Kumatori, July 7, 2023

Ken Kurosaki

Director, KURNS

CONTENTS

3. Reactor Physics and Reactor Engineering

4. Material Science and Radiation Effects

5. Geochemistry and Environmental Science

6. Life Science and Medical Science

7. Neutron Capture Therapy

I. ANNUAL SUMMARY OF EXPERIMENTAL RESEARCH ACTIVITIES

I-1. PROJECT RESEARCHES

Project 1

PR1 Development on Neutron Imaging Application

Y. Saito

Institute for Integrated Radiation and Nuclear Science, Kyoto University

1. Objectives and Allotted Research Subjects: Neutron imaging provides valuable information which cannot be obtained from an optical or X-ray imaging. The purpose of this project is to develop the imaging method itself and also the experimental environment for expanding the application area of the neutron imaging. The allotted research subjects are as follows:

ARS-1: Measurements of Multiphase Dynamics by Neutron Radiography (Y. Saito *et al.*)
ARS-2: Effect of Water Accumulation in Polymer Electrolyte Fuel Cell and the Cell Performances due to the Difference in the Surface Pressure (H. Asano *et al.*)
ARS-3: Influence of Luminance Scatter in Darkbox for Visualization by using Neutron Raidography (H. Umekawa *et al.*)
ARS-4: Frost Deposition Distribution Estimated by Neutron Imaging and its mechanism (R. Matsumoto *et al.*)
ARS-5: Effect of the moisture content of high-strength concrete on the spalling phenomenon under fire (M. Kanematsu *et al.*)
ARS-6: Effects of the mixer shape in a flow-type supercritical hydrothermal reactor as evaluated by neutron radiography (S. Takami *et al.*)
ARS-7: Neutron Imaging of Plant Roots in Soil Containing Organic Materials (U. Matsushima *et al.*)
ARS-8: Development of a method for quantitative estimation of neutron imaging (M. Kitaguchi *et al.*)
ARS-9: In-situ Lithium diffusion behavior in NASICON-Type Structured Lithium Ion Conductive Composite by Means of Neutron Radiography (S. Takai *et al.*)
ARS-10: Flow Visualization of Liquid Infiltrating into Complex Structures (M. Kaneda *et al.*)

2. Main results and the contents of this report: To develop neutron imaging, our imaging system was developed so that high-speed imaging could be performed at thermal neutron flux of 10^7 n/cm^{2}s. Such improved system was shared with all of the project members and valuable results were obtained as follows:

ARS-1 performed visualization of high temperature boiling two-phase flow by high-speed imaging. Test section is a stainless-steel pipe with an inner diameter of 10mm, which was heated by Joule-heating. The neutron experiments were performed at the B4 port. The imaging system used in this study consists of an op-tical image intensifier, a high-speed camera, and an 85 mm optical lens (F1.2) [1]. The frame rate is 1000 fps, and the exposure time is 0.5 ms. From experimental results, it was found that The electrical field effect of the image intensifier due to the Joule heating and the pipe stretching due to the high-temperature cause the image degradation, and they should be clarified for highly accurate void fraction measurement by high-speed neutron imaging.

ARS-2 applied to neutron imaging to water accumulation in Polymer Electrolyte Fuel Cell (PEFC). A PEFC having a single-serpentine gas channel with a cross-sectional area of 1 × 1 mm^2, an electrode area of 20 mm × 20 mm was used. By varying the surface pressure, the water accumulation was measured in the gas diffusion layers (GDLs). From the experimental results, it is considered that the cell performance decreased due to the increase in the diffusion resistance caused by the water accumulation in the GDL.

ARS-3 investigated the effect of neutron scattering on the accuracy of neutron imaging. By using a phantom and a grid system, the influence of the luminescence in a dark box was roughly estimated.

ARS-4 did not perform experiments due to the difficulties for experimental setup.

ARS-5 applied neutron imaging to analysis of vapor pressure in fire spalling of high-strength concrete. Measuring moisture transfer inside concrete quantitatively, how vapor pressure inside concrete affect spalling was considered.

ARS-6 proposed a mixer for the instantaneous heating of the reactant solution and performed neutron radiography measurements to confirm how supercritical water and room-temperature water mixed in the proposed mixer. From the experimental results, it was found that the proposed mixer was expected to produce metal oxide nanoparticles with smaller sizes and a narrower size distribution.

ARS-7 applied neutron imaging to visualization of plant roots in soil containing organic materials. By using heavy water instead of light water, the plant roots could be clearly visualized by neutron imaging at the E2 port.

ARS-8 was trying to develop a method for quantitative estimation of neutron imaging. For this, transmission images of industrial materials such as screws were acquired at different measurement times. From the measurements, it was found that even short imaging time and/or CT could meet the requirements for some purposes.

ARS-10 performed flow visualization of liquid infiltrating into a complex structures simulating an actual vehicle stator coil. Experiments were performed at the B4 port, by varying the flow rate and the heat applied to the structure. From the experimental results, it was concluded the initial liquid temperature is more crucial for effective coolant spreading and cooling.

PR1-1 Measurements of multiphase flow dynamics using neutron radiography

Y. Saito, D. Ito and N. Odaira

Institute for Integrated Radiation and Nuclear Science, Kyoto University

INTRODUCTION: Neutron radiography (NRG) is very useful for visualizing multiphase flow. The flow structure and dynamics of boiling two-phase flow can be measured. In this work, high-speed neutron imaging was applied to observe the phase change behavior in a heated pipe. The axial change of void fraction distribution at different mass fluxes was evaluated.

VOID FRACTION DISTRIBUTIONS OF BOILING TWO-PHASE FLOW: The boiling two-phase flow in the stainless-steel pipe heated by Joule heating is visualized by high-speed neutron imaging. The schematic diagram of the test section is illustrated in Fig.1. The inner diameter of the stainless steel pipe is 10 mm, and the heated length is 300 mm. The heated length is larger than the visualization area of the neutron imaging, so a manual z-axis stage moves the test section axially. In this experiment, image sequences at five places are acquired and arranged because the height of the image is about 75 mm. The neutron imaging experiments are conducted at the B-4 port in KUR. The imaging system used in this study consists of an optical image intensifier, a high-speed camera, and an 85 mm optical lens (F1.2) [1]. The frame rate is 1000 fps, and the exposure time is 0.5 ms. The empty, water-filled, and two-phase images can estimate the void fraction distribution. The experiments are performed by varying mass flux, heat flux, and water subcooling.

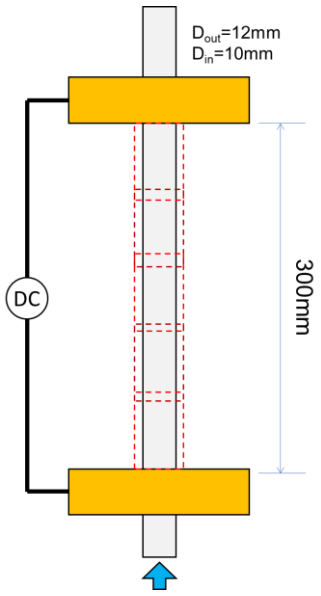

Fig. 1. Schematics of the test section of boiling two-phase flow experiments.

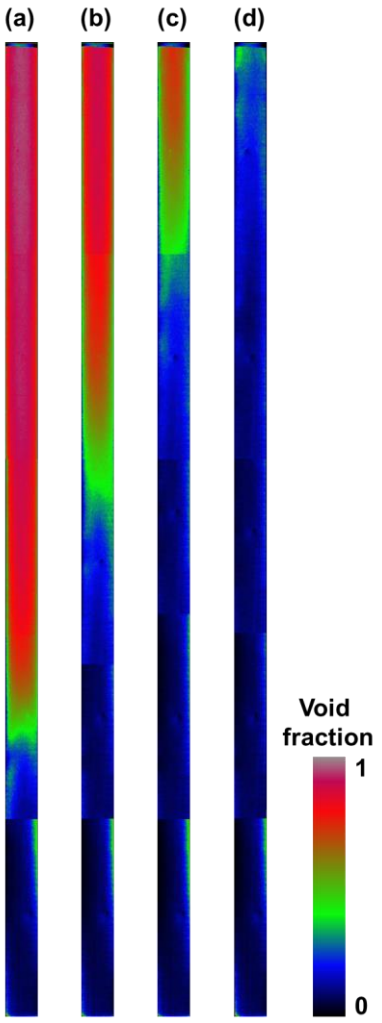

Fig. 2. Void fraction distributions of boiling two-phase flow in a heated pipe; (a) G = 100 kg/m^{2}s, (b) G = 200 kg/m^{2}s, (c) G = 300 kg/m^{2}s, (d) G = 400 kg/m^{2}s.

Fig. 2 shows temporally averaged void fraction distributions estimated from the neutron transmission images. The axial change of the void fraction is investigated by changing the mass flux at q= 290 kW/m^2 and ΔT_{sub}=20K. The boiling two-phase flow structure can be easily understood from these figures. The onset of nucleate boiling moves downstream as the mass flux increases.

The electrical field effect of the image intensifier due to the Joule heating and the pipe stretching due to the high-temperature cause the image degradation, and they should be clarified for highly accurate void fraction measurement by high-speed neutron imaging.

REFERENCES:

[1] D. Ito and Y. Saito, Materials Research Proceedings, **15** (2020) 262-267.

PR1-2 Effect of Water Accumulation in Polymer Electrolyte Fuel Cell and the Cell Performances due to the Difference in the Surface Pressure

H. Murakawa, T. Katanaya, K. Sugimoto, H. Asano, D. Ito[1] and Y. Saito[1]

Graduate School of Engineering, Kobe University
[1]Institute for Integrated Radiation and Nuclear Science, Kyoto University

INTRODUCTION: A polymer electrolyte fuel cell (PEFC) consists of a proton exchange membrane (PEM) sandwiched between gas diffusion layers (GDLs) and gas channels. Water transport in the PEFC is a key topic for fuel cell performance. If water is accumulated in the GDL, it may suppress the air supply to the cathode reaction site. It is well known that the water contents in the PEM are related to the ionic conductivity resulting in a change in the PEFC performances [1]. One of the important parameters for the PEFC setting is the surface pressure, P, of the cell. If the pressure is much higher than the appropriate pressure, the porosity of the GDL may decrease resulting in the decrease of the gas diffusivity. On the other hand, low pressure may lead to an increase in contact resistance. In this study, we focused on the effect of water transport and the cell performances due to the difference in the surface pressure.

EXPERIMENTS: Neutron radiography and electrochemical impedance spectroscopy (EIS) were employed for our investigations. B4-port in Kyoto University Research Reactor was used for the neutron radiography measurements. A PEFC having a single-serpentine gas channel with a cross-sectional area of 1 × 1 mm^2, an electrode area of 20 mm × 20 mm was used. Nafion® membrane and GDLs (SGL 22BB) with a thickness of 200 μm were used. Two-dimensional water distributions were obtained every 60 sec during the PEFC operation for 21 minutes using neutron radiography. The EIS measurement was performed between 20 and 21 minutes after the start of the PEFC power generation for evaluating the PEM resistance and the reaction resistance. The experiments were carried out at room temperature.

RESULTS: Fig. 1 shows an example of the two-dimensional water distribution at a current density, i, of 600 mA/cm^2. The color contour represents the thickness of water along the neutron beam. The gas inlet is placed on the upper right channel. At 5 min, water accumulation is confirmed mainly from between the channels and the ribs. It is considered that the water evacuation from the GDL to the channel easily occurred around the channel corner. At 21 min, much water is confirmed in the gas channel. The water accumulation is greater on the channel than that on the rib position. The average water thickness at the 5th rib which is placed at the center of the serpentine channel was calculated for evaluation of water accumulation in the GDL. Fig. 2 represents the comparison of the time series of the water thickness with different P. The change in the water thickness mainly occurred due to the accumulation in the GDL. For all conditions, the water accumulation occurred significantly during 5 minutes from the power generation start. After that, the change in the water thickness becomes moderate with the operation time. As confirmed by Fig. 1, the change in the water accumulation in the GDL becomes smaller when the water starts to be discharged into the channel. The amount of water accumulation varied depending on the difference in P and the water accumulation was the lowest at P = 1.0 MPa. Table 1 shows the reaction and ohmic resistances at 21 min. The resistances for P = 1.0 MPa take the lowest, indicating the cell performance was the best. Compared with the results in Fig. 2, it can be seen that the cell performance improved due to less water accumulation in the GDL. At P=0.5 and 2.0 MPa, it is considered that the cell performance decreased due to the increase in the diffusion resistance caused by the water accumulation in the GDL.

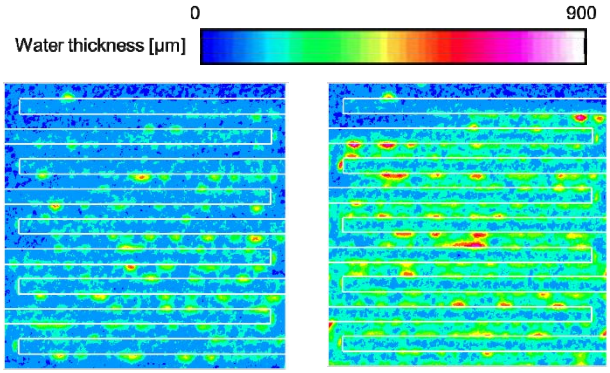

(a) 5min (b) 21 min

Fig. 1. Two-dimensional water distribution at P = 1.0 MPa

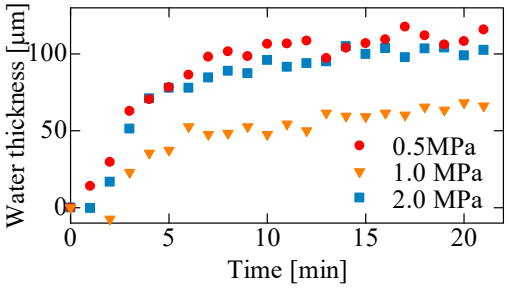

Fig. 2 Time variation of water thickness under the 5th rib.

Table 1. Reaction and ohmic resistances at 21 min.

Surface pressure	Reaction resistance	Ohmic resistance
0.5 MPa	140 mΩ	279 mΩ
1.0 MPa	117 mΩ	117 mΩ
2.0 MPa	131 mΩ	365 mΩ

REFERENCES:

[1] T. E. Springer *et al.*, J. Electrochemical Society, **138** (1991) 2334-2342.

PR1-3 Influence of Luminance Scatter in Darkbox for Visualization by using Neutron Raidography

H. Umekawa[1], Y. Kamiya[1], K. Akiyama[1], T.Ami,
N. Odaira[2], D. Ito[2], Y. Saito[2] and M.Matsubayashi[3]

[1]*Department of Mech. Eng., Kansai University*
[2]*Institute for Integrated Radiation and Nuclear Science, Kyoto University*
[3]*Japan Atomic Energy Agency*

INTRODUCTION: To improve the accuracy of Neutron Radiography, the influence of neutron scatter cannot be neglected. For the calibration of neutron scatter typically three kinds of methods are widely used, as shown in Fig.1. Although these procedures are mainly composed to calibrate the scatter of the neutron, the scatter of luminescence in dark box may also occur. In this report, the influence of the luminescence in a dark box was roughly estimated.

EXPERIMENTAL APPALATUS: For the estimation, the grid system of Fig.2 was used. The Grid and Base Grid , which are made of aluminum, have same configurations. Grids has slits (W:3mm D:6mm), and $Gd(NO_2)_3 \cdot 6H_2O$ is filled and covered by aluminum tape. Base Grid is put above the converter, and Grid set at 100mm distance from the converter. Thus, Base grid absorbs almost of all neutron including the neutron scatter, but the shadow of Grid at 100mm includes the neutron scatter and blur of neutron. Between two Grids, a wedge shape phantom which can be filled by water, is equipped, and transparent length 0mm at the bottom end and 30mm at the top end. Figure 3 is the example of visualization image of these grid system and phantom from the front side.

EXPERIMENTAL RESULTSS: The Gray levels under several experimental conditions at the level of yellow line in Fig.3 are shown in Fig 4. Especially, the difference of gray level between the Base Grid part and the Offset obviously suggests the existence of the scatter of luminescence in the Dark box.

Example of calibration results are shown in Fig.5. In this figure, water thickness of phantom along vertical direction are estimated by using several kinds of Offset values. Especially, to visualize the large attenuation object (thicker part), the influence of luminescence scatter cannot be neglected. This result also suggested that the limitation of the adapting of neutron radiography is approximately 15mm.

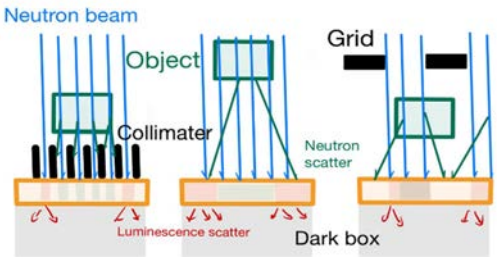

(a) Collimater (b)Gradel (c) Ambra
Fig.1. Calibration methods of Neutron Scatter.

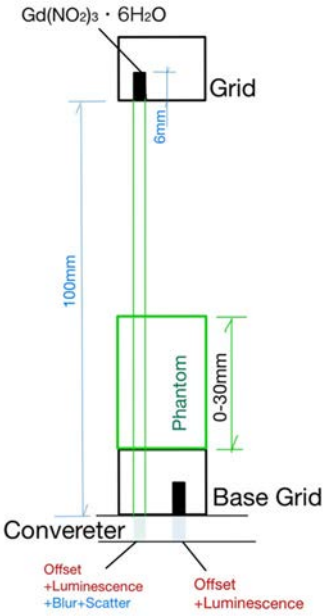

Fig.2. Grid system.

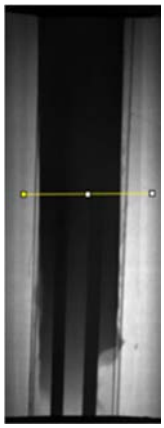

Fig.3. Visualization Image of Phantom and Grid system (Front View) .

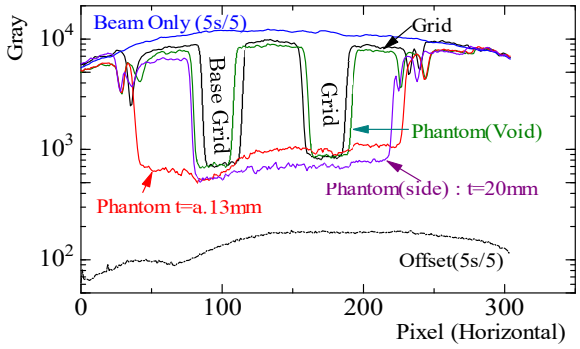

Fig.4. Gray level at the yellow line in Fig.3.

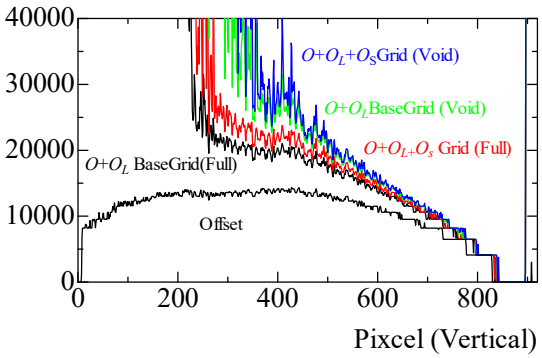

Fig.5. Calibration results. (In this figure, $\log((S_{VOID} - O)/(S - O))$, which is linear to water thickness, is plotted.) .

PR1-4 Effect of the moisture content of high-strength concrete on the spalling phenomenon under fire

M. Yoshioka, T. Hosokawa, E. Noda, M. Kawakami, J. Kim, M. Kanematsu, Y. Nishio[1], N. Odira[2], D. Ito[2] and Y. Saito[2]

Graduate School of Science and Technology, Department of Architecture, Tokyo University of Science
[1]Building Research Institute
[2]Institute for Integrated Radiation and Nuclear Science, Kyoto University

INTRODUCTION: Generally, reinforced concrete buildings are fireproof because they have cover concrete to resist heat from a fire. However, spalling [1] phenomena may occur to lose their cover concrete when the structures were heated by fire, especially when using high strength concrete. In past research, the explanations for this phenomenon have been widely accepted by thermal stress and vapor pressure due to evaporation of internal moisture, or both phenomena. On the other hand, it has been pointed out that the spalling does not occur at the low water content but at the high moisture content. In this study, the effect of moisture content on the spalling phenomena of high-strength concrete was investigated by using the neutron imaging technique.

EXPERIMENTS: Heating experiments were performed on test specimens with target relative moisture contents of 0%, 80%, and 100% in the KUR-B4 port of KURNS. Transmission images were obtained using neutron radiography to detect the moisture behavior inside the concrete. At the same time, temperatures at 10 mm and 20 mm from the heating surface were measured by thermocouples. In addition, the vapor pressure at 10 mm from the heating surface was measured. Stainless steel pipes and silicone oil were used for the measurement to vapor pressure. Fig.1 shows the schematic diagram of the test equipment used in the experiment. The concrete specimens are 100×70×30 mm (width × height × thickness) of reinforcing rebar with a cover depth of 30mm. The compressive strength of concrete measured on the day (25 days after the mixing) of the heating experiments was 135N/mm^2.

RESULTS: Fig.2, shows the distribution of moisture in concrete specimens, a location where the relative moisture content was higher at the time of the explosion than the initial state was confirmed. However, no increase in relative moisture content was observed in the range of 1 mm to 3 mm from the heating surface where the explosion occurred. Therefore, it was not possible to conclude that the movement of water contributed to the occurrence of the explosion inside the concrete. In addition, as shown in Fig.3, the vapor pressure inside the concrete increased as the heating time progressed. This increase was similar to

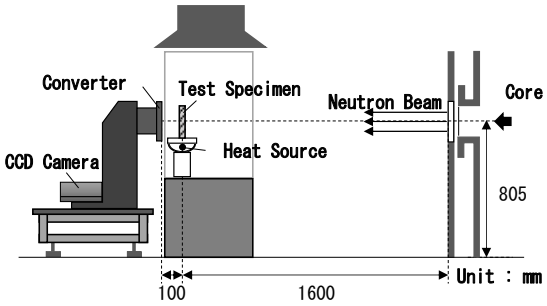

Fig. 1. Schematic diagram of the heating experiment.

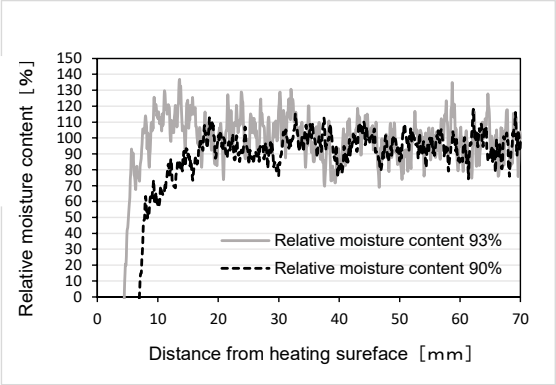

Fig. 2. The effect of initial relative moisture content on the relative moisture distribution just before the spalling.

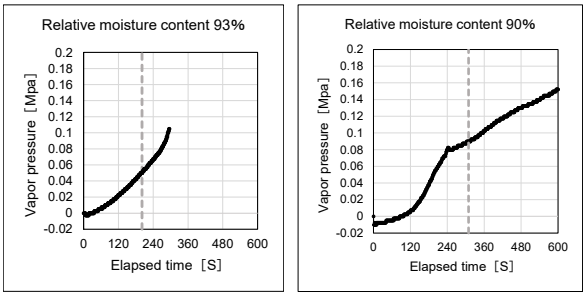

Fig. 3. Temporal changes in vapor pressure inside concrete.

the pressure increase observed in previous studies on test specimens with similar temperature increases. Therefore, it is considered the pressure was measured correctly. Some of the water inside the heated concrete is believed to have produce vapor pressure and exerted force on the concrete. The pressure at the time of the explosion at a position 10 mm from the heating surface was low, ranging from 0.045 MPa to 0.085 MPa, and it is not believed that this value alone caused the explosion. On the other hand, the initial occurrence of the explosion in this experiment was confirmed in the range of 1 mm to 3 mm from the heating surface, so it is possible that the pressure was further increased in this location. In the future, it is necessary to grasp the behavior of moisture at a position closer to the initial location of the explosion and measure the pressure.

REFERENCES:

[1] JCI Committee Report, (2017) JCI-TC-154A.

PR1-5 Effects of the mixer shape in a flow-type supercritical hydrothermal reactor as evaluated by neutron radiography

K. Sato, R. Sasaki, B. Xie, S. Takami, M. Kubo[1], T. Tsukada[2], K. Sugimoto[3], N. Odaira[4], D. Ito[4] and Y. Saito[4]

Graduate School of Engineering, Nagoya University
[1]Graduate School of Engineering, Tohoku University
[2]New Industry Creation Hatchery Center, Tohoku University
[3]Graduate School of Engineering, Kobe University
[4]Institute for Integrated Radiation and Nuclear Science, Kyoto University

INTRODUCTION: Nanoparticle synthesis has attracted considerable attention over the past few decades because nanomaterials exhibit different physical and chemical properties than their corresponding bulk materials. Among various synthesis methods, supercritical hydrothermal synthesis has attracted much attention to synthesize metal oxide nanoparticles. During supercritical hydrothermal synthesis using flow-type reactors, a stream of metal ion aqueous solution was instantaneously heated by mixing with a stream of heated water in a mixer. The previous studies suggested that the reaction rate of metal ions was fast and the products were affected by the course of mixing. In this study, we proposed a mixer for the instantaneous heating of the reactant solution and performed neutron radiography measurements to confirm how supercritical water and room-temperature water mixed in the proposed mixer.[1]

EXPERIMENTS: In this study, we conducted neutron radiography measurements to visualize the mixing behavior in a flow-type reactor. The measurements were performed at the B4 port of the Kyoto University Reactor. The KUR was operated at a 5 MW output with a neutron flux of ca. 5×10^7 n/cm^2 s at the beam exit of the B4 neutron guide tube. The experimental setup (Fig. 1) was similar to that used in previous studies.[2-4] The neutron radiography images were processed to obtain images of the average water density in the mixer. In this study, we used a conventional and designed mixer shape as shown in Fig. 2a and 2d.

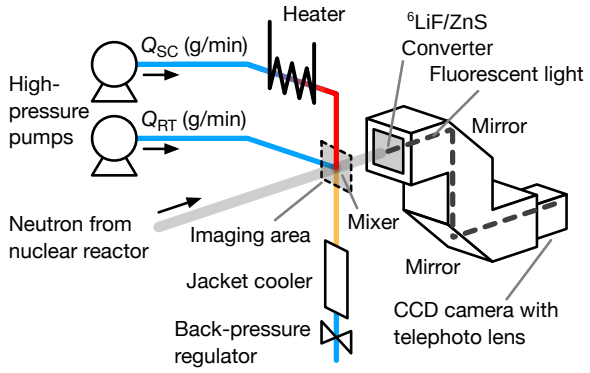

Fig. 1. Diagram of the experimental apparatus.

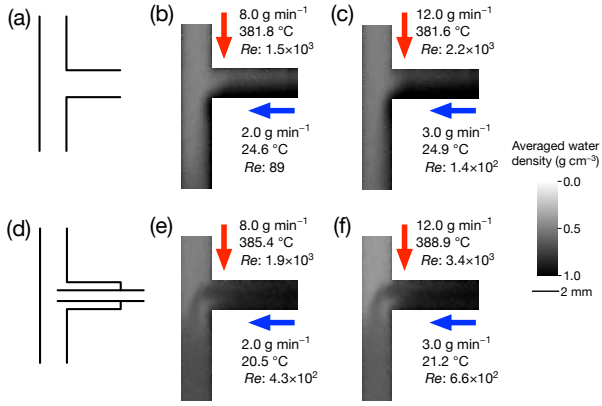

Fig. 2. (a, d) Schematic of conventional (top) and proposed (bottom) mixer and average water density profiles of the (b, c) conventional and (e, f) proposed mixers.

RESULTS: Figs. 2b, 2c, 2e, and 2f show the average water density profiles of both mixers when the flow rates of the supercritical water (Q_{SC}) and room-temperature water (Q_{RT}) were Q_{SC}=8.0 and Q_{RT}=2.0 g/min (Figs. 2b and 2e), and Q_{SC} =12.0 and Q_{RT} =3.0 g/min (Figs. 2c and 2f). The temperatures of the streams are shown in Fig. 2. In Fig. 2, the darker area corresponds to a higher water density, which corresponds to a lower temperature. Figs. 2b and 2c show that room-temperature water supplied from the side flowed along the right wall of the vertical tube after mixing under both flow conditions in the conventional mixer. The supercritical water supplied from the top flowed along the left side of the vertical tube, and the two streams gradually mixed. This mixing behavior resulted in a lower heating rate of the reactant solution, which caused gradual hydrothermal reactions and nanoparticle nucleation. Conversely, this tendency of mixing was apparently different for the proposed mixer shown in Figs. 2e and 2f. The stream of room temperature water flowed out from the side tube with an inner diameter of 1.0 mm and uniformly mixed with the supercritical water supplied from the top. he supplied room-temperature water quickly mixed in the vertical tube after the T-junction. Therefore, the proposed mixer was expected to produce metal oxide nanoparticles with smaller sizes and a narrower size distribution.

REFERENCES:

[1] K. Sato *et al.*, Chem. React. Eng., in press.
[2] S. Takami *et al.*, J. Supercrit. Fluids, **63** (2012) 46-51.
[3] K. Sugioka *et al.*, AIChE J., **60** (2014) 1168-1175.
[4] S. Takami *et al.*, Phys. Proc., **69** (2015) 564-569.

R4P1-6

PR1-6 Neutron Imaging of Plant Roots in Soil Containing Organic Materials

U. Matsushima[1], D. Ito[2], N. Odaira[2], Y. Saito[2]

[1]*Faculty of Agriculture, Iwate University*
[2]*Institute for Integrated Radiation and Nuclear Science, Kyoto University*

INTRODUCTION: Neutron imaging is a technique that takes advantage of the fact that the penetration of neutron beams varies with the material. For example, the thickness of the half-value layer, which is the thickness at which the neutron beam permeability becomes 1/2, is 2 mm and 72 mm for water and silicon, respectively, which are commonly found in soil. This neutron beam can be used to visualize plant roots, which are organic matter containing large amounts of water. When metal-rich soil and water-rich roots were compared in a neutron transmittance image, the image of roots in the soil appeared darker than that of the roots in the soil. However, when organic matter was mixed into the culture medium, the neutron transmittances of the culture medium and roots were similar, making it difficult to distinguish the root image from that of the culture medium. Therefore, roots were visualized in soil containing a high ratio of organic matter using heavy water, which has a lower neutron transmission rate than that of water, as a contrast agent and having the plant roots absorb it.

EXPERIMENTS: Rice husk medium (rice husk:soil = 3:1 by volume) was used as an organic matter-containing medium. The rice husk medium was filled into aluminum containers and Komatsuna (*Brassica rapa* var. *perviridis*) planted into aluminum containers. To allow comparison with neutron images, the thickness of the soil in the direction of neutron irradiation was 2 cm. Neutron images were obtained using the E2 neutron imaging apparatus installed in the research reactor KUR at the Institute for Integrated Radiation and Nuclear Science, Kyoto University. Heavy water was supplied to the roots by immersing them 2 cm deep from the bottom of the sample container in heavy water. Following neutron imaging, the aluminum plates of the growing container were removed and visual images of the roots on the surface of the medium were captured.

RESULTS: First, the distribution of the plant roots within the region of interest (ROI) in the neutron image was estimated by extracting the root region from the optical image of the culture medium surface using binarization (Fig.1-b). In the binary images of the roots, there was no significant difference in the distribution of roots on the surface and underside of the rice husk medium. Therefore, it was analogous that roots in the space inside the medium were also located near the roots that appeared on the surface. In the neutron image of the same ROI, although particles of rice husk medium were observed, the elongated image characteristic of roots was not observed (Fig.1-b). In the rice husk medium supplied with heavy water for waterlogging, only the particle distribution of the medium was observed in the neutron image (Fig.2-a). Therefore, the neutron image at 60 min after the heavy water supply was divided by the image immediately after the heavy water supply to emphasize the change in neutron transmittance. Consequently, an elongated root-like image was observed in the enhanced image (Fig.2-c). This indicated that heavy water was absorbed by the roots from the waterlogged area and replaced the water inside the roots, resulting in lower neutron transmittance in the roots in that area, and the difference appeared as an image. In other words, the use of heavy water as a contrast agent made it possible to visualize the inner roots even in a medium containing a higher ratio of organic matter.

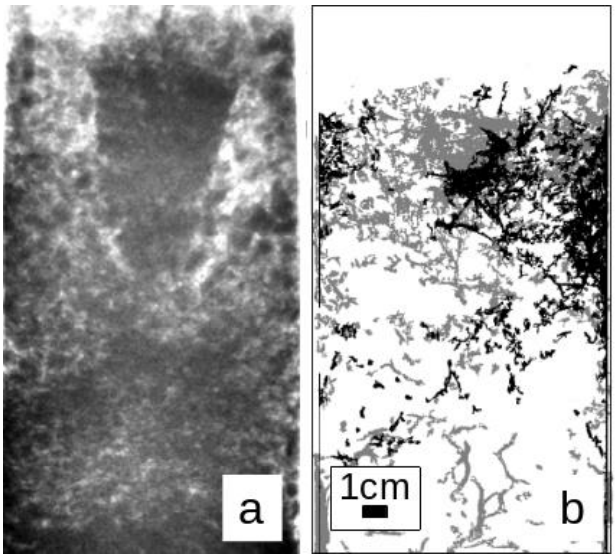

Fig. 1. Neutron image (a) of rice husk medium planted with komatsuna and root zone extracted from an optical image of the same ROI (b). b: Roots on the surface and underside of the sample are shown in black and gray, respectively.

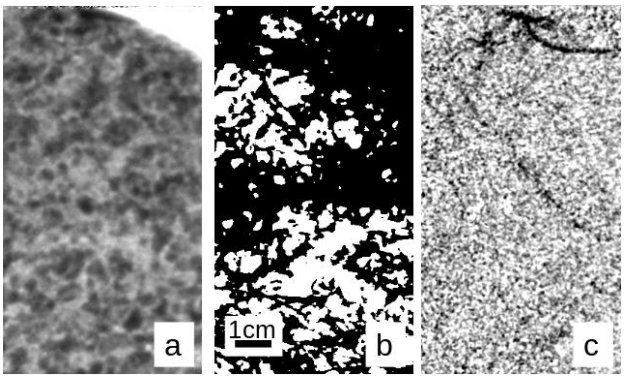

Fig.2. Neutron image (a) of a rice husk medium in which komatsuna was planted, root zone extracted from an optical image of the same ROI (b), and root image contrasted with heavy water (c).

PR1-7 Development of a method for quantitative estimation of neutron imaging

M. Kitaguchi, H. M. Shimizu[1], D. Ito[2], and Y. Saito[2]

KMI, Nagoya University
[1]*Graduate School of Science, Nagoya University*
[2]*Institute for Integrated Radiation and Nuclear Science, Kyoto University*

INTRODUCTION: Neutron imaging and computed tomography (CT) are becoming increasingly important in the development of industrial products. The visualization of microstructures between metals and the distribution of water and organic matter, which cannot be observed with the conventional methods directly, is widely desired. In order to meet the increasing demand, limited beamtime must be allocated and meaningful data must be acquired appropriately. Because neutron imaging differs from visible light and X-rays in many respects in the optical characteristics of the source and device, the experimental setups and measurement times were set empirically. This study aims to establish a technique to quantitatively predict the time required for the measurements. This will enable us to optimize the use of neutrons and to get meaningful conclusions even with small neutron sources with low beam intensity. In addition, the optimal design of new beamline can be performed.

EXPERIMENTS: The measurement was performed at the E2 port where the environment for transmission image measurement was provided. Transmission images of industrial materials such as screws were acquired at different measurement times. In this study, the object was a screw of 2 cm in diameter through a metal part. The contact between the screws and the grease between the parts was the object of interest. The images were taken with the measurement time from 10 seconds to 5 minutes. The internal structure can be seen even with short measurement time.
The CT images were also taken with normal and very-short exposure time. Although the low number of transmitted neutrons make it impossible to analyze the detailed internal structure of a bulk sample, the short-time CT can be used for specific and actual purposes, such as to determine the rough distribution of organic matter inside the sample. We shared the results with the company that provided the test samples and discussed the feasibility of a measurement that would meet their objectives.

DISCUSSION: It was found that even short imaging time and/or CT could meet the requirements for some purposes. It is considered necessary to quantify the requirements.

PR1-8 Observation of Lithium Migration in NASICON-Type Solid Electrolyte by Means of Neutron Radiography

S. Takai[1], H. Takagi[1], T. Yabutsuka[1], T. Yao[2], D. Ito[3], Y. Saito[3]

[1]*Graduate School of Energy Science, Kyoto University*
[2]*Kyoto University*
[3]*Institute for Integrated Radiation and Nuclear Science, Kyoto University*

INTRODUCTION: LISICON-type structured LATP ($Li_{1.3}Al_{0.3}Ti_{1.7}(PO_4)_3$) or LAGP ($Li_{1.5}Al_{0.5}Ge_{1.5}(PO_4)_3$) are promising materials for the solid electrolyte of All-Solid-State Batteries (ASSBs). We have focused on the enhancement of lithium-ion conductivity of these compounds by means of the dielectric particle dispersion technique [1-3]. In recent years, we have successfully measured the tracer diffusion coefficient of lithium ions in LATP by means of neutron radiography emphasizing the contribution of $LaPO_4$ particle dispersion [4]. The isotope of ^6Li well attenuates the neutron flux while ^7Li does not. We applied ^6Li tracer on the LATP block consisting of ^7Li and measured the neutron-transmitted images to obtain the diffusion profiles.

While the lithium diffusion was performed simply by annealing in the above study, the lithium-ion migrates between the electrode through the electrolyte in the actual battery operations. Then, we planned to visualize the lithium migration during the solid-state cell operation by constructing test cells. In the previous study, we fabricated the MnO_2 / ^{7}Li-LATP / ^{N}Li-LATP / $Li_{1.33}Ti_{1.67}O_4$ cells to electrolyze for neutron imaging. The natural isotope ratio of ^6Li / ^7Li is referred to ^NLi. However, the lithium transfer at the interface is relatively difficult to observe the lithium migration in ^{7}Li-LATP. In last year, we constructed the $LiMn_2O_4$ / ^{7}Li-LATP / $LiMn_2O_4$ symmetry cell to reduce the solid-solid interface. Nevertheless, the lithium migration across the solid-solid interface is still difficult. In the present study, we employed the LiMn2O4 slurry mixed with acetylene black and PVdF as the electrode materials to keep intimate contact between the electrode and electrolyte.

EXPERIMENTS: ^{7}Li-LAGP ($Li_{1.5}Al_{0.5}Ge_{1.5}(PO_4)_3$) and ^{N}Li-$LiMn_2O_4$ pellets were prepared by the conventional solid-state reaction method. Both sides of the LAGP pellet were polished to achieve the flat plane. $LiMn_2O_4$ powder was mixed with acetylene black and PVdF in the ratio of 8: 1: 1 in weight, which were applied on the both surfaces of the LAGP pellet with a small amount of NMP to fabricate the $LiMn_2O_4$ / ^{7}Li-LAGP / $LiMn_2O_4$ symmetry cells. The typical amount of applied $LiMn_2O_4$ is 3 mg for each side.

The test cell was set in a heater equipment as shown in Fig. 1 and the electric field was applied up to 10 V by using a potentio-galvanostat (Hokuto, HA151). The sample was heated up to 200°C to facilitate the electrolysis. The subjected current density is selected as 0.2 C.

After the electrolysis was started, the entire apparatus was subjected to a direct neutron beam for 45 minutes at B4 port of KUR (generated at 1MW). Neutron radiography images were taken by the CCD camera (5 min exposure) every 15 minutes. The configuration of the apparatus is also shown in Fig. 1.

RESULTS: The applied voltage gradually increased from 5 V to 10 V, which is the limit for the constant current operation. After reaching the limit potential of 10 V, the electrolysis was continued in constant voltage mode. Fig. 2 represents the typical radiography image after the electrolysis for 60 min. In the present case, any separation of electrode/electrolyte pellets was not observed due to the rigid contact using PVdF. The analysis of transmitted neutrons in the LAGP is presently carried out.

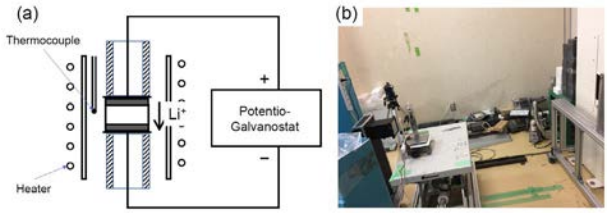

Fig. 1. (a) Schematic diagram of electrolysis equipment and (b) photograph of the experimental configuration.

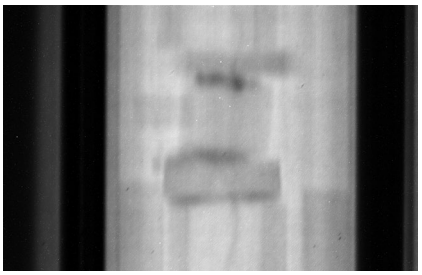

Fig. 2. Typical neutron radiography image of ^{7}Li-LAGP after electrolysis for 60 min.

REFERENCES:

[1] H. Onishi *et al*., Electrochemistry. **84** (2016) 967.
[2] F. Song *et al.,* J. Alloys Compds., **853** (2021) 157089.
[3] F. Song *et al*., *Materials,* **14** (2021) 3502.
[4] F. Song *et al*., *Solid State Ionics,* **377** (2022) 115873.

PR1-9 Flow Visualization of Liquid Infiltrating into Complex Structures

M. Kaneda, Z. Li, and K. Suga

Department of Mechanical Engineering, Osaka Metropolitan University

INTRODUCTION: Electric motors used in electric vehicles have required higher performance, more power, and compactness [1]. This results in higher Joule heating from the motor package and the effective cooling scheme of the heated stator coil has been important. The actual vehicle stator coils are cooled by the coolant poured from a nozzle above. Chen et al. [2] experimented to estimate the removed heat by the coolant from the covered stator coil. In this case, the fundamental characteristic was not clarified in terms of heat and fluid flow. Previously, we experimented with the visualization of the coolant liquid inside the layered structure but it was at room temperature without structure heating. Therefore in this study, the structure was heated by Joule heating and the coolant profile inside the structure was visualized by using neutron radiography.

EXPERIMENTS: The schematic model of the experiment is shown in Fig.1. The coolant liquid was pumped up from the bath and poured onto the horizontal simplified coil structure. The stator coil was presumed by the four-layered accumulated serpentine aluminum plates shown in Fig. 2 which was simplified from the actual stator coil structure where the coolant touches down. The coolant temperature at the nozzle was set at 35 and 50 deg.C to investigate the effect of the initial coolant viscosity. Additionally, the flow rates of the coolant were tested at 500 and 650 mL/min. The applied heat was 100 and 200W. The neutron radiography was conducted inside the structure from the horizontal direction.

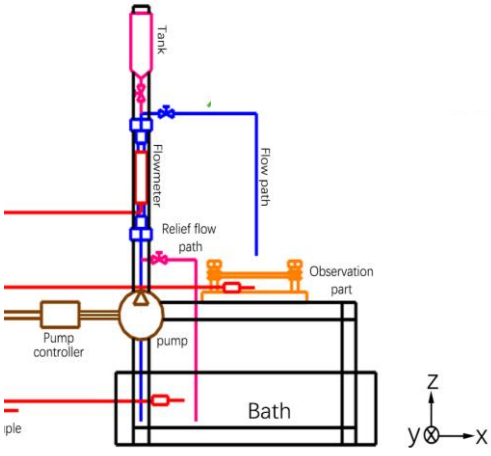

Fig. 1. Experimental setup.

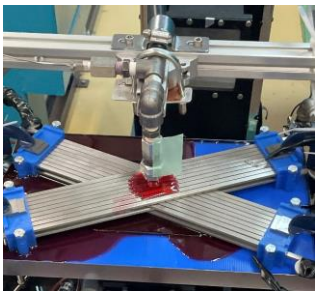

Fig. 2. Simplified heated stator coil.

RESULTS: The visualized coolant profile inside the layer structure is shown in Fig.3. As shown in Figs.3(a) and 3(b), it is found that the coolant profile does not largely depends on the applied heat. This implies the liquid temperature does not increase so much inside the structure so does the liquid viscosity. Indeed, experiments at 50 degC were less affected by the heating amount. Nevertheless, since the heat capacity of the liquid is large enough, sufficient heat removal can be expected. It was confirmed in our laboratory experiment.

Instead of the effect of heating, the liquid profile was largely affected by the coolant temperature at the nozzle (initial temperature) as shown in Fig. 3(c). This is because the liquid viscosity is much smaller at a higher temperature than that at a lower one. Therefore, it can be concluded the initial liquid temperature is more crucial for effective coolant spreading and cooling.

(a) 35 deg C, 100W

(b) 35 deg C, 200W

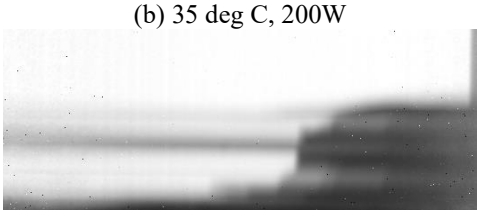

(c) 50 deg C, 100W

Fig. 3. Liquid profile inside the structure at the flow rate of 500 mL/min.

REFERENCES:

[1] N. Kobayashi and T. Ikegami, Thermal Sci. Eng., **15(2)** (2007) 49-54.

[2] P. Chen *et al.,* Appl. Therm. Eng., **220** (2023) 119702.

I-1. PROJECT RESEARCHES

Project 2

PR2 Advancement of integrated system for dose estimation in BNCT

Y. Sakurai

Institute for Integrated Radiation and Nuclear Science, Kyoto University

BACKGROUNDS AND PURPOSES:

Several types of accelerator-based irradiation system for boron neutron capture therapy (BNCT) are under development at present. But, there are a number of subjects, which should be improved for the further advance and generalization of BNCT.

In the viewpoints of medical physics and engineering, the advance for dose estimation is one of the important subjects. For the characterization of irradiation field, quality assurance and quality control (QA/QC), clinical irradiation to actual patient, and so on, an ultimate goal is to perform the three-dimensional and real-time dose estimation in discriminating for thermal, epi-thermal and fast neutron doses, gamma-ray dose, and boron dose, with simplicity and low effort. Considering about this ultimate dose estimation, several kinds of dose estimation method are studied. It is so difficult to realize the ultimate dose estimation using only one method, but it is necessary to use simultaneously more than two methods.

The purposes of this project research are the advance for various dose estimation methods, and the establishment of an integrated system for dose estimation in BNCT.

In the third year of this research project, 2022, the advancement for the respective dose estimation methods were forwarded mainly using Heavy Water Neutron Irradiation Facility (HWNIF) and E-3 Neutron Guide Tube (E-3) at KUR, sequentially the previous year. In addition, the integrated system was considered for the simultaneous usage of several dose estimation methods

RESEARCH SUBJECTS:

The collaboration and allotted research subjects (ARS) were organized as follows;

ARS-1 (R4P2-1): Establishment of characterization estimation method in BNCT irradiation field using Bonner sphere and ionization chamber (VI). (Y. Sakurai, A. Sasaki, N. Matsubayashi, M. Nojiri, D. Fu, T. Takata, H. Tanaka)

ARS-2 (R4P2-2): Study on neutron energy spectrometry for epi-thermal neutrons. (S. Yoshihashi, A. Yamazaki, K. Watanabe, Y. Oshima, A. Uritani, Y. Sakurai)

ARS-3 (R4P2-3): Development of Bonner sphere spectrometer using small lithium-glass scintillator for intense neutron beams. (A. Masuda, T. Matsumoto, S. Manabe, K. Watanabe, A. Ishikawa, H. Tanaka, Y. Sakurai, H. Harano, T. Takata, A. Uritani)

ARS-4 (R4P2-4): Improvement of the SOF detector system for energy-dependent discrimination and long-term stability. (M. Ishikawa, S. Ishiguri, K. Takamiya, Y. Sakurai)

ARS-5 (R4P2-5): Improvement of absolute fast neutron flux intensity monitor for BNCT. (I. Murata, K. Sagara, R. Kawahata, S. Tamaki, S. Kusaka, H. Tanaka, Y. Sakurai, T. Takada)

ARS-7 (R4P2-7): Neutron image sensor for boron neutron capture therapy. (M. Taniguchi, T. Meguro, H. Tanaka, S.-I. Kuroki)

ARS-8 (R4P2-8): Preliminary survey of nuclide for epithermal neutron measurement using gel detector. (K. Tanaka, Y. Sakurai, T. Kajimoto, H. Tanaka, T. Takata, S. Endo)

ARS-9 (R4P2-9): Measurements of neutron fluence and gamma ray distribution using thermoluminescence slabs. (K. Shinsho, N. Sugioka, E. Sasaki, H. Tanaka, T. Takata, W. Chang, S. Matsumoto, G. Wakabayashi, G. Okada, Y. Koba)

ARS-11 (R4P2-11): Development and evaluation of 3D gel dosimeter for the measurement of dose distribution in BNCT. (S. Hayashi, Y. Sakurai, M. Suzuki, T. Takata)

ARS-12 (R4P2-12): Establishment of beam-quality estimation method in BNCT irradiation field using dual phantom technique (VI). (Y. Sakurai, N. Kondo, T. Takata, H. Tanaka, M. Suzuki)

ARS-13 (R4P2-13): Development of real-time boron-concentration estimation method using gamma-ray telescope system for BNCT. (Y. Sakurai, D. Fu, T. Takata, H. Tanaka, M. Suzuki)

ARS-14 (R4P2-14): Development of scintillator for thermal neutron detector in BNCT. (N. Matsubayashi, H. Tanaka, S. Kurosawa, A. Yamaji, T. Hanada, T. Takata)

ARS-15 (R4P2-15): Quantitative measurement of 478 keV prompt gamma-rays of boron-neutron capture reaction. (S. Komura, T. Mizumoto, Y. Sakurai, T. Takata, T. Tanimori, H. Kimura, A. Takada)

ARS-16 (R4P2-16): Visualization of boron dose distribution on a borosilicate glass plate by neutron irradiation. (A. Nohtomi, Y. Kojima, H. Maeda, T. Yamane, G. Wakabayashi, Y. Sakurai, T. Takata)

ARS-18 (R4P2-18): Investigation of thermal neutron-induced soft errors in semiconductor devices. (H. Tanaka, R. Nakamura, T. Kato)

ARS-19 (R4P2-19): Dosimetric characteristics of optimized bolus for boron neutron capture therapy. (T. Takata, M. Nojiri, A. Sasaki, Y. Sakurai, H. Tanaka, M. Suzuki)

ARS-23 (R4P2-23): Three dimensional humanized oral cancer in vitro model for BNCT. (K. Igawa, K. Izumi, E. Naito, M. Suzuki, N. Kondo, Y. Sakurai)

ARS-24 (R4P2-24): Boron-10 uptake distribution in 3D oral cancer model using CR-39 solid state nuclear track detector. (K. Igawa, R. Ogawara, T. Kusumoto, Y. Sakurai)

ARS-6, ARS-10, ARS-17, ARS-20, ARS-21 and ARS-22 could not be performed mainly because of the influence of COVID-19 infection.

PR2-1 Establishment of characterization estimation method in BNCT irradiation field using Bonner sphere and ionization chamber (VI)

Y. Sakurai, A. Sasaki[1], N. Matsubayashi[1], M. Nojiri[1], D. Fu[1], T. Takata and H. Tanaka

Institute for Integrated Radiation and Nuclear Science, Kyoto University
[1]Graduate School of Engineering, Kyoto University

INTRODUCTION: Development in accelerator-based irradiation systems for BNCT is underway. In the near future, BNCT using these newly developed systems may be carried out at multiple facilities across the world. Considering this situation, it is important that the estimations for dose quantity and quality are performed consistently among several irradiation fields, and that the equivalency of BNCT is guaranteed, within and across BNCT systems. Then, we are establishing QA/QC system for BNCT.

As part of the QA/QC system, we are developing estimation method for neutron energy spectrum using Bonner sphere [1]. For our spectrometer using Bonner sphere, liquid such as pure water and/or boric acid solution is used as the moderator. A multi-layer concentric-sphere case with several sphere shells is prepared. The moderator and its diameter are changeable without entering the irradiation room, by the remote supply and drainage of liquid moderator in the several layers. For the detector, activation foils are remotely changed, or online measurement is performed using SOF detector, etc.

In 2022, verification experiments for the prototype Remote-changeable Bonner-sphere Spectrometer (RBS) were performed using Heavy Water Neutron Irradiation Facility installed in Kyoto University Reactor (KUR-HWNIF) as in the previous year [2].

MATERIALS AND METHODS: In the neutron energy spectrometry by Bonner-sphere, the combinations of the moderator material and diameter should be previously decided and prepared. Of course, the more information can be obtained as the more moderators and detectors are prepared. However, the information number from those measured data is less than the combination number, because of the overlapped regions among the combinations. The selection is important, in which the more information number is obtained for the combination number.

The combination of moderator and detector is decided, for that the response functions cannot be approximated by the linear functions of the other response functions. The accuracy and precision for the spectrometry can be higher, because the independent information can be obtained from the measurement by the respective combinations. We were developed the selection method, High Independence Selection (HIS) [3].

On the assumption of the application in the standard epi-thermal neutron irradiation mode of KUR-HWNIF, the combination of the moderators for boron-10 concentration and diameter was optimized by HIS. Based on this optimization, the prototype RBS was revised. Some experiments were performed for the characteristic verification of the revised prototype RBS at KUR-HWNIF.

RESULTS: The configuration of the revised RBS was decided as follows. A five-layer concentric spherical acrylic shell is used as a container. Each acrylic wall is 1 mm in thickness. The moderator injection part is 9 mm in thickness for each layer. Pure water and 0.12-wt% boric acid water for boron-10 were used as liquid moderators. A LiCaF scintillation detector was used as the detector. Figure 1 shows the outline of the revised prototype RBS.

Unfolding was performed by GRAVEL using the response function of each Bonner sphere corrected by multiplying the ratio for measured/calculated values. The nominal spectrum of the epi-thermal neutron irradiation mode was input as an initial guess.

The comparison between the nominal spectrum and unfolded spectrum was performed. The spectrum obtained by the unfolding reproduced the nominal spectrum relatively and absolutely well. It was confirmed that the accuracy of the revised prototype RBS was more improved than the previous version.

CONCLUSION: We have the plans to perform (1) the further revision of the prototype RBS and (2) the preparation of a Bonner sphere spectrometer including the remote mechanism for the supply and drainage of the liquid moderators.

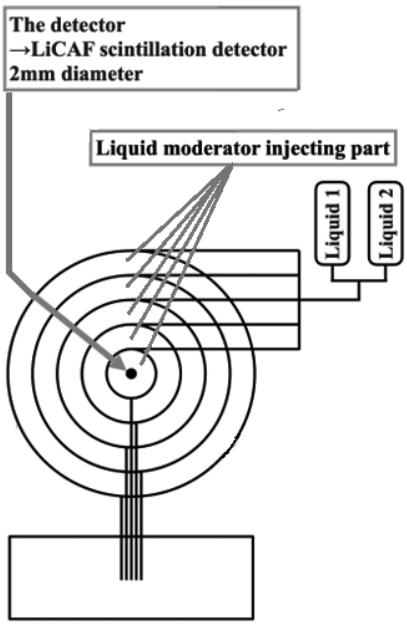

Fig. 1. Outline of the revised prototype of RBS.

REFERENCES:

[1] S. Shiraishi *et al.,* Appl. Radiat. Isot., **163** (2020) 109213.
[2] Y. Sakurai and T. Kobayashi, Nucl. Instr. Meth. A, **453** (2000) 569-596.
[3] H. Ueda, Doctoral Thesis, Kyoto Univ., (2016).

PR2-2 Study on neutron energy spectrometry for epi-thermal neutrons

S. Yoshihashi, A. Yamazaki, K. Watababe[1], Y. Oshima[1], A. Uritani and Y. Sakurai[2]
Graduate School of Engineering, Nagoya University
[1]Graduate School of Engineering, Kyushu University
[2] Institute for Integrated Radiation and Nuclear Science, Kyoto University

INTRODUCTION: Boron neutron capture therapy (BNCT) is one of the radiotherapies. This is a combined modality of radiotherapy and chemotherapy for cancer treatment. In the BNCT, a boron-containing agent, which is concentrated into tumor cells, are irradiated with thermal neutrons and $^{10}B(n,\alpha)$ reactions are induced. The BNCT is radiotherapy using neutrons. Recently, an accelerator-driven neutron source has actively been developed instead of nuclear reactors, owing to its simplicity of management. The energy spectrum of neutrons, which is irradiated to patients, should be evaluated in order to assure safety of patients.

The conventional technique for neutron spectrometry is the Bonner sphere method. The similar concept is the liquid moderator type neutron spectrometer, in which a small neutron detector can be moved and various neutron responses can be acquired. In this study, we are developing a new neutron detector using an optical fiber. So far, in order to realize the optical fiber type neutron detector showing a neutron peak in the pulse height spectrum, bright neutron scintillators, such as Eu:$LiCaAlF_6$ or LiF/Eu:CaF_2 eutectics, have been used [1]. Recently, we attempted to replace them with the faster Li glass scintillator[2]. For the both cases, we have never controlled a shape of scintillators because the scintillator size have been too small. Since they had random shapes, the Monte-Carlo simulation based study was difficult to be conducted. In order to evaluate the accurate detector response, the scintillator shape is required to be controlled.

We proposed that a transparent composite Li glass scintillator, in which fine Li glass scintillator powder and resin are mixed. This type of scintillator is expected to be easily shaped because it is a resin-based material. In this study, we fabricate the optical fiber type neutron detector using the transparent composite Li glass scintillator and evaluate its response to thermal neutron irradiation.

EXPERIMENTS: We fabricated the optical fiber type neutron detector using the transparent composite Li glass scintillator. First, fine powder of the Li glass and UV curable resin were mixed. The mixed resin was attached on a tip of an optical fiber. The resin was spontaneously shaped to a hemispherical shape by surface tension. And then, the mixed resin was irradiated with UV light to solidify it. Figure 1 shows a photograph of the fabricated the optical fiber type detector using the transparent composite Li glass scintillator. The detector was irradiated with thermal neutron beam at E-3 beam port of Kyoto University Reactor.

RESULTS: Figure 2 shows the signal pulse height spectra obtained when the fabricated optical fiber type neutron detector was irradiated with thermal neutron beam at E-3 beam port. The fabricated optical fiber type neutron detector shows a clear neutron peak in the signal pulse height spectrum. The detector can be expected to be used for the neutron energy spectrometer.

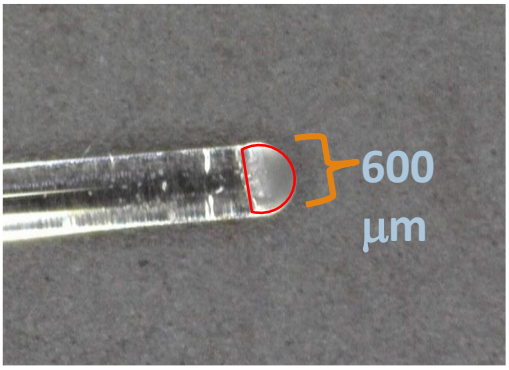

Fig. 1. Photograph of the fabricated optical fiber type neutron detector using the transparent composite Li glass scintillator.

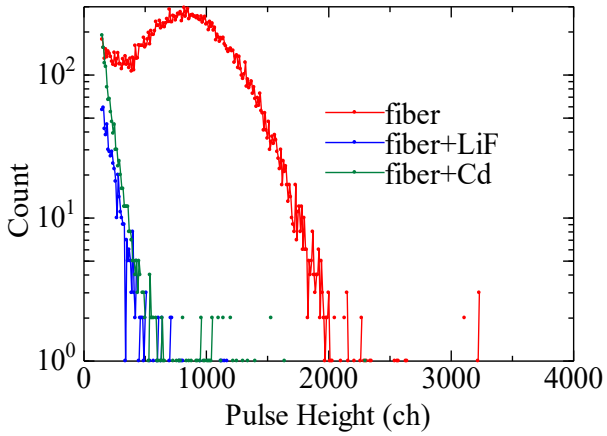

Fig. 2. Signal pulse height spectra obtained from the fabricated optical fiber type neutron detector.

REFERENCES:

[1] K. Watanabe *et al.*, Nucl. Instrum. Methods. Phys. Res. A , **802** (2015) 1-4.
[2] A. Ishikawa *et al.*, Sensors and Materials, **32** (2020) 1489-1495.

PR2-3 Development of Bonner Sphere Spectrometer using Small Lithium-Glass Scintillator for Intense Neutron Beams

A. Masuda, T. Matsumoto, S. Manabe, K. Watanabe[1], A. Ishikawa[2], H. Tanaka[3], Y. Sakurai[3], H. Harano, T. Takata[3] and A. Uritani[2]

National Metrology Institute of Japan, National Institute of Advanced Industrial Science and Technology
[1]Graduate School of Engineering, Kyushu University
[2]Graduate School of Engineering, Nagoya University
[3]Institute for Integrated Radiation and Nuclear Science, Kyoto University

INTRODUCTION: Neutron spectral fluence of intense neutron beams for boron neutron capture therapy (BNCT) should be measured to ensure therapeutic efficacy and safety. Bonner unfolding method is the best known and proven method for measuring neutron spectral fluence [1]. In this study, a small lithium-glass scintillator is adopted to Bonner sphere detectors to suppress the sensitivity of these detectors to accommodate the therapeutic-level neutron intensity.

EXPERIMENTS: A small lithium-glass scintillator coupled with an optical fiber [2] and a photomultiplier tube (PMT, Hamamatsu R9880U-21) was placed at the center of the high-density polyethylene moderator sphere using gapless HDPE fillers, to configure the Bonner sphere detector. Electrical outputs of PMT were processed by a preamplifier (Ortec 113) and a signal processing and acquisition system (Amptek PX5). Diameter of the moderators of the Bonner sphere detectors were 3”, 3.5”, 4”, 4.5”, 5”, 6”, 7” and 8”.
Bonner sphere detectors were placed at a fixed position and irradiated by the standard mixed neutron in the heavy water irradiation facility of the KUR [3], as shown in Fig.1.

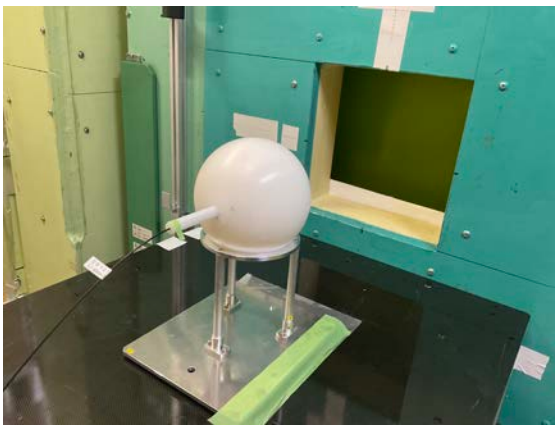

Fig. 1. A Bonner sphere detector equipped with a small lithium-glass placed at the measurement position of the heavy water irradiation facility of the KUR.

RESULTS: Fig. 2 shows output pulse-height spectra from the Bonner sphere detectors with the small lithium -glass scintillator. Pulse signals were properly analyzed and collected by the system, and neutron-induced signals can be discriminated from the photon-induced signals based on the pulse height. Signals above 225 ch were regarded as the neutron induced signals. The background signals which were acquired while neutron beam is off, were negligible. The difference in detection efficiency depending on the sphere diameter was also reasonable. These results show that the developed Bonner sphere detector performed appropriate measurements for intense neutrons.

However, parameters of the signal processing system have not yet been optimized. The effect of the optimization on measurement accuracy is significant, especially in high counting rate measurements. In the future, after optimizing the parameters of the signal processing, spectrum evaluation will be performed by the unfolding method.

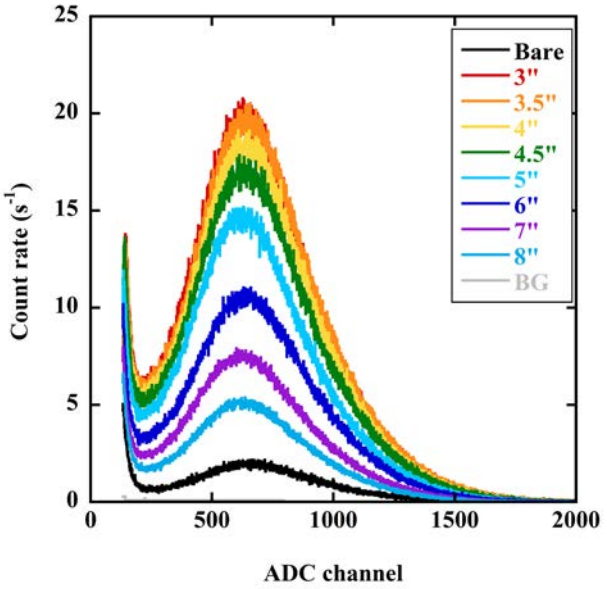

Fig. 2. Pulse-height spectra of the Bonner sphere detector acquired by the signal processing and acquisition system.

REFERENCES:

[1] A. Masuda *et al.,* Appl. Radiat. Isot., **127** (2017) 47-51.
[2] A. Ishikawa *et al.,* Sensors and Materials, **32** (2020) 1489-1495.
[3] Y. Sakurai and T. Kobayashi, Nucl. Instrum. Methods Phys. Res. A, **453** (2000) 569-596.

This study is supported by Grant-in-Aid for Scientific Research, Japan Society for the Promotion of Science (JSPS KAKENHI Grant Number JP22K12667).

PR2-4 Improvement of the SOF detector system for energy-dependent discrimination and long-term stability

M. Ishikawa[1,2], Shu Ishiguri[2], K. Takamiya[3] and Y. Sakurai[3]

[1]*Faculty of Health Sciences, Hokkaido University*
[2]*Graduate School of Biomedical Science and Engineering, Hokkaido University*
[3]*Institute for Integrated Radiation and Nuclear Science, Kyoto University*

INTRODUCTION: We have been conducting research on SOF detectors as thermal neutron flux monitors in BNCT for many years. [1,2] However, degradation of the SOF detector due to long-term irradiation has been reported.[3] As anti-degradation methods, we have replaced plastic optical fibers, which cause degradation, with quartz fibers, and developed degradation monitors using UV photons. In addition, since epithermal neutron irradiation has become mainstream in recent years, it is desirable to be able to measure the epithermal neutron flux.

EXPERIMENTS: In last year's experiment, the measurement was performed with thermal neutron flux of 1×10^{11}[n/cm^2/s] (~30 cm above from the bottom of the slant hole), but this year, measurement was performed with 1×10^{12}[n/cm^2/s] (bottom of the slant hole), one order of magnitude higher neutron intensity. Figure 1 shows the deterioration monitoring system using pulsed UV-LED. In addition to the 1-second interval measurement by the SOF detector, the scintillation light excited by the UV-LED was measured once every 10 seconds to assess the deterioration of the SOF probe. Figure 2 shows the signal count rate of the SOF detector during irradiation. From the Fig. 2, the SOF detector signal attenuated by about 84% during 5 hours of irradiation. The signal attenuation was well represented by a two-component exponential function. The signal from the UV-LED for monitoring showed a constant value and degradation could not be monitored. This is assumed to be because impurities and other contaminants adhered to the connector surface and the excited photons by the UV light were detected as a signal. As a future improvement, visible light which can induce scintillator emission, should be used instead of ultraviolet light.
On the other hand, we tried to establish energy-dependent SOF detector by using different neutron sensitizers, but no effective signal could be obtained. Instead of using different sensitizers, we tried estimating neutron energy spectrum from the measured thermal neutron flux distribution. Figure 3 shows the experimental geometry, a linear actuator was set on a 20 x 20 x 20 cm^3 PMMA phantom filled with water, and thermal neutron flux measurements were performed with SOF detectors at 5 mm-interval in the range of 0.5 to 14.5 cm from the phantom surface. Figure 4 shows that the energy spectrum estimated by unfolding using MLEM. From Fig. 4, good agreement was observed for neutron energies above 1 eV, but a rather large discrepancy in the thermal neutron region. For future work, we would like to improve the MLEM algorithm to increase accuracy in the thermal neutron region.

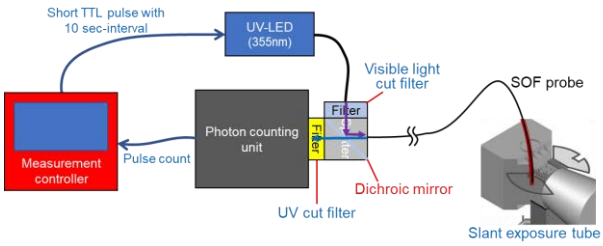

Fig. 1. Schematic illustration of deterioration monitor using pulsed UV-LED.

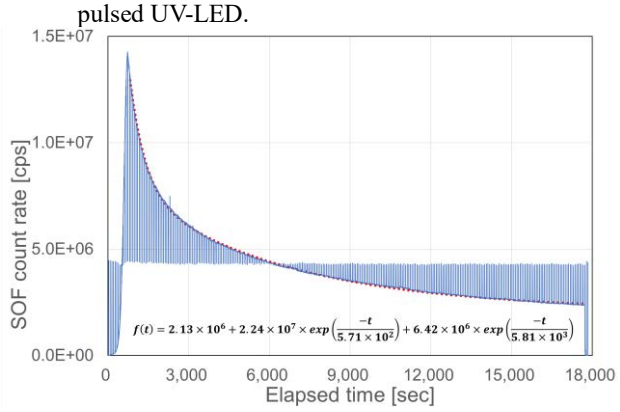

Fig. 2. SOF detector measurement with UV-LED signals.

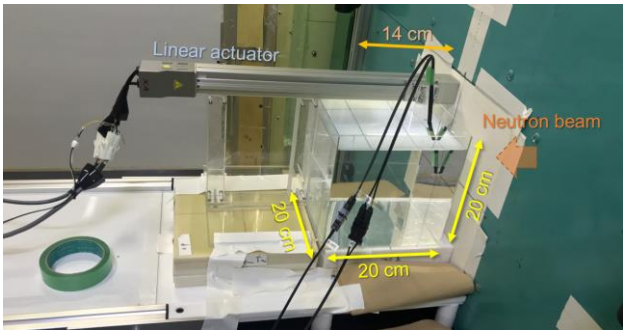

Fig. 3. Measurement geometry for neutron energy spectrum estimation using MLEM unfolding method.

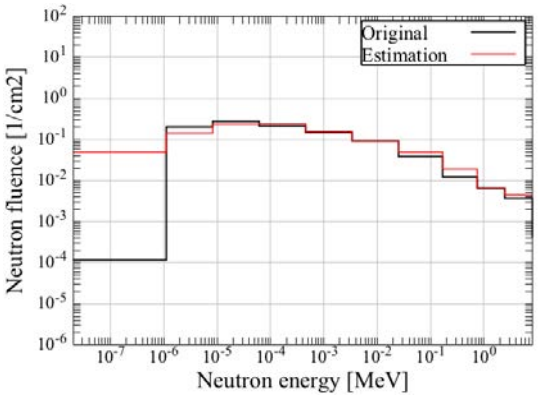

Fig. 4. Estimated neutron energy spectrum by SOF detector.

REFERENCES:

[1] M. Ishikawa *et al.*, Appl. Radiat. Isot., **61** (2004) 775-779.
[2] M. Ishikawa *et al.*, Nucl. Instr. Meth. A, **551** (2005) 448-457.
[3] M. Komeda *et al.*, Appl. Radiat. Isot., **67** (2009) 254-257.

PR2-5 Improvement of Absolute Fast Neutron Flux Intensity Monitor for BNCT

I. Murata, K. Sagara, R. Kawahata, S. Tamaki, S. Kusaka, H. Tanaka[1], Y. Sakurai[1], T. Takada[1]

Graduate School of Engineering, Osaka University
[1]Institute for Integrated Radiation and Nuclear Science, Kyoto University

INTRODUCTION: BNCT is a promising cancer therapy which kills tumor cells while suppressing exposure dose to normal tissues. Normally, the neutron field of BNCT has an energy distribution spreading within thermal and fast regions in addition to epi-thermal region. Because fast neutrons are harmful to the human body, we must measure the fast neutron flux intensity to evaluate the exposure dose of the patient accurately. However, it is quite difficult to know the intensity directly and accurately because there is no suitable neutron spectrometer or no activation material covering epi-thermal or fast neutrons separately. We are therefore developing new monitors to precisely measure the absolute integral flux intensities of fast neutrons (10 keV ~ 1 MeV). [1] In the previous research using the developed detectors to measure the fast neutron flux intensity, the experimental value was underestimated by about 87 % compared to the calculated value. [2] This is because the sensitivity of the previous monitor below 10 keV is not perfectly zero, and the epi-thermal neutron contribution in the neutron spectrum in KUR, Kyoto University, is so large. Therefore, the objective of this study is to modify the monitor to improve its sensitivity and validate it experimentally.

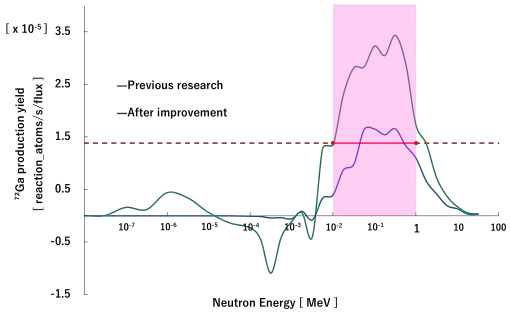

Fig. 1. Comparison of sensitivity between previous monitor and modified monitor.

EXPERIMENTS: According to the previous study, to extract the fast neutron flux intensity, two detectors are used. One of them has a small block-like B_4C in a cubic PE and a GaN foil covered with a Cd sheet at the center of the cubic PE (B_4C type). The other one consists of a cubic PE surrounded by a B_4C sheet and a GaN foil covered with a Cd sheet placed at the center of the cubic PE (PE type). In addition to the above, we designed the detectors by using a ^{10}B neutron shield to suppress the monitor's sensitivity below 10 keV. The modified monitor can estimate the absolute fast neutron flux intensity by making difference of the two ^{72}Ga activities created via $^{71}Ga(n, \gamma)^{72}Ga$ reaction. Fig. 1 shows the comparison of sensitivities between the previous monitor and modified monitor. In this study, the performance of the fast neutron monitor was verified experimentally at KUR. Epi-thermal neutron irradiations were carried out for 50 min in 1 MW operation for each detector.

RESULTS: From Fig. 1, the monitor's sensitivity below 10keV is successfully improved (suppressed to be ~0) by the revision using a ^{10}B neutron shield. The improved monitor was tested at KUR. The activities of ^{72}Ga in the monitors were measured just after their irradiations using an HP-Ge detector. The absolute fast neutron flux was deduced from the obtained activities with the improved sensitivity shown in Fig. 1. The results are summarized in Table 1. In the table, the nominal value means the value formally evaluated at KUR.

Table 1. Absolute fast neutron flux intensity obtained by the improved monitor.

	Experimental value (E)	Nominal value (C)	C/E
^{72}Ga activity*1 [Bq]	$(1.44\pm0.03)\times10^2$	—	—
^{72}Ga activity*2 [Bq]	$(1.48\pm0.04)\times10^2$	—	—
ϕ_{fast} [n/cm^2/sec]	3.52×10^7	1.08×10^7	0.31

*1 For the PE type detector.
*2 For the B_4C type detector.
*3 The estimated error is about 38 %

From Table 1, the experimental value is larger than the nominal value by the C/E value of 0.31, while in the previous result the C/E value was 7.8. This means, the result was surely improved, however, it is still largely different from the nominal value. Consequently, though the monitor was modified, the monitor was confirmed not to be able to measure the fast neutron flux intensity properly. This is due to incoming scattered neutrons during irradiation, i.e., neutrons are scattered on the wall of the irradiation window and enter the detectors from outside of the collimator. Scattered neutrons cause an error of activity of the GaN foil and it leads to a large error between the experimental and nominal values. Now we are making further revisions of the design to shield scattered neutrons.

REFERENCES:

[1] K. Aoki, Master Thesis, Osaka Univ. (2021).
[2] S. Tada, Bachelor Thesis, Osaka Univ. (2022).

PR2-6 Neutron Image Sensor for Boron Neutron Capture Therapy

M. Taniguchi[1], T. Meguro[1], H. Tanaka[2], and S.-I. Kuroki[1]

[1]Research Institute for Nanodevice, Hiroshima University
[2] Institute for Integrated Radiation and Nuclear Science, Kyoto University Graduate School of Science, Kyoto University

INTRODUCTION: Boron neutron capture therapy (BNCT) has been attracting attention as an advanced treatment method on cancer, because of its merits with a minimally invasive and selective treatment. In the BNCT, for making therapy more accurate one, it is better to measure the neutron beam profile in real time. On the other hand, silicon carbide (SiC) semiconductor has a strong radiation hardness, and then is expected as base semiconductor for radiation hardened devices. The purpose of this study is to develop a two-dimensional neutron image sensor with SiC devices.

EXPERIMENTS: The structure of our neutron sensor is based on a three-transistor type image sensor pixel. The neutron sensor is based on an image sensor pixel using SiC, which has been developed in our laboratory, focusing on stable operation under neutron irradiation for a long time. The neutron sensors are equipped with boron-10 layer as a neutron conversion layer. In this layer, the injected neutrons have a reaction with boron-10, and then, alpha and lithium particles are emitted. The alpha particles penetrate the device, and generate electron-hole pairs, electrons are collected at gate electrode of SF(source-follower) transistor, and then the induced charge is detected as the output voltage from the sensor.

The neutron radiation experiments were carried out in KUR Heavy Water Neutron lrradiation Facility.

RESULTS: The neutron exposure experiment were carried out with neutron flux of $5x10^9$ $cm^{-2}s^{-1}$. The neutron sensor was biased with VDD=10 V, RST gate voltage of 0-10 V with pulse form. By the neutron beam exposure, the differential output voltage became 50 mV. The value was difference between output voltage with and without neutron beam. As the results, we can detect the neutron with this device. As the further study, we need to optimize the structure of the devices.

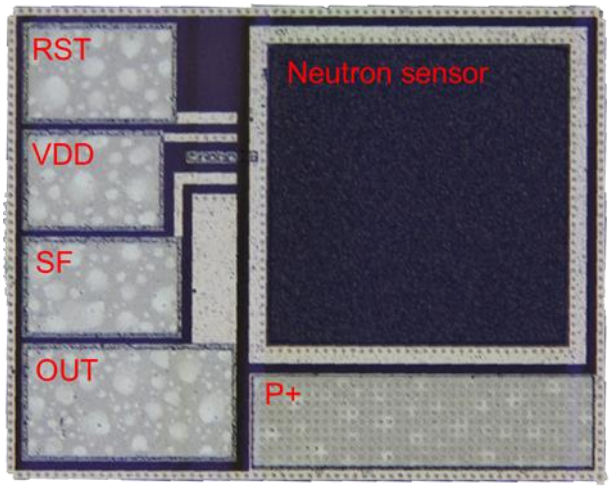

Fig. 1. SiC Neutron Sensor: This sensor consists of neutron sensor and three transistors.

REFERENCES:

[1] M. Tsutsumi *et al.,* IEEE Electron Device Lett., **44 (1)** (2023) 100-103.
[2] T. Meguro *et al.,* IEEE Electron Device Lett., **43 (10)** (2022) 1713-1716.

PR2-7 Preliminary survey of nuclide for epithermal neutron measurement using gel detector

Kenichi Tanaka, Yoshinori Sakurai[1], Tsuyoshi Kajimoto[2], Hiroki Tanaka[1], Takushi Takata[1], Satoru Endo[2]

Division of Liberal Arts Sciences, Kyoto Pharmaceutical University
[1]Institute for Integrated Radiation and Nuclear Science, Kyoto University
[2]Graduate School of Advanced Science and Engineering, Hiroshima University

INTRODUCTION: For boron neutron capture therapy, measurement of beam fluence spatial distribution is required for quality assurance in the irradiation field. This study investigated the use of the multi polymer gel detector system which consists of gels including different beam component converters. The preliminary selection of converter nuclide for epithermal neutrons is reported.

EXPERIMENTS: As an initial candidate, the $^{33}S(n,\alpha)^{30}Si$ reaction was considered based on the work of Porras [1] which showed a dose increase from the epithermal neutron component. As a method, the cross section library JENDL-4.0 was surveyed for the reactions with high cross section for epithermal neutrons [2]. Of particular interest were reactions that produced charged particles such as (n,p), (n,α), and (n,t) which result in charged particles depositing energy in the polymer gel detector. The data in Fig. 1 is an example of the cross section used in this study.

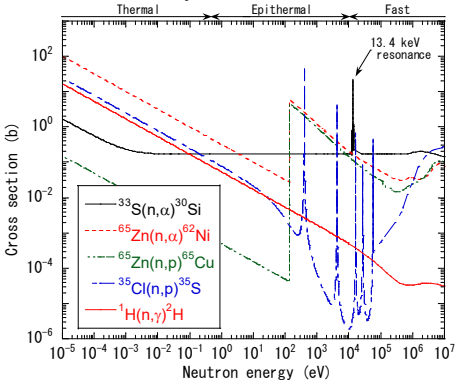

Fig. 1 Cross section used in this study.

RESULTS: The maximum of the cross section at each energy region of thermal (-0.5eV), epithermal (0.5eV-10keV), and fast (10keV-) is shown in Fig. 2, from the survey of nuclear reactions. The ratios of the cross section at the epithermal region in Fig. 2 to those at other regions are shown in Fig. 3. The reactions $^{65}Zn(n,\alpha)^{62}Ni$, $^{65}Zn(n,p)^{65}Cu$, and $^{35}Cl(n,p)^{35}S$ were selected as the candidates to enhance the epithermal neutron sensitivity of the gel detector. This is because their epithermal neutron cross sections in Fig. 2 and cross section ratios in Fig. 3 were comparable to those of $^{33}S(n,\alpha)^{30}Si$.

The nuclide ^{65}Zn with a half life of 244 days does not exist in nature, among the candidates selected. It should be produced by the neutron induction to ^{64}Zn (natural abundance: 49%). However, the reactions $^{65}Zn(n,\alpha)^{62}Ni$ and $^{65}Zn(n,p)^{65}Cu$ have a wide peak over 100 eV and low cross section at thermal and fast regions from Fig. 1, and they are expected to efficiently enhance the influence of epithermal neutrons than other candidate nuclides. Therefore, we decided to investigate ^{65}Zn as a promising option as well as ^{33}S and ^{35}Cl, apart from the convenience in practical use.

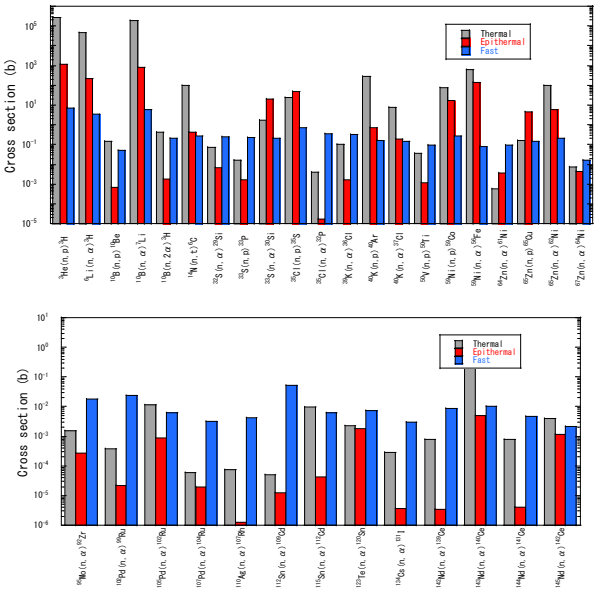

Fig. 2 Maximum cross section in energy range

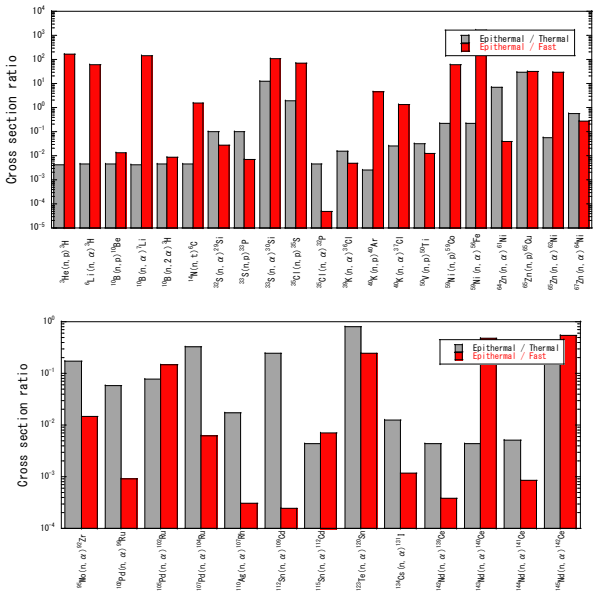

Fig. 3 Ratio of maximum cross section in epithermal region to that in other regions

REFERENCES:

[1] I.Porras *et al.* Appl. Rad. Isot. **69** (2011)1838-1841.
[2] K.Shibata *et al.* J. Nucl. Sci. Tech. 48 (2011)1-30.

PR2-8 Development and evaluation of 3D gel dosimeter for the measurement of dose distribution in BNCT

S. Hayashi, Y. Sakurai[1], M. Suzuki[1], and T. Takata[1]

Department of Clinical Radiology, Hiroshima International University
[1] Institute for Integrated Radiation and Nuclear Science, Kyoto University

INTRODUCTION: Three-dimensional (3D) gel dosimeters have been developed for the 3D dose measurement of complex dose distributions in clinical applications [1]. These devices utilize radiation-induced chemical reactions in the gel to preserve information about the radiation dose. The 3D absorbed dose distribution is deduced from the distribution of the reactant measured by imaging modalities, such as MRI (magnetic resonance imaging), X-ray CT (computed tomography), and optical CT. These gel dosimeters have excellent dose properties such as high sensitivity, dose rate independence, and a wide dose range, on X- and gamma-rays, and the potential as a 3D dosimeter has been expected.

In recent years, we have been studying the application of radiochromic gel dosimeters to dose evaluation in neutron irradiation. The optical dose-response of the PVA-I (PVA-GTA-I) radiochromic gel dosimeter [2, 3], which utilizes radiation-induced oxidation of iodide and its complex formation with polyvinyl alcohol (PVA), has been applied to neutron irradiation. The dose-response to beams with different energy spectra from a nuclear reactor has been studied and their availability has been investigated. Addition of a hydrated electron scavenger as a sensitizer showed significant dose-response improvement, while addition of boric acid as a neutron sensitizer significantly inhibited the fructose-induced initialization reaction.

Therefore, this year, we again optimized the composition, especially varying the concentration of fructose as a reducing agent and investigated its effect on the dose response.

EXPERIMENTS: The standard PVA-GTA-I gel dosimeter is composed of partially saponified PVA, potassium iodide (KI), glutaraldehyde (GTA), fructose, glucono-δ-lactone (GDL), and water, where fructose is a reducing agent and GDL is acid catalysis to promote the cross-linking, respectively. As sensitizers, boric acid $B(OH)_3$ containing ^{10}B of 20% naturally and potassium nitrate (KNO_3) as an electron scavenger were added into the gel dosimeter. A concentration of fructose was optimized to stabilize the dose-response property. The resulting solution was subdivided by pouring into PMMA cuvettes (4.5 mL, 1 cm path length). The neutron irradiations were performed using the Heavy Water Neutron Irradiation Facility (HWNIF) of Kyoto University Research Reactor (KUR, power of 1 MW). The samples were irradiated in the air at room temperature. The three different modes (thermal neutron-rich, epi-thermal and fast neutron-rich, and the mixed modes) of neutron beams made by heavy water spectrum shifter and cadmium thermal-neutron filters were applied to the samples.

RESULTS: Previously, it was feared that excess fructose would cause dosimeter fading. However, when we examined the dose-response at increasing fructose concentrations (0.1 M - 1.0 M), no significant fading was observed. In addition, the effect of suppressing autoxidation, which leads to an increase in the background, was also confirmed. It has been found that the rate of initialization can also be increased. On the other hand, excess fructose was also observed to inhibit responses at low doses. From the results of this work, it was found that the addition of about 0.3 M fructose is more effective. In the future, we plan to verify the effects of neutron sensitizer and other various sensitizers on the obtained new compositions.

REFERENCES:

[1] M. Marrale and F. d'Errico, Gels, **7** (2021) 74.
[2] S. Hayashi *et al.,* Radiat. Meas., **131** (2020) 106226.
[3] S. Hayashi *et al.,* J.Phys.; Conf. Ser., **2167** (2022) 012014.

PR2-9 Establishment of beam-quality estimation method in BNCT irradiation field using dual phantom technique (VI)

Y. Sakurai, N. Kondo, T. Takata, H. Tanaka and M. Suzuki

Institute for Integrated Radiation and Nuclear Science, Kyoto University

INTRODUCTION: Development in several types of accelerator-based irradiation systems for boron neutron capture therapy (BNCT) is underway. Many of these systems are nearing or have started clinical trials. Before the start of treatment with BNCT, the relative biological effectiveness (RBE) for the fast neutrons (over 10 keV) incident to the irradiation field must be estimated.

Measurements of RBE are typically performed by biological experiments with a phantom. Although the dose deposition due to secondary gamma rays is dominant, the relative contributions of thermal neutrons and fast neutrons are virtually equivalent under typical irradiation conditions in a water and/or acrylic phantom. Uniform contributions to the dose deposited from thermal and fast neutrons are based in part on relatively inaccurate dose information for fast neutrons.

The aim of this study is the establishment of accurate beam-quality estimation method mainly for fast neutrons by using two phantoms made of different materials, in which the dose components can be separated according to differences in the interaction cross-sections. The fundamental study of a "dual phantom technique" for measuring the fast neutron component of dose is reported [1].

In 2022, verification experiments for the dual phantom technique were performed using Heavy Water Neutron Irradiation Facility installed in Kyoto University Reactor (KUR-HWNIF) as in the previous year. Biological experiments were performed using the solid phantoms, which were made based on the simulation results [2].

MATERIALS AND METHODS: One of the dual solid phantoms was made of polyethylene with natural lithium fluoride for 30 weight percent (LiF-polyethylene phantom), and the other phantom was made of polyethylene with 95%-enriched lithium-6 fluoride for 30 weight percent (^{6}LiF-polyethylene phantom).

Glioblastoma U87MG ΔEGFR cells were cultured in Dulbecco Modified Eagle medium (DMEM) with 10 % fetal bovine serum in 5 % CO_2 incubator at 37 ℃. The cells were divided in two groups. One was p-boronophenylalanine (BPA, consisting of ^{10}B) treated group, and the other was non-treated group. The treatment group was cultured with 25 ppm BPA containing medium overnight.

The neutron flux and gamma-ray dose rate were measured using activation foils and thermo-luminescent dosimeter, respectively. The depth dose distributions for the thermal neutron, fast neutron and gamma-ray components were determined based on the simulation calculation results normalized referring to the measured values.

The epi-thermal neutron irradiation mode was used for the phantom experiments.

RESULTS: Figure 1 shows the cell survival fraction for the BPA administration group, BPA(+), and the non-administration group, BPA(-), in the LiF-polyethylene phantom. The items on the horizontal axis are arranged in ascending order of thermal neutron flux, such as "Control", "8-cm depth", "5-cm depth" and "2-cm depth". The values are normalized to be 1 with "Control" cells. "BPA(+)" corresponds to BPA-treated cell and "BPA(-)" corresponds to non-treated cell. The survival fraction became smaller as the thermal neutron flux became larger. The survival fraction for the non-treated cell was higher than that in BPA-treated cell.

Figure 2 shows the cell survival fraction in the ^{6}LiF-polyethylene phantom. The survival fraction showed no difference between non-treated and BPA-treated cells.

CONCLUSION: The ^{6}LiF-polyethylene phantom absorbs thermal neutrons although it has not significant effect in fast neutron dose. No difference in survival fractions between non-treated and BPA-treated cells with ^{6}LiF-polyethylene phantom indicated fast neutrons might not effect cell survival. On the other hand, due to mixture of thermal neutron in LiF-polyethylene phantom, BPA-treated cells were killed effectively compared with non-treated cells through n-alpha reactions.

ACKNOWLEDGMENT: This work was supported by JSPS KAKENHI Grant Number JP 16H05237.

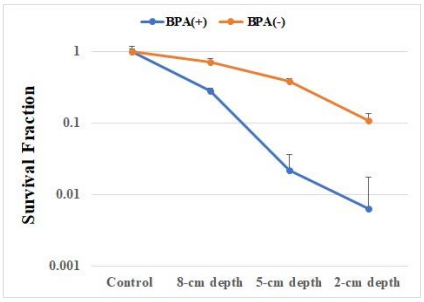

Fig. 1. Cell survival fraction in the LiF-polyethylene phantom.

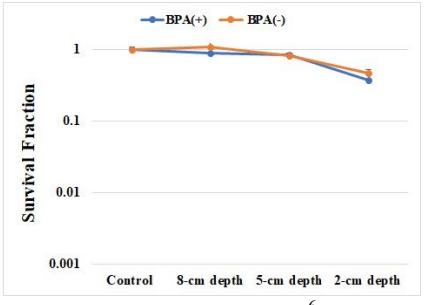

Fig. 2. Cell survival fraction in the ^{6}LiF-polyethylene phantom.

REFERENCES:

[1] Y. Sakurai *et al*., Med. Phys. **42** (2015) 6651-6657.

[2] Y. Sakurai and T. Kobayashi, Nucl. Instr. Meth. A, **453** (2000) 569-596.

PR2-10 Development of real-time boron-concentration estimation method using gamma-ray telescope system for BNCT

Y. Sakurai, D. Fu[1], T. Takata, H. Tanaka and M. Suzuki

Institute for Integrated Radiation and Nuclear Science, Kyoto University
[1]Graduate School of Engineering, Kyoto University

INTRODUCTION: It is important to decide the boron concentrations for tumor and normal parts in the dose estimation for BNCT. The on-line and real-time estimation method for the spatial distribution of boron concentration is expected for the advancement in dose estimation. The information about the boron concentration distribution can be obtained using the prompt gamma-ray analysis (PGA) for the 478-keV prompt gamma rays generated due to the nuclear reaction of boron-10 (B-10) with thermal neutrons.

The improved gamma-ray telescope system is settled at Heavy Water Neutron Irradiation Facility (HWNIF) of Kyoto University Reactor (KUR) [1-3]. This system is composed of an HPGe semiconductor detector and a collimation system including two lead collimators. The gamma rays through the two collimators can be detected, and the view-filed of the telescope can be expanded or reduced by moving the two collimators independently.

The experimental verification for the improved telescope system was performed. The experimental data was compared with the simulated data to calculate the specification coefficient.

MATERIALS AND METHODS: The phantom experiment was conducted in the irradiation room in KUR-HWNIF. The size of the phantom was 20 cm × 20 cm × 20cm. Within the phantom, a 5-cm diameter acrylic hollow sphere was placed as the tumor. Both the phantoms and tumor spheres were filled with different concentrations of boric acid water. The tumor spheres with the B-10 concentration of 70, 100, and 200 ppm were put into a phantom with B-10 concentration of 20 ppm.

The phantom was irradiated by the epithermal neutron irradiation mode. The irradiation field was set to 12 cm in diameter. Figure 1 shows the phantom and beam collimator placement in the irradiation room. The tumor sphere was fixed at the center of the telescope's view field. The 1st and 2nd telescope collimators were set at the bottom of the telescope (0-0 cm). A total of four irradiation experiments, including background tests, were conducted, each with an irradiation time of 15 minutes.

The specification coefficient is defined as $\tau = C/C`$, where C and C` are the experimental and simulated data, respectively. Regarding this coefficient, it is necessary to compare the counts of 478 keV prompt gamma rays in experiments and simulations with the same parameters. Since the input file of the detector in the simulation is made based on the energy distribution of the beam, and the data obtained from the simulation is flux, therefore the specification coefficients also carry the magnitudes. By comparing them with three B-10 concentrations of tumor spheres, the error in the calculation can be reduced.

RESULTS: From the experimental results, the spectra with different parameters were obtained. Figure 2 shows the spectrum from the experiment performed on a 70 ppm tumor sphere. The characteristic peaks are 478 keV for B-10 prompt gamma-ray, 511 keV for annihilation gamma-ray and 2220 keV for H-1 prompt gamma-ray. In the case of the 70 ppm tumor sphere, the experimental count rate was 29.6 cps (s^{-1}), simulated flux was 8.97×10^{-5} $cm^{-2}\cdot s^{-1}$, and the specification coefficient τ was 3.30×10^{5} $cps/cm^{-2}\cdot s^{-1}$. The average of the specification coefficient was calculated to 3.48×10^{5} $cps/cm^{-2}\cdot s^{-1}$, for the tumor spheres of 70 ppm, 100 ppm and 200 ppm.

CONCLUSION: From the results of the experimental verification, the effectiveness and usefulness of the improved gamma-ray telescope system were confirmed, and the specification coefficient was obtained. The more precise estimation will be performed for the B-10 concentration, size and position of the tumor sphere, and for the position of two telescope collimators. Moreover, the effective range for the discrimination between tumor and normal parts will be clarified.

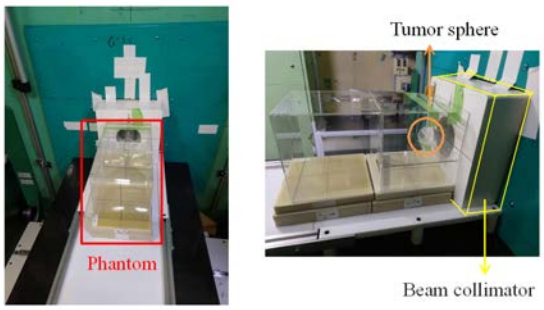

Fig. 1. Experimental setup for the phantom and beam collimator in the irradiation room of KUR-HWNIF.

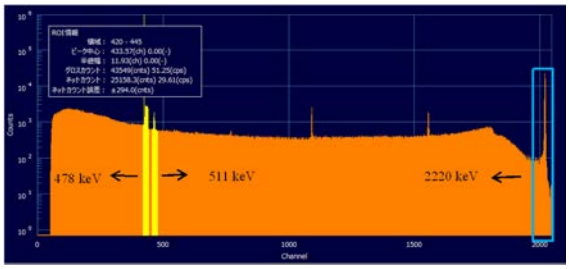

Fig. 2. The obtained spectrum from the experiment performed on a 70 ppm tumor sphere.

REFERENCES:

[1] Y. Sakurai *et al.,* Appl. Radiat. Isot., **61** (2004) 829-833.
[2] Y. Sakurai *et al.,* Appl. Radiat. Isot., **165** (2020) 109256.
[3] Y. Sakurai and T. Kobayashi, Nucl. Instr. Meth. A., **453** (2000) 569-596.

PR2-11 Development of scintillator for thermal neutron detector in BNCT

N. Matsubayashi, H. Tanaka[1], S. Kurosawa[2], A. Yamaji[2], T. Hanada[2], T. Takata[1]

Graduate School of Engineering, Kyoto University
[1] Institution for Integrated Radiation and Nuclear Science, Kyoto University
[2] Institution for Materials Research, Tohoku University

INTRODUCTION: Boron neutron capture therapy (BNCT) is a radiation therapy with thermal neutrons and ^{10}B. The particles emitted by the reaction of ^{10}B (n, α) ^{7}Li have cell dimensions and can selectively destroy tumor cells. In recent years, accelerator-based BNCTs have been constructed near hospitals, and clinical cases are increased. The activation method has been used for measurement of thermal neutron flux, but cannot measure in real-time. The development of neutron monitors capable in BNCT irradiation field is needed. The neutron monitor using Eu:$LiCaAlF_6$ (LiCAF) scintillator with quartz fiber was developed [1]. It is necessary for using the scintillator as neutron monitor to determine the relationship between the counts obtained by the detector and thermal neutron flux. Considering the increase in the clinical cases, we must calibrate the neutron monitor in primary national standard field. However, the neutron intensity of the standard field is much lower than that of the BNCT, and it takes about 5 days to calibrate the monitor available in BNCT. In this study, we develop new scintillator with faster response and higher detection efficiency than the LiCAF scintillator.

EXPERIMENTS: As the neutron detector in BNCT irradiation field, a scintillator with 0.3~0.6 mm long side is mounted on the tip of the fiber to reduce gamma-ray sensitivity. In this study, we selected the eutectic because very small scintillator can be used in BNCT irradiation field. LiBr/$CeBr_3$ and Ce:LiBr/$LaBr_3$ eutectic, which have fast response and high light yield, were grown and mounted on the fiber[2][3]. Since the grown scintillators are hygroscopic, they were packaged using glass and cement to prevent exposure to the outside air. The irradiation tests of each detector were performed in Cyclotron-based epithermal neutron source (C-BENS). The scintillator light entered the fiber and reached a photomultiplier tube (PMT). The signal from the PMT was then processed by a multi-channel analyzer (ANSeeN, ANS-HSMCA4416). To measure sensitivity to gamma-ray, the irradiation tests were carried out with ^{60}Co gamma-ray source.

RESULTS: Fig. 1 and 2 show the pulse height distributions of LiBr/$CeBr_3$ and Ce:LiBr/$LaBr_3$ in C-BENS and ^{60}Co gamma-ray source, respectively. As shown in Fig. 1 and 2, both scintillators have peaks corresponding to neutron event in the high channels. Comparing that of ^{60}Co gamma-ray source, it is confirmed that the eutectics can discriminate neutron and gamma-ray events. Since the neutron event obtained by LiCAF scintillator was observed near 720 Ch, we found that LiBr/$CeBr_3$ and Ce:LiBr/$LaBr_3$ have the same and twice the light yield of LiCAF, selectively. However, the neutron detection efficiencies of these eutectics were lower than that of LiCAF scintillator.

In conclusion, we developed neutron monitor for BNCT using LiBr/$CeBr_3$ and Ce:LiBr/$LaBr_3$ eutectic scintillator. The characteristics of these scintillators were not sufficient compared to conventional scintillator. However, the development of neutron monitors using a eutectic scintillator with hygroscopic has novelty. In the future, we will reselect the materials of scintillators and optimize the size and detection system.

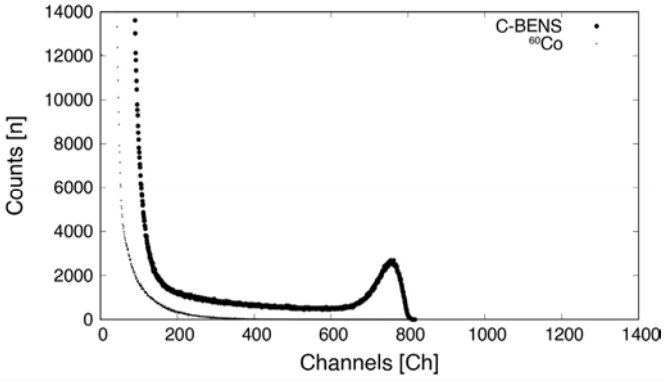

Fig. 1. Pulse height distribution of LiBr/$CeBr_3$ in C-BENS and ^{60}Co gamma-ray source.

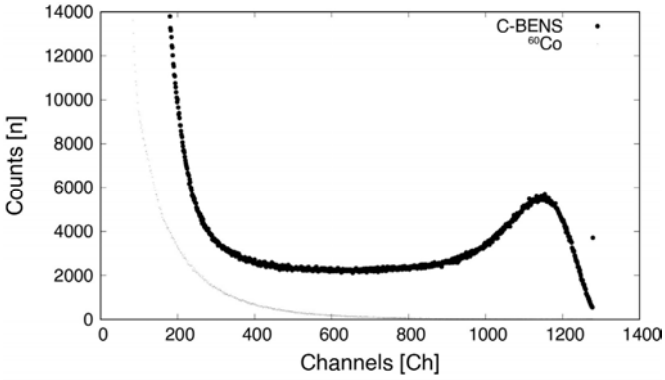

Fig. 2. Pulse height distribution of Ce:LiBr/$LaBr_3$ in C-BENS and ^{60}Co gamma-ray source.

REFERENCES:

[1] H. Tanaka *et al.*, Rev. Sci. Instrum., **88 (5)** (2017) 056101.
[2] R. Yajima *et al.*, Jpn. J. Appl. Phys., **61**, (2022) SC1028.
[3] Y. Takizawa *et al.*, Nucl. Instrum. Methods. Phys. Res A., **1028** (2022) 166384.

PR2-12 Quantitative Measurement of 478 keV Prompt Gamma-rays of Boron-neutron Capture Reaction

S. Komura, T. Mizumoto, Y. Sakurai[1], T. Takata[1], T. Tanimori[1], H. Kimura[2] and A. Takada[3]

J-BEAM Inc.

[1]*Institute for Integrated Radiation and Nuclear Science, Kyoto University*

[2]*Kyoto Pharmaceutical University*

[3]*Graduate School of Science, Kyoto University*

INTRODUCTION: In boron neutron capture therapy (BNCT), there is no method to measure the boron concentration in each tissue in the patient's body, which results in uncertainty in treatment planning. There is also no method to monitor the actual boron dose administered to the patient during neutron irradiation. Imaging of 478 keV prompt gamma rays produced by boron neutron capture reactions has the potential to solve these problems. To achieve quantitative imaging in neutron environments, we have been developing an electron tracking Compton camera (ETCC), which provides strong noise rejection by utilizing the information of the measured electron track. We conducted the following three types of experiments based on previous studies [1].

EXPERIMENTS AND RESULTS:

Exp. 1: We performed a three-dimensional prompt gamma-ray imaging test of a phantom using two ETCCs placed orthogonally to each other, as shown in Fig. 1. The phantom was a 45 mm tall tube with a 4.5 mm diameter, filled with a boric acid solution with a ^{10}B concentration of 1000 ppm. It was placed just above one of the ETCCs and irradiated with thermal neutron beam, with a diameter of approximately 1 cm, for 1.5 hours at E-3 under 1-MW operation. Both ETCCs successfully generated back-projection images of the phantom viewed from two different directions. The bright areas in both images corresponded well with the regions of the phantom that were irradiated by neutrons. Currently, we are conducting an integrated analysis of the data obtained from the two ETCCs to create a 3D image.

Exp. 2: A three-dimensional prompt gamma-ray imaging study of mice was performed in the same way as in Exp. 1. Nude mice, which were carrying U87MG tumors of approximately 1 cm in diameter on their shoulder, received a single dose of 1000 mg/kg BPA via tail vein injection. Each mouse was anesthetized, fixed in an acrylic container, and exposed to thermal neutron beams at the tumor site for 2 hours at E-3 under 5-MW operation. As in Exp. 1, we confirmed that the bright positions in the back-projection images of 478 keV gamma-rays corresponded well to the irradiation position of the mouse tumor . We are currently analyzing the data to create a 3D image.

Exp. 3: To demonstrate the effectiveness of ETCC in a real BNCT environment, we performed image monitoring of phantoms during neutron irradiation at HWNIF, as shown in Fig. 2. The phantom consisted of a 10-cm cubic acrylic container filled with a boric acid solution with a ^{10}B concentration of 230 ppm. The 478 keV prompt gamma rays emitted from the phantom passed through a cylindrical hole in the ceiling and were measured by ETCC. In a previous experiment conducted last year, the phantom was successfully imaged during 1-MW operation. This year, we switched the gas used in the gaseous electron tracker of ETCC from Ar-based gas to Ne-CF4 mixed gas to reduce accidental coincidence noise at high counting rates. At 1-MW operation, we obtained a gamma-ray image with a better signal-to-noise ratio than with conventional gases. However, under 5-MW operation, although ETCC operated stably, the gamma-ray image did not correspond well with the phantom installation position. We are currently analyzing the causes.

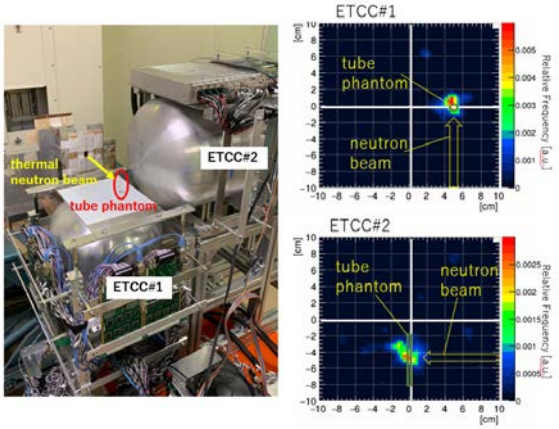

Fig.1. Photograph and measured 478 keV gamma-ray images in Exp.1.

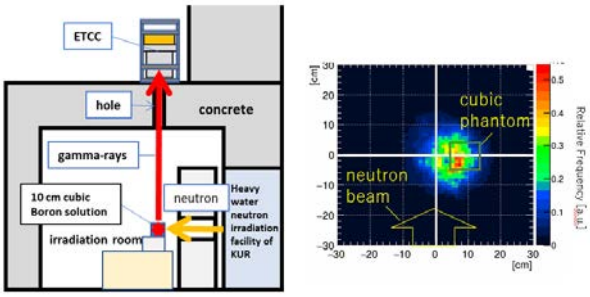

Fig.2. Schematic view and measured 478 keV gam-ma-ray image at 1-MW operation in Exp.3.

REFERENCES:

[1] T. Mizumoto *et al.*, KURNS Progress Report 2021.

PR2-13 Visualization of Boron Dose Distibution on a Borosilicate Glass Plate by Neutron Irradiaiton

A. Nohtomi, Y. Kojima, H. Maeda, T. Yamane, G. Wakabayashi[1], Y. Sakurai[2] and T. Takata[2]

Graduate School of Medicine, Kyushu University
[1]Atomic Energy Research Institute, Kindai University
[2]Institute for Integrated Radiation and Nuclear Science, Kyoto University

INTRODUCTION: Boron dose plays a critical role to kill tumor cells for the boron-neutron capture therapy (BNCT). Therefore, simple method of boron dose distribution measurement is much desirable for QA/QC purposes of BNCT. In the present study, boron dose distribution on a borosilicate glass plate, in which contains approximately 4 wt% natural boron (Table 1), has been visualized by using a CMOS camera during thermal neutron irradiation. High energy lithium ion and alpha particles generated by ^{10}B-neutron capture reactions were detected by the glass itself which acted as scintillator.

EXPERIMENTS: A borosilicate glass plate (100 x 100 x 20 mm^3, COSMOS VID Co., LTD.) was irradiated by thermal neutrons (~10^6 n/cm^2/s) during 600 s and 1200 s at E-3 irradiation port of KUR [1]. Luminescence of the glass plate was observed by a cooled CMOS camera (BITRAN, CS-67M) during the irradiation in a black box as shown in Fig. 1. For comparison, another soda lime glass plate (100 x 100 x 19 mm^3, COSMOS VID Co., LTD.) was irradiated and observed in the same manner.

RESULTS: As shown in Fig. 2, when the borosilicate glass plate was irradiated by neutrons, the cross section of beam profile was clearly visualized as luminescence distribution for 1200 s neutron irradiation. When the irradiation time was 600 s, the luminescence was weaker than that for 1200 s. On the other hand, no visible luminescence was observed for the soda lime glass, in which boron was not contained. The beam profile obtained by the borosilicate glass plate was compared with that measured by the decaying self-activation method of a CsI scintillator plate at the exit window of E3-port [2]. As indicated in Fig. 3, both profiles evaluated by different methods showed a reasonable agreement.

From the facts described above, it is evident that the observed luminescence is originated from lithium ion and alpha particles generated by ^{10}B-neutron capture reactions. This technique will be applicable for the daily QA/QC purposes of BNCT, because instantaneous neutron irradiation may be enough for observation of the actual intense neutron beam of clinical BNCT field (~10^9 n/cm^2/s).

Table 1. Typical composition and density of general glass.

	Composition (wt%)						Density (g/cm^3)
	SiO_2	B_2O_3	Al_2O_3	Na_2O/K_2O	CaO	others	
borosilicate glass	81	13	2	4	-	-	2.2
soda lime glass	70～74	-	0～2	12～16	6～12	MgO	2.5
quartz glass	100	-	-	-	-	-	2.2

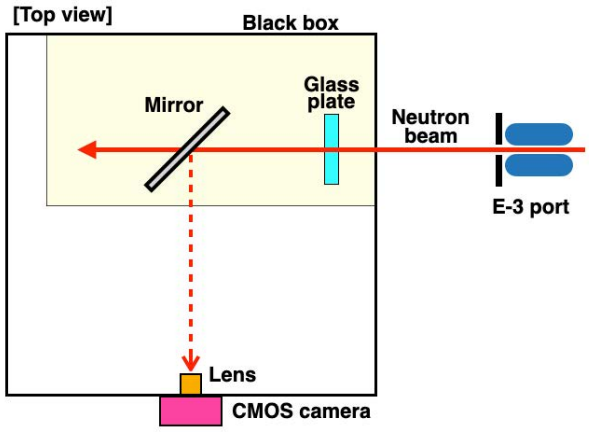

Fig. 1. Schematic drawing of experimental arrangement.

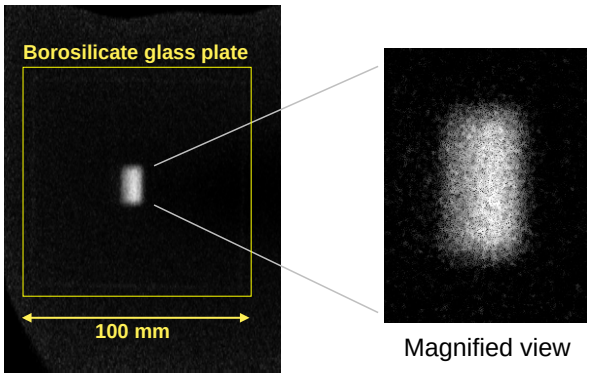

Fig. 2. Visualized boron dose distribution on a borosilicate glass plate observed by a CMOS camera during 1200 s neutron irradiation.

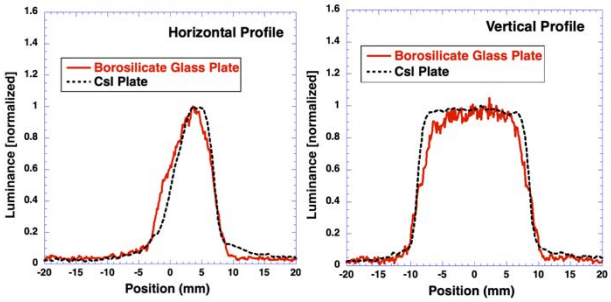

Fig. 3. Comparison between the profile obtained by luminescence of borosilicate glass plate and that measured by the self-activation of a CsI plate.

ACKNOWLEDGEMENT: This work was supported by JSPS KAKENHI Grant Number JP19K08202 and JP22K07697.

REFERENCES:

[1] T. Kobayashi and, K. Kand, Nucl. Instrum. Meth., **204** (1983) 525-531.
[2] A. Nohtomi *et al.*, Radiol. Phys. Technol., **15** (2022) 37-44.

PR2-14 Investigation of Thermal Neutron-Induced Soft Errors in Semiconductor Devices

H. Tanaka, R. Nakamura[1], and T. Kato[1]

Institute for Integrated Radiation and Nuclear Science, Kyoto University
[1]Reliability and Engineering Department, Socionext Inc.

INTRODUCTION: Soft errors are radiation-induced errors in semiconductor devices. With aggressive scaling down of transistor size and operating voltage, the semiconductor devices are becoming more susceptible to the soft errors. Therefore, to assess the reliability of electronic systems, it is necessary to investigate the characteristics of the soft errors.

In the terrestrial environment, the major radiation source for the soft errors is cosmic-ray-induced neutrons. The energy spectrum of the terrestrial neutron ranges from thermal to high-energy. The semiconductor devices are sensitive to the thermal neutrons when the devices contain abundant ^{10}B atoms, which produces He and Li ions through neutron-induced fission reactions [1].

It has been reported that in recent semiconductor devices the thermal neutron-induced soft errors appear due to the contamination of ^{10}B atoms during manufacturing processes [2, 3]. In previous experiments, the authors have demonstrated that the detailed characteristics of the thermal neutron-induced soft errors in static random-access memories (SRAMs) [4].

This study investigates the thermal neutron-induced soft errors in an advanced SRAM. Soft error rates (SERs), which are the occurrence rates of radiation-induced errors, are evaluated by neutron irradiation testing at KUR.

EXPERIMENTS: Neutron irradiation tests were performed using Heavy Water Neutron Irradiation Facility (HWNIF) of KUR [5]. The irradiation modes used were "OO–0000F" and "CO–0000F." Fig. 1 shows the energy spectra of these modes together with that of the terrestrial environment [6]. The "OO–0000F" and terrestrial spectra are similar to each other. This means that the neutron source is suitable for the investigation of the terrestrial neutron-induced soft errors. The thermal neutron sensitivity was examined by comparing results between the "OO–0000F" and "CO–0000F" modes.

The test samples were SRAM chips manufactured in an advanced CMOS process, which were labeled as Device C. During the irradiation, the SRAM chips were remotely operated, and the error events were measured. The SERs were then statistically calculated according to the JEDEC standard [7]. Thermal neutron fluxes at the locations of the samples were measured by the gold activation method. The results were compared with the previous results for Device A and B.

RESULTS: Fig. 2 presents the measured SERs of Device A, B and C, where the results of "OO–0000F" and "CO–0000F" are shown. Note that the SER values are normalized by the value of Device A with "OO–0000F".

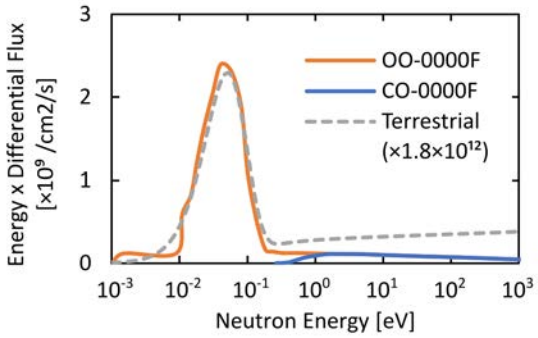

Fig. 1. Neutron energy spectra of KUR HWNIF [5] and terrestrial environment [6] .

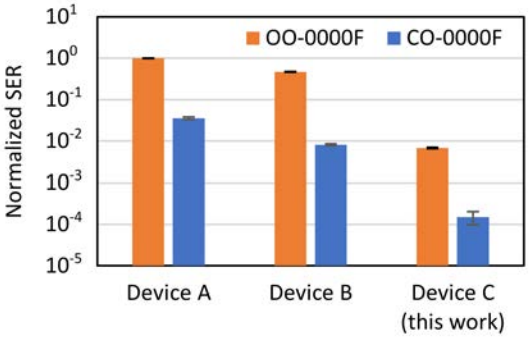

Fig. 2. Measured SERs of Device A, B and C for "OO–0000F" and "CO–0000F" modes.

For Device C, the SER of "CO–0000F" was significantly lower than that of "OO–0000F," as similarly observed in Device A and B. This result clearly shows that Device C is sensitive to thermal neutrons and contains nonnegligible amounts of ^{10}B atoms.

At the same time, the SER for Device C was greatly reduced compared to Device A and B. This indicates that the concentration of ^{10}B atoms for Device C is lower than Device A and B because basically the thermal neutron SER is proportional to the ^{10}B concentration.

Our experiments successfully demonstrated the difference in the thermal neutron sensitivity of the three SRAM devices. This result suggests that thermal neutron irradiation testing is essential to assess the soft error reliability.

REFERENCES:

[1] R. Baumann *et al.,* Proc. IEEE Int. Reliab. Phys. Symp. (IRPS), **152** (2000).
[2] S. Wen *et al.,* Proc. IEEE Int. Reliab. Phys. Symp. (IRPS), **SE.5.2** (2010).
[3] Y. Fang *et al.,* IEEE Trans. Device Mater. Rel., **14** (2014) 583.
[4] T. Kato *et al.,* IEEE Trans. Nucl. Sci., **68** (2021) 1436.
[5] Y. Sakurai *et al.,* Nucl. Instr. Meth. A, **453** (2000) 569.
[6] T. Sato, PLoS ONE, **10(12)** (2015).
[7] JEDEC Standard JESD89A (2006).

PR2-15 Dosimetric Characteristics of Optimized Bolus for Boron Neutron Capture Therapy

T. Takata, M. Nojiri[1], A. Sasaki[1], Y. Sakurai, H. Tanaka and M. Suzuki

Institute for Integrated Radiation and Nuclear Science, Kyoto University
[1]Graduate School of Engineering, Kyoto University

INTRODUCTION: In Boron Neutron Capture Therapy (BNCT), an epithermal neutron beam has been utilized to penetrate a deep site of a patient's body. However, thermal neutron buildup near a beam incident surface, associated with thermalization of epithermal neutrons, causes dose deficiency in a case where a tumor extends to vicinity of patient surface. For such a case, a thermal neutron compensation bolus consisting of a hydrogen-rich material has been utilized to improve the dose distribution. In present clinical BNCT, a bolus with a uniform thickness and a simple shape has been adopted. This study aims to increase the dose ratio of tumor to normal tissues more aggressively, by optimizing the bolus shape. An overview of the optimizing method was described in the previous report [1]. Verification using a water phantom has been attempted through experimental measurements, where the phantom with/without a simple-shaped bolus were used [2,3]. In this report, we describe comparison of dosimetric characteristics between the cases without bolus, with rectangular bolus and the optimized bolus.

MATERIALS AND METHODS: A cylindrical water phantom with a height of 20 cm and diameter of 20 cm was used, assuming a head-and-neck case with a parotid gland cancer irradiated from the lateral direction. A spherical volume with a 4-cm diameter centered at a 2-cm depth from the side surface of the cylinder was defined as a planning target volume (PTV), assuming a tumor extended to a subcutaneous region. A tubular volume with a 3-cm diameter along the center axis of the cylinder was defined as an organ at risk (OAR), assuming a mucosal tissue of oral cavity and pharynx [2].

Dose calculations were performed by using SERA, a treatment planning system for BNCT, for the cases without bolus, with rectangular bolus and the optimized bolus [4]. Figure 1 shows the geometry modeling in SERA for these cases. The rectangular bolus with the dimension of 7.5 × 7.5 × 1.1 cm^3 and the optimized bolus, each modeled as light-water region, were mounted on the beam axis on the side surface of cylinder. The optimization procedure of bolus shape was described in detail in Ref.1 and 2. An epithermal neutron beam of KUR Heavy Water Neutron Irradiation Facility with an aperture of 12-cm diameter was assumed in the calculations [5].

RESULTS AND DISCUSSION: Figure 2 shows the depth distributions of thermal neutron flux along the beam axis calculated for three cases. The figure also shows the measured distributions with adjusted depth for the cases without bolus and with the rectangular bolus [3]. In the case without bolus, thermal neutron buildup caused reduction of flux in the shallower region, resulting in lower minimum dose of PTV. In the case with the rectangular bolus, the distribution shifted toward the depth direction and the dose in the shallow region was increased. In the case with the optimized bolus, the PTV region had equalized fluxes at the entrance and distal sides, leading to higher dose coverage. However, minimum dose of the PTV was comparable between for the cases with rectangular and optimized bolus under constraint of OAR dose. The optimization method needs to be improved to further increase PTV dose.

ACKNOWLEDGMENT: This work was supported by JSPS KAKENHI Grant Number JP 17K17838.

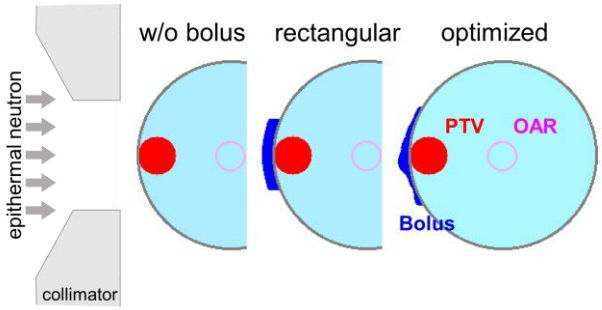

Fig. 1. Modelling of cylindrical water phantom without bolus, with rectangular bolus and with optimized bolus.

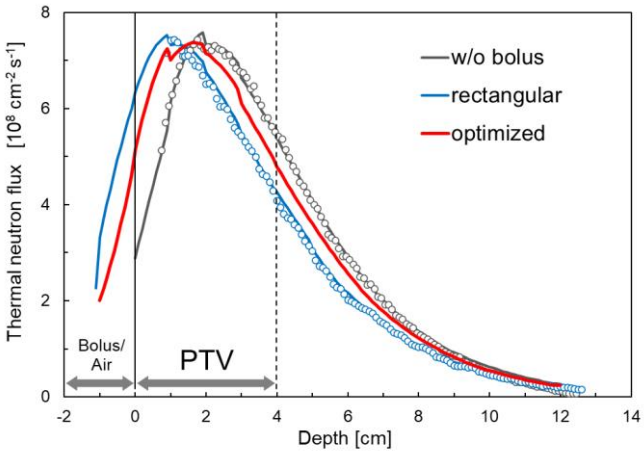

Fig. 2. Depth distributions of thermal neutron flux for cases without bolus, with rectangular bolus and with optimized bolus.

REFERENCES:

[1] T. Takata *et al.*, KURNS Progress Report 2019, (2020) 56.
[2] T. Takata *et al.*, KURNS Progress Report 2020, (2021) 83.
[3] T. Takata *et al.*, KURNS Progress Report 2021, (2022) 68.
[4] D. E. Wessol *et al.*, INEEL/EXT-02-00698 (2002).
[5] Y. Sakurai and T. Kobayashi, Med. Phys., **29** (2002) 2328-2337.

PR2-16 Three dimentional humanized oral cancer in vitro model for BNCT

K. Igawa, K. Izumi[1], E. Naito[1], M. Suzuki[2], N. Kondo[2], Y.Sakurai[2]

Neutron Therapy Research Center, Okayama University

[1] Graduate School of Medical and Dental Sciences Oral Life, Niigata University

[2] Institute for Integrated Radiation and Nuclear Science, Kyoto University

INTRODUCTION:

The preclinical animal test for BNCT is challenging from the ethical point of view of animal welfare and animal protection, as well as from the legal point of view of animal management in radiation-controlled areas. Since only a few facilities in Japan are capable of performing neutron irradiation tests on animals, there is a strong demand for alternative animal test models.

Recently, the various three-dimensional (3D) cancer models such as spheroids, organoids, and scaffold-based constructs have been developed and widely used in cancer research due to their ability to mimic multiple features of the tumor microenvironment. The 3D models are promising for the safety and efficacy assessment. Therefore, we have developed the 3D oral cancer in vitro model with human oral cancer cells and patient derived normal oral fibroblasts for BNCT. The optimal conditions of the 3D oral cancer model for BNCT have been inves-tigated. In this study, we report the histopathological fea-tures of 3D oral cancer model after BNCT.

EXPERIMENTS: First, we fabricated humanized 3D oral cancer in vitro model. The patient derived oral mucosal fibroblast cells（Niigata University, 2015-5018 ） were embedded and cultured on type Ⅰ-A collagen (Nii-tagelatin, Japan) for 7 days and oral squamous cell lines （HSC3, Riken Cell Bank）were seeded on the top of surface of 3D collagen matrix for additional 7days in α MEM medium (Wako, Japan) supplemented with 10 % fetal bovine serum (Sigma -Aldrich, USA) and 100 unit/ml penicillin and 100 μg/ml streptomycin (1% p/s) (Thermo Fisher Scientific, USA) [1]. Next, before neu-tron irradiation, Boron (Steboronine®, Stella pharma, Japan) or Phosphate Buffered Saline （PBS, Sigma -Aldrich, USA）was added to the oral 3D model and incubated for 2 hours and washed by PBS. The 3 D mod-els were irradiated by neutron for 20 minutes and cul-tured under a humidified atmosphere of 5% CO_2 at 37 ◦C for 2 hours for another 3 days. Finally, the 3D models were fixed with 10 % formalin, embedded in paraffin, cut in 5 μm sections and stained with hematoxylin and eosin. All images of the sections were obtained with an all-in-one fluorescence microscope (BZ-X800, KEYENCE, Osaka, Japan). The data are shown as means± standard deviation (S.D.) A p-value of less than 0.05 was considered statistically significant.

RESULTS: The histological examinations of the 3D oral cancer model after 3days of neutron irradiation were shown in Figure 1 and Table 1. The thickness of the HSC cells layer in the model after BNCT reduced from the multilayer to monolayer. However, there are no difference in the thickness of fibroblast-embedded collagen gel between the two (Figure 1). The size of HSC cells in the 3D oral cancer model after BNCT became about twice as large compared to the control, on the other hand, the fibroblasts was the same size with or without BNCT (Table 1) . These results indicate the 3D humanized oral cancer in vitro model would be an alternative tool to animal test for BNCT.

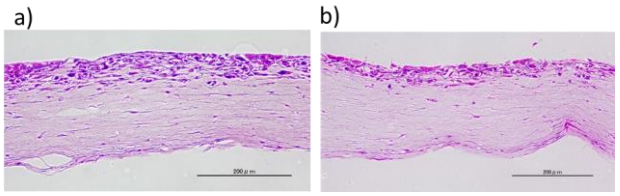

Figure 1. Microscopic image of the histological section of 3D oral cancer in vitro model at 7 days after neutron irradiation. (a) Control, (b)BNCT.

Table 1. BNCT induced histological changes 3D oral cancer in vitro model.

	Control	BNCT
Cancer cells layer [layer]	7.0±1.8	2.5±1.3
Tumor area rate [%]	21.6 ±2.7	16.7±1.4
Size of a cancer cell [μm^2]	51.6±8.9	125.6±57
Stromal tissues area rate [%]	78.4±4.6	83.3±3.7
Size of a fibroblast [μm^2]	48.5±29	43.9±12

DISCLOSURE: This research was partially supported by JSPS KAKENHI Grant Number JP20K12714.

REFERENCES:

[1] K. Haga *et al.,* Translational Oncology **12** (2021) 101236.
(doi)10.1016/j.tranon.2021.101236

PR2-17 Boron-10 uptake distribution in 3D oral cancer model using CR-39 solid state nuclear track detector

K. Igawa, R. Ogawara[1], T. Kusumoto[2], and Y. Sakurai[3]

Neutron Therapy Research Center, Okayama University

[1] Advanced Research Center for Beam Science, Institute for Chemical Research, Kyoto University

[2] Center for Advanced Radiation Emergency Medicine, National Institutes for Quantum and Radiological Science and Technology

[3]Institute for Integrated Radiation and Nuclear Science, Kyoto University

INTRODUCTION:

Boron neutron capture therapy (BNCT) for oral cancer is expected as a function-preserving therapy to maintain and improve the quality of life of cancer patients. The key to the success of BNCT is to accurately confirm the distribution of boron accumulation in the tumor and surrounding the normal regions including the tumor margins. Then, we have developed an estimation system for absolute values of a boron-10 uptake distribution in a tissue slice measured by single tracks from 10 B(n, α) 7 Li reactions using CR-39 nuclear track detector at accelerator-based neutron field.

Recently, the various three-dimensional (3D) cancer models such as spheroids, organoids, and scaffold-based constructs have been developed rapidly and are promising for the safety and efficacy assessment compared with simple 2D model. The patient delivered 3D model has demonstrated high predictive performance to predict the clinical response of the new cancer treatment. We have also developed the 3D oral cancer in vitro model with human oral cancer cells and patient derived normal oral fibroblasts for the radiation treatment.

In this study, using CR-39 nuclear track detector, the boron distribution and concentration of oral cancer regions in 3D oral cancer in vitro models is validated.

EXPERIMENTS:

The 3 D oral cancer in vitro model was fabricated with human primary normal oral fibro-blasts（Niigata University 2015-5018）and the human oral squamous carcinoma cell lines（JCRB）. The 3D oral cancer model administered with Boron (Borofaran, Stella pharma, Japan) for 2 hours was cleaned by PBS twice and embedded by O.C.T. compounds (Tissue Tek, Sakura, Japan) on a dry ice. The section at a range of 5 μm was mounted on the CR-39 plastic nuclear track detector (TechnoTrack, Chiyoda Technol Corp., Japan) using cryostat. After the neutron irradiation (KURRI) of 3D oral cancer tissue on the surface of CR-39, the tissue was removed from the CR-39. After chemical etching by a potassium hydroxide-ethanol-water (PEW-45; KOH 15 wt%, ethanol 45 wt%, water 40wt%), the microscopic image of a-particle tracks on the CR-39 was acquired with a high-speed imaging microscope (HSP-1000, SEIKO Time Systems Inc., Tokyo, Japan).

RESULTS:

The histological section of 3D oral cancer model on surface of CR-39 was irradiated for 20 mins at 2 X10^{12}/cm^2 thermal neutron fluence. The growth of etch pit diameter of a CR-39 was 3.5 μm controlled by PEW-45 at 50 ℃. The microscopic images of etch pits on CR-39 detectors were obtained as shown Figure 1 A. The number of etch pits in tumor regions (Figure 1 A-❶)was significantly higher than in stromal regions（Figure 1 A-❸）. After the analysis of etch pits, the etch pit density distribution map of a histological section 3D oral cancer model was acquired as shown Figure1 B. The results indicated that the boron concentration in tumor regions was significantly higher than in stromal regions. However, the quantitative analysis was difficult in high boron concentration areas. The further studies are needed for the optimal etch pits analysis for the 3D oral cancer model.

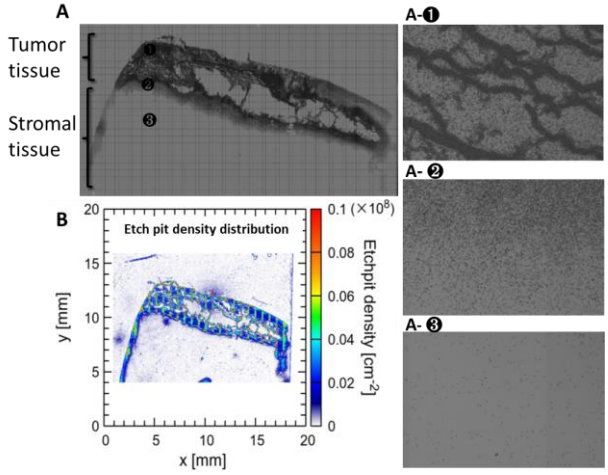

Figure 1. A）Microscopic images of a histological section of 3D oral cancer model and etch pits of CR-39 after neutron irradiation. The microscopic images of etch pits of CR-39 at ❶tumor regions ❷ tumor margins ❸stromal regions. B）Etch pit density distribution map of a histological section of 3D oral cancer model.

DISCLOSURE: This research was partially supported by JSPS KAKENHI Grant Number JP20K12714.

REFERENCES:

[1] K. Haga *et al.,* Transl Oncol., **14(12)** (2021) 101236.

[2] T. KONISHI *et al.,* J. Radiat. Res., **48** (2007) 225-261.

I-1. PROJECT RESEARCHES

Project 3

PR3 Project Research on Advances in Isotope-Specific Studies Using Muti-Element Mössbauer Spectroscopy

M. Seto

Institute for Integrated Radiation and Nuclear Science, Kyoto University

OBJECTIVES OF RESEARCH PROJECT:

Mössbauer spectroscopy is effective to extract several information such as electronic states for a specific isotope. The objective of this project research is to progress the investigation in the frontier of the materials science and the development of advanced experimental methods by using multi-element Mössbauer spectroscopy. Promotion of variety of Mössbauer isotope provides more useful and valuable methods in modern materials science even for complicated systems.

In this project research, each group performed their research by specific isotopes:

^{57}Fe in R4P3-1, R4P3-2, R4P3-3, R4P3-4, R4P3-5, R4P3-6

^{61}Ni in R4P3-7

^{197}Au in R4P3-8, R4P3-9

Other developments in R4P3-10, R4P3-11

R4P3-2(H. Fujii) was not performed this year.

MAIN SUBJECTS AND RESULTS OF THIS REPORT:

Main subjects and results are as follows:

(R4P3-1, K. Shinoda) Intensity tensor of Fe^{2+} in the *M1* Site of diopside by single crystal Mössbauer spectroscopy

K. Shinoda *et al.* successfully characterized the intensity tensor of quadrupole doublet of diopside, which is Ca-rich and Fe-poor pyroxene, in a natural mineral by Mössbauer microspectrometer.

(R4P3-3, I. Mashino) Electrical conductivity and the iron valence state of silicate glasses up to Mbar pressures

I. Mashino *et al.* investigated Fe-bearing enstatite glasses with variable amounts of iron components. The Mössbauer spectroscopy at room and low temperatures is used to determine the composition ratio and of Fe^{2+} and Fe^{3+}components.

(R4P3-4, M. Tabuchi) Change in Fe valence state of Fe and Ni substituted Li_2MnO_3 positive electrode material during different synthetic method by ^{57}Fe Mössbauer spectroscopy

M. Tabuchi *et al.* performed ^{57}Fe Mössbauer spectroscopy for several samples of Fe and Ni substituted Li_2MnO_3 electrode materials with different preparation method to improve the electro-chemical performance as positive electrodes in Li-ion batteries.

(R4P3-5, Y. Kamihara) Research on magnetism and electronic phase in a H-doped iron-based superconductor

Y. Kamihara *et al.* prepared iron-based superconductors, H-doped SmFeAsO by high-temperature and high-pressure synthesis and evaluated magnetic properties to investigate the mechanism of superconducting electron pair formation and destruction. The Mössbauer spectroscopy will be performed for this evaluated samples.

(R4P3-6, K. Yonezu) Experimental Preliminary Approach on the Precipitation Mechanism of Banded Iron Formation (BIF): Part 2

K. Yonezu *et al.* performed ^{57}Fe Mössbauer Spectroscopy of silica scales from operating geothermal power plant to understand the banded iron formation mechanism of chemically precipitated sedimentary rock at Precambrian age.

(R4P3-7, T. Kitazawa) ^{61}Ni Mössbauer Spectroscopy for Hofmann-type Supramolecular Bridging Cyanide Complexes

K. Kitase *et al*. synthesized three Hofmann-type Fe-and Ni-contained coordination polymer and investigated them by ^{61}Ni Mössbauer spectroscopy to evaluate the Ni environments in these compounds.

(R4P3-8, H. Ohashi) Chemical species for precursor of supported gold cluster catalysts presumed from Recoil-free fraction in ^{197}Au Mössbauer Spectroscopy

H. Ohashi *et al*. investigated precursor of supported Au cluster and presumed chemical species of the precursor as an analogous complex of $[Au(SH)_2]^-$ by ^{197}Au Mössbauer Spectroscopy.

(R4P3-9, Y. Kobayashi) Recoilless Fraction on ^{197}Au Mössbauer Spectroscopy(2)

Y. Kobayashi *et al.* investigated the evaluation method of the Debye temperature by measuring temperature dependence of Mössbauer spectra for several Au compounds.

(R4P3-10, R. Masuda) EuS property as the energy standard material at ^{151}Eu Mössbauer spectroscopy

R. Masuda *et al*. evaluated the temperature dependence of the isomer shifts of EuS as a Eu^{2+} standard material for ^{151}Eu Mössbauer spectroscopy.

(R4P3-11, S. Kitao) Development of ^{119}Sn Mössbauer Source

S. Kitao *et al*. have attempted to produce a ^{119}Sn Mössbauer source by using $CaSnO_3$ compounds in long-term neutron irradiation.

PR3-1 Intensity tensor for Fe^{2+} at the *M*1 site of diopside by single crystal Mössbauer spectroscopy

K. Shinoda[1], D. Takagi[1], Y. Kobayashi[2]

[1]*Department of Geosciences, Graduate School of Science, Osaka Metropolitan University*
[2]*Institute for Integrated Radiation and Nuclear Science, Kyoto University*

INTRODUCTION: Pyroxene is a major rock-forming mineral and a typical multi-site solid solution. Common chemical formula of natural pyroxene is $(Ca, Fe, Mg)_2 Si_2 O_6$. Occupying sites of divalent cations are the *M*1 and *M*2 sites. In pyroxene, Fe^{2+} in *M*1, Fe^{2+} in *M*2 and Fe^{3+} in *M*1 sites are possible. Fukuyama et al. (2022) emphasized that the intensity tensor for Fe^{2+} at the *M* sites of pyroxene is very important for analyzing Mössbauer spectra of single-crystal pyroxene thin sections, because intensities of a quadrupole doublet of a thin section as a single crystal are asymmetric and vary depending on the angle between the direction of incident γ-rays and the crystallographic orientation. Intensity of quadrupole doublet (I^h / I^{total}) means a ratio between area of the peak of the higher energy (I^h) and total area of the doublet ($I^{total}= I^h + I^l$) (sum of I^h and area of the lower energy (I^l)). Intensity can be calculated from the intensity tensor. Intensity tensors of Ca-rich and Fe-rich pyroxenes (augite and hedenbergite) were revealed by Fukuyama (2022) [1]. However, Intensity tensor of diopside, that is Ca-rich and Fe-poor pyroxene, was not measured. In this study, intensity tensor for Fe^{2+} at the *M*1 site of diopside was measured to confirm compositional dependence of the intensity tensor for Fe^{2+} at the *M*1 site in Ca-rich pyroxene by single crystal Mössbauer spectroscopy.

EXPERIMENTS and RESULTS: Single crystals of diopside from Horado, Seki, Gifu prefecture, Japan were used for this study. Chemical analyses of the diopside indicates the formula $(Ca_{0.97}Fe_{0.06}Mg_{0.94})_{\Sigma 1.97}(Si_{1.99}Al_{0.03})_{\Sigma 2.02}O_6$ by EDS. The molar contents of Mg and Ca were 0.94 and 0.97, respectively. The results suggest that Ca ions almost fully occupy the *M*2 sites and that the Mg ions are not sufficient to occupy the *M*1 sites. Therefore, the major part of the Fe^{2+} ions occupy the *M*1 sites. Three crystallographically oriented thin sections perpendicular to ***a***, ***b*** and ***c*** were prepared by measuring X-ray diffraction using Laue and precession cameras. Eight Mössabuer spectra of oriented thin sections were measured. In this study, Cartesian coordinate (*X Y Z*) is set as *X*//***c****, *Y*//***a***, *Z*//***b***, where ***c**** are reciprocal lattice vectors of diopside. Mössbauer measurements were carried out in transmission mode on a constant acceleration spectrometer with an Si-PIN semiconductor detector (XR-100CR, AMPTEK Inc.) and multi-channel analyzer of 1024 channels. A 3.7GBq ^{57}Co/Rh of 4mmϕ in diameter was used as γ-ray source. An ^{57}Fe-enriched iron foil was used as velocity calibrant. The two symmetric spectra were folded and velocity range was ± 4mm/s. Thickness corrections of raw spectra were not done.

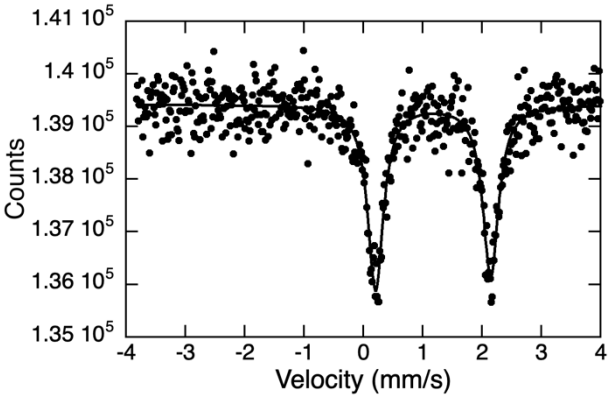

Fig.1. Mössbauer spectrum of diopside measured under γ-ray parallel to the ***a***-axis.

Fig.1 shows Mössbauer spectrum of diopside measured under incident γ-ray parallel to ***a***-axis. A doublet due to Fe^{2+} in *M*1 site of diopside was observed. Averages of isomer shift (δ), Q-splitting (Δ), and line width (Γ) were 1.176(2) 1.919(4) and 0.310(4) mm/s, respectively. From eight sets of intensity of quadrupole doublet, Four components (I_{XX}, I_{YY}, I_{ZZ}, I_{XY}) of the intensity tensor of Fe^{2+} in the *M*1 site of diopside are obtained as 0.328(7), 0.480(5), 0.692(12) and 0.050(15).

DISSCUSSION: The four components (I_{XX}, I_{YY}, I_{ZZ}, I_{XY}) of this study were compared with those of Ca-rich pyroxenes of different chemical compositions in Fukuyama et al. (2022) [2]. According to Fukuyama et al. (2022), the intensity tensor due to Fe^{2+} at the *M*1 sites of diopside, hedenbergite, and augite is dependent on the Wo content, but independent of the Fs content. This result suggests that components of the intensity tensor due to Fe^{2+} at *M* sites in Ca-Mg-Fe pyroxene minerals that contain equal Wo and different Fs components are almost constant.

REFERENCES

[1] Fukuyama., Master thesis, Osaka City Univ. (2020).
[2] D. Fukuyama *et al.,* J. Mineral. Petrol. Sci., **117(1)** (2022) 220506.

PR3-2 Electrical conductivity and the iron valence state of silicate glasses up to Mbar pressures

I. Mashino, T. Yoshino, S. Kitao[1], T. Mitsui[2], R. Masuda[3], M. Seto[1]

Institute for Planetary Materials, Okayama University
[1]Institute for Integrated Radiation and Nuclear Science, Kyoto University
[2]Synchrotron Radiation Research Center, Kansai Photon Science Institute, Quantum Beam Science Research Directorate, National Institutes for Quantum and Radiological Science and Technology
[3]Graduate School of Science and Technology, Hirosaki University

INTRODUCTION: The existance of gravitationally stabilized melts at the bottom of the Earth's mantle has been proposed because a density crossover between melts and crystals is expected to occur. However, whether the crossover occurs in the lower mantle or not strongly depends on the chemical composition of both the melt and crystals. The valence and spin states of iron are believed to affect the iron partitioning between melts and crystals, thus also control a depth of the density crossover [1]. In order to understand the valence/spin states of iron in silicate melts, we firstly conducted high-pressure electrical conductivity measurements of iron-bearing enstatite glass which has a representative composition of the mantle, because silicate glasses have been considered as good analogues of silicate melts.

EXPERIMENTS: ^{57}Fe-bearing enstatite glasses with variable amounts of iron (13 mol% Fe, 19 mol% Fe, and 10 mol% Fe, Al) were synthesized from reagent MgO, $^{57}Fe_2O_3$ and SiO_2 powders by an electric furnace. The conventional ^{57}Fe-Mössbauer spectroscopy was performed using a ^{57}Co source in Rh matrix with nominal activity of 1.85 GBq at Institute for Integrated Radiation and Nuclear Science, Kyoto University. The velocity scale is referenced to α-Fe. To determine the $Fe^{3+}/\Sigma Fe$ and confirm recoilless fractions of Fe^{2+} and Fe^{3+} in the enstatite glasses, we obtained the spectra both at room temperature and at low temperature (22-25 K).

RESULTS: According to the Mössbauer spectroscopy, iron in the enstatite glasses was found to be present as shown in Table 1. Compared with hyperfine parameters in silicate glasses previously reported at ambient condition [2, 3], doublets can be associated with Fe^{3+} or Fe^{2+} in octahedral site.

The ratio of the absorption areas of Mössbauer doublets produced by Fe^{3+} and Fe^{2+} ($A\,(Fe^{3+})_T$, $A\,(Fe^{2+})_T$) are related to the abundances of the ions ($N(Fe^{3+})$, $N(Fe^{2+})$) and the recoilless fraction (f_T) of each ion, according to

$$\frac{A\,(Fe^{3+})_T}{A\,(Fe^{2+})_T} = C_T \frac{N(Fe^{3+})}{N(Fe^{2+})},\ C_T = f(Fe^{3+})_T / f(Fe^{2+})_T, \quad (1)$$

Fig. 1 shows the comparison of Fe^{3+}/Fe^{2+} ratios of Fe-enstatite glasses at room temperature (300 K) and low temperature (22K or 25 K), suggesting that a correlation factor, C_{RT}/C_{LT} is higher than 1. The similar tendency has been observed in previous study on silicate glasses [4].

In-situ high-pressure synchrotron Mössbauer spectroscopic experiments and electrical conductivity measurements have been performed for the Fe-bearing enstatite glasses in a diamond anvil cell. We observed the trend changes in the pressure dependence of electrical conductivity and also the shape changes in Mössbauer spectra at around 80-100 GPa. We are now discussing the obtained results and then geophysical implications.

Table 1. Fitting results of the conventional Mössbauer spectra of Fe-enstatite glasses at ambient pressure.

Sample	Temp. (K)	IS (mm/s)	QS (mm/s)	Width (mm/s)	Aria (%)	Site
13 mol% Fe-enstatite glass						
doublet 1	22	1.19	2.16	0.92	57.3	Fe^{2+}
doublet 2	22	0.49	1.26	0.92	42.7	Fe^{3+}
doublet 3	300	1.05	1.97	0.75	47.7	Fe^{2+}
doublet 4	300	0.36	1.27	0.75	52.3	Fe^{3+}
19 mol% Fe-enstatite glass						
doublet 5	25	1.18	2.18	0.9	45.9	Fe^{2+}
doublet 6	25	0.45	1.25	0.9	54.1	Fe^{3+}
doublet 7	300	1.04	1.98	0.73	39.1	Fe^{2+}
doublet 8	300	0.33	1.22	0.73	60.9	Fe^{3+}
10 mol% Fe, 10 mol% Al-enstatite glass						
doublet 9	22	1.19	2.12	0.91	64.9	Fe^{2+}
doublet 10	22	0.49	1.24	0.91	35.1	Fe^{3+}
doublet 11	300	1.06	1.96	0.75	56.6	Fe^{2+}
doublet 12	300	0.35	1.26	0.75	43.4	Fe^{3+}

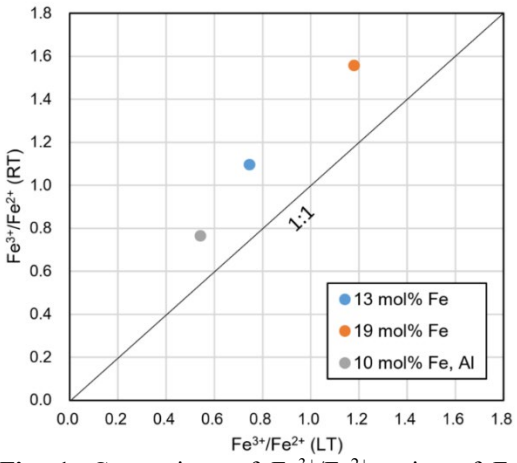

Fig. 1. Comparison of Fe^{3+}/Fe^{2+} ratios of Fe-enstatite glasses at room temperature (RT, 300 K) and low temperature (LT, 22K or 25 K).

REFERENCES:

[1] R. Nomura *et al.,* Nature, **473** (2011) 199.
[2] M. Dyar, Am. Mineral., **70** (1985) 304 .
[3] B. Mysen and P. Richet, Silicate Glasses and Melts (Elsevier, 2019).
[4] H. L. Zhang *et al.,* Chem. Geol., **479** (2018) 166 .

PR3-3 Change in Fe valence state of Fe and Ni substituted Li_2MnO_3 positive electrode material during different synthetic method by ^{57}Fe Mössbauer spectroscopy

M. Tabuchi and Y. Kobayashi[1]

National Institute of Advanced Industrial Science and Technology (AIST)
[1]Institute for Integrated Radiation and Nuclear Science, Kyoto University

INTRODUCTION: The 10% Fe and 20% Ni substituted Li_2MnO_3 ($Li_{1+x}(Fe_{0.1}Ni_{0.2}Mn_{0.7})_{1-x}O_2$, $0<x<1/3$) is an attractive positive electrode material having high discharge voltage (>3.5 V) and capacity (>200 mAh/g). However, further effort is needed to improve the electrochemical performance. In this report, we examine the change in Fe valency and local structure using ^{57}Fe Mössbauer spectra after applying ternary calcination process.

EXPERIMENTS: The sample was prepared by co-precipitation - calcination method. Water soluble Fe, Ni and Mn salts (Fe:Ni:Mn molar ratio=1:2:7) dissolved in distilled water and dripped into NaOH solution at +20°C for 2-3 h. The coprecipitate was oxidized by bubbling with O_2 flow for 2 days.

The product was washed with distilled water and then was filtered to make precursor. The precursor mixed with Li_2CO_3 (Li/(Fe+Ni+Mn)=2) into distilled water to make homogeneous slurry. The dried slurry was used as a starting material for calcination. The precursor was powdered using vibration mill and then was primary calcined at 650 °C for 5 h in air. The product was milled again and secondary calcined at 900 °C for 1h in N_2 flow. As a final calcination process, powdered sample was calcined at 450 °C for 3 h in 4%H_2-96%N_2 flow (ternary calcination process). The product was washed with distilled water and then continue to the filtration and drying processes. The obtained sample was named as sample HN. For comparison, the sample was prepared separately by secondary calcination at 900 °C for 10 h in N_2 flow. The sample name was sample N after washing with distilled water and drying processes.

The samples were characterized by X-ray diffraction (XRD), chemical analysis and half-cell tests. The lithium metal foil and 1.5 M Li PF_6/EC-DMC (3:7 in volume) were used as anode and electrolyte, respectively. The velocity axis of each ^{57}Fe Mössbauer spectrum was calibrated by α-Fe.

RESULTS: The X-ray diffraction pattern for both samples showed that each of them consisted of a single phase of monoclinic Li_2MnO_3 type structure. The 5th charge and discharge capacities corresponded to initial specific capacity, because stepwise-charging protocol until 5th cycle was applied to activate this material. The 5th charge and discharge capacities for Li/sample HN cell (267 and 257 mAh/g) were higher than those (242 and 241 mAh/g) for Li/sample N cell. To find the origin of the difference in the electrochemical performance, ^{57}Fe Mössbauer spectroscopy was used. Fig. 1 shows that ^{57}Fe Mössbauer spectra for samples N and HN.

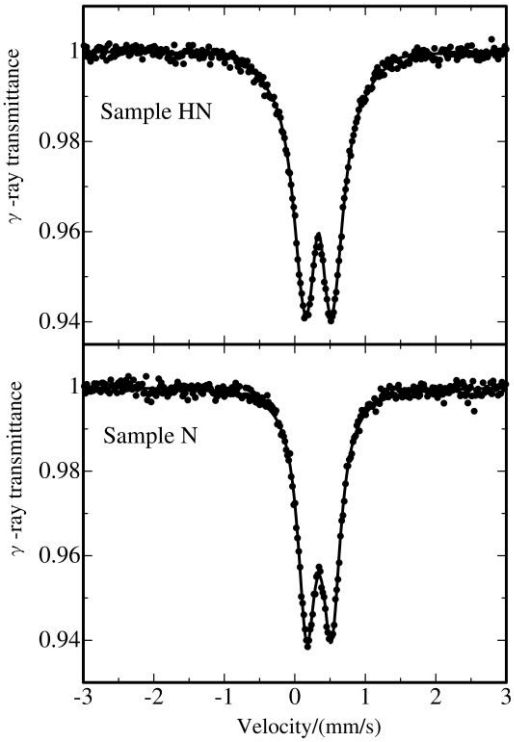

Fig. 1. ^{57}Fe Mössbauer spectra for samples N and HN.

The observed isomer shift (IS) values for samples N and HN were +0.3442 (10) and +0.3362 (10) mm/s, respectively. The Fe valency was assigned as the high-spin trivalent state from the IS data. The fact indicates that trivalent Fe ion was not reduced after calcination in the H_2-N_2 atmosphere. The QS value for the sample HN was 0.43 (3) mm/s, which was larger than that for sample N (0.3522 (17) mm/s). In general, QS value tend to large with increasing variation of local structure. The X-ray Rietveld analysis indicate that transition metal (TM) ion ordering was destroyed on TM-Li layer and part of TM ion in TM-Li layer moved to Li layer for sample HN. The TM distribution disordering was one of origin for larger QS value.

From the ^{57}Fe Mössbauer data, increase in variation of local structure around Fe^{3+} ion is one of important strategy for maximizing of specific capacity for $Li_{1+x}(Fe_{0.1}Ni_{0.2}Mn_{0.7})_{1-x}O_2$, ($0<x<1/3$) positive electrodes.

PR3-4 Research on magnetism and electronic phase in a H-doped iron-based superconductor

Y. Kamihara, T. Kawamatsu, M. Matoba, S. Kitao[1], and M. Seto[1]
Department of Applied Physics and Physico-Informatics , Faculty of Science and Technology, Keio University
[1]Institute for Integrated Radiation and Nuclear Science, Kyoto University

Superconductivity is a property of conductors, which is confirmed by two properties: zero electrical resistivity below its transition temperature (T_c) and the Meissner effect, which completely eliminates magnetic flux in the conductor.

The performance of power cables using superconductors (SC wire) is determined by the critical current density (J_c), the upper critical magnetic field (H_{c2}), and the irreversible magnetic field (H_{irr}) at the operating temperature below T_c. Here, H_{irr} is the magnetic field defined as the threshold value at which the magnetic flux entering the conductor is unpinned and begins to move due to the application of a magnetic field to the superconductor. In general, the irreversible magnetic field is smaller than the upper critical field. Under a magnetic field larger than the irreversible magnetic field, the zero resistance of the superconductor disappears. In other words, the upper limit of the performance of SC wire is determined by J_c at T below T_c and H below H_{irr}.[1]

Among iron-based high-Tc superconductors (Fe-SC), the J_c of materials with Tc above 20 K can be measured only under the extreme high magnetic field, which is difficult to realize in an ordinary laboratory.[2]

Among the Fe-SC, $SmFeAsO_{1-x}F_x$ (F-doped Sm1111) and $SmFeAsO_{1-x}H_x$ (H-doped Sm1111), whose mother compound is an antiferromagnetic (AFM) metal SmFeAsO, exhibit T_c ~55 K under ambient pressure. [3]

This feature is similar to an electronic and magnetic phase diagram for high-T_c cuprate superconductors, whose mother compound exhibit antiferromagnetic phase of copper sublattice.

Fe ions in SmFeAsO, which is a mother compound of a Fe-SC, exhibit AFM phase at T < 150 K. By partial substitution of about 4.5 at.% fluorine or hydrogen at the oxygen sites, the AFM phase disappears and a bulk superconducting phase appears.

At a phase boundary between the superconducting and normal-conductive phases with fluorine or hydrogen atoms around 4.5 at.%, the bulk magnetic phase almost disappears in Sm1111. [4]

However, in this state, local spin density waves (SDW), which indicate a magnetic order at short distances, may exist in a coexisting or phase-separated phases with SC phase. In the case of Sm1111 with higher concentration of fluorine or hydrogen, coexistence or phase separation of SDW and superconducting phase at short range is expected to be realized under high magnetic field.

Focusing on the formation of superconducting electron pairs (Cooper pairs) at the phase boundary between the superconducting and normal-conducting phases under a magnetic field.

The phase boundary in Sm1111 is expected to exhibit a special mechanism of superconducting electron pair formation and destruction, so-called Fulde–Ferrell–Larkin–Ovchinnikov (FFLO) phase. []

In this study, we will demonstrate T_c, J_c, H_{irr}, and Mössbauer spectra under magnetic field for H-doped Sm1111, whose chemical composition has been quantitatively analyzed. Our research aim to define the FFLO state, which exists as a concept, for H-doped Sm1111 experimentally.

EXPERIMENTS: The research in 2022 is the first year of a three-year plan to clarify the bulk electrical and magnetic properties of polycrystalline H-doped Sm1111 prepared by high temperature and high pressure synthesis as a preliminary step for Mossbauer spectroscopy in 2023. The magnetic moment (M) of polycrystalline H-doped Sm1111 was measured using a SQUID magnetometer (Quantum Design MPMS) at several temperatures (T) and magnetic fields (H).

RESULTS: The magnetic moment (M) of polycrystalline H-doped Sm1111 was measured using a SQUID magnetometer (Quantum Design MPMS) at several temperatures (T) and magnetic fields (H).
The magnetic Jc of H-doped SmFeAsO was quantified from the hysteresis of M-H curves using an extended Bean model. [7] The magnetic J_c of our H-doped Sm1111 is 22.3 kA/cm^2.

REFERENCES:

[1] M. Sato, Ph.D. Thesis, Seikei Univ. (2018) (in Japanese).
[2] M. Fujioka, Ph. D thesis, Keio Univ. (2012) (in Japanese).
[3] Y. Kamihara *et al.,* New J. Phys. **12** (2010) 033005.
[4] Y. Kamihara *et al.,* American Physical Society March Meeting, Dallas, USA (2011). (unpublished)
[5] P. Fulde and R. A. Ferrell, Phys. Rev. **135** (1964) A550 .
[6] A. I. Larkin and Yu. N. Ovchinnikov, Sov. Phys. JETP., **20** (1965) 762.
[7] E. M. Gyorgy *et al.,* Appl. Phys. Lett. **55** (1989) 283.

PR3-5 Experimental Preliminary Approach on the Precipitation Mechanism of Banded Iron Formation (BIF): Part 2.

K. Yonezu, H. Hirano[1], K. Arisato[1], Y. Kobayashi[2] and T. Yokoyama[3]

Department of Earth Resources Engineering, Faculty of Engineering, Kyushu University
[1]Department of Earth Resources Engineering, Graduate School of Engineering, Kyushu University.
[2]Institute for Integrated Radiation and Nuclear Science, Kyoto University
[3] Department of Chemistry, Faculty of Sciences, Kyushu University

INTRODUCTION: Banded Iron Formation (BIF) is chemically precipitated sedimentary rock at Precambrian age. Currently iron resource widely used in our industries largely depends on BIF. The formation of BIF was closely related with seafloor hydrothermal activity. In addition, the hydrothermal water, anoxic water was mixed with oxic seawater (e.g., Otake and Otomo, 2021). However, there are many mysteries on the formation mechanism. One of the biggest issues are the alternation of iron mineral and silicate (+carbonate) minerals. Therefore, this study aims to understand the formation mechanism, especially redox condition during the formation of BIF. Here, we would like to report the chemical state of iron in siliceous deposit from geothermal power plant to elucidate the precipitation behavior of iron-bearing siliceous deposit in natural system.

EXPERIMENTS: The siliceous deposit samples used here were collected from operating geothermal power plant. These samples are so called silica scale, and those were analyzed by XRF, XRD, XAFS, NMR in addition to Mossbauer analysis.

RESULTS: Five of silica scale samples were analyzed by Mossbauer spectrophotometry. Those were directly precipitated from geothermal water. Iron concentration in geothermal water is below detection limits of ICP-AES (less than 0.01 ppm), while iron concentration as Fe_2O_3 in silica scale were up to 15% (Tab. 1). This fact suggested that iron is specifically concentrated during silica scale formation.

Iron bearing components observed from the samples were hematite (shown as red in Tab. 2), magnetite/maghemite (shown as orange for A site and pink for B site), goethite (shown as green), iron silicate (shown as purple and blue) and ferric iron (shown as water blue). Sample 1 and Sample 4 shows a similar characteristic from Mossbauer analysis. In addition, those have relatively lower iron and high aluminum contents. Sample 3 consists of the same iron components with Sample 1 and Sample 4, however the ratio of each component is quite different. Sample 3 contains more ferric component than ferrous one. This might be related to high magnesium contents in the sample and the formation of smectite. In contrast, Sample 2 and Sample 5 clearly contain iron oxide, hematite and magnetite/maghemite and goethite.

Tab. 1. Chemical composition of silica scale used in this study.

	Unit	Sample 1	Sample 2	Sample 3	Sample 4	Sample 5
H2O(-)	%	0.0	5.4	2.5	3.8	0.9
H2O(+)	%	15.5	8.3	7.6	9.2	8.6
Fe2O3	%	0.2	12.0	12.3	4.8	15.6
Al2O3	%	12.9	7.0	6.6	10.5	9.3
Na2O	%	1.6	0.8	0.6	1.4	1.4
K2O	%	1.8	0.7	0.3	1.2	1.2
CaO	%	4.5	2.5	1.4	2.3	3.7
MgO	%	0.4	10.5	18.9	7.0	1.7
SiO2	%	75.3	55.6	49.1	70.2	67.3

Tab. 2. Mossbauer parameters obtained from 5 silica scale samples. Cell colors correspond to the component.

	Ratio	IS (mm/s)	Hin (T)	QS (mm/s)	FWHM (mm/s)
Sample 5	11.8%	0.374	51.5	-0.216	0.289
	15.4%	0.308	49.1	-0.053	0.441
	10.5%	0.648	45.9	0.008	0.405
	21.0%	0.238	35.0	-0.420	1.518
	13.1%	1.128		2.614	0.392
	28.2%	0.346		0.720	0.525
Sample 3	29.8%	1.130		2.579	0.365
	26.0%	0.351		0.708	0.430
	44.2%	0.374		1.325	0.532
Sample 2	11.8%	0.369	51.5	-0.208	0.261
	17.8%	0.291	49.0	-0.025	0.373
	21.7%	0.659	45.9	0.007	0.452
	10.4%	0.292	35.6	-0.275	1.674
	13.6%	1.130		2.594	0.394
	24.6%	0.325		0.664	0.460
Sample 4	58.1%	1.106		2.627	0.381
	13.9%	0.308		0.705	0.354
	28.0%	0.475		1.049	0.531
Sample 1	57.0%	1.107		2.616	0.406
	19.8%	0.308		0.705	0.354
	23.2%	0.475		1.049	0.531

Sample 5 is considered to be formed more oxidizing condition based on the ratio of A site and B site. This is also supported by the higher ration of goethite in this sample. By NMR analysis of Sample 5 suggested the presence of only 4-coordinated aluminum and zeolite like structure, while Sample 2 shows the presence of 6-coordinated aluminum suggesting that smectite group mineral harmonious with high magnesium contents.

The formation of silica scale is not monotonous but iron speciation reveals the redox condition of geothermal fluid. In geothermal fluid from geothermal power plant, there are several redox conditions derived from the mixing with oxidizing fluid and/or exposed to atmospheric condition in natural system.

We are going to apply iron Mossbauer spectroscopy for artificial BIF under known redox condition to understand the redox condition of the precipitation environment of BIF.

REFERENCES:

[1] T. Otake and Y. Otomo, Shigen-Chishitsu, **71** (2021) 57-73.

PR3-6 ^{61}Ni Mössbauer Spectroscopy for Hofmann-type Supramolecular Bridging Cyanide Complexes

K. KITASE[1], T. KITAZAWA[1,2], Y. DOI[1], Y. KOBAYASHI[3], S. KITAO[3], T. KUBOTA[4] and M. SETO[3]

[1]*Faculty of Science, Toho University*
[2]*Research Centre for Materials with Integrated Properties, Toho University*
[3]*Institute for Integrated Radiation and Nuclear Science, Kyoto University*
[4]*Agency for Health, Safety and Environment, Kyoto University*

INTRODUCTION: The Mössbauer Effect has been found for about 100 nuclear transitions in some 80 nuclides in nearly fifty elements. The technique is a very valuable and helpful tool to the material sciences linking to molecular magnetisms. It is well-known that 3-d block transition metal complexes with d^4-d^7 configuration in an octahedral crystal field have a possibility of SCO between the low spin (LS) and the high spin (HS) state. Octahedral iron(II) SCO systems with $3d^6$ can be transited between the diamagnetic $(t_{2g})^6$ and the paramagnetic $(t_{2g})^4(e_g)^2$ configuration. Hofmann-type structure is one of coordination polymer consist of center metal ion, bridging cyano metalate, and axial ligand molecule. The first Hofmann-type SCO complex was Fe^{II}(pyridine)$_2$Ni(CN)$_4$ reported in 1996 [1]. Many type of Hofmann-type SCO complex was reported [2-8] due to its tunable properties.

EXPERIMENTS: We freshly synthesized three Hofmann-type coordination polymer Fe(Ethyl Isonicotinate)$_2$Ni(CN)$_4$ and Fe(Allyl Isonicotinate)$_2$Ni(CN)$_4$. These complexes were synthesized by direct method.

^{61}Ni Mössbauer source production associated with ^{62}Ni(γ, p)^{61}Co was done using activation with Bremsstrahlung from the Electron beam of the KURNS-LINAC. ^{61}Ni Mössbauer measurements were carried out conventional methods, since the half-life of ^{61}Co is about 100 minutes, about three hours measurements were done for one cycle. For one SCO compound sample, three times cycles are carried out in order to get suitable Mössbauer spectra. All spectra were obtained at 16 K. Ni-14at%V alloy was used for characterizations of velocities.

RESULTS: Fig. 1 and 2 show/ ^{61}Ni Mössbauer spectra of synthesized complexes. Which show singlet peak. The absorbance of these of Hofmann-type complexes is relatively low. This result can be explain that Hofmann-type structure is relatively soft structure. The obtained Mössbauer parameters have relationship with the square planar crystal field of $[Ni(CN)_4]_2$- units. The parameters for two SCO complexes are slightly different due to slightly different Ni(II) environments, indicating environments of Ni(II) ions are associated with those of Fe(II) ions.

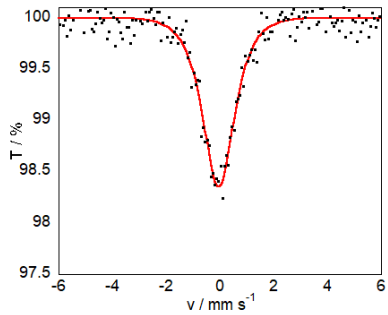

Fig. 1. ^{61}Ni Mössbauer Spectra for Fe(Ethyl Isonicotinate)$_2$Ni(CN)$_4$ (left)

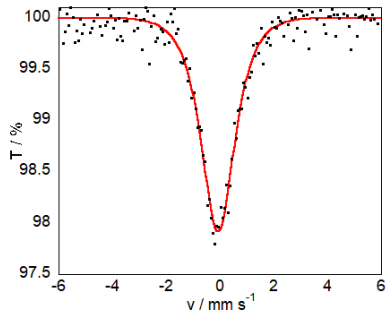

Fig. 2. ^{61}Ni Mössbauer Spectra for Fe(Allyl Isonicotinate)$_2$Ni(CN)$_4$.

REFERENCES:

[1] T. Kitazawa *et al.,* J. Mater. Chem., **6(1)** (1996) 119-121. (doi)10.1039/JM9960600119.
[2] T. Kitazawa, Crystals, **9(8)** (2019) 382. (doi)10.3390/cryst9080382.
[3] K. Kitase *et al.,* Dalton Trans., **52** (2023) 2571-2579. (Back Cover).
[4] K. Kitase *et al.,* Inorg. Chem., **60(7)** (2021) 4717-4722.
[5] K. Kitase and T. Kitazawa, Dalton. Trans., 49 (2020) 12210-12214. (Back Cover).
[6] M. Gábor *et al.,* Chem. Phys. Lett., **423(1-3)** (2006) 152-156.
[7] T. Kitazawa *et al.,* Mol. Cryst. Liq. Cryst. Sci Tech. A, **341**(2000) 527-532. (doi)10.1080/10587250008026193.
[8] T. Kitazawa *et al.,* J. Radioanal. Nucl. Chem., **239(2)** (1999) 285-290. (doi)10.1007/BF02349498.

PR3-7 Chemical species for precursor of supported gold cluster catalysts presumed from Recoil-free fraction in ^{197}Au Mössbauer spectroscopy

H. Ohashi, R. Tawatari, T. Fukae[1], H. Murayama[1], M. Tokunaga[1], Y. Kobayashi[2], S. Kitao[2]

Faculty of Symbiotic Systems Science, Fukushima University
[1]Faculty of Sciences, Kyushu University
[2]Institute for Integrated Radiation and Nuclear Science, Kyoto University

INTRODUCTION:

Though sulfide deposition-precipitation (SDP) method was a kind of new DP method, it was a very unique method and different from DP on several points such as preparation pH. However, until now, the structure of gold sulfide as a precursor synthesized by the SDP method was unknown. ^{197}Au Mössbauer spectroscopy is effective for obtaining information on the precursor.

In previous study, it was estimated that the Debye temperature derived from recoil-free fraction in ^{197}Au Mössbauer spectroscopy for the precursor of heterogeneous gold catalysts by SDP method. In this study, we presumed chemical species for precursor of supported gold cluster catalysts from Recoil-free fraction in ^{197}Au Mössbauer spectroscopy.

EXPERIMENTS:

Gold sulfide (Au_2S_x) and activated carbon supported gold sulfide (Au_2S_x/C) were synthesized by the similar SDP method already reported[1]. ^{197}Au Mössbauer spectra were measured at Kyoto University Research Institute of Nuclear Science. The ^{197}Pt isotope ($T_{1/2}$ = 18.3 h), γ-ray source feeding the 77.3 keV Mössbauer transition of ^{197}Au, was prepared by neutron irradiation of isotopically enriched ^{196}Pt metal at the Kyoto University Reactor. The measurement temperature was 14 - 20 K, and the measurement was performed by the transmission method.

RESULTS:

The ^{197}Au Mössbauer spectra for gold foil (standard) and precursor of supported gold cluster catalysts were measured. These spectra were normalized by the content of gold (n) in measured sample. Each area (A) of normalized spectrum was calculated. There is a following relationship between recoil-free fraction (f) and area;

$$f = a\,A/n \quad \text{(eq.1)}$$

where "a" is proportional constant in this measurement equipment.

No peaks were shown in ^{197}Au Mössbauer spectrum for Au_2S_x/C this time either. However, normal peaks for Au L_3 edge XAFS were obtained and EXAFS analysis showed the presence of S-Au-S chemical bonds.

Figure 1(a) shows a correlation diagram between the reciprocal of the molecular weight of the gold compound and the recoil-free fraction in the ^{197}Au Mössbauer spectrum presented by Parish [2]. Figure 1(b) shows the relationship between the ln$f$ of the prepared gold catalysts and the reciprocal of the molecular weight. ln$f$ was estimated from the area of ^{197}Au Mössbauer spectrum for each catalyst using the value of the constant "a" in eq (1) estimated in the previous report. Molecular weights were calculated from particle sizes estimated from EXAFS analysis. Comparing Fig.1(a) and (b), the tendency of the plots is similar, suggesting that eq (1) was generally satisfied. Spectral noise of the sample without Mössbauer absorption showed that ln$f$ was below -4.6, and the supported gold species was estimated to have a molecular weight of about 250 (Fig.1(b)). Therefore, this gold species was presumed to be an analogous complex of $[Au(SH)_2]^-$.

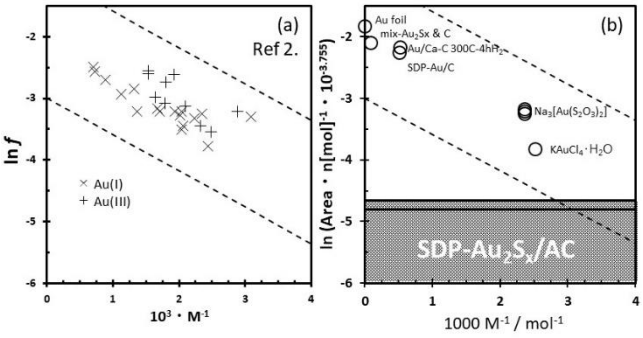

Fig.1.(a) Correlation diagram between the reciprocal of the molecular weight of the gold compound and the recoil-free fraction in the ^{197}Au Mössbauer spectrum [2]. (b) The relationship between the ln$f$ of the prepared gold catalysts and the reciprocal of the molecular weight.

REFERENCE:

[1] H. Ohashi *et al.,* "Method for dispersing and immobilizing gold fine particles and material obtained thereby", Patent No. 5010.

[2] R. V. Parish: in *Modern Inorganic chemistry* by Jolly, W. L, (McGraw-Hill College, 1984) 609-611.

PR3-8 Recoilless Fraction on ^{197}Au Mössbauer Spectroscopy (2)

Y. Kobayashi[1] and H. Ohashi[2]

[1]*Institute for Integrated Radiation and Nuclear Science, Kyoto University*

[2]*Faculty of Symbiotic Systems Science, Fukushima University*

INTRODUCTION: As a study of new materials, we are conducting Mössbauer spectroscopy of Au-supported cat-alysts. When studying the Au catalyst prepared by the calcination of Au compounds, the ratio of each component is important. In the Mössbauer spectra, the spectral ab-sorption area appears as the product of the component ratio of each state and the recoilless fraction. In the ^{57}Fe Mössbauer spectra, the difference in recoilless fraction due to the chemical form of Fe is not significant in most cases. However, in the ^{197}Au Mössbauer spectra, the recoilless fraction is known to differ between Au^{1+} and Au^{3+} [1]. In addition, it is considered that the recoilless fraction be-comes small when the Au metal becomes tiny particles [2]. As the basic data for Au Mössbauer measurements, we measured the absorption area of the spectra in multiple chemical states.

Measuring the absolute amount of the recoilless fraction is difficult due to the background fluctuations in the ^{197}Au Mössbauer measurement. Therefore, we investigated a method for estimating the Debye temperature from the temperature dependence of the spectral absorption inten-sity and confirmed its validity.

EXPERIMENTS: ^{197}Au Mössbauer measurement was conducted using a constant-acceleration spectrometer with a NaI scintillation counter. The ^{197}Au γ-ray source (77.3 keV) was obtained from ^{197}Pt (half-life; 18.3 hours) generated by neutron irradiation to 98%-enriched ^{196}Pt metal foil using KUR. The γ-ray source and samples were cooled to the same temperatures using a helium refrigerator. We prepared Au metal, $Au(OH)_3$ as Au^{3+} and Au_2S as Au^{1+} for measuring sample. The isomer shift value of a gold foil was referenced to 0 mm/s.

RESULTS: Figure 1 shows the Mössbauer spectra of Au_2S at each temperature. Although the counts of the respective spectra are different, the vertical axis ratio is the same. The absorption areas on the spectra decrease at higher temperatures, indicating that the recoilless fraction decreases. Figure 2 shows the temperature dependence of the absorption area on the Mössbauer spectra of each sample. The absorption areas are normalized by the value at 20K. The lines are the calculated value from the equation using each Debye temperature. The absorption areas are proportional to the product of the recoilless fraction of the γ-ray source and the absorber. The Debye temperature of the g-ray source is 270K, which is the Debye temperature of platinum metal.

The temperature dependences of the absorption areas of Au metal and $Au(OH)_3$ are almost the same and agree with the calculated value at the Debye temperature of 164K. 164K is the reported Debye temperature of Au metal. On the other hand, the absorption areas of Au_2S decrease at lower temperatures, which agrees with the calculated value at the Debye temperature of 100K. This result suggests that $Au(OH)_3$ and Au_2S significantly differ in lattice binding strength.

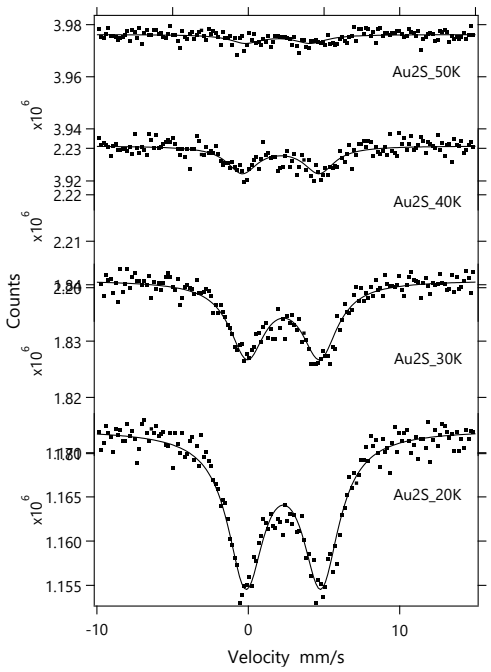

Fig. 1. Mössbauer spectra of Au_2S at each temperature. The ratio of the vertical axis is the same.

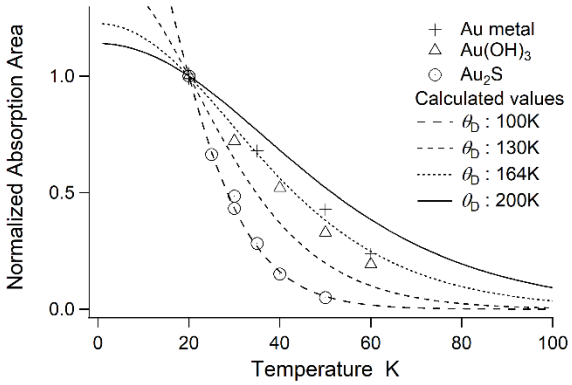

Fig. 2. Temperature dependence of the absorption area on the Mössbauer spectra. The markers are the observed ab-sorption areas (normalized by the value at 20K), and the lines are the calculated values.

REFERENCES:

[1] Jan Stanek, J. Chem. Phys., **76** (1982) 2315.

[2] M. P. A. Viegers and J. M. Trooster, Phys. Rev. B, **15** (1977) 72.

PR3-9 EuS property as the energy standard material at ^{151}Eu Mössbauer spectroscopy

R. Masuda, S. Kitao[1], Y. Kobayashi[1], M. Kurokuzu[1], T. Yamashita[1], and M. Seto[1]

Graduate School of Science and Technology, Hirosaki University
[1]Institute for Integrated Radiation and Nuclear Science, Kyoto University

INTRODUCTION: Mössbauer spectroscopy is usually known as a powerful method for the study of the microscopic state of iron in compounds through the nuclear probe of ^{57}Fe. Despite, there are many other elements the state of which in compounds we can study by Mössbauer spectroscopy. Europium is one of these elements for which we use ^{151}Eu as the probe nuclide. We usually use trifluoride, $^{151}SmF_3$, as the γ-ray source for ^{151}Eu Mössbauer spectroscopy; EuF_3, generated after the β decay of ^{151}Sm in SmF_3, is suitable for the chemical compound for the γ-ray source, because it satisfies almost all the following conditions: i) high recoilless fraction ii) no hyperfine splitting in relating nuclear levels, iii) stability in ambient condition, i.e., the 1 atm, around 300 K, and air atmosphere. Here, the structure of EuF_3 is orthorhombic *Pnma*, thus there might be room for improvement in condition ii), although it is usually sufficiently small in normal study. That is, if we use an alternative chemical specimen with higher symmetry in crystal structure, it might satisfy condition ii) further; that result in the narrow linewidth in instrumental function. In this experiment, we study cubic EuS (*Fm3̄m*) as a candidate for the alternative chemical specimen and measured the temperature dependence of ^{151}Eu Mössbauer spectra to compare the suitability of the specimen as a Mössbauer source.

EXPERIMENTS: The sample was non-enriched EuS purchased from Kojundo Chemical Laboratory Co. Ltd. The purity was 99.9% in the specification sheet. The sample was shaped to the pellet with the cross section of 10 mmφ and the thickness of 43.7 mg EuS/cm^2. The sample was cooled down by a cryostat using Liquid N_2 as the coolant. The Mössbauer spectroscopy was performed at Tracer Laboratory at KURNS. The γ-ray source was $^{151}SmF_3$ at room temperature and the transmitted γ-rays after the EuS sample was detected by Xe proportional counter.

RESULTS: Fig. 1 shows the typical ^{151}Eu Mössbauer spectra of the sample. We can clearly see the signal of EuS as a single-line absorption around the velocity of + 12 mm/s, which indicates Eu^{2+} state in EuS. However, we can also see the other component around +0.7 mm/s, which indicates Eu^{3+} state in this minor component. The area ratio of the minor component is around 15%. We note that the experimental center shift agrees with that of Eu_3S_4 in the literature [1].

Now we focused on the main EuS component. The temperature dependence of the area ratio of the spectra normalized by that at room temperature is shown in Fig. 2. The ratio increased as the temperature of the sample decreased. Because no phase transition is known for EuS between 78 K and room temperature, this change should be due to the recoilless fraction. To estimate the upper limit of the fraction, we estimated the Mössbauer characteristic temperature using the Debye model, ignoring the saturation of the area ratio to the fraction, and obtained that the characteristic temperature is less than 250 K, which corresponds to the recoilless fraction less than 0.544 at room temperature. In the case of this recoilless fraction, the spectral linewidth with the thinnest EuS sample is 1.4 mm/s, which is narrower than the typical experimental linewidth of EuF_3 in ref. 1; that is, EuS might satisfy condition ii) more. Here, we should note that the characteristic temperature of EuF_3 is 283 K [2], and thus the condition i) is less satisfied at EuS.

In summary, EuS might be better than EuF_3 in linewidth, but worse in the recoilless fraction. We will explore further suitable chemical specimens.

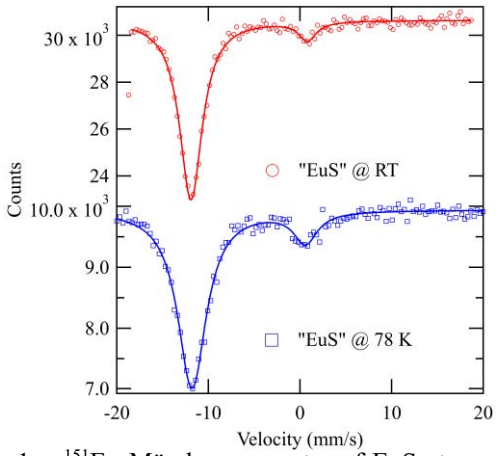

Fig. 1. ^{151}Eu Mössbauer spectra of EuS at room temperature and 78 K.

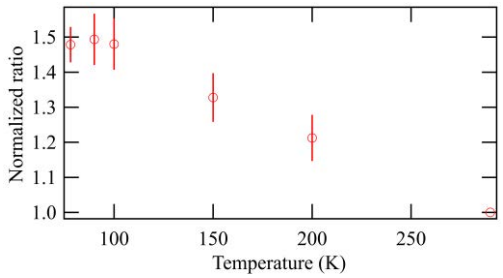

Fig. 2. Temperature dependence of the EuS component in Mössbauer spectra, normalized by that at room temperature.

REFERENCES:

[1] E. R. Bauminger *et al.*, in Mössbauer Isomer Shifts edited by G. K. Shenoy and F. E. Wagner, (North-Holland, Amsterdam, 1978).
[2] C. I. Wynter *et al.*, Hyperfine Interact. **166** (2005) 499-503.

PR3-10 Development of ^{119}Sn Mössbauer Source

S. Kitao[1], Y. Kobayashi[1], M. Kurokuzu[1], T. Kubota[2], H. Tajima[3], H. Yamashita[3], H. Ota[3], R. Masuda[4], and M. Seto[1]

[1]*Institute for Integrated Radiation and Nuclear Science, Kyoto University (KURNS)*

[2]*Agency for Health, Safety, and Environment, Kyoto University*

[3]*Graduate School of Science, Kyoto University*

[4]*Faculty of Science and Technology, Hirosaki University*

INTRODUCTION:

The Mössbauer spectroscopy is one of the most powerful methods to investigate electronic states and magnetic properties by extracting the information of a specific isotope[1]. Mössbauer spectroscopy in general is performed for quite limited isotopes, such as ^{57}Fe and ^{119}Sn. This is partly because only ^{57}Co source for ^{57}Fe and ^{119m}Sn source for ^{119}Sn are commercially available at present. On the contrary, the neutron irradiation facility at Kyoto University Reactor (KUR) at KURNS can be used to product various radioactive isotopes(RIs) for the Mössbauer sources. Moreover, some RIs can be complementarily produced by high-energy γ-ray irradiation converted from electron beam from the electron linear accelerator (KURNS-LINAC). We have been developing practical methods for Mössbauer spectroscopy for various isotopes. Available Mössbauer isotopes at present are as follows (source nuclides in parentheses): ^{61}Ni(^{61}Co), ^{125}Te(^{125m}Te), ^{129}I(^{129}Te,^{129m}Te), ^{161}Dy(^{161}Tb), ^{166}Er(^{166}Ho), ^{169}Tm(^{169}Er), ^{170}Yb(^{170}Tm), ^{197}Au(^{197}Pt), etc.

Although the ^{57}Co and ^{119m}Sn sources are commercially available, it becomes important to produce these sources by ourselves, because these sources are mainly produced in Russia and the international affairs concerning Russia is unstable recently. Therefore, we have been developing a practical production method of ^{57}Co and ^{119m}Sn Mössbauer sources using KUR and KURNS-LINAC.

In this report, an attempt for ^{119m}Sn source production for ^{119}Sn Mössbauer spectroscopy is described. The ^{119m}Sn with a half-life of 293.1 d can be produced by long-term neutron irradiation of ^{118}Sn. As a source material, several compounds are practically used, but degradation by some radiation damage of these compounds by neutron irradiation is unclear. It is necessary to establish a practical production method suitable for the facility at KURNS.

EXPERIMENTS AND RESULTS:

Among several source materials, an attempt with a typical source material, $CaSnO_3$ was studied. The neutron irradiation was performed at long-term irradiation plug of KUR nominally for 12 weeks, which has a net irradiation time of 425 h for 1 MW operation and 84 h for 5 MW operation. Since a natural Sn contains ^{118}Sn with an abundance of 24.23 %, natural Sn was used for this experiment. The $CaSnO_3$ powder was pelletized with Al powder. In order to reduce shorter lived by-product RIs, the irradiated source has used after waiting for a few months from the end of irradiation. The obtained nominal activity of ^{119m}Sn by using 100 mg of Sn was about 880 kBq after 1 month waiting. Since natural Sn contains a number of stable isotopes, several by-product RIs were produced with the neutron irradiation. Short-lived by-products such as ^{117m}Sn with a half-life of 13.6 d, ^{125}Sn with 9.6 d were reduced by waiting for a few months. However, some long-lived by-products such as ^{113}Sn with 115.1 d, ^{123}Sn with 129.2 d remained. Even though these long-lived RIs remained, the Mössbauer γ-rays with the energy of 23.9 keV from ^{119m}Sn can be separated from the γ-rays from other radioactive by-products. The main concern is how to separate Sn KX-rays with energies of around 25 keV to improve measurement efficiency, which cannot separate well by proportional counters or scintillation counters.

Figure 1 shows ^{119}Sn-Mössbauer spectrum of $BaSnO_3$ absorber using obtained $CaSnO_3$ source. The Mössbauer sources are required to be a single-line spectrum with a narrow linewidth. However, the spectrum of irradiated $CaSnO_3$ has not showed a single-line shape. It is possibly because the radiation effect in the $CaSnO_3$ occurs in the irradiated sample and different electronic states appeared in the spectrum. The experiment shows the natural Sn can be used to produce ^{119m}Sn RI source. The radioactive effect from other by-product RIs was not crucial. However, the source material for irradiation and the production method needs to be improved.

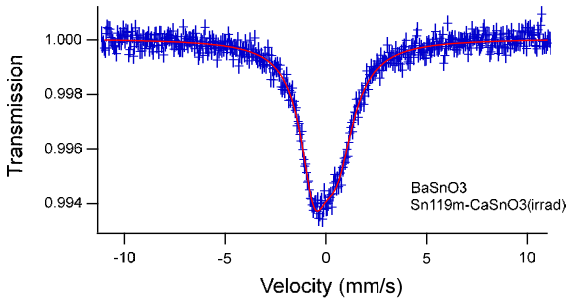

Fig. 1. ^{119}Sn-Mössbauer spectrum of $BaSnO_3$ using ^{119m}Sn source in $CaSnO_3$ at room temperature.

In summary, it is confirmed that ^{119}Sn Mössbauer spectroscopy can be performed by a ^{119m}Sn source obtained by neutron irradiation of natural Sn. However, further improvement of the source material and measurement efficiency must be required for a practical spectroscopy.

REFERENCES:

[1] "Mössbauer Spectroscopy" N. N. Greenwood and T. C. Gibb (Chapman and Hall, London, 1971).

I-1. PROJECT RESEARCHES

Project 4

PR4 Preclinical studies for appling BNCT to veterinary medicine

M. Suzuki

Institute for Integrated Radiation and Nuclear Science, Kyoto University

Recently, a concept of "One health" is considered important. The concept is a collaborative, multisectional, and transdisciplinary approach – working at the local, regional, national, and global levels – with the goal of achieving optimal health outcomes recognizing the interconnection between people, animals, plants, and their shared environment. Due to the commonality of human and animal disease collaboration between medicine and veterinary medicine will improve the heath of both.

In 2020, accelerator-based boron neutron capture therapy (BNCT) for head and neck cancer using was approved by Japanese Ministry of Health, Labor, and Welfare. At two medical institutes, BNCT for head and neck cancer has started under the insurance coverage. Common malignancy encountered in companion animals include head and neck cancer of the dog. BNCT group in Argentina reported the results of BNCT for head and neck cancers in dogs using a research reactor. In Japan, human head and neck cancers have been treated with BNCT as mentioned above. Considering these circumstances, this project was planned to obtain scientific evidence for the adaptation of BNCT to veterinary medicine.

In this research project, six research projects were included. The four researches were planned by veterinarians. Unfortunately, two researches were not carried out. Details of four projects are referred to each progress report. I hope that this project will arouse much interest in BNCT among veterinarians.

P4-1: The Basic Study Aimed at Performing the Boron Neutron Capture Therapy for Canine Osteosarcoma.

In this project, to investigate the possibility of applying BNCT to canine osteosarcoma, LAT-1 expression in canine osteosarcoma cell lines were examined, and the amount of intracellular boron using the BPA was measured. By Western blotting, LAT1 proteins in two osteosarcoma cell lines, POS and HMPOS, were found at approximately the same levels of LMeC and CMec-1 which were canine malignant melanoma and used as a positive control. By incubation with BPA at the concentration of 14, 28, 57 ppm, there were dose-dependent increase in ^{10}B uptake in both osteosarcoma cell lines. These results indicate that BNCT can be applied to canine osteosarcoma.

P4-2: Caninization of Anti BSH Antibody Prepared from Rabbit Lymphocytes

In this study, the complimentary-determining regions (CDRs), which are BSH-binding sequences, from rabbit anti-BSH antibody was identified. A canine anti-BSH antibody was prepared by replacing the regions other than the CDRs with canine sequences.

P4-3: Antibody conjugated BNNT/β-1,3-glucan complex as a boron agent for BNCT.

In this study, as a new boron agent, HER-2 recognizing antibody modified boron nitride nanotube/β-1,3-glucan complex was investigated. In addition, for the conjugation of antibody, protein A mimicking ligand molecules (PAM) were introduced to BGL (PAM-BGL). Conjugation of HER-2 recognizing antibody enhanced cellular uptake of BNNT/BGL in human ovarian cancer cells (SK-OV3 cell). This new novel boron agent has possibility to be applicable for BNCT.

P4-4: Investigation of the relationship between the therapeutic efficacy of boron neutron capture therapy and the persistence of boron in tumors.

In this study, the effect of tumor tissue diversity (stromal volume and blood flow distribution) on BPA residence time and the antitumor effect of BNCT. Two human pancreatic carcinoma cells, Capan-1 containing high stroma and PSN-1 containing low stroma, were used. Accumulation of BPA in the Capan-1 was lower than that in the PSN-1. However, in the preliminary in vivo BNCT study, the same anti-tumor effects were observed in both Capan-1 and PSN-1 tumors. These results may indicate that low boron concentration in the tumor with high stroma has been successfully treated with BNCT. In the further study, using the canine or feline tumor cells with high stroma, relationship between boron accumulation and anti-tumor effect will be investigated.

PR4-1 The Basic Study Aimed at Performing the Boron Neutron Capture Therapy for Canine Osteosarcoma

R. Iwasaki, R. Yoshikawa, T. Mori, Y. Sakurai[1] and M. Suzuki[1]

Faculty of Applied Biological Sciences, Gifu University
[1]Institute for Integrated Radiation and Nuclear Science, Kyoto University

INTRODUCTION:

Canine osteosarcoma, which commonly occurs in the extremities, is generally treated with leg amputation followed by the postoperative adjuvant chemotherapy. On the other hand, if surgery is not performed due to comorbidities, distant metastases, or the owner's wishes, radiation therapy can also be a treatment option. However, osteosarcoma is generally resistant to X-rays and carries the risk of damaging surrounding normal tissue for tumor control.

Boron neutron capture therapy (BNCT) is a therapeutic method that selectively destroys the tumor while leaving normal tissues almost unharmed by utilizing the nuclear reaction with neutron and boron, which tends to accumulate in the cancer cells. In human, LAT1, an amino acid transporter that has been found to be particularly involved in the intracellular transport of boron compound, is shown to be overexpressed in many malignant tumor cells.

In this study project, we investigated the possibility of applying BNCT to canine osteosarcoma by examining LAT1 expression in canine osteosarcoma cell lines and by measuring the amount of intracellular boron when using the BPA as boron compound.

EXPERIMENTS: Two cell lines derived from canine osteosarcoma, POS and HMPOS, were used for this study. As boron compound, p-boronophenylalanine (BPA) was prepared at a dose of 30 mg/ml.

Western blotting Cultured cells were collected and lysed with RIPA lysis buffer. After measuring the concentration with Lowry assay, 15 µg/lane of proteins were separated by SDS-PAGE for 70 min. Proteins were transferred onto the PVDF membrane and probed with LAT1 antibody overnight. After being probed with HRP-linked secondary antibodies, bound antibodies were detected with Immobilon Forte Western HRP substrate (EMD Millipore). Two cell lines of LMeC and CMeM-1 derived from canine malignant melanoma and anti-β-actin mouse monoclonal antibody were used as positive and loading control, respectively.

Inductively coupled plasma atomic emission spectrometry (ICP-AES) 1×10^6 cells of POS and HMPOS were co-incubated with BPA for 0.5, 1, 2 and 4 h. The boron-10 (^{10}B) concentrations in BPA solution were adjusted with culture medium to 14, 28 or 57 ppm, respectively. Each sample was digested by heating overnight in nitric acid (60%), then diluted with distilled water and divided into three test tubes. After measuring the boron concentration in these tubes using ULTIMA2 (HORIBA, Ltd., Kyoto, Japan), their average was taken as the amount of the sample and expressed in "ng ^{10}B / 10^6 cells."

RESULTS: Fig. 1 shows the LAT1 expressions in POS and HMPOS by the Western blotting. In both cell lines, LAT1 proteins were found at approximately the same levels of LMeC and CMeC-1.

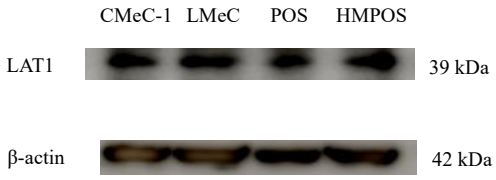

Fig. 1. Expression assessment of LAT1 protein in canine osteosarcoma cell lines of POS and HMPOS by Western blotting.

Fig. 2 shows the intracellular ^{10}B uptake measured by the ICP-AES. In both cell lines, ^{10}B concentrations decreased gradually by increasing the co-incubation time with low concentrations of BPA (14 ppm). On the other hand, co-incubation with BPA at 28 and 57 ppm had little time-dependent changes in^{10}B uptake. Furthermore, by incubation with BPA for 2 h and 4 h, there were dose-dependent increases in ^{10}B uptake in both cell lines.

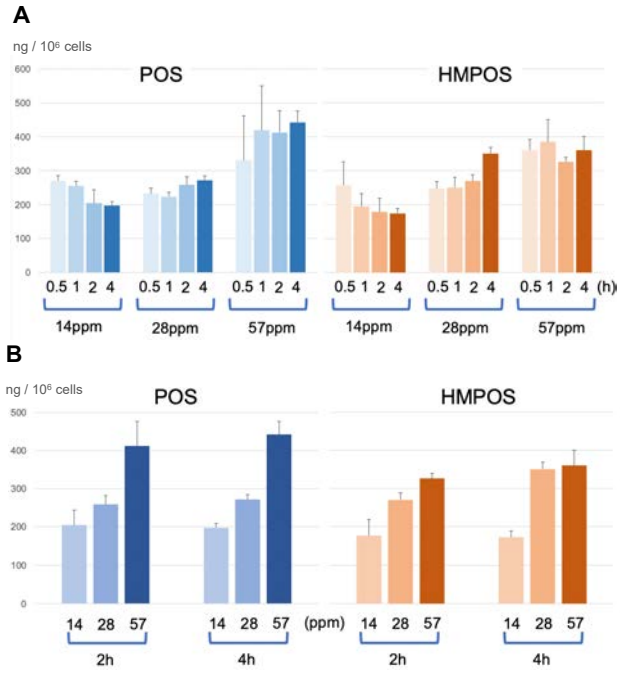

Fig. 2. Intracellular ^{10}B concentrations in POS and HMPOS by ICP-AES. (A) and (B) show the amount of ^{10}B in each cell line by BPA co-incubation time and the concentration, respectively.

CONCLUSION: Our results indicate that BNCT can be applied to canine osteosarcoma because the sufficient amount of ^{10}B uptake was confirmed in this study. It is necessary to perform the *in vitro* or *in vivo* irradiation assessment compared with X-ray and neutron beam without BPA to verify the anti-tumor effect considering the current results.

PR4-2 Caninization of Anti BSH Antibody Prepared from Rabbit Lymphocytes

N. Ueda, N. Yasukawa, R. Kawasaki[1], Y. Sakurai[2], H. Tanaka[2], Y. Sanada[2], N. Kondo[2], M. Suzuki[2], and T. Nagasaki

Graduate School of Engineering, Osaka Metropolitan University
[1] Graduate School of Advanced Science and Engineering, Hiroshima University
[2]Institute for Integrated Radiation and Nuclear Science, Kyoto University

INTRODUCTION: Recently, tumor diseases have increased in dogs as they have aged due to the development of veterinary medicine and therapy [1]. However, 30% of the causes of death are malignant tumors. Three major therapies such as surgical treatment, drug therapy, and radiation therapy, are used, but in many cases, there are limitations due to the burden on the dog's body, side effects, and therapeutic effects. Boron neutron capture therapy (BNCT) is expected as a new therapeutic strategy [2].

One of the boron agents used in BNCT is BSH. BSH is a boron cluster with a unique icosahedral structure, with twelve ^{10}B atoms per molecule. It has also the advantage on extremely high water-solubility and low toxicity.

In our previous research, rabbit anti-BSH antibody have been prepared [3]. In this study, we identified the complementarity-determining regions (CDRs), which are BSH-binding sequences, from this antibody, and prepared a canine anti-BSH antibody (caBSH IgG) by replacing the regions other than the CDRs with canine sequences.

EXPERIMENTS: We identified the CDRs from the rabbit anti-BSH antibody, and synthesized DNA by caninizing the other sequences. Using canonized DNA sequences, the antibody gene was amplified by PCR. Antibody genes were incorporated into plasmids by restriction enzyme treatment and ligation to construct caninized anti-BSH heavy and light chain expression vectors. A caninized anti-BSH antibody (caBSH IgG) was prepared by co-transfecting heavy and light chain expression vectors into Chinese hamster ovary-derived ExpiCHO cells. After seven days culture, the supernatant was purified using a protein A column and analyzed by SDS-PAGE.

An antigen (BSH-modified BSA) was immobilized, and ELISA was performed using an HRP-labeled secondary antibody to evaluate the antigen-binding ability of the produced antibody.

RESULTS: caBSH IgG was purified from the culture supernatant using a protein A column. As a result of SDS-PAGE analysis, although the purity was low, bands at approximately 27 kDa (light chain) and approximately 50 kDa (heavy chain) were detected, confirming that the caninized anti-BSH antibody (caBSH IgG) had been successfully produced. In addition, it was found that the antibody production amount per 1 L of medium was 0.94 mg, which was very low efficiency. It is necessary to improve the production efficiency in order to use caBSH IgG *in vivo* experiments in the future.

As shown in Fig. 1, when the antibody prepared were analyzed by ELISA, the absorbance at 450 nm increased with increasing antibody concentration. Therefore, caBSH IgG is considered to have the ability to bind to BSH.

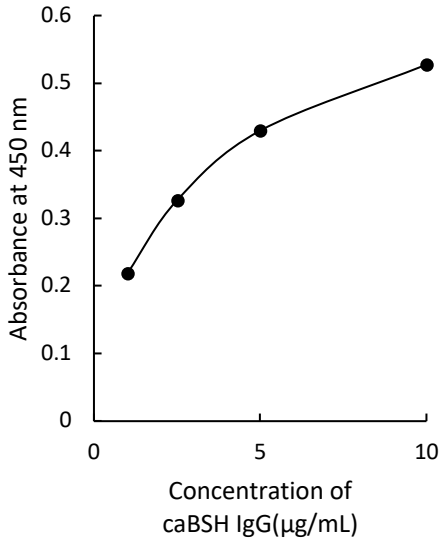

Fig. 1. Evaluation of antigen binding ability of caBSH IgG using ELISA.

In the future, we aim to improve the expression efficiency of caBSH IgG and also attempt to prepare a chimerized anti-BSH antibody that is expected to have high expression efficiency. After success of developing a mass production system for canine or chimerized antibodies, bispecific antibodies with cancer antigen Her2 will be created and evaluated as canine BNCT drugs.

REFERENCES:

[1] F. Cavallo *et al*., Can. Immunol. Immunother., **64** (2015) 137-148.
[2] A. E. Schwint *et al*., Biol., **9** (2000) 327.
[3] unpublished data.

PR4-3 Antibody conjugated BNNT/β-1,3-glucan complex as a boron agent for BNCT

K. Yamana,[1] R. Kawasaki,[1] K. Kondo,[1] H. Hirano,[1] S. Kawamura,[1] Y. Sanada,[2] K. Bando,[3] A. Tabata,[3] H. Azuma,[3] T. Takata,[2] Y. Sakurai,[2] H. Tanaka,[2] T. Nagasaki,[3] and A. Ikeda[1]

[1]*Applied Chemistry Program, Graduate School of Advanced Science and Engineering, Hiroshima University*
[2] *Institute for Integrated Radiation and Nuclear Science, Kyoto University*
[3]*Department of Chemistry and Bioengineering, Graduate School of Engineering, Osaka Metropolitan University*

INTRODUCTION: With high specificity and strong affinity, antibodies are powerful means to endow nanomaterials with targeting properties. For instance, antibody-drug complexes, which are covalently conjugated with strong toxin such as auristatin E are clinically available anti-cancer agents due to their therapeutic benefits. However, there are several issues in delivery including limitation in loading moieties, linker stability, and leakage of drugs, which can lead undesirable severe side effects on patients. For these points of views, combination of antibody with noninvasive modalities are ideal in achieving cancer therapy. Today, photodynamic immunotherapy, which is achieved by antibody conjugated photosensitizers, enabled to kill cancer cells without any harmful side effects. Here, photodynamic therapy requires several days-incubation under dark condition to avoid side effect, that is known as photosensitivity, after treatment. Here, boron neutron capture therapy (BNCT), which is achieved by nucleic reaction between boron atom and thermal neutron, is more noninvasive because boron atom does not affect on cell viability.

In this study, we demonstrated HER-2 targeted BNCT using HER-2 recognizing antibody modified boron nitride nanotube/β-1,3-glucan complex (BNNT/BGL complex, Figure 1). BNNT has been expected as a boron agent with one-dimensional morphology and large boron content in each nanorod and β-1,3-glucan is a polysaccharide with one-dimensional morphology comprising triple helix structure, which enables to trap hydrophobic compounds within their cavity. Previously, we reported facile preparation method using mechanochemical approaches for water dispersible inclusion complex of carbon nanotube, which is structural analogue of BNNT, with BGL without forming precipitate in aqueous media [1]. These advantages encouraged us to develop water dispersible BNNT/BGL complex as a boron agent for BNCT.

RESULTS: BNNT/BGL complex was prepared by high-speed vibration milling, which is based on mechanochemical approach, and the resulting mixture was extracted with water. The morphology of the complex obtained were observed by transmission electron microscopy. In case of without staining condition, bundle like structure of BNNT were found and their length were less than 200 nm, which is corresponding to the size for enhanced permeation and retention effect. In this work, we synthesized protein A mimicking ligand molecules (PAM) for the conjugation of antibody because mechanochemical system can disrupt conventional crosslinker for the modification of proteins including alkyne *via* click reaction and maleimide *via* Michael addition. The PAM were introduced to BGL (PAM-BGL). After preparation of BNNT/PAM-BGL complex, HER-2 recognizing antibodies were introduced *via* molecular recognition of PAM. We next investigated HER-2 selective BNCT activity of HER-2 antibody conjugated BNNT/PAM-BGL complex *in vitro*. Here, we employed human ovarian cancer cells (SK-OV3 cell) as HER-2 overexpressed cell line. Conjugation of HER-2 recognizing antibody enhanced cellular uptake of BNNT/BGL. Moreover, pre-treatment with anti HER-2 antibody could suppress the cellular uptake amount of boron agent. These results clearly indicate that the modified antibody work as pilot molecules for cancer targeting. The targeting properties in tumor accumulation could enhance BNCT activity toward SK-OV3 cells and the activity using HER-2 antibody conjugated BNNT/PAM-BGL complex was much higher than that using commercially available boron agent, L-BPA. These results clearly indicate that current system is potentially applicable for BNCT.

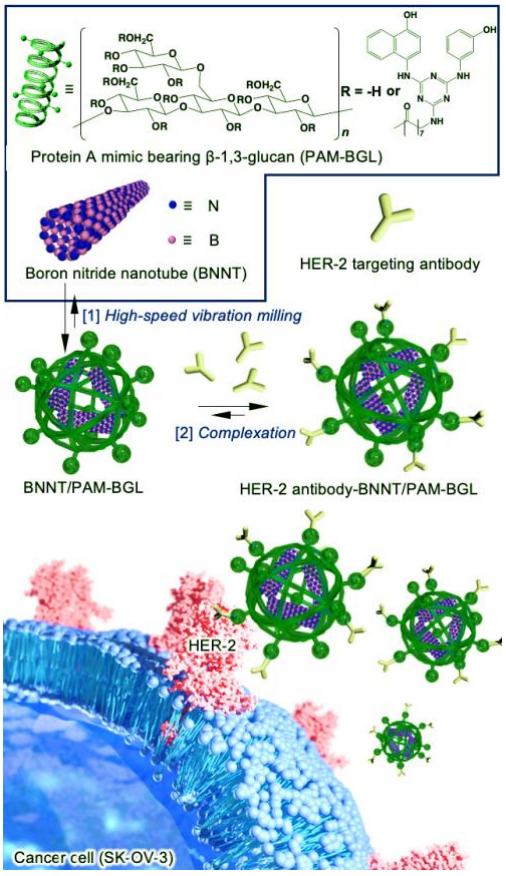

Fig. 1. BNCT using BNNT/BGL complex

REFERENCES:

[1] A. Ikeda *et al.,* Chem. Commun., **11** (2004) 1334-1335.

PR4-4 Investigation of the relationship between the therapeutic efficacy of boron neutron capture therapy and the persistence of boron in tumors

Y. Wada[1,2] and M. Suzuki[2].

[1] *Veterinary Medical Center, Osaka Prefecture University*

[2] *Particle Radiation Oncology Research Center, Institute for Integrated Radiation and Nuclear Science, Kyoto University*

Introduction

When BNCT is performed, the decision on the indication for BNCT depends on the ratio of tumor uptake of 18FBPA to normal tissue (T/N ratio) in 18F-BPA-PET scans. However, it has recently been reported that prolonged residence time of BPA in tumors contributes to improved therapeutic efficacy of BNCT.[1)] Therefore, BPA uptake alone may not be sufficient to predict therapeutic efficacy. Therefore, in this study, we investigate the effects of tumor tissue diversity (stromal volume and blood flow distribution) on BPA residence time and the antitumor effect of BNCT.

Experiments

Tumor-bearing mice: we used pancreatic carcinoma cells with high stroma (Capan-1) and pancreatic carcinoma cells with low stroma (PSN-1). Each cell was inoculated in the thigh of a nude mouse and used in the experiment when it reached a certain size.

Measurement of boron concentration in tumor tissue: 250 ng/kg of BPA was administered subcutaneously to the mice created, and tissue was sampled at regular intervals after administration, and the amount of BPA uptake was measured by ICP-AES.

Evaluation of the effect of BNCT on tumor growth inhibition: 250 ng/kg of BPA was administered subcutaneously to the mice, and the tumor volume was measured periodically by neutron irradiation at 1 hour after the administration.

Result

The changes of the boron concentration in the tumor tissue periodically after BPA administration are shown in Fig. 1.

Capan-1 and PSN-1 inoculated mice were performed BNCT and the subsequent changes in tumor volume are shown in Fig. 2. Tumor growth of both cell lines tended to be suppressed in the BNCT group.

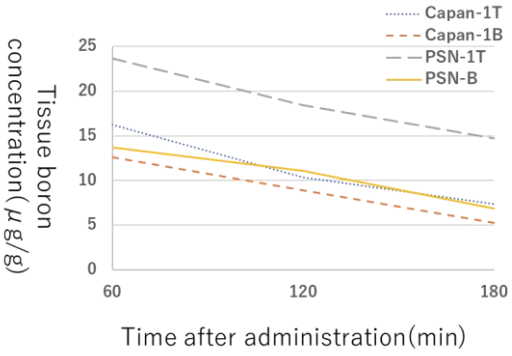

Fig.1. The boron concentration in the tumor tissue after BPA administration.

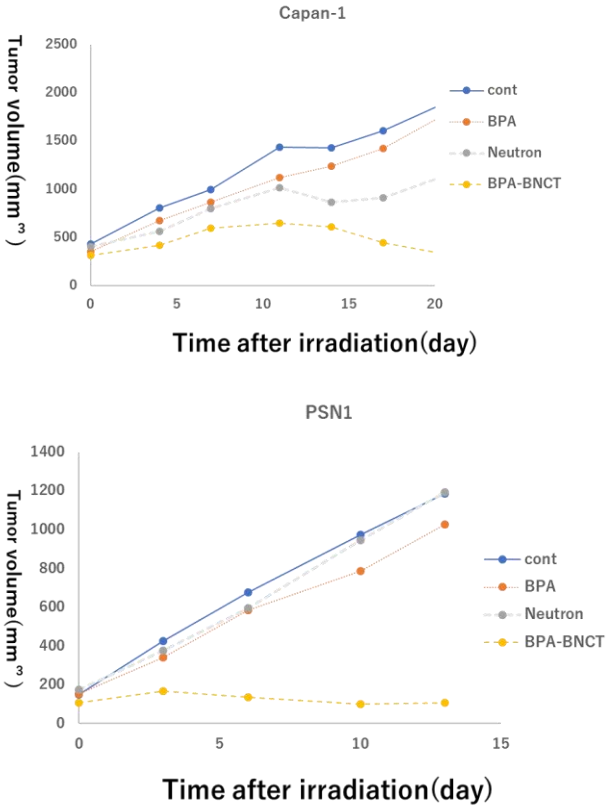

Fig.2. Growth curve of subcutaneous implantation tumor volume.

Reference

[1] T. Nomoto *et al.*, Sci Adv., **6** (2020).

I-1. PROJECT RESEARCHES

Project 5

PR5 The effect of BNCT on normal tissues

M. Suzuki

Institute for Integrated Radiation and Nuclear Science, Kyoto University

In 2020, accelerator-based boron neutron capture therapy (BNCT) for head and neck cancer was approved by Japanese Ministry of Health, Labor, and Welfare. At two medical institutes, BNCT for head and neck cancer has been started under the insurance coverage.

At Institute for Integrated Radiation and Nuclear Science, Kyoto University (KURNS), BNCT for body trunk tumors such as malignant pleural mesothelioma, liver tumors, and breast cancers had been carried out using Kyoto University Research Reactor (KUR) until 2019. These malignancies will be expected to be treated with accelerator-based BNCT in the medical institutes. For planning clinical trials of BNCT, the preclinical studies are very important. Especially the scientific findings on safety of BNCT are indispensable for first-in-men clinical trials. Therefore, I have started this project investigating the effect of BNCT on normal tissues or organs. Unfortunately, due to shortening of operation of KUR in 2022, three of six researches were not carried out. Details of three projects are referred to each progress report. I hope that this project will arouse much interest in BNCT researchers and shed new light on radiation biology.

P5-3: Phenotypic Change of Macrophage/Microglia in the Brain after BNCT.

Glioblastoma (GBM) had been treated with BNCT using Kyoto University Research Reactor (KUR) until 2019. With BNCT, better control and survival benefit was achieved. However, adverse effects such as brain edema or brain necrosis may sometimes occur after BNCT. It is known that microglia and macrophages change phenotype to control the inflammation in brain. Typically, M1type is known to induce inflammation and M2 type is known to reduce inflammation in tissue repair.

In this study, the phenotypic change of microglia/macrophage after BNCT in the surrounding normal brain in glioma baring mice. At 2 days after BNCT, M1 marker tended to increase compared to non-irradiated control. At 8 days after BNCT, M2 marker tended to increase compared to non-irradiated control.

P5-4: The effect of boron neutron capture therapy (BNCT) on esophagus in mice

Boron neutron capture irradiation (BNCR) using boronophenylalanine (BPA) to whole thorax of mice induced severe weight loss and death within one week when irradiation time was over 20 minutes. We speculated the cause of the severe acute adverse events was ascribed to the damage of esophagus. According to the report investigating the effect on esophagus by X-ray irradiation, we examined the change of numbers of basal cells in esophageal membrane. The number of basal cells was lowest at 7 days after BNCR to the whole thorax. In further experiments, the number of the basal cells at 7 days after various treatment will be compared to investigate the effect of BNCT on esophagus.

P5-6: The Influence of Boron Neutron Capture Therapy on Bone Grow in Young Mice.

According to the experiment performed in this project last year, the tibial growth in the young mice was slightly suppressed in the higher dose of boron neutron capture irradiation (BNCR) using BPA. In this year, the pathological analysis was carried out to elucidate the morphological change of bones in young mice at 3 months after BNCR.

The tibias were collected from the mice of the following the four cohorts, Control (no irradiation), X-ray irradiation, Neutron irradiation, and BNCR. Histological changes in the tibias in the young mice after BNCR were less than dose in the X-ray group.

PR5-1 Phenotypic Change of Macrophage/Microglia in the Brain after BNCT

N. Kondo[1], Y. Sakurai[1] T. Takata[1] and M. Suzuki[1]

[1] *Institute for Integrated Radiation and Nuclear Science, Kyoto University (KURNS)*

INTRODUCTION: Boron Neutron Capture Therapy (BNCT) have been applied to recurrent malignant glioma and even after standard therapy (surgery, chemo-radiation therapy) because of the selective damage to the tumor. Especially, glioblastoma (GBM) is the most miserable cancer, whose patient survival is 14.6 months and remarkably resistant to chemo-radiation and immunotherapy. With BNCT, we achieved better local control and survival benefit in malignant glioma using thermal neutrons produced by the reactor in Kyoto University. However, adverse effects (brain edema or brain necrosis, *etc*) may sometimes occur after BNCT. Microglia and macrophages change phenotype to control the inflammation in brain. Typically, M1 type is known to induce inflammation and M2 type is known to reduce inflammation in tissue repair. In this study, we examined the phenotypic change of microglia/ macrophage after BNCT in the surrounding normal brain in glioma bearing mice.

EXPERIMENTS: We implanted $2x10^5$ GL261 murine glioma cells in the C57BL/6 mouse brain stereotactically after anesthsia. About two weeks later, we administrated 500mg/kg of boronophenylalanine (BPA) subcutaneously and irradiated thermal neutrons to mouse brain in the Heavy Water Neutron Irradiation Facility of the KUR.

We collected brains with time course (2, 8, and 14 days) after BNCT and fixed them in 10 % formalin, replaced with 10 to 20 % sucrose and kept samples in deep freezer.

We immune-stained the thin-sliced tissue with M1 (iNOS: inducible nitric oxide synthase) and M2 (CD206, Macrophage mannose receptor 1) markers.

RESULTS: We showed the tissue of non-irradiated control and 2days after BNCT stained with M1 marker in fig. 1A and B respectively. After 2 days, M1 marker tended to increase compared to non-irradiated control.

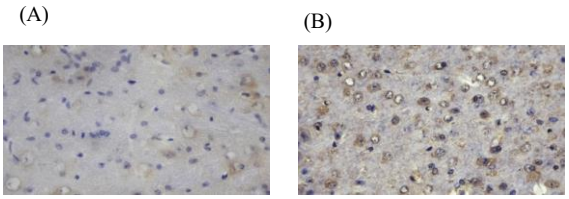

Fig.1. Typical immunostaining of brain tissue with M1 marker, iNOS in non-irradiated control (A) and 2 days after BNCT (B) .

Next, we showed the tissue of non-irradiated control and 8 days after BNCT stained with M2 marker in fig. 2A and B respectively. After 8 days, M2 marker tended to increase compared to non-irradiated control.

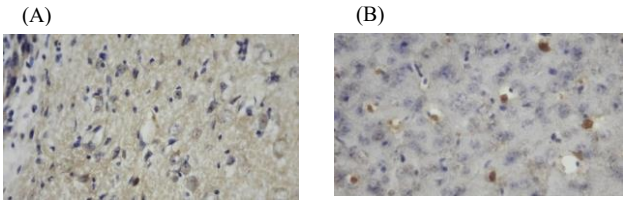

Fig. 2. Typical immunostaining of brain tissue with M2 marker, CD206 in non-irradiated control (A) and 8 days after BNCT (B) .

We will continue to immune-staining of these samples till we obtain enough numbers of samples.

PR5-2 The effect of boron neutron capture therapy (BNCT) on esophagus in mice

M. Suzuki, H. Tanaka, Y. Sakurai, T. Takata
Institute for Integrated Radiation and Nuclear Science Kyoto University

INTRODUCTION: In 2020, accelerator-based boron neutron capture therapy for head and neck cancer was approved by Japanese Ministry of Health, Labor, and Welfare. At two medical institutes, BNCT for head and neck cancer has started under the insurance coverage.

For BNCT to be applied to other malignancies such as lung cancer or liver cancers, the effect of BNCT on normal tissues should be investigated. To investigate the effect of BNCT on lung tissues, we performed boron neutron capture irradiation (BNCR) to whole thorax of mice using boronophenylalanine (BPA) as a boron compound. In the cohort of mice irradiated for 30-m BNCR, all the mice were dead within 7 days after the irradiation. No apparent abnormality was observed in the extracted lungs from the dead mice.

We speculated that cause of death would be acute side effect of the esophagus since esophagitis is known to acute side effect in radiotherapy for lung cancer or esophageal cancer. Ando et al. reported the effect of X-ray irradiation on cell kinetics of esophageal membrane cells in mice. According to this report, numbers of basal cell decreased up to 4 days after the irradiation, then rapidly increased. With reference to this report, we investigated the effect of BNCT on esophagus using mice.

EXPERIMENTS:

Mice

Ten- to twelve-week-old female C3H/He mice were used. The mice were purchased from Japan SLC, Inc.

BNCR and measurement of thermal neutron and γ-ray

In this study, BPA was administered subcutaneously at the dose of 500 mg/kg before the whole thorax irradiation. At the each BNCR, three mice were held within a specially designed acrylic box. LiF plates (5-mm thick) were used to shield the whole body except for chest.

Neutron fluences were measured by radio activation of gold foils (3mm diameter; 0.05 mm thick) on the anterior and dorsal surface of the mice. Thermoluminesent dosimeters were used for γ-ray dosimetry.

Assessment of numbers of basal sells in mouse esophageal membrane

The extracted esophagus was fixed in the 10% neutral formaldehyde. The fixed samples were processed for preparation of the section and hematoxylin-eosin (HE) staining. Using a software, basal cell numbers per 90-120 μm length were counted at 10 parts in each sample as shown in Fig.1.

Fig.1. HE staining of mouse esophagus.

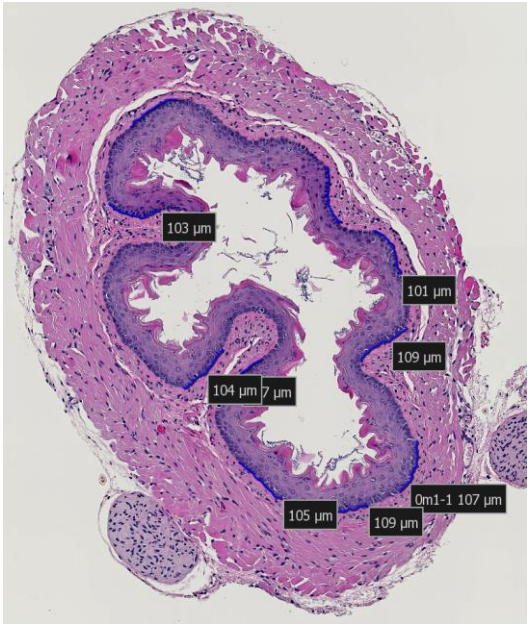

RESULTS

Dosimetry

The anterior and posterior surface of mice were irradiated with thermal neutron beam at the thermal neutron flux of 5.3 and 1.3 n/cm^2/s, respectively. The γ-ray was irradiated at the dose rate of 0.045 Gy/min.

Change in numbers of esophageal basal cells after BNCR

To investigate the change of numbers of esophageal basal cell, BNCR with fixed irradiation time (20 min) was performed. Irradiated mice were sacrificed at 2, 4, 7, and 10 days after the BNCR. Three mice were irradiated at each timepoint. Fig.2 shows the numbers of esophageal basal cells at each time interval after BNCR.

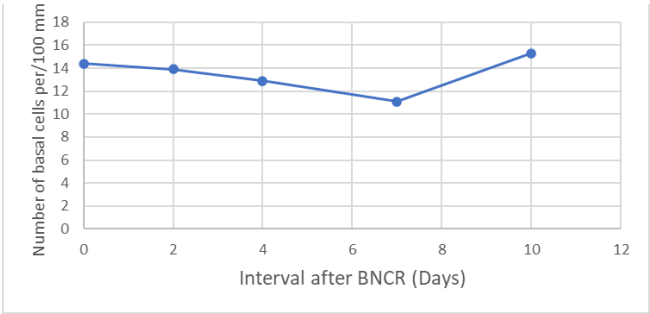

Fig.2. Change in number of esophageal basal cells after BNCR.

At 7 days after BNCT, the number of basal cells in esophageal membrane was lowest. In the further experiments to compare the effect of BNCR on esophagus at different fluence of thermal neutrons or X-ray irradiation, 7-day interval after BNCR will be selected for the assessment of the numbers of basal cells.

PR5-3 The Influence of Boron Neutron Capture Therapy on Bone Growth in Young Mice

R. Iwasaki, R. Yoshikawa, R. Kido, T. Mori, K. Ono[1], Y. Sakurai[2], and M. Suzuki[2]

Faculty of Applied Biological Sciences, Gifu University
[1] Kansai BNCT Medical Center, Osaka Medical College
[2]Institute for Integrated Radiation and Nuclear Science, Kyoto University

INTRODUCTION:

There are various tumors in which normal bone is included in the irradiation field, such as bone and soft tissue sarcoma, head and neck cancer, gynecologic cancer, prostate cancer, and tumors that have metastasized to the bone. In particular, there is a high incidence of bone tumors such as osteosarcoma, chondrosarcoma and Ewing's sarcoma in the adolescent and young adult generation. As a result, radiation-induced bone toxicity, such as fracture, necrosis, and impairment of skeletal growth, can be occurred.

On the other hand, compared with the X-ray irradiation, boron neutron capture therapy (BNCT), a tumor cell-selective particle radiation therapy, is considered to be more effective without any late effects to the normal bone. However, in our previous study using the adult mice, the higher accumulation was seen in the epiphyseal cartilage including the growth plate. This finding indicates that the higher radiation doses might be delivered to the growth plate and may cause the impairment of skeletal growth.

Last year in this project, we found that the tibial growth in the young mice was slightly suppressed in the higher doses of BNCT. Therefore, in this year, we investigated the pathological analysis to elucidate the morphological change of bones in young mice 3 months after irradiation.

EXPERIMENTS: Female four-week-old C3H/He mice were used for the study (n = 5 in each group). As boron compound, p-boronophenylalanine (BPA) was prepared at a dose of 30 mg/ml. The X-ray and neutron irradiation was performed at Gifu University and Kyoto University Reactor, respectively.

X-ray irradiation Mice were irradiated at a dose rate of 250 cGy/min to their right hind limb at single doses of 4, 8, 12, 16, 20, 24, 28, 32 and 36 Gy. Non-irradiated mice were also set as a control.

Neutron irradiation Each neutron irradiation at a power of 1 MW was carried out as follows; neutron beam only (for 30 or 60 min), neutron beam for 30 or 60 min after subcutaneously injected into mice at doses of 125, 250, and 500 mg/kg of BPA. Based on the results of the biodistribution of BPA, irradiation was started at 30 min after the injection.

Histological analysis Tibias were collected at 12 weeks post-irradiation. Subsequently, the specimens were decalcified in 10% formic acid, dehydrated with graded ethanol and embedded in paraffin. The 5-μm longitudinal histological sections of the epiphysis were stained with Hematoxylin and Eosin.

RESULTS:

In the specimens of the growth plate region from the control group, chondrocytes and hypertrophic chondrocytes surrounded by the cartilage matrix were found in the lower growth cartilage (Fig. 1A & a). The pathological findings of 4 and 8 Gy irradiation in the X-ray group, those of neutron irradiation for 30 or 60 min in the neutron group, and those of neutron irradiation for 30 min after BPA 125, 250 and 500 mg/kg in the BNCT group were similar to those in the non-irradiated group (Fig. 1b–d).

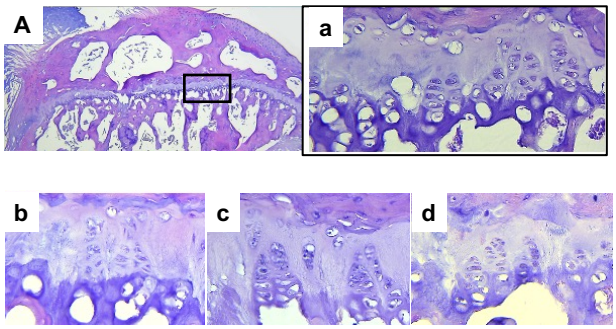

Fig. 1. Histological images of control (A, a), 8 Gy irradiation of X-ray (b), 30 min irradiation of neutron after 500 mg/kg of BPA (c) and 60 min irradiation of neutron (d).

In the growth plate from 12, 16 and 20 Gy irradiation of X-ray and 60 min irradiation of neutron after 125, 250 and 500 mg/kg of BPA, the regular arrangement of chondrocytes was disturbed, and increasing chondrocytes were found within the cartilage matrix (Fig. 2e & f). Besides the disturbance of the chondrocyte arrangement, the cartilage matrix was increased at 24 Gy irradiation of X-ray (Fig. G & g). A marked increase in cartilage matrix was observed at more than 30 Gy of X-ray (Fig. H & h). No increase in cartilage matrix was observed in the BNCT and neutron radiation groups.

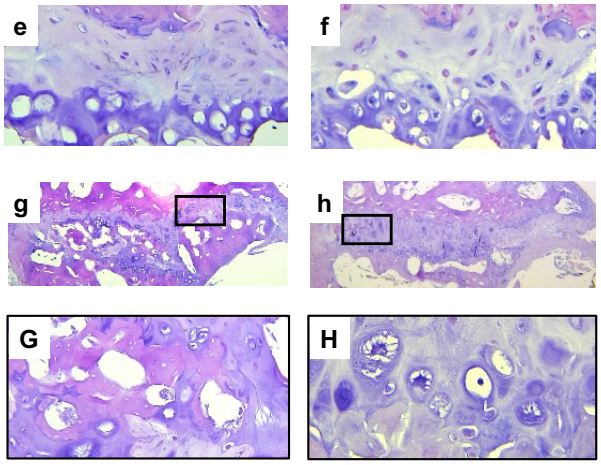

Fig. 2. Histological images of 20 Gy (e), 24 Gy (G, g), and 30 Gy (H, h) irradiation of X-ray and 60 min irradiation of neutron after 500 mg/kg of BPA (f).

CONCLUSION: The results show that the histological changes in the young mice after BNCT were less than those in the X-ray group. Further investigation to verify the effects of longer-term observation are warranted.

I-1. PROJECT RESEARCHES

Project 6

PR6 Production of medical RI by reactor irradiation

T. Yamamura[1], Y. Nakamoto[2], H. Kimura[3], Y. Shimizu[4], K. Washiyama[5]

[1]*KURNS, Kyoto University*

[2]*Department of Diagnostic Imaging and Nuclear Medicine, Graduate School of Medicine, Kyoto University*

[3]*Department of Analytical and Bioinorganic Chemistry, Division of Analytical and Physical Sciences, Kyoto Pharmaceutical University*

[4]*Division of Clinical Radiology Service, Kyoto University Hospital*

[5]*Advanced Clinical Research Center, Fukushima Medical University*

INTRODUCTION:

Remarkable results have been achieved in the treatment of metastatic cancer with β-ray emitting radionuclides such as ^{177}Lu, which can be easily produced in nuclear reactors. In recent theranostics, the incidentally emitted gamma rays can also be used for diagnosis. ^{177}Lu production is also possible with naturally occurring (n, γ) ^{176}Lu, but the specific activity is low and cannot be used for antibody labeling. Indirect methods using Yb irradiation require separation and purification after irradiation (Fig. 1). However, since the specific activity of natural Yb is not high enough, the use of enriched isotope ^{176}Yb is also necessary, but it is difficult to obtain and expensive, and a scheme to recover ^{176}Yb must be established. Research and clinical use of nuclear medicine in Japan has been lagging behind that of other countries due to various regulations and restrictions, and we would like to start basic research on β-ray emitting nuclei that can be produced by nuclear reactors in cooperation with RI production, pharmacology, and medicine during the short time we have before KUR ceases operation. Research activities in this community are also expected to contribute to design activities for RI production in the Fukui reactor, which is considered to be on the scale of a beam reactor.

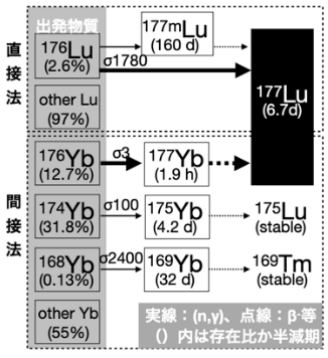

Fig. 1. Starting materials (Lu and Yb, respectively) for the production of ^{177}Lu by direct and indirect methods, and the existence ratio, half-life, and uninvolved or impure nuclides that determine the specific activity.

EXPERIMENTS:

The first fiscal year of the project has been devoted to the setting up the experimental environment and initial test experiments. Each of research fields has made their progress as followings:

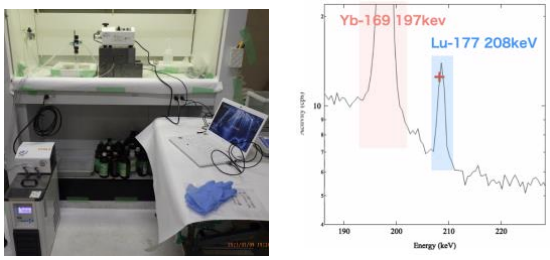

Fig. 2. Experimental set-up for separation of Lu-177 from Yb-176.

(1) H. Kimura *et al.* has carried out their experiments as followings:

^{177}Lu Production: To obtain ^{177}Lu, Lu_2O_3 and Yb_2O_3 were irradiated at 1 MW for 24 hours and 5 MW for 6 hours.

Labeling reaction with ^{177}Lu: Labeling studies were conducted using ^{177}Lu and NOTA-conjugated antibodies. NOTA-binding antibody and $^{177}LuCl_3$ were added to 0.3M AcONa solution and allowed to react at 40°C for 1 hour. The rate of reaction progress was evaluated using Radio-TLC.

SPECT/CT imaging: SPECT imaging was performed to confirm the quality of the ^{177}Lu produced.

(2) Projects of Y. Nakamoto *et al*. and Y. Shimizu *et al*. were not implemented due to the impact of the new coronavirus infection.

RESULTS:

(1) Both direct and indirect methods were confirmed to produce ^{177}Lu. In the indirect method, it was found that ^{177}Lu breaks down slowly against the large excess of ^{176}Yb, and that the specific activity of ^{177}Lu can be greatly improved by separating the eluted portion up to the breakdown (first fraction) and the eluted portion after that (second fraction) (Fig. 2).

This measurement was carried out in two ways: the first method was used to determine the specific activity of ^{176}Yb, ^{177}Lu, ^{177m}Lu, *etc*. It was found that the overlap of numerous γ rays was so pronounced that they could not be separated with the small detector Kromek (16 keV), and a germanium semiconductor detector was required. Although manual fraction collection was performed in this study, it was found necessary to proceed with collection by fraction collector and continuous measurement by a portable detection system in the future.

Since the first fraction could be recovered, we are ready to proceed with the experiment using ^{176}Yb-enriched isotope in the future.

Labeling experiments were conducted using ^{177}Lu produced by the direct method. When an antibody with 7-8 NOTAs bound as ligands was used, labeling of ^{177}Lu proceeded quantitatively. However, when the number of NOTAs introduced was small, the labeling rate of ^{177}Lu was extremely low. SPECT imaging was performed by administering $^{177}Lu_2O_3$ through the tail vein of mice; successful imaging of ^{177}Lu indicated that monitoring of therapeutic effects was also possible.

PR6-1 Development of tumor-targeted radiotheranostics probes and its clinical application

H. Kimura[1], T. Yamamura[2], K. Shirasaki[3]

[1] Department of Analytical and Bioinorganic Chemistry, Division of Analytical and Physical Sciences, Kyoto Pharmaceutical University
[2]Institute for Integrated Radiation and Nuclear Science, Kyoto University
[3]Institute for Materials Research, Tohoku University

INTRODUCTION:

Theranostics is a new medical technology that combines therapeutics and diagnostics. The key to the realization of theranostics is a drug known as theranostic probes. The characteristic of the radiotheranostics probes we are developing is that we consider a single molecule as an aggregate of target recognition units, linker units, and chelating units, and design molecular probes based on the concept of "unit-coupling molecular probes," in which independently developed units are freely combined. This drug design theory is not only effective for designing molecular probes with relatively large molecules such as antibodies and other proteins and bioactive peptides as the nucleus, but also can also be applied to organic small molecular compounds. In this study, we will utilize the theory of creation of unit-coupling molecular probes to develop drugs that can ultimately be applied clinically. First, a basic study of the production of ^{177}Lu in the KUR was conducted.

EXPERIMENTS:

^{177}Lu Production: To obtain ^{177}Lu, Lu_2O_3 and Yb_2O_3 were irradiated at 1 MW for 24 hours and 5 MW for 6 hours.

Labeling reaction with ^{177}Lu: Labeling studies were conducted using ^{177}Lu and NOTA-conjugated antibodies. NOTA-binding antibody and $^{177}LuCl_3$ were added to 0.3M AcONa solution and allowed to react at 40°C for 1 hour. The rate of reaction progress was evaluated using Radio-TLC.

SPECT/CT imaging: SPECT imaging was performed to confirm the quality of the ^{177}Lu produced.

RESULTS AND DISCUSSION:

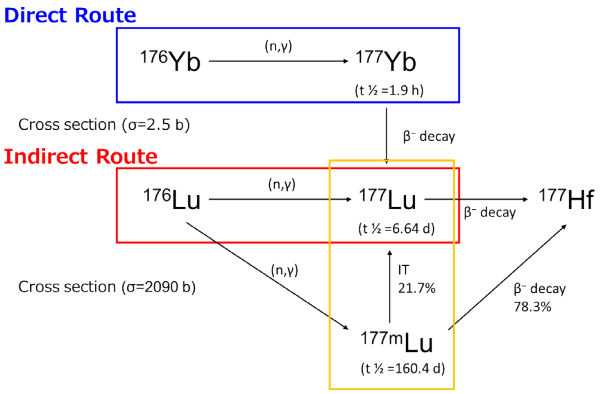

Fig. 1. ^{177}Lu Production Process

The production of ^{177}Lu was confirmed for both direct and indirect methods (Fig1)[1)]. The indirect method is under investigation for separation and purification, and we plan to continue our research to establish a purification method.

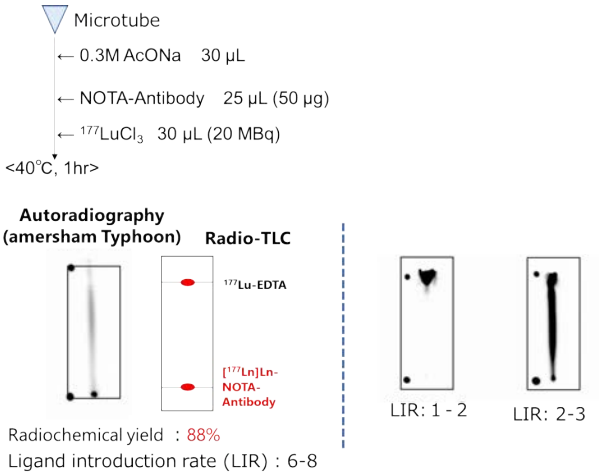

Fig.2.^{177}Lu Production Process.

Labeling experiments were performed using ^{177}Lu produced by the direct method. When antibodies with seven to eight bound NOTA as ligands were used, labeling of ^{177}Lu proceeded quantitatively. However, the labeling rate of ^{177}Lu was found to be extremely low when the number of NOTAs introduced was small (Fig2). The production of high purity ^{177}Lu by the indirect method is considered more suitable for drug development. In fact, ^{177}Lu is produced by the indirect method for pharmaceutical use worldwide.

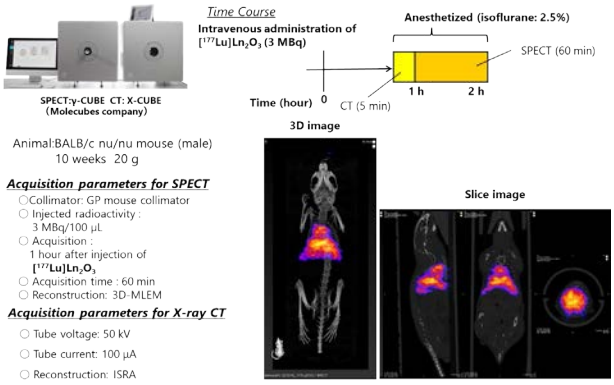

Fig. 3. SPECT/CT imaging: $^{177}Ln_2O_3$

$^{177}Ln_2O_3$ was administered via tail vein of mice and SPECT imaging was performed. The successful imaging of ^{177}Ln indicated that it is also possible to monitor treatment efficacy (Fig3).

REFERENCES:

[1] A. Dash *et al.,* Nucl Med Mol Imaging., **49** (2015) 85-107.

PR6-2 Preliminary study on the development of online monitoring system for column separation of ^{177}Lu from ^{nat}Yb irradiated target

K. Washiyama[1], R. Okumura[2], K. Shirasaki[3], K. Ogawa[4], T. Yamamura[2]

[1]*Advanced Clinical Research Center, Fukushima Medical University*
[2]*Institute for Integrated Radiation and Nuclear Science, Kyoto University*
[3]*Institute for Materials Research, Tohoku University*
[4]*Institute for Frontier Science Initiative, Kanazawa University*

INTRODUCTION: Lutetium-177 (^{177}Lu) is a beta-emitting radionuclide suitable for medical use. However, the production of ^{177}Lu and research on the development of ^{177}Lu-labeled radiopharmaceuticals have not been active in Japan, and must be addressed in the future for involvement in the global ^{177}Lu supply chain and the development of ^{177}Lu-labeled radiopharmaceuticals in Japan. The goal of this study is to produce and purify no-carrier-added ^{177}Lu using Kyoto University's research reactor, KURR, and provide it to users, and to optimize column separation conditions for separating ^{177}Lu from Yb target and by-products, which are essential for this purpose. The CZT detector has a narrower FWHM and higher resolution than the NaI detector, and some CZT detectors are small and can be powered by USB, making them suitable for online measurement. In this study, we conducted a preliminary investigation of online measurement of column separation using a CZT detector.

EXPERIMENTAL: The CZT detector used for the measurements was a RadAngel manufactured by kromek. A Ge detector (ORTEC) was used as the detector for comparison. The Yb and Lu samples to be irradiated were elemental standards for ICP-MS with natural isotopic abundances. Each sample (Yb, 0.5 mg: Lu, 0.1 mg) was added to a quartz tube, heated and concentrated to dryness, and then vacuum-sealed. The samples were then loaded into a water hydraulic transport tube of a research reactor at the Institute for Integrated Radiation and Nuclear Science, Kyoto University, and irradiated for 24 hours. A part of the Yb and Lu solutions was taken out and used for the γ-ray spectrometry with a CZT detector and a Ge semiconductor detector to set the ROI for the monitoring. The remaining Yb solution was poured into a column and about 500 mL of 1.5 M HNO_3 was added to separate the Yb target and ^{177}Lu. Extraction chromatography resin LN2-Resin (Eichrom) was used for column separation. A jacketed 11 mmφ x 240 mmL glass column (Kiriyama Chemical) was used as the separation column. The tube containing the eluted solution from the column was brought into contact with the CZT detector for online measurement of the solution. Then all eluents were collected in a fraction collector with 250 drops as one fraction. The collected solution was then subjected to γ-ray spectrometry with a Ge detector and compared to the elution curve obtained with the CZT ROI.

RESULTS and DISCUSSION: A Ge detector confirmed the production of ^{177}Lu, ^{175}Yb, and ^{169}Yb in the irradiated sample from γ-ray spectrometry. Figure 2 shows the elution curves obtained with the Ge detector, and Figure 3 shows the elution curves obtained with the CZT detector, which were obtained by setting the ROI to the channel between the 396 keV of ^{175}Yb and 208 keV of ^{177}Lu photoelectric peaks.

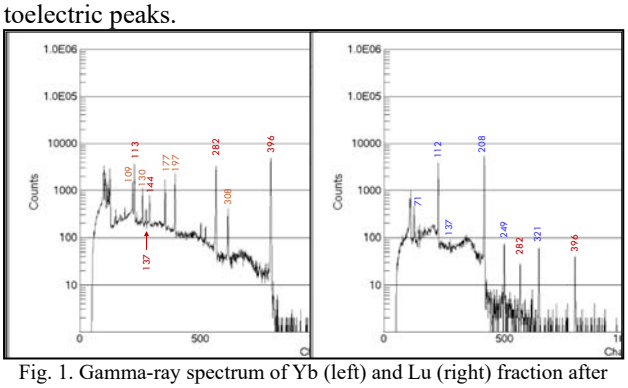

Fig. 1. Gamma-ray spectrum of Yb (left) and Lu (right) fraction after column separation using Ge-detector.

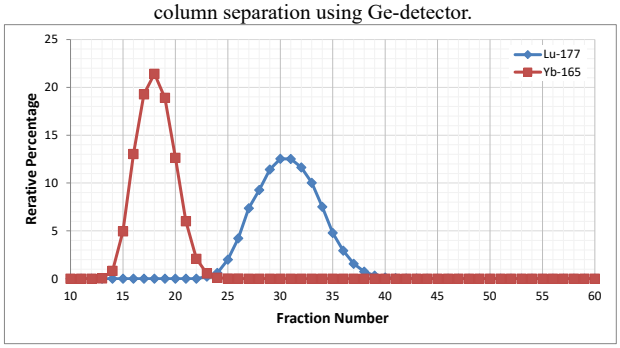

Fig. 2. Elution profile of extraction chromatography with an 11 mmφ × 240 mmL column packed with LN2 resin measured with a Ge detector.

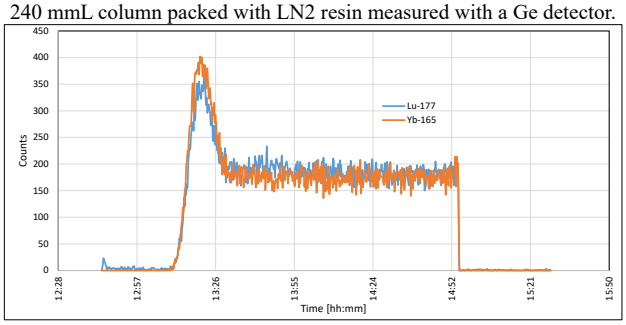

Fig. 3. Elution profile of extraction chromatography with an 11 mmφ × 240 mmL column packed with LN2 resin measured with a CZT detector.

The x-axes of Figures 2 and 3 show the elution curve of ^{165}Yb, although the units differ. On the other hand, ^{177}Lu was not detected by the CZT detector. This is probably because ^{177}Lu generates less radioactivity than ^{165}Yb and the background around the detector is high. Therefore, further study on the measurement conditions is necessary.

CONCLUSION: In this study, a preliminary investigation of online γ-ray measurements in column separations was performed. A small CdZn detector demonstrated the possibility of online measurement in column separation; however, further investigation is warranted.

I-1. PROJECT RESEARCHES

Project 7

PR7 Chemical and electronic properties of Actinide compounds and their applications

T. Yamamura[1], Y. Haga[2], M. Abe[3], M. Nakase[4], K. Shirasaki[5], S. Kanbe[6], N. Ishikawa[7], T. Suzuki[8], M. Nogami[9]

[1]*KURNS, Kyoto University*
[2]*Advanced Science Research Center, JAEA*
[3]*Graduate School of Advanced Science and Engineering, Hiroshima University*
[4] *Lab. for Adv. Nuclear Energy, Tokyo Inst. of Tech.*
[5]*Institute for Materials Research, Tohoku University*
[6] *Advanced Science Research Center, JAEA*
[7]*Department of Chemistry, Tokyo Metropolitan University*
[8]*Nagaoka University of Technology*
[9] *Graduate school of Electronic Eng., Kindai University*

INTRODUCTION:

Actinide compounds shows a unique chemical and electronic nature due to the partial and insufficient shield of 5f orbital electrons as inner transition elements. We have a deep interest in the aspect of the electronic properties of the actinide compounds and formed the group consisting of three major fields: (1) inorganic and coordination chemistry, (2) electronic properties and (3) theoretical chemistry and its users. These studies will be also useful for application research area such as the handling of the 1F debris and developments of nuclear medicines.

Such research environments to handle actinides elements are extremely difficult to build in ordinary university institutes. The hot laboratory of the KURNS offers unique opportunities for the above-mentioned characteristic research activities.

EXPERIMENTS:

The first fiscal year of the project has been devoted to the setting up the experimental environment and initial test experiments. Each of research fields has made their progress as followings:

(1) S. Kanbe and Y. Haga *et al*, has investigated the molten salt flux (MSF) method as a route to grow high-quality single crystals of UTe_2 with minimal U vacancies. The single-crystalline samples of this compound have been investigated by the measurements of crystallographic and thermodynamic properties.

(2) M. Abe *et al.* has developed new programs for calculating electronic states and properties of actinide compounds with high accuracy, based on the X2C relativistic Hamiltonian.

(3) M. Nakase *et al.* has studied properties of Phthalocyanine (Pc) as a ligand for an effective extraction of U. Moreover, they tried to construct the prediction models from the complex structure.

(4) N. Shirasaki *et. al.* has synthesized some uranium(III) halide complexes, and a commercially unavailable BDI potassium salt to obtain the starting material. The procedure to synthesize BDI potassium salt improved regarding stoichiometry and reflux time [3].

(6) N. Ishikawa *et al*. has measured VT-VH-MCD in the visible energy region for the monolayer Pc complex of U(IV) as well as that of Th(IV), structure of which is $PcAn(acac)^2$ (An=U or Th), to investigate magnetic interaction between the $(5f)^2$ system and the ligand π-conjugate system in a photo excited state.

(7) T. Suzuki *et al.* has the investigated dissolution of CeO_2 as simulant material of ThO_2 and searched the optimum condition of dissolution. 4 kinds of halides are used as reactant chemicals for thermochemical conversion.

(8) M. Nogami *et al*. has examined applicability of the factor "formation of planner five-coordinated complexes" to monoamide compounds.

RESULTS:

(1) Crystallographic parameters demonstrated that the main source of impurity in UTe_2 is the uranium defects. It hinders not only superconductivity but also the normal state electronic/magnetic excitations of UTe_2 as demonstrated by specific heat measurements [1]. Having established this, the possible route to prepare higher quality UTe_2 samples is to prevent uranium deficiency [2].

(2)The electronic ground state of UO_2^{2+} in the gas phase was used for this test with small basis sets. They confirmed that the parallelization was successfully accomplished, and the CPU times linearly scaled up to around 32/128 cores in CASCI/CASPT2 calculations. For instance, a single-core calculation of CASPT2 took five and a half hours, while using 128 cores reduced the time to only four minutes.

(3) A simple regression model of the solubility prediction by other chemicals was tested on the KNIME software (with Python modules), which enables machine learning in a low-code environment.

(4) They investigated the obtained complexes by by ICP-AES (uranium ratio), CHN elemental analysis, and XRD spectrum. Although purification of the complexes for single crystal structure analysis are desired in the future, they have obtained fundamental knowledge of the preparation of uranium trivalent complexes through this series study.

(6) Temperature dependence of MCD spectra of complexes were showed that clear evidence for the existence of a magnetic interaction between the $(5f)^2$ system and the photo-excited circular π conjugation.

(7) They found that the almost all CeO_2 can be dissolved by the thermochemical conversion method using CCl_4, CCl_3CCl_3, and CBr_4 as reactant. Moreover, they also confirmed that almost all ThO_2 can be dissolved by thermochemical conversion method. The highest percentage of dissolution was obtained in the case of CBr_4 as reactant and dissolution by HCl.

(8) Their study suggests that formation of five-coordinated complexes by monoamide compounds may be possible if realization of preferential coordination of other ligands than NO_3^- to UO_2^{2+} is achieved.

REFERENCES:

[1] Y. Haga *et al*., J. Phys.: Condens. Matter, **34**, (2022) 175601.
[2] H. Sakai *et al*., Phys. Rev. Mater., **6** (2022) 073401.
[3] W. Clegg *et al.,* Inorg. Chem., **37** (1998) 2317-2319.

PR7-1 Effect of uranium deficiency in unconventional superconductor UTe_2

Y. Haga, P. Opletal, Y. Tokiwa, E. Yamamoto, Y. Tokunaga, S. Kambe, H. Sakai

Advanced Science Research Center, Japan Atomic Energy Agency

INTRODUCTION: Since the discovery of superconductivity in UTe_2, extremely unconventional aspects of physical properties are investigated both experimentally and theoretically [1]. Experimentally, however, the strong sample dependence on superconducting properties is now recognized as a serious problem to elucidate its intrinsic behavior. In this study, we report the origin of strong sample dependent behavior in UTe_2. We report detailed analysis on crystallographic structure and discuss the electronic property of this compound.

EXPERIMENTS: Single crystals of UTe_2 were grown either from chemical vapor transport method using iodine as a transport agent. Samples were characterized using an electron probe microanalysis for the stoichiometry and homogeneity. Crystallographic parameters were determined using single-crystal X-ray diffraction techniques. Superconductivity was verified by electrical resistivity measurements using the four-probe method. Specific heat was measured using a home-built calorimeter in a ^{3}He cryostat.

RESULTS: Figure 1 shows the typical data on the temperature dependence of electrical resistivity measured on superconducting (SC) and non-superconducting (NS) samples. The data are normalized at room temperature. Apparently, SC sample showing a resistance drop at 1.8 K corresponding to superconducting transition has low residual resistivity than NS sample, demonstrating that SC sample shows less impurity scattering and therefore higher quality.

Crystallographic parameters determined for both NS and SC samples are shown in Table 1. Here, UTe_2 crystallizes in the orthorhombic cell with space group Immm. There are three fractional coordinate parameters U (0 0 z), Te1 (1/2 0 z) and Te2 (0 y 1/2). There is no significant difference in these parameters. However, the equivalent isotropic atomic displacement parameter B_{eq} for the uranium site of NS sample is abnormally large. It is even larger than Te sites with lower atomic number. Detailed analysis of scattering intensity strongly suggests that uranium site occupancy for NS sample is strongly deviated from full occupancy. By treating uranium site occupancy as a fitting parameter, the best fit was obtained at $U_{0.962(2)}Te_2$. This result is fully consistent with the composition analysis using EPMA. Note also that the lattice parameter of NS is slightly smaller than that of SC sample, in consistent qualitatively with X-ray diffraction. However, the reduction of the volume is too small from the expected value if uranium deficiency is substituted by tellurium. It is therefore suggested that 4 % of uranium sites are left vacant in NC samples. [2]

The present results demonstrated that the main source of impurity in UTe_2 is the uranium defects. It hinders not only superconductivity but also the normal state electronic/magnetic excitations of UTe_2 as demonstrated by specific heat measurements [2]. Having established this, the possible route to prepare higher quality UTe_2 samples is to prevent uranium deficiency. Recent improvements of crystal growth technique using molten salt flux technique successfully achieved this and resulted in extremely high-quality single crystals [3].

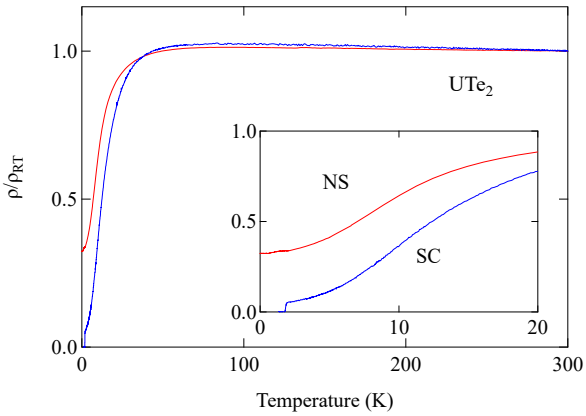

Fig. 1. Temperature dependence of electrical resistivity normalized at room temperature for UTe_2.

	NS	SC
a	4.1600(2)	4.1618(5)
b	6.1219(4)	6.1355(7)
c	13.9476(9)	13.9698(13)
U (z)	0.13545(5)	0.13520(4)
Te1 (z)	0.29755(5)	0.29780(10)
Te2 (y)	0.24895(5)	0.24910(3)
B_{eq} (U)	0.687	0.513
B_{eq} (Te1)	0.562	0.576
B_{eq} (Te2)	0.515	0.529

Table 1. Crystallographic parameters of UTe_2 for NS and SC samples.

REFERENCES:

[1] D. Aoki *et al.,* J. Phys.: Condens. Matter, **34** (2022) 243002.

[2] Y. Haga *et al.,* J. Phys.: Condens. Matter, **34** (2022) 175601.

[3] H. Sakai *et al*., Phys. Rev. Mater., **6** (2022) 073401.

PR7-2 Development of relativistic multireference electron correlation methods for actinide compounds

M. Abe,[1,2] A. Sato,[2] A. Yoshida,[2] S. Iwamuro,[2] Y. Masuda,[1] Masahiko Hada[2], N. Nakatani[2], A. Sunaga,[3] C. Tabata, [3,4] T. Yamamura[3]

[1]*Department of Chemistry, Hiroshima University*
[2]*Department of Chemistry, Tokyo Metropolitan University*
[3]*Institute for Integrated Radiation and Nuclear Science, Kyoto University*
[4]*Japan Atomic Energy Agency*

INTRODUCTION: Elucidating the properties of actinide compounds is important for both engineering and academic research. Theoretical calculations along with experimental approaches can aid in clarifying their properties and conducting safe verification studies.

For theoretical studies of actinide compounds, precise handling of relativistic and electron correlation effects is essential. As atomic number Z increases, the relativistic effect becomes significant, and conventional scalar relativistic treatment or perturbative correction of spin-orbit interaction may not be accurate. To account for rigorous relativistic effects, the four-component Dirac or the exact two-component (X2C) relativistic Hamiltonians should be applied. Additionally, since all *s*, *p*, *d*, and *f* orbitals are valence orbitals for actinide atoms, static electron correlation may not be negligible, which limits the effectiveness of conventional single-reference methods such as density functional theories. Multi-reference electron correlation theory is necessary, but its computational complexity poses a challenge.

Our group has developed new programs for calculating electronic states and properties of actinide compounds with high accuracy, based on the X2C relativistic Hamiltonian. Specifically, we have developed programs for the CASCI-CASPT2 and DMRG-CASPT2 methods, which employ multiconfigurational wave functions (CASCI/DMRG) as the 0th-order state of perturbation. CASPT2 is a well-established perturbation theory in non/quasi-relativistic frameworks [1].

METHODS: The free software DIRAC [2,3] already provides the Hartree-Fock and molecular orbital integral transformation with the X2C relativistic Hamiltonians. Therefore, we have developed CASCI-CASPT2 and DMRG-CASPT2 programs, which can be implemented subsequently to the DIRAC software. The primary aim of this research is to develop the X2C-DMRG-CASPT2 method. DMRG (density matrix renormalization group) [4] is a more suitable method than CASCI for dealing with a larger active space, albeit at the cost of high computational complexity.

The study will be conducted in three phases: (1) developing the X2C-CASCI-CASPT2 method, (2) developing the X2C-DMRG method, and (3) integrating the first two phases into the X2C-DMRG-CASPT2 method. Phases 1 and 2 will be carried out concurrently and merged into the third phase when sufficient progress has been made.

In the current year, we have completed Phase 1 by implementing an interface program from DIRAC to CASCI-CASPT2. Furthermore, we have accomplished the parallelization of the CASCI-CASPT2 program, enabling us to conduct large-scale calculations using supercomputers.

RESULTS: Figure 1 shows the scheme of the current programming in the left panel, and the CPU times of parallelized calculations in CASCI and CASPT2 in the right panel. The electronic ground state of UO_2^{2+} in the gas phase was used for this test with small basis sets. We confirmed that the parallelization was successfully accomplished, and the CPU times linearly scaled up to around 32/128 cores in CASCI/CASPT2 calculations. For instance, a single-core calculation of CASPT2 took five and a half hours, while using 128 cores reduced the time to only four minutes. This allows us to perform computations for more realistic systems with larger active spaces, which will be addressed in the coming year.

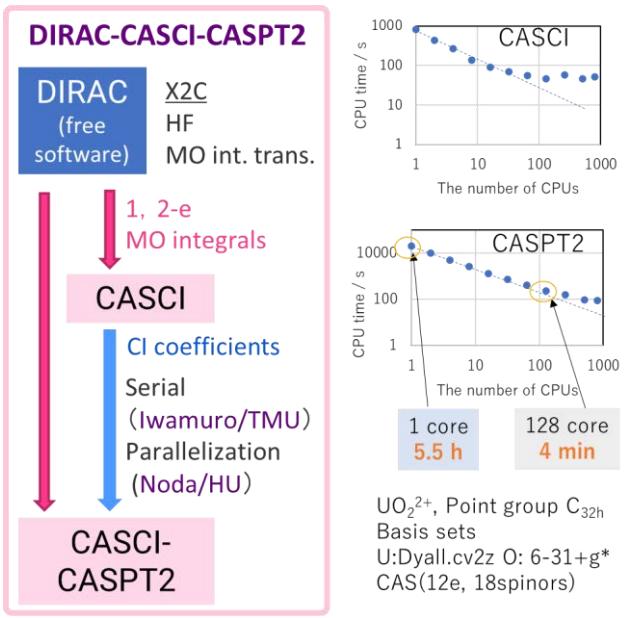

Fig. 1. Scheme of phase 1 programming and computation CPU time for parallelization in UO_2^{2+}.

REFERENCES:

[1] K. Anderson *et al.*, J. Phys. Chem., **94** (1990) 5483-5488.
[2] DIRAC, a relativistic ab initio electronic structure program, Release DIRAC22 (2022), written by H. J. Aa. Jensen *et al.*
[3] T. Saue *et al.*, J. Chem. Phys., **152** (2020) 204104.
[4] S. R. White, Phys. Rev. Lett., **69** (1992) 2863.

PR7-3 Synthesis of novel phthalocyanine derivatives and effect of substituent on recognition of light actinide and chemical property-4

M. Nakase[1], M. Harigai[1], C. Tabata[2], T. Yamamura[3]

[1]*Institute of Innovative Research, Tokyo Institute of Technology*
[2]*Materials Sciences Research Center, Japan Atomic Energy Agency*
[3]*Institute for Integrated Radiation and Nuclear Science, Kyoto University*

INTRODUCTION: Understanding Actinide chemistry is essential in any aspect, including the reprocessing of spent nuclear fuels, treatment of wastes generated in Fukushima Daiichi Nuclear Power Station, medical use of Actinium, and so on. I am especially interested in the Th fuel cycle, which does not produce heavy actinides such as Am and Cm. Instead, understanding the chemistry of light actinides such as Th, Pa, and U is essential. The Th fuel cycle needs an effective separation of U from Th and other fission products in spent Th fuels. To enable such separation, the thorium–uranium extraction (THOREX) process, like the plutonium–uranium redox extraction (PUREX) process, has been studied [1]. In the THOREX process, UO_2^{2+} is extracted by tri-*n*-butyl phosphate (TBP) with $Al(NO_3)_3$. Some other extractants which consist of C, H, O, and N atoms (CHON principle), such as monoamide, are recently reported for U/Th separation [2]. In this study, Phthalocyanine (Pc) was selected as the main structure of the extractant, which also satisfies the CHON principle, and intensively studied their characteristics. The Pc derivatization is ongoing to make the Pc soluble in an organic solvent. The purification technique suitable for Pu-Actinide complexes was investigated, and the Pc-Zn complex was synthesized as reference species previously. Next, we aim to synthesize the Pc-U complexes in the organic solvent. In FY2023, we prepared the pure U(IV) and implemented the synthesis of U(IV) acetylacetonate.

EXPERIMENTS: U(IV) acetylacetonate was synthesized following the procedure prepared in the Yamamura lab at Kyoto University. The black UO2 powder was first added to the concentrated HCl, and the mixture was heated to 100 C to dissolve. The solution was filtrated, and the green filtrate was forwarded to the next step. The electrochemical reduction to U(III) was implemented with Pt and Hg electrodes. After the reduction to U(III), the color of the solution became dense, and finally, pale red with the incandescent lamp was seen, as shown in **Figure 1 (a)**. Then the oxidation to U(IV) occurs at room temperature, which gives the green color as shown in **Figure 1(b)**. Then, the excess acetylacetonate was added to the U(IV) solution while heating at 50 C. The pH was adjusted to about 6 by dropwise addition of 3 M NaOH, and precipitation was formed. The precipitation contains some impurities, such as unreacted acetylacetone and hydrated U; recrystallization by methanol was implemented. Finally, the U(IV)-acetylacetonate complex was obtained. The U(IV)-acetylacetonate complex is the precursor of other Pc-U complexes. The final U(IV) acetylacetonate is shown in **Figure 2**

Fig. 1. Prepared U solution; (a) U(III) and (b) U(IV) in HCl solution.

Fig. 2. The synthesized U(IV) acetylacetonate.

SOLUBILITY PREDICTION: If a prediction of the solubility of the complexes is possible, it can effectively minimize the number of experiments, and the minimization of the radioactive waste generation becomes possible. Therefore, we tried to construct the prediction models from the complex structure. This year, a simple regression model of the solubility prediction by other chemicals was tested on the KNIME software (with Python modules), which enables machine learning in a low-code environment. The solubility data of Pc and U-Pc complexes must be accumulated from the literature or experiments.

PLANS: We will synthesize the U(IV)-Pc complex in the next fiscal year with newly synthesized Pc derivatives. The synthetic work was halted due to the maintenance and change in the layout of the chemical Lab in Tokyo Tech. The chemical lab upgrade was finished, and gradually, the synthesis was restarted. The prediction model of the solubility of U-Pc complexes will be further tested, and obtaining the complementary data from the literature and prediction of the characteristics will be implemented.

REFERENCES:

[1] R. H. Rainey and J. G. Moore, Nucl Sci Eng., **10(4)** (1961) 367-371.
[2] P.N. Pathak, Solv Ext Ion Exch, **20(3)** (2002) 293-311.

PR7-4 Fundamental preparation study to access functional uranium(III) complexes

K. Shirasaki, K. Miyahara, C. Tabata[1,2], A. Sunaga[1,3], T. Yamamura[1]

Institute for Materials Research, Tohoku University
[1]Institute for Integrated Radiation and Nuclear Science, Kyoto University
[2]Materials Science Research Center, JAEA
[3]Graduate School of Science, Kyoto University

INTRODUCTION: The electron configuration of uranium(III) is $5f^3$ whose electrons are influenced by the shielding effects of 5*s* and 5*p* less than 4*f*, thus the complexes with uranium(III) often have unique properties. On the other hand, uranium(III) is easily oxidized and changed into uranium(IV) or uranyl(VI). Thus, to maintain the oxidation state, limited ligands are required to use for complexation with uranium(III). In 2013, King et al. synthesized uranium(III) β-diketoiminate (BDI) complex such as $(BDI)UI_2$ [1] and in 2020, Boreen et al. reported that the single molecule magnet (SMM) behavior was observed in low temperature using $(BDI)U(OAr)_2$ (OAr = 2,6-Diisopropylphenyl) [2]. Because of the steric hindrance of BDI ligands, low-coordination complexes with BDI ligands are relatively easy to achieve. Of course, BDI ligands can be the supporting ligands not only for uranium(III) but also for uranium(IV), uranyl(V), and uranyl(VI) complexes [3].

The purpose of this study is to investigate suitable preparation method of uranium complexes with BDI ligands and to characterize low valent uranium BDI complexes. We also synthesized a commercially unavailable BDI potassium salt to obtain the starting material.

EXPERIMENTS: uranyl(VI) chloride solution (1M) was reduced into uranium(III) through an electrolytic reduction in 1M hydrochloric acid 20ml for approximately 3 hours. Subsequently, the solution evaporated and the purple compound, presumably $UCl_3 \cdot (H_2O)_{3.85}$ was obtained. It was estimated by ICP-AES (uranium ratio) and CHN elemental analysis. On the other hand, uranium iodide was achieved by reaction in ethanol. This reaction route required to use very thin uranium metal and iodine. After stirring vigorously for 7 days, the reaction didn't be finished completely. At that time, we collected the red brown powder which was rendered at that reaction. The uranium ratio was 38.45% which was close to the uranium ratio of UI_3.

The procedure to synthesize BDI potassium salt was followed by the one reported by Cleg in 1998 with fine modifications regarding stoichiometry and reflux time [4]. On top of that, a similar compound also can be synthesized by using the same equipment.

RESULTS: BDI potassium salt is soluble in THF and according to past reports, uranium (IV) trichloride BDI complex is not soluble in THF. Unfortunately, there was no residue after stirring solution, so the reaction products with uranium chloride hydrate seem to be soluble. It is necessary to use different solvents or an additional step if the uranium chloride hydrate use as starting material. In the case of uranium iodide, to prevent oxidization of low valent uranium ion, carbon tetrachloride was used as the solvent. After stirring about 12 hours, the solution was removed from the residue, and washing by toluene to extract potassium iodide. The obtained brown powder was measured by XRD equipment (MiniFlex II, Regaku). To know the difference between uranium BDI compound and lanthanide BDI compound, the attempt to react BDI potassium salt (Fig. 1, lower) with cerium compound was done. Unlike uranium, the lanthanide trichloride hydrates didn't dissolve in most polar solvents. Therefore, cerium nitrate hexahydrate was used in this experiment and consequently pink powder can be obtained.

When it comes to XRD spectrum in uranium BDI complex and cerium BDI complex, same peaks can be found. One of the different points was that the number of peaks of uranium BDI complex (Fig. 1, upper) was many more than that of cerium BDI compound.

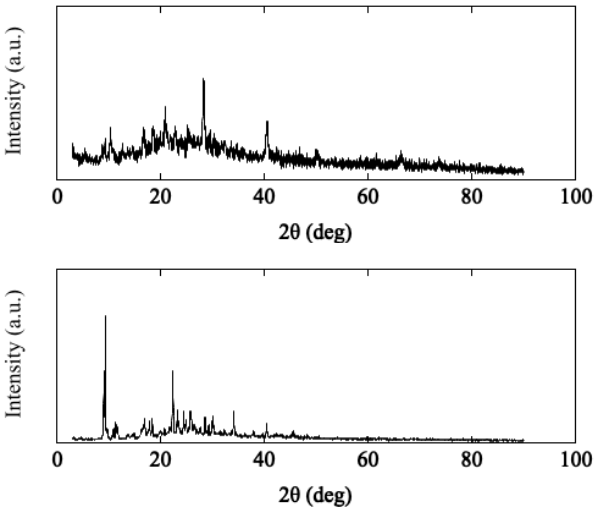

Fig. 1. XRD patterns obtained from uranium BDI complex (upper) and potassium BDI complex (lower).

Although purification of the complexes for single crystal structure analysis are desired in the future, we have obtained fundamental knowledge of the preparation of uranium trivalent complexes through this series study.

REFERENCES:

[1] D. M. King *et al.*, Angew. Chem. Int. Ed., **52** (2013) 4921-4924.
[2] M. A. Boreen *et al.,* Dalton Trans., **49** (2020) 7938-7944.
[3] P. Waldschmidt *et al.,* Inorg. Chem., **62** (2023) 2013-2023.
[4] W. Clegg *et al.,* Inorg. Chem., **37** (1998) 2317-2319.

PR7-5 Synthesis of ultra-pure UTe_2 by molten salt flux method

S. Kambe, H. Sakai, Y. Tokunaga, Y. Haga, Y. Tokiwa, P. Opletal, E. Yamamoto and [1]A. Yamamura

Advanced Science Research Center, Japan Atomic Energy Agency

[1]Institute for Integrated Radiation and Nuclear Science, Kyoto University

INTRODUCTION: Uranium ditelluride (UTe_2) has attracted considerable attention since the compound exhibits a number of novel superconducting (SC) features. Ran *et al.* [1] first reported that UTe_2 exhibits an unconventional superconductivity be- low T_c = 1.6 K, and extremely large upper critical field H_{c2} exceeding the Pauli-limiting field. In this paper, we report the molten salt flux (MSF) method as a route to grow high-quality single crystals of UTe_2 with minimal U vacancies. Such stoichiometric UTe_2 crystals grown by the MSF method exhibit the highest T_c of 2.1 K with a remarkably large RRR ~ 1000, which is much better than that grown by chemical vapor transition (CVT) method.

EXPERIMENTS: In the MSF method, an equimolar mixture of sodium chloride and potassium chloride (NaCl + KCl) was chosen, which has a eutectic melting point of about 650 °C [2]. In each growth procedure, a piece of lightly etched U metal and granule of Te metal were weighed to adjust the target molar ratio of Te/U. Then, the metals were placed together in the bottom of a carbon crucible. The carbon crucible filled with the metals and salt mixture was placed in a quartz tube with an inner and outer diameter of 15 and 18 mm, respectively. The carbon crucible filled with the metals and salt mixture was placed in a quartz tube with an inner and outer diameter of15 and 18 mm, respectively. It was heated at 200 °C for several hours under dynamic vacuum to dehydrate the contents. Then, the carbon crucible was vacuum-sealed into the quartz tube. The sealed quartz tube was inserted into a home-built vertical electric tube furnace. First, it was preheated at 450 °C for 24 h, then raised to 950 °C over 24 h, and kept for 24 h to produce a uniform melt. Then, the temperature was slowly lowered to a final-step temperature (T_f) with a ramp rate of 0.02–0.03 °C per min. The temperature was maintained at T_f for 24 h for annealing. After cooling down, the molten salts were easily dissolved in water, and the millimeter-sized crystals were picked up, washed with ethanol, and immediately dried in a vacuum atmosphere.

RESULTS: Figure 1 shows the temperature dependence of normalized resistivity $\rho(T)/\rho(300\ K)$ along the a axis for the representative single crystals of non-superconducting NS), superconducting SC1, and SC2. The RRR value was estimated using the $\rho(0)$ obtained by fitting to $\rho(T) = AT^2 + \rho(0)$ in the range of $T_c<T<4K$, assuming a Fermi liquid state just above T_c. The $\rho(0)$ of the NS crystal in Fig. 1 was 2.2μcm, whereas that of the SC2 was 34μcm. The considerably higher residual resistivity of the NS crystal indicates higher density of its scattering centers. $U_{1-\delta}Te_2$ may be described as $U^{4+}_{1-5\delta}[V_U]_\delta U^{5+}_{4\delta} Te^{2-}_2$, where $[V_U]$ means the vacancies of U sites. A $[V_U]$ of~4% in the NS crystal significantly changes the 5f electron count because of the simultaneous generation of U^{5+} and U vacancies which cause strong scattering of conduction electrons. Therefore, even if the uranium deficiency of the SC crystals is less than 1%, extra electron scattering may occur, and/or the corresponding residual density of states may exist in the SC state.

The MSF method is a promising technique for crystal growth of SC UTe_2 to control the T_c value and prevent any disorder caused by uranium vacancies. The MSF method would also be useful for various uranium chalcogenides because it is applicable at relatively low tem-peratures to avoid volatilization of the constituent chal-cogens. This will be certainly useful for nuclear fuel technology in future.

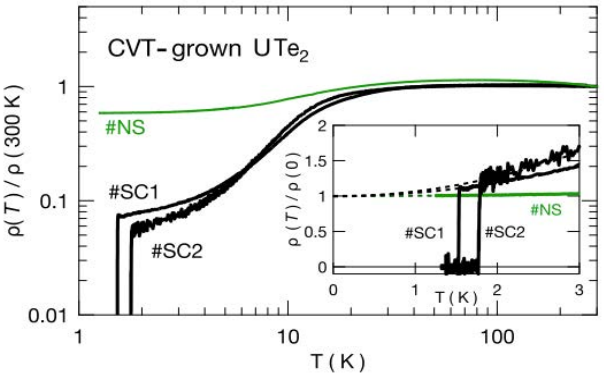

Fig. 1. Temperature dependence of normalized resistivity [3], $\rho(T)/\rho(300\ K)$, for the CVT-grown single crystals of UTe_2. The resistivity is measured along the a axis. The inset shows the enlarged plot of $\rho(T)/\rho(0)$ with regard to $\rho(0)$ in the low-temperature part. The value of $\rho(0)$ was estimated by fitting to $\rho(T) = AT^2 + \rho(0)$ in the range of $T_c<T<4$ K.

REFERENCES:

[1] S. Ran *et al.*, Science, **365** (2019) 684.
[2] D. Coleman and P. Lacy, Mater. Res. Bull., **2** (1967) 935.
[3] H. Sakai *et al.*, Phys. Rev. Mat., **6** (2022) 073401.

PR7-6 Exploration of new interactions between actinide 5f electron systems and photo-excited organic π-electron systems

N. Ishikawa

Department of Chemistrys,Graduate School of Science, Osaka University

INTRODUCTION: Lanthanide and actinide complexes have high magnetic anisotropy due to the orbital angular momentum component in the total angular momentum of the f-electronic systems. Unlike 4f electrons, 5f electrons are characterized by a large covalency involved in chemical bonding. On the other hand, phthalocyanine (Pc), one of the representative macrocyclic ligands, has a cyclic π-conjugated system and acquires orbital angular momentum in the π-π* excited state.

Our group has confirmed the existence of a magnetic interaction between these two angular momenta (J-L interaction) in rare-earth Pc complexes by temperature- and magnetic-field-dependent magnetic circular dichroism (HT-VH-MCD) spectroscopy.

Previously, our group has identified the existence of a magnetic interaction between these two angular momenta (J-L interaction) in rare-earth Pc complexes by temperature- and magnetic-field-dependent magnetic circular dichroism (HT-VH-MCD) spectroscopy [1][2]. This interaction has been observed in sandwich-type bilayer complexes [Pc2Ln] (Ln=Tb, Dy) and monolayer complexes [PcLn(cyclen)]. Similar interaction was confirmed in the sandwich bilayer complex [Pc_2Ln] and the monolayer complex [PcLn(cyclen)].[3][4]

In this study, we measured VT-VH-MCD in the visible energy region for the monolayer Pc complex of U(IV) as well as that of Th(IV), structure of which is shown in Fig.1, to investigate magnetic interaction between the $(5f)^2$ system and the ligand π-conjugate system in a photo excited state.

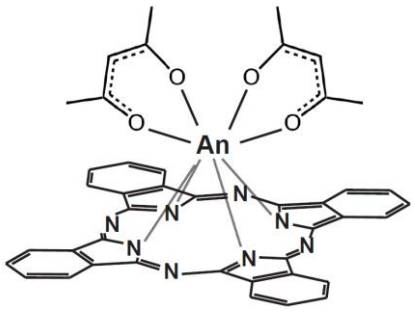

Fig. 1. Structure of PcAn(acac)$_2$ (An=U or Th).

EXPERIMENTS: Bisacetylacetonatophthalocyaninnatouranium(IV), PcU(acac)$_2$, was prepared according to the literature method from lithiumphthalocyanine and tetraacetylacetonatouranium(IV), latter of which was provided by Dr Yamamura (Institute for Integrated Radiation and Nuclear Science、Kyoto University). MCD measurements were performed using a J-Spectroscopy J-720 circular dichroism dispersometer equipped with an Oxford SM4000 superconducting magnet cryostat. The uranium complex was doped in a thin film of polymethyl methacrylate (PMMA) and subjected to measurements. VT measurements were performed in the temperature range from 1.5K to 100K under the magnetic field of IT and VH measurements were in the magnetic field from 0T to 6T at 1.5K.

RESULTS: The U and Th complexes show very similar absorption spectra in the visible energy region due to the ligand centered π-π* transition. Both complexes exhibit a sharp absorption band called Q band at around 14000-15000 cm^{-1}, which is typical for monolayered Pc complexes. MCD spectrum of this band shows a characteristic differential profile called A-term MCD. This indicates that the excited state is doubly degenerate and split by Zeeman effect. The Th complex with no 5f electron showed no temperature dependence in the MCD spectrum. On the other hand, the U complex with $(5f)^2$ system showed a significant temperature dependent MCD, as shown in Fig. 2. This is clear evidence for the existence of a magnetic interaction between the $(5f)^2$ system and the photo-excited circular π conjugation.

In order to quantify this interaction, a numerical simulation analysis was performed. Currently, an assumption that lowest substate in the J=4 multiplet is Jz=4 gives the best agreement to the experimental result. Quantum-chemical RASSCF-RASSI calculation has been performed to evaluate the validity of the assumption and the numerical model used.

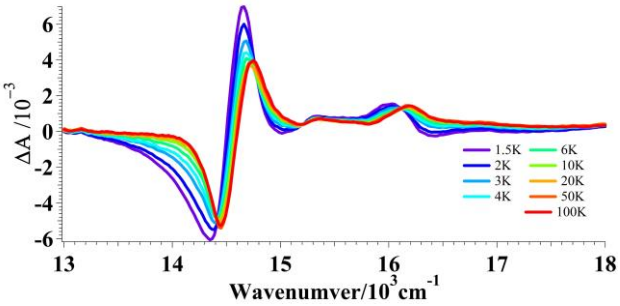

Fig. 2. Temperature dependence of MCD spectra of PcU(IV)(acac)$_2$ in visible range at the temperatures from 1.5K to 100K under magnetic field of 1T.

REFERENCES:

[1] K. Kizaki *et al., Chem. Commun.,* **53** (2017) 6168-6171.
[2] T. Fukuda *et al.,* CHEM.-EUR. J., **23(64)** (2017) 16357-16363.
[3] K. Kizaki *et al.,* Inorg. Chem., **60(3)** (2021) 2037-2044.
[4] K. Kizaki *et al.,* Inorg. Chem. Front., **10** (2023) 915-925.

PR7-7 Fundamental Study on Extraction/Separation of Actinides and Their Decay Products for Medical Nuclide Production – Dissolution Methods of ThO_2 by Themochemical Conversion –

T. Suzuki[1], F. Yin[1], S. Fukutani[2], M. Toyama[2], and T. Yamamura[2]

[1]*Department of Nuclear System Safety Engineering, Ngaoka University of Technology*
[2]*Institute for Integrated Radiation and Nuclear Science, Kyoto University*

INTRODUCTION: Many amounts of decay products are generated from uranium and/or thorium chemicals which are stored in long term. If these decay products are extracted and/or transmuted, we can obtain the several kinds of nuclides and can apply them to many fields such as medicine. While, concern of nuclear therapy using α-nuclides recently increases. Especially, Ac-225 is one of the most concerning α-nuclides. However, Ac-225 don't exist in nature, because it is nuclide in Np decay series. There are several kinds of generation methods of Ac-225, e.g., $^{226}Ra(n,2n)^{225}Ra \rightarrow {}^{225}Ac$. We have proposed $^{229}Th/^{225}Ac$ generator, Th-229 is generated by $^{228}Ra(n,\gamma)$ reaction. Our plain of obtaining Ra-228 is recovery of decay products from thorium. We have plan to use the residue of rare earth ore and/or long storage thoria, because the old thorium under the condition of radioactive equilibrium is desirable. For obtaining this type generator, development of the dissolution method of thorium compounds, extraction of Ra-228 from thorium and other decay products, manufacturing of stable target, irradiation of neutron, and separation of Th-229, etc. are required. In this year, we investigated the dissolution method of ThO_2 by thermochemical conversion.

EXPERIMENTS: Firstly, we investigated dissolution of CeO_2 as simulant material of ThO_2 and searched the optimum condition of dissolution. 4 kinds of halides are used as reactant chemicals for thermochemical conversion. Weight ratio of CeO_2/halides was 1/10. These mixtures were put into Swagelok capsule and heated. After heating, the obtained products were dissolved by conc. HCl or HNO_3. After filtration, the concentrations of Ce were measured by ICP-MS, and the dissolution percentage were calculated. The dissolution experiments of ThO_2 were carried outby by the same procedures as CeO_2, but temperature and heating time were kept to one condition, 300°C, and 4h.

RESULTS: The dissolution results of CeO2 are shown in Fig. 1. We confirmed that the dissolution rate by HCl is higher than HNO_3, and temperature affects the dissolution rate. We found that the almost all CeO_2 can be dissolved by the thermochemical conversion method using CCl_4, CCl_3CCl_3, and CBr_4 as reactant. By the way, the experiments using CCl_4 was carried out as reference experiments, because CCl_4 was forbidden the engineering use. The dissolution results of ThO_2 are shown in Fig. 2. We also confirmed that almost all ThO_2 can be dissolved by thermochemical conversion method. The highest percentage of dissolution was obtained in the case of CBr_4 as reactant and dissolution by HCl.

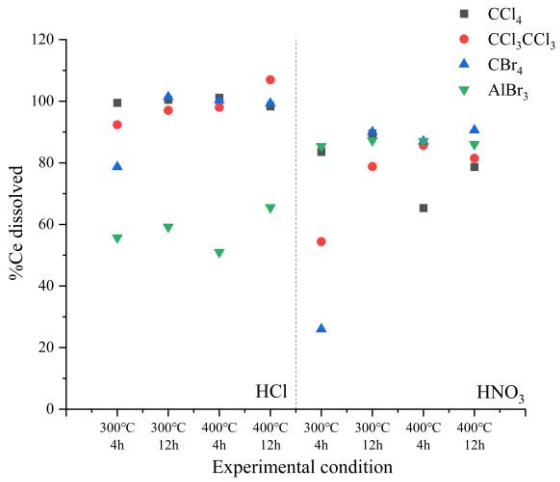

Fig. 1. Dissolution percentage of CeO_2 by thermochemical conversion.

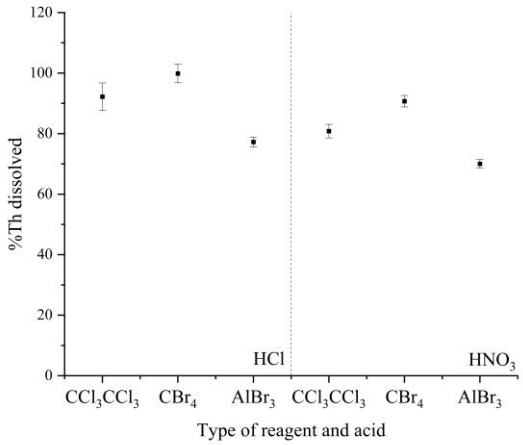

Fig. 2. Dissolution percentage of ThO_2 by thermochemical conversion.

PR7-8 Potential Another Factor to Give Selective Complex Formation between Monoamide Compounds and Actinyl Ions

M. Nogami[1] and T. Yamamura[2]

[1]*Faculty of Science and Engineering, Kindai University*
[2]*Institute for Integrated Radiation and Nuclear Science, Kyoto University*

INTRODUCTION: Development of highly selective compounds for actinyl ions has been important. We have been focusing on monoamide compounds as promising candidates, considering the possibility of complete incineration of waste compounds (so-called "CHON principle"[1]). Earlier we have considered two factors for interaction between monoamides and actinyl ions; one is "chelating effect" of the ring formed by polymer monoamides and actinyl ion(s), and the other is "flexibility" of monoamide. For our synthetic organic resins with a monoamide structure as the functional group, we have not found any clear tendency between the chemical structure of functional monoamide and the adsorptivity[2].

Recently we have found that another research group has tried to develop compounds which are selective for uranium(VI) (UO_2^{2+}) species. According to the group, UO_2^{2+} ion prefers to form "planner five-coordinated complexes" which are scarcely seen in other metal ions, and based on the knowledge they developed H_2saldian-type ligands[3]. In addition, as one of the application of those ligands, a novel adsorbent for recovery of U in seawater was synthesized, where complex formation occurs outside of main chain of polymer[4]. In this report, applicability of this factor "formation of planner five-coordinated complexes" to monoamide compounds we have examined was discussed.

RESULTS: Our main target solvent for using monoamide compounds is nitric acid. A typical coordination style of a monoamide compound to UO_2^{2+} in HNO_3 media is shown in Fig. 1. It can be seen that one UO_2^{2+} ion is surrounded by two carbonyl oxygen atoms of two monoamide molecules and in total four oxygen atoms of two nitrate ions, forming a six-coordinated complex. Judging from the figure, it would difficult to form a five-coordinated complex under usual circumstances.

While, as an example apart from monoamide compounds, we have been investigating one of triphosphine trioxides, 1,1,3,5,5-pentaphenyl-1,3,5-triphosphapentane trioxide (PPTPT : Fig. 2) for a potential versatile extractant [3]. Although PPTPT has high selectivity for U(VI) in HNO_3 of high concentrations, the most distinguished nature of it would be its unusual high selectivity for U(VI) in HNO_3 of very low concentrations. Our preliminary structure analysis of an PPTPT-UO_2^{2+} nitrate complex by single X-ray has revealed that one UO_2^{2+} ion is surrounded by two PPTPT molecules by in total four phosphoryl groups and one oxygen atom from H_2O, forming a five-coordinated complex. This suggests that formation of five-coordinated complexes by monoamide compounds may be possible if realization of preferential coordination of other ligands than NO_3^- to UO_2^{2+} is achieved. Such an approach may be investigated next year.

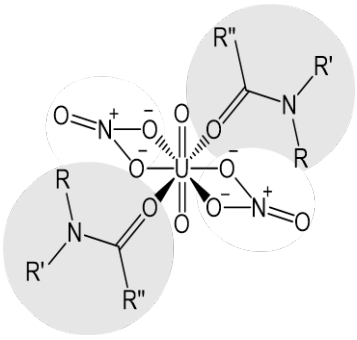

Fig. 1. Typical coordination style of a monoamide compound to UO_2^{2+} in HNO_3

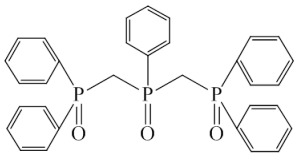

Fig. 2. Chemical structure of PPTPT.

REFERENCES:

[1] M. G. B. Drew *et al.*, Dalton Trans., (2007) 244-251.
[2] M. Nogami *et al.*, KURNS Progress Report 2019, (2020) PR13-5.
[3] T. Mizumachi *et al.*, Inorg. Chem., **61** (2022) 6175-6181.
[4] K. Ito *et al.*, 2023 Annual Meeting, Atomic Energy Soc. Jpn, Mar. 2023, 1H08.

I-1. PROJECT RESEARCHES

Project 8

PR8 Fundamental Research on Decommissioning of Reactor Facility

J. Hori

Institute for Integrated Radiation and Nuclear Science, Kyoto University

OBJECTIVES and RESEARCH SUBJECTS:

The main objective of this research project is to improve the method and the fundamental information on decommissioning of KUR and the Fukushima-Daiichi NPPs. This project consists of seven research subjects from four institutions, as follows.

R4P8-1: Neutron Flux Measurement for Activation Modeling of KUR facility (T. Sano *et al*., Kindai Univ.)

R4P8-2: Measurement of Activation in the Structure Materials of Reactor for Decommissioning Process (K. Takamiya *et al*., Kyoto Univ.)

R4P8-3: Fundamental Research about Radioactive Contamination Survey on Nuclear Reactor Facility (S. Fukutani *et al*., Kyoto Univ.)

R4P8-4: Neutron Capture Cross-Section Measurements with TC-Pn in KUR for Some Nuclides targeted for Decommissioning (S. Nakamura *et al*., JAEA)

R4P8-5: Identification of Nuclear Material in Spent Fuel (Y. Nauchi *et al*., Central Research Institute of Electric Power Industry)

R4P8-6: External Neutron Source for Non-Destructive Analysis of Fuel Debris (Y. Nauchi *et al*., Central Research Institute of Electric Power Industry)

R4P8-7: Study on Non-destructive Analysis Method for Fuel Debris using Neutron Resonance Absorption (J. Hori *et al*., Kyoto Univ.)

One research project (R4P8-3) could not be reported in this fiscal year since a sampling inspection of the object is under way.

MAIN RESULTS and CONTENTS of this REPORT:

T. Sano *et al*. (R4P8-1) installed an "ERYNGII" neutron detector system around E-4 of the biological shield. The detector system consists of a BF_3 detector, a polyethylene moderator, and a cadmium plate for measuring the epi-thermal neutron flux. The results indicate that the ERYNGII can be used to efficiently observe the epi-thermal neutron flux on the surface of the KUR biological shielding.

S. Fukutani *et al*. (R4P8-3) corrected core samples from the KUR stack made of RC (Reinforced Concrete) and γ-spectrometry by a high-purity Ge detector was performed. As for the inner side sample, no significant artificial nuclide was detected by 200,000 second measurement. In contrast, Cs-137 was detected in the outer side sample with enough long measuring time. The detected Cs-137 was considered to be from fallout of atmospheric nuclear test in 60s～70s.

S. Nakamura *et al*. (R4P8-4) measured the neutron capture cross-sections of ^{45}Sc, ^{63}Cu, ^{64}Zn, ^{109}Ag, ^{113}In and ^{186}W, which were important reactions from the viewpoint of clearance level in decommissioning. The activation experiments were performed by using the TC-Pn of KUR. For the cross-section of ^{45}Sc, it was found that its evaluation is appropriate. For the other nuclides, their results deviate from the guideline, and therefore it follows that their thermal-neutron capture cross-sections must be modified to match the guideline.

Y. Nauchi *et al.* (R4P8-5) measured the gamma-ray spectrum from the short-lived fission products (FPs) by irradiating a uranium and aluminum alloy sample at the LINAC neutron source facility. They focused on the gamma-ray events out of phase (OOP) of the pulsed source by using a TOF method. In the time region from 20 to 50 ms, the gam-ma-ray peaks due to the short lived FPs such as ^{90}Rb, $^{95, 97}$Y, and ^{136}Te were identified in the gamma-ray pulse-height spectrum. In this work, possibility of spectroscopy for OOP events was explored for measurement of FP from ^{235}U.

Y. Nauchi *et al.,* (R4P8-6) obtained the response of the neutron induced gamma ray spectroscopy (NIGS) for an 2.45 MeV neutrons generated by fusion reactions of deuterium in plasma formed in an inertial electrostatic confinement device (IEC source). Gamma rays from the stacks of sheets of uranium and polyethylene were measured with a BGO detector. As the current conclusion, the IEC neutron source is preferable to detect fission prompt gamma rays. If we want to quantify capture gamma-rays from SS contained in waste with nuclear material, gamma ray shielding from the IEC device itself would be required.

J. Hori *et al*., (R4P8-7) performed the neutron resonance densitometry (NRD) imaging test using natural uranium, minor actinides such as ^{237}Np and ^{243}Am, Cd as a neutron absorber. A gas electron multiplier (GEM) detector was used for transmission neutron detection. By using TOF information, small amount of ^{237}Np behind the Cd sheet was able to be identified. It was found that the NRA imaging technique with the GEM detector will be a useful tool for screening the fuel debris.

PR8-1 Neutron Flux Measurement for Activation Modeling of KUR facility

T. Sano, S. Ikeda, H. Fukuda, J. Hori[1], Y. Yashima[1], Y. Takahashi[1], K. Terada[1], Z. Zhang[1], Y. Fujihara[1]

Atomic Energy Research Institute, Kindai University
[1]Institute for Integrated Radiation and Nuclear Science, Kyoto University

INTRODUCTION: For the decommissioning of the KUR, it is important to evaluate the amount of radioactivation in the generated waste. In particular, it is important to evaluate the radioactivation in the equipments around the biological shield and the neutron tubes. In general, the evaluation of the activation dose is mainly based on numerical calculations (deterministic or probabilistic models), although some part of the activation dose is measured. In numerical calculations, the neutron spectrum and absolute neutron flux are important input information.
In recent years, the performance of computers has improved to the point where it is now possible to calculate neutron flux for the entire facility, including buildings, and to evaluate the injected neutron spectrum into facilities and equipment. However, the absolute values often differ by several 10% or more between the calculated and measured values.

Therefore, the purpose was to compare calculated and measured values in this study. In last year's study, a neutron detector was installed on the surface of the KUR biological shield, and preliminary experiments were conducted to evaluate the measurement time and other factors.

EXPERIMENTS: In this experiment, an EneRgY selective Neutron detector containment device for thermal Group neutron InterruptIon "ERYNGII" neutron detector system [1] was installed to measure the epi-fast neutron flux at the surface around E-4 of the biological shield. The ERYNGII shown in Fig.1 consists of a BF_3 detector, a polyethylene moderator, and a cadmium plate. The ERYNGII cuts off the thermal neutron by cadmium cover and improves the sensitivity to the epi-fast neutron by neutron moderation in the polyethylene. Neutron flux measurements were performed at the KUR thermal power of 1 MW, and the measurement time was 450 sec.

RESULTS: A measured pulsed height spectrum is shown in Fig.2. The wall effect of the counting tube can be observed near 750 ch and 1500 ch, and peaks due to alpha particles and ^{7}Li particles can be observed near 2400 ch and 2950 ch, respectively. The total counts over 800 ch, which are the signal due to neutrons, were 60867 counts, and the counting rate was 135.3. These results indicate that the ERYNGII can be used to efficiently observe the epi-fast neutron flux on the surface of the KUR biological shielding.

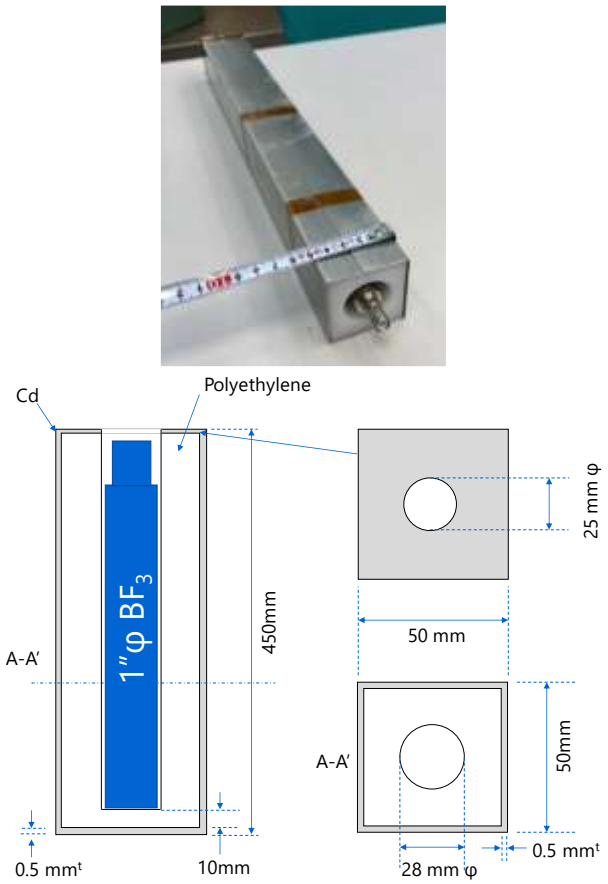

Fig. 1. Photograph and schematic diagram of neutron detector installation to the ERYNGII.

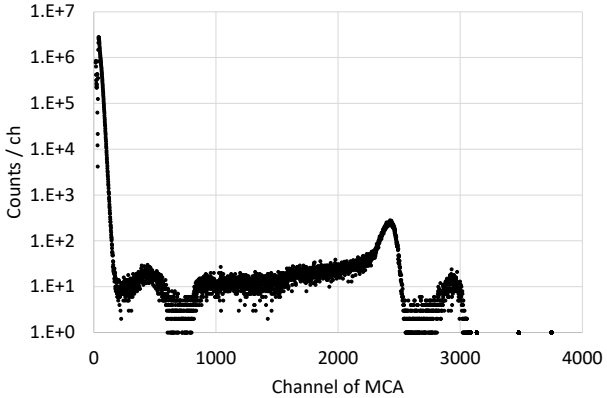

Fig. 2. Measured pulsed height spectrum.

REFERENCES:

[1] R. Kimura *et al.*, Proc. PHYSOR2022, Pittsburgh, USA, **2824** (2022).

PR8-2 Fundamental Research about Radioactive Contamination Survey on Nuclear Reactor Facility

S. Fukutani, J. Hori and K. Takamiya

Institute for Integrated Radiation and Nuclear Science, Kyoto University

INTRODUCTION: It is important to survey radioactive contamination for decommission of nuclear reactor facilities. The KUR stack made of RC (Reinforced Concrete) was demolished in 2013, and radioactive contamination of the demolition waste of the stack was surveyed. The stack was built in 1963.

EXPERIMENTS: In demolishing, coring the core was conducted to hang and transport the stack. Core samples were corrected at the time, and were used in this study. One of core samples, shown in Fig. 1, length: 16.2cm, weight: 3440g, was chosen, and about 1mm from the surface of the inner and outer side by using a grinder, respectively. The inner side is contacting side with exhaust gas from the reactor room. The cut sample by the grinder is in powder form, and about 10g of each sample, the inner and the outer, was enclosed into U8 type container, and measured γ-ray by HPGe detector (Ortec GEM 30-70).

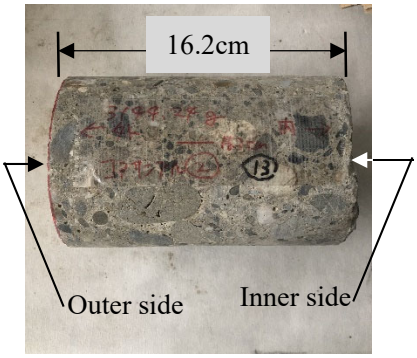

Fig. 1. Core sample from KUR stack.
Inner side is contacting side with exhaust gas, and outer side is faced side with outside air.

RESULTS: γ-spectrometry by HPGe detector was analyzed by the software of Gamma Studio® (SEIKO EG&G). As for the inner side sample, no significant artificial nuclide was detected by 200,000 second measurement. Using the γ-ray peak position of Cs-137 (661.6keV) and that peak area, Activity of Cs-137 was calculated by the Gamma Studio® and standard radiation source manufactured by JRIA (Japan Radioisotope Association). Radio activity and detection limit value of the 661.6 keV peak area for measurement times were shown in Fig. 2. The detection limit gradually decreased in proportion as measurement time increase. However, the radio activity of the 661.6 keV peak area was under the detection limit value at 200,000 second measurement time. In contrast, Cs-137 was detected in the outer side sample. Radio activity and detection limit value of the Cs-137 for measurement times

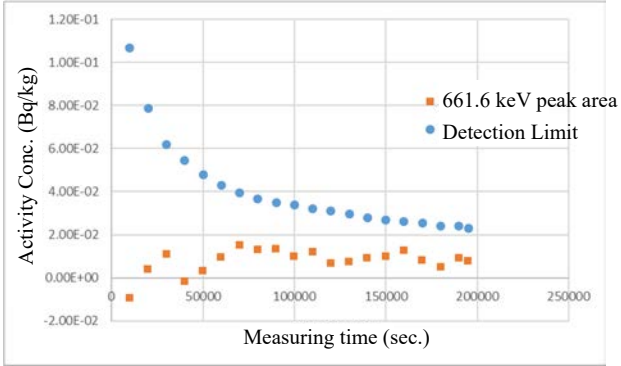

Fig. 2. Changes of activity concentration of 661.6 keV peak area and detection limit with respect to measurement time.

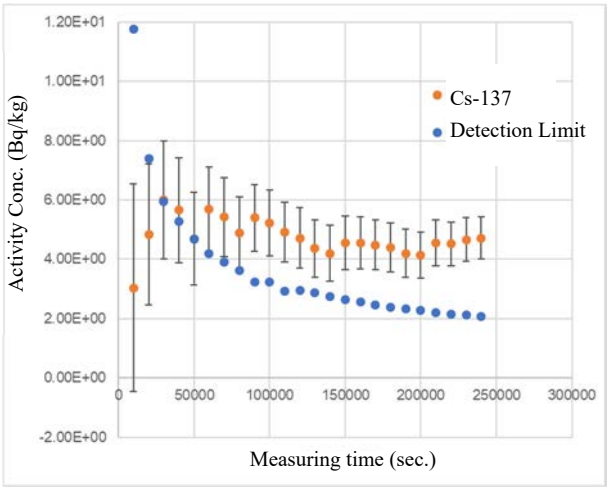

Fig. 3. Changes of activity concentration of Cs-137 and detection limit with respect to measurement time.

were shown in Fig. 3. In short measuring time, 10,000～30,000 second, significant activity of Cs-137 was not detected. But, with enough long measuring time, Cs-137 was detected significantly for detection limit. The detected Cs-137 was considered to be from fallout of atmospheric nuclear test in 60s～70s.

ACKNOWLEDGEMENT: Authors would like to thank members of Technical Staff Office for their contribution to preparation of measuring samples.

PR8-3 Neutron Capture Cross-Section Measurements with TC-Pn in KUR for Some Nuclides targeted for Decommissioning

S. Nakamura[1], S. Endo[1], A. Kimura[1], Y. Shibahara[2]

[1]*Japan Atomic Energy Agency*
[2]*Institute for Integrated Radiation and Nuclear Science, Kyoto University*

INTRODUCTION: Structural materials, piping and equipment of nuclear reactor facilities are generated as radioactive wastes by neutron activation. In the decommissioning of a facility, it becomes necessary to evaluate the amount of radioactivity produced, and this is why accurate neutron capture cross-section data will be required. We have demonstrated that the thermal-neutron capture cross-sections can be accurately derived using the TC-Pn of KUR by measuring ^{181}Ta [1] and ^{237}Np [2]. It is possible to systematically measure neutron capture cross-sections with use of the TC-Pn irradiation equipment. Consequently, from the viewpoint of clearance level in decommissioning, the present study selected the following nuclides and measured their neutron capture cross-section: ^{45}Sc, ^{63}Cu, ^{64}Zn, ^{109}Ag, ^{113}In and ^{186}W.

EXPERIMENTS: High-purity metal samples were prepared for neutron irradiation. A gold-aluminum alloy wire, a cobalt foil and a molybdenum foil were used to monitor the neutron flux at an irradiation position. **Figure 1** shows a schematic of irradiation targets. The samples were arranged so as not to interfere with each other as drawn as "Target (a)" in Fig.1. Due to the inner size of the target capsule, the Zn sample was placed at a different position together with a set of neutron monitors as "Target (b)". To make use of the well-thermalized neutron field, two dummy capsules were sent into the TC-Pn, and followed by the target capsule. The targets were irradiated for 1 hour in 1-MW operation of the KUR.

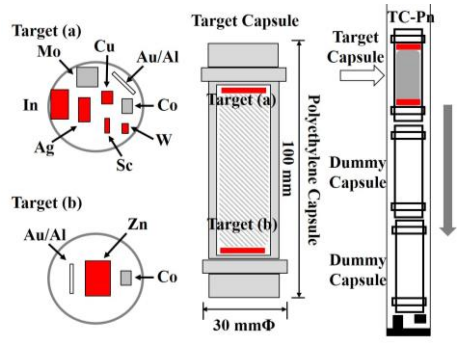

Figure 1. Schematic of irradiation targets.

After irradiation, the target capsule was opened, samples and flux monitors were enclosed in a vinyl bag one by one, and then γ rays emitted from the samples and monitors were measured with a high-purity Ge detector. The sample was placed at a distance of 100 mm from the front surface of the Ge detector. The γ-ray peak efficiencies of the Ge detector were measured with a ^{152}Eu calibration source and a mixed source. In consideration of the radioactivity and half-life of the nuclides, the samples were measured one by one so that sufficient γ-ray peak yields could be obtained.

ANALYSIS and RESULTS: The reaction rates of flux monitors (^{197}Au, ^{59}Co and ^{98}Mo) were obtained from their γ-ray yields. Using these reaction rates, the thermal-neutron flux component was derived on the basis of *Westcott*'s convention [3], and found to be (5.92±0.10) ×10^{10} *n*/cm^2/sec at the position of Target (a) as shown in **Figure 2**. The thermal flux component is indicated by the guideline in Fig. 2. The obtained rection rate divided by the evaluated thermal-neutron capture cross-section is also plotted for each nuclide in Fig.2. If the thermal-neutron capture cross-sections are appropriate, the results must fit on the guideline. For the cross-section of ^{45}Sc, it was found that its evaluated thermal-neutron capture cross-section is appropriate. So was the cross-section of ^{64}Zn of Target (b). For the other nuclides, their results deviate from the guideline, and therefore it follows that their thermal-neutron capture cross-sections must be modified to match the guideline. Considering the uncertainty evaluation, we currently proceed with the analysis toward the derivation of the final results of the thermal-neutron capture cross-sections.

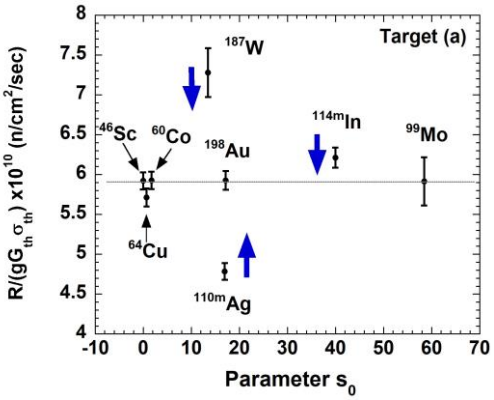

Figure 2. Discrepancies in neutron flux components between the flux monitors and metal samples.

REFERENCES:

[1] S. Nakamura *et al*., J. Nucl. Sci. Technol., **58 (10)** (2021) 1061.
[2] S. Nakamura *et al*., J. Nucl. Sci. Technol., **59 (11)** (2022) 1388.
[3] C.H. Westcott *et al*., "Proc.2nd Int. Conf. Peaceful Use of Atomic Energy, Geneva", **16** (1958) 70.

PR8-4 Identification of Nuclear Material in Spent Fuel

Y. Nauchi, J. Hori[1], T. Sano[2], K. Terada[1], S. Sato

Energy Transformation Research Laboratory, Central Research Institute of Electric Power Industry
[1]Institute for Integrated Radiation and Nuclear Science, Kyoto University
[2]Atomic Energy Research Institute, Kindai University

INTRODUCTION: We have conducted γ ray spectroscopy for reactions induced by thermal and resonance energy neutrons at the LINAC neutron source facility in KURNS [1]. In the facility, accelerated pulsed electron is injected onto a tantalum (Ta) target to generate neutrons. The neutrons are moderated in light water surrounding the target. We put a sample at distance 11~12 m from the target and measure the γ ray spectrum from the sample. By measuring time difference between the pulse injection and the γ ray counting, we can determine the energy of neutrons inducing the reactions. The flight time of thermal neutrons (25 meV) from the water to the sample is about 5 ~ 5.5 ms. By setting the pulse frequency 50 Hz, we can obtain the prompt γ ray emission events induced by the thermal and the resonance energy neutrons.

When we measured γ ray spectrum from an Uranium (U) sample of natural ^{235}U enrichment irradiated by neutrons radiated periodically in frequency of 50 Hz, we found γ ray emission in the time region after decay-out of the thermal energy neutron. γ ray spectroscopy for such **o**ut **o**f **p**hase (OOP) events might give information of radioactivity of short half-lives induced by neutrons on the phase of the pulsed source. In this work, possibility of spectroscopy for OOP events was explored for measurement of fission products (FP) from ^{235}U.

50Hz MEASUREMENT: An U and aluminum (Al) alloy sample was measured in this work. The ^{235}U enrichment is 97 wt%. The time spectrum of γ ray counting starting from the injection of the pulsed electron is shown in Fig. 1. The spectrum is terminated at the pulse period of 20 ms. The thermal energy peak appears around 3.3 ms. After that, the counting rate decays out and asymptotes to a constant. The spectrum was also measured for a condition where cadmium (Cd) plate is placed upstream of the sample to filtrate out the thermal energy neutrons. By comparison of the count rates with and without the Cd plates in time region from 16 ms to 20 ms, significant count rate of OOP events originated in reaction of ^{235}U induced by the thermal energy neutron are found.

The γ ray pulse height spectra in time regions are shown in Fig. 2. In the thermal energy peaks from 2 ms to 6 ms, count rate is large and continuum components due to ^{235}U fission is significant as well as capture γ rays from ^{27}Al and ^{1}H. Such prompt components decay with time but ^{27}Al(n,γ) and ^{1}H(n,γ) appear until 14 and 16 ms, respectively. Contrarily, 1.778MeV γ ray from decay of ^{28}Al becomes significant as the time increase. ^{28}Al is generated by ^{27}Al(n,γ) reaction and its half-life is 2.245 min. This γ ray is preferable to check stability of pulse height gain.

20Hz MEASUREMENT: To focus on the radioactivity of short-lived FPs free from the prompt γ rays, time region is extended up to 50 ms by changing the pulse frequency to 20 Hz. As shown in Fig. 1, the count rate around the thermal energy peak is reduced to 40 % due to reduction of the beam current compared to the 50 Hz operation. The count rate in the OOP region from 16 to 20ms is also reduced, but the time spectrum becomes stable in time region. The γ ray pulse height spectrum in the time region from 20 to 50ms is shown in Fig. 3. By comparing the measured spectrum to the data in JENDL / FPY & FPD-2011, ^{90}Rb, ^{95,97}Y, ^{136}Te, etc. are identified.

REFERENCES:

[1] Y. Nauchi *et al.,* KURNS pro-gress report 2020 (2021) 93.
[2] J. Katakura, JAEA-Data/Code 2011-025, 2012.

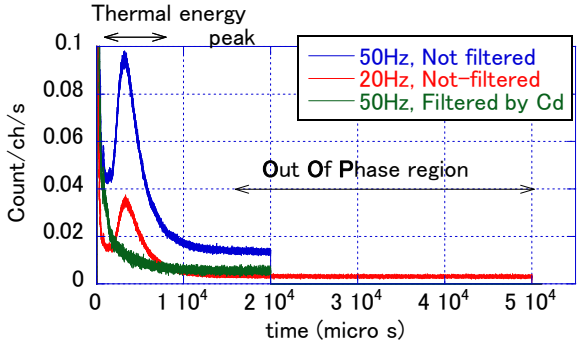

Fig. 1. Time spectrum of γ ray counting from electron pulse injection onto Ta target.

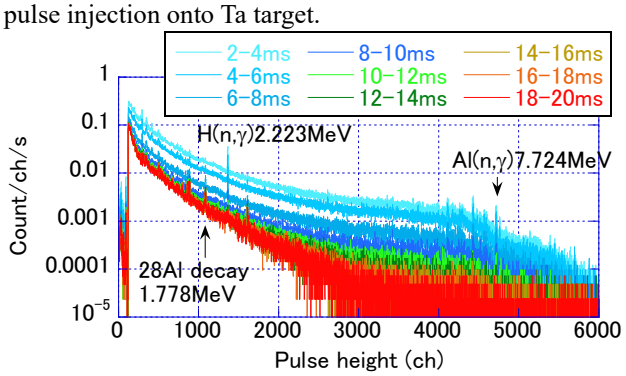

Fig. 2. γ ray pulse heigh spectrum for time region.

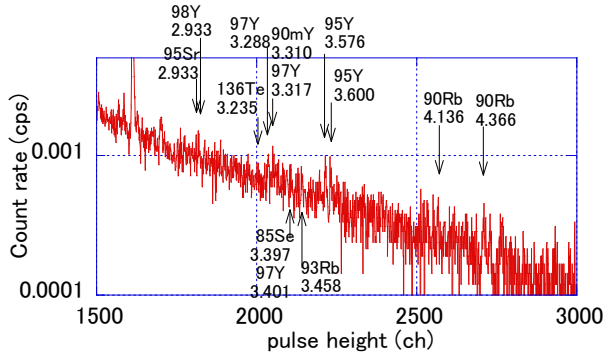

Fig. 3. γ ray pulse spectrum measured for time region from 20 to 50 ms (pulse frequency is 20 Hz).

PR8-5 External Neutron Source for Non-Destructive Analysis of Fuel Debris

Y. Nauchi, Y. Takahashi[1], T. Shiba[2], M. Kaburagi[3], J. Hori[1], K. Terada[1], S. Sato

Energy Transformation Research Laboratory, Central Research Institute of Electric Power Industry
[1]Institute for Integrated Radiation and Nuclear Science, Kyoto University
[2]Integrated Support Center for Nuclear Nonproliferation and Nuclear Security, Japan Atomic Energy Agency
[3]Collaborative Laboratories for Advanced Decommissioning Service, Japan Atomic Energy Agency

INTRODUCTION: Waste retrieved from primary container vessels of unit 1, 2, and 3 of Fukushima dai-ichi nuclear power plant (1F) must be stored safely and efficiently. Unless the amount of nuclear material in the waste is confirmed to be less than a limited value, the waste should be treated caring for criticality safety. Such storage would be a burden for operators. To reduce the burden, we should identify and quantify the nuclear material. For the purpose, the authors have studied the neutron induced gamma ray spectroscopy (NIGS) [1, 2]. By NIGS, the fissile can be identified by measuring fission prompt γ ray. The count rate indicates the products of the amount of nuclear material and the neutron flux in a sub-critical system. For NIGS, we use an external neutron source. One of the candidates for the source is 2.45 MeV neutrons generated by fusion reactions of deuterium induced in plasma formed in an inertial electrostatic confinement device (IEC source). In this study, we obtained response of NIGS for an IEC source in the measurement room of the KUCA facility.

EXPERIMENTS: We used stacks of U sheets of 5.08 cm × 5.08 cm × 0.524 cm together with polyethylene (PE) sheets of 0.3085 cm in thickness. 20 sets of U and PE sheets were used for a stack and three stacks (U+PE sample) were used for the measurement as shown in Fig. 1. In additional measurement, stacks of U sheets without PE sheets were also used for the sample (U sample). We employed bismuth germinate scintillator (BGO) of 7.62cm in diameter and 7.62cm in thickness. To shield thermal neutron, ^{6}LiF sheets are placed surrounding the BGO. Polyethylene blocks of 15 cm in thickness was placed between the sample and the BGO to shield the BGO from fast neutrons. The sample was irradiated by neutrons from the IEC source. In the IEC source, deuteron plasma is formed in a cylindrical chamber of radius of 30 cm. The wall of the chamber is made of stainless steel (SS). Lower energy X ray radiated from the plasma is shielded by sheet of lead.

RESULTS: The measured spectra are shown in Fig. 2. The U+PE sample itself radiates considerable amount of γ ray of energy less than 2 MeV, represented by 1.001 MeV γ ray from ^{234m}Pa. The count rate is reduced in energy region greater than 2.615 MeV (green line). Then we focus on the γ ray emission in the energy range greater than 3 MeV in NIGS, as in the case applied for 1F. By the neutron radiation on PE from the IEC source, H(n,γ) 2.223 MeV γ ray is found (blue, red, black line). Without the samples (blue line) irradiated by neutrons from the IEC source, rather flat spectrum is spread up to 7.7 MeV. That is due to neutron capture reactions in wall of chamber of the IEC source made of SS. That is an intrinsic background when we use the IEC neutron source. The γ ray spectrum from U+PE irradiated by the IEC source (red line) differs from the No Sample case (blue line) in the energy region from 3 to 4.5 MeV. The difference indicates the fission prompt component targeted in this work. This component is also identified when the U sample without PE was used (black dashed line). It is preferable that we can obtain signature of fissile for different neutron moderation condition since the moderation conditions is difficult to be quantified in the waste in 1F.

As the current conclusion, the IEC neutron source is preferable to detect fission prompt γ ray since background γ rays in energy range from 3 to 4.5 MeV is rather flat and the count rate is not significant. If we want to quantify capture γ rays from SS contained in waste with nuclear material, γ ray shielding from the IEC device itself would be required.

REFERENCES:

[1] Y. Nauchi *et al.*, J. Nucl. Sci. Technol., **52(7-8)** (2015) 1074-1083.
[2] T. Shiba *et al.*, Proc. FDR2022, 2022.

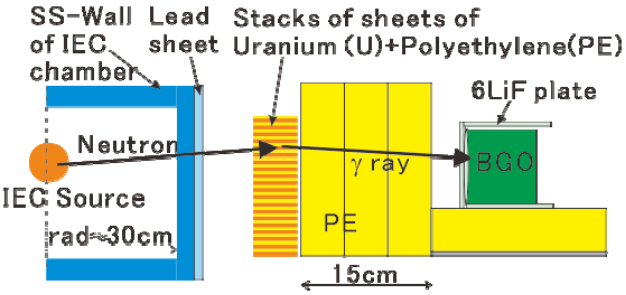

Fig. 1. Schematic view of experimental setup.

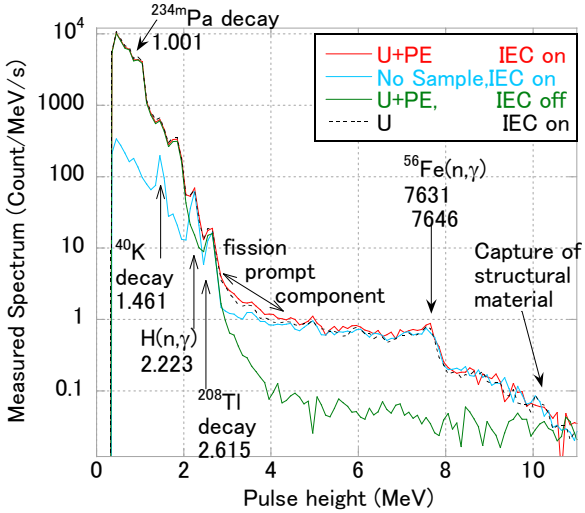

Fig. 2. Pulse height spectrum of γ rays from U+PE or U samples irradiated by neutrons from IEC source.

PR8-6 Study of Non-destructive Analysis Method for Fuel Debris using Neutron Resonance Absorption

J. Hori[1], T. Sano[2], Y. Takahashi[1], H. Yashima[1],and K. Terada[1]

[1]*Institute for Integrated Radiation and Nuclear Science, Kyoto University*
[2]*Atomic Energy Research Institute, Kindai University*

INTRODUCTION: In the units 1 to 3 of Fukushima Daiichi Nuclear Power Plant, the fuel, the metal cladding, and the control rods were melted and large amount were re-solidified in the bottom of the pressure vessel as fuel debris. Characterization of fuel debris is one of the most important issues in the process of the decommissioning. As the fuel debris contains high level radioactive materials such as fissile materials, fission products, and minor actinides, it is difficult to analysis of component directly in the high-dose-rate field. Therefore, the development of non-destructive analysis is necessary for the characterization of fuel debris. We have studied the neutron resonance densitometry (NRD) [1]. In this project research, the NRD technique will be applied to neutron imaging of radioactive material.

EXPERIMENTS: The experiment was performed at the 46-MeV electron linear accelerator in Institute for Integral Radiation and Nuclear Science, Kyoto University. The linac was operated with a repetition rate of 200 Hz, a pulse width of 100 ns, a peak current of about 5 A. The pulsed neutron beam was collimated to 50 mm in diameter. Samples were placed on an aluminum plate of the square of 4 cm. We attached natural uranium foils to the whole plate. Moreover, the sealed minor actinide (MA) samples were placed on the plate. Neptunium-237 and Americium-243 oxide powder were packed in aluminum disk containers, whose inner diameters were 20 mm. The activities of ^{237}Np and ^{243}Am were 26 MBq and 950 MBq, respectively. The right half of the plate was covered with a Cd sheet of thickness 0.5 mm. The sample arrangement of the experiment is shown in Fig. 1. The sample plate was placed in the center of beam line at a distance of about 12 m from the neutron source. The beam spot was indicated by a dot line as shown in Fig. 1.

Transmission neutrons were measured by a gas electron multiplier (GEM) detector (THIN-GEM; Bee Beans Technologies Co., Ltd.). We obtained a TOF spectrum for each pixel. The spatial resolution is 0.8 mm and the total area is 10×10 cm^2.

RESULTS: The neutron radiographs obtained by gaiting on a TOF region are shown in Fig. 2. In the case of thermal neutron region, the part of Cd sheet was only observed and MA samples were not observed. It indicated that small amount of MA cannot be detected with the conventional neutron imaging. On the other hands, the ^{237}Np sample was identified by gating on the resonance region of ^{237}Np. The 23Np sample behind the Cd sheet was also observed. It is found that the NRA imaging technique has high nuclide identification capacity.

The NRA imaging technique with the GEM detector will be a useful tool for screening the fuel debris.

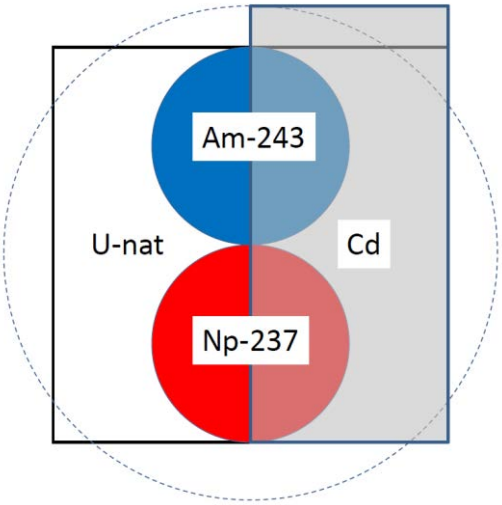

Fig.1 Sample arrangement of U-nat, Am-243, Np-237, Cd for the NRD neutron imaging experiment.

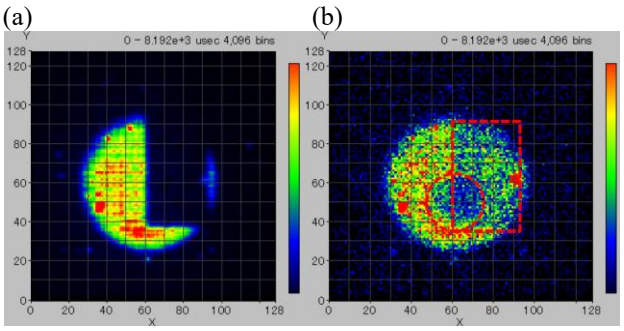

Fig.2 Neutron radiographs obtained by (a) gating on the thermal region and (b) gating on the resonance region of Np-237.

REFERENCES:

[1] J. Hori *et al*., EPJ Web Conferences, **146** (2017) 09042.

I-2. COLLABORATION RESEARCHES

1. *Slow Neutron Physics and Neutron Scattering*
2. *Nuclear Physics and Nuclear Data*
3. *Reactor Physics and Reactor Engineering*
4. *Material Science and Radiation Effects*
5. *Geochemistry and Environmental Science*
6. *Life Science and Medical Science*
7. *Neutron Capture Therapy*
8. *Neutron Radiography and Radiation Application*
9. *TRU and Nuclear Chemistry*
10. *Health Physics and Waste Management*
12. *Others*

CO1-1 Improvement of multilayer mirrors for neutron interferometer

M. Kitaguchi, T. Fujiie[1], and M. Hino[2]

KMI, Nagoya University
[1]*Graduate School of Science, Nagoya University*
[2]*Institute for Integrated Radiation and Nuclear Science, Kyoto University*

INTRODUCTION: Neutron interferometry is a powerful technique for studying fundamental physics. Numerous interesting experiments [1] have been performed since the first successful test of a single-crystal neutron interferometer [2]. However, the single-crystal interferometer is inherently not able to deal with a neutron that has a wavelength longer than twice its lattice constant. In order to investigate problems of fundamental physics, including tests of quantum measurement theories and searches for non-Newtonian effects of gravitation, the interferometry of cold neutrons is extremely important, since the sensitivity of interferometer for small interaction increases with the neutron wavelength. A large scale of interferometer also has the advantage to increase the sensitivity to small interactions.
One of the solutions is an interferometer using neutron multilayer mirrors [3]. We succeeded in developing a multilayer interferometer for cold neutrons in which two paths are completely separated for the first time using wide-gap etalons [4]. We can easily control parameters such as Bragg angle, reflectivity, and Bragg peak width by selecting the deposited material and tuning the bilayer thickness and the number of layers.
We have started the development of multilayer interferometer at the beamline 05 NOP in MLF. From 2019, we are continuing the experiments with etalons with monochromatic mirrors in order to demonstrate the performance of the interferometer. Figure 1 shows the interference fringes with etalons according to time-of-flight. The phase of interferogram depends on the wavelength of neutrons. We are testing the practical application of the interferometer. Neutron coherence scattering length of the material can be measured by inserting the sample into a path of the interferometer. The results of the trial measurements were consistent with the literature values.
Because the mirrors have narrow bandwidth of the neutron reflectivity, the number of neutrons contributing to the interference is limited. When the neutron supermirrors whose lattice constants vary gradually are utilized in the interferometer, the effective range of neutron wavelength can be broadened to be applicable to a pulsed source. In addition, the wavelength dependence of the interactions can be measured simultaneously by using pulsed neutrons.

EXPERIMENTS AND RESULTS: We are continuing to fabricate the neutron mirrors with wide band for the interferometer by using Ion Beam Sputtering facility in KURNS. The mirrors should have the wide and smooth top of the reflectivity with the range of momentum transfer from 0.4 nm^{-1} to 1.0 nm^{-1}. Especially, half mirrors with the wide range of neutron wavelength are needed for the interferometer. In 2022, we have been able to fabricate multilayer mirrors with stable performance. We also measured the reflectivity at MINE2 in JRR3. Figure 2 shows the reflectivity of the half mirrors on the fused silica substrates. Neutron wavelength was 0.88 nm and the bandwidth of the beam was 2.7% of the wavelength. We will try to create an interferometer with the mirrors shortly.

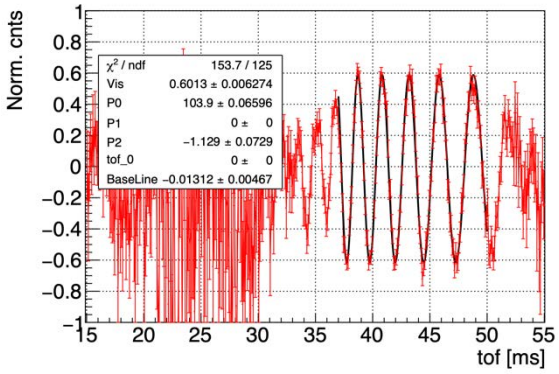

Fig. 1. Normalized interference fringes with multiplayer mirrors for pulsed neutrons.

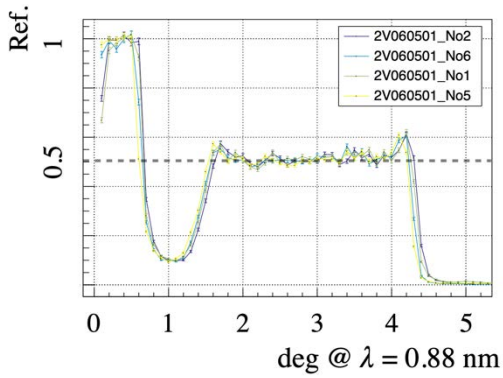

Fig. 2. Reflectivity of the half mirror with wide band of neutron wavelength. Colors represent the sample ID.

REFERENCES:
[1] H. Rauch and S. Werner, Neutron Interferometry Oxford University Press, Oxford, 2000;
J. Byrne, Neutron, Nuclei and Matter Institute of Physics Publishing, London, 1994, Chap. 7;
Mater Wave Interferometry, edited by G. Badurek, H. Rauch, and A. Zeilinger North-Holland, Amsterdam, 1988.
[2] H. Rauch *et al.,* Phys. Lett., **47A** (1974) 369 .
[3] M. Kitaguchi *et.al.,* Phys. Rev. A, **67** (2003) 033609.
[4] Y. Seki *et. al.,* J. Phys. Soc. Jpn., **79** (2010)124201.

CO1-2 Development of a Spin Analyzer for Ultra-Cold Neutron

S. Kawasaki, T. Higuchi[1], S. Imajo[1], H. Akatsuka [2], K. Mishima[3], M. Kitaguchi[2], and M. Hino[4]

Institute of Particle and Nuclear Study, KEK
[1]Resarch Center for Nuclear Physics, Osaka University
[2]Graduate School of Science, Nagoya University
[3]Institute of Material Structure Science, KEK
[4]Institute for Integrated Radiation and Nuclear Science, Kyoto University

INTRODUCTION: Existence of non-zero permanent electric dipole moments (EDM) of the fundamental particles violates time reversal symmetry. Under CPT conservation, T violation implies CP violation. Thus, a precise measurement of an EDM may reveal the origin of the matter dominant universe. The TUCAN (TRIUMF Ultra-Cold Advanced Neutron source) collaboration aims to measure a neutron EDM with a sensitivity of 10^{-27} ecm, which is one order better sensitivity than the current best measurement.

The neutron EDM is measured by precise measurements of spin precession frequency of neutrons. Ultracold neutrons (UCNs) , whose kinetic energies are less than a few 100 neV, are used for the measurement. One of the key components of the measurement is a spin analyzer of UCNs. The kinetic energy of an UCN is so low that magnetic potential can be used as a spin filter. When iron, which has a large saturation magnetization of 2.2 T, is used for the spin filter, the effective potential V_{eff} is

$$V_{eff} = V_{Fe} \mp |\mu| \cdot |B| = 90 \text{ neV, or } 330 \text{ neV}$$

Where $V_{Fe} = 210$ neV is the Fermi potential of the iron, $\mu = 60$ neV/T is the magnetic moment of the neutron, and $B = 2.2$ T. Only one spin state of UCNs with kinetic energies between 90 neV to 330 neV can transmit the iron magnetic potential. Therefore, magnetized iron film functions as an UCN spin filter. In order to reduce UCN absorption, the iron layer should be as thin as an order of 100 nm.

EXPERIMENTS: The thin iron films were prepared by an ion beam sputtering facility at the Institute for Integrated Radiation and Nuclear Science, Kyoto University (KURNS). We produced thin iron on Si substrates and Al foils similar to the actual UCN spin analyzer size of 83 mm in diameter. Figure 1 shows the way of iron film fabrication by the sputtering.

We conducted experiments to evaluate the spin-analyzing power of the ion films at Beamline 05 of the Material Life Science Experimental Facility at J-PARC, where pulsed UCNs were available. Figure 2 shows the setup of the experiments. Two sets of electromagnets are used to magnetize iron films. One is used as a spin polarizer and the other is used as a spin analyzer. Two spin flippers are installed between the spin polarizer/analyzer. A UCN detector is used to measure the UCNs transmitted through those components. The spin polarizer/analyzer performance is evaluated from the UCN counts with the spin flippers on and off. Using the time-of-flight information, we can evaluate the performance according to the energy of the UCNs.

Fig. 1. Thin iron film

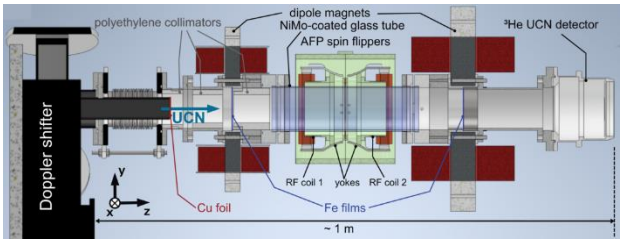

Fig. 2. Experimental Setup

The iron films on the Si substrates and on the Al foils were tested. As we reported last year and [1], the iron films on the Si substrates have much smaller coercivity than that on Al foil. In order to evaluate the dependence of polarizer/analyzer performance on the applied magnetic field, several measurements with different magnetic fields were conducted.

RESULTS:

Figure 3 presents the preliminary results of the measurements. The polarization/analysis power shows as a function of UCN wavelength. In figure 3(a), a comparison between the iron films on the Si substrates and that on the Al foils in the same magnetic field on 120 Oe. The iron film on Si substrates has slightly higher performance. Figure 3(b) shows a comparison of different magnetic fields. We can observe a significant increase between 60 Oe and 120 Oe, On the other hand, it looks saturates higher magnetic fields. However, further analysis is required to finalize the analysis.

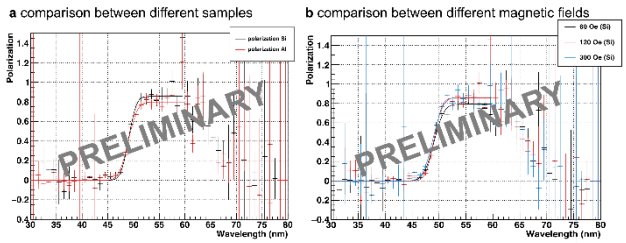

Fig.3. Preliminary Results. The solid lines indicate a fit to a model. (a) The energy dependent polarization of UCNs of iron films on Si substrates and on Al foils. (b) The magnetic field strength dependence on the UCN polarization.

REFERENCES:

[1] H. Akatsuka *et al.,* JPS Conf. Proc., **37**, (2022) 020801.

CO1-3 Development of High-resolution Cold/Ultracold Neutron Detectors Using Nuclear Emulsion

N. Naganawa, M. Hino[1], H. Kawahara[2], M. Kimura[3, 4], M. Kitaguchi[2, 5], K. Mishima[6, 7], A. Muneem[8], N. Muto[2], J. Yoshida[8]

Institute of Materials and Systems for Sustainability, Nagoya University,
[1]Institute for Integrated Radiation and Nuclear Science, Kyoto University
[2]Graduate School of Science, Nagoya University
[3]Nagoya Proton Therapy Center, Nagoya City University West Medical Center
[4]Graduate School of Medical Sciences, Nagoya City University
[5]Kobayashi-Maskawa Institute for Origin of Particles and the Universe (KMI), Nagoya University
[6]High Energy Accelerator Research Organization (KEK)
[7]J-PARC Center
[8]High Energy Nuclear Physics Laboratory, Cluster for Pioneering Research, RIKEN

INTRODUCTION:

Experiments measuring spatial distributions of ultracold neutrons in the Earth's gravitational field have been conducted [1-3]. Quantum behaviors of neutrons in the gravitational field have been studied and unknown short-range forces have been searched by them. In order to measure the spatial distributions with a higher resolution, authors have been developing a high-spatial-resolution cold/ultracold neutron detector [5] using a fine-grained nuclear emulsion [4] whose silver halide crystals' diameter is 40 nm. The detector is fabricated by sputtering a converter layer of $^{10}B_4C$(50 nm)-NiC(60 nm)-C(20 nm) on one side of a 0.4 mm-thick Si wafer and applying the fine-grained nuclear emulsion gel of 10 μm-thick directly on the converter layer. The sputtering was done by an ion-beam sputtering system in KURRI (KUR-IBS) [6]. The detector has a spatial resolution of less than 100 nm [5]. We conducted test experiments at Institut Laue-Langevin (ILL) to obtain spatial distributions of ultracold neutrons in the gravitational field in collaboration with qBOUNCE group, and the distribution was successfully obtained [9]. Also, studies for applications to high-resolution neutron imaging started [7, 8]. To prepare for the next measurement of spatial distributions at ILL and studies for neutron imaging, we sputtered the converter layer on Si wafers and checked its stability by applying the fine-grained nuclear emulsion gel, exposing it to α-ray, developing it, and observing the emulsion layer under the microscope.

EXPERIMENTS:

Six Si wafers with thickness of 0.5 mm were sputtered of $^{10}B_4C$(200 nm)-NiC(50 nm)-C(10 nm) layer by KUR-IBS. A piece of wafer of 1 cm × 2 cm was cut out from one of the sputtered wafers. Next, fine-grained nuclear emulsion gel was applied on the piece and dried under the room temperature. Next, the piece was exposed to α-ray using ^{241}Am source. After that, it was developed with a developer, XAA, for 20 minutes in 20℃. The sputtered layer and the emulsion layer were checked of their stability during the development. Finally, the emulsion layer was observed by epi-illumination microscope.

RESULTS:

The both layers were stable during the development. Tracks of α-particles were clearly observed without decrease of grain densities. There was no fog increase. It was confirmed that the mechanical and chemical stability of the converter layer was sufficient for experiments.

REFERENCES:

[1] V. V. Nesvizhevsky *et al.*, Nature, **415** (2002) 297.
[2] H. Abele *et al.,* Nucl. Phys. A, **827** (2009) 593c–595c.
[3] G. Ichikawa *et al.,* Phys. Rev. Lett., **112** (2014) 071101.
[4] T. Asada *et al.*, Prog. Theor. Exp. Phys., **2017.6** (2017) 063H01.
[5] N. Naganawa *et al.,* Eur. Phys. J. C., **78** (2018) 959.
[6] M. Hino *et al.,* Nucl. Instrum. Methods Phys. Res. A, **797** (2015) 265-270 .
[7] K. Hirota *et al.,* J. Imaging, **7** (2021) 4.
[8] A. Muneem *et al.,* J. Appl. Phys., **133** (2023) 054902.
[9] N. Muto *et al.,* JINST, **17** (2022) P07014.

CO1-4 Towards to ultra small *d*-spacing neutron monochromator

M. Hino[1], T. Oda[2], H. Endo[3], H. Yoshinaga[1]
[1]*Institute for Integrated Radiation and Nuclear Science, Kyoto University (KURNS), Japan*
[2] *ISSP, University of Tokyo, Japan*
[3] *IMSS, KEK, Japan*

INTRODUCTION: Slow neutrons are very powerful and useful in various research fields, such as material and life sciences, particle physics, fundamental engineering. It is necessary for production of neutron beam to use any nuclear reaction and it requires, in general, large facility to obtain high intensity of the neutron beam. More effective neutron intensity is still desired even in advanced large facility. It is quite important for transportation and shaping of neutron beam from the source to the experimental instrument. Recently a big project of new research reactor at the "Monju" site in Fukui prefecture has been started[1]. In case of a continuous neutron source like reactor, monochromator is very useful and smaller d-spacing multilayer is also very significant to enlarge utilization of neutron beam.

EXPERIMENTS:. The multilayer coating was conducted with ion beam sputtering machine at the KURNS (KUR-IBS) [2]. It is necessary for actual production of multilayer neutron mirror to realize large homogeneous deposition area without roughness growth. Figure 1 shows photograph of silicon wafers and glass plates placed on a substrate holder of KUR-IBS. We have optimized the deposition process by considering the deposition rate, gas pressure, the sputtering targets and geometrical condition. Then we found some parameters to fabricate smooth thin layer of which thickness was larger than 1 nm with large homogeneous area. We fabricated NiC(nickel-carbon) and Ti(titanium) multilayer of which the designed d-spacing was gradually changed from 2 nm to 2.2 nm like supermirror. The effective number of layers was 1680. The neutron experiments were conducted at CN-3 beam line at KURNS and C3-1-2(MINE) beam line of JRR-3 at JAEA.

RESULTS: Figure 2 shows measured neutron reflectivity by the multilayer mirror deposited on the silicon wafer(U0) placed on center of the substrate holder shown in Fig.1. A clear and sharp peak was observed at q_z=3.1nm^{-1}. The average d-spacing and the peak reflectivity were estimated to be 2.03 nm 1.5 %, respectively. Here reflectivity by ideal d-spacing multilayer mirror with same number of layer without surface and interface roughness was calculated to be 8%. The reflectivity of 1.5% corresponds to that by the same multilayer deposited on a substrate of which surface roughness was roughness of 0.4 nm (rms). The roughness value 0.3 nm is almost surface roughness of silicon wafer or float glass. Then it was clear that growth of interface roughness of the multilayer was well suppressed even the total thickness of multilayer was about 1.68 μm. Figure 3 shows measured neutron reflectivity by the stacking multilayer mirrors placed on the substrate holder shown in Fig.1. The peak reflectivities of various multilayers were almost same within an area of approximately 40 cm in diameter within the holder shown in Fig.1. With increasing number of stacking of multilayer mirrors, the reflectivity was increased. In case of stacking seven mirrors, we obtained peak reflectivity 8%.

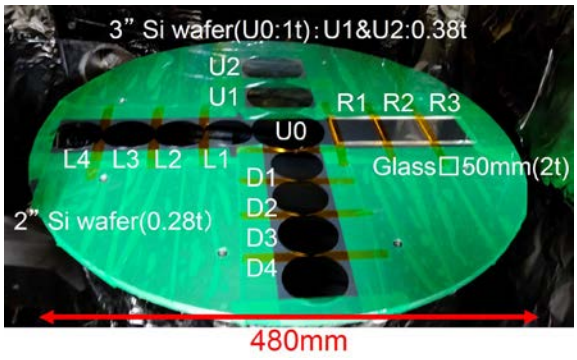

Fig. 1. The photograph of substrate arrangement on a substrate holder of KUR-IBS.

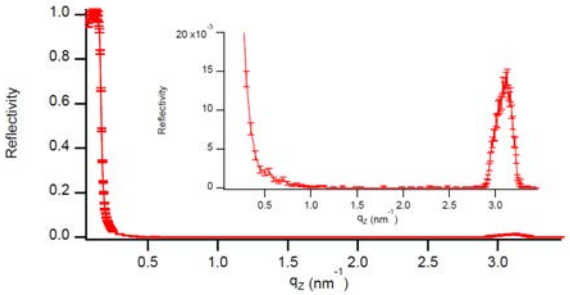

Fig. 2. Measured reflectivity of neutrons by d~2nm multilayer mirror fabricated on center position (U0) shown in Fig.1. The inserted figure is a figure with the maximum of the vertical axis set to 2%. The effective number of layers of the multilayer mirrors is 1680.

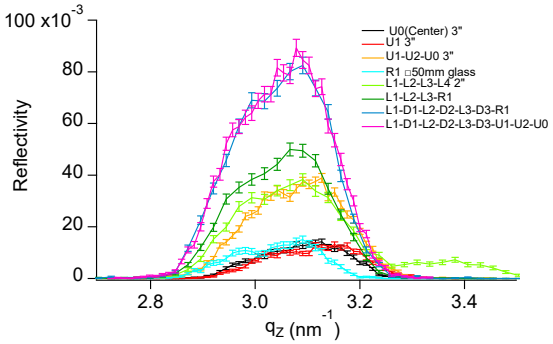

Fig. 3. Measured reflectivity of neutrons by stacking d~2nm multilayer mirrors fabricated on various positions shown in Fig.1.

REFERENCES:

[1] https://www.jaea.go.jp/news/newsbox/2023/032401/s01.pdf (in Japanese).
[2] M. Hino *et al.*, Nucl. Instr. and Meth., **797**(2015) 265.

CO2-1 β-decay spectroscopy of rare fission products with a 4π clover detector using an Isotope Separator On-Line KUR-ISOL

S. Sakakibara, Y. Miyazawa, T. Kuga[1], M. Shibata[2] and A. Taniguchi[3]

Graduate School of Engineering, Nagoya University
[1]*School of Engineering, Nagoya University*
[2]*Radioisotope Research Center, Nagoya University*
[3]*Institute for Integrated Radiation and Nuclear Science, Kyoto University*

INTRODUCTION: The decay data of the fission products are important for evaluating decay heat and determining the structure of neutron-rich nuclei. Many neutron-rich nuclei with mass numbers near 150 do not have detailed decay schemes due to their short half-lives and low fission yields. The nuclide ^{157}Nd was proposed to have a half-life of 1.15 s by Wu *et al*. with β-particle measurements [1] and a level scheme of the daughter nuclide ^{157}Pm was reported by Bhattacharyya *et al*. by the prompt γ-ray measurements of spontaneous fission fragment of ^{252}Cf [2], but, no γ rays associated with the β-decay of ^{157}Nd were reported. To identify the γ rays associated with the β-decay of ^{157}Nd, β-γ coincidence measurements were performed using a high-efficiency clover detector coupled with β-ray detectors with On-line Isotope Separator KUR-ISOL.

EXPERIMENTS: 72 mg of 93% enriched $^{235}UF_4$ target was inserted at the through-hole facility in Kyoto University Reactor. The nuclei of interest were produced by thermal neutron-induced fission of ^{235}U. The nuclei were transported by He-N_2 gas jets and ionized in a thermal ionization ion source. The mass-separated radioactive beams were collected on a thin Mylar tape and periodically transported to the center of the detector by a computer-controlled tape transport system, and were measured with detectors. The clover detector has four large Ge crystals with a diameter of 80 mm and a length of 90 mm arranged in the shape of a four–leaf clover around a through hole with a diameter of 15 mm. Two identical β-ray detectors were made of plastic scintillators 105 mm long, 12.6 mm wide, and 1 mm thick, contacted with a semi-cylindrical light guide with a radius of 6.5 mm. A 3×3 mm^2 MPPC (Multi-Pixel Photon Counter) module C13367 made by Hamamatsu Photonics was mounted on the end of the light guide. The β-detectors were inserted in a through-hole of the clover detector. The whole detector was shielded with 10 cm thick lead bricks and 10 cm thick boron-doped polyethylene blocks outside them to reduce background neutrons and γ-rays. Data were recorded on APV8008 and APV8016 DSP data acquisition systems made by Techno AP Corporation with list mode including time information. The nuclide ^{157}Nd was measured for 39 hours with the both periods of collection and measurement were set 3.0 s. After the experiments, time dependent spectra were extracted to analyze the decay properties of γ rays and KX-rays.

RESULTS and DISCUSSION: To identify the γ rays associated with the β-decay of ^{157}Nd, the decay properties of the γ rays and Pm KX-rays, and also their coincidence relations were analyzed. The coincidence time was set to 700 ns. Fig.1 shows the γ-ray singles and β-γ coincidense spectra for the A=157 radioactivities. It was confirmed that nuclides with adjacent mass numbers 156 and 158 did not mix in the mass-separated A=157 beams. In the β-γ coincidence spectrum, the background radiation such as the γ-ray associated with the decay of ^{41}Ar produced with ^{40}Ar(n, γ) reaction or capture γ-rays of Ge crystals by the neutron in the reactor room were reduced effectively. The peaks were analyzed using the peak fitting program developed by Yamada *et al*. [3] Most γ rays and KX-rays were originated from the β-decay of daughter nuclide ^{157}Pm ($T_{1/2}$=10.56 s) [1] and ground daughter nuclide ^{157}Sm ($T_{1/2}$=8.03 m) [4]. However, from the analysis of the time dependent β-γ coincidence spectra each 1 s as shown in Fig.1(b), and also the add-back of four crystals, and singles spectra, the 66 keV γ-ray and the KαX-ray region correspond to Pm were observed to disintegrate with a half-life shorter than ^{157}Pm. In the prompt γ-ray measurements with ^{252}Cf [2], the 66 keV γ-ray were proposed as the transition from the first excited state to the ground state in ^{157}Pm. The γ ray is possible to be associated with the β-decay of ^{157}Nd. In addition, the KαX-ray region of Pm also disintegrate with almost the same half-life. The precise analyses are in progress.

REFERENCES:

[1] J. Wu *et al*., Phys. Rev. Lett., **118** (2017) 072701.
[2] S. Bhattacharyya *et al*., Phys. Rev., **C98** (2018) 04316.
[3] S. Yamada, KURRI-TR-430.
[4] N. Nica, NDS. **132** (2016)1.

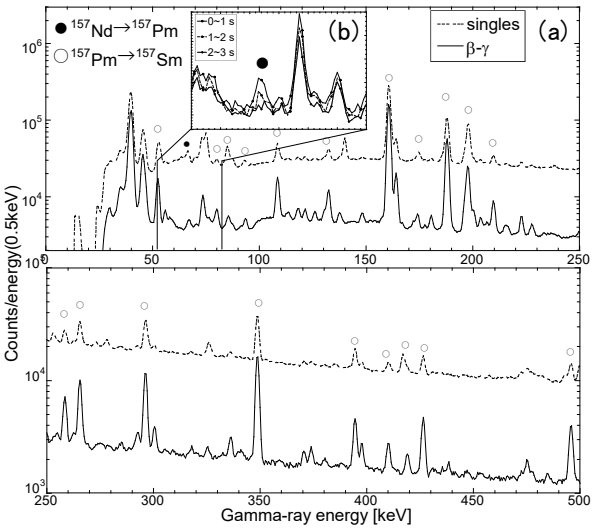

Fig. 1. Singles and β-γ coincidence spectra for the mass-separated beam of A=157 (a). The γ rays marked as ○ are associated with the decay of ^{157}Pm and that of ● is possible to be associated with the decay of ^{157}Nd. The inset (b) shows the time dependent β-γ coincidence spectra each 1 s.

CO2-2 Development and test of a current-mode ^{3}He gas neutron detectors for an intense neutron beam

T. Matsumoto, S. Manabe, A. Masuda, H. Harano, J. Hori[1], K. Terada[1]

National Metrology Institute of Japan, National Institute of Advanced Industrial Science and Technology

[1] Institute for Integrated Radiation and Nuclear Science, Kyoto University

INTRODUCTION: It is necessary to measure the neutron flux for a large dynamic range to connect between a BNCT field in a hospital and a neutron calibration field in the National Institute of Advanced Industrial Science and Technology (AIST). The difference of neutron fluxes between the BNCT field and the calibration field is more than 5 orders of magnitude. We have developed a new ^{3}He gas detector with a thimble ion chamber with a 10-mm diameter and a 10-mm length. Unlike ordinary ionization chambers that are used for gamma-ray measurements, the neutron detector has a structure that allows for gas replacement and gas sealing. The gas detector is expected to be high radiation resistance in comparison with a photo-multiplier tube in the scintillation detector [1]. In the present study, the sensitivity of the neutron detector to thermal and epi-thermal neutrons will be experimentally confirmed from time-of flight (TOF) measurements as a first step.

EXPERIMENTS: A collimated neutron beam with 30-mm diameter was obtained by the photo neutron reaction using a tantalum target with a water moderator at the KURNS Linac [2]. A BF_3 proportional counter was used as a neutron monitor. Figure 1 shows a typical experimental setup. The chamber of neutron detector was filled with ^{3}He gas at 1 atm and N_2 gas at 0.2 atm. A relative gas monitor was also installed to check for gas pressure fluctuations due to gas leakage. The neutron detector was measured by means of the TOF method to confirm that thermal and epi-thermal neutrons were detected. The measurements were performed for both pulse and current modes. In the pulse mode, signals from the ^{3}He proportional counter were obtained using a pre-amplifier (ORTEC 142PC) and main amplifier (ORTEC 570). High voltage (+500 V) was applied to the center electrode. In the current mode, the signals were obtained using a current integrator (ORTEC 439). Hight voltage (+500) was applied to the outer electrode to suppress the dark current. Finally, TOF data were extracted using a multi-stop time to digital converter and a multi-channel analyzer (Fast Com Tec MPA3).

RESULTS: Figure 2 shows TOF results obtained from the measurements in the pulse mode for conditions with and without neutron beam. From figure 2, the structure of thermal bump is clearly observed. Thermal and epi-thermal neutrons were successfully detected. Therefore, it was confirmed that it was not a mistake as the design of the neutron detector structure. On the other hand, it is also found that the background including gamma rays and electric noise observed without the neutron beam is very large. Furthermore, in the current mode, only a very small current on the order of pA was obtained. Because of the small size of the chamber of the neutron detector being developed, with the gas composition used in the present experiments, many of the protons and tritons produced by the ^{3}He(n,p)T reaction were not completely stopped inside the chamber. Therefore, the pulse height output in the pulse mode was very small and the background to signal ratio was poor. For the same reason, the output current was very small in the current mode. We will obtain heavier mass number gases such as Kr and Ar, next year. By filling the chamber with heavier mass number gases instead of N_2 gas, the outputs will be larger than those obtained in the present experiments because many of the protons and tritons produced by the ^{3}He(n,p)T reaction will stop inside the chamber. We plan to use the neutron detector in the current mode. In that case, it is impossible to discriminate gamma rays from output signals. Therefore, a chamber filled with ^{4}He instead of ^{3}He will prepared to subtract the gamma components.

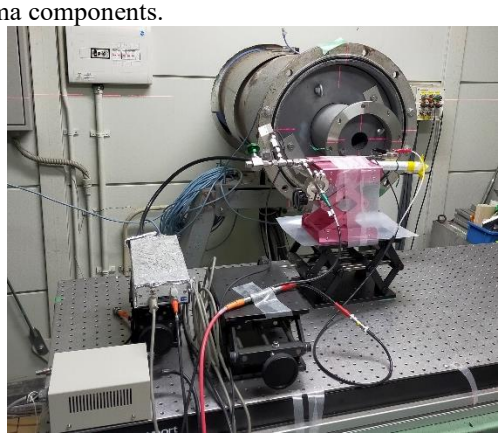

Fig. 1. Experimental setup for the neutron detector at at approximately 12 m away from the target.

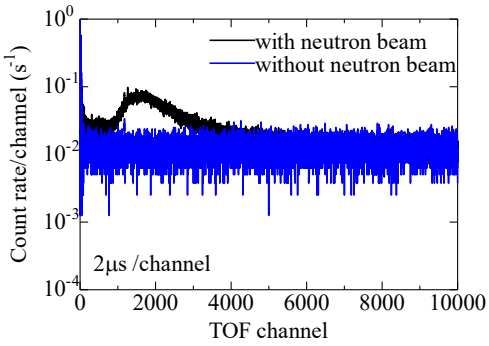

Fig. 2. TOF spectra obtained from the measurements in the pulse mode for conditions with and without neutron beam.

REFERENCES:

[1] T. Matsumoto *et al.,* Radiat. Prot. Dosim., **188 (1)** (2020) 142.

[2] K. Kobayashi *et al.,* Annu. Rep. Res. Reactorinst. Kyoto Univ., **22** (1989) 142.

This work was supported by JSPS KAKENHI (21H03755 and 19K12638).

R4125

CO2-3 Development of neutron resonance analysis technique using a neutron time-of-flight method

J. Lee[1], K. Hironaka[1], M. Koizumi[1], J. Hori[2], T. Sano[3], and Y. Matsuo[3]

[1]*Integrated Support Center for Nuclear Nonproliferation and Nuclear Security, Japan Atomic Energy Agency*
[2]*Institute for Integrated Radiation and Nuclear Science, Kyoto University*
[3]*Atomic Energy Research Institute, Kindai University*

INTRODUCTION: Passive neutron and gamma-ray detectors are widely used for nuclear material measurements in nuclear safeguards and security. However, those techniques could not directory apply for measurement of samples in a shield or with radioactive accompanies. In order to overcome the difficulties, the Japan Atomic Energy Agency (JAEA) is developing neutron interrogation techniques [1]. Neutron resonance transmission analysis (NRTA) is one of the developing active non-destructive assays (NDA) techniques, in which pulsed neutron beam is used to measures a neutron transmission TOF spectrum [2,3]. From the observed nuclide characteristic resonance spectrum, the thickness of each nuclide can be deduced. Nevertheless, measurement of trace fissile materials, such as ^{235}U, and ^{239}Pu, in a sample can be still difficult. To improve the sensitivity to those materials, a use of fission neutron measurement has been proposed. Hereafter, we call the technique as neutron resonance fission neutron analysis (NRFNA), in which fast neurons are measured by using neutron TOF technique. Pulse shape discrimination (PSD) plastic scintillation detectors [4] were employed to distinguish fission neutron events from gamma ray events. In this paper, we report a demonstration experiment of NRFNA carried out at the KURNS-LINAC using ^{nat}U samples.

EXPERIMENTS: The KURNS-LINAC was operated with an acceleration energy of about 30 MeV, and an average current of about 42 μA. Pulsed neutrons were produced by the impact of the accelerated electrons of 50-Hz repetition rate and 2-μs pulse width. The neutrons were slowed down in a moderator, then collimated and guided to a hut for 12-m TOF experiments. The ^{nat}U samples used were 1.5, 3.0, and 6.0 mm in thickness. Eight quadrangular and two hexagonal PSD plastic scintillation detectors (Eljen, EJ-276) were used for fast neutron detection as shown in **Fig. 1**. 20-mm Pb sheets were placed between the detectors and the sample to reduce the gamma ray events from the sample. The output signals of the detectors are directly sent to a digitizer (CAEN V1730D, 14 bit, 500 MSample/s). Processed data was recorded by a computer as a list data.

RESULTS: The achieved data were analyzed. Neutron and gamma ray events are discriminated [4]. Achieved TOF spectra for fission neutron and gamma ray are given in **Fig. 2**. The resonance peaks of 6.67, 20.87, 30.68, and 66.02 eV of the black line are from (n,γ) reactions of ^{238}U, and those of 1.13, 3.14, 3.62, 8.76, 12.39, 19.30, and 35.17 eV of red line are from (n,f) reactions of ^{235}U. Thermal bumps of ^{235}U and ^{238}U were also observed at around 4 ms. Using the PSD scintillation detector system, we successfully separate neuron events from gamma ray events. Further analysis will be performed using Multilevel Resonance Parameter Least Square Fit (REFIT) to establish a method for quantitative analysis. A mutual analyzing method of NRFNA and NRTA will be studied because MRTA measurement can be performed simultaneously using neuron beams passing through the NRFNA system.

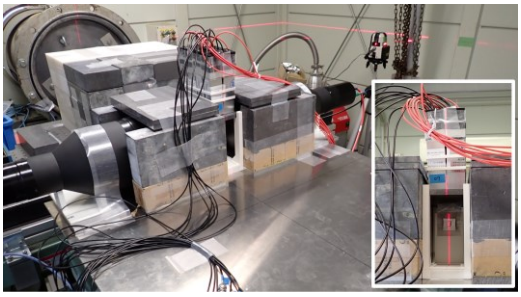

Fig. 1. Experimental setup of NRFNA. The red bricks surrounding the PSD scintillation detector system is for room background reduction.

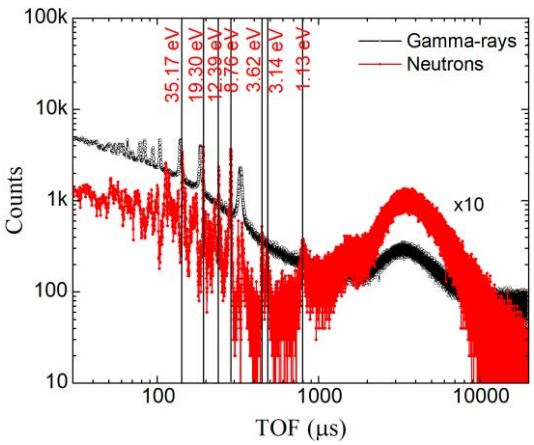

Fig. 2. TOF spectra obtained by the NRFNA experiment.

ACKNOWLEDGEMENTS: This research was implemented under the subsidy for “promotion of strengthening nuclear security and the like” of the MEXT (the Ministry of Education, Culture, Sports, Science, and Technology of the Japanese government).

REFERENCES:

[1] M. Koizumi *et al.*, Proc. of INMM & ESARDA Meeting 2021, #201.
[2] P. Schillebeeckx *et al.*, Nuclear Data Sheets, **113**, (2012) 3054-3100.
[3] H. Postma and P. Schillebeeckx, Neutron Resonance Capture and Transmission Analysis, John Wiley and Sons, 2009.
[4] M. Koizumi *et al.*, Nucl. Instr. Methods. A, **1042** (2022)167424 .

CO2-4 Technique of Transferring Radioactive Atomic Nuclei Implanted in Dry Ice Film

A. Taniguchi, P. Strasser[1] and M. Tanigaki

Institute for Integrated Radiation and Nuclear Science, Kyoto University
[1]Muon Science Laboratory, IMSS, KEK

INTRODUCTION: The nuclear charge radius is one of the fundamental parameters. It gives information about the effective interactions on the nuclear structure. Muonic atoms are an ideal tool for obtaining this parameter because the energy levels of the muon in a muonic atom can be accurately described by the electromagnetic interaction between the negative muon and the nucleus, taking into account the charge distribution of the nucleus, and the effect can be observed as the energies of the X-rays emitted from the muonic atom [1]. However, mainly because of the large amount of radioactivity required, the study of muonic atoms for unstable nuclei has made little progress. We have recently developed a new method for the high-efficiency production of muonic atoms by means of a solid film of hydrogen. In this method, negative muons (μ^-) are injected into a solid film of deuterium (D) in which nuclei of interest (A) have been implanted beforehand, resulting in the formation of muonic atoms via the highly-efficient muon transfer reaction: $\mu^-D + A \rightarrow D + \mu^-A$. The feasibility of this method was demonstrated for some stable isotopes and promising results were obtained [2]. In this study, the expected technical difficulties in applying this method to unstable nuclei, in particular the highly efficient recovery of residual radioactivities in the deuterium film after the experiments, are addressed using a radioactive-isotope beam from the Kyoto University Reactor-Isotope Separator On Line (KUR-ISOL) and a dry ice film instead of a solid hydrogen film.

EXPERIMENTS: At the beamline of KUR-ISOL, an apparatus was installed which is capable of implanting radioactivities in a dry ice film [3]. This apparatus consists of two cuboid movable copper blocks that can be cooled using liquid nitrogen (LN_2) as a coolant and a CO_2 gas diffuser in the vacuum chamber. A film of dry ice is formed on the surface of a cooled block (catcher) by spraying CO_2 gas through the diffuser and radioactivities are implanted into the film. The amount of radioactivities transferred from the catcher to the other block (trap) are examined under different conditions of film formation. In recent experiments, to improve the reproducibility of the transfer efficiency, the film-forming parameters were more finely controlled by recording the vacuum level in the chamber and the temperatures of the copper blocks using a data logger. In addition, "standing collars" were attached on the four sides of the film-forming surface so that more CO_2 gas could be retained near the surface during film formation, and during transfer, the collars covered the catcher-trap gap to allow more CO_2 gas to agglomerate again on the trap block. However, until now, the thickness of the film has not been measured because the white film on the catcher could be visually confirmed, even though the thickness is an important factor in considering the stop position of the implanted ions in the film.

In this experiment, two new gate valves were installed between the vacuum chamber and the two turbomolecular pumps at the apparatus. These valves isolate the vacuum chamber and prevent CO_2 gas from escaping, allowing the experiments to determine film thickness and try out new ways of forming films. A pressure transducer (Swagelok, PTI-S, pressure range: -0.1~0.3 MPa) was also mounted to measure the pressure in the chamber filled with CO_2 gas.

RESULTS AND DISCUSSION: Typically, 300 cc of CO_2 gas at 1 atm was gently sprayed through the diffuser onto the cooled catcher in film formation. It was estimated that 270 cc of CO_2 gas was used to form the film by comparing the pressure at which the isolated vacuum chamber was filled with a given amount of CO_2 gas with the pressure at which the film formed by spraying the same amount of gas sublimated. Assuming that a uniform film was formed on the catcher (25 × 25 mm) with this amount of gas, and using the density of dry ice (1.687 g/cm^3 at 77 K) [5], the thickness of the film was estimated to be approximately 0.39 mm. This suggests that when ideal dry ice is formed on the catcher, the film is thick enough for the implanted ions.

The transfer efficiencies of ^{146}Ce and ^{146}Pr from the catcher to the trap were obtained by detecting the γ-rays emitted from each of the blocks after implantation of about 10^6 ions of $^{146}LaO^+$ into the dry ice film formed in the chamber isolated from the TMPs. (See ref [4,6] for details.) The 454 keV gamma-ray peak counts of ^{146}Pr for the catcher and for the trap were derived by taking into account the detection efficiency of each Ge detector and a ratio of the counts for the trap to those for the catcher was 4:1. This result was not as high as those of previous values [6] and was within the range of variation.

Experiments are needed to develop a highly efficient recovery method while searching for better conditions for dry ice film formation hereafter. In addition to the development, experiments are also planned to focus on the scattering of radioactivities during the implantation.

ACKNOWLEDGMENTS: This research was partially supported by the Ministry of Education, Science, Sports and Culture, Grant-in-Aid for Scientific Research (C) (24540303, Akihiro Taniguchi, and 15K05103, Akihiro Taniguchi).

REFERENCES:

[1] I. Angeli and K.P. Marinova, At. Data Nucl. Data Tables, **99** (2013) 69-95.
[2] P. Strasser *et al*., Hyperfine Interact., **193** (2009) 121-127.
[3] A. Taniguchi *et al*., KURRI Prog. Rep. 2013, p.98.
[4] A. Taniguchi *et al*., KURNS Prog. Rep. 2019, p.4.
[5] T.P. Mangan *at al*., Icarus, **294** (2017) 201-208.
[6] A. Taniguchi *et al*., KURNS Prog. Rep. 2020, p.100.

CO2-5 Validation Experiment of Thermal Neutron Scattering Law Data for Innovative Reactor

J. Hori[1], Y. Takahashi[1], T. Sano[2], K. Terada[1], and H. Yashima[1]

[1]*Institute for Integrated Radiation and Nuclear Science, Kyoto University*
[2]*Atomic Energy Research Institute, Kindai University*

INTRODUCTION: In order to consider the design of innovative reactors, accurate thermal neutron scattering laws (TSLs) for moderator materials are necessary. Calcium hydride is one of the candidate solid moderator materials of a small modular reactor (SMR) [1]. However, TSLs of CaH_2 are not evaluated and stored in JENDL-5 [2]. As for light water which is the most important moderator in a thermal reactor, TSLs were newly evaluated with the molecular dynamics simulation in JENDL-5 and modified remarkably from those of JENDL-4.0 [3]. Validation of the modified evaluated data is needed.

Pulse-neutron die-away (PNDA) experiments have been reported as promising benchmarks for validating TSLs in the previous work [4]. In this study, we suggested a new method to detect the pulse-neutron die-away time by measuring the neutron capture gamma-rays directly. The leakage neutrons from the sample assembly were also measured with a TOF method simultaneously.

EXPERIMENTS: The experiment was performed at the 46-MeV electron linear accelerator in Institute for Integral Radiation and Nuclear Science, Kyoto University. Pulsed fast neutrons were produced from a water-cooled Ta target as a photo-neutron source without moderator. A beam width and a frequency were 100 ns and 200 Hz, respectively. A Cd sheet of 0.5 mm in thickness was inserted into the TOF beam line to suppress overlap of thermal neutrons from the previous pulses. The flight path used in the experiment is in the direction of 135 degrees to the electron beam. The pulsed neutron beam was collimated to 30 mm in diameter.

Each sample assembly was placed at about 10 m from the Ta target. The cylindrical containers made of aluminum were filled with light water or CaH_2 powder. The diameters of the containers were 20 cm and 6 cm for light water and CaH_2 powder, respectively.

The 2.2MeV gamma-rays emitted from the neutron capture by hydrogen in the assembly were measured by a BGO detector. The timing information means die-away time distribution in the assembly. On the other hands, the neutrons moderated in the assembly were also measured by a ^{6}Li-glass detector with a TOF method. The distance between the center of the assembly and the surface of the ^{6}Li-glass detector was 40 cm.

RESULTS: The comparisons of the preliminary experimental results with the calculated ones using JENDL-4.0 and JENDL-5 are shown in Figs. 1 and 2. The Calculations were performed using the MCNP code. The calculated values considering the S(α,β) are close to the experimental results compared to the calculated with the free-gas model. In Fig. 2, the present results show a tendency to support JENDL-5 more than JENDL-4.0.

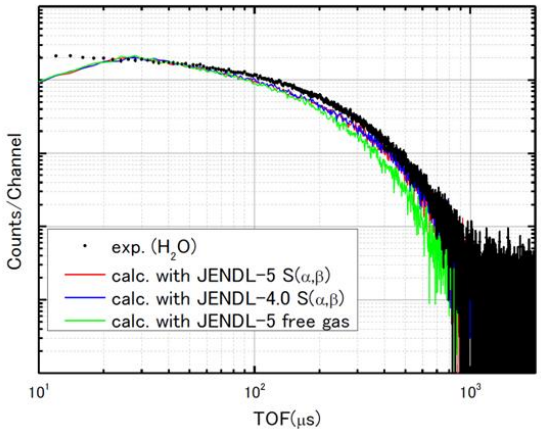

Fig.1. Comparison of the experimental neutron die-away time distribution in the light water assembly with the calculated ones.

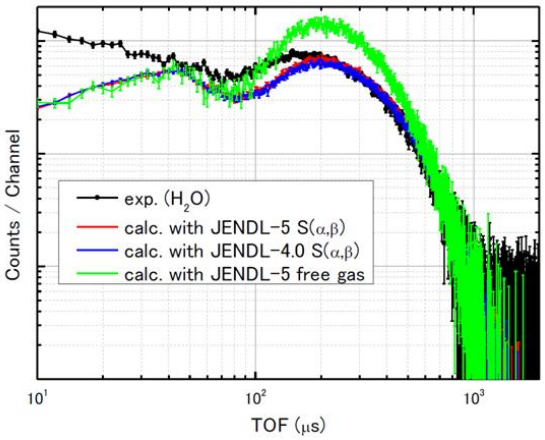

Fig.2. Comparison of the experimental neutron TOF spectrum from light water assembly with the calculated ones.

ACKNOWLEDGEMENT:
This work is supported by the Innovative Nuclear Research and Development Program from the Ministry of Education, Culture, Sports, Science and Technology of Japan.

REFERENCES:
[1] R. Kimura, S. Wada, Nucl. Sci. Eng., **193** (2019) 1013-1022.
[2] O. Iwamoto *et al.,* J. Nucl. Sci. Technol., **60** (2023) 1-60.
[3] K. Shibata *et al.,* J. Nucl. Sci. Technol., **48** (2011)1.
[4] D. Sieman *et al.,* Nucl. Sci. Eng., **197** (2023)14-24.

CO2-6 Measurement of C-13 neutron cross-section for new nuclear battery

T. Wallace-Smith[1], T. Scott[1], Y. Takahashi[2], k. Terada[2], J. Hori[2]

[1]*SouthWest Nuclear Hub, University of Bristol*
[2]*Institute for Integrated Radiation and Nuclear Science, Kyoto University*

INTRODUCTION:

The UK houses 60% of the world's store of irradiated nuclear graphite waste totalling 90,000 tonnes, with Japan also housing large quantities in repositories. This waste contains several key radioisotopes which contribute significantly to the total activity of the waste. Tritium and Carbon-14 are highlighted as commercially useful radioisotopes each with a half-life of 12.32 and 5,700 years respectively. In extracting value from nuclear waste via radioactive material, this reduces the cost burden on Governments in storing waste as removing activity lowers the waste level rating from high to low-level. These beta-emitting radioisotopes are ideally suited for use in beta-voltaics as the energy released during radioactive decay can be harvested using specialised semiconductors. The University of Bristol has several decades experience in the fabrication of such semiconductors like Chemical Vapour Deposition (CVD) diamond, which is exceptionally radiation hard and chemically inert. By incorporating Tritium and C-14 into CVD diamond a highly efficient beta-voltaic power cell can be formed, capable of lasting for decades to centuries with a wide range of uses spanning from the internet of things (IoT) to space exploration. Determining the overall quantity of C-14 in graphite waste poses several challenges, where the best approach is to simulate the burnup of nuclear fuel within a reactor where graphite shielding, or moderator material is used. However, these simulations rely on the nuclear data libraries which are based upon fundamental experimental data. In the case of C13(n, γ)C14, the data is sparse and has a large degree of uncertainty, as seen in Figure 1. Where the latest published experiments which contributed to nuclear data were performed by A. Wallner et al in 2016[1] are expressed as 3 red points. These 3 data points revealed a large resonance in C-13, changing the overall predicted Carbon-14 content in graphite waste by a large degree.

In this project, a new approach to measuring the neutron cross section of C-13 is suggested where multiple methods are used to cross-check one another. Previous work by A. Wallner used sub-1-gram samples irradiated in a nuclear reactor where the generated C-14 was measured by Accelerated Mass Spectrometry (AMS), a method usually associated with carbon dating. At the University of Bristol, the largest ever high purity (>99%) C-13 sample has been prepared by a newly developed method of ethanol slurry compaction, weighing 60 grams. The sample will be neutron irradiated at the Tokyo-Tech using the Pelletron Accelerator where secondary gammas from the C13(n, γ)C14 reaction will be detected, allowing for the measurement of the neutron capture cross section. Additionally, smaller samples will be irradiated at KUR in KURNS for AMS measurements, neutron scattering and activation-analysis. The combined method has never been deployed on a single sample to measure all aspects of neutron interaction in this way. By measuring the C13 neutron interaction cross sections in unparalleled detail, allowing for a more accurate calculation of the quantity of C-14 which can be reused for producing beta-voltaic devices, strengthening the case for repurposing otherwise value-less nuclear waste.

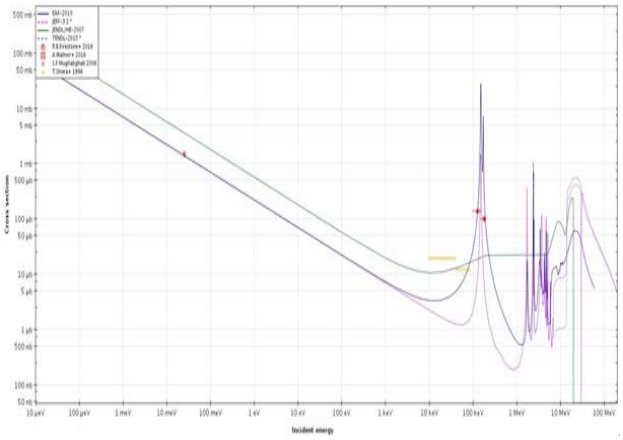

Fig. 1. C13(n, γ)C14 neutron capture cross section from different nuclear data libraries and experiments. The three dots in red represent the 2016 AMS experiments by A. Wallner.

For the prototype Tritium beta-voltaic device, a brand-new manufacture method has been developed. Wherein the diamond Schottky structure, consisting of an ohmic (Boron doped) and Schottky junction, undergoes ion implantation with Helium-3 which quickly transmutes to Tritium during neutron irradiation. This allows for incorporation of Tritium into the diode lattice, improving device efficiency from the previous documented maximum of 24% for radioactive sources situated outside of the lattice, to above 60%. By April 2022, He-3 implanted CVD diodes will be manufactured at the University of Bristol ready for irradiation.

EXPERIMENTS and PRESENT STATUS

Several smaller 1-gram pellets as well as seventeen 20 mg samples in vacuum-sealed ultrapure quartz vials had been prepared for Pelletron accelerator experiment and KUR reactor irradiation. The sample has been irradiated in the hydraulic neutron irradiation chamber at KUR. The sample is currently cooling in KURNS, and we plan to conduct beta ray measurements after cooling.

REFERENCES:

[1] A. Wallner *et al.,* Phys. Review, **C93** (2016) 045803.

CO2-7 Measurement of Energy Resokution in the KURNS-LINAC Pulsed Neutron Facility[3]

T. Sano, Y. Matuo, T. Kanda, Y. Takahashi[1], K. Terada[1], H. Yashima[1] and J. Hori[1]

Atomic Energy Research Institute, Kindai University
[1]Institute for Integrated Radiation and Nuclear Science, Kyoto University

INTRODUCTION: The electron linear accelerator at the Research Reactor Institute, Kyoto University (KURRI-LINAC) had been originally established in 1965 by the High Voltage Engineering Co., USA and started as a 23 MeV machine. In 1971, the machine power had been increased to 46 MeV. The KURRI-linac has two different operation pulse modes. One is a long mode with a maximum repetition rate of 120 Hz, a pulse width of 0.1–4.0 μs and a peak current of about 0.5 A for the measurement at low energies below 10 eV. Another is a short mode with a maximum repetition rate of 300 Hz, a pulse width of 2–100 ns and a peak current of about 5 A for the measurement at high energies above 1 eV. It is worth noting that the peak current of short mode is ten times as large as that of long mode. In measurements of nuclear data, a water-cooled tantalum (Ta) target as a photo-neutron target and a light water moderator are used. There are two kinds of the moderator. One is a water tank type and another is an octagonal shape moderator called "pac-man type". In order to measure accurate nuclear data, it is very important to evaluate the energy resolution (ΔE/E) of a moderator. In 2021, measurement and detail evaluation of energy resolutions for the water tank type moderator has been carried out [1]. In that experiment, prompt gamma radiation from a sample was measured using 12 BGO detectors. The signals from each BGO detector were integrated by a Dual Sum Inverter. It is necessary to evaluate a contribution of that signal integration to the energy resolution.

Then, TOF measurements were performed with and without the Dual Sum Inverter. In the experiment without the Dual Sum Inverter, TOF measurement was performed using a single BGO detector.

EXPERIMENTS: In this study, the energy resolution of KURNS-LINAC was obtained by transmitted neutron flux via ^{181}Ta sample. In order to measure a TOF spectrum, a cylindrical moderator tanks which have 19 cm diameter and 30cm height was installed at the target room. The tanks were filled with light water. We used the neutron at "12 m room" which is located on 135 deg. axis from the electron beam line. The flight path of neutron flux between the sample and the moderator was 12.65 m as shown in Fig.1. The two ^{181}Ta samples which has 0.2 mm and 0.03 mm thickness were employed to consider self-shielding effects at each resonance. The TOF spectrum was measured with 12 BGO detectors or single BGO detector. The signal circuits are shown in Fig.2 and Fig.3. In the experiments, the beam frequency and pulse-width of KURNS-LINAC were 200 Hz and 100 nsec.

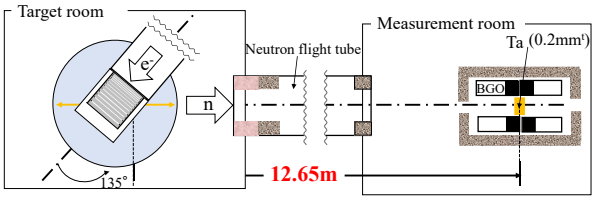

Fig. 1. Experimental geometry.

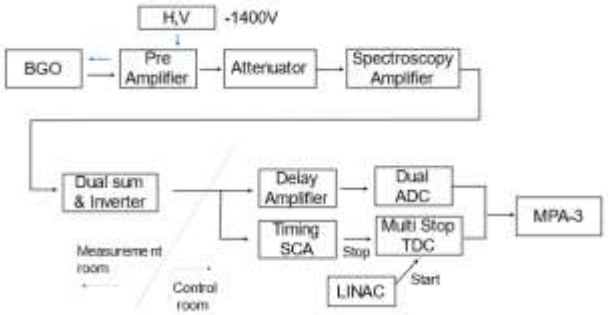

Fig. 2. Signal circuits with a single BGO detector.

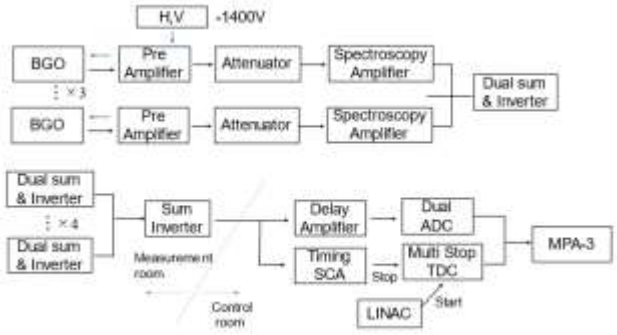

Fig. 3. Signal circuits with 12 BGO detectors.

RESULTS: The energy resolutions were evaluated by comparison between the experimental and the calculated values of FHWM at the resonance absorptions in the obtained TOF spectrum. For the first and second resonances, the sample with 0.03 mm thickness was used for evaluation, and for other resonances, the results of the 0.2 mm thick sample were used. As the results, there was no significant difference of the energy resolutions between the single and 12 BGO systems. Therefore, the contribution of the Dual Sum Inverter to the time resolution of the TOF measurement is sufficiently small.

REFERENCES:

[1] Y. Matsuo, *et. al.,* AESJ 2022 spring meeting, (2022) 2A07.

CO2-8 Search for Tetraneutron Bound State Emitted with Uranium Fission

H. Fujioka, R. Tomomatsu, K. Takamiya[1]

Department of Physics, Tokyo Institute of Technology
[1]Institute for Integrated Radiation and Nuclear Science, Kyoto University

INTRODUCTION: Whereas typical atomic nuclei are composed of both protons and neutrons, there are various attempts to search for multi-neutron systems, such as tetraneutron (^{4}n), which consists of four neutrons. Recently, two experimental groups independently reported positive results on the existence of tetraneutron. T. Faestermann *et al.* used the ^{7}Li(^{7}Li,^{10}C)^{4}n reaction to populate tetraneutron, and found a peak in the ^{10}C energy spectrum. They interpreted it as an indication of the formation of a bound tetraneutron with the binding energy of 0.42±0.16 MeV [1]. On the other hand, M. Duer *et al.* observed a resonance-like structure of tetraneutron in the missing-mass spectrum of the ^{8}He(p,p^{4}He)^{4}n reaction [2], and they extracted an energy of 2.37 ± 0.38(stat.) ± 0.44(sys.) MeV and a width of $\Gamma = 1.75 \pm 0.22(\text{stat.}) \pm 0.30(\text{sys.})$ MeV. While the latter result suggests the tetraneutron would fall apart into four neutrons, the former result implies the tetraneutron would decay via weak interaction, i.e. $^4\text{n} \rightarrow {}^4\text{H} + e^- + \bar{\nu}_e$, with a substantially long lifetime. The existence of a tetraneutron system as a resonance or a bound state is still an open question.

If the tetraneutron system is a bound system of four neutrons, it may activate an isotope in a sample by inducing a secondary reaction, such as a (^{4}n,n) reaction. Tetraneutron search with the activation technique had been extensively utilized in the 1960s and 70s, based on the hypothesis that the tetraneutron bound state could be produced in fission [3]. In particular, samples of amitrole ($C_2H_4N_4$) and pure aluminum were irradiated in a nuclear reactor, CP-5, to search for a signature of ^{17}N and ^{28}Mg, respectively, resulting in a negative result [4]. An upper limit of the production rate of 5×10^{-9} per fission was deduced.

Motivated by the recent findings, we revisited the approach in Ref. [4], and proposed an irradiation experiment at KUR, adopting an approach similar to the instrumental neutron activation analysis. It should be worth stressing that this approach is sensitive only to the bound tetraneutron, which can escape from the fuel elements. Its existence can be addressed in term of the production rate per uranium fission.

METHOD: We adopted a ^{88}Sr sample in the form of strontium carbonate ($SrCO_3$). The primary reason to use ^{88}Sr is that ^{91}Sr, which is to be produced in the ^{88}Sr (^{4}n,n) reaction, has a moderately long half-life and emit 750 keV and 1024 keV γ rays (I_γ=0.237(8) and 0.335(11)) after its β decay. Another important aspect is that the neutron capture cross section of ^{88}Sr is not too large, and the product ^{89}Sr hardly emits γ ray (only 909 keV γ ray with $I_\gamma=9.56(5)\times10^{-5}$) after its β decay, which enables us to irradiate the sample for a long time at the center of the reactor core without inducing high radioactivity.

Two kinds of samples, strontium carbonate with natural abundance ($SrCO_3$) and ^{88}Sr-enriched strontium carbonate ($^{88}SrCO_3$), were irradiated in November 2022 and February 2023, respectively. In the first irradiation, we confirmed that ^{85}Sr (half life: 64.849(7) days), ^{85}Sr^m (half life: 67.63(4) minutes), and ^{87}Sr^m (half life: 2.815(12) hours) are main sources of γ-rays, even though the natural abundances of ^{84}Sr and ^{86}Sr are much smaller than that of ^{88}Sr, in accordance with our expectation. Based on the result, the experimental plan in February 2023 has been established. A 570-mg $^{88}SrCO_3$ sample was irradiated at the center of the reactor core for two hours, using the hydraulic conveyer. After the irradiation, it was cooled for half a day before treatment. Then, we measured γ rays from the $^{88}SrCO_3$ sample with a germanium detector. We repeated the 30-minutes measurements for 48 times.

PRELIMINARY RESULT: Figure 1 displays a preliminary γ-ray energy spectrum. In addition to two prominent photopeaks and their escape peaks from ^{24}Na, we have identified the photopeak due to ^{87}Sr^m, which was produced by neutron capture in ^{86}Sr in the sample (abundance: 0.02%), and many photopeaks due to bromine contamination in a silica tube. If ^{91}Sr isotopes were produced in the ^{88}Sr (^{4}n,n) reaction, we would expect to observe 750 keV and 1024 keV photopeaks in the spectrum. We are carefully analyzing the spectra to evaluate the area of these photopeaks, which is necessary to deduce the production rate of tetraneutron bound states in uranium fission.

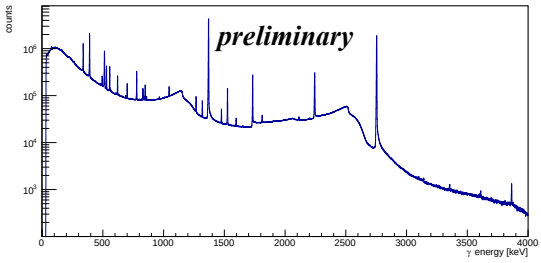

Fig.1. The γ-ray energy spectrum from the $^{88}SrCO_3$ sample. The data from 48 sets of 30-minute measurements are combined.

ACKNOWLEDGMENT: This work is supported by Grant for Basic Science Research Projects from the Sumitomo Foundation.

REFERENCES:

[1] T. Faestermann *et al.,* Phys. Lett. B, **824** (2022) 136799.
[2] M. Duer *et al.*, Nature, **606** (2022) 678.
[3] F. Miguel Marqués and J. Carbonell, Eur. Phys. J. A., **57** (2021) 105.
[4] J. P. Schiffer and R. Vandenbosch, Phys. Lett., **5** (1963) 292.

CO3-1 Basic Research for Sophistication of High-power Reactor Noise Analysis (V)

S. Hohara[1], T. Sano[1], A. Sakon[1], M. Goto[2], T. Kanda[2], K. Hashimoto[1]

[1]Atomic Energy Research Institute, Kindai University
[2]Graduate School of Science and Engineering, Kindai University

INTRODUCTION: Reactor noise for high-power reactors were actively measured in the 1960's and 1970's. The major focuses of those researches were for the abnormality diagnosis or the output stabilization diagnosis, and almost researchers were in the field of system control engineering or instrumentation engineering. High-power reactor noise measurements for dynamics' analysis of reactivity change, reactivity feedback or reactor characteristics itself were few in the time (1960's and 1970's), because of the powerless measurement system. In this research, we plan to measure KUR's output with present-day measurement system and plan to analyze with several analysis methods. The results of this work will supply some knowledges and technics in the aspect of sophistication of reactor noise analysis or simulation methods.
In this year, we tried to measure the reactor nuclide noise of the critical state KUR core via a ^{6}Li Lithium glass scintillator (GS20: Scintacor) at B-3 port focused on epi-thermal neutrons. The experimental work was done on 24th November 2022. As the result of the experiment, a result looks like the nuclear reactor noise was observed in 100W critical state.

EXPERIMENTS:
In this experiment, the output signal of the ^{6}Li Lithium glass scintillator was put into Spectro Scopy AMPs (2022: Canberra and 590A: ORTEC), and the output of the SSAs were measured with a time-series measurement system (HSMCA4106_LC: ANSeeN Inc.). A schematic view of the measurement is shown in Fig.1, and the counter installation overview is shown in Pic.1.

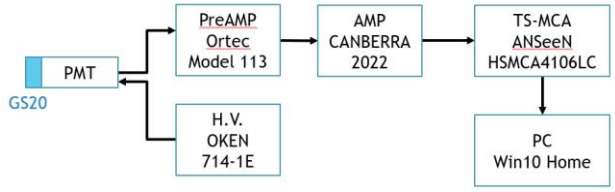

Fig. 1. Schematic view of the measurement.

The experimental condition is shown in Table.1. The reactor Power was set in 100W. The measurement time was 1,000 sec.

Pic. 1. An overview of the counter installation.

Table 1. Experimental condition.

Reactor Power [W]	Measurement Time [sec]	Count Rate [cps]
100	1,000	23 ～ 26

RESULTS:
The measurement results were analyzed by Feynman-α / bunching method and Rossi-α method.
As a result of the Feynman-α analysis, plot shapes like Feynman's theoretical formula were not obtained, because of the automation operation of the KUR.
As a result of the Rossi-α analysis, plot shapes like Orndoff's theoretical formula were obtained on the result.
An analysis results of the Feynman-α and the Rossi-α analysis are shown in Fig.2. The result of this work has large error bar even with the high-counting efficiency counter; GS20, and it means that the nuclide noise of the water moderate reactor has a trend to be trapped in a water moderator "prison".

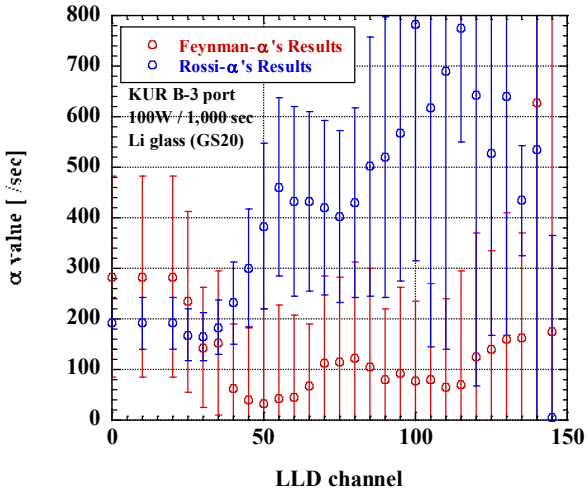

Fig. 2. A result example of Rossi-α analysis.

R4066

CO3-2 Reactor Keinetics Experiment in KUR

T. Sano, J. Hori[1], Y. Takahashi[1], K. Terada[1],
K. Hashimoto

Atomic Energy Research Institute, Kindai University
[1]Institute for Integrated Radiation and Nuclear Science, Kyoto University

INTRODUCTION: Reactor kinetics is the response of the reactor power obtained when the reactivity is inserted into a reactor core. This response is usually obtained as a change in reactor power and includes information on reactor kinetics parameters. Typically, reactor kinetics experiments are conducted using low-power reactors or critical assemblies. On the other hand, data obtained from reactor kinetics experiments in power reactor or high-power research reactor include various feedback reactivity that does not occur in low-power reactors or critical assemblies, so obtaining these data is very important for understanding reactor safety. However, in these high-power reactors, kinetic experiments are mostly measurements for tests and inspections for facility management, and it is impossible for researchers to utilize these data with some exceptions.

Therefore, the purpose of this study is to observe the KUR-specific feedback reactivity, and so on, by measuring the reactor power change during the startup of the KUR. The obtained data is important because such the kinetics experiments can be conducted only at KUR in Japan.

EXPERIMENTS: An experiment was conducted at the startup of the KUR as following processes.

1. Time series data of the startup system from two fission chambers, linear power meter, core outlet temperature and primary clear up system inlet temperature were measured at critical state with a thermal power of 20W. At this time, the A to D control rods has same positions, and criticality adjustment was operated by R rod.
2. The D rod was withdrawing out from the critical position and the time series data were measured. Here, the drawing distance was 1.21 cm. In addition, control rod maneuvers for negative reactivity compensation were not performed until the end of the measurement.
3. When the reactor power achieved about 15.6 kW, the measurements were completed. Because the negative reactivity by core temperature increasing compensated for the positive reactivity by control rod withdrawal, sot that the reactor power did not increase.

The time series data were obtained using a digital data collection system for operator assistance called the Harmonas system already installed on the KUR control console.

The KUR core location was shown in Fig.1. and table 1 shows the control rod positions and core outlet temperature at the low power (20W) criticality. The KUR was operated by natural circulation cooling mode. Thus, the generated heat was not cooled by the cooling system and increases the core temperature.

RESULTS: Fig. 2. shows the time series data of the reactor power by linear power meter. The initial reactor period (795 sec to 882 sec in the figure) by D rod withdrawing was 125.5 sec. Without feedback reactivities, a reactor power would increase exponentially. However, because of the heat generation in the KUR core, a negative feedback reactivity was observed in the time range from 1200 sec to 2200 sec.

	1	2	3	4	5	6	7	8	9
い	G	R rod	F	F	F	F	SSS	G	G
ろ	G	Pl	F	A rod	F	B rod	F	G	G
は	G	Pl	F	F	HYD	F	F	LI	G
に	G	G	F	C rod	F	D rod	F	G	Pn-2
ほ	G	G	G	F	F	F	G	G	Pn-3
へ	Pl	G	G	G	G	G	G	G	Pn-1

Fig. 1. Core location of the KUR .
F : Fuel element, G : Graphite reflector
Pl : Water plug, LI : Long irradiation element

Table 1. Control rod positions and core outlet temperature at the criticality with thermal power of 20 W.

A rod	41.65 cm
B rod	41.65 cm
C rod	41.65 cm
D rod	41.65 cm
R rod	24.98 cm
Core outlet temperature	23.83 ℃

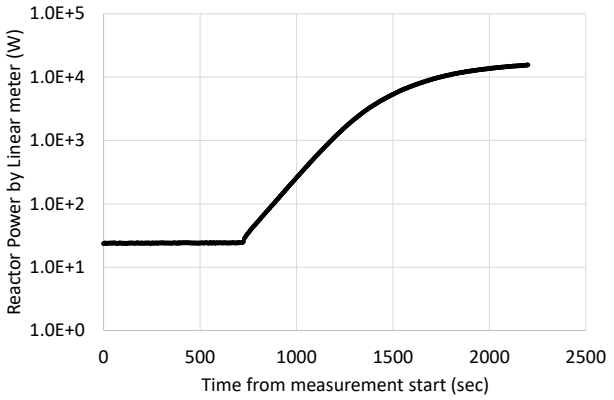

Fig. 2. Reactor power.

CO4-1 Study on HPLC Elution Behavior of Heavy Lanthanide Metalloufullerenes

K. Akiyama[1], D. Nakamura[1], T. Kuroda[1], K. Takamiya[2], and S. Kubuki[1]

[1]*Department of Chemistry, Tokyo Metropolitan Univer-sity*
[2]*Institute for Integrated Radiation and Nuclear Science, Kyoto University*

INTRODUCTION: Metallofullerene (EMF) is a clathrate compound encapsulating metal atom in fullerene molecule. Lanthanide (Ln) EMFs: $Ln@C_{82}$ have two or three charge transferred electrons on the C_{82} cage from the encapsulated Ln atom, and their electronic states reflecting the number of charge transfer electrons [1]. From the view point of inorganic chemistry, It is interesting to know that the effect of the electronic state for a series of the encapsulated 10 lanthanide elements (La, Ce, Pr, Nd, Gd, Tb, Dy, Ho, Er, Lu) with the electronic states of $(Ln^{3+})@(C_{82}^{3-})$ on the electronic state of the $Ln@C_{82}$ molecule from the difference in interaction with pylenyl stationary phase. So far, we have made clear the retention time in the pyrenyl stationary phase for five types of $Ln@C_{82}$ from La to Gd by the thermal neutron activation method. On the other hand, the high-performance liquid chromatography (HPLC) retention time of $Ln@C_{82}$ with heavy lanthanide elements have not been obtained because the half-life of the radio nuclide produced by thermal neutron irradiation such as Dy and Er is very short, and the interference by the production of $Ln_2@C_{82}$ and $Ln_2C_2@C_{80}$, whose production rate increase competitively with $Ln@C_{82}$ as the increase of the atomic number of Ln. In previous work, we used already purified $Ln@C_{82}$ of heavy lanthanide by HPLC column of a 5PBB for the neutron activation and developed at three different temperature using newly developed column cooler to obtained detailed HPLC retention time of these $Ln@C_{82}$s and successively evaluated the adsorption-desorption enthalpy (ΔH) at room temperature (RT), 0 °C, and -10 °C for $Ln@C_{82}$ of La, Ce, Pr, Tb, Dy, Ho, and Er on a pyrenyl stationary phase [2]. However, obtained HPLC retention time and evaluated ΔH for Ce and Tb were slightly larger than that for other lanthanide considering about the similarity of chemical properties of lanthanide elements. In the previous experiment, we had to develop $Ln@C_{82}$ for short half-life (La, Pr, Dy, Ho, and Er) and long half-life radioisotopes (Ce and Tb) by HPLC separately due to the limitation of the half-life. In this time, we used HPLC-separated samples of mixed $Ln@C_{82}$ solution regardless of their half-lives as irradiated samples in order to confirm the reproducibility of the retention times previously obtained.

EXPERIMENTS: Already isolated $La@C_{82}$, $Tb@C_{82}$ and $Dy@C_{82}$ were dissolved in toluene and mixed to prepare samples for HPLC development. These samples were injected into a Buckyprep column and the eluate was fractionated every 20 seconds at RT and every 1 minute at -10 °C. These fractionated eluates were evaporated to dryness and re-dissolved to carbon disulfide and then dropped onto paper filters with 12 mm diameters and dried. These samples were sealed into polyethylene bags and irradiated in ethylene vial and activated by a thermal neutron in the KUR of the Institute for Integrated Radiation and Nuclear Science, Kyoto university. After the irradiation, the g rays emitted from the samples were measured by a Ge detector.

RESULTS: Figure 1 show HPLC elution behavior of $Ln@C_{82}$s studied in this work obtained at room temperature and -10 °C. HPLC retention time (t_R) of these $Ln@C_{82}$ were evaluated from the least square fitting with extreme function and determined as 60.41, 62.41, and 61.36 for La, Tb, and Dy at RT and 86.53, 90.24, and 88.58 for La, Tb, and Dy at -10 °C, respectively. The separation coefficient (α) of $Tb@C_{82}$ and $Dy@C_{82}$ to $La@C_{82}$ were evaluated from obtained t_R and $\alpha_{Tb@C82}$ at -10 oC was found to be quite smaller than that obtained in previous work. From these results, it was clarified that the retention time of $Tb@C_{82}$ at -10 °C obtained in the previous study was overestimated, as well as that of Ce determined using long half-life nuclides.

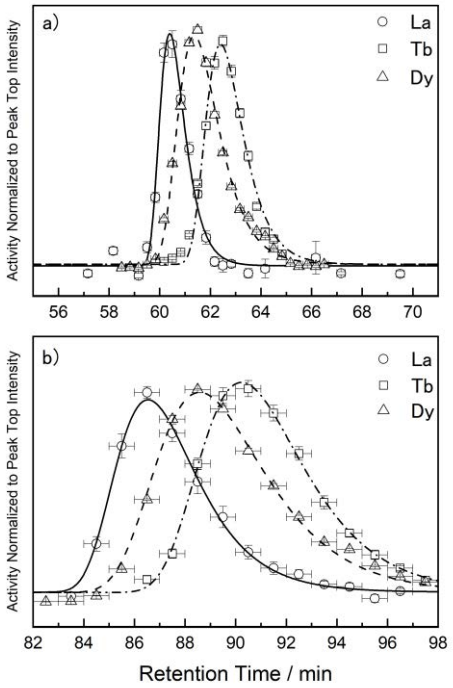

Fig. 1. HPLC elution behavior of $Ln@C_{82}$s studied in this work obtained at a) room temperature and b).

REFERENCES:

[1] H. Shinohara, Rep. Prog. Phys., **63** (2000) 843-892.
[2] K. Akiyama *et al*., KURNS Prog. Rep. 2021, CO4-20.

CO4-2 Radiation Tolerance of SiC p+n Junction-Diodes for High-Energy Physics Experiments

T. Kishishita, H. Yashima[1], R. Kosugi[2]

High Energy Accelerator Research Organization, KEK
[1] Institute for Integrated Radiation and Nuclear Science, Kyoto University
[2] National Institute of Advanced Industrial Science and Technology

INTRODUCTION: Silicon carbide (SiC) has been considered as a potential alternative to Si for the manufacture of dosimeters, spectrometers, and charge particle detectors in high energy physics experiments, by virtue of its operation capability in strong radiation and/or high-temperature environments. To take advantage of such properties for future radiation detectors with a comparable size of silicon, we investigated the influence of the bulk defects on the radiation sensor characteristics under the reverse-bias condition, by irradiating neutrons at Institute for Integrated Radiation and Nuclear Science, Kyoto University.

EXPERIMENTS: The reverse blocking characteristics and leakage current characteristic are primary concerns of the radiation effects. The radiation-induced effects are generally divided into bulk and surface defects. The formers are caused by the displacement of crystal atoms, introducing to the increase of the leakage current and degraded reverse blocking characteristics. The latter include all effects in the covering dielectrics and the interface region. Since the bulk damage caused by the elastic nuclear scattering of the lattice nuclei has a profound effect in our device, we irradiated fast neutrons to SiC pn-diodes under the bias condition of 1 kV [1]. The irradiation test was conducted at KUR. Fig. 1 shows the photograph of the measurement setup. We installed two SiC sensors at the front of the rail-instrument. After the 1MW operation, we carried out measurements of the leakage current and compared with those of the pre-irradiation samples.

RESULTS: The typical I-V characteristics before irradiation is shown in Figure 2. The data before the irradiation are plotted in white and black, while those after the irradiation are shown in colors. We note that the data around 1 kV are overlapped and the leakage current characteristics is not changed in the irradiation. The reverse blocking property was also retained up to 1 kV, which is required for full depletion of the SiC devices. Irradiation tests at higher fluences are performed in FY-2023. We note that the 1 MeV neutrons have the same efficiency in the detector degradation as 24 GeV protons at a comparable neutron equivalent fluence. The theoretical nonionizing energy loss (NIEL) calculation performed on SiC can be found in Lee et al. [2]. The primary radiation defects produced by single particles (protons and pions) or gamma-rays were not evaluated in this measurement, however, the number of primary defects is reported as low as that of diamond. Thus, we conclude that the bulk defects introduced by irradiation at the 10^{12} neutron equivalent fluence is ignorable, even with the reverse bias of 1 kV.

Fig. 1. Photograph of the measurement setup.

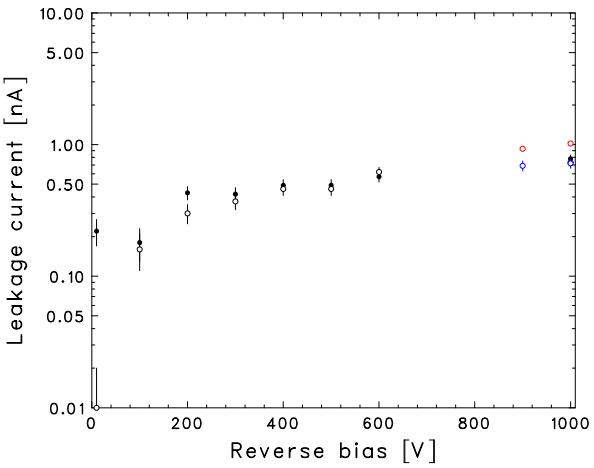

Fig. 2. Leakage currents before (plotted in white and black) and after (plotted in colors) 1 MeV neutron irradiation of 10^{12} n_{eq}/cm^2.

REFERENCES:

[1] T. Kishishita *et al.,* IEEE Trans. Nucl. Sci., **68** (2020) 2787-2793.
[2] K. K. Lee *et al.,* Nucl. Instrum. Methods Phys. Res. B, **210** (2003) 489-494.

CO4-3 Positron Annihilation Spectroscopy in Neutron-irradiated Fe-Cr Alloys

K. Sato, Y. Noshita, R. Kasada[1], Q. Xu[2], A. Yabuuchi[2], A. Kinomura[2]

Graduate School of Science and Engineering, Kagoshima University
[1]Institure for Materials Research, Tohoku University
[2]Institute for Integrated Radiation and Nuclear Science, Kyoto University

INTRODUCTION: Ferritic stainless and heat resistant steels used as nuclear reactor peripheral materials have high Cr content [1]. In these materials, ductility and toughness remarkably decrease, and hardness and tensile strength increase by aging from 593 to 813 K. This phenomenon is caused by the formation of Fe-rich and Cr-rich phase, and is called 475˚C embrittlement [2]. These changes in mechanical properties are an important issue in terms of evaluation of aged deterioration when it was used as a reactor structural material. The phase separation process of Fe-Cr binary alloys have studied by the small angle neutron scattering method [3], Mossbauer spectroscopy [4] and atom probe field ion microscopy [5] etc. Chen et al. detected phase separation in Fe-9.7%Cr irradiated with neutrons at 573 K by atom probe tomography [6], and reported that irradiation-induced excessive defects promote phase separation even at a temperature of less than 593 K.

Positron annihilation spectroscopy (PAS) is very powerful tool to obtain the information of vacancy-type defects (even single vacancies) and precipitates. Xu et al. reported the positron annihilation lifetimes of vacancy clusters and the change in spectra of coincidence Doppler broadening (CDB) in association with the formation of Cu precipitates in neutron-irradiated Fe-Cu alloys [7]. In Fe-Cu alloys, positron affinity of Cu is lower than that of Fe [8], and the formation of Cu precipitates leads to the change in spectra of CDB. In Fe-Cr alloys used in this study, positron affinity of Fe is lower than that of Cr [8]. Therefore, we can detect the formation of Fe-rich phase in phase separation of Fe-Cr alloys using PAS. The purpose of this study is to detect the progress of phase separation using PAS, and to obtain the correlation between the hardness and phase separation in Fe-Cr binary alloys irradiated with neutrons at 473K and 573 K.

EXPERIMENTS: Fe-x wt.%Cr (x = 0, 9, 15, 30, 45, 50, 70, 85, 91, and 100) binary alloys were used in this study. The weight of high purity Fe (99.99%) and Cr (99.99%) were measured, and samples were melted by the arc melting. For neutron irradiation, samples with diameters of 3 mm and thickness of 0.25 mm were cut using the wire electric discharge machine. Fe-xCr (x = 30, 45, 50, 70, 85, 91, and 100) were annealed at 1273K for 1h, and Fe-xCr (x = 0, 9, 15) were annealed at 1073K for 1h in a vacuum (< 4×10^{-4} Pa), and then water-quenching was performed for the suppression of phase separation. The neutron irradiation was carried out at the Material Controlled Irradiation Facility (SSS) of Kyoto University Reactor (KUR) [9]. The irradiation doses were 0.44×10^{-3} , 0.5×10^{-3} and 2.1×10^{-3} dpa. The irradiation temperature was 473K (0.5×10^{-3} dpa) and 573K (0.44×10^{-3} and 2.1×10^{-3} dpa). All samples were electropolished after neutron irradiation to remove the oxidation layers. Measurements of positron annihilation lifetime (PAL) were performed at room temperature. The PAL spectrometer had a time resolution of 190 ps (full width at half maximum) and each spectrum was accumulated to a total of 4×10^{6} counts. PAL spectra were analyzed using PALSfit package [10].

RESULTS: Vacancy clusters consisting of 8−12 vacancies were formed in the 473 K irradiation expect for Fe-70Cr, Fe-85Cr, Fe-91Cr. Larger vacancy clusters were detected in pure Fe and Cr. In pure metals, because the solute atoms, which suppress the migration of vacancies, do not exist, vacancy clusters are larger than in alloys. In the 573 K irradiation, no vacancy clusters were observed expect for pure Cr. Yoshiie et al. reported that the density of vacancy clusters in pure Fe irradiated with neutrons at 473 K was higher than that at 573 K from the results of PAL measurements. They also indicated that the low density of vacancy clusters was detected in the irradiation at 573 K at a dose of 2.1×10^{-2} dpa [11]. In this study, the irradiation doses were so low that we could not detect vacancy clusters in the 573 K irradiation. In the next step, we will discuss why we cannot detect vacancy clusters in Fe-70Cr, Fe-85Cr and Fe-91Cr irradiated at 473 K.

REFERENCES:

[1] R.L. Klueh *et al.,* J. Nucl. Mater., **191** (1992) 116.
[2] R.O. Williams, Trans. AIME, **212** (1958) 497.
[3] M.H. Mathon *et al.,* J. Nucl. Mater., **312** (2003) 236.
[4] H. Kuwano *et al.,* J. Japan Inst. Metals, **45** (1981) 457.
[5] S.S. Brenner *et al.,* Scripta Metall., **16** (1982) 831.
[6] W.Y. Chen *et al.,* J. Nucl. Mater., **462** (2015) 242.
[7] Q. Xu *et al.,* Philos. Mag. Lett., **88** (2008) 353.
[8] M. J. Puska *et al.,* J. Phy. Condes. Matter, **1** (1989) 6086.
[9] T. Yoshiie *et al.,* Nucl. Instr. Meth. Phys. Res. A, **498** (2003) 522.
[10] J.V. Olsen *et al.,* Phys. Stat. Sol., **C4** (2007) 4004.
[11] T. Yoshiie *et al.,* J.Nucl.Mater., **325**(2007) 367-370.

CO4-4 The change of free volume in highly-hydrogenated DLC film due to thermal desorption

K. Kanda, D. Niwa, T. Inoue, F. Hori[1], A. Yabuuchi[2] and A. Kinomura[2]

Laboratory of Advanced Science and Technology for Industry, University of Hyogo
[1]Osaka Metropolitan University
[2]Institute for Integrated Radiation and Nuclear Science, Kyoto University

INTRODUCTION: Highly-hydrogenated diamond-like carbon (H-DLC) films containing more than 40% hydrogen have been reported to take a low coefficient of friction even in a vacuum and are expected to be used as lubricants for use in a vacuum [1]. In order to use H-DLC film as a lubricant, it is necessary to know its temperature characteristics. We have performed thermal desorption spectrometry (TDS) measurements on H-DLC films and observed that hydrogen desorption occurs around 360°C and hydrocarbon desorption around 400-450°C. In this experiment, we used PAS to measure how the free volume in the highly-hydrogenated DLC films changes with increasing temperature.

EXPERIMENTS: H-DLC film was deposited on Si wafers by using an amplitude-modulated radio-frequency plasma-enhanced chemical vapor deposition method. (Nippon ITF Co.) The desired film thickness was 200-nm-thick. The hydrogen content of H-DLC film was estimated to be ≈50 at.%.

The temperature of the H-DLC films was raised in an electric furnace of the TDS system. The vacuum before the temperature increase was 5.5×10^{-5} Pa, and the temperature increase rate was 5°C/min. These were the same condition as the TDS measurements. Samples were prepared by stopping the temperature increase at 200, 360, 400, 450, 550, and 700°C. After the temperature was raised, the samples were cooled naturally in a vacuum and then removed from the furnace and stored in a dry box.

Positron lifetime spectroscopy (PAS) measurement was performed at the slow positron beam system (B-1) at Kyoto University research Reactor (KUR). Doppler broadening profiles of annihilation γ-rays were obtained using a Ge detector for each positron energy. The low and high momentum parts of spectra were characterized by the *S* and *W* parameters. *S* and *W* parameters as a function of energy were measured in the range of 0 - 30 keV. Positron annihilation lifetime spectroscopy (PALS) was performed at an energy of 2 keV, corresponding to the DLC film on Si. A Kapton (polyimide) film was measured before and after measurements of the DLC samples as a control sample. Obtained lifetime spectra were analyzed by the PALSfit code assuming one-lifetime component.

RESULTS: Figure 1 shows the temperature-dependence of positron annihilation lifetime (PAL) and the *S* parameter. The film thickness decreased due to desorption of species from the H-film as the temperature rose. Therefore, we could only measure PAL up to a sample with a temperature rise of 360°C. The *S* parameter of the H-DLC film before temperature rise was ≈0.484 and it increased to ≈0.488 by temperature rise to 200°C. The *S* parameter showed no significant change in temperature range from 200°C to 400°C, followed by a sharp increase to 450°C. The *S* parameter kept ≈0.497 in the temperature range above 450°C. On the other hand, the PAL of the H-DLC film before temperature rise was 0.382 ns and it increased to 0.415 ns by temperature rise to 360 °C.

In the TDS spectrum of H-DLC film, desorption of endohedral gas, which was the source gas left in the film during film deposition, was observed at ≈200°C. The increases in the *S* parameter and PAL of the H-DLC film at 200°C is thought to be due to the increase in free volume resulting from desorption of the endohedral gas.

Hydrogen desorbed from DLC at around 360°C in TDS measurements. The increase in PAL between 200°C and 360°C can be attributed to the increase in free volume in the H-DLC film due to hydrogen desorption from carbon skeleton of DLC. On the other hand, the *S* parameter did not increase in this temperature range. This is due to the fact that the free-volume periphery has changed from hydrogen, which has only valence electrons, to carbon, which has inner-shell electrons.

Desorption of hydrocarbons - i.e., destruction of the carbon skeleton - was observed near 450°C in the TDS spectrum. The steep increase in the *S* parameter from 400 to 450°C is thought to be due to the increase in free volume resulting from desorption of the hydrocarbons. In this temperature range, graphitization of the film proceeded rapidly, and at higher temperatures the film thickness gradually decreased due to desorption.

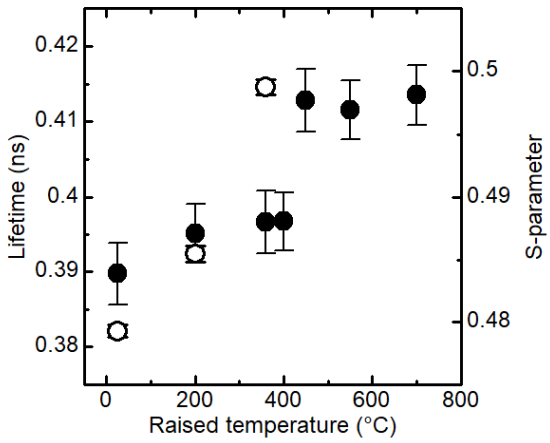

Fig. 1. The temperature-dependence of positron annihilation life-time (○) and the *S* parameter (●).

REFERENCES:

[1] C. Donnet *et al.*, Surf. Coatings Technol., **68-69** (1994) 626–631.

CO4-5 Effect of gamma radiation on ultra-micro structure of hardwood cell-wall

K. Murata, Y. Imataki, M. Nakamura, T. Saito[1]

Graduate School of Agriculture, Kyoto University
[1]Institute for Integrated Radiation and Nuclear Science, Kyoto University

INTRODUCTION: Space-wood project (LignoStella project) is performed by Kyoto University collaborating with Sumitomo forestry Co Ltd in order to challenge to use wood-material in outer space. Firstly, possibility to use wood material in outer space has to be confirmed because a small wooden artificial satellite is going to launch until 2023. Space exposure test of wood specimen started on ExBAS at ISS in March 4, 2022. The wood specimen was exposed for about 1 year and came back to Earth in March, 2023. They were affected by atomic oxygen and cosmic ray. In this study, effect of gamma-ray irradiation on cell-wall of wood material was studied on the ground in parallel with the exposure tests in outer space.

EXPERIMENTS: The sample was Honoki (*Magnolia obovate*), which is 100 mm (length) ×10 mm (radial) × 0.6 mm (tangential) in size. They were conditioned in 20 °C and 60%RH (dry wood) or 20℃ and 97%H (wet wood) for a few weeks before the doze test. They were wrapped in polyethylene film to prevent moisture content changes during irradiation. They were irradiated for 24 hours, and five types of doze was performed, which is 50 kGy, 16 kGy, 10 kGy, 4 kGy adn 1 kGy. After irradiation, ultra-micro structure of cell wall was observed using a Wide-Angle X-Ray Diffraction (WAXD) (Shimadzu, XRD-7000s). X-ray diffraction (wave length 0.154 nm) was measured under the conditions that the scan speed is 1°/min and the sampling width is 0.02°, and scanning range is 2θ=10~30°. Crystallite size or the degree of crystallinity were measured using diffraction profiles.

RESULTS: As shown in Fig. 1 and Fig. 2, the degree of crystallinity were obtained using integral intensity values of crystalline and non-crystalline peaks. They did not change by irradiation. Aoki *et al*. [1] state that the degree of crystallinity of wood remained almost unchanged up to 300 kGy of gamma rays doze, but started to decrease rapidly at about 1000 kGy. This result corresponds with that of Aoki *et al*. As shown in Fig. 3 and Fig. 4, crystallite size was obtained using Scherrer's equation. The size was identified as diameter of cellulose micro fibril (CMF), so we consider that the WAXD measurement results is appropriate. In the case of dry wood, diameters of CMF increased slightly by 50 kGy irradiation (statistically significant differences, based on t-test, $p < 0.050$). We believe that this may be due to the decomposition of the hemicellulose surrounding CMF by high-dose irradiation, but we need to consider about this reason.

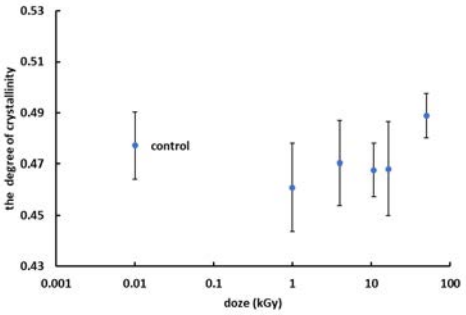

Fig. 1. Change of the degree of crystallinity of wet wood by gamma irradiation.

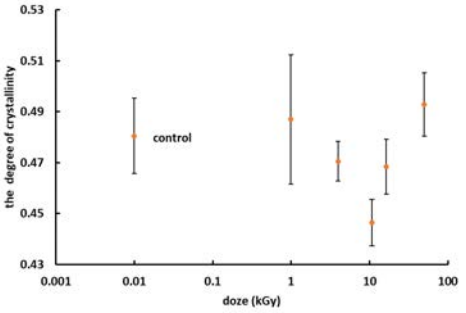

Fig. 2. Change of the degree of crystallinity of dry wood by gamma irradiation.

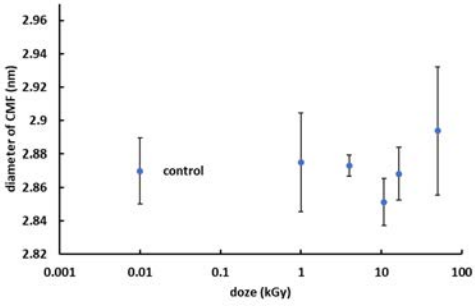

Fig. 3. Change of diameter of CMF of wet wood by gamma irradiation.

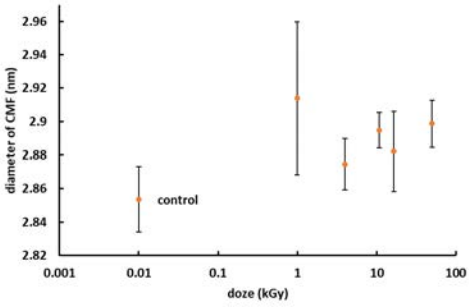

Fig. 4. Change of diameter of CMF of dry wood by gamma irradiation.

REFERENCES:

[1] T. Aoki *et al.*, bulletin of the Wood Research Institute Kyoto Univ. **62** (1977) 19-28.

CO4-6 Investigation of Concentration Dependence on Local Structures at Cd Sites in $Cd_xSr_{1-x}TiO_3$

S. Komatsuda, W. Sato[1], A. Taniguchi[2], M. Tanigaki[2], and Y. Ohkubo[2]

Institute of Human and Social Sciences, Kanazawa University
[1]*Institute of Science and Engineering, Kanazawa University*
[2]*Institute for Integrated Radiation and Nuclear Science, Kyoto University*

INTRODUCTION: Strontium titanate ($SrTiO_3$) is a cubic perovskite compound of ABO_3 type. Among ABO_3 perovskites, $SrTiO_3$ has a wide band gap values of 3.2 eV, and doping effect of $SrTiO_3$-based materials is attracting much attention. It is known from many previous reports that chemical and physical properties of $SrTiO_3$ change depending on the kind of dopant ions and the surrounding local structures[1]. For a practical use of $SrTiO_3$, it is necessary to obtain microscopic information on various impurity sites. Therefore, we applied the time-differential perturbed angular correlation (TDPAC) method to study the local structures at impurity sites in $SrTiO_3$. In our previous TDPAC study of $Cd_xSr_{1-x}TiO_3$ with the $^{111}Cd(\leftarrow{}^{111m}Cd)$ probe, concentration dependence of occupation site of Cd was observed: Cd occupies random site up to an Cd ratio $0.005 \leqq x < 0.04$, and at Cd ratio x = 0.06, Cd dopants replace Sr^{2+} and Ti^{4+} in the lattice sites where defect exists in the vicinity of the probes. In order to obtain further information on concentration dependence of local structures at Cd sites in $Cd_xSr_{1-x}TiO_3$, we have thus performed TDPAC measurements for $Cd_xSr_{1-x}TiO_3$ with $^{111}Cd(\leftarrow{}^{111m}Cd)$ probe by doping wide concentration of Cd ions ($0.06 \leqq x \leqq 0.20$).

EXPERIMENTS: Stoichiometric amount of $SrCO_3$, $CdCO_3$, and TiO_2 powders were mixed in the mortar. The powders were pressed into disks. For TDPAC measurements, about 3 mg of CdO enriched with ^{110}Cd was irradiated with thermal neutrons in Kyoto University Research Reactor, and radioactive ^{111m}Cd was generated by $^{110}Cd(n, \gamma)^{111m}Cd$ reaction. The neutron-irradiated CdO powder was dissolved in 6M HCl and added in droplets onto the pre-sintered $Cd_xSr_{1-x}TiO_3$ disk. The disk was sintered in air at 1373 K for 90 min. The TDPAC measurement was carried out for the 151-245 keV cascade γ rays of $^{111}Cd(\leftarrow{}^{111m}Cd)$ probe with the intermediate state of $I = 5/2$ having a half-life of 85.0 ns.

RESULTS: Figure 1 shows the TDPAC spectra of $^{111}Cd(\leftarrow{}^{111m}Cd)$ (a) in $Cd_xSr_{1-x}TiO_3$ (x = 0.04), (b) in $Cd_xSr_{1-x}TiO_3$ (x = 0.06), and (c) in $Cd_xSr_{1-x}TiO_3$ (x = 0.20) at room temperature. The directional anisotropy on the ordinate, $A_{22}G_{22}(t)$, was deduced with the following simple operation for delayed coincidence events of the cascade:

$$A_{22}G_{22}(t) = \frac{2[N(\pi,t) - N(\pi/2,t)]}{N(\pi,t) + 2N(\pi/2,t)}. \qquad (1)$$

Here, A_{22} denotes the angular correlation coefficient, $G_{22}(t)$ the time-differential perturbation factor as a function of the time interval, t, between the relevant cascade γ-ray emissions, and $N(\theta,t)$ the number of the coincidence events observed at angle, θ. With respect to Fig. 1(a), the spectral pattern is damped. The spectral pattern was fit-ted with two static electric quadrupole frequencies which have large distribution widths (%)21(28 ,%)7(72 = δ). These large values of distribution widths indicate local randomness at $^{111}Cd(\leftarrow{}^{111m}Cd)$ probe sites in $Cd_xSr_{1-x}TiO_3$. As for the spectrum in Figs. 1(b) and 1(c), spectral patterns can be reproduced by a fit with unique quadrupole fre-quencies. It is suggested from our previous study that Cd dopants replace Sr^{2+} and Ti^{4+} in the lattice sites where de-fect exists in the vicinity of the Cd probes at Cd ratio x = 0.06 and x = 0.20. These results indicate that Cd ions dis-persed into $Cd_xSr_{1-x}TiO_3$ perovskite structure at high con-centration $0.06 \leqq x \leqq 0.20$. These concentration depend-ences of local structure at Cd site might be attributed to the change of lattice constant of $Cd_xSr_{1-x}TiO_3$. For more in-formation on these concentration dependence, investiga-tions of lattice constants of $Cd_xSr_{1-x}TiO_3$ perovskite are now in progress.

REFERENCE:

[1] C. M. Culbertson *et al.*, Scientific Reports, **10** (2020) 3729.

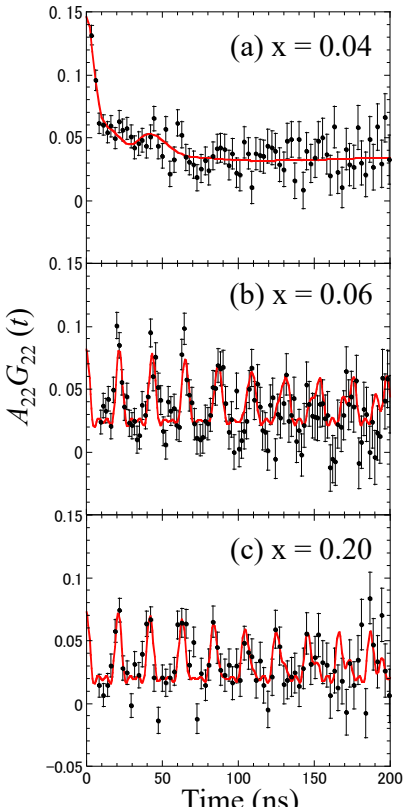

Fig. 1. TDPAC spectra of $^{111}Cd(\leftarrow{}^{111m}Cd)$ (a) in $Cd_xSr_{1-x}TiO_3$ (x = 0.04), (b) in $Cd_xSr_{1-x}TiO_3$ (x = 0.06) and (c) $Cd_xSr_{1-x}TiO_3$ (x = 0.20) at room temperature.

CO4-7 Hydrogen trapping behavior at vacancy in Fe-Al alloy with electron irradiation

F. Hori, S. Hirayama, H. Obayashi, J. Tian, K. Ohsawa[1], Q. Xu[2], N. Abe[2] and K. Yasunaga[3]

Osaka Metropolitan University
[1]*Res. Inst. of Appl. Mech., Kyushu University*
[2]*Institute for Integrated Radiation and Nuclear Science, Kyoto University*
[3]*Wakasa-wan Energy Research Center*

INTRODUCTION: Intermetallic compound of Fe-Al alloy is used as high strength at high temperature material because of its good properties such as specific strength to weight ratio, oxidation resistance. However, it is known that Fe-Al alloy with B2 ordered structure is easy to form vacancy and anti-site atom defects. These defects strongly affect the physical and mechanical properties. We have investigated the nature of defect structures in B2 type Fe-Al alloy [1,2]. On the other hand, the vacancy type defects in this alloy first principles calculation result indicate that not only one hydrogen atom but also several hydrogen atoms can be trapped in a single vacancy in B2 ordered Fe-Al alloy. However, the interaction between vacancies and hydrogen atoms in this type of Fe-Al alloy is not cleared yet. Our previous works have shown that hydrogen atoms are trapped in the introduced vacancies introduced by electron irradiation. We have also reported that hydrogen atoms trapped in the vacancies are released by annealing above 500 K [3].

EXPERIMENTS: B2 ordered Fe-Al alloys were prepared by arc melting method in argon gas atmosphere. Sliced samples with the thickness of 0.5 mm were annealed at 1273 K for 20 h and cool down to 973 K slowly and then quenched into water. These specimens were irradiated with 8 MeV electron up to the fluence of 4×10^{18} /cm^2 at KURRI, Kyoto University. Irradiation was carried out at about 330 K with temperature controlling water cool system. Hydrogen was injected for electron irradiated samples at 0.1 mA/cm^2 in a NH_4SCN solution bath added 0.001 mol/L H_2SO_4 by electro chemical method for 8, 16, 80 and 160 hours. These samples were examined by positron annihilation coincidence Doppler broadening measurement. Also, the thermal desorption spectroscopy (TDS) was measured with heating rate of 1 K/s.

RESULTS: Figure 1 shows the CDB ratio curves of H-injected Fe-Al alloy normalized to that of the alloy before hydrogen injection. The ratio curve changes with H-injection and decreases around 0 m_0c suggesting that hydrogen atoms are trapped in the vacancies. Fig. 2 shows the TDS spectra for hydrogen injected Fe-Al alloys after 8 MeV electron irradiation. This figure clearly shows that the amount of absorbed hydrogen becomes larger with hydrogen charging time. In addition, absorption peak appears around 650 K shifted to lower temperature with increasing hydrogen charging time. This may be due to the change in the ratio of vacancies to hydrogen atoms, which may result in a change in the state of hydrogen trapping. This result also suggests that multiple hydrogen may be trapped in a single vacancy.

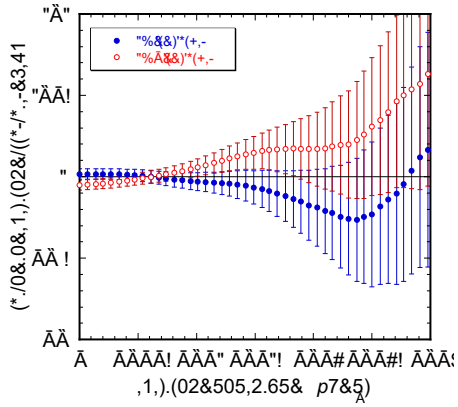

Fig. 1. CDB ratio spectra of 16 and 160 hr hydrogen injected Fe-Al alloy after electron irradiation.

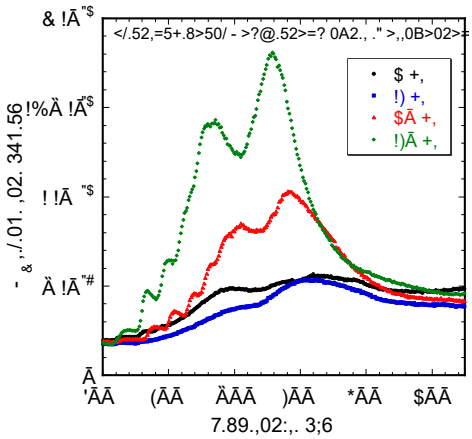

Fig. 2. TDS spectra of Fe-Al alloy electrochemicaly implanted with hydrogen after electron irradiation.

REFERENCE:

[1] T. Haraguchi, *et al.,* Intermetallics, **9** (2001) 763-770.
[2] F. Hori *et al.,* JJAP Conf. Proc., **9** (2023) 011107.
[3] F. Hori *et al.,* KURRI Progress Report 2021, (2022)114.

CO4-8 Metal nano-composites formation in water solution by electron irradiation reduction

F. Hori, S. Matsuo, T. Matsui[1], N. Taguchi[2], S. Tanaka[2], H. Tanimoto[3] and Q. Xu[4]

[1]*Osaka Metropolitan University*
[2]*AIST, Kansai Center*
[3]*University of Tsukuba*
[4]*Institute for Integrated Radiation and Nuclear Science, Kytoto University*

INTRODUCTION: Metal nanoparticles (NPs) have some specific properties, which are not appeared in bulk materials such as catalytic activities, magnetic properties, electric conductivity and light absorption. They have many possibilities to applied for various industrial fields. However, it is not easy to fabricate multi elemental alloy NPs with controlling their size, shape and structure. Generally, many kinds of metal NPs commercially are synthesized by using chemical reaction method, which is not necessarily in water solution. Recently, it is possible to fabricate some metal NPs under irradiation reduction fields such as ultrasonic, solution plasma, electron beam, ion beam and gamma-ray [1]. On the other hand, metal nanoparticles with high electronic conductivity are expected for the fields of printed electronics technologies as a metal nano-ink. Cu is the high electronic conductivity and one of the most abundant resources on earth. However, the fabrication of Cu nanoparticle has a difficulty because its oxidation property. So far, we have successfully synthesized pure Cu nanoparticles by gamma-ray reduction method. In this study, we have tried to synthesize Ag-Cu-X (X=Au, Ni) nano size composite particles by electron irradiation reduction.

EXPERIMENTS:

Aqueous solution with a 0.5 mM copper complex ($(CH_3COO)_2Cu \cdot H_2O$), 0.5 mM gold complex ($NaAuCl_4 \cdot 2H_2O$) with an additive of sodium dodecyl sulfate (SDS) and 8.5 vol% ethylene glycol was prepared. 0.5 mM $AgNO_3$ and 0.5 mM $NiCl_2$ was added into each solution, separately. The solutions were argon gas purged and sealed into polystyrene vessels. They were irradiated 7.5 MeV electron with total dose of 15 kGy in about 52 sec by linear accelerator at KURRI Kyoto University. After irradiation, the samples were measured for UV–vis absorption, X-ray Photoelectron Spectroscopy (XPS) and X-ray absorption fine structure (XAFS) at KEK BL-27 and small angle X-ray scattering (SAXS) at KEK BL-6. Moreover, dried and filtered samples were measured by X-ray diffraction and TEM (JEM-2000FX and FEI-Titan).

RESULTS:

In each sample, color of solution was clearly changed by electron irradiation, suggesting that the solute ions were reduced and formed nanoparticles. Fig. 1 shows the XRD profiles of AgCuNi and AgAuCu samples. In both cases, clear CuO (110) bragg peak and some peaks of fcc Ag are observed. On the other hand, the results of XAFS and XPS show that Cu-Cu and Cu-Ni atomic bonds were confirmed. Fig. 2 shows the SAXS profiles of the AgCuNi and AgAuCu solutions after electron irradiation and the reduced sample after gamma-ray irradiation as a comparison. This figure shows that the size of the formd particles in the case of AgCuNi are similar between electron and gamma-ray irradiation, while the size and other state of the formed particles in the case of AgAuCu are different. These results indicate that when the three types of ions are reduced simultaneously by electron irradiation, oxides are formed, but Cu and Ni are also reduced based on Ag, and complexes containing small amounts of other ions are formed.

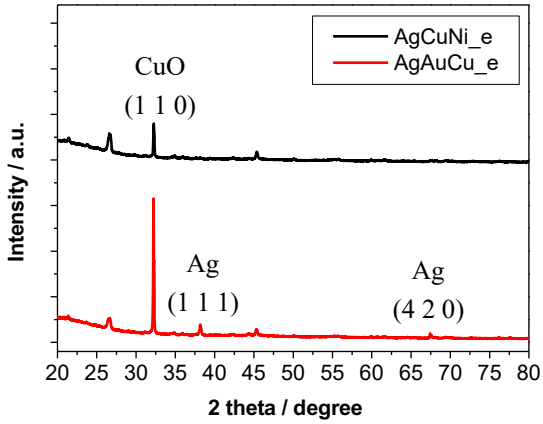

Fig.1. XRD profiles of electron irradiated AgCuNi and AgAuCu samples.

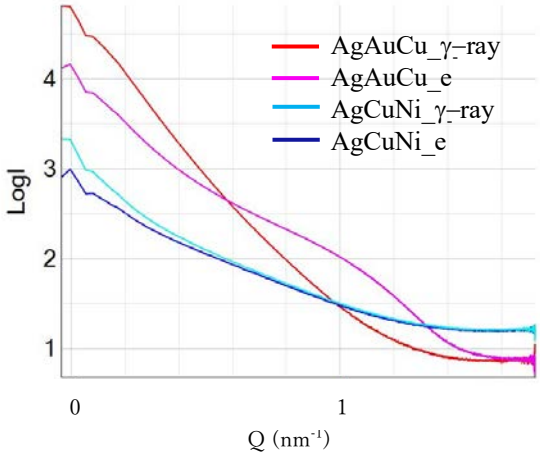

Fig. 2. SAXS spectra of AgAuCu and AgCuNi solutions after electron and gamma-ray irradiation.

REFERENCES:

[1] N. Taguchi *et al.,* Rad. Phys. Chem., **78** (2009) 1049-1053.

CO4-9 Slow Positron Beam Analysis of Polymer Composite Materials

Z. Chen, Y. Kobayashi[1], A. Yabuuchi[2] and A. Kinomura[2]

Department of Material Science and Engineering, Wuhan Institute of Technology, People's Republic of China

[1]Waseda Research Institute for Science and Engineering, Waseda University

[2]Institute for Integrated Radiation and Nuclear Science, Kyoto University

INTRODUCTION: 2D membranes based on the 2D materials, such as graphene oxide (GO) and $Ti_3C_2T_x$ (MXene), can be applied for molecular sieving with high flux and energy efficiency. It was believed that the interlayer spacing between the nanosheets was one of the key factors those influence the molecular sieving effect. So far, the popular method to evaluate the interlayer spacing is XRD. And the interlayer distance can be calculated using Bragg's law. However, this distance includes the thickness of the nanosheet and the electronic clouds of the polar groups grafted on the nanosheet. In fact, the channel for the molecules permeating through the 2D membrane is an 'empty' space in the interlayer spacing. To achieve the selective rejection of the 2D membranes, different groups were grafted on the nanosheets. In this case, the XRD results may not be so precise to predict membrane performance. It is necessary to develop new method to measure the voids between the nanosheets which are in charge of the ion permeation.

In this study, positron beam was utilized to evaluate the voids between the nanosheets. Doppler broadening spectroscopy coupled with positron beam was used to analyze the layer structure of the 2D membranes, while the positron lifetime measurement coupled with positron beam was applied to probe the voids between the 2D nanosheets.

EXPERIMENTS: GO/MXene/substrate and MXene/GO/substrate membranes were prepared by vacuum filtration method. First, 20-ml GO/water solution with a concentration of 0.005 mg/ml was filtrated by polyether sulfone (PES) substrate at 0.1 MPa. And then the 20-ml MXene/water solution with a concentration of 0.005 mg/ml was filtrated by GO/substrate membrane. And the obtained sample was MXene/GO/substrate. The GO/MXene/substrate membrane was obtained with the similar method. The as prepared membranes were heated in oven for 4 hours at 170 °C, and labeled as heated ones. Positron annihilation Doppler broadening and lifetime measurements were performed with the positron beam system at the Institute for Integrated Radiation and Nuclear Science, Kyoto University.

RESULTS: As shown in Fig. 1, the layer structure of the four samples can be distinguished from *S*-*E* curves. It can be seen that, the *S*-*E* curves can be divided into three stages, surface layer (0~5 keV), beneath layer (5~12 keV) and substrate. It is seen that the heat treatment of the beneath layer results in lower *S* parameters. Moreover, the positron lifetime results at an incident energy of 8 keV in Table 1 show that the long-lived *ortho*-positronium (*o*-Ps) component is present in the as prepared samples but not in the heated ones. It can be concluded that the heat treatment led to the inhibition of the formation of positronium (Ps).

Traditionally the size of the void for molecule permeation through the 2D membrane was calculated by coupling the results from XRD and AFM [1]. The interlayer spacing distance can be determined by XRD, and the thickness of a single platelet can be probed by AFM. Considering that the electronic clouds around graphene sheets extend over a distance of ~ 3.34 Å, the 'empty' space available for gas molecules to diffuse is estimated around 5 Å for the GO membranes by Ibrahim and Lin [2]. The positron beam experiment has the potential for independent estimation of this 'empty' space. We further seek this possibility in this ongoing research.

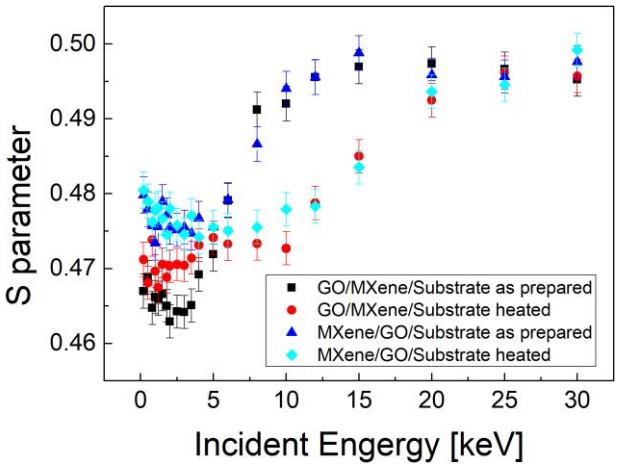

Fig.1. The *S*-*E* plots for the samples.

Table 1. *o*-Ps lifetime results at 8 keV.

	o-Ps lifetime (ns)	*o*-Ps intensity (%)
GO/MXene/Sub	1.54±0.03	14.8±0.4
GO/MXene/Sub heated	-	-
MXene/GO/Sub	1.62±0.03	13.8±0.3
MXene/GO/Sub heated	-	-

REFERENCES:

[1] R.R. Nair *et al.*, Science, **335** (2012) 442-444.

[2] A. Ibrahim and Y. S. Lin, J. Membrane Sci., **550** (2018) 238-245.

CO4-10 Characterization of Precipitates in Cu alloy using Small-Angle X-ray Scattering

Y. Oba and H. Sasaki[1]

Materials Sciences Research Center, Japan Atomic Energy Agency
[1]Furukawa Electric Co., Ltd.

INTRODUCTION: Cu alloys are one of the most important materials supporting a wide variety of industries with excellent electric and mechanical properties. In the Cu alloys, precipitation strengthening is effective to further improve the strength with reasonable conductivity [1,2]. In the precipitation-strengthened Cu alloys, the size and morphology of the precipitates are directly connected to the strength, while the alloying elements dissolved in matrix decreases the conductivity. Therefore, quantitative characterization of the precipitates is required to optimize the precipitation conditions. Small-angle X-ray scattering (SAXS) is a powerful means for such quantitative characterization of the nanostructures in metals and alloys [3,4]. In this study, we performed the SAXS measurement of Cu-Ni-Si, which is a typical precipitation-strengthened Cu alloy.

EXPERIMENTS: The chemical composition of the samples was Cu-2.5mass%Ni-0.6mass%Si. The ingot was solution-treated and aged for two hours at various temperatures. SAXS measurements were performed using the SAXS instrument with Mo *K*α radiation. Scattering patterns were measured using a photon-counting-type two-dimensional detector (PILATUS 100k). The converter was a silicon with the thickness of 1000 μm to detect the high energy X-ray from Mo efficiently. The X-ray path between an entrance slit and a detector window was in vacuum to reduce background scattering from air. The data reduction was conducted using our original program written in Igor Pro software.

RESULTS: In two-dimensional scattering patterns, all the samples show isotropic scattering. This means that the precipitates are isotropically dispersed in the samples (Fig. 1). Fig. 2 shows the circularly averaged scattering profiles. All the samples have higher intensities than the background. For the as-solution-treated sample, the scattering profile decreases exponentially with increasing q and then exhibits a plateau at $q > 3$ nm^{-1}, where q denotes the magnitude of the scattering vector. This q dependence is a typical background contribution from solution-treated alloys [4], where no precipitates are dispersed ideally. Compared to the as-solution-treaded sample, the other profiles have a shoulder, which indicates the formation of the precipitates. With increasing aging temperature, the shoulder shifts toward lower q. This means that the precipitates become larger. As a result, we successfully ob-served the formation of the precipitates and their growth with aging temperature in Cu-Ni-Si using SAXS. These results agree well with the tendency obtained using small-angle neutron scattering (SANS) [5].

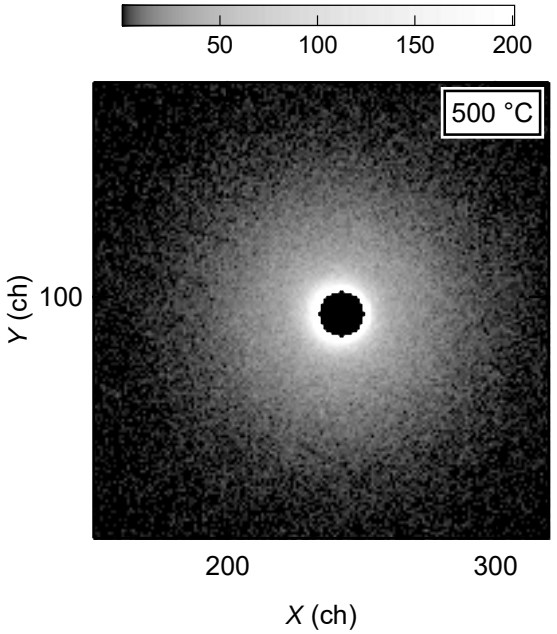

Fig. 1. Typical two-dimensional scattering pattern of Cu-Ni-Si aged at 500 °C.

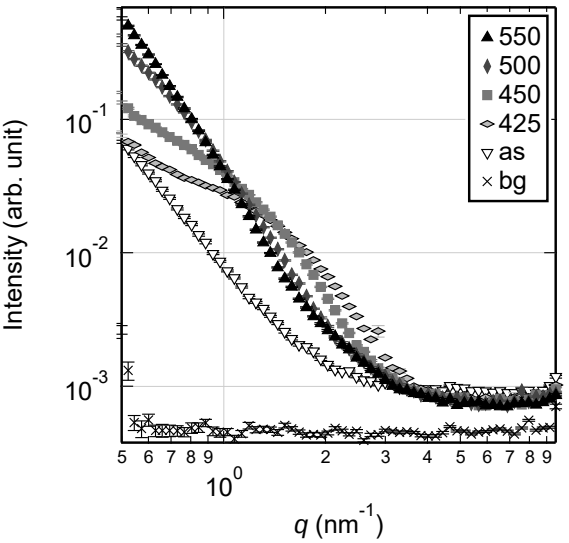

Fig. 2. Scattering intensity of Cu-Ni-Si aged at 425, 450, 500, and 550 °C as well as solution-treated.

We are now characterizing the detail of the internal structure of the precipitates from the comparison of SAXS and SANS [5].

REFERENCES:

[1] S. A. Lockyer *et al.*, J. Mater. Sci., **29** (1994) 218-226.
[2] H. Fujiwara *et al.*, J. Jpn. Inst. Metals, **62** (1998) 301-309.
[3] M. Ohnuma *et al.*, Acta Mater., **57** (2009) 5571-5581.
[4] Y. Oba *et al.*, ISIJ Int., **55** (2015) 2618-2623.
[5] H. Sasaki *et al.*, Mater. Trans., **63** (2022) 1384-1389.

CO4-11 Gamma-ray induced photo emission from GaP single crystal wafer: Comparison with GaN

T. Nakamura[1], T. Nishimura[1], K. Kuriyama[1], Atsushi Kinomura[2]
[1]*Research Center of Ion Beam Technology, Hosei University, Koganei, Tokyo 184-8584, Japan*
[2]*Institute for Integrated Radiation and Nuclear Science, Kyoto University, Kumatori, Osaka 590-0494, Japan*

INTRODUCTION: Gallium phosphide (GaP) is usually employed in the manufacture of low-cost red, orange, and green light-emitting diodes (LEDs). We recently succeeded in detection of the gamma-ray induced photo emission from GaN [1] and ZnO [2] single crystal wafers. Whether the luminescence by the excitation of gamma-ray is observed at room temperature in GaP as similar to GaN and ZnO is important as it may be used as an application as a gamma-ray detector. In the present study, we investigate the luminescence properties in gamma-ray excition of GaP, and the difference in gamma-ray induced photo emission from GaN, which is transparent to visible light.

EXPERIMENTS: GaP single crystal wafers with a size of several cm square and a thickness of several 100 μm meters were used for the present study. The crystals were irradiated at room temperature with gam-ma-rays of 1.17 and 1.33 MeV from a cobalt-60 source of Institute for Integrated Radiation and Nuclear Science, Kyoto University. The gamma-ray irradiation induced photo emission measurements were performed by using a charge coupled device (CCD) equipped spectrometer (QE Pro, Ocean Insight Co. Ltd.). Each measurement was performed under 20 min, gamma-ray irradiation and each spectrum was acquired for 2 min, CCD exposure time. One end of a 10-meter long optic fiber cable made of SiO_2 was set on the front face of GaP placed near the Co source and the other end was led to the analysis room with the spectrometer. The transmission of this fiber is about 90 % at wavelengths from 475 to 1300 nm and about 50 to 85 % at wavelength from 380 to 475 nm. Therefore, gamma-ray induced photo emission measured using this fiber cable may reduce the band edge emission of wide gap semiconductors such as GaN.

RESULTS: Figure 1 shows Gamma-ray induced photo emission spectra of GaP and GaN single crystal wafers. Both spectra are broad. The greater breadth of the spectra observed in GaP can be attributed to donor-acceptor pair transitions [3]. These spectra are usually broad because of strong phonon-assisted transitions arising from the tight binding of the O donor.Emission intensity of GaP is lower than that of GaP wafer. This lower emission intensity is observed in normal photoluminescence measurement using a He-Cd laser. The peak intensity from impurity doped GaP is about 1/200 of GaN. The transparent GaN has a larger penetration depth for the He-Cd laser and a higher emission intensity. On the other hand, it is suggested that GaP is opaque, has less penetration of He-Cd laser light than GaN, and also shows the low emission intensity. More importantly, un-doped GaP show no photoluminescence. In GaN with native defects, the defect level behaves as the emission center without adding impurities. Yellow luminescence (YL) observed in GaN has been proposed as a transition from a shallow donor to gallium vacancy (VGa) located at about 1.1 eV above the valence band [4]. Our previous study [5] reported that the high-dose gamma-ray irradiation of 160 kGy mainly induces N vacancies (VN) located at about 50 meV below the conduction band. Therefore, the gamma-ray induced YL observed in GaN is attributed to a shallow donor to VGa transition due to the excitation from valence band to conduction band by Compton electrons.

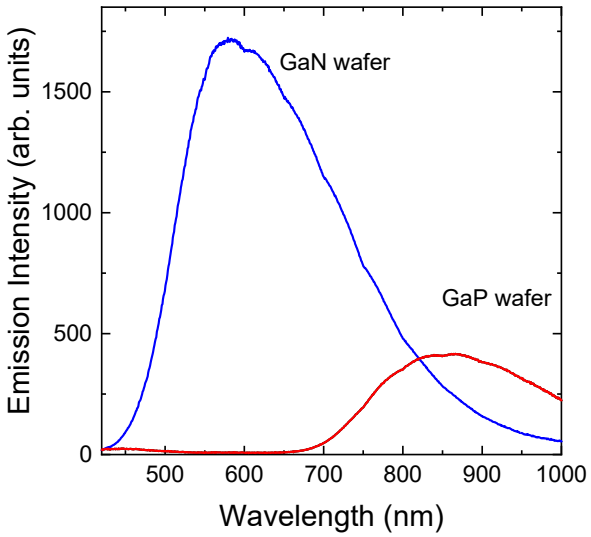

Fig. 1. Gamma-ray induced photo emission spectra from GaN and GaP single crystal wafer.

Part of this research was submitted to Nuclear Instruments and Methods in Physics Research Section B: Beam Interactions with Materials and Atoms.

REFERENCES:

[1] T. Nakamura *et al.*, Appl. Phys. Lett., **118** (2021) 032106.
[2] T. Nakamura *et al.*, Solid State Commun., **336** (2021) 114413.
[3] P. J. Dean *et al.*, Phys. Rev., **168** (1968) 812.
[4] J. Neugebauer *et al.*, Appl. Phys. Lett., **69** (1996) 503.
[5] Y. Torita *et al.*, J. Phys.: Conf. Series, **864** (2016) 012016.

CO4-12 Porosity control of diamond-like carbon films

S. Nakao, X. Qu[1], A. Yabuuchi[1] and A. Kinomura[1]

Innovative Functional Materials Research Institute, National Institute of Advanced Industrial Science and Technology
[1]Institute for Integrated Radiation and Nuclear Science, Kyoto University

INTRODUCTION: Diamond-like carbon (DLC) films which sometimes include hydrogen have attracted much attention because of their excellent properties. However, their properties are strongly degraded at elevated temperature. It is considered that the degradation should be related to the release of hydrogen and the structural changes at feverish temperature. Moreover, the behavior of pores which are presented due to amorphous nature also may be significant role on the degradation. Regrettably, the behavior of the pores in the films is not always clarified up to now.
Positron annihilation spectroscopy (PAS) using energy-variable monoenergetic positron beams (slow positron beams) is a useful technique which enables to investigate the behavior of pores in amorphous thin films. It is known that S parameters obtained from Doppler broadening annihilation radiation (DBAR) measurement reflect the size and density of open-volume defects or pores with the information of annihilation sites in the films. On the other hand, positron lifetime obtained by positron annihilation lifetime spectroscopy (PALS) mainly reflect the size of open volume defects or pores. Therefore, it is expected that both DBAR and PALS measurements should be useful for the examination of the behavior of pores as a function of annealing temperature.
In this study, DLC films are prepared by a bipolar-type plasma-based ion implantation and deposition (PBIID) system. The samples are annealed in vacuum in the range of 200 – 800 ºC. The behavior of pores is examined by PAS measurement.

EXPERIMENTS: The bipolar-type PBIID system [1] was used for sample preparation. Toluene (C_7H_8) or acetylene (C_2H_2) was used as source gas for the deposition of DLC films which were denoted as sample A and sample B, respectively. Silicon (100) wafers were used as substrates which were cut into 2 x 2 cm. The substrates were put on the sample holder where positive pulse voltage was applied, and then negative pulse voltage was applied at a frequency of 2 kHz. The deposition time of sample A and B were 40 and 60 min, respectively.
The samples were annealed in vacuum by infrared image furnace. The furnace was evacuated less than 3 x 10^{-3} Pa by a turbo molecular pump. The heating rate was 100 ºC/min and the annealing time was 60 min. The annealing temperature was set ranging from 200 to 800 ºC. The samples were kept in vacuum after annealing process and naturally cooled down to room temperature. PAS measurement was performed with a slow positron beam line. S parameters as function of energy (S-E curves) were measured in the range of 0 – 26 keV. Lifetime measurement was also conducted with a positron beam at an energy of 2 keV.

RESULTS: To investigate the pores in DLC films, the relationship between the S parameter and lifetime is plotted in Fig. 1. For sample A, the S parameter only decrease up to 400 ºC. This result seems that the pores decrease in number. However, it is noted that S parameter may be insensitive to the number of pores due to the saturation effect. Therefore, it is considered that the decrease of S parameter should be caused by the increase of π electron in number. At 800 ºC, the lifetime increases accompanied with decreasing S parameter. This suggests that the pores increase in size and π electrons increase in number. For the sample B, the S parameter mainly increases up to 400 ºC, suggesting that the pores mainly increase in size. At the same time, π electrons possibly increase in number, which is competitive effect to S parameter. At further increase of annealing temperature, the trend is a little bit complicated. At 600 ºC, the lifetime and S parameter increase. However, both values are rapidly decrease at 800 ºC. From the results, it is suggested that the pores once increase in size at 600 ºC. And then the pores decrease in size and π electrons possibly increase in number at 800 ºC.

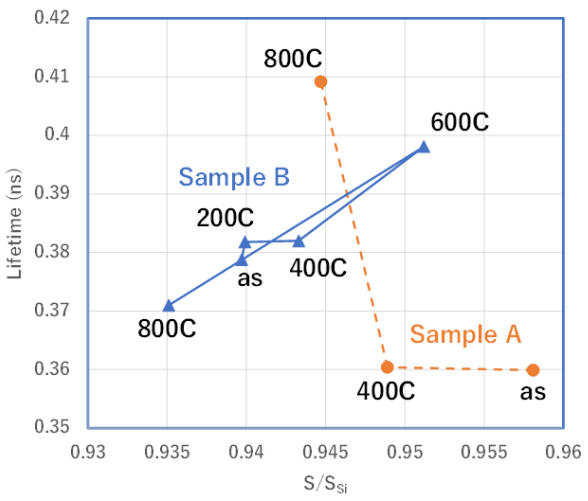

Fig.1. Relationship between the S-parameters and the lifetimes for respective samples A and B.

REFERENCES:
[1] S. Miyagawa *et al.*, Surf. Coat. Technol., **156** (2002) 322-327.

CO4-13 Hyperfine Fields in $La_{0.7}Ca_{0.3}Mn_{0.45}Fe_{0.55}O_3$ Measured by Means of Mössbauer and TDPAC Spectroscopies

W. Sato, H. Uchino[1], K. Takanashi[2], S. Komatsuda[3], A. Taniguchi[4], M. Tanigaki[4], and Y. Ohkubo[4]

Institute of Science and Engineering, Kanazawa University
[1]Graduate School of Science and Technology, Kanazawa University
[2]School of Chemistry, Kanazawa University
[3]Institute of Human and Social Sciences, Kanazawa University
[4]Institute for Integrated Radiation and Nuclear Science, Kyoto University

INTRODUCTION: $La_{0.7}Ca_{0.3}MnO_3$ is a metal oxide with a perovskite structure in which La and Ca occupy the *A* site and Mn the *B* site, respectively [1]. This compound has been receiving high expectations for applications to spintronics devices because of the effect of colossal magnetoresistance below T_C ~ 250 K arising from double exchange interaction caused by the electron transfer between Mn^{3+} and Mn^{4+} [2]. The CMR effect is expected to be applied to a variety of functional materials such as magnetic heads and resistance change memories. For wide applications of this compound, it is preferable to control its magnetic property for each practical use. As the first trial to control its magnetic property, in the present study, we tried to raise the transition temperature T_C to the vicinity of room temperature by introducing Fe to the *B* site substituting for Mn by 55% to synthesize $La_{0.7}Ca_{0.3}Mn_{0.45}Fe_{0.55}O_3$ (LCMFO). For the measurements of the local magnetic fields, we employed ^{57}Fe transmission Mössbauer and TDPAC spectroscopies. Here, a preliminary result is reported.

EXPERIMENTS: Stoichiometric amounts of La_2O_3, MnO_2, Fe_2O_3, and $CaCO_3$ were mixed well in a mortar, and the powdery mixture was calcined at 1273 K for 12 h. The sample was again ground to uniformity and was pressed into a disk. The disk was then sintered at 1473 K for 96 h. Successful synthesis of LCMFO was confirmed by the powder X-ray diffraction pattern.
A ^{57}Fe Mössbauer spectrum was obtained for the sample at room temperature (RT). The velocity of the source was calibrated with α-Fe at RT.
Neutron irradiation was performed for cadmium oxide (CdO) enriched with ^{110}Cd in Kyoto University Reactor to produce radioactive ^{111m}Cd. The radioactive Cd(^{111m}Cd)O powder was mixed well with the powdery LCMFO sample. The mixture was then pressed into a disk and was sintered in air at 1373 K for 45 min. A TDPAC measurement was carried out for the ^{111}Cd(←^{111m}Cd) probe with the intermediate state of I = 5/2 having a half-life of 85.0 ns. In the present work, we obtained the spectrum with four detector system to observe delayed coincidence events at 90 and 180 degrees' angular correlation of the 151-245 keV cascade γ rays.

RESULTS: The RT ^{57}Fe Mössbauer spectrum obtained for $La_{0.7}Ca_{0.3}Mn_{0.45}Fe_{0.55}O_3$ is shown in Fig. 1(a). The spectrum is dominated by an intense doublet, suggesting that most of the ^{57}Fe spins are paramagnetically fluctuated at this temperature. However, a quite broad resonant component is also observed in the spectrum, possibly indicating a transitional shift of the spin state between paramagnetic and ferromagnetic ordering. This observation may suggest that T_C has successfully been raised to RT or higher. For more information, we obtained a TDPAC spectrum of the ^{111}Cd(←^{111m}Cd) probe at RT as shown in Fig. 1(b). The spectrum shows a wide distribution of the electric quadrupole frequency for the precession of the probe. Although the fit was based on the assumption that the probes are perturbed by the electric quadrupole interaction with the outer charge distribution, the wide distribution could be attributed to slow fluctuation of the spins of the magnetic Mn and Fe ions at the *B* site. For more detailed discussion, low temperature measurements are underway.

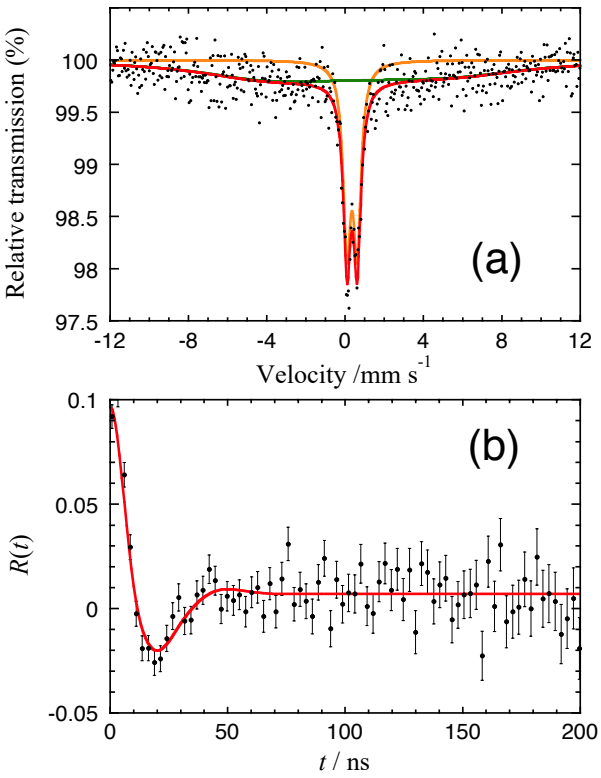

Fig. 1. (a) ^{57}Fe Mossbauer spectrum and (b) TDPAC spectrum of ^{111}Cd(←^{111m}Cd) obtained for $La_{0.7}Ca_{0.3}Mn_{0.45}Fe_{0.55}O_3$ at room temperature.

REFERENCES:

[1] H. Y. Huang *et al.*, Phys. Rev. Lett., **75** (1995) 914-917.
[2] W. Sato *et al.*, Phys. Rev. B, **100** (2019) 184111/1-7.

CO4-14 A study of guar-gum hydrogels using small angle X-ray scattering

T. Tominaga[1], R. Inoue[2], and M. Sugiyama[2]

[1]*Neutron Science and Technology Center, Comprehensive Research Organization for Science and Society (CROSS)*
[2]*Institute for Integrated Radiation and Nuclear Science, Kyoto University*

INTRODUCTION: One of the characteristics of soft matter is its capability of large deformation. Polyvinyl alcohol-borate hydrogel (so-called slime), consisting of polyvinyl alcohol (PVA), borax, and water, has long been known as a toy, and is a soft matter known to be capable of large deformation. Additives to hydrogels inhibit/promote the mechanical properties of the hydrogel.

Cross-linking agents, which are used to retain the gel morphology to some extent, lead the hydrogel less deformable, depending on the additive amount. Lubricants that act between polymer chains also be introduced to make polymer chains smoother and facilitate large deformations.

Hydrogels prepared with guar gum (GG), a galactomannan, can be greatly deformed by the addition of appropriate amounts of borax (cross-linking agent), glycerin, and vinyl acetate resin particles, compared to GG gel, which has only borax as an additive.

In this experiment, for hydrogels created with GG, the internal structural changes of the hydrogels due to the addition of borax (cross-linking agent), lubricants, and particles were evaluated by small-angle X-ray scattering (SAXS).

EXPERIMENTS: GG hydrogels were prepared in the following weight ratios: GG: approximately 2–3 wt.%, glycerin 7 ml, borax: approximately 0.4 g, vinyl acetate granular resin: approximately 2–3 g, and water: approximately 88 g.

The sample thickness of hydrogels was approximately 0.5 mm and sandwiched between a polyetherimide resin (Sperio, Mitsubishi, Japan). The Cu-SAXS (RIGAKU Nanopix) available at Institute for Integrated Radiation and Nuclear Science, Kyoto University of high-resolution mode was utilized. The empty cell was subtracted to account for the transmission, and the scattering profile, $I(Q)$ was obtained by circular averaging.

RESULTS: SAXS profiles of GG hydrogels are shown in Fig. 1. The simple GG (+ water) scattering profile shows that the addition of borax increases the slope and the addition of glycerol decreases the slope; the addition of resin increases the slope at $Q < 0.2$ Å^{-1}.

Considering that the change in slope is correlated with the internal structural inhomogeneity of the substance, glycerol has a structural homogeneity effect on slime, borax has a structural imhomogeneity effect, and resin has a structural inhomogeneity effect at $Q < 0.2$ Å^{-1}. Although the size of the resin is in the order of micrometers, the effect of the resin on the polymer chains could be observed in this SAXS Q range.

PVA is known to easily form nanocrystals with a size of approximately 7 nm [1]. The effects of the introduction of additives on hydrogel structure were evaluated in the same way as for GG hydrogels. The effects of each additive on the structure of PVA were similar to those of GG, however the effects were not strong enough to block the formation of nanocrystals. In the case of GG hydrogels, no internal structure corresponding to microcrystals was observed in the scattering profiles of PVA hydrogels, suggesting that the ability to form microcrystalline structures is an obstacle to large deformation.

Data were also obtained on the structure of the hydrogel in the case of other galactomannan species, the effect of lubricants other than glycerol, and the size-dependence of glass particles as a substitute for the resin. The data will be individually investigated and compiled into an original paper.

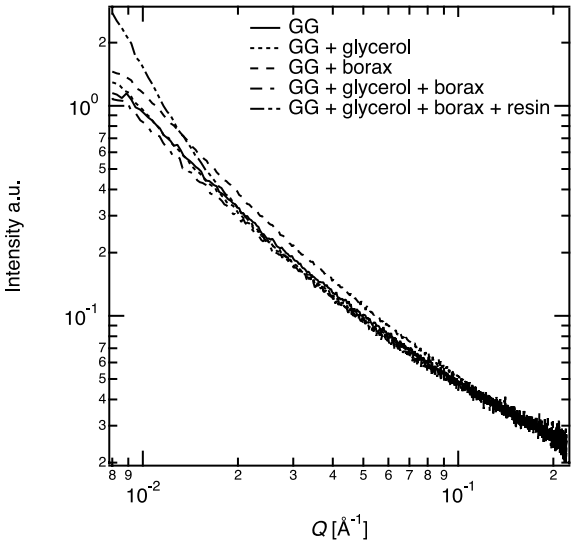

Fig. 1. SAXS profile of GG + water with additives (glycerol, borax, and vinyl acetate granular resin). Each profile corresponds to the presence or absence of the additives.

REFERENCES:

[1] T. Kanaya *et al.,* Polymer Journal, **44** (2012) 83-94.

CO4-15 Tritium recovery behavior for tritium breeder Li_2TiO_3-Li_4SiO_4 biphasic materials with various phase ratios and Pb addition

Y. Oya[1], A. Sanfukuji[2], Q. Zhou[3], G. Tan[4], F. Sun[5], Y. Feng[6], X. Wang[6], H. Wang[7], M. Kobayashi[8], Y. Iinuma[9] and R. Okumura[9]

1 Faculty of Science, Shizuoka University
2 Graduate School of Integrated Science and Technology, Shizuoka University
3 School of Materials and Science Engineering, Wuhan University of Technology
4 School of Materials and Science Engineering, University of Science and Technology Beijing.
5 School of Material Science and Engineering, Hefei University of Technology
6 Fusion Technology Research Division, Center for Fusion Science, Southwestern Institute of Physics
7 College of Physics, Sichuan University
8 National Institute for Fusion Science
9 Institute for Integrated Radiation and Nuclear Science, Kyoto University

INTRODUCTION:

In the fusion reactor blanket, tritium is produced by (n, α) reaction with lithium. Lithium titanate (Li_2TiO_3) and lithium orthosilicate (Li_4SiO_4) are considered as candidates for solid tritium breeding materials. Li_2TiO_3-Li_4SiO_4 mixed ceramic materials are expected to have both advantages. Lead (Pb) is a neutron multiplier that contributes to the improvement of the tritium breeding ratio and tritium recovery efficiency due to lower affinity with tritium. However, the tritium recovery performance has not been evaluated. In this work, the effect of Pb addition on tritium recovery for Li_2TiO_3-Li_4SiO_4 mixed ceramic materials was investigated. Li_2TiO_3-Li_4SiO_4 biphasic materials with various phase ratios and Pb addition were used and their tritium desorption behaviors after neutron irradiation were evaluated by tritium thermal desorption spectroscopy (tritium-TDS).

EXPERIMENTS:

Three kinds of powder samples were used, including Li_2TiO_3-Li_4SiO_4 (LTO-LSO), Li_2TiO_3-0.5Li_4SiO_4 (LTO-0.5LSO), and Li_2TiO_3-Li_4SiO_4-5wt%Pb (LTO-LSO-5wt%Pb). Those samples were irradiated by neutron at Kyoto University Research Reactor (KUR) with the neutron fluence of 3.96×10^{16} n cm^{-2}. After the neutron irradiation, tritium release behavior was evaluated by tritium-TDS by heating the samples separately from R.T. to 1113 K with the heating rates of 10, 20, and 30 K min^{-1}. Liquid scintillation counter (LSC) was used to measure the total T amount trapped by the water bubbler at Shizuoka University.

RESULTS:

Fig. 1. shows the tritium-TDS spectra. By the comparison of T desorption behavior for LTO-LSO and LTO-0.5LSO, the T desorption peak has shifted toward lower temperature side as the percentage of LTO increased. With the addition of 5 wt% Pb, additional peak shift toward lower temperature side was confirmed, indicating that the addition of lead enabled tritium recovery at lower temperatures. Besides, almost all of tritium was released in the form of tritiated water (HTO), which was also confirmed by the LSC measurement, while gas-species (HT) release was observed for the LTO-LSO-5wt%Pb. This may be due to the fact that Pb, a neutron multiplier, has a low affinity for tritium. The activation energies of tritium desorption for each sample was calculated based on the kinetics analysis by heating the sample with various heating rates. The activation energies were 1.13 eV for LTO-0.5LSO, 0.76 eV for LTO-LSO, and 0.86 eV for LTO-LSO 5wt% Pb, respectively. The LTO-LSO sample has acheived the lowest value. It can be said that higher Li atomic density may facilitate stable trapping sites in LTO-LSO. In our future work, Pb concentration dependence on T release will be scheduled.

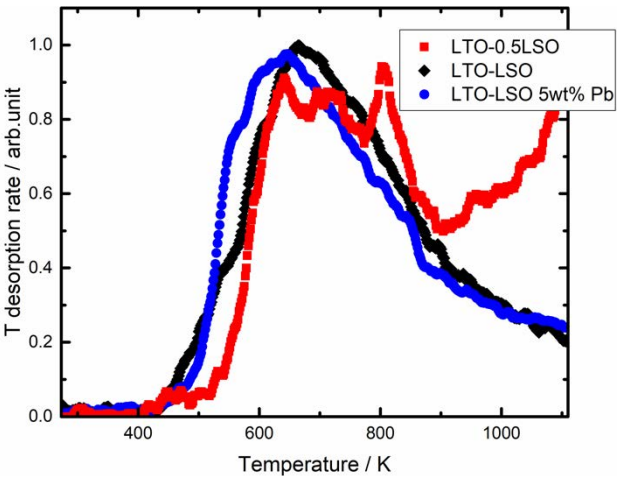

Fig. 1. Tritium-TDS spectra for Li_2TiO_3-Li_4SiO_4, Li_2TiO_3-0.5Li_4SiO_4 and Li_2TiO_3-Li_4TiO_4 5wt% Pb with the heating rate of 10 K min^{-1}.

REFERENCES:

[1] Q. Wang *et al.*, Ceramics International, **48** (2022) 26742-26749.

R4096

CO4-16 Study to improve transport and measurement performance of a slow positron beamline

A. Kinomura, N. Oshima[1], A. Uedono[2] and A. Yabuuchi

Institute for Integrated Radiation and Nuclear Science, Kyoto University
[1]National Institute of Advanced Industrial Science and Technology (AIST)
[2]University of Tsukuba

INTRODUCTION: Positron annihilation spectroscopy is an important analytical method to detect vacancy-type defects and vacant spaces of materials. Energy-variable mono-energetic positron beams (slow positron beams) are essential to perform depth-dependent positron annihilation spectroscopy of surface layers such as ion-implanted layers or thin films formed on substrates. Intense positron sources are necessary to obtain slow positron beams for practical use. In general, positron sources based on pair creation can provide higher intensity than radioisotope-based positron sources. A positron source using pair-creation by gamma-rays from a nuclear reactor have been developed by using Kyoto University research Reactor (KUR) to obtain a slow positron beam for materials analysis. In the KUR slow positron beamline, the spot size at the sample chamber is more than 10 mm in diameter. To reduce spot sizes for smaller samples, a brightness enhancement system has been developed. Simultaneously, a lifetime measurement system based on a pulsing system using a radiofrequency-driven buncher was also developed for the KUR slow positron beamline [1]. In this report, the performance of the positron lifetime system was evaluated in comparison with the system at National Institute of Advanced Industrial Science and Technology (AIST).

EXPERIMENTS: Positron lifetime spectra of Kapton and H-implanted Si samples were measured at 6 keV by the KUR slow positron beam system. The same samples were measured at 6 keV by the AIST slow positron beam system. Among the samples, the results of the Kapton sample, as a reference material, were compared to understand the characteristics of the KUR system. The design of the pulsing system of the KUR system is based on that of the AIST system. The both systems use a combination of a transmission-type chopper and radiofrequency-driven buncher electrodes. Annihilation gamma-rays are detected by scintillation detectors using photomultipliers and BaF_2 crystals.

RESULTS: Figure 1 shows the lifetime spectra of the Kapton sheet measured at KUR and AIST systems. Solid lines show the original (as-measured) spectra. Dots show the spectra after back-ground subtraction. As described in the previous study [1], the KUR lifetime measurement system is influenced by background radiation, leading to the higher background signals even with the use of background discrimination circuits. A big satellite peak around 8 ns corresponds to the buncher signal and it was not sufficiently cut by the chopper electrode. Except for this chopper-origin peak, irregular background signals were treated as a part of the resolution function. In the case of the AIST spectra, the resolution function was calculated using a YSZ (yttoria stabilized zirconia) spectrum and then it was applied for the Kapton analysis. A broad satellite peak around 12 ns can be attributed to backscattered positrons. It is interesting to note that the different lifetime measurement systems have different background shapes like fingerprints. The spectrum analysis was performed assuming a single lifetime component. The lifetimes obtained for Fig.1(a) and 1(b) were 0.3815±0.0008 and 0.3805±0.0005 ns, respectively. These values are reasonably in agreement with previously reported Kapton lifetimes.

In summary, positron lifetime measurements were performed for several samples using the KUR and AIST slow positron systems. The levels and shapes of the background signals were different but both of Kapton lifetimes were reasonably in agreement with the previously reported values.

REFERENCES:

[1] M. Nakajima *et al.,* Rev. Sci. Instrum., **91** (2020) 125109.

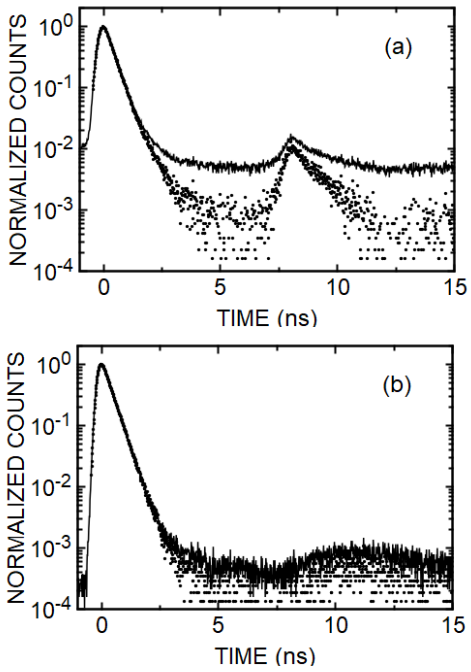

Fig. 1. Positron annihilation lifetime spectra of a Kapton sheet measured at (a) KUR and (b) AIST systems. Solid lines and dots show the original and background-subtracted spectra.

CO4-17 Complex Structure of Ions Coordinated with Hydrophilic Polymer 23. Iodine Doping with Organic Tissues.

A. Kawaguchi and, Y. Morimoto

IIRNS, Kyoto University (KURNS)

INTRODUCTION:

We have been investigating dynamical and interacted structures between iodine and polymers. Here, the term of "iodine" is not only simple iodine, I_2, but *polyiodide ions* (I_n^{m-}, *m, n*: integer, $n > 1$, "Poly-Iod(s)" mentioned below) as charged molecules, which suggest concealed potential and diverse availability for application with polymeric materials. [1,2]

"Poly-Iod"s are defined as charged molecules which are composed only by (more than one) iodine atoms as an unique element. They indicate spatial occupation, anisotropic molecular shapes, charge conjugation on molecule(s), chained structure between "Poly-Iod"s themselves through "halogen bonding (iodine bonding) ", variable distances between iodine atoms, etc; these singular behaviors are attributed to iodine as the characteristic element.

On the other hand, iodine atoms can often coordinate with other elements through lone pairs of electrons due to since its higher atomic number (Z=53). Additionally, even dipole or distributed positive charge (σ-hole) on "Poly-Iod" can be localized corresponding to their bonding with other atoms or ions. Or, though iodine is a member of halogen, mono-iodide ion, I^+, can behave as single cation with positive charge, while it does not belong to definition of "Poly-Iod". [3,4]

Such ambiguous and variable nature of "Poly-Iod" let be expected to introduce general affinity with variable polymeric structure in which dipole interaction potentially exist even whether the host polymer is hydrophilic or hydrophobic. If so, there can be expected novel functionality applied with interaction of "Poly-Iod"s with organic textures while they may not be paid attention as matrices for coordination nor be considered with hydrophilicity. [5]

EXPERIMENTS:

As host polymer originated organic texture, spallation of human throat (sputum) was sampled. As an aqueous solution of "Poly-Iod", I_2-KI(aq)/0.1N was prepared; 0.05M I_2 and 0.15M KI were solved in water. The samples were (1) casted and dried on a cover glass at first and immersed into following I_2-KI(aq)/0.1N, or (2) immersed into the solution at first and casted and dried on a cover glass (casting iodine-doped sputum on a glass substrate). After iodine doping, the samples were not rinsed with water. Mass deviation on each drying or doping process was not measured. While WAXD for the samples were observed through the cover glasses with penetrating MoKα radiation, spacing was not estimated.

RESULTS AND DISCUSSION:

While present results are not adequate for quantitative estimation, here may be hinted modification of organic tissues applied with "Poly-Iod(s)" solution.

The sampled sputum is decomposed collagen which is not polymeric material in macroscopic scale; it was solved and dispersed in water easily and was colorless.

Both process, iodine-doping after "drying and casting" and "drying and casting" after doping, indicated iodine adsorption explicitly in macroscopic observation; interacted coordination is actually realized between collagen as organic tissues and "Poly-Iod(s)". (Fig.1) [5]

On the other hand, microscopic behavior indicated in WAXD showed difference between the samples. Both samples showed arcs on diffraction; they suggested crystalline structure with host matrices (polymer or oligomer) since these diffraction (indicated with red arrows in Fig.1's) had sharp peak widths and anisotropic (?) orientation. Additionally, preceding iodine doping (Fig.1(b)) introduced other diffraction as oriented spots..

It is not clarified yet if these spots are attributed to coordinated structure between polymeric matrices and "Poly-Iod(s)" or to precipitation of low molecular substances independent of polymeric coordination. Nevertheless, arcs observed in diffraction are suggesting that iodine doping can introduce novel structure and application through interaction within organic tissues which have not been regarded as fields for functionality.

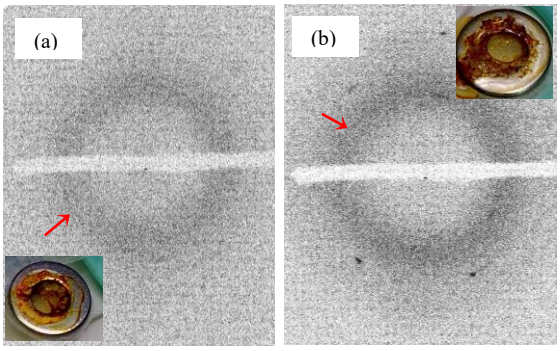

Fig.1: Adsorption as macroscopic observation and WAXD patterns indicating microscopic interaction of "Poly-Iod(s)" with collagen; (a) iodine doping after drying and (b) iodine doping before drying and casting.

REFERENCES:

[1] patent. JPN-5444559 (2014).

[2] "Projects for Practical Use from Innovation" sponsored by NEDO (2007-2009).

[3] T.J. Marks & D.W. Kalina, "Extended Linear Chain Compounds" vol.1 ch.6., ed. J.S. Miller (Plenum Press, 1982).

[4] T. Clark, *et.al.,* J Mol. Model, **13** (2007) 291-296.

[5] A. Kawaguchi, SPSJ Workshop, "58th KOHBUNSHI TO MIZU (Polymer and Water)" (on-line), (2020)1-2.

CO4-18 Chemical form of tritium released from neutron-irradiated FLiNaK mixed with Ti powder

K. Katayama, K. Kubo, T. Ichikawa, K. Masuta, M. Oya, T. Takeishi[1], K. Akashi[1], and Y. Iinuma[2]

Interdisciplinary Graduate School of Engineering Sciences, Kyushu University
[1]Faculty of Engineering, Kyushu University
[2]Institute for Integrated Radiation and Nuclear Science, Kyoto University

INTRODUCTION: As an advanced blanket concept of a DT fusion reactor, the self-cooling liquid blanket has been proposed. In this concept, primary cooling media plays two important roles of tritium transport and heat transport. Fluoride molten salts such as FLiNaBe and FLiBe are a promising liquid blanket material due to high stability at high temperatures, low reactivity with O_2 and H_2O, and low MHD pressure drop. Tritium is produced in the molten salts by the nuclear reaction between neutrons and Li. Since fluoride molten salts have a low solubility for hydrogen isotopes, the produced tritium tends to release from the molten salt. This property means that tritium can be easily recovered from the molten salt but also parts of tritium is lost to the outside of cooling tubes by the permeation on the way to the tritium recovery system. For suppressing tritium loss by increasing effective solubility for tritium, the addition of Ti powder was proposed [1]. However, few studies on molten salt materials containing Ti powder have been performed. In order to discuss the design of tritium recovery system, it is necessary to understand the fundamental behavior of tritium in the molten salt mixed with Ti powder. Since FLiNaBe and FLiBe contain highly toxic beryllium and is not easy to handle safety, FLiNaK is usually used as a simulated fluid. In this study, the solid state sample of FLiNaK mixed with Ti powder was irradiated by neutrons at Kyoto University Research Reactor, and the chemical form of tritium released from the free surface of the molten salt by heating was observed in Kyushu University.

EXPERIMENTS: In the powders of LiF, NaF and KF were mixed in a Ni crucible under Ar atmosphere. The Ni crucible was put in the stainless-steel heating pot and repeatedly heated to 600 ℃ with Ar purging to remove impurity water vapor. The heating was repeated to homogenize the FLiNaK and the plateau region of temperature change was confirmed at 454 ℃ which is melting point of FLiNaK. A part of FLiNaK was sampled for the measurement of water vapor by heating in Ar gas flow.

Ti powder was added to the part of FLiNaK with 2.5 wt% and it was heated with Ar purging. The prepared sample of FLiNaK was packed into quartz tubes in vacuum and it was installed into a polyethylene capsule. The thermal neutrons irradiation was performed by at pneumatic tube 2 (Pn-2) with the fluence of at Pneumatic Tube 2 (Pn-2) of the 1.7×10^{15} cm^{-2}.

The release behavior of water vapor from non-irradiated FLiNaK without Ti was investigated by heating at 600 ℃ in Ar gas flow with 400 cc/min. The concentration of water vapor in the outlet gas was monitored with a hygrometer (MAH-50, SIMAZU Co.). The FLiNaK granules were put in a Mo crucible and it was installed in a quartz reaction tube.

Tritium release experiment was carried out for neutron irradiated FLiNaK. The irradiated sample was put in a Mo crucible and it was installed in the quartz reaction tube. In order to melt the sample sufficiently, heating temperature was set to be to 600 ℃ or 700 ℃ with Ar purge. The chemical form of tritium released from the sample was expected to be TF, T_2 and T_2O, and these were separately quantified. Details of the quantification method were described in Ref.2.

RESULTS: The release behavior of water vapor from the FLiNaK is shown in Fig.1. Two release peaks were observed in the water vapor release curve. It is considered that the first peak is caused by the desorption of water vapor adsorbed on the surface of FLiNaK granules and the second peak is caused by the desorption contained in the bulk of FLiNaK. From the amount of released water, the concentration of water in FLiNaK including surface adsorbed water was estimated to be 1.44 wt %.

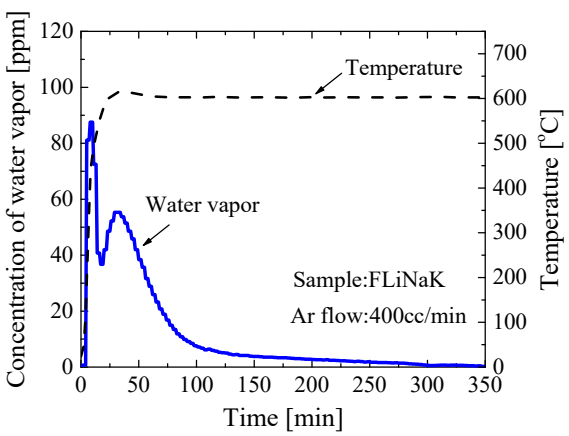

Fig.1. Water vapor release from non-irradiated FLiNaK without Ti.

It was found that about 70 % of tritium was released as T_2 and about 25 % of tritium was released as T_2O, and about 5 % of tritium was released as TF. It can be said that since the FLiNaK sample used in this experiment contained a relatively high concentration of water of 1.44 wt%, about 25 % of tritium was released as T_2O. In the Ar gas purge during FLiNaK preparation process, if the water vapor concentration in the outlet gas is measured and sufficient water vapor desorption is performed, the release ratio of T_2O is expected to be reduced.

REFERENCES:

[1] A. Sagara *et al.,* Fusion Eng. Des., **89** (2014) 2114.
[2] K. Kubo *et al.,* Fusion Eng. Des., **171** (2021) 112558.

CO4-19 Study on ^{99m}Tc separation/concentration technology from ^{99}Mo by (n, γ) method

Y. Fujita, X. Hu[1], T. Takeuchi, R. Takeda, Y. Fujihara[2], H. Yoshinaga[2], J. Hori[2], T. Suzuki[1], H. Suematsu[1] and H. Ide

Department of JMTR, Japan Atomic Energy Agency
[1]Graduate School of Engineering, Nagaoka University of Technology
[2]Institute for Integrated Radiation and Nuclear Science, Kyoto University

INTRODUCTION: Study on the production of molybdenum-99 (^{99}Mo) by the (n, γ) method has been carried for the domestic production of technetium-99m (^{99m}Tc) without using uranium. Technology to concentrate ^{99m}Tc, a daughter nuclide of ^{99}Mo, is required because the specific activity of ^{99}Mo produced by this method is low. We focused on a technique to extract ^{99m}Tc by solvent extraction using methyl ethyl ketone (MEK) and to concentrate it by alumina columns [1]. Since it has been reported that reduced ^{99m}Tc is not extracted into MEK [2], it is necessary to investigate the effect of ^{99m}Tc reduction on ^{99m}Tc yield. In this work, we attempted to reduce ^{99m}Tc by bubbling hydrogen into sodium molybdate solution (Mo solution) and investigated the effect on the yield. In addition, Raman spectroscopy of the collected ^{99m}Tc solution was performed as basic data for identifying the chemical form of ^{99m}Tc.

EXPERIMENTS: MoO_3 pellet pieces (1.5 g) were irradiated in Pn-2 at 5 MW for 20 min and dissolved in 6M-NaOHaq. This solution was mixed with non-irradiated Mo solution. The ^{99m}Tc extraction process was carried out for 3 days and the Mo solution was used repeatedly.
First, on days 1 and 3 only, the Mo solution was hydrogen bubbled for an hour using hydrogen generation by dissolving aluminum pieces in 6M-NaOHaq. Fifteen mL of MEK and the Mo solution were added to a separatory funnel and shaken for 3 min to extract ^{99m}Tc into MEK. Both solutions were stood for 3 min and separated. The separated MEK was passed through a basic column (basic alumina: 1 g) to remove the small amount of Mo solution. Second, 10 mL of fresh MEK was flowed through the basic column to remove ^{99m}Tc remaining in the column. The two MEKs were mixed and poured into an acidic column (acidic alumina: 1 g) to adsorb ^{99m}Tc onto the column. The acidic column was washed with 30 mL of deionized water to remove MEK. Finally, 10 mL of saline was flowed through the acidic column to elute ^{99m}Tc. The activity of the solutions obtained in each process was measured by γ-ray spectrometer.
Raman spectroscopy analyzed a decayed ^{99m}Tc solution (about 445 pg-Tc/mg) using a laser with an excitation wavelength of 785 nm.

RESULTS: The ^{99m}Tc content in the substance for each process was shown Fig. 1. The ^{99m}Tc content is the ratio of the ^{99m}Tc amount in each substance to the one in the Mo solution just after extraction. The activity of ^{99m}Tc in the Mo solution was calculated from the one of ^{99}Mo. The activity of ^{99m}Tc was decay corrected based on the start of extraction. The results showed a clear decrease in ^{99m}Tc adsorption rate on an acidic column only on the days 1 and 3, in which the Mo solution was hydrogen bubbled. In contrast, the effect on ^{99m}Tc extraction to MEK reported in the paper was not confirmed. Therefore, it was shown that hydrogen bubbling into Mo solution didn't affect ^{99m}Tc extraction to MEK but may interfere with ^{99m}Tc adsorption to an acidic column. However, since the chemical form of ^{99m}Tc has not been determined, further experiments are needed to determine if ^{99m}Tc reduction is the cause.

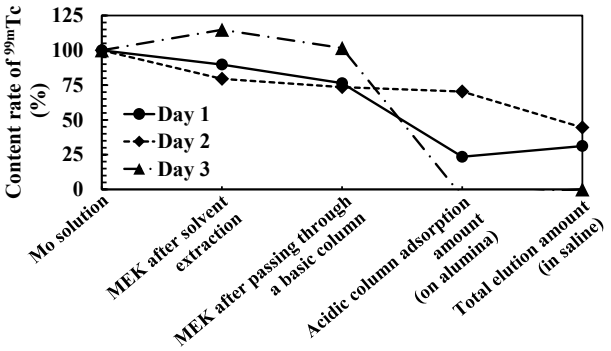

Fig. 1. ^{99m}Tc content in each process.

The Raman spectrum of ^{99m}Tc solution is shown in Fig. 2. The upper figure shows the superimposed spectra of the ^{99m}Tc solution and the saline, and the lower one is the spectrum created by subtracting the saline one from the ^{99m}Tc solution one. A sharp and weak peak at around 1050 cm^{-1} was observed. This peak is assumed to be the Raman peak of TcO_4^-. In the future, we will investigate the difference of the Raman peak due to the chemical form of Tc and so on.

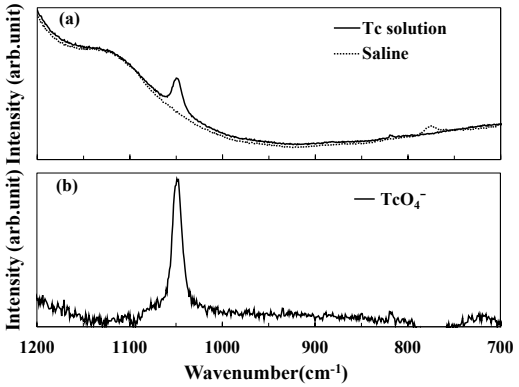

Fig. 2. Raman spectra; (a) Tc solution and saline (b) TcO_4^-

REFERENCES:

[1] S. Chattopadhyay *et al.*, Appl. Radiat. Isot., **68** (2010) 1-4.
[2] R. E. Boyd *et al.*, Radiochim. Acta, **30** (1982) 123-145.

CO4-20 Observation of Low Fluence Irradiated Accident Tolerant Control Rod Material

H. Ohta[1], K. Nakamura[1], Y. Takahashi[2], H. Unesaki[2]

[1]*Energy Transformation Research Laboratory, Central Research Institute of Electric Power Industry*
[2]*Institute for Integrated Radiation and Nuclear Science, Kyoto University*

INTRODUCTION: Various concepts of enhanced-accident tolerant fuels and core components have been developed to improve core safety under any operation conditions including severe accidents (SAs), while maintaining or improving the economic efficiency of light water reactors (LWRs). Central Research Institute of Electric Power Industry has been developing the accident tolerant control rods (ATCRs) where the novel neutron absorbing materials including rare-earth oxides (RE_2O_3) are applied[1] to prevent control rods (CRs) from damaging prior to fuel rods in the early stages of SAs. Preliminary analyses [1] revealed the ATCRs can improve the reactor shutdown margin and neutronic lifetime. RE_2O_3 (RE=Sm or Eu) has excellent high temperature compatibility with the stainless steel of CR cladding, and is not damaged less than 1200°C [2, 3]. On the other hand, RE_2O_3 is known to be highly hygroscopic and chemically unstable, but it was experimentally confirmed that physicochemical stability is improved even under high temperature steam atmosphere by mixing and sintering with MO_2 (M=Zr or Hf) [3]. In addition, it is necessary to confirm the neutron irradiation stability of RE_2O_3-MO_2 to evaluate its applicability as an ATCR material. For that purpose, irradiation experiments of Sm_2O_3-ZrO_2 with neutron fluences of 2.39×10^{19} n/cm^2 and additional 2.13×10^{19} n/cm^2 have been completed by 2020. Then, postirradiation observations of the Sm_2O_3-ZrO_2 samples irradiated up to a total fluence of 4.51×10^{19} n/cm^2 will be performed in this study.

EXPERIMENTS and RESULTS

Sample Preparation: The powders of Sm_2O_3 and ZrO_2 were mechanically mixed at a molar ratio of 1 : 1 and sintered to form a pellet with a density of 6.55 g/cm^3 corresponding to 93.7 %TD. Since any sintered mixture of RE_2O_3 and MO_2 (RE = Sm or Eu, M = Zr or Hf) with a molar ratio of 1 : 1 forms a fluorite-type crystal structure, the results of irradiation experiments with Sm_2O_3-ZrO_2 samples are considered to be applicable to the other combination materials. To reduce the radioactivation induced by the neutron irradiation as low as possible, the sintered pellet was cut into small pieces. The appearance and surface microstructure of the cut sample pieces before irradiation was observed with an optical microscope and scanning electron microscope (SEM), and their weights were measured.

Irradiation Conditions: Two campaigns of irradiation experiment were carried out using long-term irradiation plug in Kyoto University Research Reactor (KUR). Three Sm_2O_3-ZrO_2 sample pieces were enclosed in an Al capsule dedicated for long-term irradiation experiment. The irradiation periods were 530.7 hours in the 1st campaign and 475.2 hours in the 2nd campaign at an equivalent reactor power of 1 MW. The irradiation temperature in the long-term irradiation plug is pre-evaluated as 85-90°C. The neutron fluences at the end of 1st and 2nd irradiation experiments are evaluated to be 2.38×10^{19} n/cm^2 and 4.51×10^{19} n/cm^2, respectively, which is almost equivalent to irradiation fluence for 1-1.5 days in typical PWRs.

Postirradiation observations: After cooling for each irradiation campaign, the appearances of the irradiated samples were observed, and their weights were also measured. The results of weight measurement before and after irradiations were shown in Table I. No systematic weight change was observed between the 1st and 2nd irradiations in these samples. Although the smallest sample (1) showed a maximum weight change of about 3% (0.06 mg) during 2nd irradiation, it was confirmed that there was no significant weight change considering the measurement accuracy of ± 0.05 mg. Figure 1 shows the appearance of each sample before irradiation and after 2nd irradiation. No changes in the appearance and the dimensions due to neutron irradiation were confirmed.

Table I. Weight changes of Sm_2O_3-ZrO_2 samples before and after irradiation [4].

Sample No.	(1)	(2)	(3)
Before irradiation	1.95 mg	6.21 mg	5.15 mg
After 1st irradiation	1.97 mg	6.15 mg	5.11 mg
After 2nd irradiation	1.91 mg	6.24 mg	5.16 mg

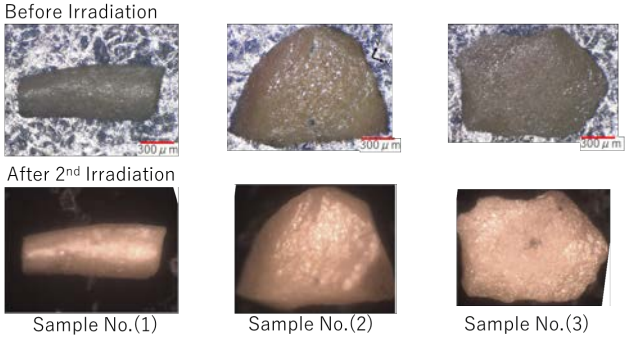

Fig. 1. Optical micrographs of Sm_2O_3-ZrO_2 samples before irradiation and after 2nd irradiation.

CONCLUSION: Postirradiation observations of sintered Sm_2O_3-ZrO_2 samples irradiated in KUR showed that the no significant changes occurred in the weight and dimensions of the ATCR neutron absorbing materials under a neutron fluence of 4.51×10^{19} n/cm^2.

REFERENCES:

[1] H. Ohta *et al.,* TopFuel 2016, (2016).17556.
[2] K. Nakamura *et al.,* AESJ 2017 spring meeting, 1I06.
[3] K. Nakamura *et al.,* 27th Int. QUENCH Workshop, (2022).
[4] H. Ohta *et al.,* NuMat 2022, O1.5 (2022).

CO4-21 Evaluation of Irradiation Damage on Semiconductor Surfaces during Plasma Etching using the Positron Annihilation Method

J. Yanagisawa, R. Shigesada, Q. Xu[1], A. Yabuuchi[1], K. Takamiya[1], and A. Kinomura[1]

School of Engineering, The University of Shiga Prefecture
[1]*Institute for Integrated Radiation and Nuclear Science, Kyoto University*

INTRODUCTION: We have been studying the ion irradiation-induced damage on semiconductor surfaces using the positron annihilation method. In our previous report [1], to study the effect of the ion-irradiation induced damage at lower ion energy and lower ion fluence, SF_6 plasma-exposed Si wafer chips were investigated. It is found that damages, such as vacancies and voids, were induced inside Si surfaces after the etching by the SF_6 plasma treatment. In the present study, another gas species, such as CHF_3 and Ar, were used to form the plasma, and damages inside Si surfaces induced by such plasma treatment were investigated using the positron annihilation method.

EXPERIMENTS: Chips cleaved from Si (100) wafer with the size of 18 mm x 18 mm were used in the present study. After wet cleaning using acetone and 2-propanol, the samples were exposed to RF plasma at a power of 5 W with a gas pressure of 30 Pa using SF_6 (sample number: #6), CHF_3 (#8), or Ar (#10) gas. No plasma exposed sample (#1) was also used as a reference of bulk Si. S parameters and life time spectra of the positrons for the Si samples were measured using slow positron beam system (B-1) in KUR at beam energies of 0 – 30 keV.

RESULTS AND DISCUSSION: Fig. 1 shows the S parameters for the samples as a function of the incident positron energy. Fig. 2 shows the spectra of the life time of positrons in the Si samples. In Fig. 1, S parameters near the surface region (positron energy: 0 – 15 keV) of the samples #6 and #10 were larger than that of un-treated Si (#1), indicating that the damages were induced by SF_6 and Ar plasma. However, that of the sample #8 was smaller than that of Si (#1). Although resemble behavior was observed for BF_2^+ ion implanted Si [2], the reason for the reduction of the S parameter from the bulk Si is not known at present. However, the life time of the positrons of 401.7 ns (#6), 466.8 ns (#8) and 444.4 ns (#10), which were calculated using Fig. 2, were larger than that of the bulk Si (218.1 ns (#1)), indicating the formation of damages by the plasma treatment.

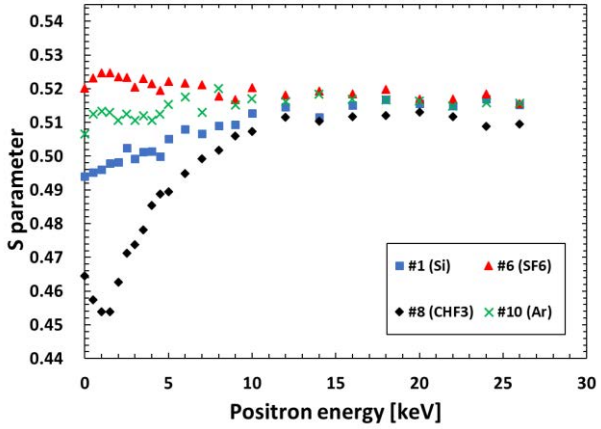

Fig. 1. S parameters for plasma treated (#6(SF_6), #8(CHF_3), #10(Ar)) and untreated (#1) Si wafer samples as a function of positron energy. The introduced gas pressure of 30 Pa and the RF power of 5 W were used to form each plasma.

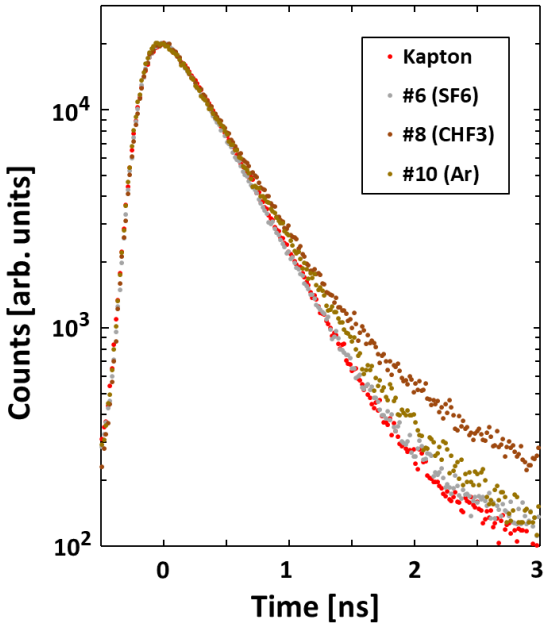

Fig. 2. Life time spectra of positrons in plasma treated (#6, #8, and #10) Si wafer samples measured at 1 keV. The result for a Kapton film is also shown as a reference.

CONCLUSION: Although the effects of the plasma on Si using SF_6, CHF_3 or Ar gas might be different from each other, it is found that damages were induced by the plasma treatment. The difference of the effects using different gases for the plasma formation should be clarified.

REFERENCES:

[1] J. Yanagisawa *et al.*, KURNS Progress Report 2021 (Kyoto University), CO4-11 (R3078).
[2] A. Uedono *et al.*, Jpn. J. Appl. Phys. **36** (1997) 969.

CO4-22 Correlation between irradiation defect density and hydrogen isotope retention in tungsten

M.I. Kobayashi[1,2], N. Abe[3] and T. Takahashi[3]

[1]*National Institute for Fusion Science, National Institutes of Natural Sciences*
[2]*The Graduate University for Advanced Studies, SOKENDAI*
[3]*Institute for Integrated Radiation and Nuclear Science, Kyoto University*

INTRODUCTION: In a deuterium-tritium (D-T) fusion reactor, tungsten (W) will be exposed to energetic particles such as fast neutrons. By the collision of these energetic particles, W atoms in the lattice points are displaced to form irradiation defects. Hydrogen isotopes are trapped in the irradiation defects, leading to a loss of fuel in the reactor. A previous study showed about two orders of magnitude larger deuterium retention in neutron irradiated W compared to non-irradiated W [1]. In addition, the deuterium desorption temperature shifted higher in neutron-damaged W. These results suggest that irradiation defects trapped hydrogen isotopes, and consequently, the retention and the desorption behaviors of hydrogen isotopes in W drastically changed. Therefore, this study aims to evaluate the quantitative correlation between irradiation defect density and hydrogen isotope retention in W irradiated with electron beam which can introduce only point defects.

EXPERIMENTS: The W sample was purchased from Nilaco co. The thickness of the sample was 25 μm. A sample was annealed at 1173 K for 6 hours under the pressure below 10^{-5} Pa (The annealed W) at National Institute for Fusion Science (NIFS). Then, samples were shipped to KURNS-LINAC for electron irradiation. The electron acceleration voltage was 8 MV. The dose was evaluated as 4.3×10^{-3} dpa according to an atomic displacement cross-section of 70.4 barns and a displacement threshold energy of 84 eV [2]. The irradiation temperature was less than 353 K due to the water coolant.

For the evaluation of the interaction between hydrogen isotopes and irradiation defects in W, the deuterium gas permeation system was prepared in NIFS. A disc shaped thin metal samples can be mounted to separate the vacuum system in this device. A side of the vacuum system can be filled with deuterium gas with desired pressure and temperature (upstream side). Another side of the system is evacuated by a turbo molecular pump (downstream side), and the desorption of permeated deuterium was monitored by a quadrupole mass spectrometer.
As the benchmark experiment, we used a nickel (Ni) foil with the thickness of 50 μm. Then, the W samples were examined. We report here the results on the annealed W and the as-received W (un-annealed W).

RESULTS: Figure 1 shows the summary of deuterium permeability in Ni as a function of the reciprocal temperature. The deuterium permeability increased exponentially with the elevated temperature. The permeation processes of hydrogen isotopes consist of diffusion and solution processes. The rates of these processes vary with the temperature according to the Arrhenius's law. Therefore, the deuterium permeability has the exponential temperature dependency.

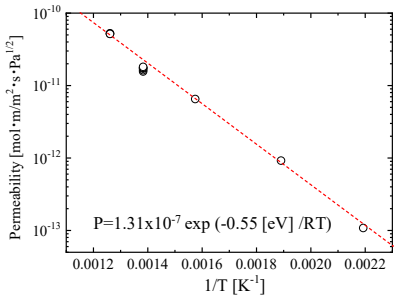

Fig.1. Deuterium permeability in Ni.

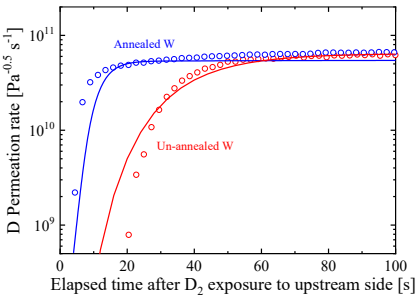

Fig.2. Time evolution of deuterium permeation flux in annealed W and un-annealed W.

Figure 2 shows the transient curves of deuterium permeation flux in W samples after the beginning of deuterium gas exposure to the upstream side. A gradual increase of deuterium permeation flux and a subsequent steady-state permeation flux comes from the evolution of deuterium distribution in W samples. It can be seen that the annealed W achieved a steady-state deuterium permeation quickly compared to the unannealed W. This indicates the trapping effects of diffusing deuterium by defects in W which apparently decrease the deuterium diffusion rate in W. Using a simulation code in which the diffusion behavior of hydrogen isotopes with competitive trapping/detrapping processes in W can be solved [3], the deuterium permeation fluxes for these samples were analyzed, and the deuterium permeation curves were roughly reproduced as found in Fig. 2. From this analysis, the trapping site density for annealed W was evaluated to be 1.5×10^{-3} at.%, besides, that in un-annealed W was 3.5×10^{-3} at.%. We will perform the similar series of experiments for electron irradiated W, and the increase of the trapping site density will be estimated.

REFERENCES:

[1] Y. Hatano *et al.*, Nucl. Fusion, **53** (2013) 073006.
[2] K. Sato *et al.,* Nucl. Mater. Ene., **9** (2016) 554.
[3] M.I. Kobayashi *et al.*, Fusion Eng. Des., **168** (2021) 112635.

CO4-23 Characteristics of Improved Tetrode Configuration for Radiation Tolerant Image Sensor

Y. Gotoh, Y. Neo[1], M. Nagao[2], and N. Sato[3]

Graduate School of Engineering, Kyoto University
[1]Research Institute of Electronics, Shizuoka University
[2]National Institute of Advanced Industrial Science and Technology, AIST
[3]Institute for Integrated Radiation and Nuclear Science, Kyoto University

INTRODUCTION: In decommissioning of Fukushima Daiichi Nuclear Power Plant, observation of inside of the reactor pressure vessel is one of the most important issues. We have been developing an image sensor based on field emitter array (FEA), which is a two-dimensional miniaturized electron source. Radiation tolerance of the components of this image sensor has already been demonstrated [1]. Last year, light-detection test under γ-ray irradiation was attempted with a proto-type image sensor, and it was found that the device yielded a small signal of light even under γ-ray irradiation [2]. The signal was very weak, and one of the reasons would be the electrode configuration of the image sensor; the distance between the FEA and the anode which accumulates photo-signal was too large. In this study, some of the metal and insulator plates which supported the mesh electrode and photoconductor were eliminated in order to locate the anode much closer to the FEA. With the improved configuration, the characteristics of the device was investigated with and without γ-ray irradiation.

EXPERIMENTS: The image sensor consisted of an FEA, mesh, and anode. The FEA used in this study was the identical one to the previous experiment [3]. In the previous experiment, the mesh was fixed with two 1 mm-thick metal plates, and the photo-conductor was also fixed in a similar way to the mesh. Between the mesh and the photoconductor, a 1 mm-thick insulting plate was inserted to maintain the gap of the electrodes. In the present device, the mesh was spot-welded to a 1-mm thick metal plate, and the anode was set close to the mesh without using an insulating layer. The distance between the mesh and the photoconductor in the previous study, and that between the mesh and a metal anode was reduced more than 2 mm. The device was installed in the identical vacuum vessel used in the previous study. A non-evaporative getter pump was activated to evacuate the vessel. The pressure before the experiment was less than 1 x 10^{-6} Pa. The FEA used in the present study was the same one as used in the present study [3]. The emitter was grounded, and the gate was positively biased between 46 and 50 V. The mesh electrode was biased to 200 V. The mesh current ranged from 2.5 μA to 7 μA. The emitter current could not be measured due to circuitry problem. The anode characteristics were acquired varying the anode voltage 0 to 60 V with and without γ-ray irradiation. The dose of irradiation was estimated to be 410 Gy h^{-1} at the anode plate.

RESULTS: Figure 1 shows anode characteristics with and without γ-ray irradiation. The gate potential was 50 V. The abscissa is the anode voltage and the ordinate is the anode current. The solid and open circle indicate the characteristics with and without γ-ray irradiation, respectively. The anode current began to increase at 10 V. The anode current showed a maximum at 20 V, and then turned to decrease. The maximum anode current without γ-ray irradiation was 1.2 μA, which is sufficient to act as an image sensor. At the gate voltage of 46 V, the maximum anode current was 600 nA. The increase of the anode current would be attributed to the reduction of the decelerating electric field between the mesh and the anode. The decrease of the anode current higher than 20 V would be attributed to the increase of the secondary electron emission coefficient due to higher incident energy of electrons. The anode characteristics showed little difference with γ-ray irradiation. Slight difference is due to the difference of the beam current, which was proven from the anode current normalized by the mesh current showed a good agreement. It was already shown that γ-ray irradiation with the dose rate of irradiation of higher than 1 kGy h^{-1} did not affect the characteristics of the triode [4]. The present result indicated that the newly constructed device configuration realized sufficient anode current, and the performance was not affected by the γ-ray irradiation. The effect of γ-ray irradiation to the photo-detection performance will be tested in the following experiments.

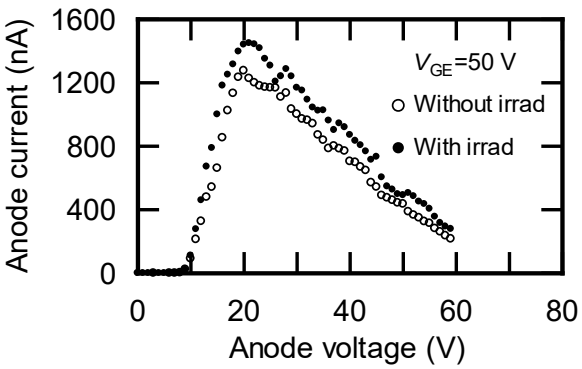

Fig. 1. Anode characteristics with and without γ-ray irradiation.

REFERENCES:

[1] Y. Gotoh *et al.*, IEEE Trans. ED, **67** (2020) 1060-1065.
[2] Y. Gotoh *et al.*, KURRI Progress Report 2021, (2022) CO4-8.
[3] T. Sato *et al.*, J. Vac. Sci. Technol. B, **21** (2003) 1589-1593.
[4] T. Morito *et al.*, IEEE 31st International Vacuum Nanoelectronics Conference, Kyoto, July 9-13, 2018 (2018) 96-97.

CO4-24 Characterization of $YBa_2Cu_3O_y$ and $FeSe_{0.5}Te_{0.5}$ superconducting films using a slow positron beam

T. Ozaki, H. Sakane[1] and A. Yabuuchi[2]

School of Engineering, Kwansei Gakuin University
[1]SHI-ATEX Co., Ltd.
[2]Institute for Integrated Radiation and Nuclear Science, Kyoto University

INTRODUCTION: Cuprate and iron-based superconducting films are expected for magnet applications in areas of basic science, medicine and levitation. For these applications, raising critical current, which is a maximum value of zero-resistivity current, property in magnetic fields is very important. The critical current in applied magnetic fields could be improved by introducing structural defects with nano-meter size using ion-irradiation techniques. Positrons are sensitive to vacancy-type defects, and they are useful for characterizing irradiation-induced defects. In this study, we probed two kinds of pristine superconducting films, cuprate superconductor $YBa_2Cu_3O_y$ (YBCO) and iron-based superconductor $FeSe_{0.5}Te_{0.5}$ (FST), using a slow positron beam, so that we will evaluate the irradiation defect in these films using the positron annihilation measurement.

EXPERIMENTS: The YBCO and FST thin films were deposited on $SrTiO_3$ (STO) single crystal substrates by pulsed laser deposition (PLD) method using a Nd:YAG laser (λ = 266 nm). These films were probed by the KUR slow positron beam and the Doppler broadening of annihilation radiation (DBAR) spectra were acquired with incident positron energies E_+ = 9 keV. The sharpness of the DBAR spectra is evaluated by a value called the *S*-parameter, which becomes generally lower when positrons annihilate in a perfect lattice, and higher when positrons are trapped into vacancies [1].

RESULTS: Fig. 1 shows the *S*-parameters of the YBCO thin film as functions of the incident positron energy. For higher implantation energies $E_+ > 7$ keV, a fraction of positrons annihilates in the STO substrate whereas for $E_+ < 4$ keV positrons also annihilate at the film surface. The *S*-parameters in the energy region of 4−7 keV correspond to positron annihilation in the YBCO layer. The low *S*-parameters at 4−7 keV could indicate that the YBCO layer contains a low concentration of vacancy-type defects. Fig. 2 shows the *S*-parameters of the FST thin film as functions of the incident positron energy. The *S*-parameters at 1−4 keV would be indicative of the positron annihilation in the FST layer. The *S*-parameter values in the FST layer is clearly higher than those in the STO substrate. This could be attributed to: (i) *S*-parameter values in the FST layer would be essentially higher than those in the STO substrate, or (ii) the vacancy-type defects would be formed in the FST layer during the film growth process. In order to determine whether which one is highly likely, we need to carry out first principle calculation on the *S*-parameters of each materials.

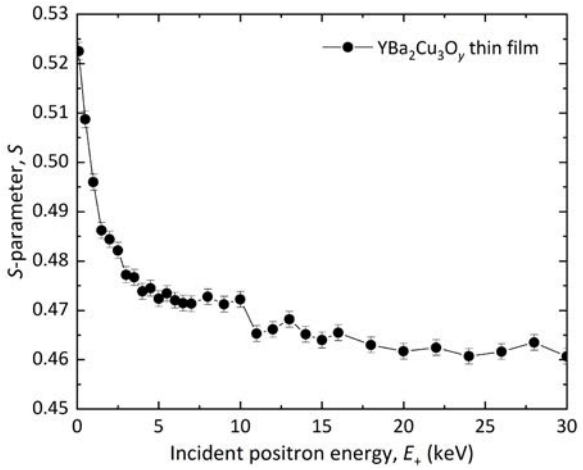

Fig. 1. *S*-parameters as functions of the incident positron energy for the $YBa_2Cu_3O_y$ thin film.

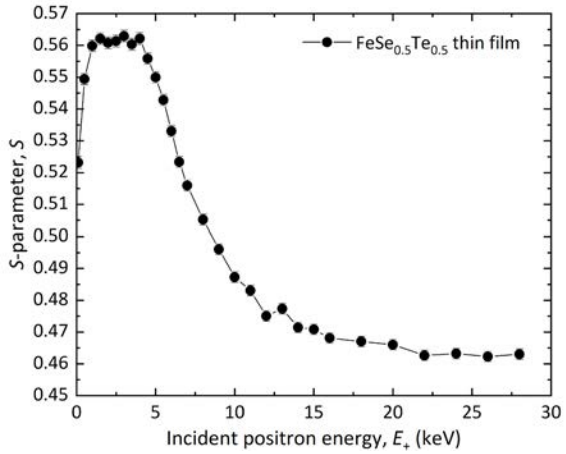

Fig. 2. *S*-parameters as functions of the incident positron energy for the $FeSe_{0.5}Te_{0.5}$ thin film.

REFERENCES:

[1] R. W. Siegel, Ann. Rev. Mater. Sci., **10** (1980) 393-425.

CO4-25 Neutron irradiation tests for components of ITER plasma diagnostics

M. Ishikawa, T. Ushiki, E. Yatsuka, K. Torimoto, M. Inamine, H. Murakami, K. Shimizu, T. Sugie, S. Kono and Y. Nunoya

National Institutes for Quantum Science and Technology

INTRODUCTION: ITER [1] is being built in France by international cooperation. Components of diagnostic systems installed in the ITER tokamak are exposed to high radiation. Therefore, it is important to investigate the radiation resistance of those components. In this study, neutron irradiation effects on optical elements such as lens and glasses used for Infrared Thermography system (IRTh) and Edge Thomson Scattering system (ETS) were investigated, respectively. The effects of neutron irradiation on an electronic device, the preamplifier of the Microfission chamber system (MFC), were also evaluated. Considering the neutron conditions at the installation location of the electronic device, the irradiation test was conducted at CN-3. Details are given below.

(1) Irradiation Tests of Si for Optical Lens of IRTh

IRTh is planning to use Si lenses in the ITER. The authors recently conducted separate gamma-ray and neutron irradiation tests. The gamma-ray irradiation test showed that the transmittance of Si is not significantly degraded in the wavelength range used by IRTh (1.5 μm - 4.5 μm). The neutron irradiation test showed that the transmittance of Si is not significantly degraded up to about 2.5 x 10^{15} (n/cm^2). However, no investigation has been conducted so far on the changes in refractive index due to irradiation. Change in refractive index could affect the chromatic aberration, focus position and optical performance of IRTh optics. Therefore, in this study, the authors investigated the changes in refractive index of Si before and after neutron irradiation tests.

EXPERIMENTS: For the irradiation test of Si samples, the slant exposure tube was used. Several Si samples were irradiated at multiple neutron fluences up to 1.0 x 10^{16} (n/cm^2). Refractive index measurement was taken at three wavelengths (3.35 μm, 4.19 μm and 4.45 μm) before and after neutron irradiation.

RESULTS: Fig. 1. shows the example of irradiation test result of Si samples. As shown in Figure 1, refractive index of Si decreased slightly due to neutron irradiation up to 1.0 x 10^{16} (n/cm^2). The impact on of the refractive index change on chromatic aberration, focus position, and opti-cal performance of IRTh will be quantitatively investigated in the future.

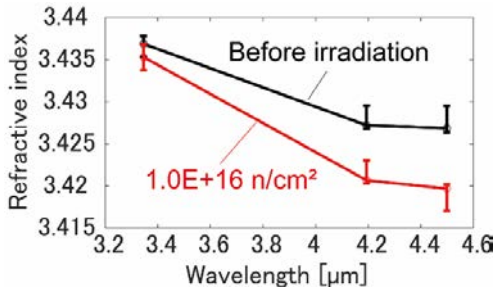

Fig. 1. Refractive index of Si before and after irradiation

(2) Irradiation Tests of Glass for compensating chromatic aberration of ETS

ETS will measure the spectrum at wavelengths of approximately 600-1060 nm to determine the electron temperature and density in the ITER fusion plasma. If the collection optics were constructed using only fused silica, the focal position would change for each wavelength due to the wavelength dependence of the refractive index (dispersion). Therefore, a glass material with a different refractive index and dispersion from fused silica is required. Cerium-doped glass, which is said to be durable against irradiation of cosmic rays including gamma rays, is considered promising. Estimated neutron fluence at the position where the glass is placed is of the order of 10^{16} (n/cm^2).

EXPERIMENTS: Cerium-doped glass called SF6G05 manufactured by Schott was irradiated up to 4x10^{15} (n/cm^2) for fast neutron and 2x10^{16} (n/cm^2) for thermal neutron, which is several times higher the 20-year cumulative fluence at the location of lens optics for ETS in ITER. The performance deterioration due to neutron irradiation was investigated by comparing the wavelength dependence of transmitted signal before and after irradiation.

RESULTS: Fig. 2. shows the spectral transmission of cerium-doped glass SF6G05 having the thickness of 10 mm before and after irradiation. In the end of 2021, deterioration in transmittance was observed in some samples, so a reproducibility test was performed. In February 2023, all the samples show the same tendency, and the decrease in transmittance is not remarkable at wavelengths above 600 nm, which is important for ETS. It is not clear why the results differed from those before. Perhaps the details of the manufacturing method, such as the heat history during glass molding and anti-reflection coating, are different.

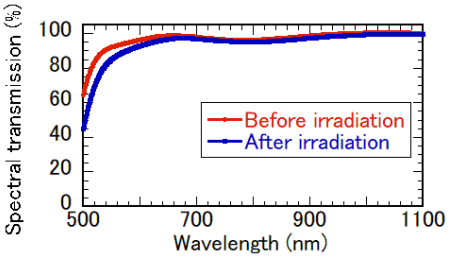

Fig. 2. Spectral transmission of cerium-doped glass (SF6G05) before and after irradiation

(3) Irradiation Tests of the preamplifier of MFC

The preamplifier of the MFC amplifies and converts a weak signal from the MFC detector into a nose tolerant strong output. The preamplifier will be installed in the port cell area and maximum neutron flux at the installation position of the preamplifier with neutron shielding could become about 2.4 x 10^3 n/cm^{2}s. However, the effects on neutrons have not been evaluated yet. Therefore, in order to investigate whether a preamplifier can be applied under the current shielding design. The neutron irradiation test on the preamplifiers was conducted at CN-3.

EXPERIMENTS: The preamplifier was installed near the conduit exit of CN-3 so that the semiconductor elements of the Preamplifier would be most exposed and neutrons were irradiated up to 1.0 x 10^{11} (n/cm^2), corresponding to neutron fluence for 20 years under the current shielding design. To properly investigate the effects of neutron irradiation, output power from the preamplifier, power consumption and temperature of the preamplifier were constantly monitored in situ during irradiation.

RESULTS: No change in output signal was observed, including no change in amplitude and no noise generation. On the other hand, a change in the current consumption of the preamplifier was observed, but this was consistent with the temperature, confirming that it was not due to neutron irradiation. This result suggests that the preamplifier can be used without replacement under its current design.

REFERENCES:

[1] B. Bigot, Fusion Eng. Des., **146** (2019) 124.

CO4-26 Study of resonant frequency change with irradiation dose of piezoelectric PZT element

M. Kobayashi, T. Miyachi, S. Takechi[1], Masaya Danjohbara[1] and Haruki Oh'ishi[1], Shoki Maeda[1], Shuhei Tominaga[1]

Planetary Exploration Research Center, Chiba Institute of Technology
[1]Graduate School of Engineering, Osaka Metropolitan University

INTRODUCTION: This study aims to establish an inexpensive method for dosimetry in high-dose environments. We consider changes in piezoelectric properties of piezoelectric elements due to irradiation for dosimetry in high-dose environments. For this purpose, the mechanism of radiation-induced change of piezoelectric properties has been investigated.

In a previous experiment conducted at NIRS/HIMAC, piezoelectric PZT elements were irradiated with 400 MeV/n Xe particles, and the decrease in the electromechanical coupling coefficient k was investigated [1][2]. As a result, it was found that k_r of the irradiated PZT element was -0.35%/kJ, which is a phenomenon concerning the irradiation dose [3]. In order to investigate what happens to piezoelectric elements due to irradiation, electron beam irradiation experiments have been conducted at KURNS-LINAC. The effect of temperature, which was negligible in the Xe particle experiments, has been investigated and controlled in the experiments at KURNS-LINAC. It was found that k_r linearly decreased with increasing beam energy absorbed in the PZT element, whereas the surface temperature remained constant [4]. In terms of that, we propose a dosimeter based on piezoelectric PZT.

EXPERIMENTS IN THE FISCAL YEAR 2022: Although two machine times of LINAC experiment were scheduled for the current year, both experiments were impossible because they coincided with periods of LINAC maintenance and breakdowns.

Although we were unable to conduct electron irradiation experiments using LINAC this year, we conducted experiments using the Pneumatic transport pipe irradiation equipment in KUR to investigate changes in piezoelectricity when PZT samples are irradiated with neutrons. Since this was the first experiment, only one irradiation was conducted on one PZT sample (soft material) to demonstrate proficiency in the experiment. In the future, we would like to continue the experiment by setting multiple irradiation levels and increasing the number of types of irradiated samples.

REANALYSIS OF PAST EXPERIMENTAL DATA: A reanalysis of the data from LINAC experiments up to the previous year was conducted. In earlier analyses of experimental data, we have investigated how the electromechanical coupling coefficient k_r, as an indicator of the piezoelectricity of piezoelectric PZT, changes with electron irradiation. In addition to kr, the mechanical quality factor Q_m was also evaluated in the present study.

As an example of the experimental results, Figure 1 shows the changes of k_r and Q_m versus irradiation dose when piezoelectric PZT, a type of high-temperature soft material, was irradiated by electron beams. As shown in Figure 1, there is an inverse correlation between the increase in the value of the mechanical quality factor and the decrease in the electromechanical coupling coefficient, indicating that the hardening of PZT occurred when only the change in Q_m was examined. This behavior is in contrast to piezoelectric PZT when exposed to high temperatures. In other words, both k_r and Q_m of PZT decrease when exposed to high temperatures, while k_r decreases, but Q_m increases in the case of electron irradiation. These experimental results suggest that the cause of the decrease in k_r due to electron-beam irradiation may be the increase in Q_m; as Q_m increases, the amount of strain against external force decreases, and therefore k_r also decreases. Then, what is the cause of the increase in Q_m, i.e., the "hardening" by electron irradiation? A bold hypothesis is that electron-beam irradiation causes oxygen vacancies in PZT crystals, which in turn causes pinning that prevents the domain walls of the domain structure from moving, but this is still a matter of conjecture. We will need to examine this issue in the future, including how to verify the hypothesis.

Fig. 1. the changes of Kr and Qm versus irradiation dose when piezoelectric PZT, a type of high-temperature soft material, was irradiated by electron beams.

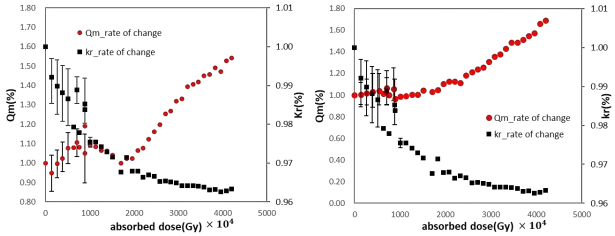

REFERENCES:

[1] M. Kobayashi *et al.,* Jpn. J. Appl. Phys., **52** (2013) 126604.
[2] M. Kobayashi *et al.,* JJpn. J. Appl. Phys., **53** (2014) 066602.
[3] S. Takechi *et al.,* Jpn. J. Appl. Phys., **60** (2021) 038003.
[4] S. Takechi *et al.,* Jpn. J. Appl. Phys., **61** (2022) 128001.
[5] H. Oh'ishi, Master Thesis, Osaka Metropolitan Univ. (2023).

CO4-27 Radiation Induced Demagnetization of Neodymium Magnets

Y. Fuwa, Y. Kuriyama[1], Y. Iwashita[1], K. Takamiya[1], T. Takayanagi

J-PARC Center, Japan Atomic Energy Agency
[1]Institute for Integrated Radiation and Nuclear Science, Kyoto University

INTRODUCTION: Magnets are essential devices in the transport and control of charged particle and neutron beams. Electromagnets have been the primary magnets used in beam experiments so far, but they are being replaced by permanent magnets due to their lower power consumption, compactness, and the fact that they do not require ancillary equipment such as power supplies and cooling water [1-3]. Demagnetization due to radiation is one of the concerns in the use of permanent magnets, but quantitative evaluation of the effect is not sufficient. The importance of this evaluation has increased in recent years due to the increasing intensity of accelerators. Therefore, we are systematically evaluating the effects of demagnetization caused by radiation using the irradiation facilities at the KUR [4].

EXPERIMENTS: In this study, differences in radiation demagnetization effects for neodymium magnets (NdFeB) were evaluated for different dysprosium contents in the material. The irradiated sample were three types of neodymium magnets; N32EZ, N43TS, N52 made by Shin-Etsu Chemical Co., Ltd. These three magnet samples differ in their dysprosium content, with N32EZ, N43TS, and N52 containing more dysprosium in that order, with N52 being a dysprosium-free magnet. The shape of the sample was cylindrical with a thickness of 1 mm and a diameter of 5 mm. The irradiation experiments were performed at KUR Pn-2 port and Tc-Pn. The irradiation time at Pn-2 ranged from 10 seconds to 30 minutes, and at Tc-Pn from 10 minutes to 30 hours. The rate of demagnetization was calculated by comparing the magnitude of magnetization before and after irradiation. The magnitude of each magnetization was evaluated by measuring the magnitude of the induced voltage generated when the magnet sample was rotated near the measuring coil [5].

RESULTS: From Fig. 1, it can be seen that the demagnetization effect of NdFeB magnets with respect to irradiation in Pn-2 is larger as the dysprosium content decreases, and for N52, the magnitude of magnetization decreases to less than 10% of that before irradiation. Similar demagnetization effects have also occurred with irradiation at Tc-Pn (Fig. 2). The thermal neutron flux irradiated at Pn-2 corresponds to 4.9 x 10^{13} n/cm^2 (10 sec.) to 8.8 x 10^{15} n/cm^2 (30 min.), and that at Tc-Pn to 7.6 x 10^{11} n/cm^2 (10 min.) to 1.4 x 10^{14} n/cm^2 (30 hour). For Pn-2 and Tc-Pn, the instantaneous neutron fluxes are 64 times different, (4.9 x 10^{13} n/cm^2/s for Pn-2 and 7.6 x 10^{10} n/cm^2/s for Tc-Pn, respectively), but the effect on demagnetization is not significantly different.

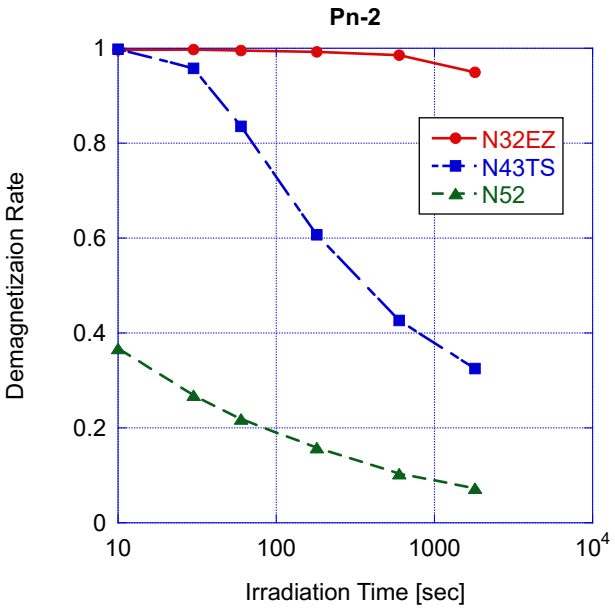

Fig. 1. Measured demagnetization rate of the NdFeB samples irradiated in Pn-2.

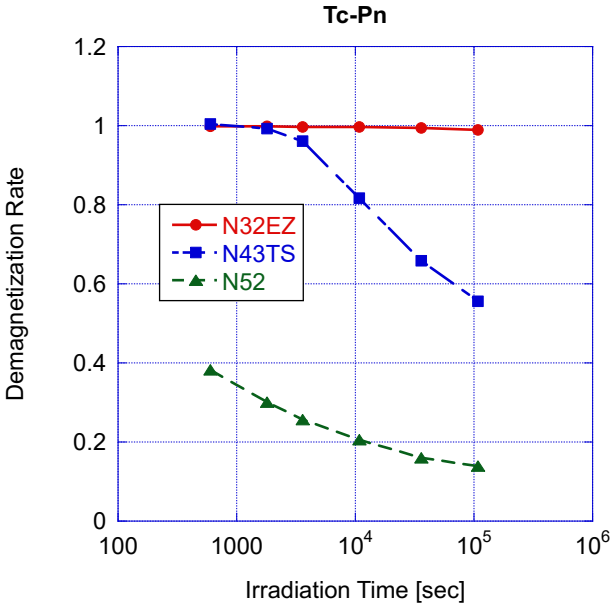

Fig. 2. Measured demagnetization rate of the NdFeB samples irradiated in Tc-Pn.

REFERENCES:

[1] Y. Fuwa *et al.,* Prog of Theor and Exper Physics, **2017(2)** (2017) 023G01.
[2] Y. Kuriyama *et al.,* IEEE Trans. Appl. Supercond., **32(6)** (2022) 4007204.
[3] M. Yamada *et al.,* Prog. Theor. Exp. Phys., **2015(4)** (2015) 043G01 .
[4] Y. Fuwa *et al.,* MT-27 Int. Conf. on Magnet Technology, (2021) TUE-P01-115-05.
[5] Y. Fuwa *et al.,* Proc. of 18th annual meeting of particle accelerator society of Japan, (2021) MOOB07.

CO4-28 Fundamental study of damage on tungsten by heat and particle loading

K. Tokunaga, M. Matsuyama[1], Y. Hatano[1], M. Hasegawa, K. Nakamura and Q. Xu[2]

Research Institute for Applied Mechanics, Kyushu University
[1]Hydrogen Isotope Research Center, University of Toyama
[2]Institute for Integrated Radiation and Nuclear Science, Kyoto University

INTRODUCTION: Refractory metals such as tungsten (W) is potential candidate for the armor of the first wall and the divertor plate of the fusion reactor because of its low erosion yield and good thermal properties. The armor material will be subjected to heavy thermal loads in the steady state or transient mode combined with high energy neutron irradiation that will cause serious material degradation. In addition, high energy runaway electrons would bombard the armor materials along the equatorial plane in fusion device. It is considered that these cause radiation damage and enhance tritium retention. It is of a great importance to clarify phenomena of implantation, retention, diffusion and permeation of tritium (T) on surface of the armor materials of the first wall/blanket and the divertor on fusion device from a viewpoint of precise control of fuel particles, reduction of tritium inventory and safe waste management of materials contaminated with tritium.
In the present works, T exposure experiments have been carried out on W samples which were irradiated by high energy electrons to investigate effects of high energy electrons irradiation on microstructure and tritium retention of W. In this fiscal year, pure W and recrystallized W were irradiated by high energy electron beam. Before and after that, positron annihilation experiment was carried out to identify the radiation defect. In addition, EBSD （Electron Back Scatter Diffraction Patterns）analyses has been carried out on the specimens before and after the electrons irradiation. Tritium exposure experiments have been carried out using a tritium (T) exposure device.

EXPERIMENTS: W samples used were ITER specification W (ALMT-grade) (SR-W) and its recrystallized W (RC-W). The SR-W was fabricated via a powder metallurgical route including cold isostatic pressing, sintering, hot rolling, and heat treating to relieve the residual stresses. Some of the machined SR specimens were subjected to a full recrystallization treatment at 2000 ºC for 1 hr in vacuum. Sizes of the specimens were 10 mm x 10 mm x 1mm (10 mm x 10 mm : ND-TD). The surface of the both samples were polished to be mirrored. High energy electrons irradiation has been carried out using LINAC in Institute for Integrated Radiation and Nuclear Science, Kyoto University. An peak energy of electron irradiated was 8 MeV and DPA was 5.8 x 10^{-3}. Temperature during the irradiation was measured by thermocouples which was contacted with a backside of the W samples. Before and after that, positron annihilation experiment was carried out to identify the radiation defect. In addition, a high energy ion irradiation experiment has stared to carry out. The sample surface was irradiated by 2.5 MeV Fe ions with a flence of 5 x 10^{18} ions/m^2 at RT. T exposure experiments have been carried out using a T exposure device in University of Toyama. Pressure of the T gas was 1.3 kPa and T exposure was kept for 4 h at 100 ºC. T concentration in the gas was about 5 %. After the exposure to T gas, T amount retained in surface layers of the sample was evaluated by imaging plate (IP) measurements and β-ray-induced X-ray spectrometry (BIXS).

RESULTS: Fig.1. shows X-ray spectra observed by BIXS for the non-irradiated SR-W(a), e-irradiated SR-W(b) and ion-irradaited SR-W(c). Temperature of T exposure is 100 ºC. In the case of SR-W(b), WM_{α}, ArK_{α} are detected. These results indicate that T exists the deeper area and the surface of the sample. On the other hand, in the case of SR(c), ArK_{α} are detected. This is attributed by surface retained T. T exposure experiment at 350 ℃ has been carried out.

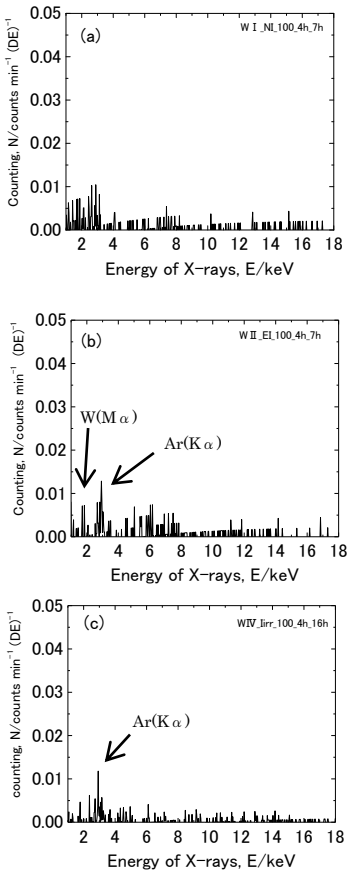

Fig. 1. X-ray spectra for non-irradiated SR-W(a), e-irradiatyed SR-W(b) and ion irradiated SR-W(c).

CO4-29 Vacancy Migration Energy in CrFeNi Medium-Entropy Alloy

H. Araki, K. Sugita, M. Mizuno, A. Yabuuchi[1] and A. Kinomura[1]
Graduate School of Engineering, Osaka University
[1]*Institute for Integrated Radiation and Nuclear Science, Kyoto University*

INTRODUCTION: Tsai *et al*. [1] originally proposed the concept of sluggish diffusion, based on a positive correlation between the activation energies for atomic diffusion, which are normalized by the melting temperature, T_m , and the number of constituent elements in the CrMnFeCoNi high-entropy alloy(HEA) and its subsystems. However, the reason for the sluggishness of diffusion is not quite clear.

In the CrMnFeCoNi HEA and its subsystems at high temperatures, atomic diffusion is expected to proceed via a vacancy mechanism because they are substitutional solid solutions. Therefore, vacancy formation and migration energies in the CrMnFeCoNi HEA and its subsystems are important indexes for understanding the sluggish diffusion. In this work we have evaluated the vacancy migration energy in CrFeNi medium-entropy alloy by observing the vacancy migration and annihilation behavior during an annealing process after electron irradiation, with the use of the positron lifetime spectroscopy.

EXPERIMENTS: An arc-melted ingot of CrFeNi alloy was homogenized at 1373K for 24 h under argon atmosphere, and cut into 10 mm × 10 mm × 0.5 mm plates. The plates were polished and then sealed in silica tubes. Solution heat treatment was carried out for 1 h at 1373 K and the samples were quenched in water. Their X-ray diffraction analysis shows that all the samples are composed of single phase with a fcc structure. Then, the samples were irradiated in water with 8 MeV electrons at a fluence of approximately, 1×10^{22} e^{-} m^{-2} below 358 K using the electron linear accelerator at the Institute for Integrated Radiation and Nuclear Science, Kyoto University. The irradiated samples were isochronally annealed in a temperature range from 373 to 673 K. The temperature step during the isochronal annealing was 25 K and the duration of exposure to each temperature was 1 h.

The positron lifetime measurements were made at 297–299 K using a fast-fast timing coincidence system with a time resolution(FWHM) of 180–183 ps.

RESULTS: Before the electron irradiation the positron lifetime spectrum for the solution-treated alloys was represented by only one component of 108 ps, which is approximately equal to the values calculated for the defect-free constituent pure metals. This indicates that positrons annihilate in the bulk for the solution-treated alloy sample. After electron irradiation, the mean positron lifetime was increased to 136 ps. The analysis of positron lifetime spectra for the as-irradiated sample shows that many positrons are trapped and annihilate in the monovacancies introduced by electron irradiation, because the lifetime component, τ_2 , of trapped positrons was 180 ps, which is in agreement with the experimental values for monovacancies in the constituent pure metals. Assming that the specific trapping rate of monovacancies, μ_v , is 10^{15} s^{-1}, the vacancy concentration in the as-irradiated sample is of the order of a few atomic parts per million.

Fig.1 shows the change in the vacancy concentration during the isochronal annealing of the irradiated sample, which was evaluated on the basis of the two- or three-component analyses for the positron lifetime spectra. In the temperature range where dislocations and monovacancies are expected to coexist, the positron lifetime spectra were analyzed on the assumption that the positron lifetime component of dislocation is 150 ps. As shown in Fig.1, the vacancy concentration decreases with annealing temperature, because the vacancies introduced by electron irradiation gradually disappear as the vacancies become mobile during the isochronal annealing. The decrease in the vacancy concentration was theoretically analyzed on the basis of Dryzek *et al*.'s model for isothermal annealing [2] .

Assuming that the vacancy migration energy is constant over the whole temperature range, there remains a few discrepancies between the theoretical fitting model and the experimental data, as shown in Fig.1. The positron lifetime measurements indicate that dislocation loop components are detected in addition to vacancies at high temperatures, suggesting that the vacancy migration process is easily influenced by the presence of dislocations. Therefore, we assumed two-component vacancy migration energies (H_m^L , H_m^H) and optimized their values to fit the experimental data. The value of H_m^L obtained in the low temperature range is 0.79 eV, which is nearly equal to 0.77 eV of effective vacancy migration energy obtained in an analysis of the void-denuded zone widths formed in a $Fe_{55.8}Cr_{16.1}Ni_{28.8}$ alloy under neutron and electron irradiation[3].

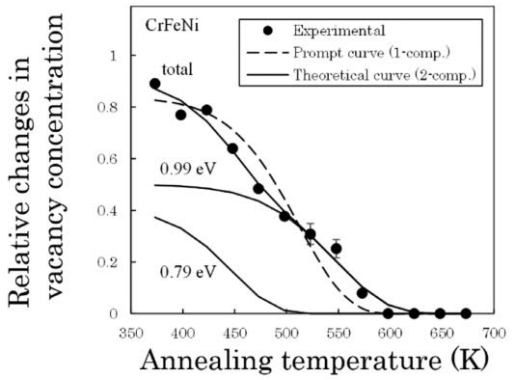

Fig. 1. The relative changes in vacancy concentration ob-tained from experiments and theoretical calculations.

REFERENCES:

[1] K. Y. Tsai *et al.,* Acta Mater., **61** (2013) 4887.
[2] J. Dryzek *et al.,* Ma-ter. Lett., **21** (1994) 209.
[3] Y. Sekino and N. Sakaguchi, Mater. Trans., **60** (2019) 678.

CO4-30 A study on destruction of cesium aluminosilicate compounds by gamma irradiation (4)

H. Ohashi, R. Tawatari, T. Saito[1]

Faculty of Symbiotic Systems Science, Fukushima University

[1]Institute for Integrated Radiation and Nuclear Science, Kyoto University

INTRODUCTION: Pollucite which is one of cesium aluminosilicate compounds have attracted attention as a fi-nal storage material of ^{134}Cs and ^{137}Cs. Pollucite is easily synthesized by hydrothermal method in low temperature below 300°C [1]. Pollucite has various properties that fa-vor the immobilization of Cs ions.

However, the damage to the aluminosilicate framework by radiation decay is concerned because it contains ^{134}Cs and ^{137}Cs. It has been reported that the effect of β-ray emis-sion and nuclide conversion by β-decay of ^{137}Cs on alumi-nosilicate framework is minor [2, 3]. On the other hand, there are few reports of effects by gamma rays on pollucite framework. Therefore, we examined the effect of gamma radiation on the aluminosilicate framework of Pollucite. In this report, we have studied on cesium leakage from pol-lucite and various aluminosilicate.

EXPERIMENTS: Sodium aluminate, sodium metasilicate and cesium chloride were dissolved in sodium hydroxide solution. The solution was placed in a Teflon inner cylinder pressure container. Pollucite was synthesized by hydrothermal method, holding the container at 180°C for 12 hours. The resulting precipitate was washed by distilled water. Thereafter, each solid was collected by filtration and dried at 110°C for 12 hours or more. Adsorption experi-ments were performed using mordenite, bentonite and Ze-olite 13X, Zeolite 4A. Each adsorbent was added to 0.1 M cesium chloride solution and stirred for 24 hours. The amount of cesium absorbed was estimated by atomic ab-sorption spectrophotometry.

The powder samples were characterized by XRD, and gamma-irradiated with 87.9 kGy by ^{60}Co source. The leaching test by PCT-A method [4] was carried out to eval-uate the change of Cs retention performance by framework damage. Concentration of cesium in solution leached was estimated by atomic absorption spectrophotometry. Leach-ing rate was calculated by equation (1).

$$\boldsymbol{LR}\ (\%) = \frac{\boldsymbol{C_{Cs}V \times 10^{-3}}}{\boldsymbol{mf_{Cs}}} \times \boldsymbol{100} \qquad (\boldsymbol{1})$$

Where C_{Cs} [mg L^{-1}] was the concentration of Cs in the solution, m was the weight of samples, f_{Cs} was the weight ratio of the Cs in the sample before leaching, V [L] was the volume of the leaching liquid.

RESULTS: It was confirmed from the result of atomic absorption spectrometry that cesium was adsorbed on the adsorbent. Figure 1 shows the XRD pattern of samples. The sample synthesized for 12 hours was confirmed to be pollucite.

Table 1. shows the results of leaching tests performed with various aluminosilicates. As a result of the table, it was turned out that pollucite had a lower leaching rate than other cesium-containing aluminosilicates.

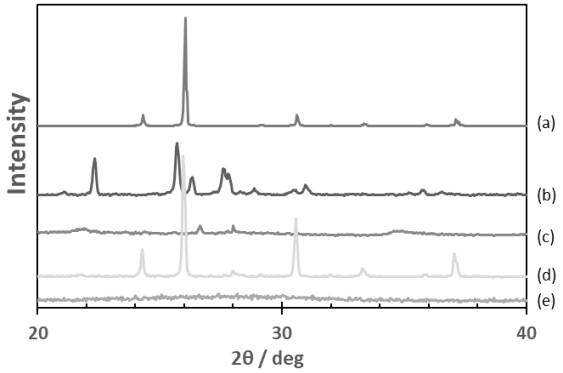

Fig. 1. XRD patterns of samples. (a)Pollucite-std, (b)Cs_{ad} Mor-denite, (c)Cs_{ad} Bentnite, (d)Pollucite, (e)Amorphous.

Table 1. Results for PCT-A-like leaching test.

Sample	T / °C	t / hr	C_{Cs} / mg L^{-1}	Leaching rate /%
Cs_{ad} MOR	**90**	**168**	**144**	**0.620**
Cs_{ad} Bentnite	**90**	**168**	**267**	**1.50**
Cs_{ad} Zeolite13X	**90**	**168**	**245**	**1.03**
Cs_{ad} Zeolite4A	**90**	**168**	**368**	**2.00**
Pollucite	**90**	**168**	**13**	**0.0425**
Amorphous	**90**	**168**	**989**	**92.3**

REFERENCES:

[1] Y. Yokomori *et al.*, Sci. Rep., **4** (2014), 4195.
[2] J. Fortner *et al*., Argonne National Laboratory, Argonne, Illinois **60439** (2001).
[3] N. J. Hess *et al.*, J. Nucl. Mater., **281** (2000), 22-33.
[4] ASTM C 1285-02 (2008).
[5] Z. Jing *et al.*, J. Hazard. Mater., **306** (2016), 220-229.

CO4-31 Radiotolerance analysis of *Deinococcus sp.* strain AKn-1 isolated from the coast of Akina bay in Amami-Oshima Island

H. Ohashi, K. Matsubara[1], T. Saito[2] and T. Sakaguchi[1]

Faculty of Symbiotic Systems Science, Fukushima University

[1]Department of Life Science, Prefectural University of Hiroshima

[2]Institute for Integrated Radiation and Nuclear Science, Kyoto University

INTRODUCTION: Since discovery of *Deinococcus spp.*, its microorganisms have been well known for their resistance to strong radiation, and have been found in many environments such as deserts, muddy soils, and aerial environments. We have studied properties of *Deinococcus spp*. Recently we have isolated the AKG-1 strain, which produces a red pigment from slime on the body surface of the yellowbarred red rockfish. Its strain was classified in *Deinococcus sp.* and had resistant to hydrogen peroxide and ultraviolet rays. The results suggested that the *Deinococcus spp*. would have a wide distribution of in the marine environment.

In this study, we examined the isolation and culture of *Deinococcus* microorganisms from samples taken from the sandy beach in Amami-Oshima Island with strong ultraviolet rays. Furthermore, the gamma ray resistance of the obtained UV-resistant isolate AKn-1 strain was investigated.

EXPERIMENTS: The sand and seawater along the coast of Amami-Oshima Island, which is assumed to be a harsh growing condition due to the high exposure to ultraviolet rays, was collected during the daytime on a sunny day and used as an isolated sample of the target microorganism. After that, normal culture and isolation operation were performed.

The strain obtained above and the *E. coli* JM109 strain were made into a suspension solution, and each suspension solution was irradiated with ^{60}Co gamma ray at the Institute for Integrated Radiation and Nuclear Science, Kyoto University.

The irradiated samples were diluted with YMs medium, inoculated and cultured on a plate. Then, Colony Forming Units (CFU) were counted. The surviving fraction was estimated from the CFU ratio of non-irradiated and irradiated samples.

RESULTS: As a result of isolating and culturing, we succeeded in obtaining an isolated strain (named "AKn-1 strain") resistant to selenate and ultraviolet rays from the sandy beach of Akina Bay, Tatsugō, Kagoshima Prefecture, Japan. The strain was cocci or diplococci with a size of 1-2 μm and had a non-migrating cell morphology. In addition, it was Gram-positive and closely resembled *Deinococcus sp.* AKG-1 strain.

Fig.1. shows a plot of the surviving fraction of cells as measured by the number of colonies formed by the surviving cells relative to the control. Both *Deinococcus sp.* AKG-1 and *Deinococcus sp.* AKn-1 strains were found to be radiotolerant compared to *E. coli* JM109 strain.

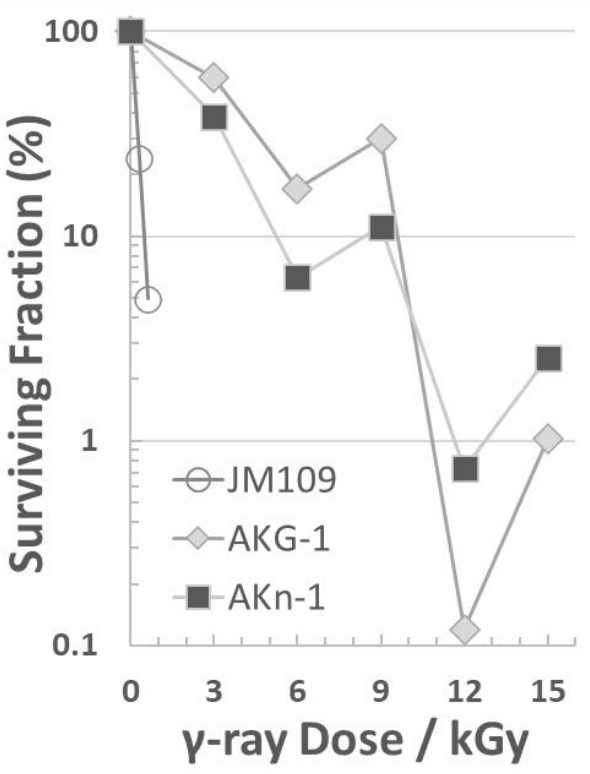

Fig.1. Surviving fraction of cells as measured by the number of colonies formed by the surviving cells relative to the control. ○: *E. coli* JM109 strain, ◇: *Deinococcus sp.* AKG-1 strain, and ■: *Deinococcus sp.* AKn-1 strain.

CO4-32 TDPAC Measurement of ^{111}Cd(←^{111}In) in Ultrafine Bubble Water

M. Tanigaki, Y. Ohkubo, A. Taniguchi, Y. Ueda[1], Y. Tokuda[2]

Institute for Integrated Radiation and Nuclear Science, Kyoto University
[1]Research Institute for Sustainable Humanosphere, Kyoto University
[2]Department of Education, Shiga University

INTRODUCTION: Ultrafine bubbles, the gaseous cavities with diameters less than one micrometer, have recently attracted much attention because of their multi-functionalities [1]. Fundamental studies on such multi-functionalities of ultrafine bubbles are not well extended because they are smaller than the wavelength of radiant rays. The time differential perturbed angular correlation (TDPAC) of ^{111}Cd(¬ ^{111}In) in the aqueous solution with ultrafine bubbles is performed for the study of the interface of ultrafine bubbles, which should be one of the essential origins of its multi-functionality.

EXPERIMENTS: Typical four-counter TDPAC measurements were performed for the 171-245 keV cascade in ^{111}Cd(¬ ^{111}In) in aqueous solutions of pH = 7~8, 10~10.5 with/without Oxygen-ultrafine bubbles. The average diameter and the density of the ultrafine bubbles in each sample were measured by Archimedes to be 115 nm and 2.45 ×10^6/mL, respectively. ^{111}In was obtained from Nihon Medi-Physics as the aqueous solution of $^{111}InCl_3$ at a pH of approximately 2. This ^{111}In solution was added to each aqueous solution sample. The pH control was performed by adding Na_2CO_3 for better pH control around pH = 7 instead of NaOH in the previous study [2]. The angular correlation term $A_{22}G_{22}(t)$ is given by the following equation,

$$A_{22}G_{22}(t) = \frac{2\big(N(180°,t)-N(90°,t)\big)}{N(180°,t)+2N(90°,t)},$$

where $N(90°, t)$ and $N(180°, t)$ are the counting numbers of the 171-245 keV γ-γ cascade at 90 and 180 degrees, respectively. The time-dependent term $G_{22}(t)$ for each sample was obtained by normalizing obtained $A_{22}G_{22}(t)$ by the asymmetry parameter of 171-245 keV cascade in ^{111}Cd, $A_{22} = -0.18$.

RESULTS AND DISCUSSIONS:
Observed $G_{22}(t)$ are shown in Fig. 1. and 2. Those were similar to the cases of pH = 7.4 and 13.4 reported by Demille [3]. The initial drops at 15 to 20 ns in $G_{22}(t)$ were more significant in Oxygen-ultrafine bubble water than those in pure water regardless of their pH. This difference may be caused by the influence of the ultrafine bubbles to the formation of hydrated ions of In. More studies, such as the detailed pH dependence, are underway.

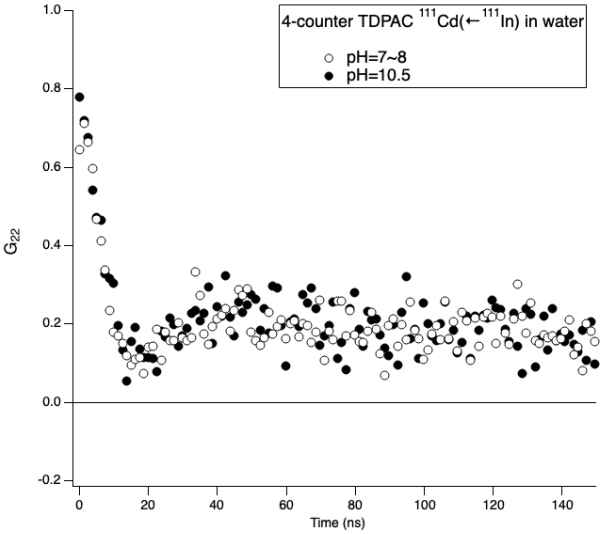

Fig. 1. TDPAC spectra of ^{111}Cd(¬ ^{111}In) in pure water at pH = 10~10.5 and 7~8.

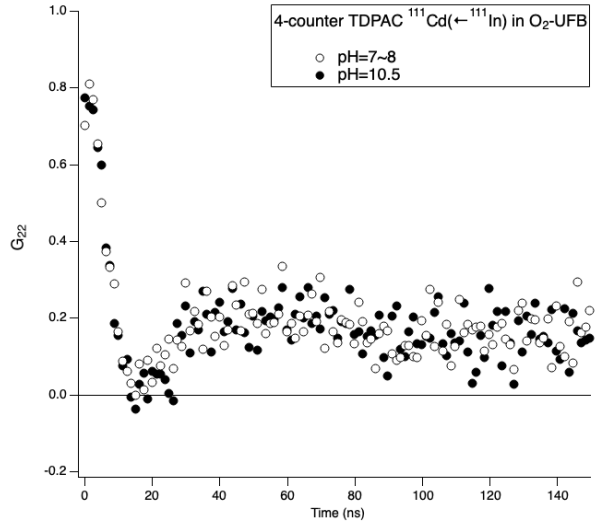

Fig. 2. TDPAC spectra of ^{111}Cd(¬ ^{111}In) in ultrafine bubble water and pure water at pH = 10~10.5.

The present work is supported by JSPS KAKENHI Grant Numbers 18K03948 and 21K03854.

REFERENCES:
[1] E. G. Denis, The fine bubble break-through. https://www.iso.org/news/2014/05/Ref1844.html.
[2] M.Tanigaki *et al.,* KURNS Progress Report 2021, (2022) 124.
[3] G. R. Demille *et al.,* Chemical Physics Letters, **44** (1976) 164-168.

CO4-33 Low Energy Positron Annihilation Lifetime Spectroscopy of Chromium Oxynytride Epitaxial Films on Magnesium oxide crystalline substrates

M. Kitaura, S. Watanabe[2], T. Sugai[3], T. Suzuki[3], J. Kinomura[4]

Faculty of Science, Yamagata University
[1]Institute of Innovative Research, Tokyo Institute of Technology
[2]Graduate school of Engineering, Nagaoka University of Technology
[3]Institute for Integrated Radiation and Nuclear Science, Kyoto University

INTRODUCTION: Epitaxially grown chromium oxide films on magnesium oxide crystal substrates have the NaCl type (B1) structure, same as chromium nitride films. Rutherford backscattering spectroscopy (RBS) measurement revealed that the compositions of chromium oxide epitaxial films is Cr_2O_3, similar to corundum type [1,2]. In order to obtain Cr_2O_3 with the B1 type structure, vacancies
have to be introduced at the chromium site. However, there is no evidence concerning the introduction of such chromium vacancies by oxygen replacement in chromium nitride. Vacancy-induced B1 structures have also been observed for other 3d transition metal monoxides such as VO and TiO. Positron annihilation lifetime spectroscopy (PALS) has been used to investigate the nature of vacancy-type defects in solids [3,4]. In the present study, PALS spectra of chromium oxynitride epitaxial films with different oxygen contents were measured.

EXPERIMENTS: Samples of epitaxially grown chromium oxynitride files on magnesium substrates were prepared by the pulse laser deposition (PLD). The average thickness of samples was 300 nm. PALS measurements were performed using slow positron beam from Kyoto University Research Reactor (KUR). The incident energy of the slow positron beam was adjusted by the Doppler broadening measurements of positron annihilation with valence electrons in chromium oxynitride epitaxial films. To obtain PALS spectra, positron annihilation gamma-rays were detected until the number of evens for it reaches 100000 counts. The lifetime was analyzed using the software LT9 [5].

RESULTS: PALS spectra of chromium oxynitride epitaxial films were reproduced by two exponential decay functions. The first component with a shorter lifetime was dominant. The intensity of the second component with a long lifetime was only a few percent. The variation of the lifetime of the first component for chromium oxynitride epitaxial films is shown in Fig. 1 for several oxygen content x. The lifetime was apparently increased with x. This fact indicates that the positron annihilation site changes with x. As mentioned above, the replacement of

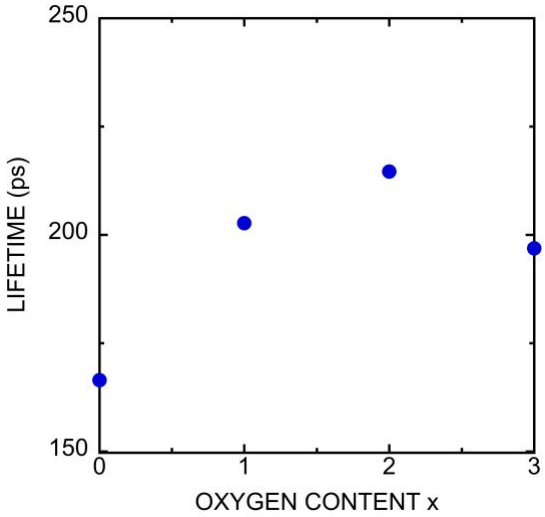

Fig.1. Variation of the lifetime of the first component for chromium oxynitride epitaxial films.

nitrogen by oxygen is expected to introduce chromium vacancies in chromium oxynitride epitaxial films. The longer lifetime of the first component suggests that most of positrons annihilation at chromium vacancy sites in chromium oxynitride epitaxial films of x=1. The lifetime was slightly increased at x=2. Divacancy or trivacancy may be predominantly formed in 1<x<2, because the lifetimes of them are slightly larger than that of monovacancy. The lifetime was slightly shortened at x=3. In refs. [1,2], stacking faults due to corundum Cr_2O_3 were increased with x. Vacancy complexes in the B1 type structure will partially participate the formation of the stacking fault, in which they are changed into the interstitial open space. This process competes with the formation of vacancy complexes in the B1 type structure. Consequently, vacancy complexes are suppressed with increasing x, and thus the lifetime is decreased at x=3.

REFERENCES:

[1] K. Suzuki *et al.*, Thin Solid Films **625** (2017) 111-114.
[2] K. Suzuki *et al.*, APL Mater. **3** (2015) 096105/1-6.
[3] K. Fujimori *et al.*, Appl. Phys. Express, **13** (2020) 085505/1-4.
[4] M. Kitaura *et al.*, Opt. Mater.: X **14** (2022) 100156/1-7.
[5] J. Kansy, Nucl. Instrum. Methods Phys. Res. Sect. A, **375** (1996) 235-244.

CO4-34 Influence of Hydrogen Isotopes on Growth of Vacancy Clusters in Tungsten-Based Materials

Y. Hatano, M. Matsumoto[1], T. Asano[1], M. Nishimura[1], T. Takahashi[2], N. Abe[2] and A. Kinomura[2]

Hydrogen Isotope Research Center, University of Toyama
[1]Guraduate School of Science and Engineering, University of Toyama
[2]Institute for Integrated Radiation and Nuclear Science, Kyoto University

INTRODUCTION: As a plasma-facing material of a future fusion reactor, tungsten (W) will be exposed to intense flux of fuel particles, deuterium (D) and tritium (T), and that of products of fusion reactions, helium and 14 MeV neutrons. Irradiation of 14 MeV neutrons induces displacement damages in a W lattice. The authors have found that neutron irradiation drastically increases fuel retention in W due to trapping effects by vacancies and vacancy clusters [1]. Understanding of vacancy formation and clustering is necessary for accurate evaluation of T inventory in a vacuum vessel of a reactor.

In previous studies [1-3], W samples were irradiated with neutrons or heavy ions first, and then hydrogen isotope was introduced by plasma or gas exposure. However, in real fusion conditions, the radiation-induced defects are accumulated under exposure to hydrogen isotope plasma. Hence, the influence of hydrogen isotopes on the development of damaged structure must be understood.

The objective of this study is to investigate vacancy clustering in W under the presence of hydrogen isotopes and to construct a kinetic model of clustering. To reach this goal, W samples with monovacancies are prepared by electron beam irradiation. Then, the irradiated samples are heated with and without hydrogen isotopes, and the difference in size distributions of vacancy clusters is examined using positron annihilation spectroscopy.

EXPERIMENTS: Samples were disks of W with 6 mm diameter and 0.5 mm thickness prepared from a rod provided by A. L. M. T. Co., Japan. After surface polishing to mirror-like finish, the samples were annealed in vacuum ($<10^{-5}$ Pa) at 1273 K for 1 h to relieve stress potentially induced during machining and polishing.

The electron linear accelerator at Institute for Integrated Radiation and Nuclear Science, Kyoto University, was used for electron beam irradiation. Eight samples were stacked in two layers of four samples, as shown in Fig. 1. The stacked samples were wrapped with aluminum (Al) foil and sealed using Al tape. Then, the samples were put into an Al chamber and irradiated with 8 MeV electrons for 77 h to 5×10^{-3} dpa. During irradiation, the samples were cooled by water circulating in the chamber over the Al tape. The temperature of the samples was measured using a thermocouple insulated with a polyimide film and attached on the Al tape. However, signal was lost during the irradiation probably due to damaging in the polyimide film. After the irradiation, the positron lifetime was measured using 1 MBq ^{22}Na source at Institute for Materials Research, Tohoku University. A total of 9×10^6 coincidence events were collected for each measurement, and the lifetime spectrum was analyzed using PALSfit software package [4].

RESULTS: Positron lifetime spectra for non-irradiated and electron-irradiated samples are given in Fig. 2. Clear increase in positron lifetime was observed after electron irradiation. The positron lifetime in the non-irradiated samples was ~130 ps. The lifetime spectra for the irradiated samples were reproduced by assuming presence of two components: ~140 ps and ~360 ps. The shorter component showed formation of monovacancies. The longer component indicated that vacancy clusters were formed during irradiation though the samples were cooled by flowing water. D will be introduced into the samples by plasma exposure and cluster growth will be investigated in the next year.

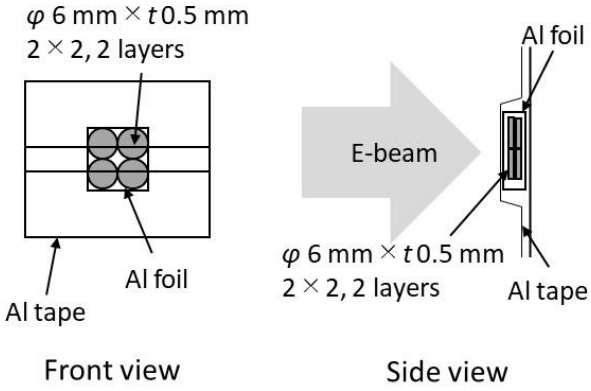

Fig. 1. Arrangements of W samples during electron irradiation.

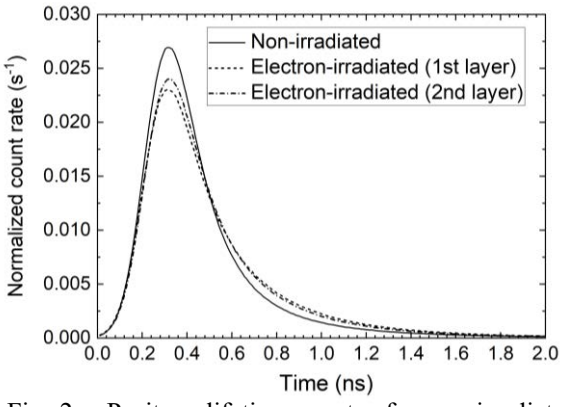

Fig. 2. Positron lifetime spectra for non-irradiated and electron-irradiated W.

REFERENCES:

[1] T. Toyama *et al.,* J. Nucl. Mater., **499** (2018) 464-470.
[2] M. Yajima *et al.*, Phys. Scr., **96** (2021) 124042.
[3] J. Wang *et al.*, J. Nucl. Mater., **559** (2022) 153449.
[4] J. V. Olsen *et al.*, Phys. Stat. Sol. C., **4** (2007) 4004-4006.

CO4-35 Magnetic Measurememts of Irons in Soda-lime Glass by Mössbauer Spectroscopy

K. Okada and Y. Kobayashi[1]
SPring-8/JASRI
[1]Institute for Integrated Radiation and Nuclear Science, Kyoto University

INTRODUCTION and AIM: Glass is used in many applications in our every-day lives and has exciting new applications related to the energy. Soda-lime glass is made of mainly silica (SiO_2) and additive many other materials, such as magnesium, sodium, calcium, aluminum, iron, sulfur, and so on. Our sample glass composition, in percent by weight (wt%), was 72.25 SiO_2, 1.75 Al_2O_3, 4.00 MgO, 8.00 CaO, 14.00 Na_2O as basic components, and 0.015-5 iron in terms of Fe_2O_3 as coloring and functional components. Iron contaminants of less than 0.0005-0.01 wt% are from raw materials, and irons up to 1.5-5 wt% are from injection. The iron oxides in a glass composition are thought to be present in forms of Fe^{3+} and Fe^{2+}. The control parameters for irons are two: (1) the total iron mass weight percent in terms of Fe_2O_3, and (2) the number ratio of Fe^{2+} to total iron ions ($\Sigma_n Fe^{2+}/(\Sigma_n Fe^{2+}+\Sigma_n Fe^{3+})$). The Fe^{3+} component adds a light yellow tint to the glass and absorption in the ultraviolet and visible band, while the Fe^{2+} component adds a blue tint to the glass and absorption in the near-infrared band (1 μm). The transmission from ultraviolet to infrared in glass cannot be explained by simple Fe^{2+} and Fe^{3+} structures. Then, to reveal the exact local structures of irons (Fe^{2+} and Fe^{3+}) is necessary. Many scientists proposed many new theories and local structures [1-4], but they did not resolve it completely.

We have prepared glass samples using the Mössbauer isotope ^{57}Fe (natural abundance is about 2.119 %). The chemical composition of iron oxide in the ^{57}Fe enrichment glass samples was from 0.015 to 5 wt%, and the $\Sigma_n Fe^{2+}/(\Sigma_n Fe^{2+}+\Sigma_n Fe^{3+})$ was from 0 to 0.6. We have investigated these samples by nuclear resonant inelastic scattering and X-ray Absorption Fine Structure methods at synchrotron radiation to reveal the local atomic structure around and neighboring iron atoms in sub-nanometer region[5]. And then we have investigated same samples by the Electron Spin Resonance and the Superconducting Quantum Interference Device measurements to reveal the magnetic property in glass. From these results, the capability of complex magnetic fields according to the only Fe^{3+} atoms or both of Fe^{3+} and Fe^{2+} atoms was suggested. By Mössbauer experiments, we can get magnetic moments and magnetic states at various temperatures. Then we proposed the Mössbauer measurements to reveal the magnetic property and the magnetic state from Fe^{3+} and Fe^{2+} atoms independently.

EXPERIMENTS: The measurements were performed using conventional Mössbauer spectrometer. The specimens for Mössbauer measurements were tuned to 10 mm-phi pellet from the ^{57}Fe enriched glass powders. We investigated one new sample including irons of 0.1 wt% with 0.6 $\Sigma_n Fe^{2+}/(\Sigma_n Fe^{2+}+\Sigma_n Fe^{3+})$ at room temperature.

RESULTS and DISCUSSION: The data of samples including iron of 0.1 wt% with 0.2 and 0.6 $\Sigma_n Fe^{2+}/(\Sigma_n Fe^{2+}+\Sigma_n Fe^{3+})$ were showed in Fig. 1. As shown in Fig. 1, there was the difference of continuous wide components between the $Fe^{2+}/(\Sigma_n Fe^{2+}+\Sigma_n Fe^{3+})$, and these structures indicated the local magnetization around iron atoms. The Fe^{3+} components with large internal magnetic field have been detected. And the results from various iron oxide content glass indicated the Fe^{3+} and Fe^{2+} atoms were in glass as separate structures.

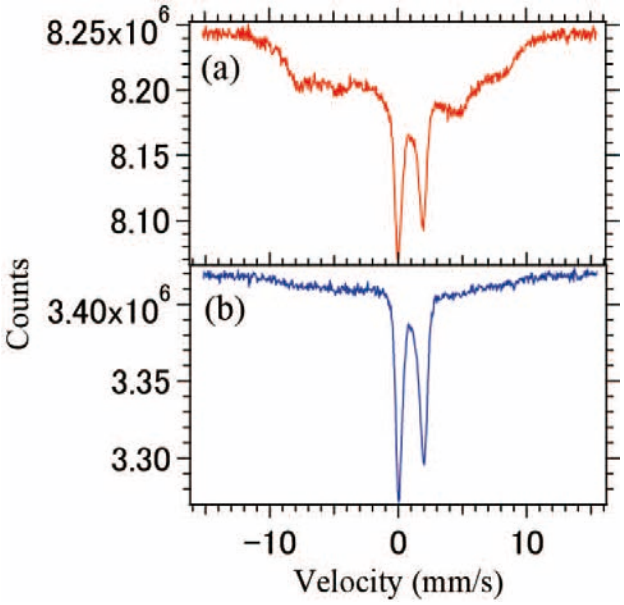

Fig. 1. Mössbauer spectra of soda-lime glass with 0.1 wt% iron oxide comprising. The **$Fe^{2+}/(\Sigma_n Fe^{2+}+\Sigma_n Fe^{3+})$** was (a) 0.2, and (b) 0.6. The measurements were performed at room temperature.

REFERENCES:

[1] C. Ruessel *et al.*, Phys. Chem. Glasses, **47** (2006) 563.
[2] T. Uchino *et al.,* J. Non-Cryst. Solids, **261**(2000) 72.
[3] F. Farges *et al.*, Physica Scripta, **T115** (2005) 957.
[4] C. Russel, Glastech. Ber., **66** (1993) 68.
[5] K. Okada *et al.*, X-ray Spectrometry, **47** (2018) 359-371.

CO4-36 Gamma-ray energy separation by shielding material for 1F debris destribution estimation

Y. Okuno[1,2] and N. Sato[2]

[1]RIKEN
[2]*Institute for Integrated Radiation and Nuclear Science, Kyoto University*

INTRODUCTION:

At TEPCO's Fukushima Daiichi nuclear power plant(1F), fuel debris removal began in December 2021, and full-scale decommissioning will take place over the next several decades. However, the location of debris has not been sufficiently identified, and sensors for debris exploration is required. The gamma rays emitted from fuel debris and the others are expected to originate from Eu-154, and Cs-134, Ba-137, Co-60, and Pr-144, respectively. Since debris-specific gamma rays are predominantly seen in the energy region above 1 MeV, designing a detector that can roughly separate the energies above and below 1 MeV will enable us to determine the rough distribution of debris. Also, since Co-60 gamma rays present the noise in the Eu-154 signal above 1 MeV, auxiliary neutron flux measurements would improve the accuracy of the fuel debris location characteristics. We envision the use of solar cell dosimeters as dosimeters for debris exploration[1]. However, it is difficult for a single element to discriminate between radiation types and energies. Therefore, in this study, a new energy-separation method is proposed that uses a radiation low-cut filter that preferentially attenuates low-energy gamma rays below 1 MeV by shielding. Using shielding materials of two or more different elements, it is assumed to analyze debris-derived gamma rays from the difference in dosimeter signals resulting from the difference in the energy dependence of the attenuation coefficients of photoelectric and Compton effects.

****

RESULTS:

As shown in Fig.1, 18.1 mm beryllium and 2 mm lead were used as low-cut filters, and the filter characteristics above and below 1 MeV were obtained using Cs-137 and Co-60 gamma sources. The current signal of the solar cell dosimeter using amorphous silicon solar cells with Pb shield attenuated just the gamma-ray from Cs-137 such as below 1 MeV gamma rays. Solar cells also can detect neutrons in the case of charged particle conversion film such as boron placed on the surface. The signal of with and without the conversion film installed InGaP solar cell under the condition of neutron irradiation using the small accelerator neutron source RANS[2]. The results show that RANS neutrons can be efficiently detected by the conversion film. Therefore, there is a possibility that information on fuel debris can be identified by scanning measurement of gamma-ray-energy-separation and gamma-ray-neutron-separation with multiple solar cell type dosimeter adjusted the structure of shield and conversion film installed at the same position, such as on a robot arm.

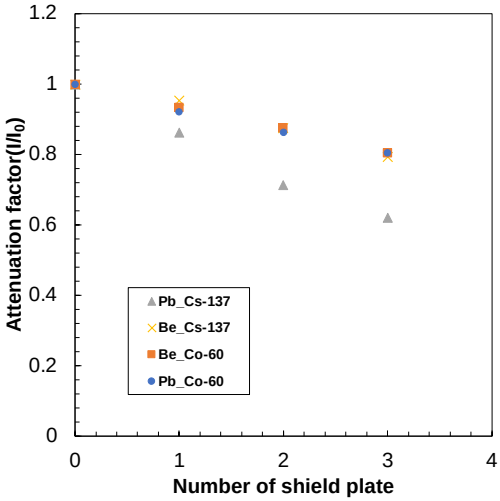

Fig. 1. Signal attenuation factor of solar cell dosimeters due to the installation of shielding material.

****

EXPERIMENTS:

The irradiation sample was amorphous silicon solar cell. Irradiation source was ^{137}Cs gamma-ray at Tokyo Metropolitan Industrial Technology Research Institute and ^{60}Co at Institute for Integrated Radiation and Nuclear Science. The sample was set at under the irradiation environment and was connected with electrometer (iDC13, Taieidenki co.) at the measurement room by using BNC cable.

****

REFERENCES:

[1] Y. Okuno *et.al,* ACS Appl. Electron. Mater., **4** (2022) 3411-3420.
[2] Y. Otake, Reviews of Accelerator-Science and Technology, **8** (2015) 181-207.

CO4-37 Study on activation of neutron optical elements in a new research reactor

H. Fujioka, K. Mishima[1], Y. Yamagata[2], and K. Takamiya[3]

Department of Physics, Tokyo Institute of Technology
[1]Institute of Material Structure Science, KEK
[2] RIKEN Center for Advanced Photonics, RIKEN
[3]Institute for Integrated Radiation and Nuclear Science, Kyoto University

INTRODUCTION: To extract neutron beams efficiently from a research reactor, it is important to increase the solid angle of extraction by using a focusing optical system, as well as to improve the performance of the cold neutron source itself. This is achieved by inserting a neutron guide tube with rotating parabolic or ellipsoidal surface as close as possible to the cold neutron source. In this case, the neutron mirror is placed in a high radiation environment near the reactor core, and the radiation resistance and activation evaluation are necessary. In addition, diamond nanoparticles (DNP) can change the direction of flight of neutrons that are not fully reflected by the mirror to the beam extraction direction by neutron scattering, and are expected to increase the extraction amount of neutrons, especially long-wavelength neutrons. In this study, we irradiate metal materials used as substrates for neutron reflectors at KUR, and investigate the activation analysis and physical damage of the substrate surface. Since physical damage caused by radiation may increase the surface roughness, we compare the surface roughness before and after irradiation. We also perform activation analysis on DNP in the same way.

EXPERIMENTS: Two DNPs and two mirrors were irradiated in the KUR nuclear reactor to investigate radiations due to impurities in them.

For DNP samples, uDiamond® Molto Nuevo (DNP#01) from Carbodeon and RT-DND-B (DNP#02) from Ray Techniques were used. Each DNP power of 0.1 g was sealed in a plastic case, inserted into the radiation field through the KUR pneumatic transport tube Pn-2, and irradiated for 12 seconds. The reactor power was 5 MW and the neutron dose was estimated to be 2.6×10^{13} n/cm^2/s. Gamma-ray spectra were obtained by a HPGe detector after irradiation, and activation analysis was performed.

For neutron mirrors, two pieces of aluminum mirror coated with electroless NiP plating (50 μm) (10 mm x 15 mm x 2 mmt) were used for the irradiation experiment. These samples were irradiated through Pn-2 port with radiation time of 6 and 360 seconds. As well as DNP, the residual Gamma-ray spectra was measured by HPGe. In addition, to check whether the surface roughness was not degraded by irradiation, a replica of the NiP was taken on a sheet and the surface condition was observed.

RESULTS: For DNPs, the post-irradiation doses were estimated to be 75 kBq for DNP#01 and 280 kBq for DNP#02. Impurities such as Na, Cl, Mg, and Ti were detected at several hundred to several thousand ppm, especially Ti in DNP#01 and Cl in DNP#02. The results were summarized in Table. 1.

When DNP is placed directly under a neutron source as a reflector, the Wigner effect [1], a phenomenon in which a material is excited by radiation and its energy remains in the material for a long period of time, may be a problem in addition to impurities. The Wigner effect requires a longer irradiation time, but the results of this study suggest that the impurities that cause activation need to be reduced.

Table. 1. Contaminations in the DNP samples with unit of atom-ppm.

Impunity	DNP#01	DNP#02
Na	28	55
Cl	106	2042
Ti	287	12
Mn	1	9

Figure 1 shows a surface morphology of replica film (cellulose acetate) taken from sample without irradiation (left) and sample irradiated for 6 minutes. Although there are number of dots, which are probably due to aggregation of cellulose acetate molecule, the surface roughness values are 0.8nm and 0.63 nm in average, respectively. This indicate that irradiation of 2.6×10^{13}n/cm^2/s flux for 6 minutes does not affect the surface roughness of the mirror. The study of the impurities of NiP mirror by Gamma-ray spectra is under analysis.

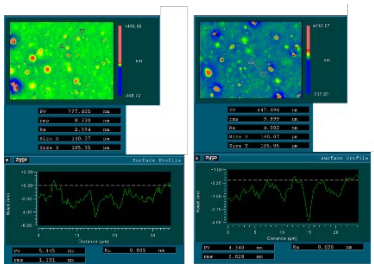

Fig. 1. surface morphology of replica film taken from NiP mirror without irradiation (left) and 6min irradiation (right).

REFERENCES:

[1] F. Cataldo *et al.*, Fuller. Nanotub. Carbon Nanostructures, **22:10** (2014) 861-865. (doi:) 10.1080/1536383X.2013.858131.

CO5-1 Track observation in muscovite irradiated by ^{241}Am sources and its thermal stability

N. Hasebe, T. Nakashima[1], K. Miura[1], U. Uyangaa[1], G.Shuukhaaz[1], K. Oohashi[2], S.Akutsu[2], Y. Iinuma[3], and K. Takamiya[3]

Institute of Nature and Environmental Technology, Kanazawa University
[1]Graduate School of Natural Science and Technology, Kanazawa University
[2]Graduate School of Science and Technology for Innovation, Yamaguchi University
[3] Institute for Integrated Radiation and Nuclear Science, Kyoto University

INTRODUCTION: ^{238}U, ^{235}U, and ^{232}Th decay through emission of alpha particles to stable lead. Alpha Recoil Track (ART) is the damage created when daughter nuclides move back in reaction to alpha decay (Fleisher, 2003). Under the known decay constants of uranium and thorium, the age since the start of ART accumulation can be calculated by measuring the number of ARTs and uranium and thorium concentrations.
The purpose of this research is to establish a method to artificially form ARTs on mineral surfaces using muscovite ART detectors to help the understanding of ART behavior in various minerals. An experiment on the annealing behavior of ARTs in muscovite was also performed.

EXPERIMENTS: A 300 Bq americium source was tested to form artificial ART at Research Institute for Complex Nuclear Science, Kyoto University. Irradiation was performed under a vacuum at various time intervals (1 hour, 3 hours, 6 hours, 12 hours, 2 days, 4 days and 1 week). The ARTs were enlarged by etching with 47 % HF for two hours and observed with a phase contrast optical microscope.
Several samples of muscovite that have been irradiated for 3 hours were prepared and annealed at different temperatures (100℃, 150℃, 200℃) and times (30 min, 1 hour, 3 hours, 5 hours, 10 hours, 20 hours, 100 hours and 352 hours) to see the stability of ARTs under the geological condition.

RESULTS: The areal density of ARTs increased linearly against the irradiation time (Figure 1). One could identify each ART one by one in samples irradiated from 1 hour to 12 hours, but the number of ARTs formed on the muscovite surface was too many to identify for samples irradiated from 2 days to 1 week. Size of artificially formed ARTs (single alpha decay) was investigated and they were larger than natural ARTs (multiple alpha decay). In general, the artificial ART is formed by a single alpha decay from ^{241}Am to ^{237}Np. In contrast, muscovite without annealing should record the ARTs by multiple decay from the parent nuclide ^{238}U, ^{235}U, and ^{232}Th to the stable ^{206}Pb, ^{207}Pb, and ^{208}Pb, respectively, so that one can expect larger natural tracks than the artificial tracks formed by irradiation.
Based on the annealing experiment, It was concluded that natural ARTs were annealed at ambient temperature for a long period of time because the size of ART tends to decrease with annealing time during the isothermal annealing experiment (Figure 2). The establishment of the artificial ART formation method will make it possible to observe the shape and characteristics of ARTs in various minerals other than mica and will contribute to further development of geochronological use of ART, especially including zircon.

REFERENCES:

[1] Fleischer R., Geochim. cosmochim. acta, **67**, (2003) 4769-4774.

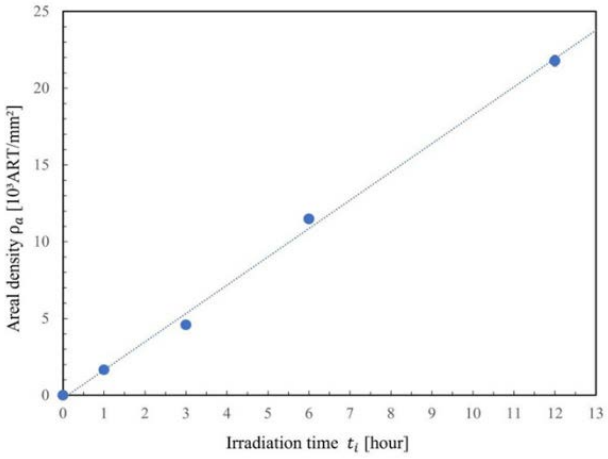

Fig. 1. Areal density of ARTs is plotted against irradiation time.

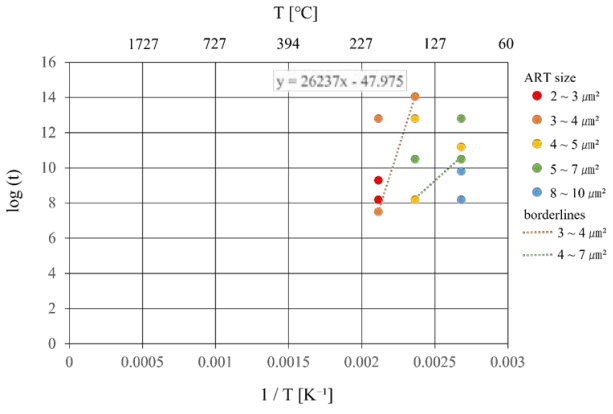

Fig. 2. The Arrhenius plot based on the annealing temperatures and times (sec).

CO5-2 Mechanisms of high-pressure transitions in $(Mg,Fe)_2SiO_4$ under differential stress

N. Tomioka[1], T. Okuchi[2], M. Miyahara[3]

[1]*Kochi Institute for Core Sample Research, Japan Agency for Marine-Earth Science and Technology*
[2]*Institute for Integrated Radiation and Nuclear Science, Kyoto University*
[3]*Graduate School of Advanced Science and Engineering, Hiroshima University*

INTRODUCTION:

Phase equilibria studies have demonstrated that olivine [$(Mg, Fe)_2SiO_4$: α-phase] transforms into a spinelloid structure (wadsleyite:β-phase) and then into a spinel structure (ringwoodite: γ-phase) with increasing pressure. Natural examples of wadsleyite and ringwoodite were first discovered in heavily shocked meteorites. Based on the characterizations of planer defects in these natural phases, shear-promoted "diffusionless" mechanisms were proposed in transformations among the olivine polymorphs [1]. The transformation models also predicted the possible occurrence of an intermediate phase, which is exhibiting the smallest unit cell among all spinel/spinelloid structures. We recently discovered the phase as a mineral poirierite (ε-phase) in shocked meteorites [2, 3]. In the present study, we have carried out a transformation experiment on olivine to understand the conditions and mechanism of the poirierite formation.

EXPERIMENTS:

Natural olivine with an Fe/(Mg+Fe) ratio of 0.09 was used in the transformation experiments. The olivine single crystal was crushed into powder with heterogeneous grain size less than 100 μm. The powder was kept at 16 GPa and 900 °C for 2 hours by using a Kawai-type high-pressure apparatus. The recovered samples were measured using an X-ray diffractometer (RIGAKU SmartLab 9 kW) at the Institute for Integrated Radiation and Nuclear Science, Kyoto University. The X-ray beam is focused to a diameter of ~100 μm. The portions at the reaction boundaries were extracted and to be ultrathin sections of ~150 nm in thickness by using a focused ion beam apparatus (Hitachi SMI-4050), and then examined by a transmission electron microscope (TEM: JEOL JEM-ARM200F).

RESULTS AND DISCUSSION:

The olivine grains are partially transformed at their grain boundaries. Micro-area powder X-ray diffraction patterns show that the product phase is exclusively ringwoodite (Fig. 1). The ringwoodite occurs as euhedral and subhedral crystals with a grain size of 490 ± 270 μm under TEM (Fig. 2). Most of the ringwoodite grains exhibit pervasive stacking faults on {110} planes. These defects have also been reported in ringwoodite in shocked meteorites [e.g. 2,3]. The selected-area electron diffraction (SAED) patterns of many ringwoodite grains with a high density of planar defects show weak extra diffraction spots corresponding to poirierite. In addition, the SAED patterns of the ringwoodite-poirierite intergrowth show that both phases have a topotaxial relationship: $(001)_\varepsilon // \{001\}_\gamma$ and $(100)_\varepsilon // \{110\}_\gamma$. The relict olivine has a high dislocation density of 1.4 x 10^9 /cm^2, corresponding to a differential stress of ~0.6 GPa according to an olivine piezometer [4].

Microstructural and crystallographic features of the sample described above suggest that polycrystalline ringwoodite grains were formed by a nucleation and growth mechanism at grain boundaries of olivine, while poirierite lamellae were metastably formed within ringwoodite grains by a shear mechanism. The latter transformation would be favored by relatively low temperature conditions, where atomic diffusion is kinetically hindered, and by high differential stress, which causes shearing of the oxygen sublattices of the spinel/spinelloid structures. The transformation experiments at different pressure conditions are currently ongoing.

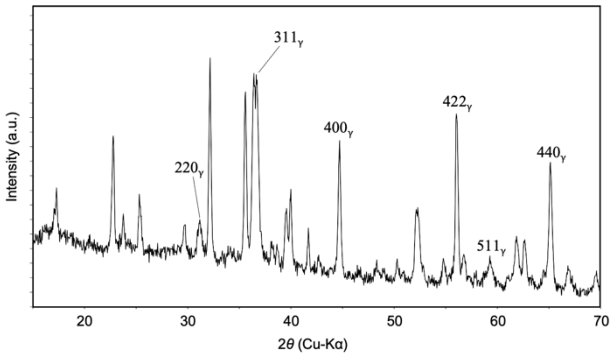

Fig. 1. Micro-area X-ray diffraction pattern taken from olivine kept at 16 GPa and 900 °C. Peaks with notations are from ringwoodite (γ), and all the other peaks are from olivine.

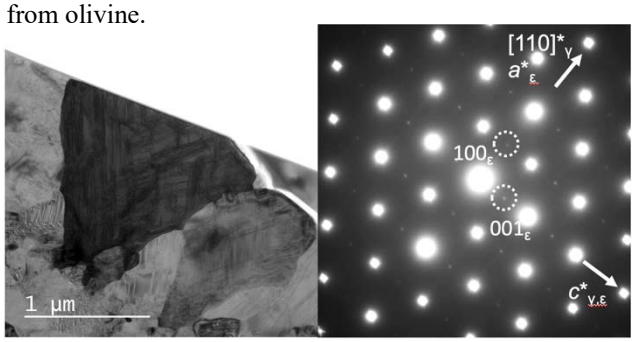

Fig. 2. Transmission electron micrograph (Left) and selected-area electron diffraction patten (Right) of a ringwoodite (γ) grain with intergrown poirierite (ε).

REFERENCES:

[1] M. Madon and J. P., Poirier, Phys. Earth Planet Inter., **33** (1983) 31–44.
[2] N. Tomioka and T. Okuchi, Sci. Rep., **7** (2017) 17351.
[3] N. Tomioka *et al.*, Commun. Earth Environ., **2**, (2021) 16.
[4] Kohlstedt *et al.* (1976). in Physics and Chemistry of Minerals and Rocks, R. G. J. Strens (ed.), (1976) 35–49.

CO5-3 Experimental evaluation of impact-induced structure transformation of planetary minerals

T. Okuchi, N. Tomioka[1], Y. Seto[2], Y. Umeda and T. Sekine[3]

Institute for Integrated Radiation and Nuclear Science, Kyoto University

[1]Kochi Institute for Core Sample Research, Japan Agency for Marine-Earth Science and Technology

[2]Graduate School of Science, Osaka Metropolitan University

[3]Center for High Pressure Science & Technology Advanced Research

INTRODUCTION: 4.6 billion years ago in a nebula surrounding the primordial sun, numerous small bodies were growing into planets and satellites through their mutual collisions. After the collisions of small bodies, some evidences had been recorded within themselves to indicate their impact histories, where materials were strongly and temporally compressed during the impact events. A typical example of such evidence is frozen dense structures occurring after such compression, which emerged through structural transformations of the mineral crystals that originally consisted the asteroids.

There are numbers of previous reports on such dense structures occurring in primitive meteorites [1]. We have been reporting some of these structures including newly discovered one, which had been very possibly recording hypervelocity impact events of the ancient asteroids [2,3]. In these meteorites, we observed that low-density olivine crystals [α-$(Mg,Fe)_2SiO_4$] were transformed into one or more of its three dense high-pressure polymorphs. These are of particular interest because they could have recorded the timescale and the pressure scale of the ancient impact processes in quantitative manner [2,3].

The purpose of the current research is to reveal the formation mechanisms of these dense mineral structures as unique evidences of evolution history of the early solar system, with particular attention to their nanoscale morphological structures and textures.

RESULTS: We experimentally evaluated the timescales of such planetary shock events and also their generated pressure scales. For that purpose, we observed the structure transformation process from α-Mg_2SiO_4 into one or more of its dense high-pressure polymorphs during experimentally-induced shock compression events, which results in an ultrafast structure transformation into ringwoodite [γ-Mg_2SiO_4] [4]. Ringwoodite is one of the most-commonly observed dense high-pressure polymorph minerals occurring in deformed primitive meteorites. For conducting this experiment, we focused a high-power laser pulse into α-Mg_2SiO_4 to apply strong shock compression, where its transformation process was time-resolved by ultrafast diffractometry using a x-ray free electron laser pulse of femtosecond time width generated at SACLA facility [5]. We observed a lattice-shear mechanism which was proceeded within several nanoseconds, much faster than any previous estimation of solid-state structure transformation mechanism of silicate minerals. The mechanism proceeded even during short-lived shocks equivalent to those induced by impacts of relatively-small (sub-kilometer-scaled) asteroids. The mechanism mostly worked during shock releases, such that the peak shock pressures deduced from the existence of shear-induced olivine polymorphs could be underesti-mated. Since shorter-duration compression events occur more frequently in asteroid impacts, the shorter events could have more frequently recorded the fast mechanism. When we carefully search for such records in meteorites and asteroids, we will be able to quantitatively recon-struct the evolution history of the early solar system through numerous impact events.

REFERENCES:

[1] M. Miyahara *et al.,* Prog. Earth Planet. Sci., **8** (2021) 59.
[2] N. Tomioka and T. Okuchi, Sci. Rep., **7** (2017) 17351.
[3] N. Tomioka *et al*., Commun. Earth. Environ., **2** (2021) 16.
[4] T. Okuchi *et al*., Nat. Commun., **12** (2021) 4305.
[5] T. Okuchi, SPring-8/SACLA Information, **26** (2021) 341-348.

CO5-4 Volcanic and Tectonic History of Philippine Sea Plate (South of Japan) Revealed by $^{40}Ar/^{39}Ar$ Dating Technique

O. Ishizuka, S. Sekimoto[1], R. Okumura[1], H. Yoshinaga[1], Y. Iinuma[1], T. Fujii[2]
Geological Survey of Japan, AIST
[1]Institute for Integrated Radiation and Nuclear Science, Kyoto University
[2]Graduate School of Engineering, Osaka University

INTRODUCTION:

Robust tectonic reconstruction of the evolving Philippine Sea Plate for the period immediately before and after subduction initiation at ~52 Ma to form the Izu-Bonin-Mariana arc is prerequisite to understand cause of subduction initiation. Understanding of nature and origin of overriding and subducting plates is especially important because plate density is a key parameter controlling subduction initiation based on numerical modelling. There is increasing evidence that multiple geological events related to changing stress fields took place in and around Philippine Sea plate about the time of subduction initiation at ~52 Ma [1]. To understand tectonics during the period of subduction initiation, it is important to understand the pattern and tempo of these geological events, particularly the duration and extent of seafloor spreading in the Mesozoic arc terrane (Daito Ridge Group), and its temporal relationship with spreading in the West Philippine Basin (WPB).

In this study we have investigated magmatism in the oldest part of the Philippine Sea Plate to reveal for the first time the age and origin of the northernmost part of the WPB and the Palau Basin. The outcome of these studies will assist in understanding the time sequence of magmatic and tectonic events which took place within a relatively short period around 52 Ma, i.e., immediately before and after subduction initiation along the Pacific margin.

EXPERIMENTS: Ages of the igneous rocks were determined using the $^{40}Ar/^{39}Ar$ dating facility at the Geological Survey of Japan/AIST. 10-15 mg of phenocryst-free groundmass, crushed and sieved to 250 – 500 μm in size, was analyzed using a stepwise heating procedure. The samples were treated in 6N HCl for 30 minutes at 95°C with stirring to remove any alteration products (clays and carbonates) present in interstitial spaces. After this treatment, samples were examined under a microscope. Sample irradiation was done either at the Kyoto University Reactor (KUR). The neutron irradiation was performed for 10 h at the hydro-irradiation port under 1 MW operation, where thermal and fast neutron fluxes are 1.6×10^{13} and 7.8×10^{12} n/ cm^2 s, respectively, or for 2 h under 5 MW operation, where thermal and fast neutron fluxes are 8.15×10^{13} and 3.93×10^{13} n/cm^2 s respectively. Argon isotopes were measured in a peak-jumping mode on an IsotopX NGX noble gas mass spectrometer fitted with a Hamamatsu Photonics R4146 secondary electron multiplier.

RESULTS: 6 samples have been dated by the laser-heating $^{40}Ar/^{39}Ar$ dating technique. Basalts from the basin floor of northernmost part of the WPB show age range between 47.5 and 49.3 Ma (Fig.1). Basalts from the Palau Basin gave age range between 45.2 and 48 Ma.

SUMMARY:

1) The new dating results from the oldest part of the WPB and the Palau Basin strongly imply that these ocean basins which are supposed to form the oldest part of the Philippine Sea Plate only formed mostly after c. 51 Ma.

2)This fact seems to provide further support for the model that the Izu-Bonin-Mariana arc was established on ocean crust formed associate with subduction initiation, but not on the older ocean crust existed prior to the subduction initiation [2]. This also confirm that the overriding plate at subduction initiation (i.e., Philippine Sea Plate) is mainly composed of Mesozoic remnant arc terrane represented by the Daito Ridge Group, and might have had not much ocean crust.

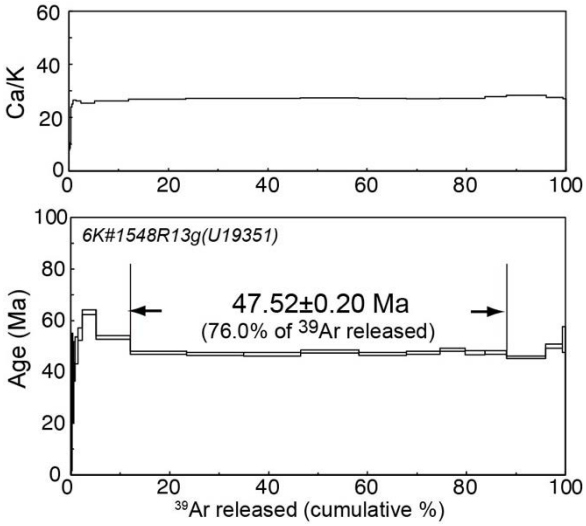

Fig. 1. Age spectrum for the basalt from the northernmost part of the WPB.

REFERENCES:

[1] O. Ishizuka *et al.*, Earth and Planet. Sci. Lett., **306** (2011) 229-240.
[2] O. Ishizuka *et al.*, Earth and Planet. Sci. Lett., **481** (2018) 80-90.

CO5-5 Temporal trends of extractable organochlorine in wild kite (*Milvus migrans*)

K. Ito[1], T. Fujimori[2], K. Oshita[1], S. Fukutani[3], H. Mizukawa[4], M. Takaoka[1], S. Takahashi[4]

[1]*Department of Environmental Engineering, Graduate School of Engineering, Kyoto University*

[2]*Faculty of Advanced Science and Technology, Ryukoku University*

[3] *Institute for Integrated Radiation and Nuclear Science, Kyoto University*

[4] *Graduate School of Agriculture, Ehime University*

INTRODUCTION: Among organochlorine compounds, persistent organic pollutants (POPs) are subject to international regulation, but the number of POPs and the diversity of alternatives and analogues with similar properties is increasing, so extractable organochlorine (EOCl) have attracted attention as a comprehensive risk assess-ment [1]. POPs are known to be concentrated in highly trophic animals through bioaccumulation in the food chain, and wild birds are considered one of the most sen-sitive organisms to pollutants.

The aim of this study is to temporally evaluate EOCl in archived wild kite liver samples. Extracts were separated by 1000 g/mol molecular weight and measured by neu-tron activation analysis (NAA) and compared to poly-chlorinated biphenyls (PCBs) concentrations in the same samples reported previous study [2] to quantitatively evaluate unidentified chlorine.

EXPERIMENTS: Kite liver samples were used from individuals which were collected at Matsuyama airport from 1977 to 2018. Samples were dissected after collec-tion and stored frozen in environmental specimen bank (*es*-BANK) in Ehime university.

The extraction method followed previous studies [1]. Samples were extracted in organic solvents using homogenizer and washed with aqueous solution. Gel permeation column chromatography was used to fractionate at a molecular weight of 1000 g/mol (lower fraction is EOCl-L), and the extract was places in polyethylene (PE) bags and dried under normal temperature and pressure. Samples were irradiated for 15 min with a thermal neutron flux of $2.0–2.4\times10^{13}$ cm^{-2} · S^{-1} at KURNS. ^{38}Cl ($t_{1/2}$ = 37.18 min, E_γ = 1642, 2168 keV) were measured by using a Ge semiconductor detector for 300 sec. Concentrations in the samples were calculated using the comparison method between those and standard samples minus the amount of chlorine from the PE bag.

RESULTS: Figure(A) shows the results of EOCl-L in kite liver samples. EOCl-L averaged 15.9 ± 18.9 μg/g lipid overall. The concentrations of EOCl-L were decreased from 1977 to 1990. This may reflect a decrease in PCBs due to environmental regulations. On the other hand, no large changes were observed for both EOCl-L and PCBs after 2001. The indicated that in addition to PCBs remaining in the environment, the compounds in EOCl-L have not changed much. And it is possible that the compounds of anthropogenic origin have been present for a long time.

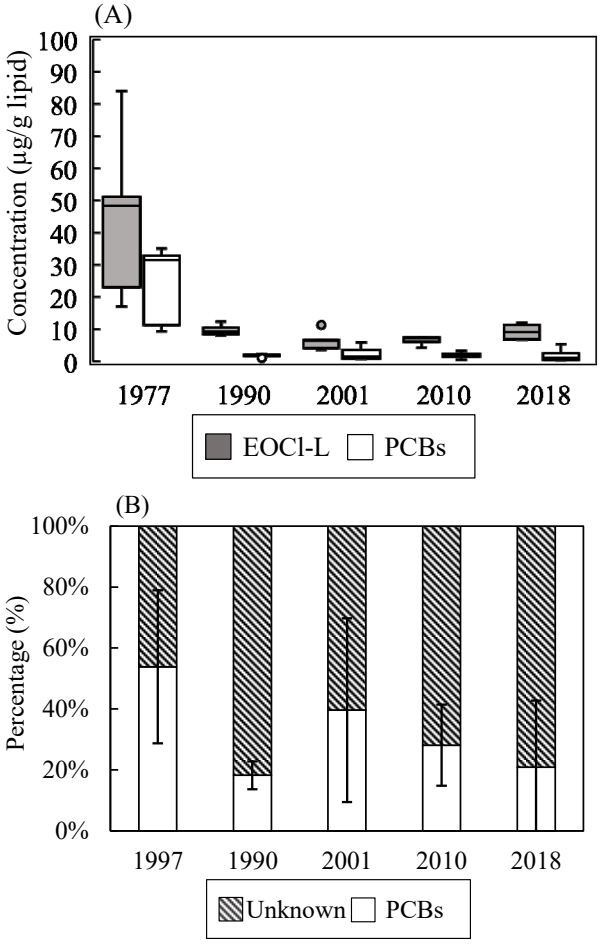

Figure(A) is the concentrations of EOCl-L and PCBs, and **Figure(B)** is the percentage of unknown Cl and PCBs in kite liver samples.

In the **Figure(B)**, the percentage of unidentified chlorine (i.e. EOCl-L - PCBs) in EOCl-L were about 50 %. The concentration of EOCl-L was also high in this year, suggesting that environmental contamination by chlorinated pesticides and other compounds had an impact for environment. In addition, the percentage of unidentified samples has been increasing since 2000, and in 2018, about 80 % of the EOCl-L were unidentified, so futher attention should be paid to this issue.

From this study, we were able to quantitatively evaluate the time change of EOCl-L and unidentified chlorine in kite liver samples. The results indicate that the threat from unidentified compounds is lower than in 1977, but the unidentified percentage has increased in recent years, suggesting the need for regular monitoring.

REFERENCES:

[1] K. Mukai *et al.*, Science of the Total Environment., **756** (2021) 143843.

[2] Watanabe *et al.,* (2021) 29th Symposium on Environmental Chemistry. Osaka, Japan.

CO5-6 Determination of Uranium in Local Fallout from A-bomb Using Fission-Track Analysis

K. Takamiya, N. Toe, M. Inagaki, Y. Oki and Y. Igarashi

Institute for Integrated Radiation and Nuclear Science, Kyoto University

INTRODUCTION: The distribution and properties of fallout materials those were released into the environment by atomic bombs and deposited on the ground surface is important to estimate exposure dose from residual radiation of the atomic bomb, as typified by the black rain. Measurements and determination of ^{137}Cs in fallout materials have been tried for collecting soil samples. However, since the origin of ^{137}Cs includes not only the atom-ic bomb fallout but also the fallout from atmospheric nuclear tests conducted around the world after 1950's, it is very difficult to identify its origin. Therefore, we considered the possibility of using insoluble particles containing uranium as an indicator of the atomic bomb-derived local fallout. Many insoluble particles containing radioactive cesium and uranium were found in the TEPCO Fukushima Daiichi Nuclear Power Plant accident [1], and similar insoluble particles could be produced by the atomic bombs. Therefore, we attempted to detect uranium-containing particles in soil using fission track method, which is used to detect trace amounts of uranium.

EXPERIMENTS: If particles in the soil contain high concentrations of uranium, these particles might have a higher specific gravity than general soil particles. Therefore, in order to efficiently detect particles containing uranium, we developed a method that combines heavy liquid separation and the fission track method [2, 3]. A sodium polytungstate (SPT) solution was used for heavy liquid separation. A part of soil sample collected in Hiroshima was mixed with SPT solution adjusted to 3.0 g/cm^3, and centrifuged at 3000 rpm for 10 minutes at room temperature to separate particles with a specific gravity more than 3.0 g/cm3. The separated particles were collected on a PTFE filter and attached to a track detector (BARYOTRAK-P, Fukuvi Chemical Industry Co., Ltd.) and wrapped by a paraffin film. Particles and the track detector were irradiated by about 3.10^{14} n/cm^2 of thermal neutrons using the pneumatic irradiation facility (TC-Pn) at Kyoto University Research Reactor. After the irradiation, the particles and filter were removed from the track detector together with the paraffin film, the surface was washed with pure water, and then etched with 8 M NaOH at 70 °C for 1 hour.

RESULTS: If a particle containing a high concentration of uranium exists, it is expected that tracks were observed radially around the particle. Fig. 1 shows an example of the results of an analysis of soil samples collected at the area where the black rain phenomenon was observed in Hiroshima Prefecture. At least two clusters of tracks can be detected in this figure. The enlarged image of the right cluster of Fig. 1 was shown in Fig. 2. The size of the particle forming the cluster in Fig. 2 is estimated to be several tens of μm. Many similar cluster of tracks were also detected in soil samples collected at the same point at different ground depths. On the other hand, such a cluster was not detected for fallout samples collected in Japan after 1960 by using similar fission track method. Therefore, the origin of this particle might not be an atmospheric nuclear test. In addition, very few clusters of tracks were detected for soil samples collected at locations about 20 km east from the hypocenter. Therefore, it is considered that the particles forming the clusters of numerous fission tracks in this experiment includes fallout materials derived from the atomic bomb.

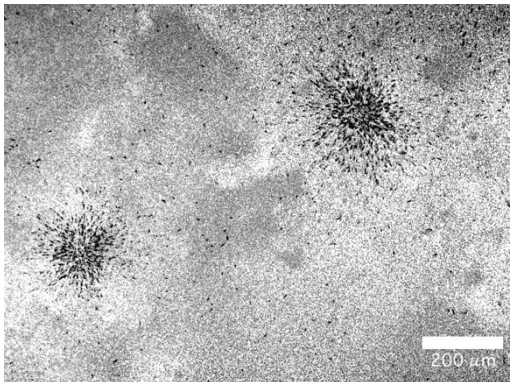

Fig. 1. Clusters of fission tracks observed on a track detector by neutron irradiation.

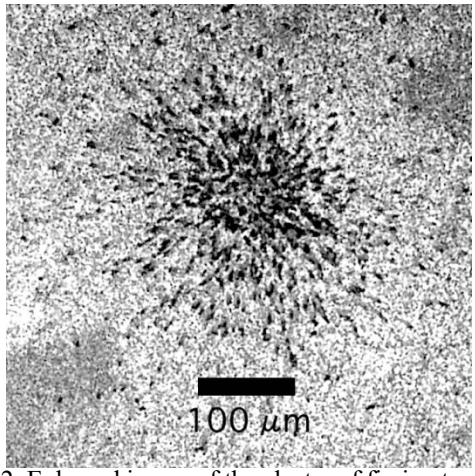

Fig. 2. Enlarged image of the cluster of fission tracks.

REFERENCES:

[1] Y. Abe *et al.,* Anal. Chem., **86** (2014) 8521-8525.
[2] K. Iguchi, J. Soc. Photogr. Sci. Tech. Jpn., **6** (2005) 59.
[3] F. Esaka *et al.*, Anal. Chem., **87** (2015) 3107-3113 .

CO5-7 Trace elements and Ar-Ar analyses of extraterrestrial materials

R. Okazaki[1], S. Sekimoto[2], N. Shirai[3], and J. Park[4]

[1]*Department of Earth and Planetary Sciences, Kyushu University*

[2]*Institute for Integrated Radiation and Nuclear Science, Kyoto University*

[3]*Department of Chemistry, Tokyo Metropolitan University*

[4]*Kingsborough Community College, the City University of New York*

INTRODUCTION: Meteorites and cosmic dust (micrometeorites) have diverse mineralogical, chemical, and isotopic compositions, which records their origins and evolution histories. Mineralogy and major element compositions can be obtained using commonly-used instruments, such as an electron micro-prove analyzer, whereas some of trace elements and Ar-Ar analyses require neutron irradiation. We have developed the analytical method to determine trace element compositions and Ar-Ar ages of individual submillimeter-sized extraterrestrial materials. This method has been applied to the Hayabusa2 samples in Projects #R3007, R3038, and R3127 using the Hydro irradiation in 2021.

EXPERIMENTS: Plagioclase and pyroxene mineral separates of 0.15-0.7 mg in weight were prepared from 7 eucrites (Agoult, HaH262, Yamato-792510, Y-792769, Y980318, Y980433, and Y983366) and a shergottite (Y002712). Bulk meteorite samples of 0.3-0.7 mg in weight (A12325 and Y002712 shergottites, DEW12007 lunar meteorite, NWA12542 nakhlite, and NWA8785 EH3 chondrite) were also prepared. The Allende CV chondrite (Provided by Smithonian museum [1]) of 0.07 mg and terrestrial minerals (orthoclase [2] and wollaston-ite) were used as the laboratory standards. Each of the samples was placed in a conical dimple (φ1, depth ~ 0.5 mm) of a sapphire disk (φ5.5, 1.5 mm thick), and covered with a sapphire disk (φ5.5, 0.3 mm thick). Each of the sapphire container was wrapped with pure aluminum foil. These Al-wrapped containers were stacked (Fig. 1) and sealed in the capsules for the Hydro irradiation. The irra-diation was operated at 1 MW for 47 h plus 5 MW for 6 h.

REUSLTS and DISCUSSION: The meteorite samples and the standard samples were irradiated in the Hydro irradiation term of Jan. 2023. One month later (on March 14-16), the irradiated samples were removed from the irradiation capsule. The Al foils that wrapped the sapphire containers were removed to avoid exposures to induced radioactivity from the Al foils. The containers were introduced into the SUS holders for transportation. In the original plan, we were going to measure gamma-rays of the irradiated samples to measure trace elements, but we gave up this measurement because of misfortune. Limited amounts of the irradiated samples were trans-ferred to Kyushu Univ., without detectable radioactivity from the samples. Each of the samples was picked up and placed into Al capsules for weighing and noble gas measurements (Fig. 2). The samples were installed into the vacuum system of the noble gas mass spectrometer at Kyushu Univ. Noble gas measurements are currently in progress.

Fig. 1. Meteorite samples and mineral standards in the sapphire containers wrapped with Al foils.

Fig. 2. Irradiated meteorite plagioclase (left column) and pyroxene (right column) samples in the Al foil capsules. The width of each photo is approximately 1 mm.

REFERENCES:

[1] E. Jarosewich *et al.*, Smithsonian Contributions to the Earth Sciences, **27** (1987) 1-49.

[2] S. Weiss, Mineralien Magasin Lapis. **16** (1991) 13-14.

CO5-8 ^{40}Ar-^{39}Ar Dating of Extraterrestrial Materials in KURNS

N. Iwata, S. Sekimoto[1], M. Inagaki[1], Y. N. Miura[2] and R. Okazaki[3]

Faculty of Science, Yamagata University
[1]Institute for Integrated Radiation and Nuclear Science, Kyoto University
[2]Earthquake Research Institute, University of Tokyo
[3]Department of Earth and Planetary Sciences, Kyushu University

INTRODUCTION: Radiometric dating is a valuable tool for unveiling the formation and evolution process of planetary material. The K-Ar and ^{40}Ar-^{39}Ar methods are invaluable to date the timing of heating events on planetesimals and asteroids (e.g. Swindle et al. (2014) [1]). The ^{40}Ar-^{39}Ar dating method with laser heating technique is suitable for tiny samples (e.g. Kelley, 1995 [2] and Hyodo, 2008 [3]). To date the extraterrestrial material by the ^{40}Ar-^{39}Ar method in KURNS, we have continued developing a ^{40}Ar-^{39}Ar dating system which includes laser-heating gas extraction and gas purification line.
Fig. 1 shows the latest schematic drawing of the system. A continuous Nd-YAG laser (~15 W) extracts gas from a neutron-irradiated sample. The extracted gas is purified using a Sorb-AC getter pump in the purification part. After the purification of extracted gas, argon isotope ratios in the gases are analyzed using an online connected quadrupole mass spectrometer. The whole of the extraction and purification parts will be evacuated by a rotary oil pump, two turbomolecular pumps and an ion pump to an ultra-high vacuum condition.

EXPERIMENTS & RESULTS: We have continued assembling the gas extraction and purification system in FY2022. Then, we could evacuate the extraction and purification parts. Pressure in the vacuum plumbing lines reaches 10^{-6} Pa at N1 on the top of the turbomolecular pump and 10^{-4} Pa at N2 under pumping (Fig. 1). The vacuum quality is several orders of magnitude higher than that of the ideal, insufficient to ^{40}Ar-^{39}Ar dating in KURNS. Bakeout is necessary to attain ultra-high vacuum conditions of the system. The vacuum condition (i.e., amounts of interfering isotopes) and the sensitivity of the quadrupole mass spectrometer (QMS) equipped with the system determine the amounts of samples required for analysis. Hence, the next step is to install the QMS to evaluate these factors.

REFERENCES:
[1] T. D. Swindle *et al.*, in Advances in ^{40}Ar/^{39}Ar Dating: from Archaeology *to Planetary Sciences*, edited by Jourdan, Mark, Verati (Geol. Soc., London, Spec. Pub. **378**, 2014) 333-347.
[2] S. P. Kelley, in Microprobe techniques in the earth sciences, edited by Potts, Bowles, Reed, Cave (Chapman & Hall, London, 1995) 327-358.
[3] H. Hyodo., Gondwana Res. **14** (2008) 609-616.

Explanation of Fig. 1. Latest schematic diagram of gas extraction and purification line in KURNS. RP, TMP, IP and Sorb-AC denote rotary pump, turbomolecular pump, ion pump and Sorb-AC getter pump, respectively. P1 and P2 are Pirani gauges. N1 and N2 are nude Bayard-Alpert ion gauges. CH denotes charcoal trap. QMS indicates quadrupole mass spectrometer. Equipment marked with dashed lines (QMS, CH, RP) is the forthcoming component.

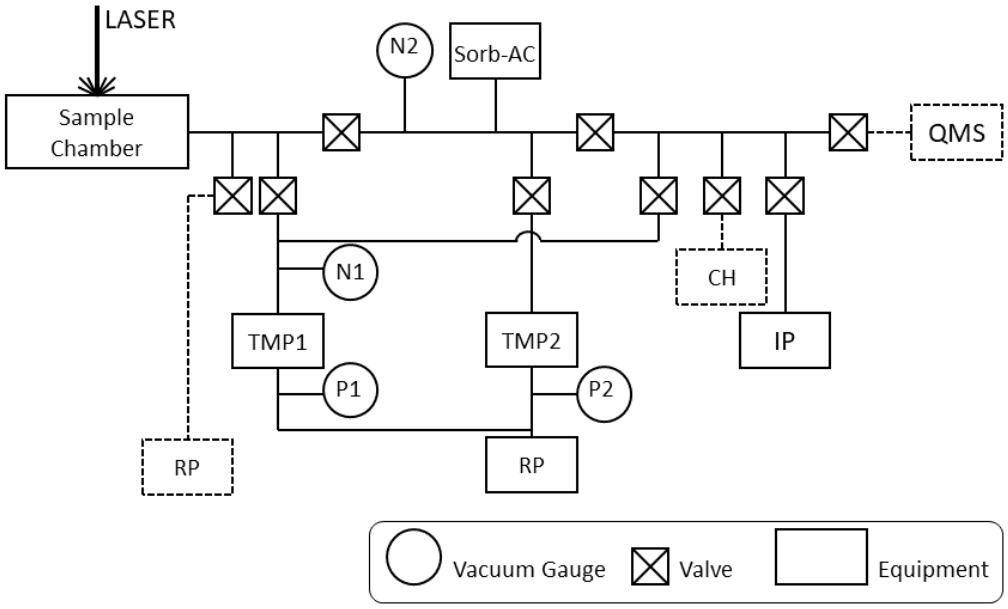

Fig. 1. Latest schematic diagram of gas extraction and purification line in KURNS.

CO5-9 Determination of Abundance of Rare Metal Elements in Seafloor Hydrothermal Ore Deposits by INAA Techniques-9: Behaviour of trace metal elements in gold-rich hydrotthermal ore deposits

J. Ishibashi, K. Kohama[1], K. Yonezu[1], T. Nozaki[2], R. Okumura[3], Y. Iinuma[3], H. Yoshinaga[3] and K. Takamiya[3]

Ocean-bottom Exploration Center, Kobe University
[1]Department of Earth Resources Engineering, Faculty of Engineering, Kyushu University
[2]Submarine Resources Research Center, Research Institute for Marine Resources Utilization, Japan Agency for Marine-Earth Science and Technology (JAMSTEC)
[3]Institute for Integrated Radiation and Nuclear Science, Kyoto University

INTRODUCTION: Instrumental neutron activation analysis (INAA) has several advantages for geochemical tools to provide useful information for mineral exploration. INAA enables highly sensitive multi-element analysis without geochemical pretreatment. We have conducted studies using mineralized samples collected from seafloor hydrothermal deposits, with a view to extend the range of application of this technique. Here, we report results of INAA analysis of some ores collected from a hydrothermal filed where occurrence of gold-rich ores had been reported [1].

SAMPLES: Ore samples collected from an active seafloor hydrothermal field on a submarine caldera volcano in Izu-Bonin Arc were provided for the study. Within the caldera, three active hydrothermal fields, Central Cone (CC) Site, South East (SE) Site and East (ES) Site, have been located. While CC site is located near the central cone, the other two sites are along the caldera wall.

EXPERIMENTS: INAA analysis was conducted by two runs. For short life nuclides, powdered samples of 10-20 mg were irradiated at Pn-3 (thermal neutron flux = 4.68×10^{12} n/cm^2/sec) for 30 seconds, and the gamma ray activity was measured for 3 minutes after adequate cooling time (3~15 minutes). For long life nuclides, powdered samples of 10-20 mg were irradiated at Pn-2 (thermal neutron flux = 5.50×10^{12} n/cm^2/sec) for 30 minutes, and the gamma ray activity was measured for 15 minutes after adequate cooling time (~30 hours).

RESULTS: As shown in Fig. 1, some interest correlations were recognized among concentrations of metal elements in the ores. Concentration of Au showed poor correlation with Zn regardless of the sampling sites (Fig. 1A). This correlation is in accordance with Au mineralization style as native Au or electrum, considering that Zn is the dominant element of the collected sulfide ores. Correlation between Ag and Sb concentrations (Fig. 1B) would be interpreted as a result of replacement in the tetrahedrite-tennantite system where Cu+As is replaced by Ag+Sb. These notable correlations suggest substantially high concentrations of Au and Ag in the hydrothermal fluid. For trace elements, In was detectable only for the SE and ES Sites showing correlation with Zn (Fig. 1C), whereas Co was detectable only for CC Site showing correlation with Fe (Fig. 1D). These correlations could be attributed to a result of replacement in the host sulfide minerals such as sphalerite and pyrite. Recognition of these trace elements in specific sites could be attributed to difference in chemical condition of the hydrothermal fluid among these three sites.

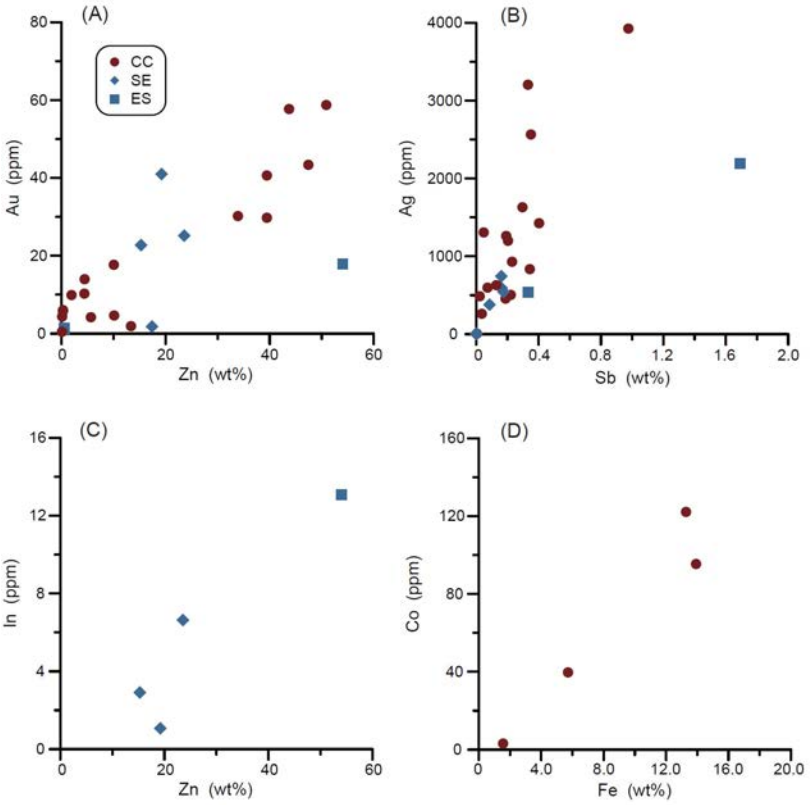

Fig. 1. Relationship between metal element concentrations of the ores. (A) Au vs Zn, (B) Ag vs Sb, (C) In vs Zn, (D) Co vs Fe

REFERENCES:

[1] K. Iizasa *et al.*, Mineralium Deposita, **54** (2019) 117-132.

R4077

CO5-10 Size distribution of metal elements in the atmospheric aerosols

N. Ito, A. Mizohata, Y. Iimura[1], H. Yoshinaga[1]

Radiation Research Center, Osaka Metropolitan University,[1] Institute for Integrated Radiation and Nuclear Science, Kyoto University

The atmospheric aerosols, the suspended particles existing anywhere in the atmosphere on the size range of 10nm-100 μm, effect our health by their depot ion(mainly fine particle) on the respiration tract and the lung, and also effect the climate by their absorption and reflect of the Sun light. To observe the size distribution and the chemical constituents of the atmospheric aerosols for the long period provide the data to analyze the air pollution effect to our health and the cause of global warming.

We have observed the atmospheric aerosols since 1995 at Sakai,Osaka and analyze the chemical components(ions,carbon elements and metals) in the atmospheric aerosols. In this report we show the size distribution data(central diameter) of the elements, which were analyzed by the neutron activation analysis using Kyoto University nuclear reactor.

We have collected the samples of the atmospheric aerosols by Andersen sampler, which collect the samples by 9 size rages(>11 μm ,11-7,7-4.7 μm ,4.7-3.3μm , 3.3-2.1,μm, 2.1-1.1 μm ,1.1-0.65 μm ,0.65-0.43μm ,<0.43μm) on the 1 week period at Osaka Metropolitan University(Osaka,Sakai). General size distribution of mass of the atmospheric aerosols, which have two peaks, fine(<2μm) and coarse(>2μm), is shown on Fig.1. Fine particles (atmospheric aerosols <2 μm m) are almost ions and carbon elements(organic and elementary carbon) and few of metals. Fine particles are produced by burning and chemical process from gaseous materials. Coarse particles(atmospheric aerosols > 2μm) are mainly soil particle and sea salt particles.

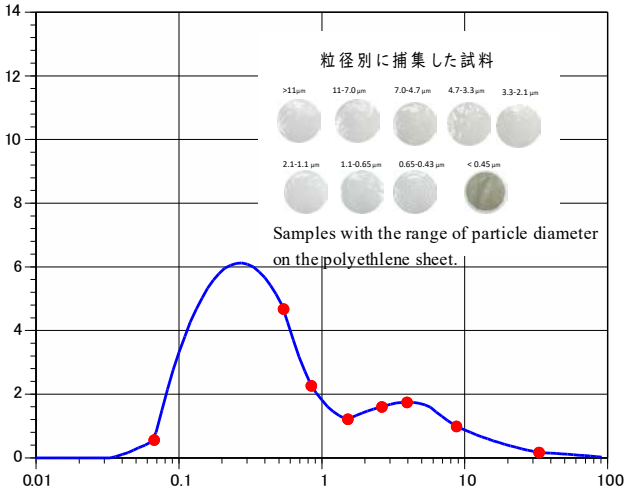

Fig.1. Example of mass size distribution of the atmosphe ric aerosols observed at Sakai, Osaka. The aerosols are cl lected by 9 size ranges.

We show the example of the size distribution of metal,V (Fig.2). The central diameter is the peak of fine particles. Result of the central diameter averaged by 70 samples from 1995 for the elements is shown via element melting point (Fig.3). The melting point of element relates to the creation of particles by the process of burning and emission from burning system.

From Fig3.,we can guess that the decrease trend of central diameter imples that high melting point element can makes fine particles that central diameter is smaller than 0.4μm. In the observed elements V and Mo which might be emitted from oil burning process, has smallest diameter and high melting point .

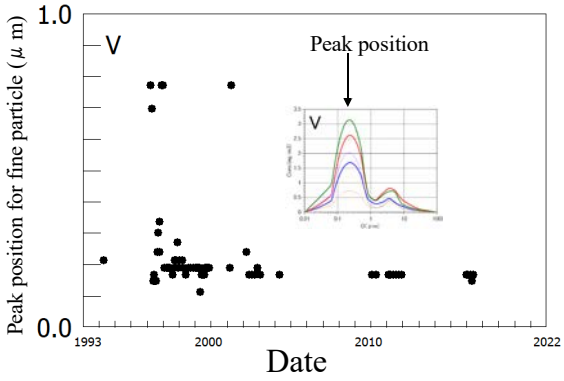

Fig.2. Central peraks and their yearly chage in va nadium(V) in the atmospheric aerosols observed at Sakai,Osaka.

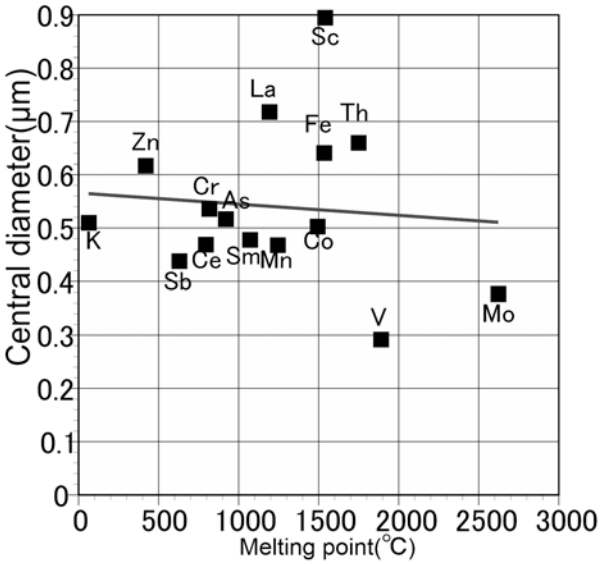

Fig. 3. Scatter graph on the central diameter and m elting point of the elements mainly observed in the fine particles.

CO5-11 Absorption of alkali metal ions by white radish sprouts (IV)

M. Yanaga, Y. Oshiro[1], T. Nakamura[1], H. Yoshinaga[2], R. Okumura[2] and Y. Iinuma[2]

Center for Radioscience Education and Research, Faculty of Science, Shizuoka University

[1]*Department of Chemistry, Faculty of Science, Shizuoka University*

[2]*Institute for Integrated Radiation and Nuclear Science, Kyoto University*

INTRODUCTION: More than 10 years after the Fukushima Daiichi Nuclear Power Plant accident, radioactive cesium still exists in the soil of the fields, and it is the cause of the harmful rumors. Separating radioactive cesium from the soil is necessary to prevent damage by rumors and to minimize the quantity of radioactive waste because simply removing the contaminated soil will result in a large amount of radioactive waste. Our previous reports have shown that the absorption of radioactive cesium ions from contaminated soil into rice plants increased by adding stable cesium ions to irrigation water, and that the possibility that the cesium ions added were replaced with radioactive cesium ions in soil [1, 2]. On the other hand, it was also found that addition of excess amount of stable cesium caused an obstacle to growth of rice plant [3].

We examined the removal of radiocesium from two types of soil, kuroboku soil (Andsols) and vermiculite, which were artificially contaminated with ^{137}Cs, through chemical treatment with various kinds of alkali ion solutions. The effect of decontamination with alkaline ions on the growth of plants was also investigated for white radish sprouts as model plants. In investigation of the behavior of trace elements in white radish sprouts, simulated decontamination with alkaline ions was performed on the soil containing no radioactive cesium and examined. White radish sprouts were also cultivated hydroponically in order to investigate the influence of alkali metal ions.

EXPERIMENTS: *^{137}Cs removal from soil* A sample (30 g) of commercially obtained vermiculite or kuroboku soil was placed in a metal mesh, immersed in 300 mL of aq. ^{137}Cs (10 Bq/mL) solution for one day, then removed from the solution and dried. After that, 35 mL of 0.014 mol/L KCl, RbCl or CsCl solution were added to a cen-trifuge tube containing 18 g of the contaminated soil and the mixture was stirred for 72 hours. Each soil was re-moved by filtration, then, washed with pure water. The same treatments were also applied to soil that was not contaminated with radioactive cesium.

Materials and Method The dried each soil mentioned above was placed in a plastic pot, wetted with pure water and 1.0 g of radish sprouts seeds were sown on it. After germination, Hyponex diluted 2000 times was added as liquid fertilizer. After that, they were cultivated for 4 - 5 days while giving only pure water as appropriate. White radish sprouts cultivated in soil without radioactive cesium were subjected to INAA. In hydroponics, seeds were sown on absorbent cotton and 30 mL of pure water was added. After germination, 10 mL of different concentrations (1.0×10^{-6} – 2.5×10^{-3} mol/L) of each alkali metal ions were added twice.

INAA The samples in polyethylene capsules were irradiated in Pn-3 for 90 seconds and in Pn-2 for 4 hours, for short and long irradiation, respectively. As comparative standards, the certified NIST Standard Reference Ma-te-rial 1577b Bovine Liver as well as elemental standard for Cs was used. The γ-ray spectroscopic measurements with an HPGe detector were performed repeatedly for the short-irradiated samples: the first measurements for 120 – 900 seconds after decay time of 5 - 15 minutes and the second one for 250 - 1200 seconds after 60 - 150 minutes. The long-irradiated samples were measured for 1 - 24 hours after an adequate cooling time (15 - 60 days).

RESULTS: Experimental results for removing radioactive cesium from soil showed that 10% or more of radioactive cesium was removed using any alkali metal ion. More than 20% of radioactive cesium was removed from vermiculite when rubidium ions or cesium ions were used. However, this high decontamination rate may be due to the fact that cesium ions are not strongly bound to vermiculite under the conditions in this experiment. When each soil that had been decontaminated once was washed with pure water, radioactive cesium was further removed, confirming that washing with water after decontamination is effective. The transfer coefficients of radioactive cesium to radish sprouts grown in soil after decontamination ranged from 0.03 to 0.16, and high transfer coefficients were shown when rubidium or cesium ions were used as decontamination agents.

The concentration of potassium ions in the hydroponically cultivated radish sprouts was decreased as the concentration of added rubidium ions or cesium ions increased, indicating a competitive relationship. However, the decrease in potassium ion concentration was not significant, but rather remained almost constant. On the other hand, the chloride ion concentration showed a different trend. Chloride ion concentration was almost constant when the added alkali metal ion (and chloride ion) concentration was in the range of 1.0×10^{-6} – 2.5×10^{-4} mol/L. However, above this range, significantly higher concentrations were shown. This indicates that changes in trace element concentration may indicate abnormalities even when no growth disorder is apparently observed. It is considered that exposure to the high-concentration solution caused abnormalities in the uptake mechanism of young roots.

REFERENCES:

[1] M. Yanaga *et al.*, NMCC ANNUAL REPORT, **22** (2015)185-190.
[2] M. Yanaga *et al.*, NMCC ANNUAL REPORT, **23** (2016)172-179.
[3] M. Yanaga *et al.*, KURNS Progress Report 2018 (2019) CO5-10.

CO5-12 Basic Study on Trace Elemental Analysis of Airborne Particulate Matters in an Environment by INAA & PIXE

N. Hagura[1,2,3], T. Matsui[3], T. Uchiyama[2], H. Matsuura[1,2,3]

[1] *Nuclear Safety Engineering, Science and Engineering, Tokyo City University*
[2] *Atomic Energy Research Laboratory, Science and Engineering, Tokyo City University*
[3] *Cooperative Major in Nuclear Energy, Integrative Science and Engineering, Tokyo City University*

INTRODUCTION: To discuss the elemental distribution of airborne particulate maters (APM) in an environment with large variability, it is necessary to accumulate a large amount of measurement data. Therefore, a sufficiently long time and a large number of samples are required. In order to efficiently perform a large number of measurements and analysis, we believe that it is important to use ion beam analysis methods in parallel with an analytical method using a nuclear reactor.
The Atomic Energy Research Laboratory of Tokyo City University (TCU-AERL) operated the Musashi reactor until 1989 and has been conducting research using neutrons, including instrumental neutron activation analysis (INAA). Although now it is in the decommissioning phase, the facility is still in operation as a facility for conducting experiments using RI. Since 2002, sampling of airborne particulate matter have been performed on our facility. In 2018, a 1.7 MV Pelletron tandem accelerator (TCU-Tandem) was installed and began performing trace element analysis using Particle Induced X-ray Emission (PIXE) [1].
In near future, unfortunately it may become increasingly difficult to conduct experiments using research reactors. Therefore, we believe that the use of accelerator ion beams is an effective means of advancing analytical methods. In addition, ion beam analysis is expected to provide more valuable measurement data, including information on chemical bonding states.
In this study, trace element analysis by instrumental neutron activation analysis and measurement by ion beam analysis using a tandem accelerator were conducted on the APM samples. And also we have considered a system concept that enables measurement with energy resolution at a level that can determine chemical form, namely, wavelength dispersive spectroscopy PIXE (WDS-PIXE) analysis method.

EXPERIMENTS: The sampling method for airborne particulate matters is explained. We use a high volume air sampler (Shibata Scientific Technology LTD., HV-1000F, filter: ADVANTEC, QR-100 (collection efficiency: 99.99% for 0.3 μm particles)) with an inhalation flow rate of 700 L min^{-1}. The radioactivity of the filter that has collected dust is measured by a high-purity germanium (HP-Ge) semiconductor detector, and a part of the filter was stored for INAA.
The conditions of the INAA method are described. Irradiation was performed at the research reactor KUR at the Institute for Integrated Radiation and Nuclear Science, Kyoto University, between the December and February with four machine times in FY2022. The irradiation conditions are shown in Table 1. The measurement of radioactivity of short half-life nuclides was carried out using the HP-Ge semiconductor detector of the hot laboratory of KUR. And long and medium half-life nuclides, after cooling for one or two weeks, transported to the TCU-AERL, and was measured by a HP-Ge semiconductor detector. JLk-1 and others were used as a comparative standard substance.

RESULTS: This year, several samples of stocked airborne dust from 2011, 2016, 2017, and 2018 were measured. In addition, PIXE analysis is being conducted at TCU-Tandem. We plan to summarize the data together with the results of past measurements. Figure 1 shows the concept of a wavelength-dispersive spectroscopy PIXE (WDS-PIXE) analysis system [2]. This concept is characterized by the application of image processing techniques to the acquisition of X-ray bright spots to improve positional resolution. The aim is to achieve high energy resolution while maintaining a compact size. We have constructed an analytical chamber and confirmed that it is possible to cover the target elemental range in the measurement of atmospheric airborne dust samples by appropriately selecting spectroscopic crystals.

Table 1. Irradiation conditions.

Irradiation			Operating power	Thermal neutron flux
date	time	position		
2022/12/6	60 min	Pn-2	1 MW	5.5 x 10^{12} n/cm^2/sec
2023/1/24	60 min	Pn-2		5.5 x 10^{12} n/cm^2/sec
2023/2/8	30 sec	Pn-3		4.7 x 10^{12} n/cm^2/sec
2023/2/14	60 min	Pn-2		5.5 x 10^{12} n/cm^2/sec

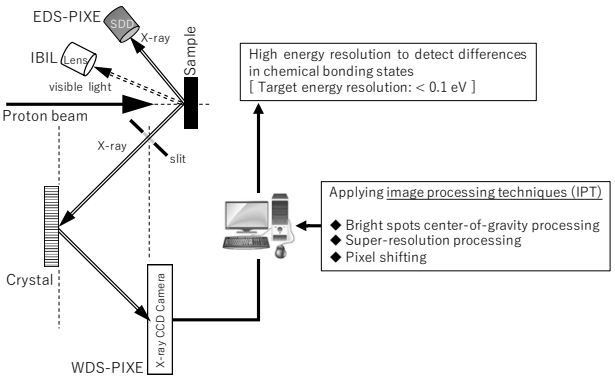

Fig. 1. Conceptual diagram of wavelength-dispersive spectroscopy PIXE analysis system [2] .

REFERENCES:

[1] N. Hagura *et al.,* Trans. At. Energy Soc. Japan, **17 (3-4)** (2018)111-117.
[2] K. Ushijima *et al.,* 2022 IEEE NSS MIC RTSD, (2021)NSS-20-154.

CO5-13 Ar-Ar Dating for Differentiated Meteorites

Y. N. Miura, R. Okazaki[1], S. Sekimoto[2], M. Inagaki[2] and N. Iwata[3]

Earthquake Research Institute, University of Tokyo
[1]Earth and Planetary Sciences, Kyushu University
[2]Institute for Integrated Radiation and Nuclear Science, Kyoto University
[3]Faculty of Science, Yamagata University

INTRODUCTION: Extra-terrestrial materials, such as meteorites and samples collected by asteroid/planetary explorations, provide a variety of information for understanding the origin and evolution of the solar system. In particular, age determination gives us direct knowledge about thermal histories as well as timing of the events occurred in solar nebular and on the parent bodies (e.g., [1, 2]). The K-Ar/Ar-Ar ages (a chronometer based on the ^{40}K-^{40}Ar pair) likely correspond to thermal metamorphism, aqueous alteration or impact heating on the parent bodies (e.g., [3]). The Ar-Ar dating method, a variant of K–Ar dating, uses ^{39}Ar as a proxy for ^{40}K; ^{39}K is converted partly to ^{39}Ar by irradiation of fast neutrons. Therefore, Ar-Ar ages can be determined by ^{40}Ar/^{39}Ar ratios for a common spot between K and Ar. In addition, reliability of the ages are examined by age spectra obtained from the step-heating method, that is a sample is heated stepwisely and released Ar of each step is measured. In order to perform Ar-Ar dating for extra-terrestrial samples, we attempt to establish the analytical protocol and apparatus at KURNS. A system consisting of gas extraction, gas purification and Ar isotope measurements is being constructed.

EXPERIMENTS and RESULTS: The gas extraction/purification line is composed of a CW Nd:YAG laser, a Sorb-ac getter, two vacuum gauges, two turbo molecular pumps (each TMP equips with a rotary pump and a pirani gauge), an ion pump, valves and connection parts (Fig. 1). For Ar isotope measurements we are preparing a quadrupole mass spectrometer (QMS), which is now attached to a vacuum line at University of Tokyo and will be connected to the line at KURNS in FY2023. Usefulness of QMS has been reported for K-Ar/Ar-Ar dating (e.g., [4-6]). The gas extraction/purification line was evacuated by the two turbo molecular pumps and its vacuum pressure reached to 10^{-6} Pa near the vacuum pump and to 10^{-4} Pa at the gas purification line (near the Sorb-ac getter). In order to measure Ar isotopes for Ar-Ar dating, vacuum condition has to be improved by bakeout and degassing the Sorb-ac getter. The Nd:YAG laser (maximum output power ~15W) was set up by attaching objective lens, eyepiece lens and an optical light (Fig. 2, a picture of the laser before attaching eyepiece lens and the optical light). Laser irradiation was performed to a test piece. During the test irradiation we controlled output power still low so that it was not enough to melt rock samples. We will adjust optical alignment and apply laser-irradiation with higher power to rock samples.

Fig. 1 A picture of the gas extraction/purification line. The line was evacuated by two turbo molecular pumps. The vacuum pressure was monitored by two ion gauges. A QMS and a sample chamber will be connected to ICF34 ports of the line.

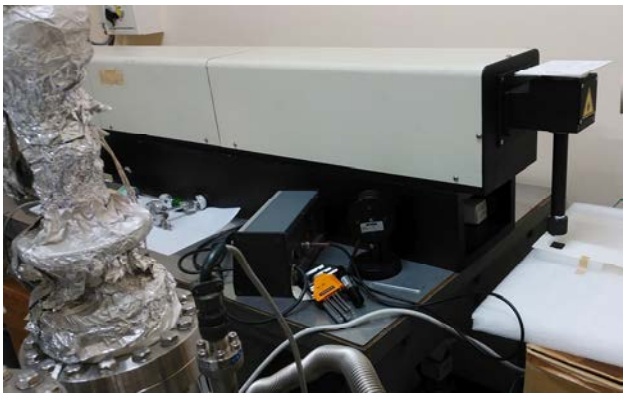

Fig 2. A picture of the CW Nd:YAG laser, which is under setup processes and will be used for extraction of Ar from rock samples.

REFERENCES:

[1] D. S. Lauretta and H. Y. McSween, Meteorites and the Early Solar System II (Space Science Series, Univ. of Arizona Press) (2006).
[2] A. Longobardo, Sample Return Missions: The Last Frontier of Solar System Exploration (Elsevier) (2021).
[3] D. Bogard, Chemie der Erde, **71** (2011) 207-226.
[4] B. Schneider *et al.,* Quaternary Geochronology, **4** (2009) 508-516.
[5] Y. Cho *et al.* Planet. Space Sci., **128** (2016) 14-29.
[6] Y. Cho and B. A. Cohen, Rap. Comm. Mass Spectrometry, **32** (2018) 1755-1765.

CO5-14 Halogen and noble gas characteristics of subcontinental lithospheric mantle beneath southwestern North America and northwestern Africa

H. Sumino, Y. Hibiya, M. Fukagawa[1], J. Ren[1], T. Oishi[1], A. Takenouchi[2], Y. IInuma[3], R. Okumura[3], H. Yoshinaga[3] and S. Sekimoto[3]

Research Center for Advanced Science and Technology, University of Tokyo
[1]Graduate School of Arts and Sciences, University of Tokyo
[2]Kyoto University Museum, Kyoto University
[3]Institute for Integrated Radiation and Nuclear Science, Kyoto University

INTRODUCTION: The subcontinental lithospheric mantle (SCLM) is generally metasomatized by intra-plate or arc magmatism, making them distinct geochemical reservoirs from mid-ocean ridge basalts (MORBs) and ocean island basalt (OIB) sources. Higher $^{3}He/^{22}Ne$ is observed in mantle-derived xenoliths from the SCLM in Patagonia, South America [1], compared to MORBs and OIBs, which reflect the composition of the convecting mantle and plume source, respectively. Based on this $^{3}He/^{22}Ne$ difference, SCLM is expected to be a distinct geochemical reservoir that has evolved differently from the convecting mantle and plume sources in terms of noble gases [2]. The average $^{3}He/^{4}He$ of SCLM-derived peridotite samples is about 6 Ra [3], where 1 Ra = 1.4×10^{-6} represents atmospheric $^{3}He/^{4}He$, suggesting that the contribution of radiogenic ^{4}He derived from the decay of U and Th to SCLM is more significant than that to the convecting mantle with $^{3}He/^{4}He$ of ca 8 Ra. In addition, Ne isotopic compositions of the SCLM samples from Patagonia in South America have been confirmed to have a more significant contribution of nucleogenic ^{21}Ne from $^{24}Mg[n,\alpha]^{21}Ne$ and $^{18}O[\alpha,n]^{21}Ne$ reactions compared to MORBs. If the SCLM is a globally homogeneous reservoir, these features are expected to be observed in SCLMs in other regions. Therefore we analyzed noble gases and halogens in SCLM-derived samples from the Lunar Crater volcanic field, Toroweap flow, the Mendocino Mountains, and Mount Emma in southwestern North America, and Beni Bousera peridotite body in northwestern Africa.

EXPERIMENTS: The samples of 5-50 mg each and standards for neutron fluence were wrapped with aluminum foil and put in aluminum capsules of ϕ10 mm x 30 mm. The capsules were irradiated with neutrons in KUR. After the irradiation, the samples were sent to the University of Tokyo. The samples were loaded into an ultrahigh-vacuum, noble gas extraction, purification, and separation line. Argon was extracted from the samples by heating up to 1800°C, purified with hot titanium-zirconium getters, separated into each noble gas with temperature-controlled cold traps, and then determined their isotope compositions with a noble gas mass spectrometer [4,5]. The fast neutron flux was estimated as (1.0–1.2) × 10^{18} neutrons cm^{-2}, from the production of ^{39}Ar from ^{39}K in the Hb3gr hornblende standard in which K contents have been determined by [8].

RESULTS: The samples from southwestern North America have $^{3}He/^{4}He$ that fall within the range of the convecting mantle. On the other hand, the $^{3}He/^{4}He$ ratios of the Beni Bousera peridotite samples are low, ranging from 0.3 Ra to 0.7 Ra. The Ne isotope ratios of the southwestern North America samples are also accounted for by mixing between air and convecting mantle endmembers. In contrast, those of the Beni Bousera peridotite samples suggest the addition of nucleogenic Ne to the atmospheric compositions. These results indicate that the SCLM is not a homogeneous geochemical reservoir of noble gases.
The MORB-like He and Ne feature of the samples from southwestern North America differs from those of other SCLMs. This result suggests that the SCLMs beneath these regions were incorporated into the mantle convection by delamination, resulting in compositional overwriting with the convecting mantle component. The contribution of nucleogenic ^{21}Ne correlates with that of radiogenic ^{4}He and is substantial in the Beni Bousera peridotite body samples. The sample was reported to have experienced deformation and dynamic recrystallization, which may have resulted in the loss of mantle-derived noble gases.
In contrast to the noble gas features, the Br/Cl and I/Cl ratios of the samples from southwestern North America and northwest Africa share similar characteristics in which Br/Cl and I/Cl range 1.2-7.8 $\times 10^{-3}$ mol/mol and 61-860 $\times 10^{-6}$ mol/mol, respectively, while I/Br showed fewer variations (0.031-0.110 mol/mol). Both samples are from the back-arc regions of the subduction zones, and a similar feature was observed for mantle-derived xenoliths in Takashima, northwestern Kyushu, Japan, which is also in the back-arc region. Therefore, it is possible that this feature is common in the back-arc regions of subduction zones and may result from Cl depletion in the mantle wedge having higher I/Cl due to the addition of iodine-rich subducted halogen component.

REFERENCES:
[1] T. Jalowitzki *et al.*, Earth Planet. Sci. Lett., **450** (2016) 263-273.
[2] N. Dygert *et al.*, Earth Planet. Sci. Lett., **498** (2018) 309-321.
[3] C. Gautheron, and M. Moreira, Earth Planet. Sci. Lett., **199** (2002) 39-47.
[4] N. Ebisawa *et al.*, J. Mass Spectrom. Soc. Jpn. **52** (2004) 219-229.
[5] M. Kobayashi *et al.*, Chem. Geol. **582** (2021) 120420.
[6] J. C. Roddick, Geochim. Cosmochim. Acta **47** (1983) 887-898.

CO5-15 Determination of Cl, Br and I contents in U. S. Geological Survey reference materials by RNAA

S. Shirai, S. Sekimoto[1], M. Ebihara[2]

Department of Chemistry, Faculty of Science, Kanagawa University
[1]Institute for Integrated Radiation and Nuclear Science, Kyoto University
[3]Department of Chemistry, Tokyo Metropolitan University

INTRODUCTION: Compared with other trace elements, cosmochemical and geochemical behaviors of halogen elements are still not well understood. The major reason is that there are a limited number of techniques available to precisely analyze the halogen contents in solid samples. As a result, large variations exist between the reported values in geological reference samples. Recently, ICP-MS has been commonly used for the determination of halogen contents. In this method, halogens are extracted from rock samples by pyrohydrolysis. As mentioned by Sekimoto and Ebihara [1], the quantitive collection of halogens cannot always be achieved by phrohydrolysis. In this study, halogen contents in rock samples are determined by radiochemical neutron activation analysis, and the obtained analytical results were evaluated.

EXPERIMENTS: Standard solutions of Cl, Br, and I were prepared by dissolving know amounts of chemical reagents (KCl, KBr, and KI) into high-purity water. For I, KOH was added to stabilize I^- in the solution. Chemical reference samples of three halogens were prepared by pipetting know amounts of these standard solutions onto filter papers.
BHVO-2 prepared U.S. Geological Survey was used in this study. This reference material was in powder and was not subjected to any additional treatment such drying. BHVO-2 weighing about 110 to 320 mg was weighed in a clean plastic vial. This geological reference materials together with a set of chemical reference samples of three halogens were irradiated with neutrons for 10 min. After cooling for 10 min, geological reference material was transferred into a Ni crucible, in which known amounts of the three halogen carriers in solution were taken and dried with a proper amount of concentrated NaOH solution. NaOH in pellets was added and heated gently for 3 min, then strongly for 5 min over a Mecker burner. After cooling for a few min, H_2O was added to the fusion cake. The precipitate was separated by centrifugation and Na_2SO_3 as a reductant was added to the obtained supernatant. 6M HNO_3 and $Pd(NO_3)_2$ in solution was added. The PdI_2 precipitate was collected onto filter paper. $AgNO_3$ in solution was added to the filtrate in order to precipitate Cl^- and Br^- as AgCl and AgBr. These precipitates were collected onto filter paper. These precipitates were dried under a heat lamp and measured for gamma rays. Chemical yields of the three halogens were determined by reactivation method. The precipitates were again irradiated with neutrons for a few seconds together with reference samples. After cooling, these samples were measured for gamma rays. The analytical procedure used in this study was essentially the same as those of Sekimoto and Ebihara [1].

RESULTS: Analytical results for the three halogens for BHVO-2 are indicated in Table 1, where literature values [2-5] are also shown for comparison. BHVO-2 was analyzed five times, and the mean values with one standard deviation repeatabilities are calculated and indicated. The three halogen contents were determined by using noble gas mass spectrometry (NG-MS) [2]. In this method, the samples were irradiated, and halogen-derived noble gas isotopes produced were analyzed. Three halogens were extracted from samples by pyrohydrolysis technique, and Cl, and Br and I were determined by ion chromatography and ICP-MS, respectively [3,4]. The analytical procedure used in [5] was the same as used in this study. As shown in Table 1, ion chromatography value for Cl [3] is higher than both literature values, and our data are consistent with literature values [2,4,5]. There are good agreements of Br values among our data and literature values. In contrast, there is a large deviation of I values. Our data are in agreement with NG-MS value [2], and inconsistent with other literature values [3-4]. There are no reasonable explanations for this discrepancy. As a careful preparation of chemical references of I was performed in this study, it is suggested that our values are more reliable.

REFERENCES:

[1] S. Sekimoto and M. Ebihara, Anal. Chem., **85** (2013) 6336-6341.
[2] M. A. Kendrick *et al.,* Geostand. Geoanal. Res., **42** (2018) 499-511.
[3] A. Michel and B. Villemant, Geostand. Geoanal. Res., **27** (2003) 163-171.
[4] H. Balcone-Boissard *et al.,* Geostand. Geoanal. Res., **33** (2009) 477-485.
[5] S. Sekimoto and M. Ebihara, Geostand. Geoanal. Res., **41** (2017) 213-219.

Table 1. Analytical results of three halogens (Cl, Br and I) in BHVO-2.

	Cl (ppm)	Br (ppm)	I (ppm)
This work (n = 5)	90.6±4.5	0.240±0.012	0.0592±0.0078
Kendrick et al. [2]	102±1	0.259±0.005	0.070±0.040
Michel and Villeman [3]	150±21	0.269, 0.277	0.016±0.002
Balcone-Boissard et al. [4]	81±11	0.29±0.10	0.020±0.012
Sekimoto and Ebihara [5]	104±1	0.240±0.013	0.307±0.050

R4166

CO5-16 Phase identification and amorphous structure analysis of chondrule-simulated samples

Y. Seto, T. Araga[1], Y. Tarutani[1], Y. Umeda[2], T. Okuchi[2]

Department of Geoscicences, Graduate School of Science, Osaka Metropolitan University
[1]Department of Mechanical Engineering and Science, Graduate School of Engineering, Kyoto University
[2]Institute for Integrated Radiation and Nuclear Science, Kyoto University

INTRODUCTION:

Chondrites are the most common type of meteorite that formed during the earliest period of the solar system. They contain spherical objects, called chondrules, with diameters ranging from 0.1 to 10mm. Chondrules are thought to have formed when aggregates of dust that coalesced and grew within the protoplanetary disk melted due to instantaneous heating, and then rapidly cooled.

It is believed that chondrules were primarily composed of glassy or low-crystallinity silicates, but their internal texture changed due to various subsequent processes (re-melting, shock-induced metamorphism, thermal metamorphism) after their formation. Unraveling the process of these changes is an important clue to deciphering the material evolution of the early solar system.

The reaction of silicate glasses to heat and shock is, however, generally slow and difficult to reproduce in the laboratory. In this study, we used GeO_2 glass as an analog of the chondrule to examine how crystallization proceeds in response to shock compression.

EXPERIMENTS:

GeO_2 glass samples were prepared by placing pelletized GeO_2 powder in a platinum container, heating and melting it at 1300-1450°C for 8-24 hours using a vertical tube furnace (at Osaka Metropolitan University) and quenching it under air.

The glass samples were carefully pulverized in a mortar, sealed in a stainless-steel container, and then subjected to shock compression (maximum pressure of 17 GPa) by striking a projectile using a single-stage powder gun (at National Institute for Materials Science).

Diffraction profiles of the samples before and after the impact compression were obtained using a fully automated multi-purpose X-ray diffractometer (Rigaku SmartLab) in the range of 5° to 120° using Cu Kα rotation anode X-ray tube. The profiles were analyzed using the software PDIndexer [1].

RESULTS and DISCUSSION:

In the diffraction profile of the glass sample before shock compression (blue line in Figure 1), there are no distinct diffraction peaks, and a halo pattern characteristic of the short-range order structure in amorphous materials can be observed.

On the other hand, in the profile after impact compression (orange line in Figure 1), slightly broad but distinct diffraction peaks were observed. Comparing the diffraction peaks with known crystal phases of GeO_2 revealed that most of them could be indexed by the quartz structure, but there were also peaks derived from the rutile structure. In the quartz structure, Ge is four-coordinated with surrounding oxygen, whereas in the rutile structure, it is six-coordinated. The latter structure exhibits a higher density compared to the former.

The present shock compression experiments and analyses of X-ray diffraction profiles show that GeO_2 glass can easily crystallize and change to a dense structure. Since the timescale of shock events in the solar system is much longer than that of laboratory shock compression experiments, it is quite possible that such crystallization and densification can occur even in silicate glasses, which have slower crystallization kinetics. In fact, a number of dense silicate minerals have been found in impact melts in meteorites [2,3]. We plan to further investigate the crystallization process of amorphous materials during shock compression by changing the shock pressure and the chemical composition of the starting materials.

REFERENCES:

[1] Seto *et al.*, Rev. High Press. Sci. Technol., **20** (2010) 269-276.
[2] Tomioka and Okuchi, Sci. Rep., **7** (2017) 17351.
[3] Tschauner *et al.*, Science, **346(6213)** (2014) 1100-2.

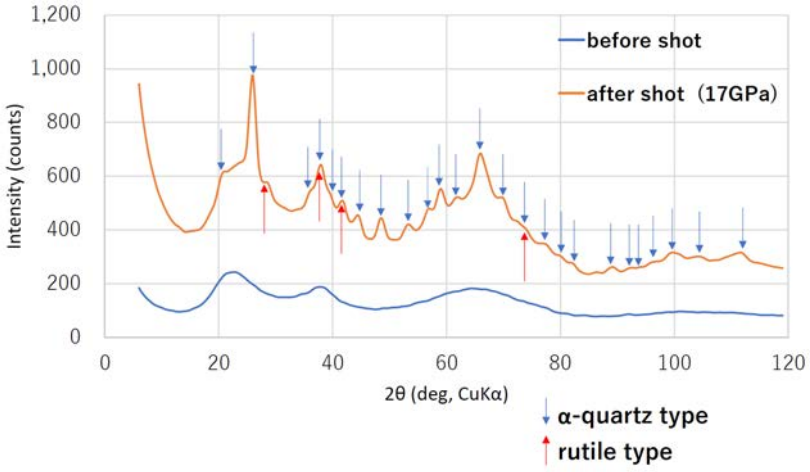

Fig. 1. Diffraction profiles of the GeO_2 samples before (blue) and after (orange) the impact compression. Before the shock, a halo pattern characteristic of glass materials was observed, but after the shock, a slightly broad diffraction peak was observed.

CO5-17 Distribution of radiocesium in forestry area in Fukushima -focusing on inner bark-

T. Ohta, S. Fukutani[1], T. Kubota[2], Y. Mahara[3]

Department of Nuclear Technology, Nagaoka University of Technology
[1] Institute for Integrated Radiation and Nuclear Science, Kyoto University
[2] Agency for Health, Safety and Environment, Kyoto University
[3] Kyoto University

INTRODUCTION: Vast forest was markedly contaminated by radioactive plums containing radiocesium in the wide range of the eastern part of Japan in 2011 [1–7]. As forests have an important role in preventing landslides and maintaining the ecological and hydrological system, the destructive forest should be avoided and an appropriately managed tree-felling should be conducted. It is necessary to know the environmental dynamics of radiocesium in forest to keep the forestry vividly.

In our previous field study [1], most of the radiocesium in the tree rings was directly absorbed by the atmospheric direct uptake via the bark and leaves rather than by roots. The chemical form of radiocesium on the leaves and bark would have been a mixture of water-soluble and insoluble forms. Another our previous study [2] demonstrated that the effluence rate of radiocesium (^{137}Cs) obtained from dissolved assay experiments on the trunks of *Cryptomeria japonica (Japanese cedar)*, indicating that the radiocesium in the trees was mainly water-soluble. We also directly measured root distribution of *Cryptomeria japonica*[3], indicating that mature it is not effective to absorb radiocesium by the root uptake due to the distribution of the fine root[3, 5].

After the accident, radioactive cesium was efficiently absorbed from the bark into xylem, but it is believed that the radioactive cesium in the bark does not migrate after that. Without a route from the inner bark to the xylem, radioactive cesium will remain on the surface of the xylem in the future. We measured the concentration of radioactive cesium the inner bark outside the xylem.

EXPERIMENTS: Barks were collected at the Koriyama, Fukushima. *Quercus serrata* was harvested prior to leaf fall at the end of September 2012 and *Cryptomeria japonica* was harvested at the end of October 2012. After cutting the trees, we carefully and completely stripped off all bark from the tree trunk. The collected the samples in the field were transported to the laboratory and stored it in the dark for 11 years. After separating the outer and inner bark, the ^{137}Cs in the inner bark was determined by gamma-ray spectrometry (HPGe). The concentration of ^{137}Cs was corrected on March 12, 2011.

RESULTS: Fig. 1.(a) and (b) show concentration of ^{137}Cs in the inner bark of the *Cryptomeria japonica* and *Quer-cus serrata*, respectively. The concentration of the ^{137}Cs in the inner bark of the *Cryptomeria japonica* was higher than that in the *Quercus serrata*. These may also depend on the ease of aerosol penetration and the shape of the bark.

The concentration of the xylem at the same site was less than 50Bq/kg collected in 2014 in the same site. The concentration of radiocesium did not increase from 2012 to 2014. The concentrations in the inner bark of the *Cryptomeria japonica* were three orders of magnitude higher than those in the xylem. We concluded that the radioceisum was not absorbed from not only the root but also inner bark effectively. However, our target trees are mature trees, and there is no guarantee whether the same tendency is observed in young trees.

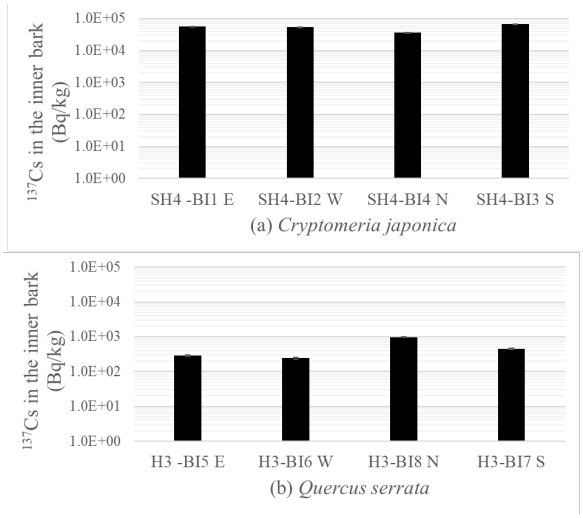

Fig. 1. Concentration of ^{137}Cs in the inner bark

REFERENCES:

[1] Y. Mahara *et al.,* Sci. Rep., **4** (2014) 7121.
[2] T. Ohta *et al.,* J. Radioanal. Nucl. Chem., **310** (2016) 109-115.
[3] Y. Mahara *et al.,* Sci. Rep., **11** (2021) 8404
[4] T. Ohta *et al.,* Radiological Issues for Fukushima's Revitalized Future, edited by T. Takahasi (Springer, 2016) 13-24.
[5] T. Ohta *et al.,* KURNS Progress Report 2021, p151
[6] T. Ohta *et al.,* Ana. Sci., **29** (2014) 941-947
[7] T. Ohta *et al.,* J. Environ. Radioact., **111** (2012) 38-41

CO6-1 Radioresistance Mechanisms Acquired by Adaptive Evolution and their Evolutionary Mechanisms III

T. Saito

Institute for Integrated Radiation and Nuclear Science, Kyoto University

INTRODUCTION: Organisms have evolved diverse forms by adapting to various environmental conditions, and some can survive in hostile environments. Studying these adaptive mechanisms can provide meaningful information regarding the evolution and biological diversity of organisms. Some radioresistant bacteria are highly resistant to ionizing radiation [1]. The mechanism through which bacteria resist ionizing radiation is an interesting research subject considering the adaptive mechanisms employed by organisms in nature. To elucidate the mechanisms of radioresistance in these organisms, the biological defense mechanisms against external stress must be investigated at the molecular level. However, studies on naturally occurring radioresistant organisms are particularly challenging, owing to limited knowledge of their genetic and biochemical properties. Therefore, in this study, radioresistant *Escherichia coli*, whose wild-type genetic and biochemical characteristics have been elucidated in detail, were generated via an adaptive evolution experiment using gamma rays as the selective pressure, and the characteristics of the evolved radioresistant *E. coli* were compared with those of the wild type. Previously, radioresistant *E. coli* have been generated with a 7.9-fold resistance compared with wild-type *E. coli* [2, 3, 4]. This report describes the differences in gene expression status between wild-type and radioresistant *E. coli*.

EXPERIMENTS: Extraction of total RNA and RNA sequencing : Total RNA was extracted from *E. coli* cells using RNAiso Plus (Takara) and further purified using NucleoSpin RNA Clean-up XS (Macherey-Nagel). The quality of total RNA was evaluated and confirmed using an Agilent 2100 Bioanalyzer (Agilent Technologies). rRNA was removed from the total RNA using a Ribo-Zero Magnetic Kit (Gram-Negative Bacteria) (Illumina). A sequence library was prepared from the resulting RNA using a TruSeq Stranded mRNA Sample Prep Kit (Illumina). The quality of the sequence library was evaluated and confirmed using an Agilent 2100 Bioanalyzer. Sequence analysis was performed using NovaSeq 6000 (Illumina), NovaSeq 6000 S4 Reagent Kit (Illumina), and NovaSeq Xp 4-Lane Kit (Illumina). Gene expression levels were analyzed using Genedata Profiler Genome (Genedata) and STAR [5]. All procedures were performed according to the manufacturer's instructions.

Analysis of gene expression status: In the analysis, gene expression data with “fragments per kilobase of transcript per million mapped fragments” values less than 1 for all samples from the two groups compared were filtered to eliminate noise data. Differentially expressed genes (DEGs) in radioresistant *E. coli* compared with wild-type *E. coli* were identified using Welch's t-test and correction for multiple testing using the Benjamini and Hochberg method (BH method) [6]. Furthermore, Kyoto Encyclopedia of Genes and Genomes (KEGG) pathway analysis of DEGs in radioresistant *E. coli* relative to wild-type *E. coli* was performed using the Database for Annotation, Visualization and Integrated Discovery bioinformatics resources ver.6.8.

Statistical analysis: Welch's t-test and the BH method were used to identify DEGs among many genes, and a q-value of less than 0.05 was considered significant. The Expression Analysis Systematic Explorer score was used to test for significance in KEGG pathway analysis, and a P-value of less than 0.05 was considered significant [7].

RESULTS: KEGG pathway analysis revealed that genes involved in metabolism-related pathways are enriched in genes up-regulated in radioresistant *E. coli* compared with wild-type *E. coli*. Previously, the high expression of genes involved in survival, cell recovery, DNA repair, and response after stress exposure was found to be involved in the radioresistance of radioresistant *E. coli* [3, 4]. Alterations in the expression of metabolism-related genes described in this report are likely to optimize the intracellular environment for survival, cell recovery, DNA repair, and response after irradiation by regulating the state of intracellular molecules.

REFERENCES:

[1] T. Saito, Viva Origino, **30** (2007) 85-92.
[2] T. Saito, KURNS ProgressReport 2019, (2020) 211.
[3] T. Saito, KURNS ProgressReport 2020, (2021) 162.
[4] T. Saito, KURNS ProgressReport 2021, (2022) 158.
[5] A. Dobin *et al.*, Bioinfomatics, **29** (2013) 15-21.
[6] Y. Benjamini and Y. Hochberg, J. R. Statist. Soc. B, **57** (1995) 289-300.
[7] D. W. Huang *et al.*, Nat. Protoc. **4** (2009) 44-57.

CO6-2 Integrated approach for structural analysis of a biomacromolecule in a polydispersed solution using analytical ultracentrifugation and small-angle X-ray scattering

K. Morishima[1], Y. Yunoki[1], A. Okuda[1], M. Shimizu[1], N. Sato[1], R. Inoue[1], M. Sugiyama[1]

[1]*Institute for Integrated Radiation and Nuclear Science, Kyoto University*

INTRODUCTION:

Small-angle X-ray and neutron scatterings (SAXS and SANS; collectively called SAS) offer overwhelming opportunities for structural analysis of a biomacromolecule in solution. Especially, state-of-the-art computational analyzing methods for SAS offer a high resolution three-dimensional structural model and/or its dynamics in the solution. To build a reliable structural model through the advanced analyses, it is essential to obtain the precise SAS profile from only a target biomacromolecule. Hence, a sample should be purified to be a monodisperse solution prior to a SAS measurement. Nevertheless, non-specific oligomers, namely aggregates, often remain in the solution even after purification. Even if the weight fraction of aggregates is a few %, the experimental SAS profile is deteriorated by them. As the result, an incorrect structural model is built as the target biomacromolecule: This is the fatal problem on the structural analysis with SAS.

To overcome this problem, a new data-reduction method, "AUC-SAS"[1], has been developed with integration of analytical ultracentrifugation (AUC) and SAS. AUC provides the weight fractions and molecular weights of all components in solution without destruction of aggregates and complexes. AUC-SAS derives the scattering profile of a target biomacromolecule from the deteriorated experimental profile using the information provided by AUC. However, the first designed AUC-SAS (first-AUC-SAS)[1] is constrained by the weight fraction of the aggregates (less than approximately 10 %). In this study, we improved AUC-SAS, which is applicable to samples with relatively large weight fraction of aggregates (> 10 %).

EXPERIMENTS:

As the demonstration of AUC-SAS, bovine serum albumin, apoferritin, catalase, lysozyme, ovalbumin, and ribonuclease A were subjected to the SAXS and AUC measurements.

SAXS measurements were carried out with NANOPIX (Rigaku). AUC measurements were conducted with a ProteomeLab XL-I (Beckman Coulter). All measurements were conduceted at 25 ºC.

RESULTS:

AUC-SAS derives the scattering profile of a target molecule through following steps;

Step 1. Derivation of forward scattering intensity.

Step 2. Derivation of scattering profile in high q region.

Step 3. Connection of forward scattering and scattering profile in high q region with Guinier approximation.

On the Step 2 in the first-AUC-SAS, the scattering profile in high q region for the target molecules is approximated to be identical with that for aggregates because it is not different in the inner local structure between the monomer and the aggregates in the sample for a general SAS measurement. However, we found that this approximation leads to the error in the target scattering profile for the samples with relatively large weight fraction of aggregates (> 10 %).

We improved the procedure of the Step 2 with carefully reconsidering the scattering profile of an aggregate. To express the scattering profile of an aggregate, we applied the random flight model. Consequently, the improved-AUC-SAS offered the correct scattering profile of the target molecule even for the sample with ~20% of weight fraction of aggregates: The improved-AUC-SAS was demonstrated to offer the consistent result with size exclusion chromatography (SEC)-SAXS for various proteins (bovine serum albumin, apoferritin, catalase, lysozyme, ovalbumin, and ribonuclease A).[2]

Because AUC-SAS does not require a large amount of sample or a very highly intensive instrument, such as synchrotron-light SAXS, it has a potential to be applied to laboratory-based SAXS. Additionally, AUC-SAS is applicable to also SANS which faces the same aggregation problem as well as SAXS. Indeed, we confirmed that the improved-AUC-SANS successfully works with the SANS data measured with SANS-U at JRR-3. Finally, we developed the software of the improved-AUC-SAS for broad SAS users (available at [http://www.rri.kyoto-u.ac.jp/NSBNG/activity.html]) [2].

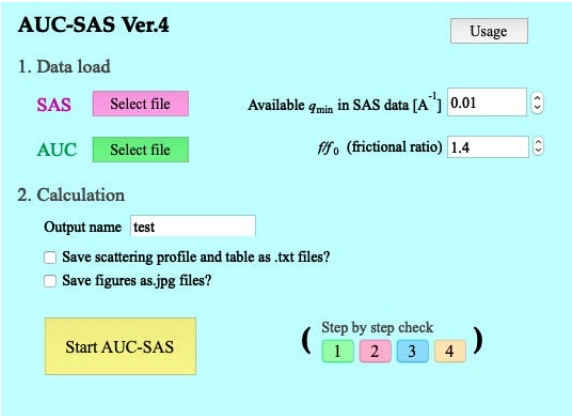

Fig. 1. Interface of AUC-SAS software on the Igor Pro.

REFERENCES:

[1] K. Morishima *et al.,* Commun. Biol., **3** (2020) 294.

[2] K. Morishima *et al.,* J. Appl. Crystallogr., (2023) in press.

R4010

CO6-3 Mutational and environmental effects on the dynamic conformational distributions of Lys48- linked di-ubiquitin chains

K. Kato, M. Yagi-Utsumi, S. Yanaka, H. Yagi, K. Morishima[1], R. Inoue[1], N. Sato[1] and M. Sugiyama[1]
Graduate School of Pharmaceutical Sciences, Nagoya City University
[1]*Institute for Integrated Radiation and Nuclear Science, Kyoto University*

INTRODUCTION: In multidomain proteins, individual domains connected by flexible linkers are dynamically rearranged upon ligand binding and sensing changes in environmental factors, such as pH and temperature. We characterize dynamic domain rearrangements of Lys48-linked ubiquitin (Ub) chains as models of multidomain proteins in which molecular surfaces mediating intermolecular interactions are involved in intramolecular domain–domain interactions [1, 2]. Using NMR and other biophysical techniques, we characterized dynamic conformational interconversions of diUb between open and closed states regarding solvent exposure of the hydrophobic surfaces of each Ub unit, which serve as binding sites for various Ub-interacting proteins. We found that the hydrophobic Ub-Ub interaction in diUb was reinforced by cysteine substitution of Lys48 of the distal Ub unit because of interaction between the cysteinyl thiol group and the C-terminal segment of the proximal Ub unit. In contrast, the replacement of the isopeptide linker with an artificial ethylenamine linker minimally affected the conformational distributions.

Small-angle neutron scattering (SANS) and small-angle X-ray scattering (SAXS) are powerful techniques for the structural characterization of biomolecular complexes. Here, we attempted to elucidate the time scale of the transit domain motions of the Lys48-linked diUb chain collaborated with SAXS and molecular dynamics (MD) simulation.

EXPERIMENTS: We prepared the Lys48-linked diUb. We performed SEC-SAXS of Lys48-linked diUb chain at 283 K using the laboratory-based SAXS instrument, NANOPIX equipped with a HyPix-6000 (Rigaku Corporation, Japan).

RESULTS: We obtained the SAXS profile of di-Ub (Fig. 1, light blue circle) and determined the radius of gyration (R_g) using Guinier analysis, which yielded $R_{g,exp}$=19.9±0.2 Å. To investigate whether the crystal structure differs from that of di-Ub in solution, we used Pepsi-SAXS [3] to calculate a SAXS curve from the crystal structure, which is shown as the black line in Figure 1. The R_g calculated from the SAXS curve was $R_{g,xtal}$=16.9 Å, indicating a structural difference between the crystal and solution states of di-Ub. This difference is likely due to domain motion in solution.

To further investigate this, we conducted all-atom molecular dynamics (MD) simulation for 100 ns at 283 K using GROMACS with the AMBER99-SB [4] force field and the crystal structure as the initial structure. From the trajectories of MD simulation, we extracted structures every 10 ps and calculated SAXS curves for each structure. We then averaged these curves to obtain the SAXS curve shown in red in Fig. 1. The R_g calculated from this curve was R_{g,MD_ave}=17.4 Å, with an average sum of squared residuals of $\chi^2_{MD\_ave}$=4.2, which was better than the scattering profile obtained from the crystal structure alone $R_{g,xtal}$=16.9 Å, χ^2_{xtal}=5.6).

We further plan to optimize the force field parameters and identify the domain motion of di-Ub in order to improve the reproducibility of the experimental data.

The conformational interconversion of Ub chains offers a unique design framework in Ub-based protein engineering not only for developing biosensing probes but also for allowing new opportunities for the allosteric regulation of multidomain proteins.

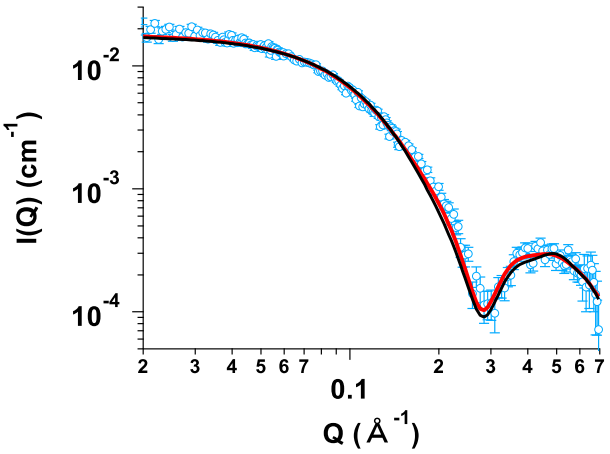

Fig. 1. Experimental SAXS curve of di-Ub (light blue circles), SAXS curve calculated from the crystal structure of di-Ub (black line), and ensemble average of SAXS curves for each structure for all atoms MD (red line).

REFERENCE:

[1] M. Hiranyakorn *et al.*, Int. J. Mol. Sci., **21** (2020) 5351. (doi) 10.3390/ijms21155351.
[2] M. Hiranyakorn *et al.*, Int. J. Mol. Sci., **24** (2023) 6075. (doi) 10.3390/ijms24076075.
[3] S. Grudinin *et al.*, Acta. Cryst., **D73** (2017) 449. (doi) 10.1107/S2059798317005745.
[4] V. Hornak *et al.*, *Proteins*, **65** (2006) 712. (doi) 10.1002/prot.21123.

CO6-4 Evaluation of BPA-Uridine conjugates as Smart Drugs for BNCT

K. Tanabe,[1] T. Nishihara,[1] and M. Suzuki[2]

[1]*Department of Chemistry and Biological Science, College of Science and Engineering, Aoyama Gakuin University*
[2]*Institute for Integrated Radiation and Nuclear Science, Kyoto University*

INTRODUCTION:

Modified nucleobases are widely used in vivo as functional materials.[1] Recently, we have shown that nucleobases can be utilized as an efficient solubilizer and carrier of hydrophobic drugs. We have employed uridine as a functional solubilizer and carrier for poorly soluble compounds BPA and constructed BPA-uridine conjugate for boron neutron capture therapy (BNCT). We had found that irradiation in the presence of the conjugate markedly enhanced the cytotoxicity of radiation.

In this study, we evaluated their cytotoxic effect against several tumor cells. In vivo study revealed that the conjugate selectively accumulated into tumor tissues and showed high cytotoxic effects upon thermal neutron irradiation.

EXPERIMENTS:

Preparation of BPA-uridine conjugate. BPA was added to the aqueous solution of uridine under basic conditions to solubilize the conjugate. After the BPA was dissolved in the aqueous solution, the resulting solution was neutralized and then subjected to in vivo experiments.

Neutron capture therapy to SAS tumor models. SAS cells in matrigel (1×10^6 cells per mouse) were subcutaneously inoculated into the right thighs of BALB/c nude mice. The tumors were allowed to grow ~1.0 month. The mouse was injected with fructose-BPA or uridine-BPA (250 mg/kg). The mice were placed in acrylic which were secured on a 5-mm-thick thermoplastic plate that contained 40 weight % (wt %) of ^{6}LiF (96% 6Li) to block thermal neutrons and had a circular hole in the center. The thigh containing the tumor was stretched over the hole, and the tumor was irradiated with epi-/thermal neutrons for 50 min, 1 h after the injection. The tumor size was measured by a caliper, and tumor volume (V) was calculated using the following equation: $V = ab^2/2$, where a and b are the major and minor axes, respectively.

RESULTS:

Last year, we found that the BPA-uridine complex dissolved smoothly in water, and it exhibited high cytotoxicity toward A549 cells under thermal neutron irradiation. Therefore, in this study, we further determined its cytotoxicity toward other tumor cells such as SAS and SCCVII cells. We evaluated the cytotoxicity of BPA-uridine conjugate against these cells, which were exposed to neutron (1 MW) in the presence of aqueous solution consisted of BPA and uridine and then incubated at 37 ˚C. After wash, cell survival was determined by WST assay. Figure 1 compares cell survivals in the presence and absence of BPA-uridine after irradiation. The cytotoxic effect of radiation was significantly enhanced when the cells were irradiated in the presence of BPA-uridine. It is likely that BPA is effectively activated in the cells and thereby exhibits high cytotoxicity against tumor cells upon irradiation.

We also evaluated the cytotoxic effect of BPA-uridine using tumor tissue planted in mice. To determine whether the BPA-uridine conjugate is effective in vivo, we administered this conjugate to BALB/cAJcl nude mice with SAS tumors. SAS cells were transplanted into BALB/cAJcl nude mice (n = 3 per group) and allowed to grow until the tumor size was about 200 mm^3. The conjugate was then administered subcutaneously and changes in tumor size after thermal neutron irradiation were recorded. As shown in Figure 1B, tumors grew significantly when no drug was administered, while administration of the BPA-uridine conjugate and neutron irradiation effectively inhibited tumor growth. The degree of inhibition was comparable to that of the previously reported BPA-fructose conjugate. These results strongly suggests that BPA-uridine is activated in tumors under irradiation conditions and exerts its cell-killing effect in vivo.

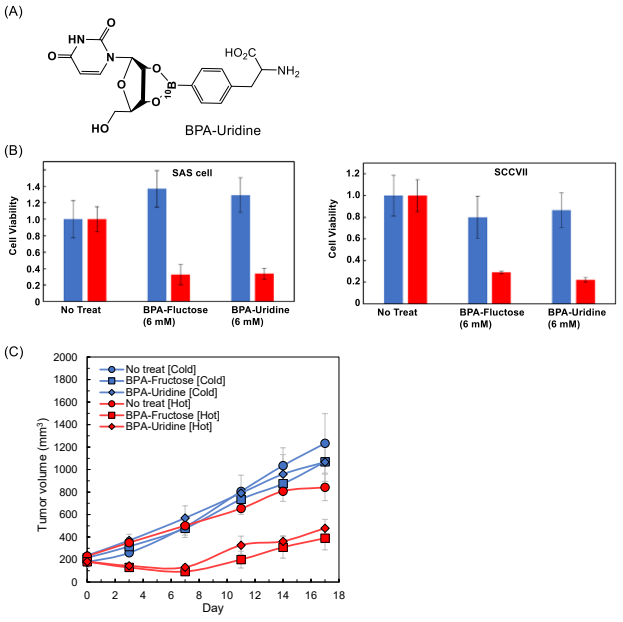

Figure 1. (A) Chemical structure of BPA-Uridine. (B) Cytotoxic effect of BPA-Uridine conjugate upon thermal neutron irradiation (1 MW, 45 min, red: irradiation (+), blue: irradiation (-)) against SAS or SCCVII cells. (C) In vivo evaluation of BPA-uridine or BPA-fluctose as an anticancer agent. Tumor (SAS cells) volumes of each group were measured, epi-/thermal neutrons: 50 min.

REFERENCES:

[1] K. Tanabe *et al.,* Org. Biomol. Chem., **7** (2009) 654.

CO6-5 BPA derivative bearing Hoechst unit for BNCT

K. Tanabe,[1] T. Nishihara,[1] M. Mizutani,[1] and M. Suzuki[2]

[1]*Department of Chemistry and Biological Science, College of Science and Engineering, Aoyama Gakuin University*
[2]*Institute for Integrated Radiation and Nuclear Science, Kyoto University*

INTRODUCTION:

Recently, "Boron Neutron Capture Therapy (BNCT)" has been attracting attention; BNCT is a therapy that selectively damages cancer cells by causing them to accumulate a ^{10}B compound that causes a nuclear reaction with thermal neutrons. However, at present, there are only two types of boron drugs available for BNCT: BPA, a phenylalanine derivative, and BSH, a boron cluster. Therefore, it is an urgent issue to develop drugs for BNCT which show effective therapeutic effects. In this study, we attempted to construct a molecular system to damage genomic DNA by delivering BPA to the cell nucleus. We designed a new boron drug by using Hoechst unit[1] (Hoechst-BPA), which have an ability to be accumulated in the cell nucleus.

EXPERIMENTS:

Neutron capture therapy to SAS tumor models. SAS cells in matrigel (1×10^6 cells per mouse) were subcutaneously inoculated into the right thighs of BALB/c nude mice. The tumors were allowed to grow ~1.5 month. The mouse was injected with fructose-BPA or Hoechst-BPA (250 mg/kg). The mice were placed in acrylic which were secured on a 5-mm-thick thermoplastic plate that contained 40 weight % (wt %) of ^6LiF (96% 6Li) to block thermal neutrons and had a circular hole in the center. The thigh containing the tumor was stretched over the hole, and the tumor was irradiated with epi-/thermal neutrons for 50 min, 1 h after the injection. The tumor size was measured by a caliper, and tumor volume (V) was calculated using the following equation: $V = ab^2/2$, where a and b are the major and minor axes, respectively.

RESULTS:

Last year, we successfully synthesized Hoechst-BPA from a BPA derivative with an azide group and a Hoechst molecule with an alkyne moiety using a cycloaddition reaction called Huisgen reaction.

Initially, the function of Hoechst-BPA was evaluated using cultured cells. A549, human lung cancer cell, was treated with Hoechst-BPA, and then the cells were observed by confocal laser microscopy. As a result, blue fluorescence derived from Hoechst was observed in the cell nucleus. Similar results were obtained when SAS, human squamous cells, and SCC7, mouse squamous cells, were used. These results suggests that Hoechst-BPA was transported into the cell nucleus and bound with genomic DNA.

Next, SAS, and SCC7 cells treated with Hoechst-BPA were irradiated with neutrons and cytotoxic effect was evaluated. We evaluated the cytotoxicity of Hoechst-BPA conjugate against these cells, which were exposed to neutron (1 MW) in the presence of aqueous solution of the conjugate and then incubated at 37 ˚C. Cell survival was determined by WST assay. Hoechst-BPA showed little toxicity without neutron irradiation, but moderate toxicity was observed upon neutron irradiation.

Finally, Hoechst-BPA was administered to tumor-bearing mice (SAS), and then the mice were irradiated with neutrons to evaluate the anti-tumor effect in vivo. One month after irradiation, the tumor volume increased significantly after neutron irradiation to mice without administration of Hoechst-BPA, whereas the increase of tumor volume was greatly suppressed when mice were treated with Hoechst-BPA. Although high cell-killing and antitumor effects were expected, the Hoechst-BPA-treated mice did not show sufficient efficacy. This may be due to insufficient accumulation of Hoechst-BPA in the tumor tissue.

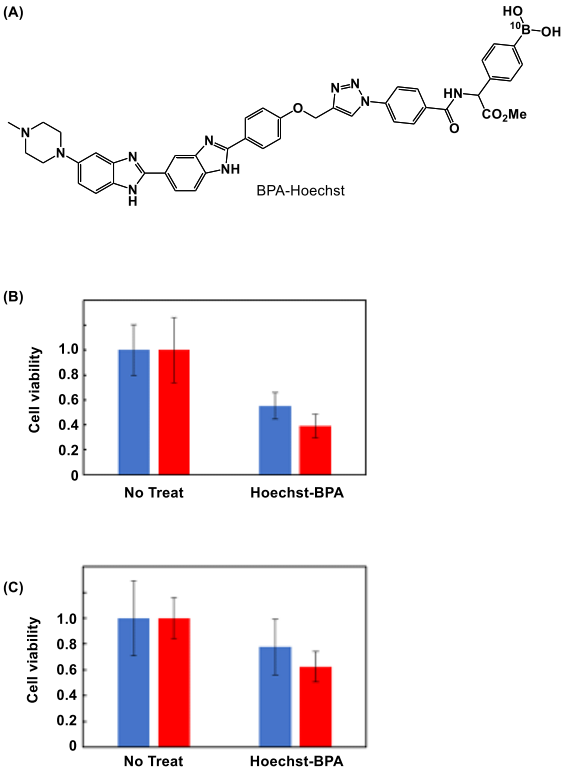

Figure 1. (A) Chemical structure of Hoechst-BPA. (B,C) Cytotoxic effect of BPA-Hoechst conjugate upon thermal neutron irradiation (1 MW, 45 min, red: irradiation (+), blue: irradiation (-)) against SAS (B) or SCCVII cells (C).

REFERENCES:

[1] K. Tanabe *et al.*, ChemBioChem., **19** (2018) 956-962.

CO6-6 Elucidating the Molecular Basis for the Increased Risk of Nuclear Cataract Development with Global Warming

N. Yamamoto[1] and T. Takata[2]

[1] *Fujita Health University*
[2] *Institute for Integrated Radiation and Nuclear Science, Kyoto University*

INTRODUCTION:
The transparency of the lens is important for focusing target onto retina. Maintaining the function of lens determines the quality of life. Lens cells contain rich structural proteins, which is called as crystallin. Those stable long-lived crystallin interactions is critical for lens functions. Many past studies have reported about post-translational modifications in crystallin species decreased solubility of crystallins and lead senile cataract formation in aged lens. Those modifications were accumulated under various stresses during life, such as heat and ultraviolet (UV) irradiation. It has also been considered that many factors in addition to UV are the main causes of nuclear cataract (NUC). In order to elucidate those factors, we performed a worldwide epidemiological survey and confirmed that the risk of NUC is significantly higher in residents living in areas where the annual number of days with temperatures of 30°C or higher is higher. Furthermore, in an *in silico* simulation study, the applicant group showed that the incidence of NUC differs within a range of internal temperature differences (35.0-37.5°C) [1]. These obvious but new results are currently the focus of worldwide attention. Based on these results, this study aims to clarify the relationship between NUC and environmental temperature. We had previously cultured lens model cells in different temperature and analyzed the modification levels of Aspartate (Asp) in crystallin. However, we had not succeeded in mass spectrometry of cell extracts cultured at different temperatures. The reason for this issue would be low amount of target peptides. Therefore, we adopted on membrane digestion and a quadrupole (qqq) mass spectrometry. Those are less comprehensive but with excellent sensitivity to identify the trace modification in peptide.

EXPERIMENTS:
Material Immortalized human lens epithelial cells (iHLEC-NY2) are cultured on different temperature (35.0-37.5°C) and collected by RIPA buffer. All cell extracts were solubilized in the sample buffer for SDS-PAGE, then separated by electrophoresis. Anti-αA crystallin antibody (Santa) was used for western blotting to identify αA-crystallin in cell extracts.
Western Blot and on membrane digestion In order to get intense peptides from isolated αA-crystallin, on membrane digestion was performed. To get a lot of proteins, molar mass of 15,000–30,000 bands from five to seven lanes membrane were collected, then used for on membrane digestion.
LC-MS analysis After trypsin digestion, each tryptic peptide was injected to RP-HPLC-MS/MS (qqq) systems (Shimadzu) to identify the expressed αA-crystallin in iHLEC-NY2. An L-column 2 metal-free (3 μm, 2.0 mm × 150 mm, CERI) was used with the following binary mobile phase compositions: solvent A (0.1% TFA acid aqueous solution) and solvent B (100% acetonitrile containing 0.1% TFA). The algorism for the database search was LabSolutions (Shimadzu) as previously reported [2].

RESULTS:
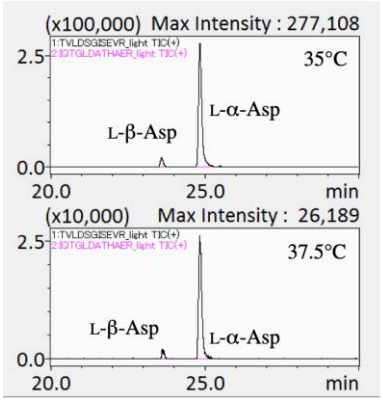

	35°C	37.5°C
Lα	2095229 (94%)	258644 (94%)
Lβ	132898 (6%)	15185 (6%)

Fig. 1. Modifications on Asp58 and Asp151 of αA-crystallin in iHLEC-NY2 extracts.

The conventional LC-MS/MS analysis from tryptic digested cell extracts could not show the peaks, but peptide from on membrane digestion could be observed on RP-HPLC-MS/MS (qqq) systems (Fig. 1). This indicated the significance of current method for identification of trace modification of amino acid residues in proteins. There is a small amount of L-β-Asp 58 in both samples without any differences. The chromatogram of peptide containing Asp151 of αA-crystallin were not observed in both. The amount of sample maybe short for the identification of Asp151, or ionization of peptide was not enough to be observed on current systems. No significant modification was observed at this temperature difference, so the reason of the formation of NUC under high temperature may not be caused by isomerization of Asp58. There were still significant changes in cell proliferation and expression of αA-crystallin, indicating that temperature-dependent changes occur during protein biosynthesis inside the cell. We, therefore, hypothesized that the folding pathways of αA-crystallin and that substrate proteins inside the cell are temperature dependent, and tried to conduct the following study focusing on temperature changes.

REFERENCES:
[1] N. Yamamoto *et al.*, Cells., **12** (2020) 2670.
[2] N. Fujii *et al.*, ACS Omega, **5** (2020) 27626-27632.

CO6-7 Elucidation of the effects of dose rate of radiation on normal and tumor tissues

T. Watanabe[1], Y. Sanada[1], T. Takata[1], G. Edward Sato[2], M. Yoshimura[2], H. Tanaka[1], M. Suzuki[1], T. Mizowaki[2]

[1]*Institute for Integrated Radiation and Nuclear Science, Kyoto University*

[2]*Radiation Oncology and Image-Applied Therapy, Graduate School of Medicine, Kyoto University*

INTRODUCTION: Radiation with different dose rates is known to have different effects on normal tissues [1]. On the other hand, the effect of dose rate on the antitumor effect is minor, and a higher dose rate may improve the therapeutic efficacy ratio of radiation [2]. The purpose of this study is to ascertain whether the dose rate alters the effects of various normal tissues. In addition, experiments were conducted to see if the antitumor effect of radiation could be differentiated by differences in dose rate, which had previously been equivalent, by using drugs that affect the antitumor effect of radiation in combination.

****

EXPERIMENTS: A mouse subcutaneous transplantation model of mouse-derived squamous cell carcinoma cells (SCC7) was used for experiments in C3H mice under the lower limb skin. The differences in the effects of irradiation with electron beams with high dose rates and X-rays with low dose rates on normal and tumor tissues were investigated. The irradiation area was limited to the lower extremities, the remaining area was shielded, and the tumor tissue was irradiated with a single 14 Gy dose. In addition, to evaluate the radiation effects on the skin of one of the normal tissues at different dose rates, the head was irradiated with 14 Gy and the body weight and the states of the irradiated area were observed for one month. Tirapazamine and amifostine were used as agents affecting the antitumor effect of radiation [3, 4]. Tirapazamine and amifostine were each administered 1 hour before irradiation, and tumor tissue was irradiated to confirm tumor size over time.

****

RESULTS: When the upper body of the mice were irradiated, the X-ray group showed significant weight loss up to 12 days after irradiation, whereas the electron beam group, which has a higher dose rate, showed less weight loss and a significant difference. The skin in the irradiated area also showed obvious alopecia and wet desquamation and dermatitis in the X-ray group, whereas the skin in the high-dose-rate electron beam group showed only slight alopecia, no wet desquamation, and no dermatitis. Compared to the X-ray group, the higher dose rate electron beam group showed less redness in the oral cavity and perinasal area. These results suggest that the difference in the degree of weight loss in the two groups was influenced by the severity of oral mucositis. When X-rays were irradiated after preadministration of tirapazamine to subcutaneous tumors in mice, the anti-tumor effect of X-rays was sensitized. Similarly, when the subcutaneous tumors of mice were irradiated with high-dose-rate electron beams after preadministration of tirapazamine, they showed a sensitizing effect of the antitumor effect of X-rays as well. However, the degree of sensitization of the antitumor effect was similar to that of X-ray irradiation, and there was no significant difference in antitumor effect in the combination group of tirapazamine and X-ray irradiation compared to the combination group of tirapazamine and electron beam irradiation. When amifostine was preadministered to mouse subcutaneous tumors followed by X-rays, it showed the same anti-tumor effect as X-rays alone. Similarly, when amifostine was preadministered to subcutaneous tumors of mice and then irradiated with high-dose-rate electron beams, the anti-tumor effect was not attenuated and was similar to that of electron beams alone. However, in this experiment, the degree of sensitization of the antitumor effect was similar to that of X-irradiation, and there was no significant difference in antitumor effect in the combined amifostine and X-irradiation group compared to the combined amifostine and E-beam irradiation group.

****

REFERENCES:

[1] Binwei Lin *et al.,* Front Oncol., **11** (2021) 644400.
[2] Elise Konradsson *et al.,* Advances in Radiation Oncology., **7** (2022) 101011.
[3] B G Siim *et al.,* Cancer Res., **57** (1997) 2922-8.
[4] Jr William Small *et al.,* Int. J. Gyn. Can., **21** (2011) 1266-75.

R4041

CO6-8 Asp racemization/isomerization in shedding products of cell adhesion molecule 1 is potentially involved in the neurodegeneration induced by elevated pressure

A. Yoneshige[1], A. Ito[1] and T. Takata[2]

[1]*Department of Pathology, Kindai University*
[2]*Institute for Integrated Radiation and Nuclear Science, Kyoto University*

INTRODUCTION: The elevation of internal pressure is often involved in neurodegeneration; intraocular and intraventricular pressure elevations over 20–30 cmH_2O cause glaucoma and hydrocephalus, respectively.
Previously, to investigate the mechanisms by which elevation of intraluminal pressure causes cell or tissue degeneration, we devised a novel two-chamber culture system that enabled us to subject cultured cells to low levels of water pressure (2-50 cmH_2O pressure load) [1,2]. We found that mouse primary neurons degenerated when the water pressure was above 30 cmH_2O, and that ectodomain shedding of synaptic cell adhesion molecule 1 (CADM1) increased in a water pressure-dependent manner [1]. We also discovered that the increase of intracellular product of CADM1 shedding (C-terminal fragment, CADM1-CTF) resulted in decreased neurite density with punctate localization of CADM1 suggesting its aggregation in neurites [1].
CADM1-CTF is rich in Asp residues neighbored by Ala residues, and the conversion of these amino acids to poly-Gly diminished its aggregation state. Since the racemization and isomerization of Asp residues contributes to aggregation of various proteins and it likely occurred when the neighboring residues are small [3,4], these insights led us to hypothesize an involvement of Asp racemization/isomerization in the neurodegeneration induced by internal pressure elevation.

EXPERIMENTS:
(1) Synthetic peptide of internal sequence of CADM1-CTF (GADDAADADTAIINAEGGQNNSEEK) was incubated at 50°C for 0-15 days and applied to LC-MS to identify Asp isomer-containing peptides.
(2) Mouse neuroblastoma cell line Neuro-2a cells with exogenously expressed CADM1-CTF were cultured under 50 cmH_2O and were prepared for LC-MS analysis.
(3) To mimic oxidative stress induced by internal pressure elevation, Neuro-2a cells expressing CADM1-CTF were treated with hydrogen peroxide and the cells were subjected to the isolation of CADM1-CTF by immunoprecipitation.

RESULTS:
(1) In LC-MS analysis of CADM1-CTF synthetic peptide, multiple peaks were detected after 1 day at pH 6.0 or pH 7.0 indicating that Asp racemization/isomerization could occurred under neutral pH.
(2) CADM1-CTF proteins in Neuro-2a cells were solubilized with water, Triton X-100 containing buffer, or SDS containing buffer after 3 days culture under 50 cmH_2O, and CADM1 immunoblot was carried out. CADM1-CTF protein yields (CADM1-CTF / total proteins) were in the order Triton X-100 > SDS > water, however, the peptide peak was not identified using with LC-MS.
(3) Previously, we found that CADM1 shedding was increased by oxidative stress as a cause of pulmonary emphysema in cigarette smoke exposure [5]. We furthermore showed that Lipocalin-2, an iron binding protein was upregulated in the retinae under 50 cmH_2O pressure [6]. Since iron dysregulation induces oxidative stress, we decided to explore the linkage between oxidative stress and Asp racemization/isomerization of CADM1-CTF. Our preliminary data demonstrated that CADM1-CTFs could isolate from Neuro-2a extracts by immunoprecipitation (Fig.1). Future experiments are planned for identification of Asp isomer by LC-MS or anti-D-Asp antibody (if available) in these immunoprecipitated CADM1-CTFs.

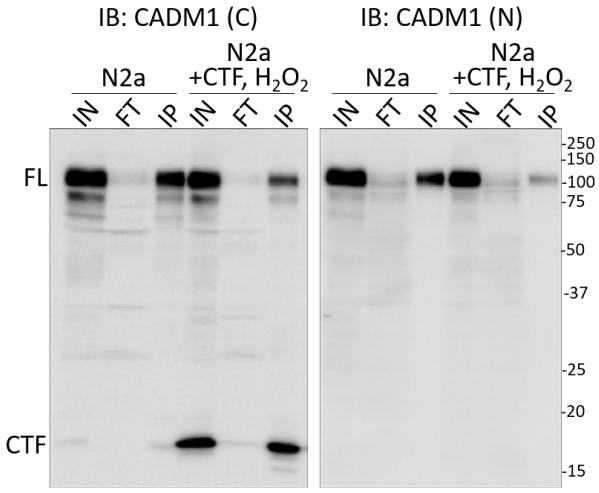

Fig. 1. Isolation of CADM1-CTFs from Neuro-2a (N2a) cell lysate by immunoprecipitation. Full length (FL)-CADM1 and CADM1-CTFs were isolated with antibody recognizing CADM1 C-terminal peptide and detected by immunoblotting (IB) with anti-CADM1 C-terminus (C) or anti-CADM1 N-terminus (N) antibody respectively. IN: input, FT: flow-through, IP: immunoprecipitated sample.

REFERENCES:
[1] A. Yoneshige *et al.*, Mol. Neurobiol., **54** (2017) 6378-6390.
[2] M. Hagiyama *et al.*, Front. Physiol., **8** (2017) 997.
[3] N. Fujii *et al.*, J. Biochem., **116** (1994) 663-669.
[4] T. Takata *et al.*, Protein Sci., **29** (2020) 955-965.
[5] A. Ri *et al.*, Front. Cell Dev. Biol., **6** (2018) 52.
[6] A. Yoneshige *et al.*, Front. Cell Dev. Biol., **9** (2021) 664327.

CO6-9 SAXS analysis for elucidating the inhibitory mechanism of the amyloid precursor of insulin B-chain through the interaction with αB-crystallin

Y. Kokuo, K. Yuzu, N. Yamamoto[1], K. Morishima[2], A. Okuda[2], R. Inoue[2], M. Sugiyama[2], J. Hayashi[3], J. A. Carver[3], E. Chatani

Graduate School of Science, Kobe University
[1]*Graduate School of Medicine, Jichi Medical University*
[2]*Institute for Integrated Radiation and Nuclear Science, Kyoto University*
[3]*Research School of Chemistry, The Australian National University*

INTRODUCTION: Amyloid fibrils are protein aggregates showing fibrous morphology and β-sheet-rich inner structure, and they are deeply involved with amyloidoses and neurodegenerative diseases. A cellular strategy for preventing the formation of amyloid fibrils is the expression of small heat shock proteins (sHsps), which have been proposed to rescue unfolded protein in an ATP-independent manner. αB-crystallin (αB-C) is a typical member of sHsps in mammals, and there have been reported its inhibitory effects against amyloid formation in vitro. However, the mechanism of the inhibition remains to be fully elucidated.

In this study, we analyzed the mechanism by which αB-C inhibits fibrillation by using insulin B-chain (B-chain) as a substrate. B-chain is an excellent model of amyloidogenic proteins, as it forms amyloid precursors prior to αB-C amyloid nucleation [1-4]. We previously found that αB-C inhibit the B-chain fibrillation through interacting with the B-chain amyloid precursors [5], and here, we performed small-angle X-ray scattering (SAXS) in combination with analytical ultracentrifugation (AUC) measurements to clarify the change in size and shape of the amyloid precursor formed under reactions in the presence of αB-C.

EXPERIMENTS: Insulin B-chain was dissolved at a final concentration of 400 μM in 50 mM Tris-HCl buffer (pH8.7) containing 5 mM NaCl and αB-C at the molar ratio ranging from 0 to 0.2. After overnight incubation at 25 °C, the samples were subjected to SAXS measurements. A SAXS profile was collected at 25 °C and 30-minute exposure with a NANOPIX equipped with a HyPix-6000 (Rigaku Corporation, Japan). A Cu K-α line (MicroMAX-007HFMR) was used as a beam source, which was further focused and collimated with a confocal multilayer mirror (OptiSAXS). The camera length was set to 1.33 nm and the range of the scattering vector q was from 0.008 to 0.20 Å^{-1}.

AUC was conducted with a ProteomeLab XL-I analytical ultracentrifuge (Beckman Coulter, USA) to analyze the weight distribution of the B-chain/αB-C complex and unbound αB-C. Sedimentation velocity analytical ultracentrifugation (SV-AUC) measurements were performed using Rayleigh interference optics at 40,000 rpm at 25 °C with a 1.2 mm path-length cell. The experimental data were analyzed with SEDFIT software. The density and viscosity of solvent, and partial specific volume of each protein was calculated from its amino acid sequence with SEDNTERP software.

RESULTS: The SAXS profiles of the B-chain-αB-C complex formed at five different molar ratios (1:0, 1:0.025, 1:0.05, 1:0.1, and 1:0.2) are shown in Fig. 1A. It was found from the AUC analysis that αB-C became excess at a higher molar ratio, and therefore, the fraction of unreacted αB-C was subtracted from the SAXS profile to obtain the profiles of the B-chain-αB-C complex selectively. The slope of the log-log plot was close to −1 for all samples, suggesting that the complex has a rod-like morphology like the B-chain amyloid precursor. To calculate the base diameter of the complex, the cross-section plot was constructed in Fig. 1B. The slope of this plot became steeper at higher molar ratio, suggesting that the complexes tend to become thicker as the concentration of αB-C increased. Although the length was difficult to be estimated from the SAXS profile because of limited Q range, the hydrodynamic diameter from dynamic light scattering has suggested that the complex tended to become shorter upon increasing the αB-C concentration.

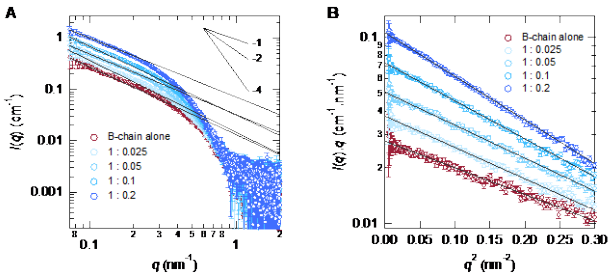

Fig. 1. (A) SAXS profiles and (B) their cross-section plots of the B-chain-αB-C complexes formed at different molar ratios of B-chain:αB-C. In this figure, unreacted αB-C is already subtracted to show the SAXS profiles of the B-chain-αB-C complexes themselves. The profile of the B-chain amyloid precursor, which is formed by B-chain alone, is also shown as a reference. The slopes in (A) in the intermediate region suggest that the complexes have a rod-like shape, and from the slopes in (B), the base diameters of the rod-like complexes have been estimated.

REFERENCES:

[1] N. Yamamoto *et al.*, Sci. Rep., **8** (2018) 62.
[2] N. Yamamoto *et al.*, Biochemistry, **58** (2019) 2769-2781.
[3] Y. Yoshikawa *et al.*, Molecules, **27** (2022) 3964.
[4] N. Yamamoto *et al.*, J. Phys. Chem. B, **126** (2022) 10797-10812.
[5] Y. Kokuo, Master Thesis, Kobe Univ. (2023).

CO6-10 Detection of the LIM Kinase 1 and Fam81a multimeric complex

T. Saneyoshi[1], T. Hirouchi[1], T. Kaizuka[2,3], A. Okuda[4], K. Morishima[4], T. Takumi[3], M. Sugiyama[4], Y. Hayashi[1]

[1] *Graduate School of Medicine, Kyoto University*
[2] *Centre for Clinical Brain Sciences, University of Edinburgh*
[3] *Graduate School of Medicine, Kobe University*
[4] *Institute for Integrated Radiation and Nuclear Science, Kyoto University*

INTRODUCTION: LIM kinase 1 (LIMK1) is a kinase involved in actin cytoskeletal regulation by phosphorylating actin binding protein cofilin. In neurons, it is involved in structural plasticity of dendritic spines. LIMK1 has been shown to dimerize upon activation but not further details are known as to its high order structure [3]. On the other hand, FAM81A is a postsynaptic density (PSD) localized protein containing coiled-coil structure [1]. We have demonstrated that recombinant mouse Fam81a undergoes liquid-liquid phase separation, interacts with PSD proteins, including PSD-95, SynGAP, and NMDA receptors, and promotes condensation of those proteins [2]. However, no further characterization has been reported about Fam81a, neither.

We therefore investigated whether recombinant mouse LIMK1 and Fam81a forms multimeric complex or not by performing dynamic light scattering (DLS) and analytical ultracentrifugation (AUC) to detect a multimeric complex of Fam81a and estimated its molecular size.

EXPERIMENTS: Full length LIMK1 fused with GST was purified from baculovirus expression system using Sf9 cells. Fam81a were produced as a GST-fused form in an *E.coli* expression system. The GST-fusion proteins were pulled down using glutathione agarose beads. After cleaving GST tag using HRV3C protease, the target protein was purified by size exclusion chromatography using HiLoad 16/600 superdex 6 pg. The purify of the proteins were assessed by CBB staining of SDS-PAGE.

RESULTS: We successfully purified both recombinant proteins. They were then examined by DLS and AUC and their oligomerization status was determined. We plan to confirm the results further by cryoEM. The LIMK1 structure will be used to design FRET probe to detect its conformational change that may represent activity. The result will be published in scientific journal.

REFERENCES:

[1] R. Li *et al.,* FASEB J., **20** (2006) 1218-1220.
[2] A. Dosemeci *et al.*, Neurosci. Lett., **699** (2019) 122-126.
[3] T. Kaizuka *et al.*, bioRxiv, (2023).
(doi) 10.1101/2023.01.23.525126.

CO6-11 Structural Analysis of Ceramide Transport Protein (CERT)

S. Morita[1], K. Morishima[2], T. Fujita[1], N. Sato[2], A. Okuda[2], K. Hanada[3], M. Sugiyama[2] and C. Kojima[1,4]

[1]*Graduate School of Engineering Science, Yokohama National University*
[2]*Institute for Integrated Radiation and Nuclear Science, Kyoto University*
[3]*National Institute of Infectious Diseases*
[4]*Institute for Protein Research, Osaka University*

INTRODUCTION: Lipids are important components of cell membranes. Lipids are synthesized in the endoplasmic reticulum and transported to the Golgi apparatus, where they are chemically modified. Lipid transfer proteins (LTPs) are known to transport lipids from the endoplasmic reticulum (ER) to the Golgi apparatus. Ceramide is one of the lipids and is transported by ceramide transfer protein (CERT). CERT consists of three segments, a PH domain that interacts with PI4P and contributes to Golgi localization, a START domain that binds to ceramide, and a middle region (MR) connecting the PH and START domains [1]. The MR is known to contain functional sites such as the FFAT motif that interacts with the ER membrane protein VAP and the serine repeat motif (SRM) that inhibits ceramide transport by phosphorylation. Among these regions, the structures of the PH and START domains have already been determined, but neither the MR nor full-length structures of CERT have yet been analyzed. Here the structural analysis of the full-length CERT was performed with the aim of elucidating the mechanism of ceramide transport mediated by CERT.

EXPERIMENTS: The wild-type and dominant-negative mutant samples of the full-length CERT were expressed using *E. coli* and purified by affinity chromatography and gel filtration chromatography. The samples were analyzed by gel filtration chromatography. The dominant-negative mutant was further analyzed by MS spectrum, analytical ultracentrifuge, and small-angle x-ray scattering.

RESULTS: Both the wild-type and dominant-negative mutant samples of the full-length CERT were successfully expressed and purified. The sample purity was evaluated by SDS-PAGE as a single band. Both samples were analyzed by the gel filtration chromatography. The apparent molecular mass evaluated from the elution volume of the gel filtration chromatography (Fig. 1) was 215 and 254 kDa for the wild-type and dominant-negative mutant samples of the full-length CERT, respectively, and close to that of the CERT trimer, 204 kDa. In the cells, the full-length CERT is reported to form a trimer [2]. The elution volume of the gel filtration chromatography depends on both molecular weight and shape. Therefore, we assumed that both samples are trimer with different molecular shapes and that molecular shape of the dominant-negative mutant sample is distorted.
To investigate this assumption, the molecular mass and shape of the dominant-negative mutant sample of the full-length CERT were evaluated by the analytical ultracentrifuge (Fig. 2). Assuming the ratio of the friction coefficients f/f_0 = 1.8, the major sedimentation coefficient for the dominant-negative mutant sample was found as 7.2 S ~ 212 kDa which is close to that of the CERT trimer, 204 kDa. The f/f_0 value 1.8 indicates the molecular shape is significantly distorted with the axial ratio ~ 12. The observed molecular mass and distorted shape of the dominant-negative mutant sample are consistent with our assumption based on the gel filtration analysis.

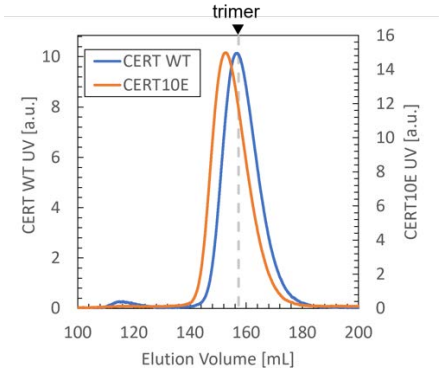

Fig. 1. The gel filtration chromatography of the wild-type (blue) and dominant-negative mutant (orange) samples of the full-length CERT. The down-closed black triangle on the top shows the elution volume of the 204 kDa protein which is the molecular mass of the CERT trimer.

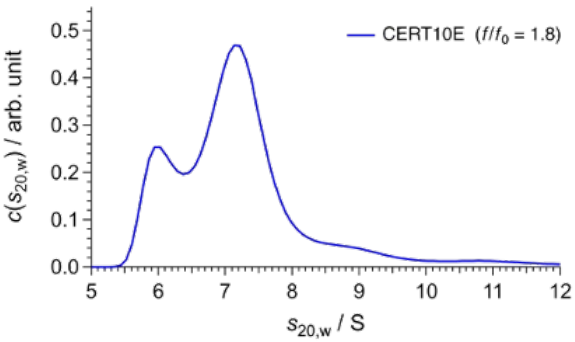

Fig. 2. The distribution function of the sedimentation coefficient obtained from the c(s) analysis of the analytical ultracentrifuge measurement for the dominant-negative mutant of the full-length CERT.

REFERENCES:
[1] K. Kumagai and K. Hanada, FEBS Lett., **593** (2019) 2366-2377 .
[2] A. Goto *et al.,* Int. J. Mol. Sci., **23** (2022) 8576.

CO6-12 Small-angle X-ray Scattering toward Understanding Chromosomal Modulation by Topoisomerases

M. Shimizu, A. Okuda, Y. Yunoki, R. Inoue, K. Morishima, N. Sato, R. Urade, and M. Sugiyama

Institute for Integrated Radiation and Nuclear Science, Kyoto University

INTRODUCTION: In both eukaryotes and prokaryotes, functions of chromosomes have a strong relationship with superhelicity of the genomic DNA. During the DNA transcription and DNA replication, complexed protein machines proceed on the genomic DNA while unwinding the DNA duplexes. These processes accumulate positive superhelicity in the direction of the molecular machines, and accumulate negative superhelicity in the opposite direction [1, 2]. As a result, progression of the complex becomes more difficult. Therefore, mechanisms are needed to control the level of superhelix and to maintain the progression of the molecular machines [3]. Conversely, DNA superhelix are also known to promote formation of a certain complexes [4]. This can be interpreted as stabilization of curved DNA structure promotes the formation of a protein complex that form across two DNA regions or that form at a DNA loop. In other words, cells sometimes deal with the DNA superhelix as an obstacle to be overcome, and at other times they utilize it. With this background, it is critical to maintain the superhelical level of the genomic DNA. DNA topoisomerases are responsible for maintaining the DNA superhelicity. There are two major types of DNA topoisomerase, type I and type II. The type I topoisomerases break covalent bond of one strand of the DNA duplex, and then restore the DNA chain after their superhelical level has changed. The type II topoisomerases cleave both DNA strands, introduce superhelicity, and restore the DNA strands [5]. The detailed process by which DNA superhelicity introduced by topoisomerases spreads over a wide area of the genomic DNA and affects transcription and replication is not yet clear. The dynamic process cannot be captured by X-ray crystallography or cryo-electron microscopy. Single-molecule measurements have studied the global conformational changes in DNA exerted by DNA topoisomerases [6, 7]. However, chromosomes in cells are more complex systems in which many factors interact. Therefore, we focused on small-angle X-ray scattering measurements, which provides information on structural ensemble of biomolecules, to study topoisomerase-induced changes in huge DNA-protein complexes. As the first step to achieve this, we examined a condition for measuring long double stranded DNA with small-angle X-ray scattering system in the Institute for Integrated Radiation and Nuclear Science, Kyoto University.

EXPERIMENTS: SAXS measurements were performed on the pUC19 linearized vector supplied with the In-Fusion HD Cloning Kit (Takara Bio USA, Inc., CA, USA, Clontech Laboratories, Inc., CA, USA). After replacing the DNA-dissolving buffer by dialysis, small-angle X-ray scattering measurements were performed for 6 hours.

RESULTS: In small-angle scattering, the scattering intensity near zero scattering vector is proportional to the square of the molecular weight of the sample. We tried to measure plasmid DNA at low concentrations because we expected that the large molecular weight would guarantee sufficient scattering intensity even at low concentrations. After replacement of buffer by dialysis, the sample concentration was 22.9 μg/mL. The radius of gyration from the SAXS profile was 36.11 ± 1.54 Å. In order to identify the structural ensemble of this DNA, it is necessary to design measurements with smaller measurement errors. In summary, the results suggest that a sample concentration of about 1 mg/mL is required even when measuring large DNA systems.

REFERENCES:

[1] L. F. Liu and J. C. Wang, Proc. Natl. Acad. Sci. USA, **84(20)** (1987) 7024-7027.

[2] L. Postow *et al.,* Proc. Natl. Acad. Sci. USA, **98(15)** (2001) 8219-8226.

[3] S. J. McKie *et al.,* BioEssays, **43(4)** (2021) 2000286.

[4] K. Kasho *et al.,* J. Biol. Chem., **292(4)** (2017) 1251-1266.

[5] J. J. Champoux, Annu. Rev. Biochem., **70** (2001) 369-413.

[6] A. Basu *et al.,* Nat. Chem. Biol., **14(6)** (2018) 565-574.

[7] D. Spakman *et al.,* Nucleic Acids Res., **49(10)** (2021) 5470-5492.

CO6-13 Character of DNA damage induced by nuclear palnt neutron beams

H. Terato, T. Hanafusa, M. Isobe, Y. Sakurai[2], and T. Saito[2]

Advanced Science Research Center, Okayama University
[1]Graduate School of Medicine, Dentistry, and Pharmceutical Sciences, Okayama University
[2]KURNS

INTRODUCTION: DNA is a main target of radiation biological effects. This is because DNA is the only molecule responsible for genetic information, and when it is broken, the life events corresponding to the broken part are stalled. This breakdown of DNA is called DNA damage, as a radiation DNA damage. Radiation DNA damage are generated by direct and indirect effects of ionizing radiation. In the former process, ionizing radiation attack and ionize DNA directly. In the latter process, ionizing radiation react water molecules, which are abundant in the organism, and various reactive oxygen species (ROS) are generated. These ROS cause oxidative damage to DNA. For oxidative DNA damage, especially oxidative base damage, the sites of ROS attack have been largely identified in the DNA molecule, and both their types and yields are fairly accurate by previous studies. In the early days of radiation research, such studies were conducted with readily available X-rays and gamma rays, but now they are conducted with a variety of radiation types, including particle beams. It has been found that the type and yield of DNA damage varies greatly depending on the wire type. We have studied for the DNA damage with heavy ion beams, previously [1, 2]. These studies indicated that the DNA damage with heavy ion beams were unique, indicating that a lot of clustered DNA damage were generated including DNA double strand break (DSB), and clustered base lesions. Clustered DNA damage is a complex damage containing multiple lesions in the local region of DNA. This damage is mainly produced by highly concentrated ROS produced by heavy ion beam. This complexed damage can inhibit DNA polymerization with high efficiently stopping of DNA polymerase moving on DNA, and this damage shows less repairable.

Neutron beam shows severe biological damage like heavy ion beams, but its elucidation is still in the middle of research. In this study, we analyze the DNA damage with neutrons from nuclear power plant to unveil the molecular mechanism of biological effect with neutron beam. In the previous study periods, we found the relatively higher yields of DNA damage with the neutron beams than gamma-rays. In this fiscal year of the research project, we conducted irradiation experiments using several DNA repair-deficient strains to determine what DNA damage species are specific to neutron radiation.

EXPERIMENTS: Cultured cells of Chinese hamster ovary (CHO) strains with various DNA repair background were irradiated with neutron beams in the Kyoto University Reactor. The cells were cultivated with the conventional method. The logarithmic growing cells were recovered by trypsinization and set into polypropylene tubes for irradiation. The estimated dose rate of neutron was 1 Gy h^{-1}. The irradiation periods were 0, 30, 60, 90, 120, 150 min. The irradiated cells were divided into two groups, one for viability and the other for DNA damage analysis. For viability, the cells were immediately dissolved again with the cultured medium and reseeded into fresh medium. The cells were cultivated for 10 days for growing the colony. The colony was fixed with ethanol and stained with methylene blue. The colony number was counted for estimation of the irradiated cell viability. Simultaneously a half of the sampled cells were analyzed by agarose gel electrophoresis for DNA damage estimation. For DNA damage analysis, the irradiated cells were immediately frozen and stored at -80°C until the analysis. The frozen cells were embedded in low melting agarose plug and treated by protease. Then the plugs were subjected by electrophoresis in the manner already reported [2]. We use the Kindai reactor in parallel to conduct our research. This is to generalize the results from the various reactors.

RESULTS AND DISCUSSION: There were a variety of DNA repair-deficient strains of CHO used in this study, but only one is reported here for reasons of space. CHO-V3 strain is deficient in DNA-PK_{cs}, which prevents the function of nonhomologous end joining (NHEJ). Thus, it is extremely susceptible to DNA double-strand breaks, the major DNA damage caused by radiation. The degree of sensitivity with D_{37} of CHO-V3 for the neutron beam was 0.22 Gy. On the other hand, the D_{37} of CHO-AA8, a wild type of CHO-V3 was 0.39 Gy. Its sensitivity to neutron radiation is ten times higher than that of gamma radiation. And NHEJ insufficiency increases that sensitivity by a factor of two. Its sensitivity to neutron radiation is ten times higher than that of gamma radiation. And NHEJ insufficiency increases that sensitivity by a factor of two. This means that neutrons produce DSBs, which are the target of NHEJ repair. However, the increase in susceptibility is only 2-fold, which may indicate that the susceptibility is already high enough, or that some other damage species other than DSBs are produced by neutrons. The contribution of gamma-rays contaminated in the reactor neutron beams must also be clarified. We will await the results of the DNA damage analysis we are going to perform and discuss.

REFERENCES:

[1] H. Terato *et al.,* J. Radiat. Res., **49** (2008) 133-146.
[2] Y. Tokuyama *et al.,* J. Radiat. Res., **56** (2015) 446-455.

CO6-14 Distribution analysis of the chemical modification of the amino acid residues in mice lens structural proteins during age-related cataract

S. Matsushita[1], A. Nakamura[1], Y. Suzuki[1] and T. Takata[2]

[1] *Dept of Materials and Applied Chemistry, Nihon University*
[2] *Institute for Integrated Radiation and Nuclear Science, Kyoto University*

INTRODUCTION:
Age-related cataracts are the leading causes of blindness in world. Several risk factors, contributing to the development of cataracts, have been reported. Above all, abnormal lens protein aggregation and insolubilization has been believed as the main process [1]. Alteration of lens protein structure, caused by covalently post-translational modifications, are thought to be critical for maintaining lens protein homeostasis. We have shown that the isomerization of Aspartate residues (iso-Asp) as a scale for a lens aging. One of those Asp is Asp151 in human lens αA-crystallin. Since the sequence of αA-crystallin was highly conserved in mammal, we also used the same method to identify the isomerization of Asp151 in porcine lens previously. As a result, we could identify the isomerization of Asp151 in adult porcine lens. However, the distribution of iso-Asp151 in lens was very obscured. Therefore, we are to address revealing the distribution of isomerized Asp containing proteins in the lens.

Imaging Mass Spectrometry (IMS) is a powerful tool for revealing the distribution of biomolecules, including proteins, on tissues. This technique requires the preparation of high-quality sections. However, it is difficult to prepare sections from water-rich tissue, such as lens. In addition, sensitivity is decreased by background peaks and ionization efficiency. Therefore, it is essential for optimizing sample preparation to analyze the target molecules/modifications.

We have tried different methods to establish the high-quality section of lens. In this study, we first attempted to contain the tissue block with 4% carboxyl methylcellulose (CMC) for preparing lens sections. Next, we attempted to sealed small biomolecules on lens by metal nanoparticles of Zinc Oxide (ZnO) and compared them with cataract and aged eyes [2].

EXPERIMENTS:
ZnO solution
ZnO was suspended in 40 mM sodium acetic acid in acetonitrile/water/trifluoroacetic acid (50/50/0.1, v/v/v) at a concentration of 1 mg/mL.
Tissue section
The cataractous and control lensed were collected from C57BL/6JJcl female mice (CLEA Japan, Inc.,). After extraction of lenses, there lensed were frozen immediately without fixation. The eyes were embedded in 4% CMC solution in liquid nitrogen, following to be sectioned into 10 μm thicknesses, then put on the indium-thin-oxide-coated glasses. The sections were coated with ZnO solution using a manual sprayer.
IMS
A JMS-S3000 SpiralTOF-MS system (JEOL) was used in the spiral-positive ion mode with a detection range of *m/z* 100-1000 for IMS.

RESULTS:
Unfortunately, huge cracks were observed in sections, even if those were embedded by CMC. We tried to use higher concentration of CMC, yet there were still occurring cracks on the lens. The CMC was easily peeled while spraying the ZnO solution, would cause the loss of sections on preparation. Therefore, we must do effort to optimize sample preparation/spraying methods for obtaining ideal images for IMS.

In current study, we found out some small biomolecules in each eye sample. In comparison of signal intensities, we found molecule, being *m/z* 103.9 from cataract tissue, was higher than that from aged eyes (Fig. 1). Distribution of the peak were located on the scleral on control aged lens, but not intense on cataract lens. To the end, we success to show difference of small molecule distribution even in clacked lens section between aged and cataractous lenses, but still need to be optimizing methodology for getting distribution of peptides in further study.

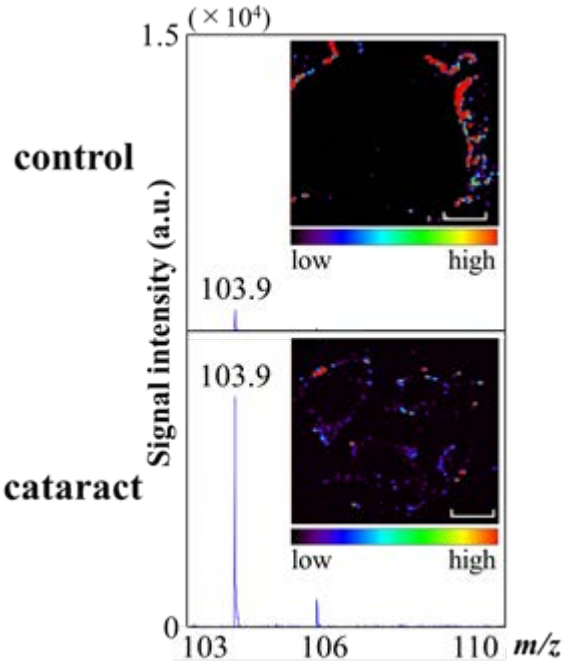

Fig. 1. MS spectra of each sample and distribution at *m/z* 103.9. (Scale bar: 0.5 mm).

REFERENCES:
[1] N. Fujii *et al.*, Biochim. Biophys. Acta, **1860** (2016) 183-191.
[2] C. Chen *et al.,* J. Am. Soc. Mass. Spectrom., **32** (2021) 1065-1079.

CO6-15 Neutron activation of medicines for development of new imaging methodology

A. Toyoshima, N. Koshikawa[1], Y. Kadonaga[2], M. Masubuchi[1], S. Takahashi[1], K. Tokoi[3], H. Aoto[4] and J. Kataoka[1]

Institute for Radiation Sciences, Osaka University
[1]Graduate School of Advanced Science and Engineering, Waseda University
[2]Graduate School of Medicine, Osaka University
[3]Graduate School of Science, Osaka University
[4]School of Science, Osaka University

INTRODUCTION: In the drug delivery system, it is desired to obtain high therapeutic effects with no side-effects by direct transportation of medicine to lesion. At present, it is impossible to simultaneously evaluate the accumulation of administrated medicine in a targeted organ and its therapeutic effect without incision. Imaging of radiations emitted from activated medicine, however, makes it possible to visualize the pharmacokinetics without incision. In our group, an advanced imaging camera available for a wide energy range of X- and γ-rays has been already developed [1]. Previously, we reported the activation of gold nano-particle (AuNP), platinum nano-particle (PtNP), Cisplatin, and Gadoteridol by thermal neutron to produce short-lived radioisotopes suitable for imaging: ^{198}Au (half-life = 2.69 d), ^{159}Gd (18.48 h), and ^{197}Pt (18.3 h) [2]. In this study, we investigated preparation and stability of activated AuNP and Cisplatin for developing a novel methodology of the radioactivated medicine imaging. In addition, we performed the visualization of activated AuNP.

EXPERIMENTS: Dried mPEG-modified gold nano-particles (AuNP-S-mPEG) in polypropylene (PP) tubes were enclosed in small plastic bags. Cisplatin was also enclosed in a small plastic bag. The prepared AuNP and Cisplatin samples were irradiated by neutron using the Pn-2 pneumatic transport system of KUR for 10 min at 5 MW. After the irradiation, these were transported to Osaka University. [^{198}Au]AuNP-S-mPEG was dissolved in deionized water. Condition of [^{198}Au]AuNP-S-mPEG was investigated by ultraviolet-visible absorption spectroscopy (UV-vis). After that, we performed imaging of the [^{198}Au]AuNP-S-mPEG with hybrid Compton camera (HCC) which can visualize wide-band X-rays and gamma rays ranging from a few tens of keV to nearly 1 MeV. The [^{198}Au]AuNP-S-mPEG sample was added into three holes with 10-mm diameters on a phantom. HCC was placed 2 cm apart from the phantom, and measurement with HCC was performed for 20 min. The energy window was set to 412±30 keV to visualize the 412-keV gamma ray emitted form Au-198. As for cisplatin, the stability of activated samples was investigated using high-purity liquid chromatography (HPLC).

RESULTS: Irradiation of neutron in KUR gave approximately 0.4 MBq of [^{198}Au]AuNP-S-mPEG, which contains 25 μg of Au. Photos of dried AuNP before irradiation and dissolved AuNP after irradiation are shown in Figs. 1 (a) and (b), respectively. The red color of the dissolved AuNP suggests that no critical aggregation occurred even after the irradiation. Obtained UV-vis Spectra are shown in Fig. 1 (c). The blue, green, and red and purple lines represent non-irradiated (cold) AuNP dissolved in deionized water, cold AuNP which was dried in PP tube and then re-dissolved in deionized water, AuNP irradiated with neutrons and then dissolved in deionized water. Peaks around 510 nm originated from AuNP. Comparing the blue/green lines (AuNP before irradiation) and red/purple lines (AuNP after irradiation), no significant peak shift was observed. This confirms that the AuNP were successfully activated without aggregation under the present condition. It should be noted that the aggregation was observed under some other irradiation conditions using the different types of AuNP or PP tubes. Therefore, further investigation is necessary to determine the optimum conditions.

The image of [^{198}Au]AuNP-S-mPEG in the three 10-mm holes on the phantom is shown in Fig. 2. The 3 holes were clearly separated, which suggests the potential of HCC as the effective device to visualize the accumulation of the AuNP in organs of a mouse.

In the results of HPLC of cisplatin, hydrolysis of Pt bonds was partly observed. This denaturation of cisplatin is under investigation; there are some possible causes other than neutron irradiation such as photolysis. We will clarify the reason of denaturation and establish the optimum method to generate radioactive cisplatin.

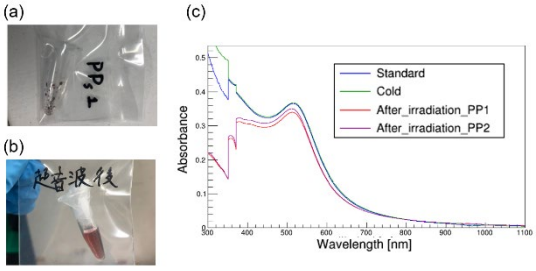

Fig.1. (a) Dried AuNP in PP tube, (b) dissolved AuNP in deionized water after neutron-irradiation, and (c) Result of UV-vis.

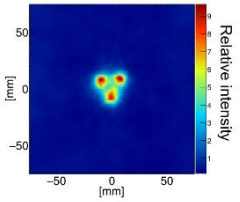

Fig. 2. Image of activated AuNP obtained with HCC.

REFERENCES:

[1] A. Omata *et al.*, Sci. Reports, **10** (2020) 14604.
[2] N. Koshikawa *et al.*, Nucl. Instrum. Methods Phys. Res. A, **1045** (2023) 167599.

CO6-16 Polyglycerol Functionalized ^{10}B Enriched Boron Carbide Nanoparticle as an Effective Bimodal Anticancer Nanosensitizer for Boron Neutron Capture and Photothermal Therapies

Y. Wang[1], G. Reina[1], H. G. Kang[1], X. Chen[1], Y. Ishikawa[2], M. Suzuki[3], and N. Komatsu[1]

[1] *Graduate School of Human and Environmental Studies, Kyoto University*
[2] *National Institute of Advanced Industrial Science and Technology, Research Institute for Advanced Electronics and Photonics, Central 5, 1-1-1 Higashi, Tsukuba, Ibaraki 305-8565*
[3] *Institute for Integrated Radiation and Nuclear Science, Kyoto University*

Boron neutron capture therapy (BNCT) is a non-invasive cancer treatment with little adverse effect utilizing nuclear fission of ^{10}B upon neutron irradiation [1]. While neutron source has been developed from a nuclear reactor to a compact accelerator, only two kinds of drugs, boronophenylalanine and sodium borocaptate, have been clinically used for decades despite their low tumor specificity and/or retentivity. To overcome these challenges, various boron-containing nanomaterials, or "nanosensitizers", have been designed based on micelles, (bio)polymers and inorganic nanoparticles. Among them, inorganic nanoparticles such as boron carbide can include much higher ^{10}B content, but successful *in vivo* applications are very limited. Additionally, recent reports on photothermal effect of boron carbide motivated us to add another modality of photothermal therapy. In this study, ^{10}B enriched boron carbide ($^{10}B_4C$) nanoparticle was functionalized with polyglycerol (PG), giving $^{10}B_4C$-PG with enough dispersibility in a physiological environment [2]. Pharmacokinetic experiments show that $^{10}B_4C$-PG fulfills the following three requirements for BNCT; 1) low intrinsic toxicity, 2) ^{10}B in tumor / tumor tissue (wt/wt) ≥ 20 ppm and 3) ^{10}B concentrations in tumor / blood ≥ 3. *In vivo* study reveals that neutron irradiation after intravenous administration of $^{10}B_4C$-PG suppressed cancer growth significantly and eradicated cancer with help of near-infrared light irradiation (Fig. 1) [3].

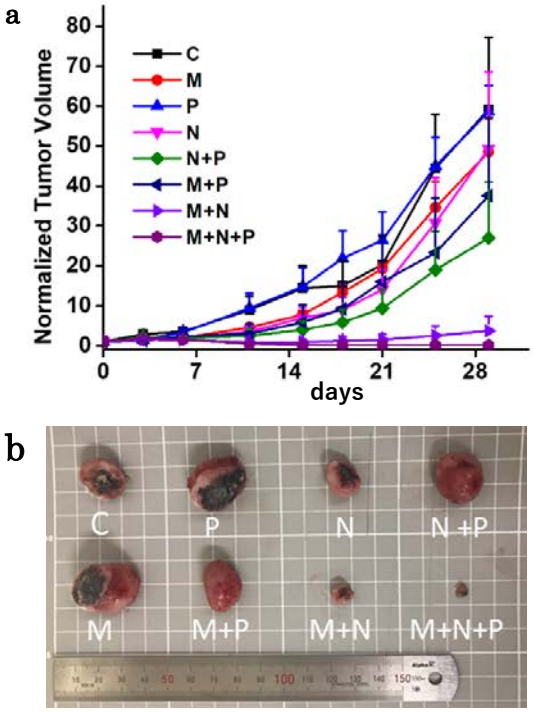

Fig. 1. Bimodal BNCT/PTT by **$^{10}B_4C$-PG**; (a) time coarse of tumor size (n = 3), (b) tumors after a month (C: control, M: $^{10}B_4C$-PG injection, P: 660 nm LED light irradiation, N: neutron irradiation) [3].

REFERENCES:

[1] M. Nishikawa *et al.*, Bull. Chem. Soc. Jpn., **94(9)** (2021) 2302-2312. [selected paper, highlighted at the inside cover].
[2] Y. Zou *et al.,* ACS Nano, **14(6)** (2020) 7216-7226.
[3] L. Zhao *et al.,* Angew. Chem.Int. Ed., **50(6)** (2011) 1388-1392. [highlighted atback cover].
[4] Y. Wang *et al.,* Small, **18(37)** (2022) 2204044.

CO6-17 Solution structure of intrinscially disordered protein

R. Inoue, T. Oda[1], and M. Sugiyama

Institute for Integrated Radiation and Nuclear Science, Kyoto University
[1]Department of Life Science, Rikkyo University

INTRODUCTION: It is considered that three-dimensional ordered structure is a prerequisite for maintain the proper development of protein's intrinsic function. In consistent with such common well-recognized knowledge, Wright and Dyson [1] for the first time reported that some proteins intrinsically lack three-dimensional ordered structure even under their functionally active state. At present, these proteins are known as intrinsically disordered proteins (IDPs) and play biologically significant biological roles, especially for those in Eukaryotes. Both high contents of hydrophilic and charged residues in IDP [2] make the destabilization of ordered structures, leading to its highly flexible structure in solution. It is considered the modulation of solution environment, such as temperature, ionic strength and so on, would affect the local configurations of above-described hydrophilic and highly charged residues. As a result, these changes in local scales could induce its overall structure as well. Among the parameters that can modulate solution environment, we especially focused on the effect of temperature change on solution structure and dynamics of IDP. In this work, we especially adopted small-angle X-ray scattering (SAXS) to analyze the ternary structures of IDP at different temperatures. As an example of IDP, we focused on intrinsically disordered region (IDR) of Hef (helicase- associated endonuclease for fork-structured DNA) (Hef-IDR) [3].

EXPERIMENTS: SAXS measurements were obtained on Photon Factory BL-6A (Tsukuba, Japan). The wavelength of the X-ray and the sample-to-camera distance were set to 1.5 Å and 2038.9 mm, respectively. The observed SAXS intensity was corrected for background, empty capillary and buffer scatterings, and transmission and converted to the absolute intensity using the scattering of water. All the data reduction was performed using the software "SAngler".

RESULTS: Figure 1 (a) shows the SAXS profiles at five different temperatures and no prominent change of SAXS profiles was observed with increasing the temperature. It means highly flexible configurations in solution state. We then calculated the temperature dependence of radius of gyration (R_g) utilizing the Guinier approximation and resulting temperature dependence of R_g is given in Fig. 1 (b). Interestingly, R_g decreased with increasing the temperature. It should be stressed that the globular proteins normally tend to lose higher-order structures with increasing temperature. Namely, the sensitivity of solution structure of IDP to the temperature change is totally different from that of globular one. Similar results were already reported by Uversky [2] as well, hence this

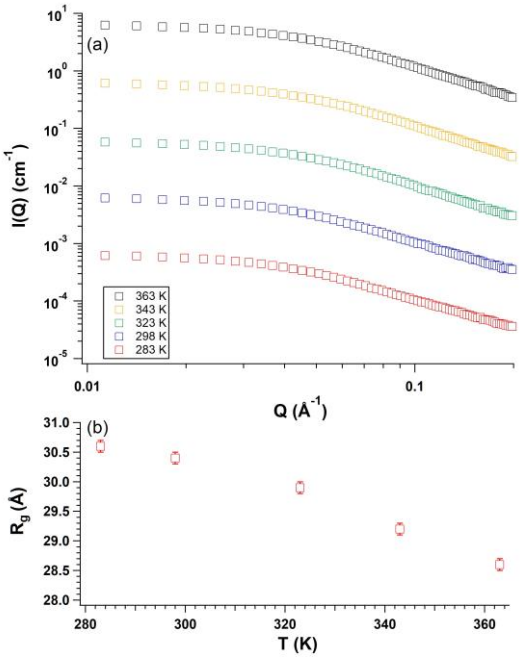

Fig. 1. (a) SAXS profiles of Hef-IDR at 283 K (red square), 298 K (blue square), 323 K (green square), 343 K (yellow square) and 363 K (black square), respectively. (b) Temperature dependence of R_g of Hef-IDR.

must be a characteristic feature of IDP. It is expected that a promotion of ordered structure with increasing temperature could be related to this experimental result. To figure out the possible mechanism of this singular result, we also started to study the dynamics of Hef-IDR in solution through quasielastic neutron scattering [4] which enables to analyze the internal of protein in solution.

REFERENCES:

[1] H. J. Dyson, P. E Wright., Curr. Opin. Struct. Biol. **12**, (2002) 54.
[2] V. N. Uversky, Protein J. **28**, (2009) 305.
[3] S. Ishino *et al*., J. Biol. Chem. **289**, (2014) 21627.
[4] R. Inoue *et al.*, Sci. Rep., **10**, (2020) 21678.

CO6-18 Oligomeric structure and interaction sites of Dpcd involved in actin bundle network formation

H. Koeda, K. Shinohara, K. Morishima[1], R. Inoue[1], M. Sugiyama[1] and M. Yohda

Department of Biotechnology and Life Science, Tokyo University of Agriculture and Technology
[1]Institute for Integrated Radiation and Nuclear Science, Kyoto University

INTRODUCTION: Cilia are organelles found on the surface of cells with hair-like protrusions. Cilia are classified into two types: motile cilia and non-motile cilia. Loss of function in motile cilia leads to primary ciliary dyskinesia (PCD). In knockout mice for the Dpcd gene, one of the causative genes for PCD [1,2], the actin bundle network, which is essential for ciliary movement, was not correctly formed in the cell surface layer. Previous studies showed that the Dpcd protein binds to actin and has the activity of bundling the fibers *in vitro*. The crystal structure analysis revealed the structure of the region from the 86th Glu to the 183rd Leu. The structure of this region showed a similar folding to small heat shock proteins. There is a characteristic positive charge cluster on the surface. The crystal structure analysis as well as structural prediction by alphafold2 suggested that K96, R107, and the region corresponding to basic amino acid residues from 185th to 191st is conserved in eukaryotes. Since the surface of actin is net negatively charged, the positive charge cluster region in the Dpcd is suggested to be involved in bundling F-actin. The fact that the concentration of Dpcd correlated with the actin-bundling activity means that oligomerization of Dpcd is necessary for activity acquisition. This study aimed to elucidate the oligomerization structure of Dpcd and the function of the positive charge cluster.

EXPERIMENTS: Mutant Dpcd genes were prepared by QuikChange method. Wild type and mutant Dpcd proteins with C-terminal His-tag were expressed in *E. coli* BL21(DE3) using pET15b vector. The *E. coli* lysate was applied on a Nickel column and Dpcd proteins were eluted with imidazole. After the removal of His-tag by thrombin, Dpcd proteins were purified by gel filtration using HiLoad 26/600 Superdex200. The affinity between actin and Dpcd proteins was examined by co-precipitation experiment with F-actin. The bundling of actin was observed by fluorescence microscopy using Rhodamine Phalloidin labelled actin. The oligomer structure of wild type Dpcd was examined by sedimentation velocity Analytical ultracentrifugation (SV-AUC).

RESULTS: Based on the structure model, we thought that Dpcd functions as a dimer or larger conformer (Fig. 1). Then, we analyzed the oligomeric structure of Dpcd wild type by AUC at various conditions (Fig. 2). Dpcd existed primarily as monomers or dimers. Although there was some change in the monomer and dimer equilibrium by the concentration and sample history, concentration dependent increase of dimer was not observed.
We conducted co-precipitation experiments between F-actin and wild-type or mutant Dpcd proteins, in which the basic amino acids on the surface were changed to acidic amino acids. Dpcd wild type was co-precipitated with F-actin, but the mutation in the positively charged surface region 1, which is predicted to be the binding site for F-actin, impaired the interaction. In contrast, mutations in the other region (region 2) did not affect the interaction. When we examined the actin-bundling activity, all mutants lost the activity. These results suggest that Dpcd binds to actin filaments by region 1 and that region 2 is required for the bundling.

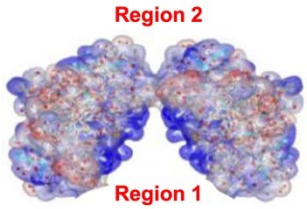

Fig. 1. Structure model of Dpcd tetramer

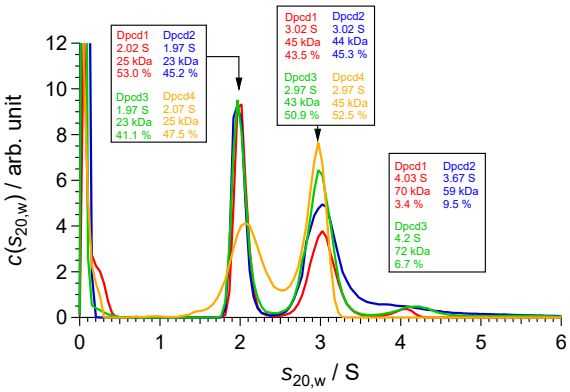

Fig. 2. SV-AUC results of Dpcd WT. Dpcd1: 1.5 mg/ml, Dpcd2: 15 mg/ml sample diluted to 1.5 mg/ml, Dpcd 3: 15 mg/ml sample diluted to 5 mg/ml, Dpcd 4: 1.5 mg/ml sample diluted to 0.3 mg/ml.

DISCUSSION: We had detected monomer and dimer of Dpcd in SV-AUC experiment. The basic amino acids on the surface of Dpcd were suggested to be involved in binding and bundling to actin.

REFERENCES:

[1] M. R. Knowles *et al.*, Am J Respir Cell Mol Biol., **30** (2004) 428-34.
[2] K. Shinohara *et al.*, Nat Commun., **3** (2012) 622.

CO6-19 Analysis of dinamic structure of intrinsically disordered protein

T. Oda, R. Oi[1], R. Inoue[2], K. Morishima[2], A. Okuda[2], M. Sugiyama[2], and M. Sato[1]

Department of Life science, Rikkyo University
[1]Graduate school of Medical Life science, Yokohama City University
[2]Institute for Integrated Radiation and Nuclear Science, Kyoto University

INTRODUCTION: Intrinsically disordered proteins (IDP), which do not have a rigid folded structure, play important roles in living cells. Because of its flexibility, it is difficult to solve its three-dimensional structure by X-ray crystallography or cryo-electron microscopy. Thus, it is hard to discuss its function based on its structure. Small-angle X-ray/neutron scattering (SAXS/SANS) is a useful method to analyze IDP because it provides structural information of IDP in an aqueous solution. In this study, we attempted to solve dynamic structures (various conformations in aqueous solution) of Hef with Ensemble Optimization Method (EOM) [1].

Hef is a protein involved in the repair of DNA damage. Hef consists of two folded domains (Helicase domain and Nuclease domain), which are connected by an intrinsically disordered region (IDR) [2]. In the previous study, we have shown that Hef tends to form aggregates (or oligomers) in aqueous solutions. The scattering data without contributions from aggregates, is required to determine the dynamic structure of Hef by EOM. For this purpose, we applied the AUC-SAS (analytical-ultracentrifugation and SAS) method [3] to the scattering data to remove contributions from aggregates.

EXPERIMENTS: The SAXS measurements were performed with BL15A2 installed at Photon Factory. The same sample solution (but not used for SAXS measurements) was used for AUC analysis. Prior to SAXS and AUC analysis, samples were subject to size exclusion chromatography to remove aggregates, and the protein concentration was adjusted to 0.5 mg/mL.

RESULTS: Since Hef tends to form aggregates (oligomers) at high protein concentrations, SAXS measurements were performed at low protein concentrations (0.5 mg/mL). AUC analysis showed that it contains a small amount of dimer. To obtain the scattering profile from monomeric Hef selectively, the AUC-SAS was applied to the observed SAXS profile. Fig. 1 shows the raw scattering data and the data after applying the AUC-SAS. The radius of gyration; R_g after applying AUC-SAS (45.6±0.9 Å) was slightly smaller than that from the raw data (46.2±0.9 Å).

Using the scattering profile of monomeric Hef, we attempted to solve the dynamic structure of Hef with EOM. EOM first created a large number of model structures (initial ensemble). Then, a small number of structure combinations (final ensemble) that can reproduce the experimental scattering curve were selected from the initial ensemble. Fig. 1(C) shows the final ensemble and the fraction of each structure. Hef showed highly flexible structure. The total fraction of compact structures in which the helicase domain and the nuclease domain are close together was relatively high (model 1 and 4, fraction 0.45 and 0.09). There were also extended structures (model 4, fraction 0.18) and intermediate structure between the extended and the compact (model 2 and 3, fraction 0.09 and 0.18). However, due to the high degree of structural freedom, the fraction of each structure cannot be accurately determined from SAXS data alone. Moreover, low contribution for scattering of IDR (consists of 100 amino acids, which is only 12.5% of Hef) makes it difficult to determine the detailed structure of IDR. Thus, further integrated analysis using SANS and molecular dynamics simulation is required.

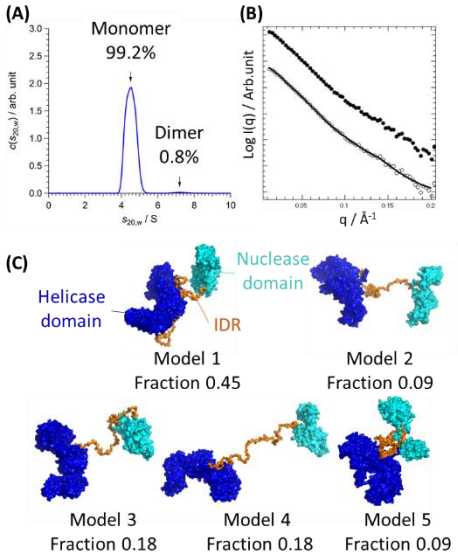

Figure 1. AUC-SAS and EOM analysis. (A) AUC analysis of Hef. (B) Raw scattering data (black filled circle), AUC-SAS (white circle), and back calculated scattering from final ensemble of EOM (black solid line). (C) Final ensemble of EOM.

REFERENCES:

[1] G. Tria *et al.*, IUCrJ. **26**(2015) 207-217.
[2] S. Ishino *et al.*, J. Biol. Chem. **289** (2014) 21627-21639.
[3] K. Morishima *et al.*, Commun Biol. **3** (2020) 294.

CO6-20 Interaction between Mint3 and FIH-1 involved in hypoxia stress responses

R. Maeda, S. Nagatoishi[1], K. Tsumoto[1], K. Morishima[2], R. Inoue[2], M. Sugiyama[2] and M. Hoshino

Graduate School of Pharmaceutical Sciences, Kyoto University

[1]Institute of Medical Science, the University of Tokyo
[2]Institute for Integrated Radiation and Nuclear Science, Kyoto University

INTRODUCTION: Oxygen is essential for many organisms to produce ATP efficiently from nutrients in food. Under the normal oxidative conditions, nutrients are metabolized through glycolytic pathway, tricarboxylic acid cycle and electron transport system. Temporal or local drop of oxygen level induces cells to change the metabolic pathway, which is known as hypoxia stress responses. The responses are mainly triggered by hypoxia inducible factors (HIFs) that activate transcription of a group of genes.

Under the normal oxygen conditions, transcriptional activities of HIFs in the cells are inhibited by the factor inhibiting HIF-1 (FIH-1). On the other hand, several cells including tumor cells and macrophages, metabolize nutrients exclusively by nonoxidative glycolytic pathway even under the normal oxygen levels. Munc-18 interacting protein 3 (Mint3) is recently found to activate the hypoxia responses by binding and inhibiting the activity of FIH-1 in these cells [1]. Although the N-terminal 214 residues (Mint3NT) are found to be necessary for the interaction with FIH-1 to inhibit its activity, little is known about inhibitory mechanisms.

We attempted to elucidate the molecular mechanism of the interaction between Mint3NT and FIH-1 by a various physicochemical methods, including small-angle X-ray scattering, analytical ultracentrifugation, and solution-state NMR.

EXPERIMENTS: High-expression systems for the N-terminal fragment proteins of Mint3 (Mint3NT) and smaller fragments (Mint3(1–117) and Mint3(101–214)), as well as full-length FIH-1 were constructed by E. coli BL21 strains. The proteins were expressed in bacteria grown in LB-broth and ^{15}N-enriched M9 minimal medium to produce unlabeled and ^{15}N-labeled proteins, respectively.

NMR experiments were performed on a Bruker Avance 600 spectrometer equipped with a triple-resonance probe. A typical ^{1}H-^{15}N HSQC experiments were performed at protein concentration of 50 μM. The solvent conditions used were 20 mM sodium acetate (pH 7.3), and 10% D_2O. The chemical shift value was referenced to DSS.

RESULTS: We measured the ^{1}H-15N HSQC spectrum of Mint3NT, and found that the dispersion of resonance peaks was very poor particularly along the ^{1}H-axis, suggesting the absence of strong hydrogen-bonding interactions (Figure 1). Furthermore, the superposition of two HSQC spectra separately recorded for the fragment proteins of Mint3NT (Mint3(1-117) and Mint3(101-214)) reproduced the spectrum of whole protein (Mint3NT), suggesting the absence of significant interaction between the N- and C-terminal regions of Mint3NT.

We also performed a titration experiment of ^{15}N-labled Mint3NT by unlabeled FIH-1, and found that the peak intensities for many residues were remarkably decreased in a concentration dependent manner. We analyzed several 3D-triple resonance experiments, and succeeded to unambiguously assign more than 95% of residues. By mapping the change in the peak intensity along the primary structure of the protein, we found that a broad range of residues were significantly affected by the addition of unlabeled FIH-1, suggesting the involvement of these residues in the interaction between Mint3NT and FIH-1.

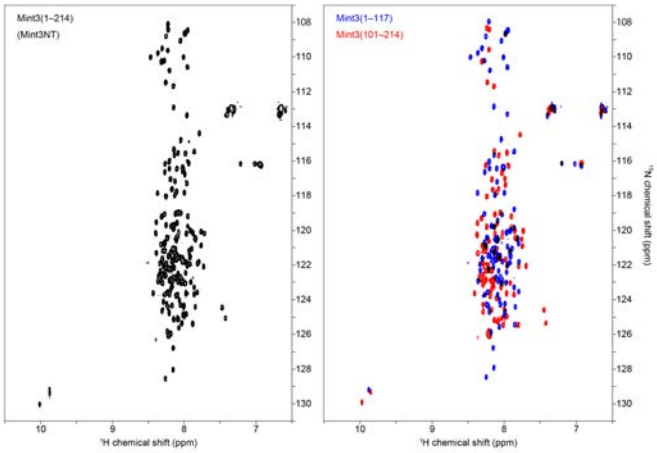

Fig. 1 ^{1}H-^{15}N HSQC spectra of Mint3(1–214) (left) and the superposition of fragment proteins (Mint3(1–117) and Mint3(101–214) (right).

We are now elucidating a change in overall dimensions of protein molecule upon complex formation between globular FIH-1 and intrinsically disordered Mint3NT by small angle X-ray scattering.

REFERENCES:

[1] T. Sakamoto *et al.,* Mol Cell Biol. **34 (1)** (2014) 30-42.

CO6-21 Analysis of novel p53-DBD aggregate for the development of anti-cancer drug

E. Hibino, R. Hijikata, K. Morishima[1], R. Inoue[1], M. Sugiyama[1] and H. Hiroaki.

Graduate School of Pharmaceutical Science, Nagoya University
[1]Institute for Integrated Radiation and Nuclear Science, Kyoto University

INTRODUCTION: The tumor suppressor protein p53 is a transcription factor that induces DNA repair proteins when DNA is damaged or induces apoptosis when DNA damage is severe, thereby preventing cells from turning cancerous. In fact, p53 mutations are found in half of all cancers, and preservation of p53 function is important in terms of cancer prevention. However, the development of therapeutic drugs targeting p53 has been challenging. It has been reported that the DNA-binding domain of p53 (p53-DBD) is aggregation-prone, that the introduction of hotspot mutations which are common in cancer increases its aggregation, and that the aggregates present heterogeneous [1,2].

We recently found that the environments in which amyloid aggregates and amorphous aggregates of p53-DBD tend to form are distinct [3]. They found that high salt and sugar concentrations inhibited amorphous aggregate formation of p53-DBD and suppressed loss of function. Inhibition compounds of aggregation of p53-DBD provides lead compounds for anti-cancer drugs that prevent loss of function of p53 [4], thus we constructed a screening system. Several compounds were evaluated and found to induce the formation of aggregates that are neither amorphous nor amyloid aggregates.

EXPERIMENTS: The p53-DBD protein solution was produced as a GST-fused form in an *E. coli* expression system. After GST-tag affinity purification, the GST-tag was cleaved with HRV3C protease and finally purified by size exclusion chromatography. 1 mg/mL p53-DBD protein solution with or without the addition of Compound A (Com. A) was incubated at 37°C for 1 h for DLS measurements.

DLS measured by using a system equipped with a 22-mW He-Ne laser, an Avalanche Photo Diode mounted on static/dynamic compact goniometer, ALV/LSE-5003 electronics, and ALV-5000 Correlator. Incident angles were 45°, 60°, 75°, 90°, 105°, 120°, and 135°, and measurements were taken three times at each angle.

RESULTS: The change in the size of p53-DBD aggregates with and without the addition of Com. A was investigated by DLS, and we found that as the amount of Com. A increased, the size of the aggregates increased. Furthermore, the heterogeneity of the aggregates decreased in proportion to the amount of Com. A.

There have been previous examples of compounds reducing the toxicity of aggregates, such as epigallocatechin gallate, which induces non-toxic oligomers rather than amyloid fibrils in the amyloid β protein [5,6]. We will further investigate the effect of this novel aggregate formation on p53-DBD function.

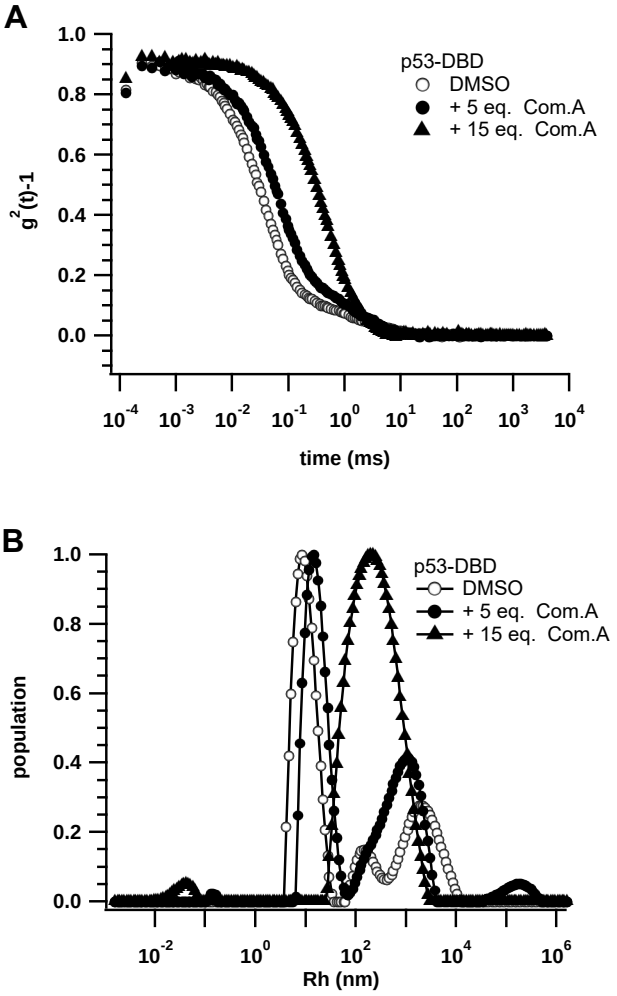

Fig. 1. Results of DLS measurements of p53-DBD aggregates without and with 5 and 15 equivalents of Com. A. (A) Auto-correlation function. (B) Histogram of hydrodynamic radius.

REFERENCES:

[1] A.P.D.A Bom *et al.,* J. Biol. Chem., **287** (2012) 28152-18162.
[2] S. Ghosh *et al.,* Cell Death Differ., **24** (2017) 1784-1798.
[3] E. Hibino *et al.,* Front. Mol. Biosci. **9** (2022) 869851.
[4] E. Hibino *et al.,* Biophys. Rev. **14** (2022) 267–275.
[5] Ehrnhoefer DE *et al.,* Nat. Struct. Mol. Biol. **15** (2008) 558-566.
[6] Bieschke J. *et al.*, Proc. Natl. Acad. Sci. **107 (17)** (2010) 7710-7715.

CO6-22 Analysis of the GATA3-nucleosome complex in solution

H. Tanaka[1], A. Okuda[2], K. Morishima[2], N. Sato[2], R. Inoue[2], M. Sugiyama[2] and H. Kurumizaka[1]

[1]*Laboratory of Chromatin Structure and Function, Institute for Quantitative Biosciences, The University of Tokyo*
[2]*Institute for Integrated Radiation and Nuclear Science (KURNS), Kyoto University*

INTRODUCTION:
In eukaryotes, genomic DNA is packaged into nucleosomes, the fundamental unit of chromatin structure. Nucleosome is the structure, in which about 150 base-pairs of genomic DNA are wrapped around a histone octamer composed of four core histones (H2A, H2B, H3, and H4). The nucleosome structure inhibits protein-DNA interactions including many transcription factors. However, a group of transcription factors called “pioneer transcription factors” is known to have the intrinsic ability to bind its target DNA motifs in the nucleosome. A pioneer transcription factor bound to the nucleosome may facilitate the recruitment of transcription factors and chromatin remodeling factors, which result in the change of the local chromatin structure.
The pioneer transcription factor GATA3 is a key regulator of developmental pathways including mammary epithelial cell differentiation and T cell development [1]. GATA3 is frequently mutated in breast cancer [2]. It has been reported that GATA3 binds to the target DNA motif in the nucleosome, and converts the chromatin structure from closed to open conformation [3]. However, it is still unknown how chromatin structure is changed by GATA3 binding. In this study, we performed analytical ultracentrifuge (AUC) and small angle X-ray scattering (SAXS) of GATA3-nucleosome complex to elucidate the structural change in nucleosome induced by GATA3 binding.

EXPERIMENTS:
The reconstituted nucleosome and the recombinant GATA3 DNA binding domain were mixed to form GATA3-nuclesome complex. The complex was purified by sucrose density gradient centrifugation to remove free GATA3. The quality of the purified sample was confirmed by non-denaturing PAGE and SDS-PAGE.
SAXS analysis was performed with a NANOPIX instrument (RIGAKU) at the Institute of Radiation and Nuclear Science, Kyoto University. We also performed AUC to correct the SAXS data by removing the SAXS profile portion derived from slight aggregates as previously described [4].

RESULTS:
We successfully purified the GATA3-nucleosome complex for AUC and SAXS analysis by sucrose density gradient centrifugation. AUC analysis confirmed the absence of free GATA3 and nucleosome in the purified GATA3-nucleosome complex fraction. On the other hands, AUC analysis showed the presence of aggregated components in the GATA3-nucleosome solution. SAXS analysis was then performed with the purified GATA3-nucleosome sample. Scattering profiles were calculated after removing the aggregated components in solution. Compared to the SAXS profile of nucleosome alone, the SAXS profile of the GATA3-nucleosome complex showed a difference, especially in the region larger than q=0.12Å^{-1}. This difference may be attributed to the increased molecular asymmetry induced by the GATA3 binding to the nucleosome.

REFERENCES:
[1] I. Ho *et al.*, EMBO J., **10** (1991) 1187-1192.
[2] B. Pereira *et al*., Nat. Commun., **7** (2016) 11479.
[3] M. Takaku *et al.*, Genome Biol., **17** (2018) 36.
[4] K. Morishima *et al*., Commun. Biol., **3** (2020) 294.

CO6-23 Measurement of the resistance of the spores of *Bacillus subtilis natto* to gamma radiation

T. Chatake, T. Saito, Y. Yanagisawa[1]

Institute for Integrated Radiation and Nuclear Science, Kyoto University
[1]Faculty of Pharmacy, Chiba Institute of Sciences

INTRODUCTION: It is well known that *Bacillus subtilis* has high resistance to ionizing radiation, because *Bacillus* forms spores [1]. *Bacillus* transform themselves into spores like seeds of plants, and the spores have high resistance to various severe conditions. On the other hand, vegetative cells of *Bacillus* are believed to have lower environmental resistance like other bacteria such as *Escherichia coli*. This radioresistance is completely different from that of radioresistant bacteria such as *Deinococcus radiodurans*, which has powerful molecular mechanisms that repair damaged DNA and protect proteins and lipids from radiation [2,3]. *B. subtilis* is a type species of *Bacillus*, and *B. subtilis natto* is one of the most famous subspecies of *B. subtilis*. It is used for the production of the traditional Japanese fermented food "natto", which contains biologically active substances: nattokinase [4], water-soluble vitamin K [5], and so on. The aim of this project is to elucidate the radioresistance of two forms (vegetative cell and spore) of *B. subtilis natto*. The two forms with the different resistances are expected to be useful for the breeding of this bacterium by gamma irradiation. The radioresistance of vegetative cells of *E. coli* has been studied in detail. In our previous study, we established an experimental procedure of to evaluate the radioresistance of *B. subtilis natto* in the same manner as that of *E. coli*, and measured the resistance of the vegetative cells to gamma radiation [6]. In the present study, the resistance of spores to gamma radiation.

EXPERIMENTS: The gamma irradiation experiment of *Bacillus subtilis natto* spores was performed out in the same manner as that of vegetative cells. The experimental protocol of the vegetative cells was previously reported in detail [6,7]. Glycerol stock of *B. subtilis natto* clone was incubated in 4 mL LB medium at 315 K with shaking (1200 rpm) for 65 h. After the incubation, 1 mL of the culture medium was centrifuged at 1,000×*g* for 10 min. After centrifugation, the supernatant was removed, and the precipitate was suspended in 1 mL Phosphate-buffered saline (PBS). The solution was heated at 353 K for 10 min in a dry block bath, in order to kill vegetative cells. Seven samples were prepared, and irradiated with gamma rays at doses of 0, 100, 200, 400, 800, 1600, and 3200 Gy at a dose rate of 10.8 Gy/min. After the irradiation, each solution was diluted with PBS, and plated. Colony formation units were counted after incubation for 8 h at 315 K.

RESULTS: As shown in Fig. 1, the resistance of the spores to gamma radiation was much higher than those of the vegetative cells. The radiation survival fraction curve of spore is a liner function, and the mean lethal dose (MLD) of spores was estimated to be 677.9 Gy. The high MLD value is expected from previous studies. On the other hand, the MLD of the vegetative cells was estimated to be 100.9 Gy, where the values at 0–50 Gy were excluded from the calculation. The difference between the two values indicates the dual nature of the resistance of *B. Subtilis natto* to gamma radiation. The MLD for the vegetative cells of *B. Subtilis natto* is close to that for *E. coli*. Meanwhile, the resistance to low radiation dose (0–50 Gy) observed in the vegetative cells of *B. subtilis natto*. was not observed in the case of the spores.

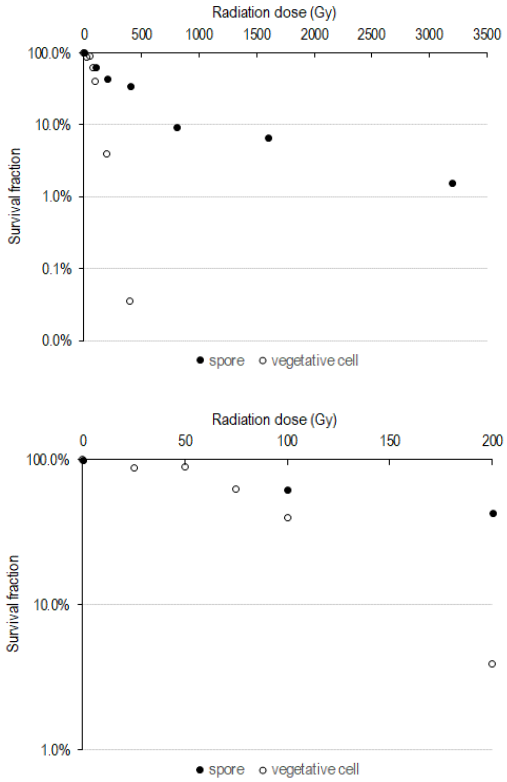

Fig. 1. The radiation survival fraction curve of *Bacillus subtilis natto* in the range of 0−3200 Gy (upper) and of 0–100 Gy (lower).

REFERENCES:

[1] P. Stelow, J. Appl. Microbiol., **101** (2006) 514−525.
[2] T. Saito, Viva Origino, **30** (2007) 85-92.
[3] A. Pavlopoulou *et al.,* Mutat. Res. Rev. Mutat. Res., **767** (2016) 92-107.
[4] H Sumi *et al.*, Experentia. **42** (1987) 1110-1111.
[5] H. Sumi *et al.,* Nippon Nogeikagaku Kaishi **73** (1999) 599-604.
[6] Y. Yanagisawa *et al.,* KURRI PROGRESS REPORT 2016, (2017) 65.
[7] T. Chatake *et al.,* Radiation biolo-gy research communications, **53** (2018) 280-290.

CO6-24 Analysis of water-soluble vitamin K complex from *Bacillus subtilis natto*

T. Chatake, A. Okoda, K. Morishima, R. Inoue, M. Sugiyama, T. Takata, Y. Yanagisawa[1]

Institute for Integrated Radiation and Nuclear Science, Kyoto University
[1]Faculty of Pharmacy, Chiba Institute of Sciences

INTRODUCTION: Vitamin K promotes bone formation; therefore, it is expected to suppress osteosis [1]. In addition, recent studies have reported that it also contributes to cardiovascular health [1]. Menaquinone-7 is a subtype of vitamin K_2 and is abundant in natto, a traditional Japanese food. Natto is produced from soybeans by fermentation using *Bacillus subtilis natto*. *Bacillus subtilis natto* produces a water-soluble macromolecular complex containing menaquinone-7, while menaquinone-7 alone is fatty-soluble. The molecular complex is of interest not only to researchers but also to companies because its solubility in water would be an advantage in nutritional, medical and pharmaceutical applications. However, the structure of the complex was not well understood. Ikeda and Doi reported that the complex was composed of peptides, and the main component was named K-binding factor (KBF) [2]. However, in the quarter of a century since this report, no further structural studies have been reported. In order to reveal the molecular structure of the complex in detail, the purification protocol of the complex was developed in our previous study [3]. The molecular weight was estimated to be ~100k, and the peptide of KBF was identified by Tris-Tricine SDS electrophoresis.

Recently, MALDI-TOF/MS of the complex shows strong peaks in the range of m/z = 1000 ~ 1100 [4], indicating that the molecular weight of KBF would be ~1k, while the previous electrophoresis suggested that the molecular weight would be ~3k [2,3]. It is an important question what are the properties of KBF: peptide length, amino acid composition, sequence, and so on. In the present study, the further analyses of KBF were carried out.

EXPERIMENTS: The water-soluble complex of menaquinone-7 (*Natto*-MK-7) was purified from the culture medium of *Bacillus subtilis natto* for several days [3]. During cultivation, *Bacillus subtilis natto* transform spores and releases cell contents into the medium in this process. The culture medium was concentrated and purified by repeating FPLC. *Natto-MK-7* was purified by triple or quadruple ion exchange chromatography (DEAE Sepharose FF) and then size exclusion chromatography (Sephacryl S300). The *natto*-MK-7 was assessed by the combination of size-exclusion chromatography and dynamic light scattering. Each fraction of size exclusion chromatography was analyzed by dynamic light scattering method.

MALDI-TOF mass spectrometry of *natto*-MK-7 was performed on a microflexLT MALDI-TOF mass spectrometer (Bruker Daltonics) in positive ion mode. Measurements were performed in the m/z ranges of approximately 300-4,000, 3,000-20,000, 20,000-201,500, and 820-14,000. Significant peaks were observed in the m/z range of 300-4,000, hence the subsequent measurement was performed only in this range. The standard amino acid analysis of *natto*-MK-7 was performed at the Instrumental Analysis Division, Global Facility Center, Creative Research Institution, Hokkaido University.

RESULTS: Fig. 1 shows the decay time of the main fraction of size-exclusion chromatography of *natto*-MK-7 used. A peak between 0.01 to 0.1 s corresponds to a single particle of *natto*-MK-7, of which hydrophobic radius (R_H) was estimated to be about 27 Å.

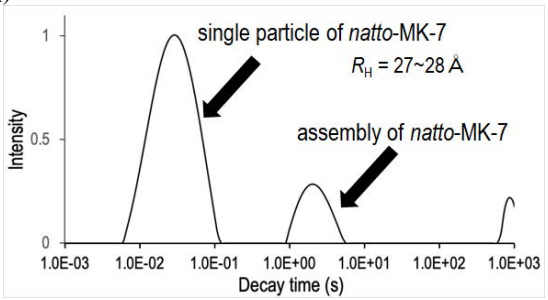

Fig. 1. The decay time of *natto*-MK-7 in DLS measurement.

For MALDI-TOF/MS and amino acid analysis, whole *natto*-MK-7 was used. Since KBF is the major component of *natto*-MK-7, the results could be considered as KBF-derived. As shown in Fig. 2, multiple peaks were found, indicating that KBF would be a 1k peptide with multiple sequence. In the amino acid analysis, hydrophilic amino acids: Asx (Asp or Asn) and Glx (Glu or Gln), and hydrophobic amino acids: Val and Leu, and small amounts of Met were found. The intervals are 14 in Fig. 2, which corresponds to a methyl group, supporting the results of MALDI-TOF/MS. Recently, KBF was extracted from natto MK-7 by reversed phase chromatography. The detailed analysis is on progress.

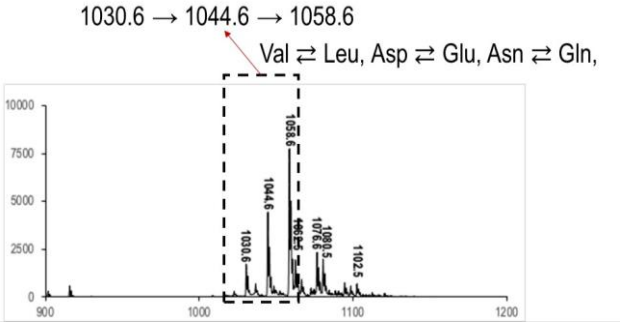

Fig. 2. The MALDI-TOF/MS chart of *natto*-MK-7.

REFERENCES:

[1] L.Wen *et al.*, Mol. Med. Rep. **18**, (1999) 3–15.
[2] H. Ikeda, Y. Doi, Eur. J. Biochem. **192**, (1990) 219-224.
[3] T. Chatake *et al.* J. Food Biochem. (2018) e12630.
[4] T. Chatake *et al.* KURNS PROGRESS REPORT 2019, (2020) CO6-20.

CO6-25 Preliminaly Study for The Development of New Treatment Method for Myxofibrosarcoma with BNCT

T. Fujimoto[1, 2], T. Andoh[3], T. Takata[4], Y. Sakurai[4]
H. Tanaka[4], M. Suzuki[4]

[1]*Department of Orthopaedic Surgery, Hyogo Cancer Center*
[2]*Department of Orthopaedic Surgery, Kobe University Graduate School of Medicine*
[3]*Faculty of Pharmaceutical Sciences, Kobe Gakuin Universityniversity*
[4]*Institute for Integrated Radiation and Nuclear Science, Kyoto University*

INTRODUCTION

Myxofibrosarcoma (MFS) is a rare malignant soft-tissue tumor observed predominantly in the extremities of elderly patients [1]. Since MFS is not sensitive enough to anticancer drugs or radiation therapy, wide surgical excision is the standard treatment for localized MFS. Nonetheless, this treatment affects, especially, the activity of daily life (ADL) of elderly patients. The present study explored the application of a more minimally invasive treatment with Boron Neutron Capture therapy (BNCT) with the use of a newly established human-derived MFS cell line-bearing animal model at the Institute for Integrated Radiation and Nuclear Science, Kyoto University (KURNS).

EXPERIMENTS

Newly established MFS cell line from a patient was used to create a cancer-bearing animal model by subcutaneously transplanting the MFS cells into the right thigh of nude mice. After the tumor grew, the animals were divided into a hot control group and a BNCT group. Only the BNCT group was administered BPA (500 mg/kg); almost 45 min thereafter, only the right lower limbs of both groups were irradiated with epithermal neutrons for 10 minutes. Immediately after termination of the animals, the tumor tissue was removed and subjected to histological examination.

RESULTS

The Newly established MFS cell line successfully formed tumors in the subcutaneous space of the nude mice. After irradiation, tumor regression was observed only in the BNCT group. Histological examination revealed destroyed tumor cells in a myxoid background of the BNCT group [Fig. 1], while tumor cells in the hot control group continued growing [Fig. 2].

FIGURES

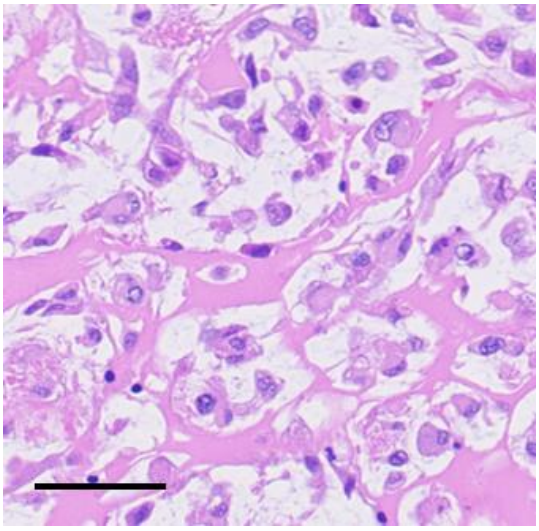

Fig. 1. Histopathological study (HE staining) of tissue from BNCT group reveals destroyed tumor cells in a myxoid background. Bar indicates 50μm.

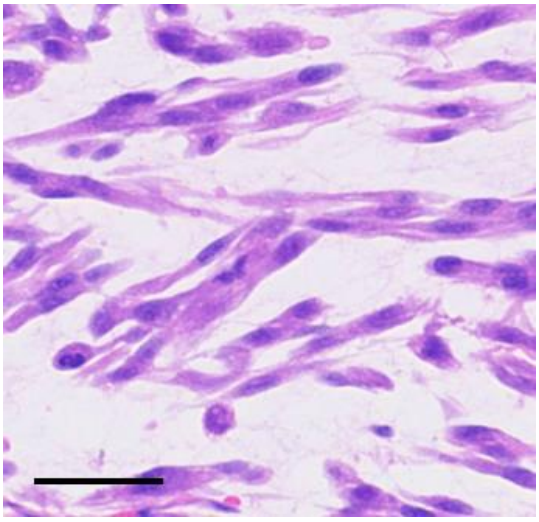

Fig. 2. Histopathological study (HE staining) of tissue from hot control group reveals no destroyed tumor cells. Tumor cells display a variably cellular spindle cell proliferation in a myxoid background. Bar indicates 50μm.

REFERENCE

[1] A. Gronchi *et al.,* Ann. Surg., **251** (2010) 506–511.

CO6-26 Development of Boron Cluster-Loaded Nanoparticles for BNCT

A. B. Fithroni,[1, 2] K. Kobayashi,[3] M. Akehi,[3] H. Inoue,[1]
S. Zhou,[1] T. F. N. Hakim,[1] H. Uji, [4] M. Ishimoto,[5]
M. Suzuki,[6] T. Ohtsuki,[1] and E. Matsuura[2, 3, 7]

[1] Department of Interdisciplinary Science and Engineering in Health Systems, Okayama University

[2] Department of Cell Chemistry, and [3]Collaborative Research Center for OMIC, Graduate School of Medicine, Dentistry, and Pharmaceutical Sciences, Okayama University

[4] Department of Material Chemistry, Graduate School of Engineering, Kyoto University

[5] Fukushima SiC Applied Engineering Inc.

[6] Institute for Integrated Radiation and Nuclear Science, Kyoto University

[7] Neutron Therapy Research Center (NTRC), Okayama University

INTRODUCTION: Boron neutron capture therapy (BNCT) is a novel nuclear therapeutic modality that can induce apoptosis in targeted cells, such as malignant cancer cells. To address the issues of limited application of clinically approved boron compounds, we designed self-assembling nanoparticles composed of polymeric micelles, namely, "Lactosome micelles" loaded with a boron cluster [1]. The particles consist of an amphipathic polydepsipeptide chain that are linked between a hydrophilic polysarcosine chain and a hydrophobic poly-L-lactic acid chain, and the polymer can assembly forms micelle-like particles. Moreover, the Lactosome micelles showed promising prospects for solid tumor accumulation via the enhanced permeability and retention (EPR) effect.

In the previous study, we aimed to develop Lactosome micelles highly loaded with a hydrophobic boron cluster that may be able to apply for the BNCT treatment [2]. In the present study, we performed *in vitro* and *in vivo* neutron irradiation to the AsPC-1 cells (human pancreatic cancer cells) and AsPC-1/CMV-Luc (their transfectant with luciferase expression) to assess BNCT effect of a boron cluster-loaded Lactosome micelles. The tumor growth was measured by bioluminescence imaging using IVIS.

EXPERIMENTS: For *in vitro* study, we irradiated AsPC-1 cells by subjected with 1 MW nuclear power for 30 min. After the neutron irradiation, colony formation assay of was performed by culturing in 60 mm dishes for 2 weeks. For *in vivo* study, the AsPC-1/CMV Luc cells-bearing mice were intravenously injected with a boron cluster-loaded Lactosome micelles, and then, the neutron irradiation was performed with nuclear power of 5 MW for 40 min. Data were represented as mean ± S.E.M. Significant differences were represented by *: $p < 0.05$.

RESULTS: In *in vitro* irradiation study, the results indicated that a boron cluster-loaded Lactosome micelles showed a significant inhibitory effect in the colony formation of the cancer cells (AsPC-1 cells) (Table 1). Furthermore, the *in vivo* irradiation study also showed that intravenous injection with a boron cluster-loaded Lactosome micelles and together with the neutron irradiation significantly suppressed the tumor growth on day 21 (after irradiation) (Table 2).

In conclusion, either *in vitro* or *in vivo* neutron irradiation studies suggest that our newly developed boron cluster-loaded Lactosome micelles are promising for boron compound candidates for BNCT.

Table 1. Effect of the neutron irradiation on *in vitro* colony formation of AsPC-1 cell treated with a boron cluster-loaded Lactosome micelles.

Group	Colony formation rate	
	0 min	30 min
Control (DPBS)	1	0.51 ± 0.01
Lactosome micelles	1	0.52 ± 0.03
-loaded with a boron cluster	1	0.14 ± 0.02*
BPA	1	0.30 ± 0.03*

Table 2. *In vivo* neutron irradiation study.

Group	Intensity (%) on day 21
Control (cold)	1129 ± 617
Control (hot)	774 ± 527
Lactosome micelles loaded with a boron cluster	177 ± 83.0*

Tumor growth in the xenografts with AsPC-1/CMV Luc cells were affected by the intravenously treated with a boron cluster-loaded Lactosome micelles and by the neutron irradiation. The tumor size was detected on day 21 after the irradiation.

REFERENCES:

[1] E. Hara *et al.,* Biochim. Biophys. Acta., **1830** (2013) 4046-4052.
[2] A.B. Fithroni *et al*., Cells, **11**(2022) 3307.

R4123

CO6-27 *C9orf72*-derived PR poly-dipeptides bind Kapβ2: discovery of secondary binding sites

E. Mori, T. Yoshizawa[1], T. Saio[2], K. Morishima[3], R. Inoue[3] and M. Sugiyama[3].

Department of Future Basic Medicine, Nara Medical University
[1]College of Life Sciences, Ritsumeikan University
[2]Institute of Advanced Medical Sciences, Tokushima University
[3]Institute for Integrated Radiation and Nuclear Science, Kyoto University

INTRODUCTION: Biomolecules such as proteins and nucleic acids form condensates in cells. These liquid-like condensates/droplets do not require membrane to keep boundaries, and thus are called membrane-less organelles. Because the process is partially explained in the context of physical chemistry, these phenomena are sometimes called biological phase separation or liquid-liquid phase separation (LLPS) in cells.

Uncontrolled phase separation is known to be associated with pathogenesis in some types of neurodegenerations. Repeat expansions in *C9orf72* cause amyotrophic lateral sclerosis (ALS) and front-temporal dementia (FTD), and the translated products, five poly-dipeptides, are thought to be the disrupters of physiological phase separations in cells, leading to cause protein aggregations. We found that Arg-rich poly-dipeptides, PRn and GRn, bound to proteins with low-complexity (LC) sequences, such as RNA-binding proteins, intermediate filaments, and FG-domains of nuclear pore complexes [1,2].

Further, we recently found that a phase modifier Kapβ2 [3] bound PRn and GRn through its nuclear localization signal (NLS) recognition motif at 1:1 ratio [4]. However, detailed mechanisms are still not clear.

EXPERIMENTS: To further analyze protein-protein interaction including weaker and dynamic affinities, analytical ultracentrifugation (AUC) was applied for complex formation of Kapβ2 and MBP-tagged PR18.

RESULTS: As shown in Fig. 1A, Kapβ2 bound at least two MBP-PR18 molecules and possibly up to 3 to 5 more MBP-PR18 bound, but not as strong as initial binding, suggesting that the affinity to the secondary binding site is weaker than that to NLS recognition motif. We made a mutant Kapβ2 that lacks potential binding sites of PRn, and found that mutant Kapβ2 could bind to only one MBP-PR18. These results suggest that Kapβ2 binds to PRn through NLS recognition motif and other specific region.

DISCUSSION: Further analysis such as NMR is required to understand detail mechanisms of Kapβ2-PRn complex formation.

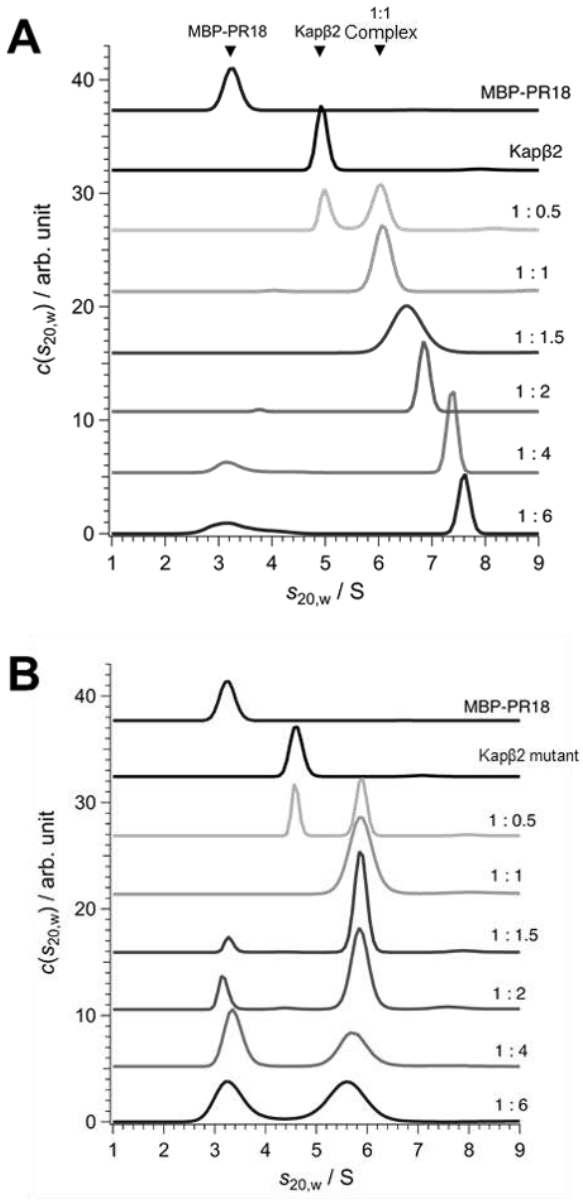

Fig. 1. AUC analysis of Kapβ2 and MBP-PR18 complex. Binding of multiple MBP-PR18 was analyzed with Wild-type Kapβ2 (A) and mutant Kapβ2 (B).

REFERENCES:

[1] Y. Lin *et al*., Cell, **167** (2016) 789-802.
[2] K.Y. Shi *et al*., Proc. Natl. Acad. Sci. U. S. A., **114** (2017) E1111-E1117.
[3] T. Yoshizawa *et al*., Cell, **173** (2018) 693-705.
[4] H. Nanaura *et al*., Nat. Commun., **12** (2021) 5301.

CO6-28 ^{11}C Medical-isotope Production via ^{12}C(γ,n)^{11}C Reaction with Carbon Nanotubes

N. Takahashi[1,2], M. Kurosawa[1], M. Tamura[1],
M. Fujiwara[1,2], T. Kubota[3], N. Abe[4], and T. Takahashi[4]

[1]*Research Center for Nuclear Physics, Osaka University*
[2]*Kyoto Medical Technology*
[3]*Agency for Health, Safety and Environment, Kyoto University*
[4]*Institute for Integrated Radiation and Nuclear Science, Kyoto University*

INTRODUCTION: L-[^{11}C]-Methionine is used as a positron emission tomography (PET) reagent for medical diagnosis of brain tumors [1]. The medical ^{11}C radioisotopes are mostly produced in a cyclotron via the ^{14}N(p,α)^{11}C reaction by bombarding enriched nitrogen gas with a proton beam [2]. In Japan, Hokkaido University and Osaka University have worked in collaboration with Sumitomo Heavy Industries to obtain the government permission for the PET examination with L-[^{11}C]-Methionine for checking the metastasis and recurrence test of the brain tumor patient [3,4].

Instead of producing ^{11}C with the cyclotron, we tried a novel method of producing ^{11}C using the bremsstrahlung γ-rays with a carbon nanotube (CNT) target to get a reasonable number of the ^{11}C activity.

EXPERIMENTS: Figure 1 shows the experimental scheme for the ^{11}C production via the ^{12}C(γ,n)^{11}C reaction. Bremsstrahlung γ-rays were produced by impinging a 40 MeV electron beam on platinum converter at the electron LINAC facility. The γ-rays were irradiated to CNT powders sealed in aluminum vessel with non-woven masks as gas inlet/outlet filter. The produced ^{11}C inside the vessel were oxidized to ^{11}CO or ^{11}CO$_2$ in O$_2$ gas, which was continuously flown during the irradiation. The ^{11}C gas (^{11}CO and ^{11}CO$_2$) were trapped in two 13X molecular sieve columns and 511-keV γ-rays from positron-electron annihilation were detected with CdZnTe detectors. Taking into account the incompleteness of trapping ^{11}C gas with molecular sieves, we prepared two molecular sieve columns to correct for the trapping efficiency.

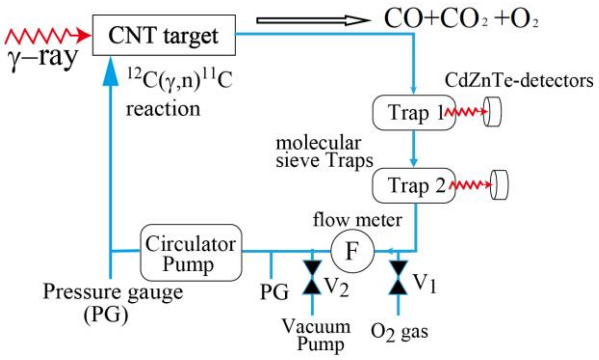

Fig. 1. Experimental scheme to produce ^{11}C and measure the extraction rate of ^{11}C gas.

In this experiment, single-walled carbon nanotube (SWCNT) powders (KH Chemicals Co., Ltd.) were irradiated under the different conditions of the bulk density of SWCNT powders, the pressure of O$_2$ gas in the vessel, and the flow rate of O$_2$ gas.

RESULTS: We confirmed that the ^{11}CO and ^{11}CO$_2$ flowed out from the vessel by observing 511-keV γ-rays from ^{11}CO and ^{11}CO$_2$ trapped in the molecular sieves. The measured decay curve obtained by measuring 511-keV γ-rays as a function of elapsed time was well in agreement with the ^{11}C half-life of 20 minutes.

The normalized activity of ^{11}C gas after the correction of the trapping efficiency for each experimental condition is summarized in Table 1. The normalized activity of ^{11}C gas was almost independent of the bulk density of SWCNT. On the other hand, the rate of ^{11}C gas reaching the trap column could increase by increasing the flow rate and pressure of O$_2$ gas. Further study is required to elucidate optimal production condition.

Table1. Normalized activity of ^{11}C gas for each condition.

Bulk density of SWCNT (mg/cm^3)	Flow rate of O$_2$ gas (cc/min)	Pressure of O$_2$ gas (MPa)	Normalized activity of ^{11}C gas (kBq/μA/g/min)
83.1	105	0.1	8.19±0.04
55.4	100	0.1	7.69±0.05
27.7	105	0.1	8.17±0.04
27.7	50	0.1	6.11±0.04
27.7	125	0.13	10.97±0.09

Biomass nanocarbon, graphene nano-powder and diamond nano-powder were also examined to achieve high yields of ^{11}C gas. The production yield of ^{11}C gas was as low as 7%, 24% and 72% that of SWCNT under the same experimental conditions, respectively.

Based on the experimental production rate of ^{11}C gas for SWCNT, we estimate that we can obtain the ^{11}C activity of 34 GBq when we use a SWCNT target under the conditions with 1) a length of 50 cm, 2) weight of 1.13 kg for 0.155 g/cm^3, 3) a 40 MeV electron beam intensity of 100 μA for 40 minutes bombardment. This 34 GBq radioactivity is enough amounts for one patient's diagnosis. The detailed report will be published in the near future [5].

REFERENCES:

[1] Y. Komatsu *et al.*, Radioisotopes, **67** (2018) 75.
[2] T. J. Ruth. A.P. Wolf, IEEE Trans., NS-26 (1979) 1710.
[3] M. Kinoshita *et al.*, J. Neurosurg **125** (2016) 1136.
[4] M. Kameyama *et al.*, Eur. J. Nucl. Med. Mol. Imaging, **43** (2016) 2267.
[5] M. Kurosawa *et al.*, to be published.

CO6-29 Molecular dynamics analysis of oxidative folding enzyme ER-60 with solution scattering measurement

A. Okuda, M. Shimizu, K. Morishima, Y. Yunoki, R. Inoue, N. Sato, R. Urade and M. Sugiyama

Institute for Integrated Radiation and Nuclear Science, Kyoto University

INTRODUCTION: ER-60, an oxidative protein folding enzyme, is a multi-domain protein, **a** and **a'** domains with catalytically active cysteine pairs and **b** and **b'** domains in the order **a-b-b-b'-a'**. In the process of oxidative protein folding, ER-60 might have the appropriate domain conformations and arrangement to function, and it is estimated that the structure fluctuates and changes according to the redox state of active cysteine pairs in the solution [1]. Inverse Contrast Matching Small-Angle Neutron Scattering (iCM-SANS) [2], which takes advantage of the large difference in neutron scattering length between hydrogen and deuterium, is useful for observing the dynamics and structures of such multi-domain proteins in solution.

When 75% deuterated and hydrogenated proteins are in 100% deuterated solvent, the deuterated proteins are scatteringly invisible, and only the hydrogenated proteins could be observed. Applying this method to multi-domain proteins, the domain of the hydrogenated domains could be selectively observed. To achieve this method for multi-domain proteins, the hydrogenated and deuterated domains must be prepared separately and then connected by the protein ligation technique.

To reveal the structure-function correlations of ER-60, we aim to analyze selective domain dynamics by iCM-SANS. The segmental deuterated proteins for this experiment were prepared by connecting the domains with the ligation enzyme *Oa*AEP [3].

EXPERIMENTS: The 75% deuterated recombinant protein was expressed in *E. coli* cultured in M9 medium containing 75% deuterium [4]. The recombinant proteins were purified using a His-tag affinity column and an ion exchange column. The deuterated and the hydrogenated domains were mixed in buffer containing 200 mM Tris-HCl (pH 7.4) / 150 mM NaCl. Then, 0.2 μM of the ligation enzyme *Oa*AEP was added to the mixture, and the protein ligation reaction was performed at 20°C for 64 hours. The results of ligation reactions were confirmed by SDS-PAGE. The deuteration rates of deuterated proteins were calculated by mass spectrometry with MALDI-TOF MS (microflexLT MALDI-TOF mass spectrometer, Bruker Daltonics) using a previously reported [3]. Analytical ultracentrifugation (AUC) experiments were performed at 60,000 rpm at 25 °C with a sedimentation velocity method using Rayleigh interference optics (ProteomeLab XL-I, Beckman Coulter). SAXS measurements were performed at 25 °C with 4 hours of exposure- time using a NANOPIX (Rigaku, Tokyo, Japan). The sample-to-detector distance (SDD) was set to 1330 mm and the q range was from 0.01 to 0.20 Å $^{-1}$.

RESULTS: The deuteration rates of deuterated **a** (*d*(**a**)) and **a'** (*d*(**a'**)) domains were calculated to be 73.5% and 74.1% respectively. The results of the protein ligation reaction are shown in Fig. 1. The band of ligation product, (*d*)**a**-(*h*)**bb'a'** and (*h*)**abb'**-(*d*)**a'**, connecting the deuterated and hydrogenated domains were observed, indicating the progress of the protein ligation reaction.

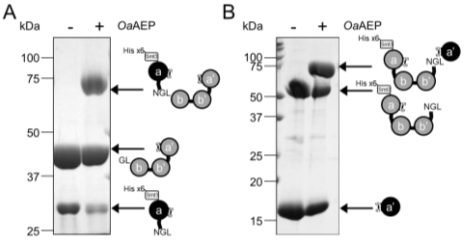

Fig. 1. The ligation products from (A) (*d*)**a** and (*h*)**bb'a'** domains and (B) (*h*)**abb'** and (*d*) **a'** domains of ER-60 by *Oa*AEP.

AUC was conducted to determine the abundance of monomers, aggregations, contaminations, and degradation products in the sample solution. It was shown that about half of (*d*)**a**-(*h*)**bb'a'** was degraded (Fig. A) and (*h*)**abb'**-(*d*)**a'** contained aggregation of 19% (Fig. B).

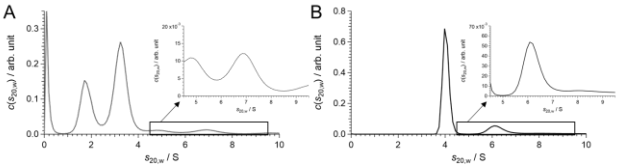

Fig. 2. Analytical ultra-centrifugation (AUC) profiles of ligation products, (A) (*d*)**a**-(*h*)**bb'a'** and (B) (*h*)**abb'**-(*d*) **a'**.

The SAXS profile of (*h*)**abb'**-(*d*)**a'** treated with AUC-SAS [5] is shown in Fig. 3.

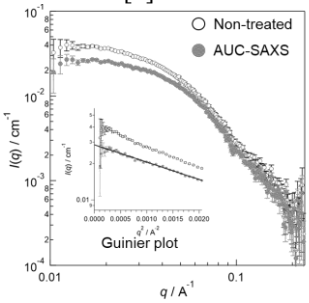

Fig. 3. The SAXS profiles of (*h*)**abb'**-(*d*) non-treated (white circles) and treated (gray circles) with AUC-SAS.

Currently, we are examining the conditions for obtaining the stable (*d*)**a**-(*h*)**bb'a'** sample, and are planning iCM-SANS measurements.

REFERENCES:

[1] A. Okuda *et al.*, Sci Rep., **11** (2021) 5655.
[2] M. Sugiyama *et al.*, J. Appl. Crystallogr., **47** (2014) 430-435.
[3] A. Okuda *et al.*, Angew Chem Int Ed Engl., **62** (2023) e202214412.
[4] A. Okuda *et al.*, Biophys Physicobiol., **18** (2021) 16-27.
[5] K. Morishima *et al.*, Commun Biol., **3** (2020) 294.

CO6-30 The regulation of the Kai proteins interaction by the KaiC hexamers that can adopt various kinds of phosphorylation states

Y. Yunoki, K. Morishima, N. Sato, R. Inoue, A. Okuda, R. Urade, M. Sugiyama

Institute for Integrated Radiation and Nuclear Science, Kyoto University

INTRODUCTION: Circadian rhythm is regulated by clock proteins. The cyanobacterial clock is controlled via interplay among KaiA, KaiB, and KaiC, which generate a periodic oscillation of KaiC phosphorylation in the presence of ATP. KaiC forms a homohexamer harbouring 12 ATP-binding sites and exerts ATPase activities associated with its autophosphorylation and dephosphorylation. Although there are as many as 700 phosphorylation states could become in the KaiC hexamer due to the presence of two phosphorylation sites in the subunit KaiC, previous reports disclose only the average phosphorylation state of the KaiC hexamer in solution. Herein, in order to understand the oscillation mechanism involved in the clock proteins, we develop the native mass spectrometry for simultaneous analyzing of the phosphorylation states in the KaiC hexamer and Kai proteins interaction as exemplified KaiA-KaiC interaction.

EXPERIMENTS: nMS measurements were recorded on a microTOF II ESI mass spectrometer (Bruker) at room temperature using the microTOF II software. KaiA and KaiC originating from thermophilic cyanobacteria, *T. elongatus* BP-1, were expressed in *Escherichia coli* and purified by an anion-exchange column (Resource Q) and size-exclusion column (superdex75). To control the phosphorylation state in the KaiC hexamer, we used two KaiC mutants, $KaiC_{AA}$ and $KaiC_{DD}$ (in which Ser431 and Thr432 were both substituted with aspartate and alanine residues, respectively), mimicking the dephosphorylated and phosphorylated states of KaiC, respectively. For preparing the group of heterogeneous phosphorylation state in the KaiC hexamers, before adding ATP, we mixed unlabeled $KaiC_{AA}$ mutant and ^{13}C labeled $KaiC_{DD}$ subunit. In this way, there are seven types of the KaiC hexamers with different phosphorylation states in solution.

RESULTS: We successed in preparation of the group of heterogeneous phosphorylation state in the KaiC hexamer (Fig. 1A). Then, we tried to reveal the KaiA-KaiC interaction by adding KaiA in this KaiC group.

As shown in Fig. 1B, our data indicate the KaiA-KaiC interaction depends on the number of $KaiC_{AA}$ in the KaiC hexamer. It means that KaiA-KaiC interaction might be controlled by the phosphorylation state in the KaiC hexamer.

To examine the possible dependence of KaiA–KaiC interaction on the phosphorylation state in the KaiC hexamer, we measured nuclear magnetic resonance (NMR) of KaiC.

NMR data show only the subunit $KaiC_{AA}$ in the KaiC hexamer released the intrinsically disordered region and becomes reactive with KaiA, leading to the enhanced KaiA–KaiC interaction.

We illustrated KaiC regulates KaiA-KaiC interaction by changing the phosphorylation state in the KaiC hexamer. We believe that these insights will contribute to the understanding of the oscillation mechanism through the dissociation and assembly of Kai proteins.

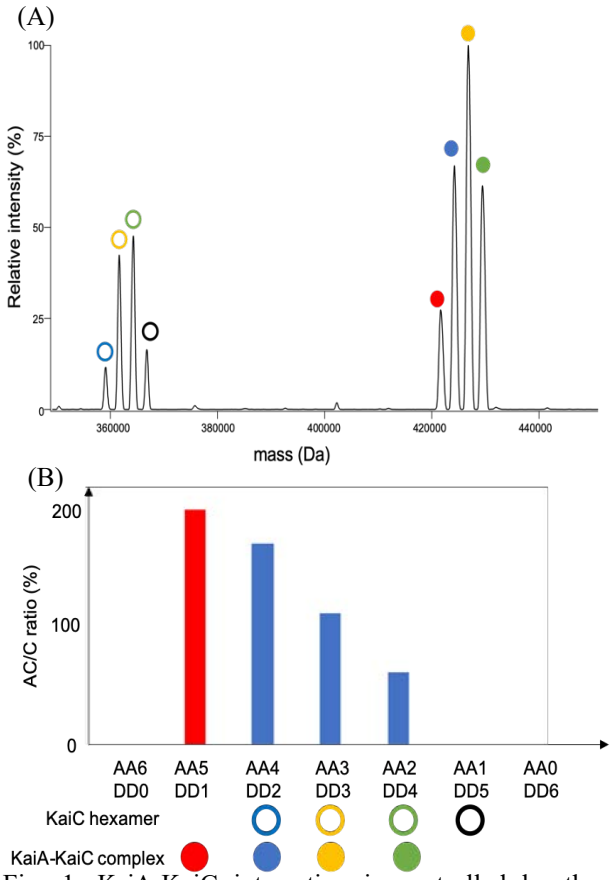

Fig. 1. KaiA-KaiC interaction is controlled by the phosphorylation state in KaiC hexamer.

(A) Native mass spectra of heterogeneous phosphorylation state in KaiC hexamer in the presence of KaiA. The open circles show the KaiC hexamer, and the closed circles show the KaiA-KaiC complex. The red, blue, yellow, green and black circles show the KaiC hexamer which is composed of 1 : 5, 2 : 4, 3 : 3, 4 : 2, 5 : 1 of $KaiC_{AA}$ and $KaiC_{DD}$.

(B) Plot of relative peak intensity of KaiA-KaiC complex versus KaiC. The color of the peak, that yielded only KaiA-KaiC complex, is red.

CO6-31 Small-angle scattering analysis of wheat protein glutenin

N. Sato, R. Urade, A. Okuda, M. Shimizu, K. Morishima, R. Inoue, and M. Sugiyama

Institute for Integrated Radiation and Nuclear Science, Kyoto University

INTRODUCTION: Food science in combination with quantum beam analyses is now attracting wide attention among researchers. Food materials have been difficult to examine their structure because they have undesirable characteristics for structural analyses, such as condensed, amorphous, opaque and multi-component features. However, quantum beam analyses are successfully applicable to those kinds of materials such as colloids, rubbers, gels, and other soft matters. It is therefore expected that quantum beam analyses can also be powerful tools for examining the structural of food materials, which has not been closely investigated by conventional methods.

There are many kinds of wheat flour foods such as bread and noodle. These foods are produced from wheat dough, which is prepared by kneading wheat flour with water and salt. Physical properties of the dough are responsible for the quality and processability of wheat flour foods. Gluten, a composite of major wheat storage proteins gliadin and glutenin, makes a significant contribution to the physical properties of wheat dough. Gliadin is a monomeric protein and exhibits viscose feature while glutenin is high-molecular-weight network protein and exhibits elastic feature. In order to clarify the properties of gluten composite, it is required to investigate the individual properties of each protein gliadin and glutenin.

Conventionally, gliadin had been extracted only with alcohols or acids. However, we found gliadin can be extracted with pure water from the dough containing NaCl. This finding enabled us to investigate the structure of gliadin in conditions closer to actual foods. It was revealed in our previous study [1] that gliadin monomers are isolated and dispersed at a low concentration of aqueous solution, but with increasing gliadin concentration, they associate together gradually to form multimolecular domains. At higher concentrations, on the other hand, gliadin is no longer soluble in water and form aggregates with density fluctuation inside. The correlation length of this fluctuation becomes smaller with increasing gliadin concentrations. Another finding is that the structure of gliadin hydrates is greatly affected by salts. The correlation length of density fluctuation becomes smaller with increasing NaCl concentration, indicating that gliadin hydrates are contracted by NaCl.

Thus we could successfully reveal the structure of gliadin. However, the structure of glutenin has not been clarified yet. Glutenin is a protein with completely different characteristics from gliadin. Therefore it is expected that the nano-structure of glutenin is also largely different from that of gliadin. In this study, we carried out SAXS measurements on glutenin hydrates and investigated the difference from the gliadin structure.

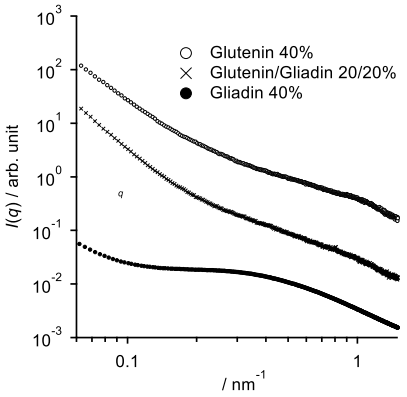

Fig. 1. SAXS profiles of glutenin, gliadin and their mixture.

EXPERIMENTS: Glutenin was obtained from the insoluble residue after gliadin preparation. Glutenin concentration was 40 wt%. SAXS measurements were performed with a laboratory SAXS instrument (NANOPIX, Rigaku) installed at Institute for Integrated Radiation and Nuclear Science, Kyoto University. The wavelength of X-ray was 1.54 Å and the camera length was 1300 mm. All measurements were carried out at 25 °C.

RESULTS: Fig. 1 shows the SAXS profiles of 40 wt% hydrates of glutenin, gliadin, and their 1:1 mixture. Gliadin shows gentler upturn in the low-q region and a broad peak around 0.3–0.6 nm^{-1}. As reported before, this result demonstrates that gliadin forms aggregates with density fluctuation inside. In other words, gliadin molecules gather together but dense and sparse regions are present within the aggregates. In contrast, glutenin shows steeper upturn in the low-q region and a small peak appears around 1 nm^{-1}. The slope in the low-q region has nearly q^{-4} dependence, indicating that a definite interface of large aggregates of glutenin is found. This result is explained by the structural difference of glutenin and gliadin. Glutenin is a high-molecular weight protein with network structure via disulfide bonds. Consequently, it forms huge aggregates in the hydrates. On the other hand, gliadin is a monomeric protein and associates each other more weakly by hydrophobic interaction. Hence it forms aggregates not so large as glutenin. The structure of the 1:1 mixture is similar to that of glutenin. This is because the molecular weight of glutenin is much higher than gliadin. In principle, scattering intensity is proportional to the square of the molecular weight. Accordingly, the profile of the mixture strongly reflects the high-molecular-weight glutenin.

REFERENCES:

[1] N. Sato *et al.,* J. Agric. Food Chem., **63** (2015) 8715.

CO6-32 Design, Synthesis, and BNCT Effect of Macrocyclic Polyamine-type Boron Carriers for BNCT

S. Aoki[1,2], H. Ueda[3], M. Suzuki[3], Tanaka, T.[1,4] S. Masunaga[3], N. Kondo[3], and Y. Sakurai[3]

[1]*Faculty of Pharmaceutical Sciences, Tokyo University of Science*
[2]*Research Institute for Science and Technology, Tokyo University of Science*
[3]*Institute for Integrated Radiation and Nuclear Science, Kyoto University*
[4]*Faculty of Pharmaceutical Sciences, Okayama University*

INTRODUCTION: Neutron capture therapy using boron-10 (^{10}B) (BNCT) is one of powerful therapies for local tumor control in the treatment of brain tumor, melanoma, and related diseases [1].

Based on high intracellular uptake pendant-cyclen (cyclen = 1,4,7,10-tetraazacyclododecane) in cancer cell, we designed and synthesized several phenylboronic acid-pendant 9-, 12-, and 15-membered macrocyclic amines such as **^{10}B-1a~3a** and their corresponding Zn^{2+} complexes **^{10}B-1b~3b** (Fig. 1) [2]. The experimental results suggest that the metal-free **^{10}B-1a~3a** are introduced into cancer cells (A549 and HeLa S3 cells) more efficiently than their Zn^{2+} complexes **^{10}B-1b~3b** with considerably high cancer/normal cells selectivity. Besides, it was found that 12- and 15-membered derivatives **^{10}B-2a~3a** exhibit a higher BNCT effect than **^{10}B-1a**, possibly because **^{10}B-2a~3a** form the corresponding Zn^{2+} complexes **^{10}B-2b~3b**, which strongly interact with DNA in living cells, resulting in the efficient breakdown of DNA double-strand upon the neutron irradiation.

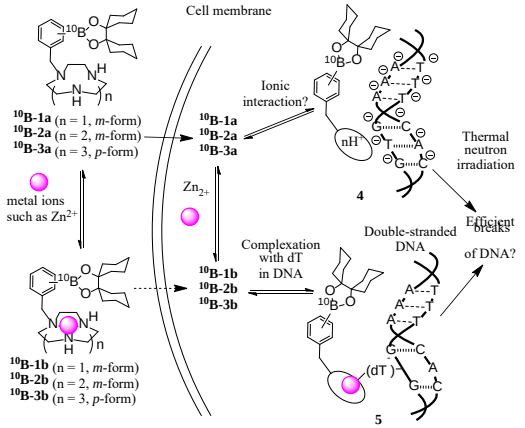

Fig. 1. Structures of boron-containing macrocyclic polyamines and the corresponding Zn^{2+} complexes and the proposed scheme of their intracellular uptake and interaction with DNA for BNCT.

EXPERIMENTS and RESULTS: The synthesis of **1a~3a** and their Zn^{2+} complexes **1b~3b** was carried out and their cytotoxicity and cellular uptake activity against cancer cell lines (HeLa and A549 cells) and normal cell line (IMR-90) were evaluated. It was found that the intracellular uptake of **1~3** is higher than that of BSH and BPA, possibly via polyamine transporter system (PTS) and that **^{10}B-2a**, **^{10}B-3a** **^{10}B-2b**, and **^{10}B-3b** exhibit more potent BNCT effect than that of BSH and BPA.

These results have prompted us to design and synthesize boron carriers that have homo- and heterodimeric macrocyclic polyamines functionalized phenylboronic acid units such as **4a~5a** (homodimers) and **6a~8a** (heterodimers) and their corresponding Zn^{2+} complexes **4b~8b** (Fig. 2), because it was well established that polymeric Zn^{2+} complexes would form more stable complexes with DNA double strand than monomeric Zn^{2+} complexes than monomeric Zn^{2+} complexes [3].

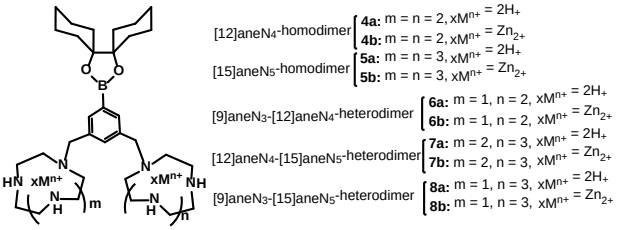

Fig. 2. Structures of boron-containing dimeric macrocyclic polyamines and Zn^{2+} complexes (**4a~8a** and **4b~8b**).

It has been found that the intracellular uptake and BNCT of ^{10}B-enriched **4a~8a** and **4b~8b** are lower than that of **1~3** (Fig. 3), possibly due to their high hydrophilicity than **^{10}B-2a** [4,5]. Our next work will be the synthesis of monomeric polyamines that are equipped with multiple boron units for more efficient BNCT effect and the observation of these B-containing agents in nucleus.

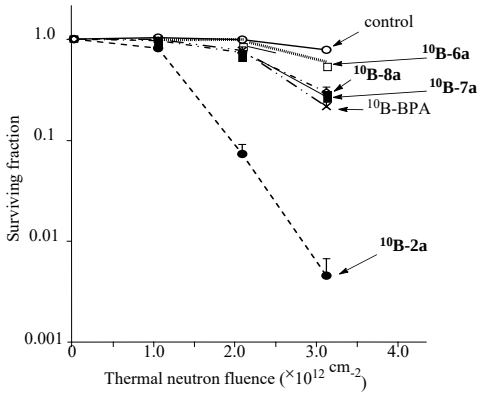

Fig. 3. Antitumor effect of ^{10}B-enriched BPA, **2a, 6a, 7a,** and **8a** (100 μM) against A549 cells upon irradiation with thermal neutron (averaged thermal neutron flux was 1.2~1.3 X 10^9 n/cm^2·s), as evaluated by a colony assay.

REFERENCES:

[1] a) R. F. Barth *et al.*, Clin. Cancer Res., **11** (2005) 3987-4002. b) R. F. Barth *et al.*, Rad. Oncol., **7** (2012) 146-166.
[2] H. Ueda *et al.*, J. Med. Chem., **64** (2021) 8523-8544.
[3] S. Aoki and E. Kimura, Chem. Rev., **104** (2004) 769-788.
[4] H. Ueda *et al.*, Eur. J. Inorg. Chem., **2022** (2022) e202100949 (24 pages).
[5] S. Aoki *et al.*, In "*Characteristics and Applications of Boron*" 2022, pp 83-105, Charchawal Wongchoosuk, Ed., IntechOpen, Croatia.

CO6-33 Radiolabeling of composite natural material chicken eggshell membrane via neutron irradiation $^{6}Li(n,\alpha)\ ^{3}H$ reaction

M. Shimizu[1], E. Fujita[1], N. Nogawa[2], K. Takamiya[3] and Y. Atomi[1]

[1]*Material Health Science, Tokyo University of Agriculture and Technology*

[2]*Isotope Science Center, The University of Tokyo*

[3]*Institute for Integrated Radiation and Nuclear Science, Kyoto University*

Chicken eggshell membrane (ESM) has been listed as an excellent wound-healing agent in Chinese pharmacopoeia book entries for 400 years. It is a non-woven fabric composed of fibrous biopolymers that are mainly protein-based and contain a large amount of extracellular matrix such as collagen and proteoglycans, as well as antibacterial proteins, cross-linked by lysyl-oxidase. Recently, proteomic analysis has revealed that it contains more than 400 different proteins. We previously found that hydrolyzed ESM provide young extracellular environment to dermal fibroblast [1] and improved skin elasticity and reduced facial wrinkles when topically applied as cosmetics [2]. Ingestion of this non-woven fabric has been reported to improve pain in knee joints and prevent liver fibrosis and ulcerative colitis in animal experiments. In our previous studies, we have found that eggshell membrane supplements improved skin elasticity, respiratory function, and locomotion (especially balance function) in healthy adults within 8 weeks of taking the supplements [3]. ESMs are secreted by cells in the narrow oviduct of the parent bird and serve as a biomineralization scaffold for eggshell formation and to protect chick embryo from drying and infection. We applied the tritium labeling of organic compounds via the 6Li(n,α)3H reaction, which has been used for radiolabeling of natural products that are difficult to synthesize and for tissue distribution in individuals, to ESM and conducted pilot experiments to determine whether ingested ESM are indeed digested and absorbed and distributed to various tissues. The labeled eggshell membrane was orally administered to mice, and was digested and absorbed. The radioactivity derived from the labeled ESM was detected in blood 2 hours after administration, peaking 6 hours later, and was also detected in almost all tissues [4]. However, in the previous irradiation experiment with JRR-4 (3.5 MW, 20 min), many parts of the sample were scorched, and the optimization of the eggshell membrane to lithium carbonate ratio and irradiation conditions remained an issue. In this study, in order to obtain tritium-labeled eggshell membranes for detailed verification of the pharmacokinetics and cellular uptake of ESM orally ingested by mice, we irradiated ESM powder samples (Almado Inc.) sealed in quartz glass (Figure 1) under milder conditions (Pn-2, 1 MW, 70 min). As a result, tritium labeling was successful and discoloration of the samples was minor. The Kyoto University furnace is beneficial for irradiating protein samples because its low power output does not raise the sample temperature during irradiation. On the other hand, since the labeling efficiencies of the two samples were different, it is necessary to monitor the actual irradiation efficiencies in the future experiment.

Fig.1 ESM powder in the custom-made quartz tubes.

REFERENCES:

[1] E. Ohto-Fujita *et al.,* Cell Tissue Res., **345** (2011) 177-190.
[2] E. Ohto-Fujita *et al.,* Cell Tissue Res., **376** (2019) 123-135.
[3] E. Ohto-Fujita *et al.,* J. Fiber Sci. Technol., **77** (2021) 258-265.
[4] E. Ohto-Fujita *et al.,* J. Fiber Sci. Technol., **77** (2021) 182-187.

CO7-1 Development of Alubmin Binding Gadolinium Complexes for MRI-Guided BNCT

S. Okada, K. Nishimura[1], Q. Ainaya[1], I. B. Sivaev[2], K. Miura, T. Takada[3], M. Suzuki[3], H. Nakamura

Laboratory for Chemistry and Life Science, Institute of Innovative Research, Tokyo Institute of Technology
[1]School of Life Science and Technology, Tokyo Institute of Technology
[2]Russian Academy of Sciences, Russia
[3]Institute for Integrated Radiation and Nuclear Science, Kyoto University

INTRODUCTION: Boron Neutron Capture Therapy (BNCT) is a promising cancer treatment of harsh and un-operatable malignant tumors. In order to obtain effective BNCT treatment of patients, it is important to control the biodistribution of the boron-containing drug and its accumulation in tumors. The conventional method to estimate biodistribution is positron emission tomography (PET) based on drugs labeled by radioactive isotopes[1], although ^{10}B isotope is non-radioactive.

We focused on Gd contrast agents for magnetic resonance imaging (MRI), which is a non-invasive method and one of the most widely used medical diagnostics. The ^{157}Gd isotope has the highest thermal neutron capture cross section of all stable nuclides in the periodic table. The thermal neutron capture cross section of the ^{157}Gd isotope exceeds that of the ^{10}B isotope by more than 60 times. The neutron capture reaction by ^{157}Gd causes complex inner shell transitions that produce prompt γ-emission displacing an inner-core electron, resulting in internal-conversion electron emission, and finally in the Auger electron emission, together with soft X-ray and photon emission. Therefore, the synthesis of compounds containing both boron and gadolinium can be useful not only to estimate biodistribution of boron drugs under MRI guide but also to develop efficient neutron capture cancer therapy. We have developed maleimide-functionalized *closo*-dodecaborate (MID) albumin conjugates that demonstrated high and selective accumulation in tumor tissue with no toxicity in the absence of thermal neutrons, hence a promising boron delivery system [2].

In this study, we synthesized Gd complexes that functionalized MID albumin conjugates aiming MRI-guided BNCT.

EXPERIMENTS: To a solution of bovine serum albumin (BSA) in 10 mM HEPES buffer (pH 7.4) was added Gd-complex ligand. The reaction solution was shaken at 800 rpm for 12 h at room temperature. The reaction solution was subjected to six cycles of ultracentrifugation with a 30 kDa filter to remove excess ligand before the addition of MID. The reaction solution was shaken for another 12 h at 37°C. The final BSA-Gd-MID conjugate was obtained after filtration of excess MID via ultracentrifugation. The concentrations of ^{10}B and Gd per BSA were estimated by using ICP-OES. The conjugate solution was diluted with PBS for the biodistribution study.

CT26 tumor bearing mice (Balb/cCrSlc nu/nu female, 5−6 weeks old, 16−20 g) were injected via the tail vein with 200 μL of MID-BSA or Gd-MID-BSA (7.5 mg [^{10}B]/kg). The plasma, liver, lung, kidney, spleen, muscle, brain, and tumor were extracted 6, 12, and 24 hours after the injection and proceeded to ashing process, followed by quantification of B and Gd via ICP-OES.

RESULTS: Previously, we demonstrated that tumor accumulation of MID-BSA was the largest 12 h after the injection[3]. Therefore, we compared the B and Gd concentration in the organs at 6, 12, 24 hours after injection. The results are shown in Fig. 1. The B concentration of Gd-MID-BSA in tumor was comparable to that of MID-BSA in all the time points, although the Gd concentration of Gd-MID-BSA was the largest in liver, followed in order by spleen and tumor. Therefore, the concentration of B was not consistent with that of Gd, indicating the release of Gd from Gd-MID-BSA due to non-specific binding of free Gd to BSA. These results indicate it is necessary to synthesize more stable Gd complexes and remove free Gd ions in reaction solution thoroughly to proceed thermal neutron irradiation experiment.

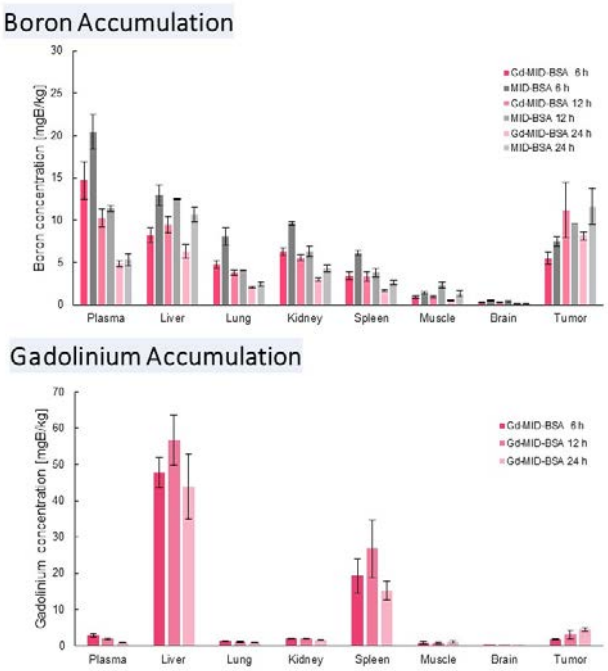

Fig. 1. Biodistribution of boron and gadolinium in colon 26 (CT26) tumor bearing mice. Gd-MID-BSA was intravenously injected at a dose of 7.5 mg [^{10}B]/kg via the tail vein, and the organs were extracted 6, 12, and 24 hours after injection. The concentration of B and Gd in organs was quantified using ICP-OES after ashing.

REFERENCES:

[1] V. Tolmachev *et al.*, Bioconjugate Chem., **10** (1999) 338-345.
[2] K. Kawai *et al.*, Mol. Pharm., **17** (2020) 3740–3747.
[3] S. Kikuchi *et al.*, J. Control. Release, **237** (2016).

CO7-2 Iodophenyl-Conjugated *closo*-Dodecaborate as a Promising Small Boron Agent for BNCT

K. Nishimura, K. Kawai, T. Morita[1], S. Okada[1], K. Miura[1], T. Takada,[2] M. Suzuki[2], H. Nakamura[1]

School of Life Science and Technology, Tokyo Institute of Technology
[1]Laboratory for Chemistry and Life Science, Institute of Innovative Research, Tokyo Institute of Technology
[2]Institute for Integrated Radiation and Nuclear Science, Kyoto University

INTRODUCTION: Boron Neutron Capture Therapy (BNCT) is attracting attention as a non-invasive radiotherapy in the treatment of cancer. The efficiency of boron agent depends highly on tumor selectivity, sufficient amount of boron agent in tumor site, non-toxicity, tumor/normal tissues ratio (>3) and absorption of thermal neutrons by boron. In March 2020, accelerator-based BNCT for head and neck cancer using 4-borono-L-phenylalanine (L-BPA) was approved by the Pharmaceuticals and Medical Devices Agency in Japan, making BNCT more accessible treatment [1]. L-BPA is known to actively accumulate into tumor cells thorough L-type amino acid transporter 1 (LAT-1). However, there are still many patients for whom L-BPA is not applicable. Therefore, the development of novel boron carriers applicable to various cancers including BPA-negative tumors is required for further expansion of BNCT.

We recently developed maleimide-functionalized *closo*-dodecaborate sodium form (MID), which conjugates not only the free SH group of a cysteine residue (Cys34) but also several lysine residues in serum albumin under physiological conditions [2,3]. The MID-conjugated albumin selectively accumulated in tumors due to the enhanced permeability and retention effect and significantly inhibited tumor growth in colon 26 tumor-bearing mice subjected to thermal neutron irradiation [2].

In this study, we focused on small molecule albumin ligands that bind noncovalently to albumin. 4-Iodophenylbutanamide (IP) was chosen as the albumin ligand and conjugated with *closo*-dodecaborate to demonstrate in vivo biodistribution.

EXPERIMENTS: Boron-conjugated 4-iodophenylbutanamide (BC-IP) was designed and synthesized from *closo*-dodecaborate. Tumor-bearing mice (female, 5-6 weeks old) were prepared by injecting subcutaneously (s.c.) a suspension of U87MG human glioblastoma cells in PBS. The mice were kept on a regular chow diet and water for a week. The tumor-bearing mice were injected *i.v.* with 200 μL of PC-IP or MID dissolved in ultrapure (Milli-Q) water at the final dose of 15μgB/g. At 3, 12, and 24 h after injection, the mice were lightly anesthetized and blood samples were collected from heart. The mice were then sacrificed by cervical dislocation and dissected. Liver, spleen, kidney, brain, and tumor were excised, washed with saline, and weighted. Each tissue was digested with 1 mL of HNO_3 at 90 ℃ for 3 h, and then the digested samples were diluted with distilled water. After filtering through a membrane filter (0.5 μmφ, 13JP050AN, ADVANTEC, Japan), boron concentrations were measured by ICP-OES. All protocols for *in vivo* studies involving the use of mice were approved by the Institutional Animal Care and Use Committee of Tokyo Institute of Technology.

RESULTS: The boron concentration in the tumor showed the highest value of 11 μgB/g at 3 h and gradually decreased to 2.4 and 2.3 μgB/g at 12 and 24 h respectively (Fig. 1A). In contrast, boron concentrations in other tissues remained below 5.0 μgB/g at all time periods, demonstrating the highest BNCT effect can be achieved with neutron irradiation at 3 h post injection. For comparison, we investigated the biodistribution of MID at 12 h post injection, the time point at which MID exhibited the highest accumulation in tumors. MID tended to accumulate in plasma, followed by lung, tumor, and kidney (Fig. 4B). The boron concentration in tumor was about 5 μgB/g and thus much lower than was observed with BC-IP. These results suggest that IP, a non-covalent albumin ligand, can enhance tumor accumulation over the maleimide, covalent ligand. Therefore, BC-IP has a potential to act as a more efficient boron carrier than MID in BNCT.

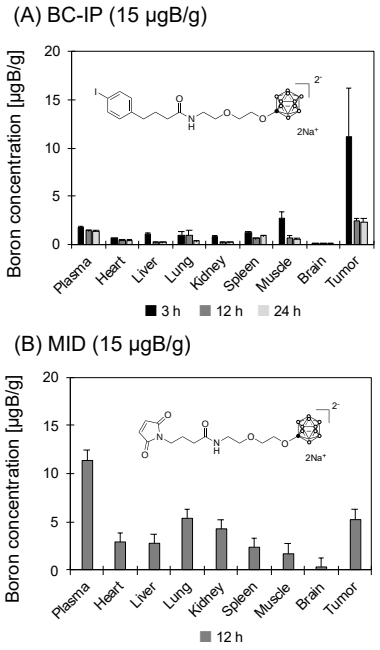

Fig. 1. Biodistribution of (A) BC-IP and (B) MID in U87MG tumor mouse models with i.v. injection. Data are expressed as mean ± SD (n = 3).

REFERENCES:

[1] H. Kanno *et al.*, The Oncologist, **26** (2021) e1250-e1255.
[2] S. Kikuchi *et al.*, J. Control. Release, **237** (2016) 160-167.
[3] K. Kawai *et al.*, Mol. Pharm, **17** (2020) 3740-3747.

CO7-3 Effects of overexpression of *LAT1* in cancer stem cell-like cells on suppression of tumor growth by boron neutron capture therapy

K. Ohnishi[1], T. Tani[2] and M. Suzuki[3]

Department of [1]Biology, Ibaraki Prefectural University of Health Sciences

[2]QST Hospital, National Institutes for Quantum and Radiological Science and Technology

[3]Institute for Integrated Radiation and Nuclear Science, Kyoto University

INTRODUCTION: Outcome from BNCT largely depends on amount of intracellular accumulation of boron compound. L-type amino-acid transporter 1 (LAT1) [1], through which boronophenylalanine (BPA) is transported into cells, is frequently expressed in various types of tumor cells including glioblastoma but not in normal cells [2]. We transfected *pCMV/LAT1-GFP* plasmids into a glioblastoma cell line, T98G, and selected several clones. The sensitivity of cancer cells to neutron and γ-ray fluences was well correlated with the expression level of LAT1 and the level of BPA uptake in the clones [3]. These results suggest that overexpression of LAT1 in cancer cells results in enhanced anticancer effects of BNCT and BNCT combined with gene therapy is beneficial for tumors with low LAT1 expression. In this study, we transfected *pCD133-TRE/LAT1-tdTomato/IRES/tTA* plasmids including a positive-feedback loop into glioblastoma cell line, T98G. The plasmids were designed to overexpress LAT1 tagged with tdTomato on cytoplasmic membranes of CD133 positive cancer cells selectively. We confirmed several clones which stably overexpress LAT1 in hypoxic microenvironment of spheroids. In this study, we examined enhanced effects of LAT1 overexpression on BNCT using the clones in which LAT1 is selectively overexpressed in CD133 positive cancer cells. We have already shown that the CD133 positive cancer cells in spheroids are model cells of cancer stem cells [4]. We transplanted the clone cells into nude mice and performed neutron irradiation on tumors.

EXPERIMENTS: We transplanted tumors formed with a clone (T98G/K10, *pCD133-TRE/LAT1-tdTomato/IRES/tTA*-transfected, LAT1-overexpressed cells in CD133 positive cell selectively), or a clone (T98G/KC2, control plasmid-transfected, LAT1-nonoverexpressed cells) into femoral region of nude mice. Accumulated amounts of ^{10}BPA in blood and tumor were measured using prompt gamma-ray assay (PGA) on 1 h after ^{10}BPA s.c. injection (100 mg/kg, 1 h before irradiation). The transplanted tumors into mice were irradiated with thermal neutron beam at the fluences of 3.3 x 10^{12} n/cm^{-2} on 1h after the ^{10}BPA injection.

RESULTS: Relative tumor volumes in ^{10}BPA-treated mice are shown in Fig. 1. Tumor growth in ^{10}BPA-treated T98G/K10 (n=3) and T98G/KC2 mice (n=3) was strongly suppressed for approximately 40 days after neutron irradiation. However, such suppression was not observed in PBS-treated T98G/K10 and T98G/KC2 mice (data not shown). Relative tumor volumes of 2 mice and 1 mouse were approximately 2 and 6, respectively on 57th day after neutron irradiation in T98G/K10 mice. In contrast to T98G/K10 mice, in T98G/KC2 mice, those of 1 mouse and 2 mice were immediately 4 and over 6, respectively on the same day after neutron irradiation. It seemed that tumor regrowth of T98G/K10 mice is delayed compared with that in T98G/KC2 mice. These results suggest that BNCT is more suppressive on tumor regrowth in CD133 expressing cell-selective LAT1 overexpression cells compared with control cells. We plan additional experiments to confirm the effect of BNCT on tumor regrowth using CD133 expressing cell-selective LAT1 overexpression cells and control cells.

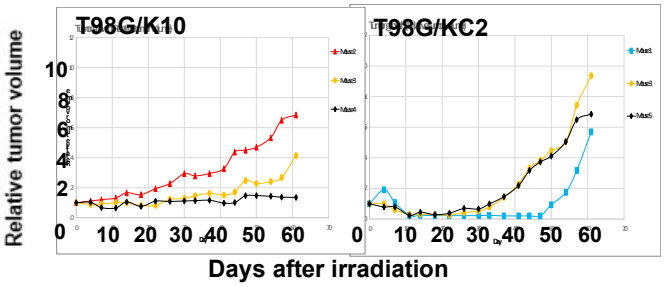

Fig. 1. Tumor growth curves in mice transplanted with CD133 expressing cell-selective LAT1 overexpressing (T98G/K10) or control cells (T98G/KC2).

CONCLUSION: We obtained preliminary data from this study, suggesting that BNCT is more effective by manipulation of cancer stem cell-selective *LAT1* gene expression. On the basis of the present data, we plan to perform further detailed experiments.

REFERENCES:

[1] Y. Kanai *et al.*, J. Biol. Chem., **273** (1998) 23629-23632.

[2] K. Kaira *et al.*, Br. J. Cancer, **107** (2012) 632-638.

[3] K. Ohnishi *et al.*, Radiat. Res., **196** (2021) 17-22.

[4] K. Ohnishi *et al.*, Biochem. Biophys. Res. Communi., **546** (2021) 150-154

CO7-4 Optimization study of polymer-BPA conjugates for non-clinical study

T. Nomoto[1,2], K. Konarita[1,2], D. Tokura[1,2], M. Suzuki[3], N. Nishiyama[1,2]

[1]*Institute of Innovative Research, Tokyo Institute of Technology*
[2]*School of Life Science and Technology, Tokyo Institute of Technology*
[3]*Institute for Integrated Radiation and Nuclear Science, Kyoto University*

INTRODUCTION: Boronophenylalanine (BPA) has been clinically used in boron neutron capture therapy (BNCT). Because BPA can be internalized into cells through LAT1 amino acid transporters expressed on many tumor cells, BPA can show selective accumulation within malignant tumors [1]. However, it was also reported that intracellular BPA is sometimes exchanged with extracellular amino acids including tyrosine due to the antiport mechanism of the amino acid transporter, causing short retention time in a target tumor [2]. Since this unfavorable efflux of intracellular BPA is likely to compromise the therapeutic effect, it is important to prolong the intracellular retention of BPA.

In this regard, we found that polymers possessing multiple hydroxy groups or sugar moieties can form complexes with BPA molecules through boronate esters in aqueous solution and that the polymer-BPA complexes are internalized into cultured tumor cells via LAT1-mediated endocytosis and entrapped mainly in endo-/lysosomes, resulting in prolonged retention in the intracellular compartment by preventing the unfavorable efflux [3, 4]. The polymer-BPA complexes can exhibit the prolonged tumor retention even in *in vivo* condition and significantly enhance the BNCT effects. In particular, poly(vinyl alcohol)-BPA (PVA-BPA) complexes showed the considerably strong BNCT effects in subcutaneous tumor models [3]. Considering the ease of manufacturability PVA-BPA, its clinical translation appears to be promising. Thus, we previously prepared PVA-BPA complexes with various compositions and compared their therapeutic effect to optimize the drug formulation. In this study, by the use of PVA-BPA with the optimized composition, we investigated the therapeutic effect in the orthotopic lung cancer mouse model inoculated with human lung cancer cells.

EXPERIMENTS: PVA-BPA and free BPA were administered by intravenous injection. Three-hour after injection, The chest was irradiated with epi-/thermal neutrons at 1 MW for 50 min using the Kyoto University Research Reactor (KUR).

RESULTS: The result is shown in Fig. 1. The free BPA exhibited obvious therapeutic effects, and PVA further improved the survival rate. The result is consistent with our biodistribution study, in which PVA-BPA prolonged the intratumoral retention. Thus, PVA-BPA may be a promising formulation for BNCT against lung cancers.

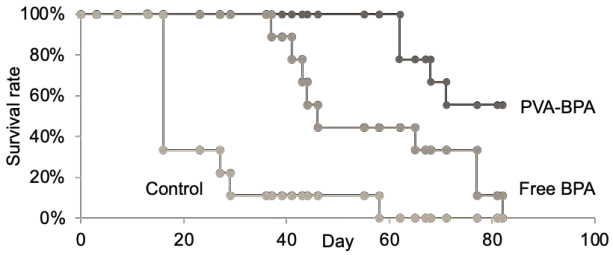

Fig. 1. Survival rate.

REFERENCES:

[1] P. Wongthai *et al.*, Cancer Science, **106** (2015) 279-286.
[2] A. Wittig *et al.*, Radiat. Res., **153** (2000) 173-180.
[3] T. Nomoto *et al.*, Sci. Adv., **6** (2020) eaaz1722.
[4] T. Nomoto *et al.*, J. Control. Release, **332** (2021) 184-193.

CO7-5 Neutron capture therapy using Gd-chelated polymeric drug delivery systems

Y. Miura[1,2], T. Nomoto[1,2], K. Konarita[1,2], D. Tokura[1,2], Y. Sakurai[3], M. Suzuki[3], N. Nishiyama[1,2]

[1]*Institute of Innovative Research, Tokyo Institute of Technology*
[2]*School of Life Science and Technology, Tokyo Institute of Technology*
[3]*Institute for Integrated Radiation and Nuclear Science, Kyoto University*

INTRODUCTION: ^{157}Gd has the high neutron capture cross section and can generate Auger electrons and γ-rays upon thermal neutron irradiation. Thus, Gd has been expected to be a promising atom in neutron capture therapy. We previously synthesized the inorganic-organic hybrid nanoparticle encapsulating Gd and demonstrated strong antitumor efficiency in subcutaneous tumor models [1]. To improve the tumor accumulation and penetration performance of drug carriers, we designed and synthesized new class of Gd-DOTA introduced polymers (polymer-drug) by using controlled polymerization techniques and selective polymer modifications. According to *in vivo* biodistribution study, obtained polymer-drug exhibited selective Gd delivery against targeted tumors, thereby inducing strong antitumor effects upon neutron irradiation. In this year, we compared the therapeutic potential of Gd-chelated polymers with BNCT of boron cluster-conjugated polymers.

EXPERIMENTS: The polymeric drugs or the low-molecular drug as a control were intravenously injected to the BALB/c mice having subcutaneous CT26 tumors. The tumor sites were irradiated with epi-/thermal neutrons 24 or 1 h after injection. using KUR at 5 MW for 10 min. The tumor volume (V) was calculated using the following equation:

$$V = 1/2 \times a \times b^2$$

where a and b denote major and minor axes of a tumor, respectively.

RESULTS: The result indicated that the polymeric drugs could show higher antitumor effects than the low-molecular drugs, which is consistent with our previous results. In addition, the boron cluster-conjugated polymers exhibited strong therapeutic effects comparable to Gd-chelated polymers. In order to elucidate the merit of Gd-NCT, it is important to further investigate detailed mechanism of Gd-NCT. With such study, our results about biodistribution and therapeutic effects may provide significant insights for the development of NCT.

REFERENCES:
[1] P. Mi *et al.*, ACS Nano, **9** (2015) 5913-5921.

CO7-6 Lipid-coated boronic oxide nanoparticles as a boron agent for BNCT

R. Kawasaki,[1] H. Hirano,[1] K. Yamana,[1] A. Oshige,[1] K. Nishimura,[1] N. Kono,[1] Y. Sanada,[2] A. Tabata,[3] N. Yasukawa,[3] H. Azuma,[3] T. Takata,[2] Y. Sakurai,[2] H. Tanaka,[2] M. Suzuki,[2] N. Tarutani,[1] K. Katagiri,[1] T. Nagasaki,[3] and A. Ikeda[1]

[1]*Program of Applied Chemistry, Graduate School of Advanced Science and Engineering, Hiroshima University*
[2] *Institute for Integrated Radiation and Nuclear Science, Kyoto University*
[3]*Department of Chemistry and Bioengineering, Osaka Metropolitan University*

INTRODUCTION: With noninvasiveness, boron neutron capture therapy (BNCT) is considered as one of the elegant therapeutic modalities in cancer treatment. In this therapy, cytotoxic particles are generated by nucleic reaction between ^{10}B and neutron, that is boron neutron capture reaction. The effective ranges of the energy from these cytotoxic particles are corresponding to the size of cells, suggesting that deliverability of boron agents to cancer cell with high specificity and efficiencies is the critical to maximize therapeutic benefits from BNCT. Today, we can use two types of boron agents, L-boronophenylalanine (L-BPA) and 1-mercaptoborocaptate (BSH), in clinical. There are still several issues in delivery including poor solubility in water and cancer selectivity. For these points of views, development of boron agents that can overcome these issues are indispensable.

In this study, we developed hybrid nanoparticles comprising boronic oxide nanoparticles and phospholipids (LCB) as a boron agent for BNCT (Figure 1) [1]. Here, phospholipids are one of the promising candidates as drug delivery nanocarrier that is widely used in liposomes and lipid nanoparticles with excellent biocompatibility and excellent water dispersibility. Boronic oxide nanoparticles possesses several advantages as a boron agent for BNCT including their large contents of boron atom in each nanoparticle with large area to enhance the efficiencies to achieve boron neutron capture reaction and their degradability to avoid undesirable side effects in accumulation of inorganic nanoparticles.

RESULTS: Boronic oxide nanoparticles with a diameter of ~10 nm were prepared by mechanochemical formulation approach as we previously reported [2]. We prepared LCB using eggPC *via* conventional liposome preparation method and their size were manipulated by extruder. Their hydrodynamic diameter was determined to be 120 nm (polydispersity index, 0.15) by dynamic light scattering measurement (DLS). Agglomerate of boronic oxide nanoparticles were found by transmission electron microscopic observation (TEM), indicating the cluster of boronic oxide nanoparticles were coated with eggPC. Moreover, our systems did not form undesirable precipitate and the boron concentration of the dispersion did not change for 1 week, indicating our systems are colloidally stable.

We next evaluated appropriateness of our system as a boron agent by estimating biocompatibility. As a result, current system did not induce cytotoxicity toward murine fibroblast cell (L929) and murine colon carcinoma cell (Colon26) even at the highest concentration, indicating our systems are safely applicable as a boron agent. Moreover, our system could efficiently deliver boron atom toward cancer cells compared to clinically available boron agent, L-BPA, resulting in the therapeutic benefit of BNCT were improved by using current system. Moreover, the anti-cancer effects were obtained even in cancer spheroid, which is used as model for 3-dimensional tumor tissues. Our system comprising boronic oxide nanoparticles and phospholipids are potentially applicable as a boron agent for BNCT.

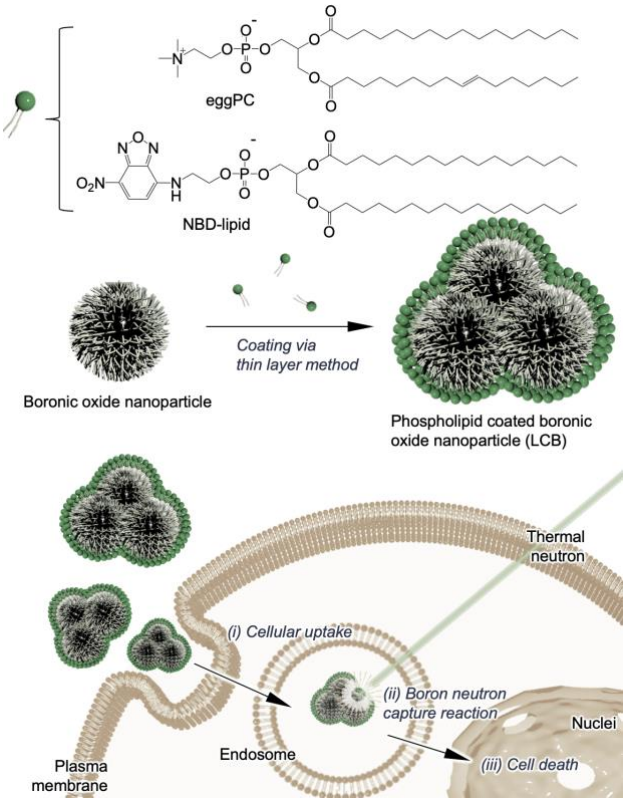

Fig. 1. Schematic illustration of BNCT using LCB.

REFERENCES:

[1] R. Kawasaki *et al.,* ChemBioChem, **in press** (doi):10.1002/cbic.202300186.
[2] R. Kawasaki *et al.,* Nanomed. Nanotechnol. Biol.Med., **49** (2023) 102659 .

CO7-7 Combination Effect of Shikonin on BPA-BNCT toward SCCVII Cells-Bearing C3H Mice

K. Bando, A. Tabata, N. Yasukawa, R. Kawasaki[1], Y. Sakurai[2], Y. Sanada[2], M. Suzuki[2], N. Kondo[2], and T. Nagasaki

Graduate School of Engineering, Osaka Metropolitan University
[1] Graduate School of Advanced Science and Engineering, Hiroshima University
[2]Institute for Integrated Radiation and Nuclear Science, Kyoto University

INTRODUCTION: Boron neutron capture therapy (BNCT) is a potent cancer therapy that exhibits cancer selectivity at the cellular level and has few side effects. However, in many cases, it will not be completely cured due to recurrence/metastasis (distant dissemination). One of the reasons is the involvement of tumor associated macrophages (TAM) present in the stroma of tumor tissue. It has become a major problem that TAM not only promotes neovascularization and tumor regrowth/metastasis, but also suppresses antitumor immunity. In this study, β-1,3-glucan is used as a novel carrier to efficiently and selectively deliver the M2→M1 polarizer to M2 macrophages by Drug Delivery System targeting dectin-1 expressed in M2 macrophages. The complex nanogel of β-1,3-glucan with shikonin as macrophage M2→M1 polarizer was prepared to suppress the malignant transformation of the tumor microenvironment, further increase the cancer immunoreactivity in cancer treatment, and increase BNCT efficiency. Combination effect of shikonin/ β-1,3-glucan nanogel on BPA-BNCT toward SCCVII tumor cells-bearing C3H mice was estimated.

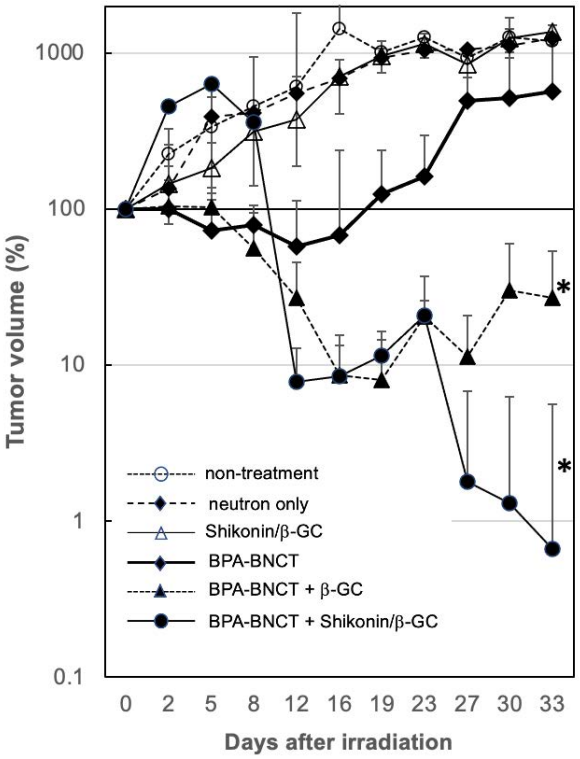

Fig. 1. Tumor volume in SCCVII allograft tumor model mice (C3H female, 6 weeks old, 18−21 g) irradiated with thermal neutron for 30 min (4.8×10^{12} neutrons/cm^2) or without irradiation. Data are expressed as means ± SD (n = 5). Statistical significance: *P < 0.05 compared with BPA-BNCT controls.

EXPERIMENTS: A subcutaneous inoculation of 6×10^5 SCCVII cells in female C3H mice was established for 14 days. Thermal neutron beam irradiation was started from the time point of 120 min after the s.c. injection of BPA (300 mg/kg)-fructose. BNCT effects were evaluated on the basis of the changes in tumor volume of the mice. In order to estimate a combination effect on shikonin, the complex of shikonin/ β-1,3-glucan ([shikonin]=100 μM, 200 μL) was administered via the tail vein at the time points of 1, 3,5 days after irradiation.

RESULTS: Takeya *et al.* reported that triterpenoid derivatives such as soyasapogenol contained in soybeans and corosolic acid in apple pomace inhibited the activation of STAT3, thereby reducing the activity of M2 macrophages [1]. In this study, shikonin, well-known STAT3 inhibitor, was used as a candidate of M2→M1 polarizer [2].

As shown in Fig. 1, clear antitumor effect was found for the combination of shikonin/ β-1,3-glucan nanogel with BPA-BNCT. With shikonin/ β-1,3-glucan treatment alone and neutron irradiation alone, tumors proliferated as well as non- treatment. Tumor regrowth was seen after 27 days on BPA-BNCT due to insufficient dose of BPA. β-1,3-glucan is known to have an immunostimulatory effect and is used as a concomitant drug for cancer radiotherapy [3]. Moreover, it has recently been reported that β-1,3-glucan acts as an M2→M1 polarizer [4]. Herein, administration of β-1,3-glucan only after BPA-BNCT also enhanced the BNCT effect. However, its effect is weaker than that of combination of shikonin/ β-1,3-glucan and BPA-BNCT.

These results on the combination of shikonin/ β-1,3-glucan nanogel with BPA-BNCT suggests our hypothesis that shikonin may induce a tumor-killing M1 macrophage in the tumor microenvironment and enhance the antitumor effect of BNCT.

REFERENCES:

[1] M. Takeya *et al*., Can. Sci., **102** (1981) 206-211.
[2] X. Gao *et al*., Int. Immunopharmacol., **19** (1981) 327-333.
[3] Y. Shimizu *et al*., Cancer, **69** (1992) 1188-1194.
[4] J. Yan *et al*., J. Immunol., **195** (2015) 5055-5065.

CO7-8 The Response of Tumor Cells to BNCT

Y. Tong[1], Gao Zhongming[1], B. Saraswat[1], A. Vadi Velu[1], Y. Sasaki[1], M. Ishiai[2,3], S. Imamichi[1,2,3], T. Nozaki[1,5], M. Suzuki[4], Y. Sanada[4], and M. Masutani[1,2,3]

1 Dept. of Molecular and Genomic Biomedicine, Center for Bioinformatics and Molecular Medicine, Nagasaki University Graduate School of Biomedical Sciences
2 Division of Boron Neutron Capture Therapy, EPOC, National Cancer Center
3 Central Radioisotope Division, National Cancer Center Research Institute
4 Institute for Integrated Radiation and Nuclear Science, Kyoto University
5 Dept. Pharmacology, Osaka Dental Univ.

INTRODUCTION: Boron neutron capture therapy (BNCT) is a novel cancer treatment method that uses high-energy alpha particles and lithium nuclei generated by nuclear reactions. This method is highly precise, short in duration, and has minimal side effects. To better optimize the therapeutic effects of BNCT, it is important to conduct in-depth analysis of its response to cancer cells and therapeutic efficacy. We conducted detailed studies on the effects of BNCT on tumor cells, including cell death and various biological responses. The use of cancer cells and xenograft mouse models can provide powerful support for this effort.

EXPERIMENTS: Neutron irradiations at KUR reactor were operated at 1 MW in all experiments. Irradiation in KUR was carried out with mode : OO-0000F mixed irradiation mode, Dr ratio at ~9.4. Gold foil activation analysis measured thermal neutron fluences and thermoluminescence dosimeter (TLD) measured the γ-ray doses including secondary γ-ray. Total physical dose calculation was carried out using the flux-to-dose conversion factor by the sum of the absorbed doses resulting from ^{1}H (n, γ)^{2}D, ^{14}N (n, p)^{14}C, and ^{10}B (n, α)^{7}Li reactions [1] (Tables 1, 3).
The human squamous cell line SAS and human malignant Melanoma A375 cells were incubated with ^{10}B-boronophenylalanine fructose complex (BPA) for 2.0 hrs. The cell survival of SAS and A375 cells was analyzed by colony formation assay after BNCT with the medium containing fetal bovine serum (FBS). The serum-free medium (SFM) was used to culture SAS and A375 cells after BNCT, and cells and supernatants were harvested at 6 and 24 hours. Cells were harvested for RNA and proteins isolation and molecular analysis was carried out. E-3 port measurement of BPA solution was carried out using teflon tubes (Table 2).
Mouse melanoma cell lines B16F10 or the variant were grafted to the hind legs and were locally irradiated using ^{6}LiF containing thermal neutron shield. Mice were injected with BPA (Catchem) at 500 mg/kg bodyweight approximately 30 min before irradiation. Mice were euthanized on days 7 and 13 after irradiation, and blood, tumors, and other organs were analyzed.

RESULTS: The measurement of thermal neutron fluence and doses for cells were as indicated (Table 1) and for mice were shown in Table 2. Analysis by colony formation assay and RNA and protein expression were carried out to elucidate early cellular and *in vivo* responses to BNCT. A potential role of HMGB1 and proteomic data as early biomarkers for evaluation of cellular and *in vivo* response to BNCT were also indicated [2, 3].

Table 1. Irradiated doses at cells from 6:32-6:42 am and 6:43-7:43 am on Nov. 16, 2022 (Single layer, E-4 rail port) .

Irradiation time [min]	Position	Fluence [/cm²]		[Gy]					
		Thermal neutron [/cm²]	Epi-thermal neutron	Thermal neutron [Gy]	Epi-thermal neutron [Gy]	Fast neutron [Gy]	Gamma-ray [Gy]	Physical Dose [Gy]	B-10* (1ppm)
10	U, Cl	1.1E+12	1.9E+11	1.4E-01	1.5E-02	1.0E-01	9.4E-02	3.6E-01	7.9E-02
	U, F	5.5E+11	9.8E+10	7.4E-02	7.9E-03	5.5E-02	9.4E-02	2.3E-01	4.1E-02
	D, Cl	1.1E+12	2.0E+11	1.5E-01	1.6E-02	1.1E-01	9.4E-02	3.7E-01	8.2E-02
	D, F	6.9E+11	1.2E+11	9.2E-02	9.8E-03	6.8E-02	9.4E-02	2.6E-01	5.1E-02
60	U, Cl	6.4E+12	1.1E+12	8.6E-01	9.2E-02	6.4E-01	6.2E-01	2.2E+00	4.8E-01
	U, F	2.8E+12	5.0E+11	3.7E-01	4.0E-02	2.8E-01	6.2E-01	1.3E+00	2.1E-01
	D, Cl	6.0E+12	1.1E+12	8.0E-01	8.5E-02	5.9E-01	6.2E-01	2.1E+00	4.5E-01
	D, F	3.5E+12	6.2E+11	4.6E-01	4.9E-02	3.4E-01	6.2E-01	1.5E+00	2.6E-01

Table 2. E-3 port measurement result of BPA solution in triplicate on Nov. 16, 2022.

Sample	Number	NET counts H	NET counts B	B/H Ratio	^{10}B conc. (ppm)
Standard ^{10}B	1	1942.0	3721.0	1.9	50.0
Samples 2-4	2	698.0	24338.0	34.9	909.9
	3	666.0	25245.0	37.9	989.1
	4	512.0	18982.0	37.1	967.5
Empty tube	5	97.0	228.0	2.4	61.3

Table 3. Irradiated doses for local irradiation of mice (cart, irradiation room) on 11:17-12:27 am, January 24, 2023 (Cart, irradiation room) .

Irradiation time [min]	Position	Fluence [/cm²]		[Gy]					
		Thermal neutron [/cm²]	Epi-thermal neutron	Thermal neutron [Gy]	Epi-thermal neutron [Gy]	Fast neutron [Gy]	Gamma-ray [Gy]	Physical Dose [Gy]	B-10* (1ppm)
60	Ce1	3.6E+12	6.4E+11	4.8E-01	5.1E-02	3.5E-01	3.2E-01	1.2E+00	2.7E-01
60	Ce2	3.3E+12	5.8E+11	4.3E-01	4.6E-02	3.2E-01	3.3E-01	1.1E+00	2.4E-01

REFERENCES:
[1] S. Nakamura *et al.,* Proc Jpn Acad Ser B Phys Biol Sci, **93** (2017) 821-831.
[2] S. Imamichi *et al.,* Biology, **11** (2022) 420.
[3] D. Perico *et al.,* Cancer Biother Radio-pharm., **38** (2023) 152-159.

CO7-9 Elucidating the effects of boron neutron capture therapy on host immunity in mice tumor models

T. Watanabe[1], Y. Sanada[1], T. Takata[1], G. E. Sato[2], M. Yoshimura[2], T. Mizowaki[2], Y. Sakurai[1], H.Tanaka[1], M. Suzuki[1]

[1]*Institute for Integrated Radiation and Nuclear Science, Kyoto University*

[2]*Radiation Oncology and Image-Applied Therapy, Graduate School of Medicine, Kyoto University*

INTRODUCTION: Boron neutron capture therapy (BNCT) is a type of radiation therapy that utilizes a reaction in which boron atoms (^{10}B) capture neutrons and cause them to fission into alpha particles and lithium nuclei [1]. By selectively delivering boron atoms in the form of drugs to tumor cells, subsequent neutron irradiation can selectively induce nuclear reactions in the delivered cancer cells, resulting in the death of the cancer cells. In particular, immune cells are known to be more radiosensitive than normal cells and can be killed even by small doses of radiation [2]. On the other hand, it has also been shown that irradiation of tumor tissue releases the immune escape mechanism, which is designed to prevent tumor tissue from being attacked by the immune system, and that irradiation of tumors makes it easier for immune cells to attack tumor cells [3]. BNCT is also a type of radiation and may have some effect on the number and function of host immune cells after BNCT, but there have been only a few reports on the immune response after BNCT in detail [4]. The purpose of this study is to elucidate the effects of BNCT on host immune cells.

****

EXPERIMENTS: A tumor model was created in which mouse-derived malignant melanoma cells B16 and mouse-derived squamous cell carcinoma SCCVII were transplanted subcutaneously into the lower leg skin of C57BL/6 and C3H mice, respectively. A tumor model was created in which mouse-derived malignant melanoma cells B16 and mouse-derived squamous cell carcinoma SCCVII were transplanted subcutaneously into the lower leg skin of C57BL/6 and C3H mice, respectively. Each mouse subcutaneous tumor model was treated with BNCT or BNCT plus immunotherapy (anti-PD-1 antibody), and subcutaneous tumor size was measured every 3 days. After X-ray therapy or BNCT was performed on the mouse tumor models, tumor tissue was removed and RNA-seq was performed using a next-generation sequencer. Tumor tissue was removed after BNCT and BNCT + immunotherapy combination treatment, and the tumor tissue was enzymatically treated and separated into single cells.

****

RESULTS: Using each mouse subcutaneous tumor model, we compared the BNCT group and the combination group of BNCT and immunotherapy (anti-PD-1 antibody), and found that the combination group of immunotherapy and BNCT showed better long-term tumor growth inhibition in the tumor curve. In addition, RNA-seq analysis of post-treatment tumors in the target group (X-ray therapy group) and the BNCT group was performed using a next-generation sequencer to examine gene expression status at the time of analysis, and revealed that the expression of chemokines (a group of proteins released into the tumor microenvironment to modulate immune function) in the tumor tissue was significantly increased in the BNCT group. The BNCT group showed significantly increased expression of chemokines (a group of proteins released into the tumor microenvironment that modulate immune function). Since the combination of BNCT and immunotherapy showed a long-term inhibition of tumor growth compared to the control group and the BNCT alone group, we focused on the memory function of lymphocytes, which is involved in immune memory and shows a long-term inhibition of tumor growth, and examined the percentage of CD3+ T cells with a memory function among the lymphocytes infiltrating the tumor. However, contrary to the hypothesis, no significant differences were found between the treatment groups or in comparison with the control group.

****

REFERENCES:

[1] RF. Barth *et al.,* Radiat Oncol., **7** (2012) 146.

[2] Guillaume Vogin and Nicolas Foray., Int J Radiat Biol., **89** (2013) 2-8.

[3] T. Watanabe *et al.,* Int J Clin Oncol., **28** (2023) 201-208.

[4] A. A. Khan *et al.,* PLoS One., **14** (2019) e0222022.

CO7-10 Development of carborane-containing amino acid derivatives for BNCT

A. Niitsu[1], R. Yamamoto[1], T. Watanabe[2], Y. Sanada[2], M. Tsuji[1], T. Hirayama[1], S. Masunaga[3], and H. Nagasawa[1]

[1] *Laboratory of Medicinal & Pharmaceutical Chemistry, Gifu Pharmaceutical University*
[2] *Institute for Integrated Radiation and Nuclear Science, Kyoto University*
[3] *Hanwha Daini Senboku Hospital*

INTRODUCTION: Cancer cells have a greatly increased requirement for amino acids to maintain rapid proliferation and active metabolism, and are particularly dependent on glutamine, which has been termed "glutamine addiction". Glutamine is transported into cells through ASCT2, and the imported glutamine can be used or exchanged through the L-type amino acid transporter (LAT1 or SLC7A5) for hydrophobic or aromatic amino acids such as isoleucine, valine, methionine, tryptophan, and phenylalanine. It is known that these transporters are overexpressed in a variety of tumor cells. Therefore, we are developing a boron carrier that efficiently accumulates ^{10}B atoms in tumors exploiting these amino acid transporters that is highly expressed in cancer. We have synthesized various amino acid derivatives containing boron clusters as hydrophobic pharmacophore and screened them by boron uptake into cells, and **BC2** was selected as a promising candidate.

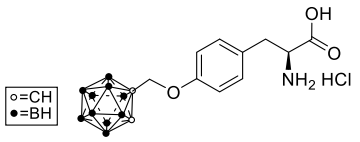

BC2

In this study, to investigate the mechanism of its cellular uptake, we evaluated the correlation between LAT1 expression and the uptake of boron carriers using genetically modified LAT1-deficient/enhanced cell lines.

EXPERIMENTS: **BC2** is synthesized by a microwave reaction in which the corresponding alkyne reacts with decaborane in the presence of a Lewis base to construct carborane. This study used cell lines generated from the SCC7 tumor cell line, a murine squamous cell carcinoma cell line that obtained spontaneously from a C3H/He mouse. LAT1-deficient (SCC7- ΔLAT1) and LAT1 overexpressing (SCC7-LAT1OE) cells were established from SCC7 cells expressing 6×His-tagged LAT1 protein (SCC7-WT), which were established previously [1]. T98G and LAT1-modified SCC7 cells were added with BPA or BC2 at 1 or 10 μg ^{10}B/mL, incubated for 15 minutes, then trypsinized and collected (Method A) or washed with cold PBS (Method B) and dissolved in nitric acid. The boron concentration was determined by ICP-AES.

RESULTS: In the collection of cells treated with boron carriers, boron uptake was found to be significantly increased when cells were dissolved in nitric acid immediately after cold PBS washing without trypsin treatment (Method B), as shown in Fig. 1. This is expected because boron compounds are excreted during trypsinization.

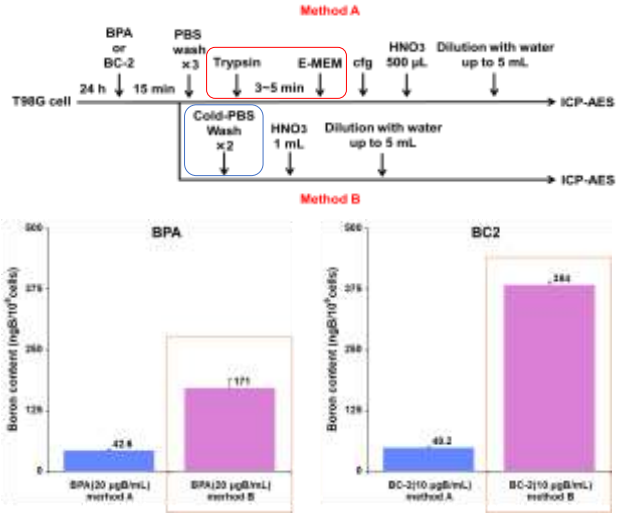

Fig. 1. Differences in boron carrier uptake with or without trypsin treatment.

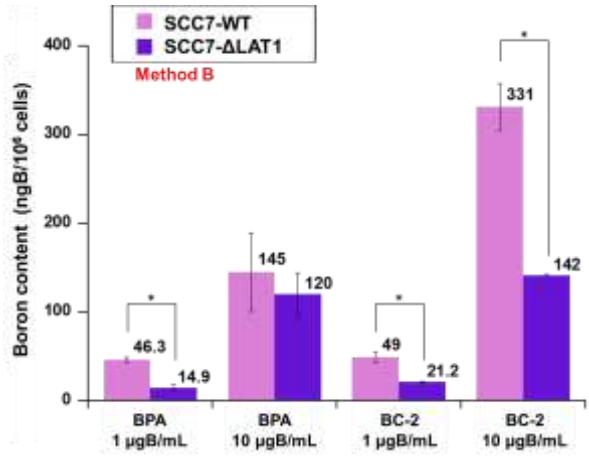

Fig. 2. Effect of LAT1 knockout on boron uptake. Student t-test, n = 2 or 3, *: $p<0.05$.

As shown in Fig. 2, boron uptake was significantly reduced in SCC7- ΔLAT1 compared to SCC7-WT, suggesting that BC-2, like BPA, is taken up into the cells via LAT1. The effects of LAT1 inhibitors and the uptake in LAT1 overexpressing cells are also under investigation.

These results indicate that BC-2 is partially taken up into the cell via LAT1 and accumulated and retained in the cell by an unknown mechanism. Its biodistribution will be investigated in the future.

ACKNOWLEDGEMENTS: This research was supported by JSPS Grants-in-Aid for Scientific Research JP19H03352 and JP26670059.

REFERENCES:

[1] T. Watanabe *et al.*, J. Rad. Res., **64** (2023) 91-98.

CO7-11 Development of Nano Carriers Installed with Gd(III)-Thiacalixarene Complex for Gd-NCT

N. Iki[1], K. Ohama, M. Komiya[1], T. Nagasaki[2], and M. Suzuki[3]

[1] Graduate School of Environmental Studies, Tohoku University
[2] Graduate School of Engineering, Osaka City University
[3] Institute for Integrated Radiation and Nuclear Science, Kyoto University

INTRODUCTION: Owing to a large thermal neutron capture cross section and total kinetic energy of $^{157}Gd(n,g)^{158}Gd$ larger than that of $^{10}B(n,a)^{7}Li$, gadolinium attracts growing attention as an alternative to boron in neutron capture therapy [1]. Because free gadolinium ($Gd(OH_2)_9$) has toxicity, a safe carrier of Gd to tumor not to release free Gd is required. We recently found that thiacalix[4]arene-p-tetrasulfonate (TCAS) self-assembled three lanthanide (Ln) cores including Gd to form a sandwich-type complex, Ln_3TCAS_2 (Fig. 1) [2], the characteristic features of which are high kinetic stability, luminescence signal [3], and 1H relaxation arising from the Ln center [4]. Nano-sized particles are frequently used as a drug carrier toward tumor by enhanced permeability and retention (EPR) effect. We have so far studied nano-carriers for Gd_3TCAS_2 such as silica nano-particle (NP) [5] and albumin NP (AlbNP) [6, 7] aiming at Gd-NCT. This FY, we devised a new AlbNP installed with Gd_3TCAS_2 inside and at the surface of NP (core-shell type) and compared the ability to kill cancer cells upon neutron irradiation with the core- and shell-type AlbNPs.

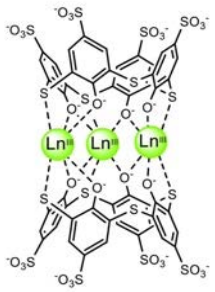

Fig. 1. Structure of Ln_3TCAS_2 complex.

EXPERIMENTS: *Preparation of core-shell AlbNP.* The trinuclear complex Gd_3TCAS_2 was prepared as reported elsewhere [2]. The AlbNP was prepared by a method reported [8]. Briefly, an aqueous mixture of BSA and Gd_3TCAS_2 solution was added EtOH, followed by addition of glutaraldehyde to afford core-AlbNP. This was further mixed with Gd_3TCAS_2 to provide Gd_3TCAS_2-installed core-shell AlbNP (denoted as core-shell AlbNP).
Cell experiment. MCF-7 cells were seeded in a 6-well plate at a cell concentration of 1.0×10^5 cells/mL and incubated for 24 h. After supernatant was removed, RPMI medium and solution containing Gd in a form of 1) shell AlbNP, 2) core AlbNP, 3) free Gd_3TCAS_2, 4) Gd-DTPA, 5) PBS (as control), and 6) core-shell AlbNP were added to each well and incubated for 24 hr. The concentration of Gd in the medium to incubate MCF-7 was set to be 25 μM for 1–3). After washing with PBS, the cells were detached from the well and transferred to tubes to be irradiated with thermal neutron for 20 min.
Assay. To the wells containing 2 mL of RPMI medium in 6-well plates, irradiated cells were seeded at the concentration of 500 cells/well. After incubation for 14 days, the colony was stained with crystalviolet.

RESULTS:
The colony formation units (CFU) normalized with one for no irradiation is shown in Fig. 2. As can be seen, there seems appreciable difference between CFU for 1) control and others except for 3) free Gd_3TCAS_2, suggesting that a suitable carrier like AlbNP is essential for delivery of Gd_3TCAS_2. Regarding the effect of the types of AlbNP, 6) core-shell showed highest ability for cell killing ability at fluence of around 7×10^{11} cm^{-2}. With higher fluence of neutron (at around 1.3×10^{11} cm^{-2}), however, core-shell showed similar ability as shell AlbNP did. On the whole, the core-shell AlbNP is promissing at lower dose of neutron. Material design on the basis of Gd_3TCAS_2 and nanomaterials enabling more efficient NCT effect is now on the way.

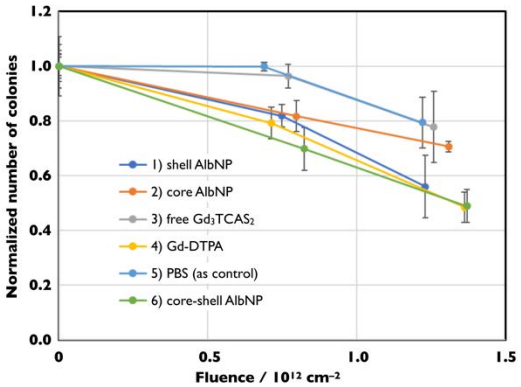

Fig. 2. Dependence of neutron fluence on the colony for-mation rate (n = 3).

REFERENCES:
[1] M. Takagaki *et al.,* Future Application of Boron and Gadolinium Neutron Capture Thrapy, in Boron Science, Ed N. S. Hosmane (CRC Press) (2012) 243.
[2] N. Iki *et al.,* Eur. J. Inorg. Chem., **2016** (2016) 5020-5027.
[3] R. Karashimada *et al.,* Chem. Commun. **52** (2016) 3139-3142.
[4] N. Iki *et al.,* Inorg. Chem. **55** (2016) 4000-4005.
[5] T. Yamatoya *et al.,* KURNS Progress Report 2019. 31P11-8, p.105,
[6] N. Iki *et al.,* KURNS Progress Report 2020. R2P5-2.
[7] N. Iki *et al.,* KURNS Progress Report 2021. R3P2-2.
[8] C. Weber *et al,.* Int. J. Pharm., **194** (2000) 91-102.

CO7-12 International Screening study of Boron / Gadolinium Compounds for NCT of malignant tumors, 2022

RR. Zairov[1], M, Neikter[2], M. Takagaki[3], N, Kondo[4], Y. Sakurai[4] and M. Suzuki[4]

[1]*Kazan Federal University, Russia*
[2]*Univrsity West, Sweden*
[3]*RCNP, Osaka University, Japan,*
[4]*IIRNS, Kyoto University, Japan*

INTRODUCTION:
The possibility of gadolinium neutron capture therapy is controversial, but the total trajectory range of heavy-charged particles generated by the ^{10}B (n, α) ^{7}Li reaction close to the cell diameter, and the total dose distribution is probably too selective. In GdNCT, it is expected that the dose distribution will be improved by the higher total kinetic energy of γ rays, electron beams, Auger electrons, etc., by a single neutron capture reaction of ^{167}Gd (n, γ) ^{168}Gd. Zairov and Neikter have prepared gadolinium inclusion novel nanoparticles, and we repeated GdNCT experiments in vitro, and have confirmed their low toxicity, tumor retention and concentration-dependent GdNCT effect in this research program.

EXPERIMENTS:
SCCVII and/or rat glioma cell line C6 were incubated with an aliquot of nano particle micelles containing natural gadolinium for 5 hrs, then their survival property has been investigated with variety of GdNCT modality; Gd-free, Gd-preincubation+, Gd-preincubation+Gd+. The survival character of GdNCT was compared with BNCT using BPA.

RESULTS:

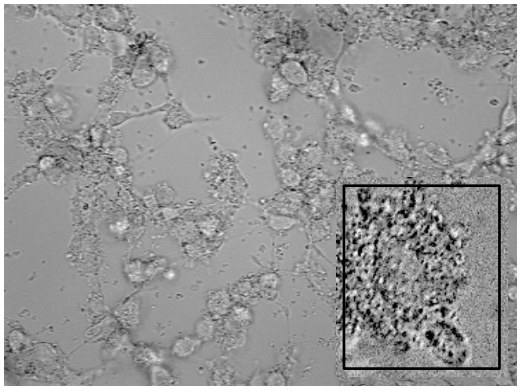

Fig. 1. Microscopic view of rat glioma cell line C6 incubating with the Gd nano micelles.

Tiny micelles are well visualized and reveals their high tumor affinity. No significant tumor damage was confirmed via microscopical observation and toxic study of IC_{50}.

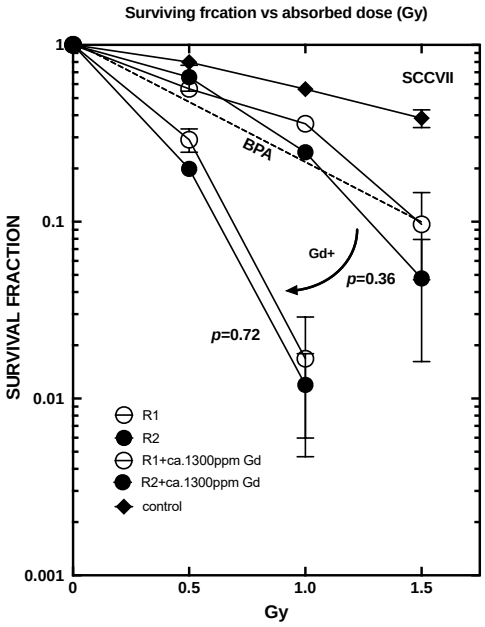

Fig. 2. The survival fraction of SCCVII after GdNCT using the Gd nano compounds of R1 and R2.

The absorbed dose yielding the D_{37} (dose used to inhibit 63% colony formation) values were 0.55 Gy for R1, 0.56 Gy for R2, and 1.50 Gy for control.
As far as the comparison under this experimental condition is concerned, the GdNCT effect was comparable to the standard BNCT effect.

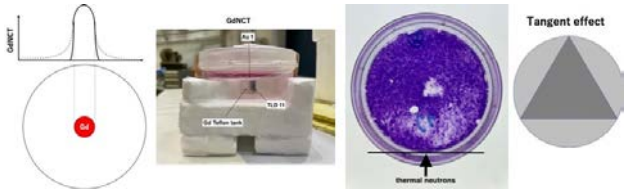

Fig. 3. Maro dose distribution of GdNCT.

Our in-vitro preliminary study using rat glioma cell line C6 for estimation of GdNCT dose distribution shows the macro lethal dose caused by GdNCT might distribute close to the tumor nest without serious damage onto the surrounding tumor cells. These data will be reported details in next time.
We will continue to investigate the possibility of GdNCT.

REFERENCES:
[1] S. Fedorenko *et al.,* Colloids Surf. A Physicochem. Eng. Asp., **559** (2018) 60–67.
[2] R. Zairov *et al.,* Sci. Rep. **7** (2017) 14010. (doi) 10.1038/s41598-017-14409-6.

R4047

CO7-13 Fluorescent Dodecaborate to Development of Theranostic Type Boron Carrier

Y. Hattori, M. Ishimura, I. Nakase[1], M. Kirihata

Research Center of Boron Neutron Capture Therapy, Osaka Metropolitan University
[1] Graduate School of Science, Osaka Metropolitan University

INTRODUCTION: Recently, boron neutron capture therapy (BNCT) has been recognized as an essential treatment for refractory cancers such as glioma, head and neck cancer, and melanoma. Although many types of boron compounds, including amino acids, peptides, nucleic acids, anticancer drugs, and liposomes have been reported as boron delivery agents for BNCT, only two compounds, *p*-borono-L-phenylalanine (L-BPA, Boropharan-10B, Fig.1-**1**) and disodium mercapto-*closo*- undecahydro-dodecaborate (**2**) ($[B_{12}H_{11}SH]^{2-}2Na^+$, BSH, Fig.1-**2**), are clinically used in the treatment of cancer with BNCT. In light of these factors, novel useful boron-pharmaceuticals for BNCT are in high demand.

BSH, a class of water-soluble boron cluster compounds with low toxicity, is clinically used as boron carrier for the treatment of brain tumors, although, tumor selectivity and cell membrane permeability of BSH is slightly low. In the course of our developing studies on new boron carrier for BNCT, we have designed and synthesized thiododecaborate ($[B_{12}H_{11}S]^{2-}$) unit-containing tumor seeking compounds such as amino acids, peptides and antibodies [1-3]. Furthermore, we reported the bifunctional type thiododecaborate containing compounds which $B_{12}H_{12}^{2-}$ cluster is linked two kinds of organic moiety through S^+ sulfaneyl groups ($B_{12}H_{11}$-S^+($-R_1$)-R_2) [4].

Recently, theranostic drug delivery is strong criteria for effective cancer treatment. In BNCT, development of theranostic type boron carrier is highly noted, because visualization of the boron distribution and determination of tumor/normal ratio by non or minimally invasive examination are very important for the planning of BNCT. To develop the theranostic type boron carrier for BNCT, we present the design and synthesis of novel bifunctional boron cluster containing compounds which linked fluorescent dye (fluorescein, BODIPY, Aza-BODIPY etc.) and alkyl linker (-COOSu, maleimide, etc.) to conjugate with tumor seeking compounds such as peptides, proteins and antibodies. Furthermore, we report the conjugation of novel bifunctional boron compounds with antibody, and the biological evaluation of boronated antibody as boron carrier for BNCT.

RESULTS and Discussion: The synthetic route of bifunctional boron cluster containing compounds was illustrated in Fig. 1. The S-alkylation of cyanoethyl BSH (**1**) with 6-bromohexanoic acid or N-Boc-3-bromopropyl amine was achieved by previously reported method in good yield [5]. After deprotection of S-cyanoethyl group, the brominated fluorescent dye (fluorescein, BODIPY, Aza-BODIPY and Cy5.5) was treated to give fluorescent sulfoniododecaborate followed by treatment with an ion-exchange resin. The succineimide ester type compound 4 was prepared by the reaction of compound 3 with di(N-succinimidyl)carbonate (DSC). The alkyl amine type compound 6 was reacted with N-methoxycarbonylmaleimide to give maleimide type fluorescent sulfoniododecaborate **7**.

The conjugation of novel bifunctional boron compounds with peptides, protein or antibody, and the evaluation of boronated compounds as boron carrier for BNCT and is now under investigation.

References:

[1] Y. Hattori *et al.*, J. Med. Chem., **55** (2012) 6980-6984.
[2] I. Nakase *et al.,* Chemm. Commun., **55** (2019) 13955-13958.
[3] I. Nakase *et al.,* ACS Omega, **5** (2020) 22731-22738.
[4] Y. Hattori *et al.,* ACS. Med. Chem. Lett., **13** (2022) 50-54.
[5] S. Kusaka *et al.,* Appl. Radiat. Isot., **69** (2011) 1768-1770.

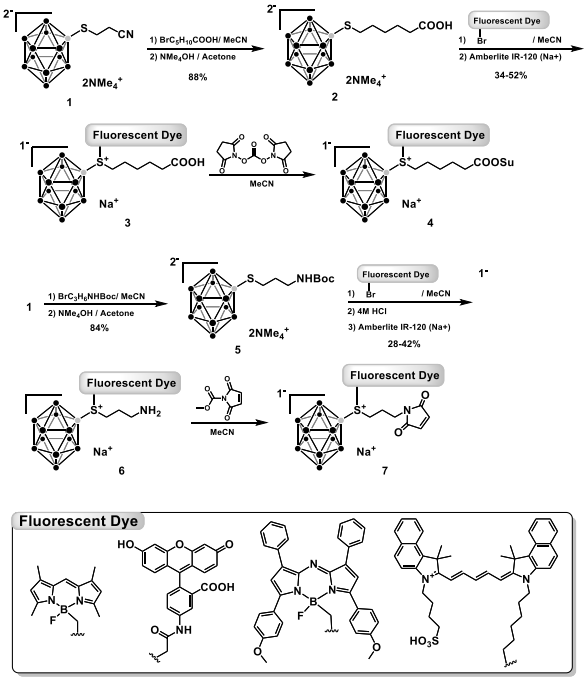

Fig. 1. Synthesis of bifunctional sulfoniododecaborate.

CO7-14 Evaluatiomn of gadolinium biodistribution and tumor-killing effects of surface-modified gadolinium-loaded chitosan nanoparticles for gadolinium neutron capture therapy

T. Andoh[1], T. Fujimoto[2], M. Suzuki[3], T. Takata[4], Y. Sakurai[4] and H. Ichikawa[1].

1Faculty of Pharmaceutical Sciences, Kobe Gakuin University, Japan.
2Department of Orthopaedic Surgery, Hyogo Cancer Center, Japan.
3Particle Radiation Oncology Research Center, Institute for Integrated Radiation and Nuclear Science, Kyoto University, Japan.
4 Division of Radiation Life Science, Institute for Integrated Radiation and Nuclear Science, Kyoto University, Japan

INTRODUCTION: Neutron-capture therapy using nonradioactive ^{157}Gd (Gd-NCT) is currently under development as a potential radiation therapy option for cancer. Gd-NCT with ^{157}Gd has several potential advantages over boron (^{10}B) neutron capture therapy (BNCT). The deep tissue penetration (100 μm) of γ-rays from the ^{157}Gd (n, γ) ^{158}Gd reaction is expected to provide tumor-killing efficacy within bulky tumors such as head and neck cancers. Furthermore, oral mucositis caused by BNCT using *p*-boronophenylalanine could be a potential dose-limiting consideration for head and neck tumors [1]. We have previously developed gadolinium-loaded chitosan nanoparticles (Gd-nanoCPs) for controlled Gd delivery in GdNCT. These nanoparticles comprised Gd-diethylenetriaminepentaacetic acid (Gd-DTPA, an MRI contrast agent), and chitosan (a naturally abundant biodegradable polysaccharide with good biocompatibility and bioadhesive characteristics). The present study investigates the *in vivo* gadolinium biodistribution and tumor-killing effects after NCT with intra-tumoral injected nanoparticulate formulations.

EXPERIMENTS: Gd-nanoCP was prepared using chitosan and Gd-DTPA through the previously developed w/o emulsion-droplet coalescence technique [2]. The condensation reaction of the amino group present in intact Gd-nanoCP and NHS-activated ester-PEG prepared direct PEG-modified Gd-nanoCP (PEG-Gd-nanoCP). The thin-film hydration method carried out surface-modification of Gd-nanoCPs with Soybean Lecithin and PEG-lipid (PEG-SL-Gd-nanoCP). Mean particle size and zeta potential of the resultant Gd-nanoCPs were measured by Zetasizer® (Malvern). Gd concentration of tumor tissue was determined by inductively coupled plasma atomic emission spectrometry (ICP-AES, SPS3100) followed by incineration of each sample. In the NCT trial, male 5-week-old C3H/HeN mice were used. SCC-VII (1×10^6 cells/mouse) were injected into the left masseter muscle [3]. The mice were divided into NCT group and HOT control group. Before injection, centrifugation concentrated Gd-nanoCPs to 6000 μg Gd/mL. Gd-nanoCPs incorporating 1.2 mg of natural Gd were injected intratumorally twice to the mice. The tumors were exposed to thermal neutron irradiation at the Institute for Integrated Radiation and Nuclear Science, Kyoto University. The tumor volume ratio before and after neutron irradiation assessed the tumor-growth suppressing effect.

RESULTS: Mean particle diameter and zeta potential of the Gd-nanoCP, PEG-Gd-nanoCP, and PEG-SL-Gd-nanoCP were 171, 168, and 179 nm, 15, 20, and -6 mV, respectively. In the intratumoral injection test, the Gd concentrations of Gd-nanoCP, PEG-Gd-nanoCP, and PEG-SL-Gd-nanoCP in the tumor tissues were 2337, 1551, and 1533 ppm, respectively. PEG-SL-Gd-nanoCP wasn't used in the GdNCT because it's shown good permeation, leaked out the tumor tissue, and accumulated to normal tissues. In GdNCT, the NCT group significantly suppressed tumor growth relative to that observed in the HOT control group. Although the Gd concentration in the tumor tissue of the PEG-Gd-nanoCP group was approximately 2/3 lower than that in the Gd-nanoCP group, the PEG-Gd-nanoCP group showed similar tumor growth suppression as the Gd-nanoCP group. This result was found to be related to the distribution behavior of Gd preparations within the tumor after administration. Unlike extensive delivery via tumor vasculature, the intratumoral injection causes particle diffusion and distribution from the injection site. Therefore, improving the permeability and diffusion of Gd preparations within the tumor tissue after injection is crucial for achieving uniform Gd distribution in the tumor tissue. The improvement in dispersion stability with surface modification possibly led to the homogenization of Gd distribution in the tumor tissue because the particle sizes of the two types of Gd formulations did not differ significantly.

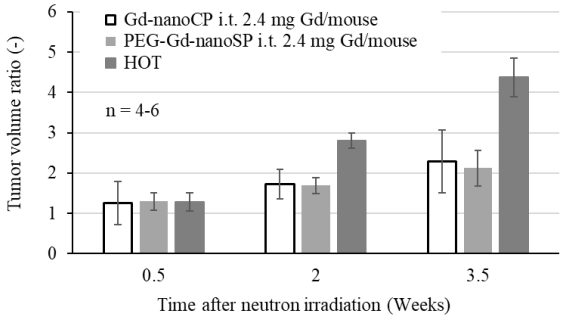

Fig. 1. Tumor volumes after thermal neutron beam irradiation of NCT and HOT control groups.

REFERENCES:

[1] J. A. Coderre *et al.,* Radiat. Res., **152** (1999) 113-118.
[2] H. Tokumitsu *et al.,* Pharm. Res., **16** (1999) 1830-1835.
[3] T. Nomura *et al.,* 5th Asian Conference on Oral and Maxillofacial Surgery, (2002) 111-115.

CO7-15 Basic research to expand the indication of boron neutron capture therapy to non-neoplastic diseases

T. Watanabe[1], Y. Hattori[3], Y. Sanada[1], T. Takata[1], G. E. Sato[2], M. Yoshimura[2], Y. Sakurai[1], H. Tanaka[1], T. Mizowaki[2], M. Kirihata[3], M. Suzuki[1]

[1]*Institute for Integrated Radiation and Nuclear Science, Kyoto University*

[2]*Radiation Oncology and Image-Applied Therapy, Graduate School of Medicine, Kyoto University*

[3]*Research Center for Boron Neutron Capture Therapy, Organization for Research Promotion, Osaka Metropolitan University*

INTRODUCTION: The purpose of this study is to explore the possibility of applying BNCT, which has been developed as a cancer therapy [1], to intractable diseases other than cancer (intractable non-tumor diseases) using mouse models, in order to further develop BNCT as a medical field and to discover potential indications for diseases other than cancer [2]. In this study, we will develop boron agents for the above purposes based on antibodies and examine their efficacy using disease-specific mouse models.

****

EXPERIMENTS: It is known that intraperitoneal administration of β-glucan to mice (Balb/c or Balb/c-derived offsprings) induces an immune response and may induce symptoms similar to collagen disease [3, 4]. In this study, we used a mouse model of inflammation induced by intraperitoneal administration of β-glucan to induce symptoms such as arthritis and enteritis, which are commonly observed in human collagen diseases. When 30 mg of laminarin, a β-glucan, was administered intraperitoneally to mice, swelling of bilateral wrist joints was observed from 7 days after administration, and 10-14 days after administration, redness of the wrist joints was observed, suggesting clear inflammation. No obvious diarrhea was observed in this mouse model or at the β-glucan dose.

To bind a boron atom to the stationary portion (Fc portion) of a commercially available IgG antibody, a boronated module was prepared by attaching a functional group that reacts against an amino group to a boron cluster. The number of boron atoms (relative ratio) was quantified by binding the FITC-bound boronated module to the isotype antibody and measuring the fluorescence intensity per antibody molecule.

To determine whether the antigen recognition ability of the antibody is maintained after binding of the boronated module, the boronated module conjugated with FITC was conjugated to a commercially available anti-mouse CD8a antibody (BioLegend), and mouse-derived splenocytes were measured together with BV421-anti-mouse CD8b antibody. The IL17 receptor was targeted by the method described above.

A new boron drug targeting the IL17 receptor was prepared by the above method, and its therapeutic effect was examined by comparing it with that of the neutron alone irradiation group, the L-BPA administration group, and the boron drug targeting the immune response group.

****

RESULTS: FITC-conjugated boronated anti-CD8a and BV421-aCD8b antibodies co-stained CD3+CD8+ T cells in splenocytes, indicating that the antigen recognition capacity of the antibodies is maintained within the protocols used in this study even when the boronated modules are bound to the antibodies. After binding a boronated module to a commercially available anti-mouse IL17 receptor (BioLegend) and administering 200 μg to a mouse model of arthritis created by intraperitoneal administration of β-glucan, the therapeutic effect on arthritis was observed by irradiating bilateral wrist joints with neutrons. Mice with arthritis were prepared under the same conditions, and the same neutron irradiation was performed on the following two control groups; control group 1: Neutron irradiated without boronated antibody, control group 2: Neutron irradiated with boronated derivatives of amino acids, which are commonly used as boron drugs for BNCT. No obvious improvement in arthritis was observed when arthritis was evaluated by scoring over time after neutron irradiation.

****

REFERENCES:

[1] RF Barth *et al.,* Radiat Oncol., **7** (2012) 146.
[2] TD Malouff *et al.,* Front Oncol., **11** (2021) 601820.
[3] S. Sakaguchi *et al.,* FEBS Letters, **585** (2011) 3633-9.
[4] K. Hirota *et al.,* Immunity, **48** (2018) 1220-1232.e5.

CO7-16 In Vivo Efficacy of BPA-Ionic Liquid as a Novel Compound for BNCT (2)

M. Shirakawa[1,2], T. Sakai[1], R. Terada[1], Y. Sato[1], N. Kamegawa[3], R. Takeuchi[3], H. Hori[3], K. Nakai[2], A. Zaboronok[2], F. Yoshida[2], T. Tsurubuchi[2], T. Sakae[2], A. Matsumura[2], T. Takata[4], N. Kondo[4], Y. Sakurai[4], M. Suzuki[4]

[1]*Department of Pharmaceutical Sciences, Fukuyama University*
[2]*Department of Neurosurgery, Faculty of Medicine, University of Tsukuba*
[3] *Morita Pharmaceutical Ind., Ltd.*
[4] *Institute for Integrated Radiation and Nuclear Science, Kyoto University*

INTRODUCTION:

L-p-boronophenylalanine (BPA) shows excellent anti-tumor effects after thermal neutron irradiation but is known to require large doses to achieve clinical efficacy because of its low solubility. Therefore, we have been investigating and reporting the use of ionic liquids (ILs) [1, 2]. Here, we have gone further and synthesized a more stable BPA-based IL (BPA-IL) and reported its in vivo antitumor effects after thermal neutron irradiation.

EXPERIMENTS:

1. Synthesis of BPA-IL

BPA-IL applied in this study was synthesized using meglumine as the cation substance and BPA as the anion substance, as in the previous study [3]. However, meglumine and BPA were mixed 2:1 and stirred at room temperature for 24 hours. After that, the water content of the IL was reduced to about 20 wt% by rotary evaporator at 80°C.

2. Anti-tumor effect using BPA-IL by BNCT

Female 3-week-old BALB/cA mice were purchased from CLEA Japan Inc. (Tokyo, Japan). The tumor model was prepared by grafting 2×10^6 of murine colon carcinoma cells (CT26) to the right thigh of mice (4 weeks old, weighing 16-20 g) to develop a tumor of 6-8 mm in diameter.

Ten days later, 34μL of BPA-IL was administrated via intravenous injection before irradiation was delivered at a dose of 24mg^{10}B/kg. Similarly, 200μL of BPA-Fru was administered. In addition, 29 μL of BPA-IL was administered intravenously over 30 minutes. Two hours after injection, thermal neutron irradiation was performed with a flux of $1.1\text{-}1.2 \times 10^9$ neutrons/cm^2/s over 60 min. The tumor size was measured over time after the irradiation until day 27, and the volume was calculated using the previously applied formula [4].

On the last measurement day, a significant difference in tumor size between the groups was calculated using the independent t-test. The *p*-values representing significant differences were marked with the following number of asterisks: *: $p<0.05$, **: $p<0.01$, ***: $p<0.005$, ****: $p<0.001$, and ns: no significant difference.

RESULTS:

As shown in Figure 1, BPA-IL (Meg-BPA) significantly inhibited tumor growth compared to the control group despite the lower dose volume compared to BPA-Fru. However, the intravenous administration of BPA-IL (Meg-BPA i.v.D) did not produce excellent therapeutic effects. As shown in Figure 2, no significant side effects (e.g., weight loss) were observed after using BPA-IL, similar to BPA-Fru.

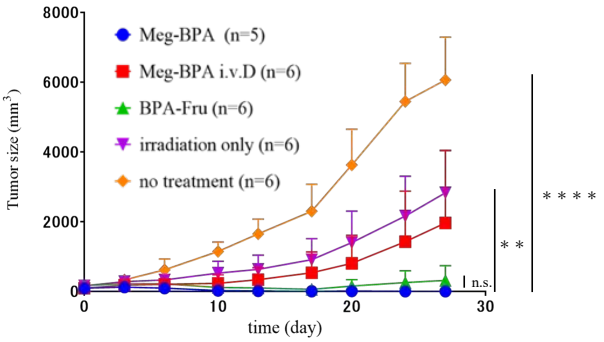

Fig.1) Meg-BPA anti-tumor effect after BNCT.

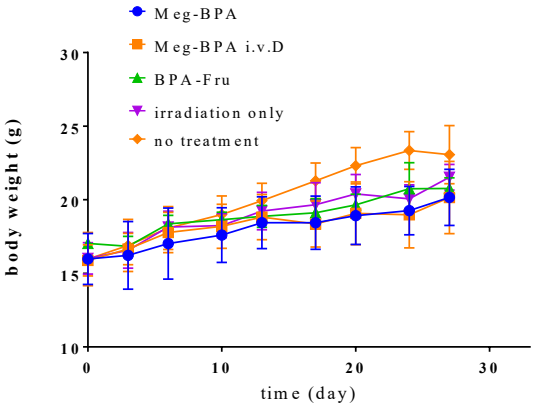

Fig.2) Mice body weight after Meg-BPA injection with further neutron irradiation.

REFERENCES:

[1] M. Shirakawa *et al.*, Patent application 2020-067196 and patent publication 2021-161093.
[2] M. Shirakawa *et al.*, Patent application 2020-136911 and patent publication 2022-032754.
[3] M. Shirakawa *et. al.*, KURNS PROGRESS REPORT 2021, (2022) 208.
[4] M. Shirakawa *et. al.*, KURRI PROGRESS REPORT 2017, (2018) 69.

R4059

CO7-17 Synthesis of a Novel Boron Compound with Potential Peptide-Related Nuclear Import (2)

M. Shirakawa[1,2], T. Nakano[1], A. Okuda[3], A. Shigenaga[1] and M. Sugiyama[3]

[1]*Department of Pharmaceutical Sciences, Fukuyama University*
[2]*Department of Radiation Oncology, Faculty of Medicine, University of Tsukuba*
[3] *Institute for Integrated Radiation and Nuclear Science, Kyoto University*

INTRODUCTION:

The therapeutic effect of BNCT is provided by the alpha -rays generated in the ^{10}B neutron capture reaction, which leads to double-strand DNA breaks in tumor cells. Based on its principle, the anti-tumor effect of BNCT is presumed to be maximized when ^{10}B is present in or near the nucleus of the tumor cell [1].

Therefore, we have been investigating and reported the peptide-BSH (TAT-GALA-BSH) [2]. Here, we have gone synthesized a novel boron peptide of other amino acid sequence and reported the obtained experimental results.

EXPERIMENTS:

Novel boron peptides were combined with mercaptododecaborate (BSH) and three functional peptides, and the synthesis was performed on Rink Amide resin (100~200 mesh) by the Fmoc solid-phase method [3]. As amino acids sequence of the peptide, we selected S19 (PFVIGAGVLGALGTGIGGI), H16 (HHHHHHHHHHHHHHHH), NLS (RREKYGI-PEPPEKRRK), and synthesized them. After that, BSH was conjugated with the peptide N-terminal region by binding chloroacetic acid. Each amino acid coupling reaction was carried out for 60 min at room temperature. De-protection and cleavage of resin were accomplished with a cleavage cocktail at room temperature, then precipitated by adding a large amount of diethyl ether. After the freeze-drying procedure, we obtained the desired compound.

RESULTS:

As shown in Fig. 1, we succeeded in synthesizing the novel boron peptide (BSH-S19-H16-NLS). In the identification of this boron peptide, ESI-TOFMS (Xevo G2-XS QTof) showed m/z 1576.1 of the tetravalent peak. However, the yield and purity were low, and not enough yield was obtained to be used in other experiments.

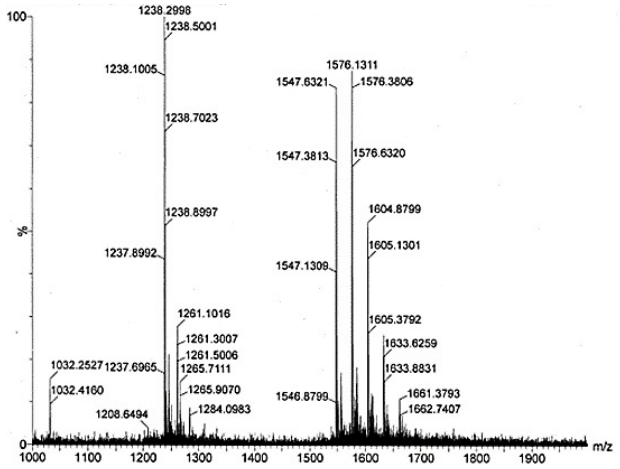

Fig.1) Identification of BSH-S19-H16-NLS by ESI-TOFMS

REFERENCES:

[1] T. Sato *et al.,* Sci. Rep., **8** (2018) 988.
[2] M. Shirakawa *et. al.,* KURNS PROGRESS REPORT 2020, (2021) 198.
[3] M. Gongora-Benitez *et al.,* ACS Comb. Sci., **15**(5) (2013) 217-228.

CO7-18 Construction of novel Boron-containing silica nanoparticles and BNCT experiments

F. Tamanoi[1], M. Laird[1], K. Matsumoto[1] A. Komatsu[1], Y. Higashi[1] A. Kubota and M. Suzuki[2]

[1]*Institute for Advanced Study*
Institute for Integrated Cell-Materials Sciences, Kyoto University
[2]*Institute for Integrated Radiation and Nuclear Science, Kyoto University*

INTRODUCTION: Borocaptate (BSH) has been developed as useful boron compound which is available for the Boron neutron capture therapy (BNCT) therapy of brain tumor. But, BSH has poorly accumulation capability into cell, so it is necessary to develop of novel type of boron compound that can effectively be transported BSH into cells. We have recently developed a mesoporous silica-based nanoparticle which has biodegradable bonds in the framework, named biodegradable periodic mesoporous organosilica (BPMO), that are coupled with BSH by thiol-ene reaction. These nanoparticles have a large surface area where BSH can be coupled for BNCT application. In this study, we investigated BSH-BPMO uptake into OVCAR8 ovarian cancer cells and spheroid, and evaluated spheroid destruction efficacy.

EXPERIMENTS: BPMO was synthesized by sol-gel synthesis of two precursors, bis[3-(triethoxysilyl) propyl] tetrasulfide and 1, 2-bis(triethoxysilyl) ethane. This resulted in the incorporation of tetrasulfide bonds into the framework of the nanoparticles. BPMO was then processed to modify with triethoxyvinylsilane that contain vinyl groups. After vinyl group modification on BPMO surface, BPMO was phosphonated and coupled with BSH by overnight nixing. The synthesized nanoparticles were characterized by using SEM, TEM, FT-IR, NMR, nitrogen adsorption-desorption analysis and zeta potential. The amount of boron attached on the nanoparticles was examined by ICP, and boron content was determined.

GFP-expressed OVCAR8 cells (5,000 cells/well)) were inoculated on U-bottom 96-well plate to form cancer spheroid for 7 days. After spheroid formation, BSH-BPMO was loaded to spheroid and evaluation of BSH-BPMO uptake by confocal microscopy. Finally, we investigated BSH-BPMO-loaded spheroid destruction with thermal neutron for 1 hour at an operating power of 1MW. After the irradiation, spheroids were cultured for 24h with 5%-humified CO_2 and evaluated the size.

RESULTS: Nanoparticles synthesized had approximately 300 nm of diameter and homogenous shapes examined by SEM and TEM microscopy. FT-IR analysis of BPMO showed diagnostic peaks of typical Si-O-Si, -$(CH_2)_2$- and -CH_2- vibrations. After coupling of BSH to BPMO, we analyzed surface charge of BSH-BPMO which was negative due to modification with phosphonate. The zeta potential of BPA-BPMO was -51.5 mV.

BSH-BPMO accumulation in theOVCAR8 cell was investigated with a confocal microscope. BSH-BPMO was effectively able to take up into cells and localized at perinuclea region. We also evaluated the amount of boron which was taken into cancer cells by ICP. 19.15±0.39% of boron were detected from cell lysate, whereas normal BPA was 0.33±0.02%. And then, we investigated spheroid uptake of BSH-BPMO by confocal microscopy. As seen in Fig.1, The red fluorescence of BSH-BPMO was overlapped with GFP fluorescence at each focal plane, and it indicated BSH-BPMO was effectively taken up into spheroid. These results indicated that BSH can effectively improve the cellular uptake and accumulation by BPMO nanoparticles.

Investigation of the spheroid destruction of cancer spheroid loaded BSH-BPMO was carried out with Kyoto University Nuclear Reactor and evaluated the spheroid size after neutron irradiation. Following solutions were loaded to spheroid with 24h incubation at 37℃ in humidified CO_2: 500 μg/ml of BSH-BPMO, 500 μg/ml of BPMO, 15.6 μg/ml of free BSH and 186 μg/ml of free BPA corresponding to 89 ng of ^{10}B. These spheroids were irradiated with thermal neutron. As seen in Fig.2, the spheroid which was loaded BSH-BPMO was completely destructed compared with free BPA-loaded cancer spheroid. We demonstrated that BPMO can be useful for effectively carrier of BSH into cells, and BSH-BPMO could be a novel boron compound with the potential to dramatically improve the BNCT efficacy.

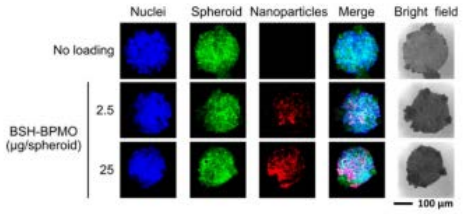

BSH-BPMO uptake in OVCAR8 spheroids with 10^4 cells: Hoechst-dyed nuclei observed at 405 nm, GFP-expressed OVCAR8 cell at 488 nm and Rhodamine B containing nanoparticles at 561 nm.

Fig.1. Spheroid uptake of BSH-BPMO.

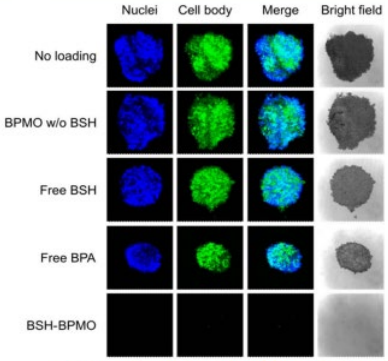

Neutron exposure results of (a) OVCAR8 spheroids observed by confocal microscopy after 1 h of neutron irradiation and three days of incubation: Hoechst-dyed nuclei observed at 405 nm and GFP modified OVCAR8 cell at 488 nm.

Fig.2. Spheroid destruction by neutron irradiation.

R4092

CO7-19 Development of Gadolinium-loaded mesoporous silica-based nanoparticles and application to cancer radiotherapy

F. Tamanoi[1], K. Matsumoto[1] and M. Suzuki[2]

[1]*Institute for Advanced Study*
Institute for Integrated Cell-Materials Sciences, Kyoto University
[2]*Institute for Integrated Radiation and Nuclear Science, Kyoto University*

INTRODUCTION: Gadolinium neutron capture therapy (GNCT) has emerged as an attractive neutron-based cancer therapy different from BNCT. Neutron exposure leads to the generation of gamma-rays and Auger electrons. We aim to develop a novel type of nanoparticles for GNCT. We have previously developed silica-based nanoparticles for BNCT [1]. Our approach for GNCT reagents is to utilize a similar approach. Mesoporous silica-based nanoparticles have the advantage of well-established synthesis methods as well as a large surface area. In addition, the nanoparticles are stable enabling various chemical modifications to be carried out.

EXPERIMENTS:
BPMO synthesis was carried out by sol-gel synthesis of two precursors, bis[3-(triethoxysilyl) propyl] tetrasulfide and 1, 2-bis(triethoxysilyl) ethane. The nanoparticles synthesized contain tetrasulfide bonds within their framework. In order to bind gadopentetic acid, we modified the nanoparticle surface with amino groups.

Gadolinium was coupled onto BPMO surface using gadolinium diethylenetriamine penta-acetic acid (DTPA).
The nanoparticles synthesized were characterized by SEM and EDX-TEM. ICP-AES was used to determine the amount of Gd attached on the nanoparticles.

Uptake of Gd-BPMO into human cancer cells was examined. In addition, CAM model established by transplanting human ovarian cancer cells OVAR8 on the CAM membrane in fertilized chicken egg was used to check the efficacy of Gd-BPMO.

After intravenously injection of Gd-BPMO, the eggs were placed at the center of emerging neutron beam and were irradiated with thermal neutron for 1 h at an operating power of 1MW. After the irradiation, eggs were incubated for 3 days at 37℃ with 65% humidity. Tumors were then cut out to evaluate the tumor size.

RESULTS: We have developed a reproducible method for Gd-BPMO. The nanoparticles had a diameter of approximately 80-100 nm, as determined by SEM and TEM microscopy. The amount of Gd that was coupled onto BPMO was 2.6% of the total weight, as determined by ICP. Scaling-up of the method was attempted.

We have established a convenient assay to examine the efficacy of Gd-BPMO for GNCT. This assay utilizes the CAM assay and examines tumor growth inhibition upon neutron exposure after injection of the nanoparticles. This assay can be used to test a variety of nanoparticles and the results obtained can be used to further improve the nanoparticles. Evaluation of Gd-BPMO efficacy using a mouse model needs to be carried out in the future.

REFERENCES:
[1] F. Tamanoi *et al*., Int. J. Mol. Sci., **22** (2021) 2251.

CO7-20 Is the boron neutron capture reaction captured using CR-39 related to boron concentration and cell viability?

K. Nakai[1], Y. Yoshitaka[1], Y. Sugawara[2] and Y. Sanada[3]

[1]*Department of Radiation Oncology, Proton medical research center, Faculty of Medicine, University of Tsukuba.*

[2]*Doctroial program in Medical Sciences, Graduate School of Comprehensive human Sciences, University of Tsukuba.*

[3]*Institute for Integrated Radiation and Nuclear Science, Kyoto University*

INTRODUCTION: Boron neutron capture therapy is a particle therapy that produces alpha rays and lithium nuclei in vivo for anticancer effect. Alpha autoradiography is also used in the BNCT field as a simple method to show the localization of alpha radiation.
As a solid range detector, CR-39 is insensitive to X-rays and gamma rays and is also a material used for neutron detection by incorporating proton radiators and alpha converters.
In the present experiment, we aimed to investigate the in-ternal alpha distribution of tubes irradiated with a horizon-tal neutron beam in a cell survival experiment system us-ing cell suspensions, which are commonly used in BNCT experiments.

MATERIAL AND METHODS:
The CR-39, which is a passive Solid-state Nuclear Track Detector cut into the shape shown in Figure 1(a) by a car-bon dioxide laser machine. The CR-39 treated with UV sterilization was placed vertically inside the sample tube at a 90-degree angle as shown in Figure 1(b). The sample was filled with 0.5 mL of solution containing cell suspension and used as the irradiation sample.
Cells: CHO, Neutron source: KUR thermal neutron beam.

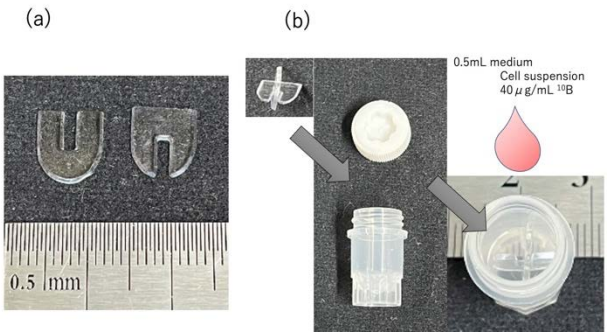

Figure 1. Schema of CR-39 shape (a) and placed inside the sample tube (b).

EXPERIMENTS: The irradiation set-up is the same as the cell survival experiments performed in KUR.
Cell suspension and samples with medium were irradiated in the reactor for 18 and 36 min. CHO cells were maintained at a boron concentration of 40 μg/ml in the medium for 2 h before irradiation and diluted with medium immediately before irradiation to 1/10 the boron concentration. Cell suspensions and samples with medium were irradiated in the reactor for 18 minutes and 36 minutes, respectively. After the irradiation, for the cell suspension samples, a colony formation assay was performed at each irradiation time, and the boron neutron capture reaction was confirmed to have occurred Figure 2.

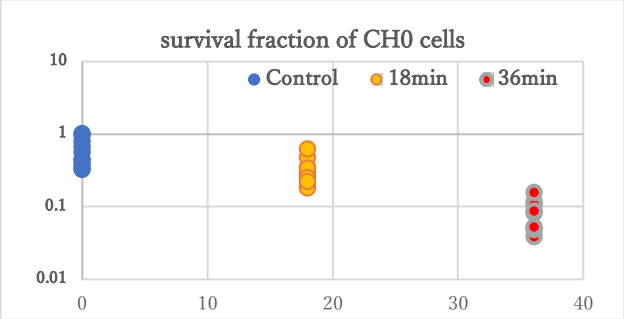

Figure 2. Survival Fraction of CHO, pretreated with 40 μg/ml ^{10}B 2hrs before irradiation. Y axis showing irradiation time of KUR.

RESULTS: The CR-39 samples inserted in the same tube, were etched in a 6N NaOH solution at 60 °C for 60min, images of the pits were acquired with an optical microscope (Figure 3).

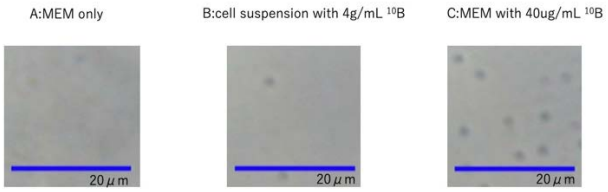

Figure 3. Blue bars are 20 μm; A: no pits observed in culture medium only, no boron; B: approximately 1-2 pits observed in 20 μmx20 μm in CR-39 irradiated with cells; C: approximately 10 pits observed in culture medium only sample with 40 μg/mL of boron.

We can now relate the correlation between boron concentration, beam direction, and viability in colony formation tests with cell suspensions when the liquid surface is in contact with CD-39 with respect to alpha autoradiography. We plan to verify this.

REFERENCES:
[1] I. Postuma *et al.*, Appl Radiat Isot., **167** (2021) 109353.
[2] H. Tanaka *et al.*, J Radiat Res., **55** (2014) 373-380.

CO7-21 L-Phenylalanine Deficiency in Human Tumor Cells Improves BNCT Therapeutic Efficiency

Y. Tamari[1, 2], R. Saba[1], T. Takata[2], M. Suzuki[2], K. Yamada[1] and H. Yamazaki[1]

[1]Department of Radiology, Kyoto Prefectural University of Medicine
[2]Institute for Integrated Radiation and Nuclear Science, Kyoto University

INTRODUCTION: Boron neutron capture therapy (BNCT) is a type of radiotherapy that utilizes the nuclear reaction between ^{10}B and neutrons, and is an excellent method of selectively destroying cancer cells. In Japan, BNCT is now covered by insurance for head and neck tumors, but one problem is the insufficient concentration of 10B, and the tumor tissue/ normal tissue (T/N) ratio of 10B concentration is often small in some patients. L-Boronophenylalanine (L-BPA), used as a boron drug, is a boronated isotope of phenylalanine and is taken up through increased amino acid metabolism in tumors. L-type amino acid transporter 1 (LAT1) is known to be the uptake pathway for L-BPA. LAT1 is an exchange transporter that releases one molecule of amino acid to the extracellular space for uptake of one molecule of amino acid into the cell [1]. Although LAT1 expression in normal cells is rather limited, with only a small amount of expression at the blood-brain barrier and placental barrier, L- BPA can be taken up by normal cells via LAT2 and other pathways, which is a major problem when BNCT is performed [2, 3]. In this study, we attempted to improve the therapeutic effect of BNCT by restricting phenylalanine and improving L-BPA uptake.

EXPERIMENTS: The cell lines used were the human tongue cancer-derived cell line SAS, the human glioblastoma-derived cell line U87MG, and the human pancreatic cancer-derived cell line Panc-1. Phenylalanine-free medium was used for phenylalanine restriction, and dialyzed fetal bovine serum was used. Intracellular boron concentration was determined for each cell line using inductively coupled plasma atomic emission spectrometry (ICP-AES). In addition, the viability of each cell line was determined by the colony formation method after neutron irradiation in a research reactor at the Institute for Integrated Radiation and Nuclear Science, Kyoto University.

RESULTS: The results of the study on L-BPA uptake by phenylalanine restriction showed that the change in uptake efficiency was greatest in SAS, with an over 4-fold increase in L-BPA uptake in the group cultured on L-Phe-free medium compared to the group cultured on normal medium. U87MG and Panc-1 also showed a significant increase in BPA uptake under phenylalanine restriction compared to the group cultured in normal medium. This increase in L-BPA uptake due to phenylalanine restriction was greatest at 24 hours after phenylalanine restriction, and was greatest when the phenylalanine concentration in the medium of SAS/Panc-1 and U87MG was 0 μM and 2 μM, respectively. The survival of cells after neutron irradiation was investigated. In all cell lines, the survival rate of the neutron-irradiated group treated with L- BPA without phenylalanine restriction was significantly lower than that of the neutron-irradiated group treated with neutrons alone. In addition, the survival rate of the L-BPA-neutron irradiated group under phenylalanine-restricted conditions was greatly reduced compared to the L-BPA-neutron irradiated group without phenylalanine restriction.

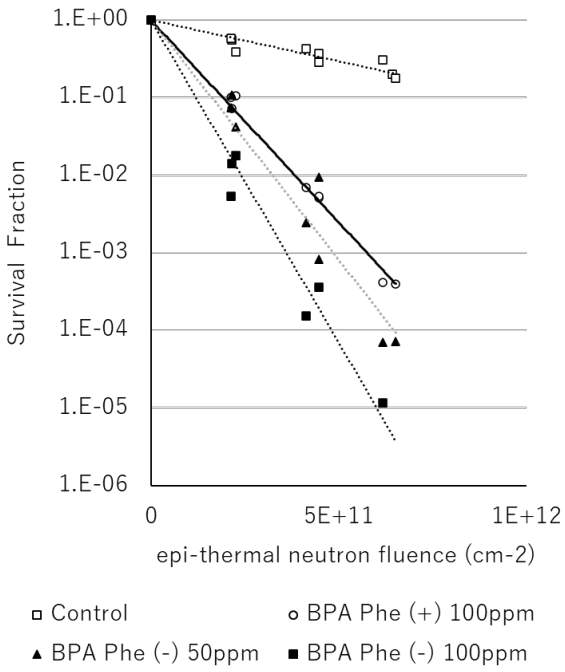

Figure 1. Effect of BNCT on phenylalanine deficiency in human tongue cancer-derived cell line SAS.

This study shows that phenylalanine restriction may improve the efficiency of L-BPA uptake in cancer cell lines and increase the therapeutic efficacy of BNCT. We will continue to investigate the improvement of therapeutic efficacy of BNCT by phenylalanine restriction in tumor-bearing mice.

REFERENCES:

[1] A. Wittig *et al.*, Radiat. Res., **153** (2000)173-180.
[2] T. Watanabe *et al.,* BMC Cancer, **16** (2016) 859.
[3] P. Wongthai *et al.,* Cancer Sci., **106** (2015) 279-286.

CO7-22 Mechanism of Glioma Resistance After BNCT Conferred by Glioma Niche

N. Kondo[1], E. Hirata[2], Y. Sakurai[1], T. Takata[1], T. Kinouchi[1] and M. Suzuki[1]

[1] Institute for Integrated Radiation and Nuclear Science, Kyoto University (KURNS)
[2]Division of Tumor Cell Biology and Bioimaging Cancer Research Institute of Kanazawa University

INTRODUCTION: Boron Neutron Capture Therapy (BNCT) have been applied to recurrent malignant glioma and even after standard therapy (surgery, chemo-radiation therapy) because of the selective damage to the tumor. Especially, glioblastoma (GBM) is the most miserable cancer, whose patient survival is 14.6 months and remarkably resistant to chemo-radiation and immunotherapy. With BNCT, we achieved better local control and survival benefit in malignant glioma using thermal neutrons produced by the reactor in Kyoto University. However, the recurrence is inevitable after BNCT. Reasons for recurrence after BNCT have not been fully elucidated.

We reported glioma stem cells which are known to be resistant to chemo-radiation therapy, take up a boron compound, *p*-boronophenylalanine (BPA) and can be targeted by BPA-BNCT [1]. Even if glioma stem cells are killed by BNCT, the glioma niche (microenvironment) cells may help recurrence of the tumor. In this study, we investigated whether the glioma niche influences the survival of glioma cells after BNCT.

EXPERIMENTS:

Cell culture: We used murine glioma cell line G261 and astrocytes which was established from a brain of baby mouse. Both cells were cultured in Dulbecco's Modified Eagle Medium（DMEM） containing 10% fetal bovine serum at 37 °C in CO_2 incubator.

Boronophenylalanine (BPA) Treatment and Thermal Neutron Irradiation: We treated G261 cells with medium containing BPA at the concentration of 20 ppm for 30 minutes. The BPA was formulated and its concentration was measured as previously described [2]. After we trypsinized and rinsed the cells, cells were collected in plastic tubes and irradiated with thermal neutron for 20 minutes.

Co-culture system: After thermal neutron irradiation, $10^{4\sim}7.5x10^4$ GL261 cells per well were disseminated into the bottom dish of 6 well plates. And $10^{4\sim}1.5x10^5$ astrocytes per well were disseminated into the insert (pore size, 0.4 μm), and co-cultured with GL261cells in 6 well plates. Three and eleven days after co-culture, GL261 cell numbers were counted and compared with mono-culture of GL261 cells.

RESULTS: On day 3, the cell numbers of BNCT mono-culture groups were smaller than those of non-irradiated mono-culture. There was no significant difference between mono and co-cultures both in non-irradiated group and BNCT group. On day 11, the cell numbers of co-culture were higher than mono-culture in non-irradiated group. In BNCT groups, there were no significant change between mono-culture and co-culture.

We are continuing these experiments and collecting cell samples and soluble factors in medium.

****

REFERENCES:

[1] N. Kondo *et al.,* Cancers, **12** (2020) 3040. (doi) 10.3390/cancers12103040.
[2] N. Kondo *et al.* Radiat. Environ. Biophys., **55** (2016) 89-94.

CO7-23 Antitumor effect of boron neurton capture therapy in vulvar cancer mouse model.

S. Terada[1], S. Tsunetoh[1], A. Toji[1], S Miyamoto[1], T. Tanaka[1], M. Ohmichi[1], J. Arima[2], K. Taniguchi[2], M. Suzuki[3]

[1]*Department of Obstetrics and Gynecology, Osaka Medical and Pharmaceutical University, Takatsuki, Japan*

[2]*Department of general and gastroenterological surgery, Osaka Medical and Pharmaceutical University, Takatsuki, Japan*

[3]*Institute for Integrated Radiation and Nuclear Science, Kyoto University, Asasiro-Nishi, Kumatori-cho, Japan*

INTRODUCTION:

Vulvar cancer is an uncommon cancer in gynecologic cancer worldwide. Squamous cell carcinoma (SCC) is the most common histologic type. The primary treatment for vulvar cancer is surgical or radiation therapy. However, the recurrences involving local and inguinal node is not uncommon. [1] Therefore, the new treatment for the vulva cancer is needed. In this study we investigated the effectiveness and safety of boron neutron capture therapy (BNCT) for vulvar cancer using mouse model.

EXPERIMENTS:

Stella Chemifa (Osaka, Japan) supplied BPA (L-isomer), which was converted into a fructose complex. Female 4–6-week-old athymic nude mice (BALB/c Slc-nu/nu) were purchased from Japan SLC. 5×10^6 A431 cells (Vulvar squamous cell line) were injected subcutaneously around the genital area of each mouse. Treatment was initiated 4-6-weeks after injection of A431 cells. The mice were divided into the hot control (neutron irradiation only) and BNCT (neutron irradiation after peritoneal BPA administration) groups. BPA (250 mg/kg) was injected intraperitoneally into mice 2.5hr before neutron irradiation in the BNCT group. After irradiation, the tumor size and the mice weight was measured, and the tumor volume was calculated as follows.

V=ab2/2

RESULTS: Fig.1 shows that the tumor volume in the hot control and BNCT groups. The tumor was suppressed in the BNCT group than in the hot control group ($P<0.05$). No adverse effects were observed in hot control and BNCT groups after irradiation. The body weight was no remarkable change in the both group,

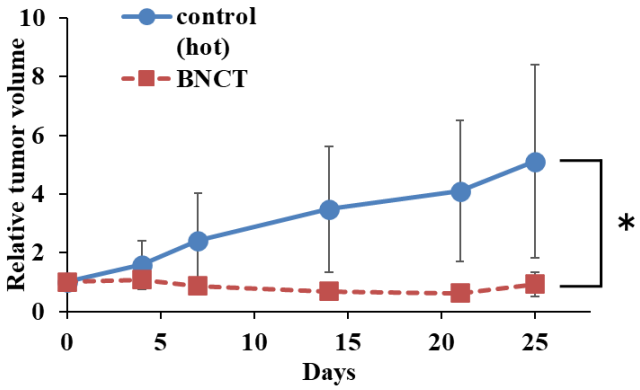

Fig.1. Antitumor effect on subcutaneous A431 tumor model.

Tumor grows curves in the hot control (irradiation only) and BNCT (irradiation after BPA administration) groups (n=7). The results are expressed as means±SD. (*P< 0.05).

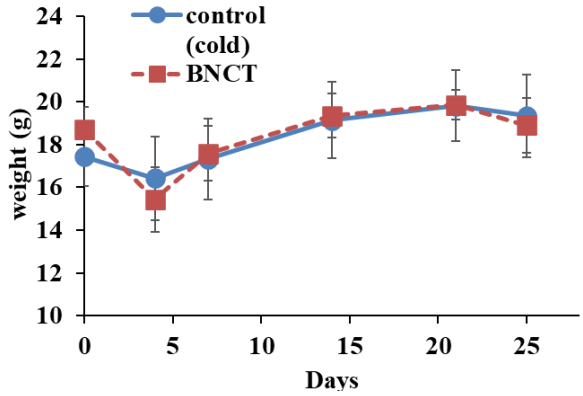

Fig.2. Body weight.

Body weight in the hot control (irradiation only) and BNCT (irradiation after BPA administration) groups(n=7).

REFERENCES:

[1] T. Maggino *et al*., Gynecol oncol., **89** (2000) 116-122.

CO7-24 Anti-tumor effect of boron neutron capture therapy in pelvic human colorectal cancer in a mouse model

J. Arima, K. Taniguchi[1], M. Yamamoto, T. Watanabe[3], Y. Suzuki, H. Hamamoto, Y. Inomata; H. Kashiwagi[2], S. Kawabata[2], K. Tanaka, K. Uchiyama, M. Suzuki[3] and S-W. Lee

Department of general and gastroenterological surgery, osaka medical and pharmaceutical university, 2-7 daigaku-machi, takatsuki, osaka 569-8686, japan

[1]Translational research program, osaka medical and pharmaceutical university, 2-7 daigaku-machi, takatsuki, osaka 569-8686, japan

[2]Department of neurosurgery, osaka medical and pharmaceutical university, 2-7 daigaku-machi, takatsuki, osaka 569-8686, japan

[3]Department of particle radiation oncology, institute for integrated radiation and nuclear science, kyoto university, 2 asashiro- nishi, kumatori-cho, sennan-gun, osaka 590-0494, japan.

INTRODUCTION:

Colorectal cancer is the most common cancer worldwide. Surgical resection is the mainstay treatment of colorectal cancer. However, local recurrence still occurs in 5% to 13% of patients after curative resection. When the tumor is unresectable, it needs alternative therapeutic strategy.
In this study, we investigated the effectiveness of boron neutron capture therapy (BNCT) to pelvic colorectal cancer using the mouse model of pelvic recurrence of colorectal cancer. [1]

EXPERIMENTS:

^{10}B-enriched BPA was provided by Stella Pharma Corporation (Osaka, Japan). An aqueous solution of the BPA D-fructose complex (250 mg/ml, 21.28 mg ^{10}B/ml) was prepared for use in the experiments. Seven-week-old female BALB/c nude mice were purchased from Japan SLC, Inc (Hamamatsu, Japan). DLD-1 cells (1.0×10^6/100 µL in 0.1 ml PBS) were injected into the pelvic retroperitoneum of each mouse, and the mice were divided into the cold control (no treatment, no neutron irradiation), hot control (neutron irradiation only), and BNCT (intraperitoneal BPA administration and neutron irradiation) groups. Irradiation was performed 7 days after the injection of DLD-1 cells. BPA was injected intraperitoneally at a dose of 250 mg/kg 4 h before irradiation.

RESULTS:

Kaplan-Meier analysis showed that survival was significantly prolonged in the BNCT group compared with that in the cold and hot control groups (vs. cold control group, P<0.0001; vs. hot control group, P<0.05). (Fig.1) Moreover, survival was significantly prolonged in the hot control group compared with that in the cold control group (P<0.05). In the BNCT group, there was no evidence of diarrhea, intestinal hemorrhage, or intestinal perforation after irradiation. Remarkable weight loss was observed in the cold and hot control groups (Fig.2).

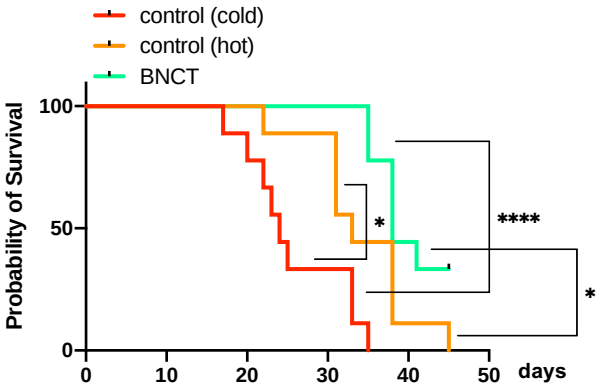

Fig.1. Kaplan-Meier plots showing the rate of survival in the cold control (red line), hot control (orange line), and BNCT (green line) groups (n=9). Survival duration was analyzed for significance using log-rank survival analysis (****P<0.0001, *P<0.05).

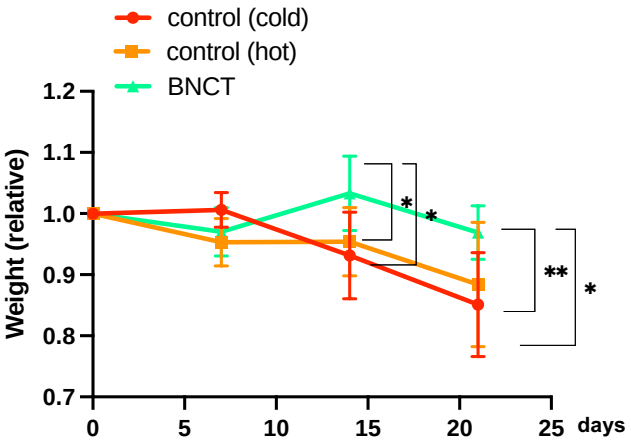

Fig.2. Body weight in the cold control (red line), hot control (orange line), and BNCT (green line) groups. Data is shown as the mean ± SEM. (**P<0.01, *P<0.05)

[1] M. Yamamoto *et al.*, Sci. Rep., **9** (2019) 19630.

CO7-25 Research and Development of New Technology for Boron Neutron Capture Therapy

M. Xu[1], T. Watanabe[3], X. Zhou[1], R. Ohgaki[1,2], C. Jin[1], H. Okanishi[1], H. Tanaka[3], M. Suzuki[3], and Y. Kanai[1,2]

[1]Department of Bio-system Pharmacology, Graduate School of Medicine, Osaka University
[3]Integrated Frontier Research for Medical Science Division, Institute for Open and Transdisciplinary Research Initiatives (OTRI), Osaka University
[3]Institute for Integrated Radiation and Nuclear Science, Kyoto University

INTRODUCTION: Boron Neutron Capture Therapy (BNCT) relies on accumulating boron-containing compounds within cancer cells, followed by irradiation with a neutron beam. To optimize the subsequent nuclear reaction between ^{10}B and thermal neutrons in cancer cells, ensuring the high accumulation of boron-containing compounds within cancer cells is crucial. One of the most widely used boron carriers for BNCT is L-*p*-boronophenylalanine (L-BPA), which is taken up by tumor cells due to their elevated amino acid transports [1]. However, a challenge in applying L-BPA for BNCT is the rapid decrease in intracellular L-BPA levels due to the release of L-BPA from cancer cells through specific transporters. This study aims to experimentally validate an approach to enhance the cytotoxic effects of neutron irradiation on cancer cells by inhibiting the transporters responsible for L-BPA efflux. Using cultured cells and tumor-bearing mice as model systems, we investigated the potential of this approach to improve the efficiency of BNCT with L-BPA.

EXPERIMENTS: For the cell irradiation experiment, the human-derived tumor cell line MCF-7 was treated with L-BPA by adding it to the culture medium. Following a washing step, cells were incubated for 60 minutes in a medium with or without inhibitors targeting transporters responsible for L-BPA release. Subsequently, cells were harvested in Hanks' Balanced Salt Solution (HBSS) and transferred to 1.5 mL tubes, serving as neutron irradiation samples. A control sample was prepared by irradiating cells without L-BPA loading. Post-neutron irradiation, the cell numbers were adjusted, and cells were seeded in 10 cm dishes. Viable cells were then collected and assessed for colony formation to measure cell survival.

For *in vivo* mouse irradiation experiment, the mouse-derived tumor cell lines 4T1 and CT26 were subcutaneously implanted into Balb/c mice to establish syngeneic tumor models. Mice were administered 8 mg of L-BPA (equivalent to 400 mg/kg) via tail vein injection, followed by the administration of transporter inhibitor responsible for L-BPA release at 1 hour and 1.5 hours post-L-BPA injection. As a control, neutron-irradiated mice were prepared without L-BPA loading but received the inhibitor treatment alone. Neutron irradiation was conducted at 5 MW for 15 minutes. The therapeutic effects on tumor regression were compared between the experimental and control groups following neutron irradiation.

RESULTS: In cell irradiation experiments, MCF-7 cells were treated with L-BPA, and after washing, the cells were divided into two groups: Group 1 was incubated for 60 minutes in a cell culture medium (RPMI1640) containing an inhibitor of the transporter responsible for L-BPA release. Group 2 was incubated for 60 minutes in a culture medium without the inhibitor. Additionally, Group 3 consisted of cells without L-BPA treatment was prepared. All groups were then subjected to neutron irradiation. After irradiation, the number of viable cells was compared by assessing colony formation in low-density cultures. The results showed no significant difference in cell survival between Group 2 and Group 3 (non-BNCT), suggesting that the intracellular L-BPA content had decreased to a level undetectable for BNCT effects within 60 minutes following L-BPA treatment. In contrast, the cell survival rate in Group 1 was significantly less than that in Group 2, indicating a significant enhancement of BNCT efficacy by inhibiting the transporter responsible for L-BPA release.

In *in vivo* mouse irradiation experiment, mouse triple-negative breast cancer-derived 4T1 cells and mouse colon cancer-derived CT26 cells were implanted into the hind limbs of mice to form allograft tumors. Mice were then administered L-BPA intravenously and divided into two groups. Group 1 received an intravenous injection of a transporter inhibitor responsible for L-BPA release 1 hour and 1.5 hours after L-BPA administration. Group 2 did not receive any inhibitor treatment following L-BPA administration. Additionally, Group 3 was prepared by administering saline instead of L-BPA, followed by injections of the transporter inhibitor at 1 hour and 1.5 hours post-saline administration. For each group, mice were anesthetized 2.5 hours after L-BPA or saline administration and subjected to neutron irradiation. Tumors were excised two weeks after irradiation, and their sizes were measured. The results indicated that, for both 4T1 and CT26 tumors, there was no significant difference between Group 2 and Group 3 (non-BNCT), suggesting that tumor L-BPA levels had decreased to an extent undetectable for BNCT effects within 2.5 hours post-administration. In contrast, tumor sizes in Group 1 were significantly smaller for both 4T1 and CT26 than Group 2, demonstrating that inhibiting the transporter responsible for L-BPA release significantly enhanced BNCT efficacy.

The results obtained in this study provide us with clues for optimizing L-BPA-based BNCT.

REFERENCES:

[1] P. Wongthai *et al.*, Cancer Sci., **106** (2015) 279-286.

CO7-26 Observation of Intracellular Boron Neutron Capture Reaction with a Novel Boron Compound

R. Nozaki,[1] Y. Takamura,[1] K. Igawa,[2] N. Kondo,[3] Y. Sakurai,[3] and H. Kakuta[1]

[1] *Division of Pharmaceutical Sciences, Okayama University Graduate School of Medicine, Dentistry and Pharmaceutical Sciences.*

[2] *Neutron Therapy Research Center, Okayama University.*

[3] *Institute for Integrated Radiation and Nuclear Science, Kyoto University.*

INTRODUCTION: A cancer treatment known as "boron neutron capture therapy (BNCT)" is based on the nuclear interaction between the element boron-10 (^{10}B) and neutrons. Since the effectiveness of this treatment depends on the collision of ^{10}B with neutrons, the amount of boron present in the tumor tissue is essential. The blood boron level for borofaran (1), the only treatment currently approved for BNCT, is used to assess the amount of boron in cancer tissue. There are no boron agents available that can quantify boron concentrations in cancer tissue. Thus, we aimed to create a BNCT drug that could identify boron levels in malignant tissue.

We focused on iodine contrast agents for X-ray CT because they can detect iodine concentrations noninvasively by X-ray CT and are given in similar large doses to BNCT agents. This idea led us to propose that boron content in tissues may be determined using this concept. We created and synthesized BS-DIP-OEF (2) (Figure 1A) to test the aforementioned concept. We then used this compound to evaluated intra-cellular concentration and a colony assay utilizing B16BL6 after neutron irradiation with the drug.

EXPERIMENTS: (Boron concentration in compound-treated cells) Compound **2** was synthesized by our group. The boron concentration in boron compound-treated cells was measured using ICP-MS in mouse melanoma B16/BL6 cells. B16/BL6 cells were seeded at 6×10^5 cells/2 mL in 60 mm petri dishes. BSH is treated at 2 mM in many references. However, this concentration is extremely high and requires large amounts of the compound. Therefore, we set an upper limit of 500 μM for the exposure concentration of **2**. In addition, borofaran exposure time is less than 3 hours in actual clinical practice. Based on the above, the compound exposure time was set to 2 hours. After compound exposure, cells were washed with PBS, collected with a scraper, and counted for live and dead cells using trypan blue. All cells were then lysed using RIPA buffer, and the boron (10B) concentration in the resulting samples was measured by ICP-MS (Agilent 7900/MassHunter).

(Neutron irradiation experiment) B16/BL6 cells prepared as in the previous section were exposed to **2** at a final concentration of 500 μM for 2 hours. The medium was aspirated off, and after trypsin treatment, 1 mL of cell suspension was prepared in 1.5 mL Eppendorf tubes to a concentration of 5.0×10^3 cells/mL. The samples were irradiated with neutrons at 5 MW for 1 hour at a thermal neutron fluence of 1.2×10^{12} cm^{-2}. After that, cells were seeded at 250 cells/well on 12 well plates and cultured for 7 days, cells were fixed and stained with crystal violet, and the number of colonies was counted. The number of colonies obtained was divided by the number of seeded cells to obtain the colony formation ratio.

RESULTS: Figure 1B shows the data obtained by the above experiment. Compound **2** was found to give an intracellular boron concentration of 1.02 μg ^{10}B/10^7 cells. This is higher than the boron concentration obtained for B16 cells exposed to 2 mM BSH for 24 h (0.75 μg ^{10}B/10^7 cells).[1] Since the cell proliferation inhibition of neutron irradiation has been expected, we applied neutron irradiation toward **2**-treated at a final concentration of 500 μM for 2 hours and performed a colony assay. As a result, a clear inhibition of cell proliferation was observed (Figure 2B).

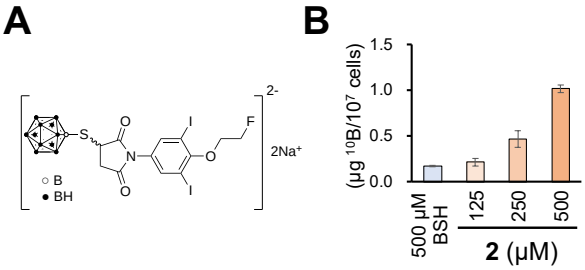

Figure 1. (A) Chemical structure of **2**. (B) Intracellular boron concentration measured by ICP-MS at the indicated concentration after 2 hr exposure. Mean ± SD (n = 3).

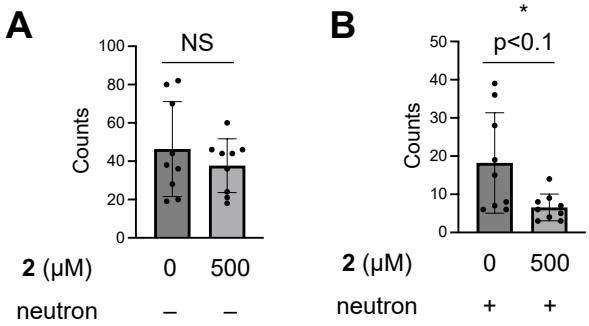

Figure 2. (A) Comparison of colony counts after com-pound treatment without neutron irradiation. (B) Com-parison of colony counts after neutron irradiation.

DISCUSSIONS AND FUTURE PLAN:
Neutron irradiation toward B16/BL6 cells treated with **2** at 500 μM for 2 hours inhibited the colony formation. Though BNCT of **2** in cancer model mice was planned (R4136), it has not yet been performed. Future in vivo studies are expected to be conducted to elucidate the compound potentials.

REFERENCE:
[1] Y. Hattori *et al.,* J. Med. Chem., **55** (2012) 6980-6984.

R4132

CO7-27 Observation of Tumor Tissue Destruction with Boron Neutron Capture Reaction

R. Nozaki,[1] Y. Takamura,[1] K. Igawa,[2] T. Sasaki,[2]
N. Kondo,[4] Y. Sakurai,[4] and H. Kakuta[1]

[1] Division of Pharmaceutical Sciences, Okayama University Graduate School of Medicine, Dentistry and Pharmaceutical Sciences.

[2] Neutron Therapy Research Center, Okayama University.

[3] Institute for Integrated Radiation and Nuclear Science, Kyoto University.

INTRODUCTION: CR-39 is known as a plastic material that can visualize and quantify the boron neutron capture reaction (BNCR) (Ref.1). Alpha rays generated by BNCR on CR-39 form small holes called "etch-pits". These are enlarged by alkali treatment. In this study, we attempted to visualize the BNCR in boron compound-treated cells and tumor tissue sections. In this experiment, BSH (1) and our boron compound **2** were used as boron agents. Compound **2** is an iodine-containing compound that can be used for X-ray CT contrast and was created to directly measure the boron concentration in cancer tissue. Exposure of mouse melanoma cells B16BL6 to 2 at 500 μM for 2 hours has been found to give a boron concentration of 1.0 μg $^{10}B/10^7$ cells.

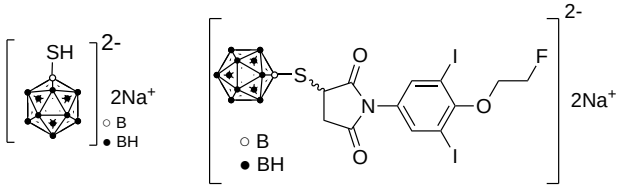

1 **2**

Figure 1. Chemical structures of **1** and **2**.

EXPERIMENTS: BNCR detection was performed by seeding cells on CR-39 as follows: cells were cultured in 35 mm petri dishes submerged in 2 cm squares of CR-39, replaced with medium containing the test compound, and exposed to the medium for 2 hours. The CR-39 cells were irradiated with neutrons. Neutron irradiation was performed at KUR at 5 MW for 1 hour (a thermal neutron fluence of 2×10^{12} cm^{-2}). The CR-39 was stirred in an alkaline solution (15 wt% KOH, 40 wt% MilliQ, 45% wt% ethanol) at 50°C for 16 min to widen the etch pit and make it quantifiable. Five fields of view of the treated CR-39 were arbitrarily imaged using a microscope, and the resulting images were analyzed using imageJ.

RESULTS: Figure 2A shows a representative example of the obtained image and 2B shows the number of etch pits analyzed using image J. As a result, **2** shows a significantly higher number of etch pits than **1**. This relationship corresponds to the intracellular boron concentration. Therefore, **2** was found to generate BNCR in the cell by neutron irradiation.

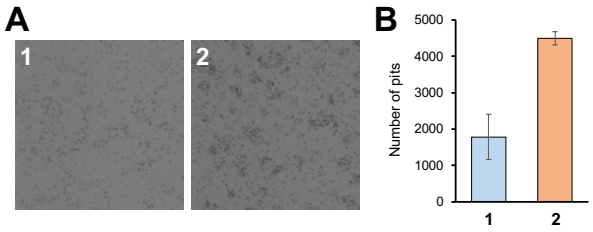

Figure 2. (A) CR-39 images after alkali treatment and (B) comparison of the number of etch pits counted using Image J.

DISCUSSIONS AND FUTURE PLAN: Compound **2**, which was found to migrate into B16BL6 cells, showed more pronounced BNCR on CR-39 as etch pits than **1**, which was less cell-migrating. The number of etch pits was also successfully quantified by imageJ. We had planned to perform the same experiment with sections of tumor-bearing mice, but we could not prepare the experimental data in time and had to give up the experiment this time. In the future, we hope to observe BNCR on CR-39 using tumor sections of tumor-bearing mice treated with **2**.

REFERENCES:

[1] T. Kusumoto *et al.,* Radiat. Res., **191** (2019) 460-465.

CO7-28 Study on Intracellular Protein Destruction by Boron Neutron Capture Reaction

Y. Takamura,[1] R. Nozaki,[1] K. Igawa,[2] M. Fujihara,[1] N. Kondo,[3] Y. Sakurai[3] and H. Kakuta[1]

[1] Division of Pharmaceutical Sciences, Okayama University Graduate School of Medicine, Dentistry and Pharmaceutical Sciences.

[2] Neutron Therapy Research Center, Okayama University.

[3] Institute for Integrated Radiation and Nuclear Science, Kyoto University.

INTRODUCTION: Boron neutron capture therapy (BNCT) is a cancer treatment based on the nuclear reaction between boron-10 (^{10}B) and neutron. The high-energy par-ticle beam after neutron capture by ^{10}B is reported to break the double-stranded DNA of cancer cells and induce apop-tosis. However, the effect of the particle beam on intracel-lular organelles has not been investigated in detail. In this study, we investigate whether protein cleavage based on neutron irradiation occurs using the retinoid X receptor (RXR), one of nuclear receptors, and a boron-containing RXR ligand.

EXPERIMENTS: The compounds shown in Figure 1A and bexarotene were synthesized by the authors. The RXR ligand binding domain (RXR-LBD) was kindly gifted by Prof. Nakano, University of Shizuoka. RXR-LBD binding assay and reporter gene assay were performed according to references 1 and 2. Neutron beam was irradiated at 1 MW for 60–240 minutes. The irradiated sample (100 µL) was prepared as below; RXR-LBD (10 µM), CBTF-EE-BODIPY (200 µM, converted to ^{10}B concentration 0.1 ppm) or CBTF-EE-BSH (200, 100, 50 µM, converted to ^{10}B concentration 24, 12, 6 ppm), bexarotene (20 µM or not), buffer (10 mM HEPES, 150 mM NaCl, 2 mM $MgCl_2$, 5 mM DTT, 5% DMSO). The irradiated sample was di-luted 10 times with above buffer and mixed with BPB-con-taining buffer in a 4:1 composition, and electrophoresed at 250 V, 20 mA for 70 minutes. The concentration of RXR-LBD was estimated using CBB staining.

RESULTS: We have reported CBTF-EE (**1a**, Figure 1) as an RXR antagonist.[1] Also, it has been confirmed that CBTF-EE-BODIPY (**1b**, Figure 1), which was designed by inducing a fluorescent group at the end of the alkoxy chain of **1a**, functions as an RXR antagonist.[2] Compound **1b** has been confirmed to bind to RXR-ligand binding domain (RXR-LBD). In addition, the fluorescence group of **1b** contains a boron atom. Thus, we have interested in RXR-LBD destruction using **1b**. When neutron beam was irradiated to 200 µM of **1b** (0.1 ppm as ^{10}B) and RXR-LBD, the destruction could not be confirmed (Figure 2A). From the point of which BNCT requires 20 ppm of ^{10}B in the tumor issue, we determined that the ^{10}B concentration was insufficient in **1b**. Thus, we designed and synthesized CBTF-EE-BSH (**1c**, Figure 1), which has ^{10}B cluster molecule BSH, and evaluated whether **1c** will function as an RXR ligand. As a result of RXR-LBD binding assessment, it has been revealed that a *K*i value of **1c** was 3.31 µM (Figure 2B). In addition, a reporter assay using COS-1 cells revealed that **1c** inhibits the transcriptional activity of RXR agonist bexarotene in a dose-dependent manner and functions as a non-competitive RXR antagonist (Figure 2C). Then, neutron irradiation was performed on each solution in which **1c** and RXR-LBD coexisted, and in which bexarotene, which is an RXR agonist and inhibits the binding of **1c** to RXR-LBD, was further added. After irradiation, the amount of RXR-LBD was estimated by SDS-PAGE. However, 240 minutes of irradiation at 1 MW did not show the destruction of RXR-LBD (Figure 2D). On the other hand, we next interested in the use of **1c** as a ^{10}B-carrier for BNCT, so that the ^{10}B introduction ability of **1c** have being evaluated.

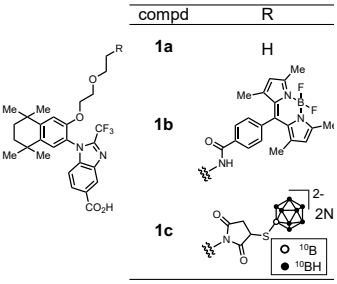

Figure 1. Chemical structures of **1a**–**1c**.

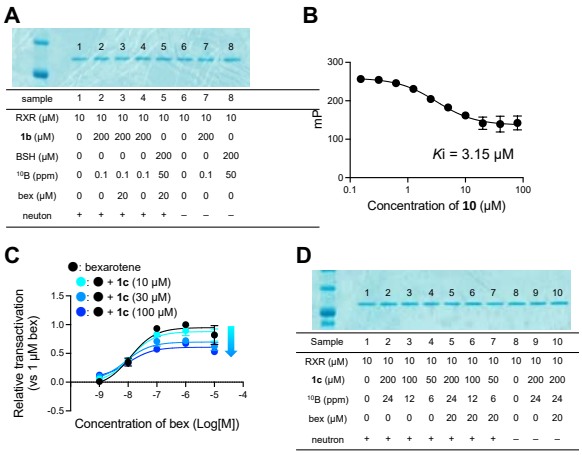

Figure 2. (A) SDS-PAGE of **1b**. (B) Binding ability and (C) antagonistic activity of **1c**. (D) SDS-PAGE of **1c**.

DISCUSSIONS AND FUTURE PLAN: The neutron irradiation to the combination of **1b** or **1c** and RXR-LBD could not induce RXR-LBD degradation. On the other hand, the intracellular introduction and its non-competi-tive antagonistic activity of **1c** has been confirmed. These results These results suggest the potential use of 1c as an intracellular ^{10}B-carrier. In recent years, various fields have been challenging to produce boron delivery agents which could replace L-boronophenylalanine (BPA). Given that the BNCT targets tumor DNA cleavage, it is of interest to use nuclear receptor ligands as boron delivery agents. The results of this research may provide useful knowledge for the development of 10B-carriers for BNCT, which bind to the nuclear receptors.

REFERENCES:

[1] M. Watanabe *et.al.,* J. Med. Chem., **64** (2021) 430-439.

[2] M. Takioku, ACS Med. Chem. Lett.,**12** (2021) 1024-1029.

CO7-29 Attempts to sensitize tumor cells by exploiting the tumor microenvironment

Y. Sanada, T. Takata, Y. Sakurai, H. Tanaka and T. Watanabe

Institute for Integrated Radiation and Nuclear Science, Kyoto University

INTRODUCTION: In the boron neutron capture therapy with BPA, SLC7A5 (LAT1) protein expression level of tumor cells is an important factor for the anti-tumor efficacy, since LAT1 is a major transporter for intracellular uptake of BPA. We previously examined the SLC7A5 expression profiles of murine squamous cell carcinoma (SCC VII) cells, and reported that its expression can be affected by hypoxia and the changes in SLC7A5 levels is likely linked to the function of Hif-1α [1]. In the present study, we examined whether the presence of SLC7A5 affected cellular survival after BNCT, using SCC VII SLC7A5-knockout cells.

EXPERIMENTS: We previously established SCC VII cells expressing SLC7A5-6xHis proteins, SCC VII-SH cells. In the present study, SLC7A5 knockout cells (SCC VII-SH-ΔSLC7A5 cells) were generated using CRISPR-Cas9 system.
In order to examine the sensitivity to BPA-BNCT and gamma-ray, these cells were exposed to neutron beams (KUR Heavy Water Facility) and gamma-ray (Co-60 Gamma-ray Irradiation Facility), respectively, and then clonogenic cell survival assays were performed.

RESULTS: In the present study, SLC7A5 deficient cells (SCC VII-SH-ΔSLC7A5 cells) were generated, and the phenotype of these cells were examined. Compared with SCC VII-SH cells, the SLC7A5 deficient cells are characterized by a relatively low proliferation rate, as previously described. Similarly, the colonies of SCC VII-SH-ΔSLC7A5 cells were smaller than those of SCC VII-SH cells.
We next examined the sensitivity of SCC VII-SH-ΔSLC7A5 cells to BPA-BNCT. When exposed to neutron-beams after treatment of BPA, SCC VII-SH-ΔSLC7A5 cells exhibited higher survival rate than SCC VII-SH cells.
We should note that the genetic disruption of SLC7A5 protein may differ from its temporal downregulation by hypoxia. For examples, knock out cells often undergo reprogramming during selection, and several pathways can permanently up- or down-regulated.
We also performed gamma-irradiation experiments for SCC VII-SH-ΔSLC7A5 cells. Surprisingly, the disruption of SLC7A5 increased the survival after gamma-ray irradiation.
One possible explanation for these results is that slow growth phenotype of these cells affected the sensitivity to radiation. It is well-known that slowly proliferating cells were radio-resistant, because the delayed cell cycle provides the cells with enough time to repair DNA damages. Therefore, it is now difficult to conclude whether the BNCT-resistance of SCC VII-SH-ΔSLC7A5 cells was caused by lower BPA uptake capacity or lower proliferation rate.

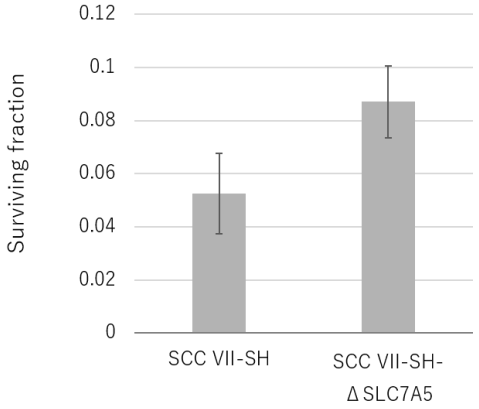

Fig. 1. Cell survival rate for SCC VII-SH or SCC VII-SH-ΔSLC7A5 cells. Cells were exposed to neutron beams (thermal neutrons at a fluence of 2.0×10^{12} n/cm^2) after treatment with BPA (20 ppm).

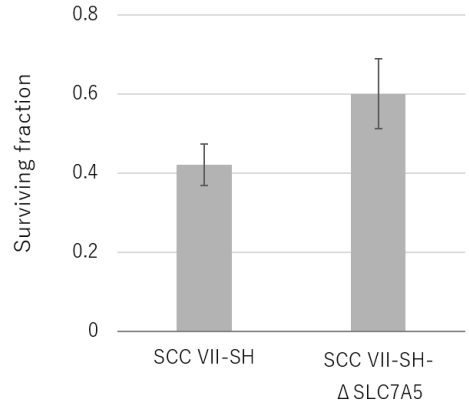

Fig. 2. Cell survival rate for SCC VII-SH or SCC VII-SH-ΔSLC7A5 cells. Cells were exposed to gamma-ray (2.5 Gy).

REFERENCES:

[1] Y. Sanada *et al.,* Int. J. Rad. Biol. **97** (2021) 1441-1449.

CO7-30 Enhancement of Tumour Growth Suppression by Bubble Liposome / Ultrasound Stimulation on Intraveneous Injection of ^{10}BSH entrapped PEG Liposome for Boron-Neutron Capture Therapy to Pancreatic Cancer Model *in vivo*

H. Yanagie[1,2,3], X. Hou4, S. Kageyama[5], K. Maruyama[5], T. Takata[6], T. Watanabe[6], M. Suzuki[6], Y. Sakurai[6], H. Tanaka[6], M. Nashimoto[3], J. Nakajima[2,7], M. Ono[2,8], T. Sugihara[3], and H. Takahashi[1,2,4]

[1] *Institute of Engineering Innovation, School of Engineering, The University of Tokyo,*
[2]*Cooperative Unit of Medicine & Engineering, The University of Tokyo Hos-pital,*
[3]*Niigata University of Pharmacy & Applied Life Sciences,*
[4]*Dept of Bioengineering, School of Engineering, The University of Tokyo,*
[5]*Faculty of Pharma-Science, Teikyo University,*
[6]*Kyoto University Institute for Integrated Radiation & Nuclear Science,*
[7]*Dept. of Pulmo-nary Surgery, The University of Tokyo Hospital,*
[8]*Dept. of Cardiac Surgery, The University of Tokyo Hospital, JA-PAN*

INTRODUCTION:

For achieving effective Boron neutron capture therapy (BNCT), we performed the experiments of boron delivery systems for BNCT using boronododecaborane($^{10}B_{12}H_{11}SH$; ^{10}BSH) [1, 2, 3].

Recently, for effective chemotherapy, drug delivery using a combination of ultrasound and microbubbles has been reported [4]. The interaction of microbubbles and ultrasound increases the local permeability of blood vessels, allowing the injected drug to move easily out of the vessel and increasing the drug concentration in the tissue. The combination of liposomal doxorubicin, microbubbles, and ultrasound has been reported to inhibit growth of tumors [5].

In this study, we evaluated the tumor growth suppression by intraveneous injection of ^{10}BSH-encapsulated PEG liposomes combined with perfluorocarbon microbubbles / Ultrasound external stimulation system to AsPC-1 human pancreatic tumor-bearing mice.

EXPERIMENTS:

Human pancreatic cancer AsPC-1 cell was used for the in vivo anti-tumor effect evaluation. We prepared AsPC-1 ($5x10^5$) model by transplanting to right lower leg. ^{10}BSH-encapsulated PEG liposomes (mean ^{10}B concentration : 4466ppm) and bubble liposomes were injected via the tail vein, and then ultrasound was applied to the tumors. The construction of Bubble liposome is DSPC : DSPG : DSPE-PEG2000-OMe = 30 : 60 : 10. The Ultrasound condition is below ; Machine : Sonitron2000, Intensity : 2 W/cm^2, Frequency : 1MHz. We performed thermal neutron irradiation at Institute for Integrated Radiation and Nuclear Science, Kyoto University (average neutron fluence of 2.0×10^{12} n/cm^2). The change in tumor growth and survival rate of the mice reflected the anti-tumor effect of ^{10}BSH-encapsulated PEG liposomes. While measuring the size of tumor, the weight change was also recorded for evaluation of the toxicity of these samples.

RESULTS:

The experimental results showed that tumor growth suppression in the group treated by ^{10}BSH-encapsulated PEG liposomes combined with perfluorocarbon microbubbles / Ultrasound external stimulation system and NCT was 3 times superior compared with non-irradiated group (only treated with ^{10}BSH PEG Lip / Bubble Lip / Ultrasound). No significant weight loss were observed after treatment suggesting low systemic toxicity of this system.

It is thought that the Bubble Liposome / Ultrasound stimulation is effective to increase the concentration of the compounds into the cytoplasms of cancer cells. We hope to apply these techniques from the surface of the body to the tumour site in the body acutually using in clinical to BNCT for local advanced cancers [6,7].

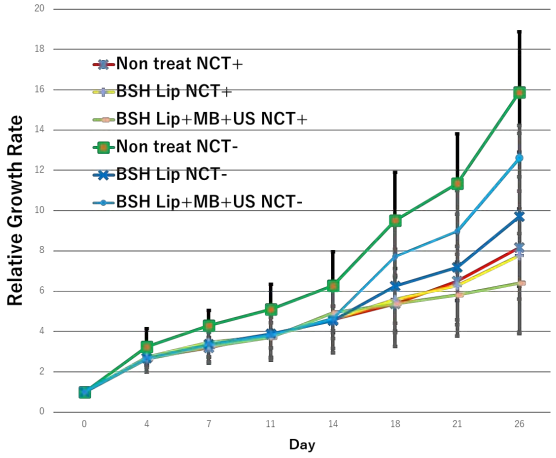

Figure 1. Tumor growth suppression by intraveneous injection of ^{10}BSH entrapped PEG Liposome combined with perfluorocarbon microbubbles / Ultrasound external stimulation system with thermal neutron irradiation on AsPC-1 model *in vivo*

REFERENCES:

[1] H. Yanagie *et al.,* Br J Cancer, **75(5)** (1997) 660-665.
[2] K. Maruyama *et al.,* J Control Release, **98(2)** (2004) 195-207.
[3] H. Yanagie *et al.,* In Vivo, **35(6)** (2021) 3125-3135.
[4] I. Yokoe *et al.,* Drug Deliv., **28(1)** (2021) 530-541.
[5] I. Yokoe *et al.,* Cancers, **12(9)** (2020) 2423.
[6] L. Lambricht *et al.,* Expert Opin Drug Deliv., **13(2)** (2016) 295-310.
[7] B. Trotovšek *et al.,* World J Gastroenterol, **27(48)** (2021) 8216-8226.

CO7-31 The basic research of boron neutron capture therapy for spinal cord gliomas in rat spinal cord glioma models

K.Tsujino[1], S. Kawabata[1], R. Kayama[1], H. Kashiwagi[1], K.Yoshimura[1], Y. Fukuo[1], H. Shiba[1], R. Hiramatsu[1], T. Takata[2], H. Tanaka[2], M. Suzuki[2], S-I, Miyatake[3] , T. Takami[1] and M.Wanibuchi[1]

[1]Department of Neurosurgery, Osaka Medical and Pharmaceutical University

[2]Institute for Integrated Radiation and Nuclear Science, Kyoto University

[3]Kansai BNCT Medical Center, Osaka Medical and Pharmaceutical University

INTRODUCTION: Boron neutron capture therapy (BNCT) is a particle therapy that can be targeted at the cellular level. So far, BNCT has been shown to be effective for intracranical malignant gliomas [1] and high-grade meningiomas [2], which are invasive cancers. Spinal cord gliomas, due to their infrequent occurrence [3-5], have no established treatment and are mostly mimicked by standard treatment for intracranial malignant gliomas. Surgery is limited to removal of the tumor mass, and the presence of numerous nerve travel routes in the spinal cord parenchyma makes it difficult to the treat for spinal cord tumors including the tumor invasion area. As a result, recurrence from residual disease is frequent and the prognosis is poor. There is also a tolerated dose to the spinal cord, which limits radiotherapy to recurrent lesions. In the face of these numerous problems, we focused on BNCT, which can target tumors at the cellular level. In the past, BNCT to the spinal cord has been used to test the safety of BNCT for intracranial malignant gliomas. In the present study, a rat spinal glioma model was used to evaluate the efficacy of BNCT for spinal cord gliomas.

EXPERIMENTS: F98 rat glioma cells were used to create a rat spinal cord glioma model. The F98 rat spinal cord glioma models were implanted 10^4 F98 rat glioma cells in 3μl Dulbecco's Modified Eagle Medium (DMEM) into the spinal cord at thoracic 9/10 level. Intravenous administration (i.v.) of BPA (12 mg B/b.w.) to the F98 rat spinal glioma model was performed to assess in vivo boron distribution. After creating the models, lower limb function was assessed using the Basso, Bresnahan and Beattie (BBB) scale. The rats were euthanized, when the BBB scale was less than or equal to 5, or severe bladder and rectal obstruction was observed. The effectiveness of BNCT for rat spinal cord glioma models was also tested by neutron irradiation experiments with the following experimental design prepared. The control group was prepared as the sham-operated group (implanted 3μL DMEM).

Study 1 for the sham-operated models
1. Sham-untreated group (n=5)
2. Sham-neutron only group (n=4)
3. Sham-BNCT BPA 2.5 h (n=3)

Study 2 for the F98 rat spinal cord tumor models
1. Untreated group (n=8)
2. Neutron only group (n=6)
3. BNCT BPA 2.5 h (n=8)

Study 3 for the normal rats
BNCT BPA 2.5 h (n=3)

RESULTS: The boron concentration in the spinal cord tumor at 2.5 h after i.v. was sufficient for BNCT, and more than 20 μg B/g. The results of the present in vivo neutron irradiation experiment are currently being analysed and cannot be shown, but the BNCT group with BPA significantly prolonged survival compared to the untreated group. The decrease in BBB scale was also significantly reduced compared to the untreated group. BNCT for normal rats did not show an obvious decrease in BBB scale after neutron irradiation. These findings suggest that BNCT for spinal gliomas may have a potential therapeutic effect, including safety. Most importantly, careful consideration is needed in terms of radiation dose in clinical application.

REFERENCES:

[1] S. Kawabata *et al.*, Neurooncol Adv., **3(1)** (2021) vdab067.

[2] S. Kawabata *et al.,* J Neurosurg., **119(4)** (2013) 837-844.

[3] A. Raco *et al.,* Neurosurgery, **56** (2005) 972–981.

[4] Parsa AT *et al.,* Clin Neurosurg., **52** (2005) 76–84.

[5] M. C. Chamberlain *et al.,* Curr Neurol Neurosci Rep., **11** (2011) 320-328.

CO7-32 Boron neutron capture therapy using folate receptor targeted novel boron carrier for F98 rat brain tumor models

K.Tsujino[1], S. Kawabata[1], R. Kayama[1], H. Kashiwagi[1], K.Yoshimura[1], Y. Fukuo[1], H. Shiba[1], R. Hiramatsu[1], T. Takata[2], H. Tanaka[2], M. Suzuki[2], S-I, Miyatake[3], K. Nishimura[4], H. Nakamura[4] and M.Wanibuchi[1]

[1]*Department of Neurosurgery, Osaka Medical and Pharmaceutical University*

[2]*Institute for Integrated Radiation and Nuclear Science, Kyoto University*

[3]*Kansai BNCT Medical Center, Osaka Medical and Pharmaceutical University*

[4]*Laboratory for Chemistry and Life Science, Institute of Innovative Research, Tokyo Institute of Technology*

INTRODUCTION: Boron neutron capture therapy (BNCT) is a particle therapy that can be targeted at the cellular level and is considered an effective treatment for malignant gliomas in which tumor cells have invaded the normal brain parenchyma [1]. Clinical trials of reactor-based BNCT for malignant gliomas have been performed and their efficacy has been reported. BNCT using an accelerator-based neutron generator has also been shown to be effective for the treatment of malignant gliomas [2,3]. Although boronophenylalanine (BPA) is commonly used in BNCT for head and neck cancer, there is an urgent need to develop novel boron carrier to improve therapeutic efficiency of BNCT, and our research group has reported various type novel boron carrier [4,5,6]. We previously reported that Pteroyl-Boron-conjugated 4-iodophenylbutanamide (PBC-IP) is effective in the F98 rat brain tumor models. PBC-IP targeted to the folate receptors which is highly expressed in malignant glioma [7]. Neutron irradiation experiments using PBC-IP administered by Convection enhanced delivery (CED), a local drug delivery system, in the F98 rat brain tumor models showed 50% long-term survival (>90 days) in the irradiation group using PBC-IP only, and even better results when PBC-IP was used in combination with BPA. With these results, we considered PBC-IP to be a promising novel boron carrier and conducted further experimental studies with a view to preclinical trials.

EXPERIMENTS: The boron concentrations in each organ were measured following by PBC-IP CED administration at 1, 3, 6, 12, 24 and 48 h after CED 24 h administration. Neutron irradiation was performed on F98 rat brain tumor models in which PBC-IP was administered by CED, and the therapeutic effect was evaluated by survival time. Neutron irradiation experiments were performed to evaluate the therapeutic effect of different catheter tip positions of the CED in consideration of the nature of the penetrating tissue, and the maintenance of drug effect by BNCT at different time points (3, 6, and 24 h after of CED 24 h administration). In the in vivo neutron irradiation experiment to evaluate the therapeutic effect of different catheter tip positions of CED, four groups were prepared as follows: group 1, untreated; group 2, BNCT PBC-IP CED to the contralateral brain; group 3, BNCT PBC-IP CED to the peritumoral brain; group 4, BNCT PBC-IP CED to the tumor body (Fig. 2.). On the other hand, in the in vivo neutron irradiation experiment to evaluate the maintenance of drug effect by BNCT at different time points, six groups were prepared as follows: group 1, PBS CED; group 2, PBC-IP CED drug only; group 3, NCT PBS CED; group 4, BNCT PBC-IP CED 24 + 3 h; group 5, BNCT PBC-IP CED 24 + 6 h; group 6, BNCT PBC-IP CED 24 + 24 h.

RESULTS: The boron concentrations in each organ shows in Fig.1. The boron concentration in almost all of the organs decreased gradually. The results of neutron irradiation have not yet been finalized and analyzed. However, in the in vivo neutron irradiation experiment to evaluate the therapeutic effect of different catheter tip positions of the CED, long-time survivors were observed in the group of BNCT PBC-IP CED to the tumor body, and BNCT PBC-IP CED to the peritumoral brain. In addition, in the in vivo neutron irradiation experiment to evaluate the maintenance of drug effect by BNCT, significantly difference was observed between the control group and all the BNCT groups through the log-rank test.

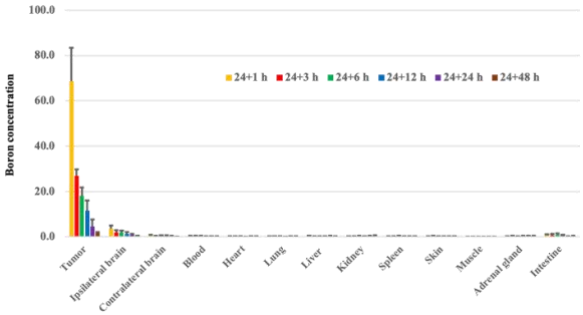

Fig. 1. The boron concentration in each organ was shown at 1, 3, 6, 12, 24 and 48 h after CED 24 h administration.

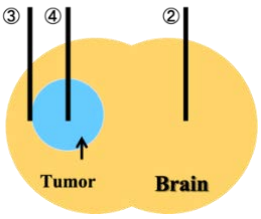

Fig. 2. This figure shows the schema of a different catheter tip positions of CED. ② shows the position of CED at the contralateral brain. ③ shows the position of CED at the peritumoral brain. ④ shows the position of CED at the tumor body.

REFERENCES:

[1] R.F. Barth *et al*., Radiation Oncology, **7** (2012)146.

[2] S. Kawabata *et al*., Neurooncol Adv., **3(1)** (2021) vdab067.

[3] S. Arami *et al.*, Cancer Biother Radiopharm. **38(3)** (2023) 201-207.

[4] T. Kanemitsu *et al.*, Radiat. Environ. Biophys., **58** (2019) 59-67.

[5] H. Kashiwgi *et al.*, Investig. New Drugs, **10** (2022) 255-264.

[6] K. Tsujino *et al.,* Biology., **12** (2023) 377.

[7] F. Nakagawa *et al.,* Cells, **9(7)** (2022) 1615.

CO7-33 Development of a Nanomaterial-based Boron Delivery System for BNCT

G. Choi[1], K. Nishimura[2], J.-H. Choy[1], Y. Sakurai[3], H. Nakamura[2,4], M. Suzuki[3]

[1]Institute of Tissue Regeneration Engineering, Dankook University
[2]*School of Life Science and Technology, Tokyo Institute of Technology*
[3]*Institute for Integrated Radiation and Nuclear Science, Kyoto University*
[4]*Laboratory for Chemistry and Life Science, Institute of Innovative Research, Tokyo Institute of Technology*

INTRODUCTION: Boron Neutron Capture Therapy (BNCT) is attracting attention as a non-invasive radiotherapy in the treatment of cancer. In order to achieve efficient BNCT effect, the boron concentration in tumor tissue needs to be more than 20 μgB/g. Moreover, tumor/normal tissues ratio of boron concentration should be more than three to decrease undesirable side effects. In March 2020, accelerator-based BNCT for head and neck cancer using 4-borono-L-phenylalanine (L-BPA) was approved by the Pharmaceuticals and Medical Devices Agency in Japan, making BNCT more accessible treatment [1]. L-BPA is known to actively accumulate into tumor cells thorough L-type amino acid transporter 1 (LAT-1). On the other hand, mercaptoundecahydrododecaborate (BSH) is a boron cluster containing 12 boron atoms although BSH does not show efficient tumor-selective pharmacokinetics. Therefore, the development of tumor-selective BSH delivery system is required for further expansion of BNCT, especially for the treatment of BPA-negative tumors.

We recently applied layered double hydroxide (LDH) to develop a nanohybrid of BSH and LDH (BSH-LDH) as a boron delivery carrier [2]. The tumor-to-blood ratio of BSH in the BSH-LDH-treated-group is found to be 4.4-fold higher than that in the intact BSH, demonstrating BSH-LDH is a promising integrative therapeutic platform for BNCT.

In this study, we estimated BNCT effect of BSH-LDH in glioblastoma mouse models.

EXPERIMENTS: BSH-LDH was designed and synthesized according to the previous report [2]. Tumor-bearing mice (female, 5-6 weeks old) were prepared by injecting subcutaneously (s.c.) a suspension of U87MG human glioblastoma cells in PBS. The mice were kept on a regular chow diet and water for a week. The tumor-bearing mice were injected *i.v.* with 200 μL of BSH-LDH (n = 6), BSH (n = 6), BPA (n = 4) and PBS (n = 4) (5.7 mg/kg and 30 mg/kg for BSH and BSH-LDH, respectively). At 2 h after injection, the tumors of mice were irradiated with thermal neutrons in the nuclear reactor for 15 min. The tumor volume and body weight of the mice were measured at 0, 4, 8, and 12 days after neutron irradiation.

RESULTS: The BNCT effect was evaluated by measuring tumor volume and body weight after neutron irradiation. The tumor volume slightly increased in all the groups 12 days after irradiation (Fig. 1A). There was no significant difference in all the groups, demonstrating that the tumor did not grow appropriately. The body weight of the mice did not change significantly in all the groups 12 days after irradiation (Fig. 1B). Therefore, BSH-LDH nanohybrid did not have critical toxicity.

These results indicate that BSH-LDH can be a promising boron carrier with lower toxicity even in high dose of administration. Further BNCT experiment is necessary to evaluate anti-cancer effect of BSH-LDH compared with BSH and BPA. For this purpose, the U87MG mice models should be constructed properly by optimizing the tumor bearing conditions such as the number of the injected cells.

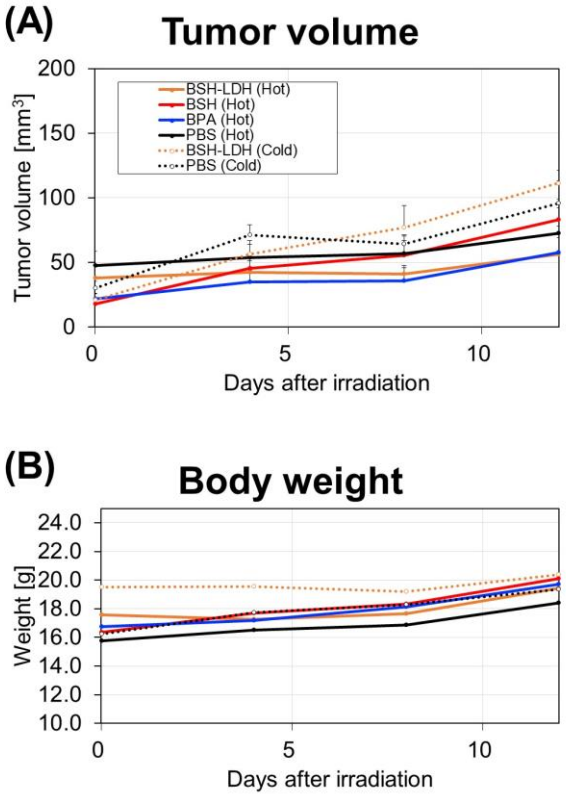

Fig. 1. (A) Tumor volume in mice after BNCT with BSH-LDH (n = 6), BSH (n = 6), BPA (n =4) and PBS (n = 4) (5.7 mg/kg and 30 mg/kg for BSH and BSH-LDH, respectively). The tumors were irradiated with thermal neutron for 15 min at 2 h after administration. Hot and cold mean with and without irradiation of thermal neutron, respectively. (B) Body weight changes of mice after BNCT. The data are shown as mean ± sem.

REFERENCES:

[1] H. Kanno *et al.*, The Oncologist, **26** (2021) e1250-e1255.
[2] G. Choi *et al.*, Adv. Func. Mater., **28** (2018) 1704470.

CO7-34 Gadolinium-containing nanoparticles grafted with polyglycerol for magnetic resonance imaging and gadolinium neutron capture therapy of cancer

L. Zhao[1], H.G. Kang[2], W. Huang[2], J. Yu[2], Y. Yoshino[3], F. Yoshino[4], M. Suzuki[5] and N. Komatsu[2]

[1] School for Radiological and Interdisciplinary Sciences (RAD-X) and Collaborative Innovation Center of Radiation Medicine of Jiangsu Higher Education Institutions, Soochow University, China
[2] Graduate School of Human and Environmental Studies, Kyoto University, Japan
[3] Department of Radiology, Kyoto Prefectural University of Medicine, Japan
[4] Department of Obstetrics and Gynecology, Shiga University of Medical Science, Japan
[5] Institute for Integrated Radiation and Nuclear Science, Kyoto University, Japan

Cancer is one of leading causes of death worldwide, accounting for nearly 10 million deaths in 2020. Gadolinium neutron capture therapy (GdNCT) is an alternative to BNCT using Gd-containing agents as a sensitizer, killing cancer cells with Auger electrons of high linear energy transfer (LET) as well as low-LET γ photons.[1] The Gd-containing agents can also serve as an efficient tracer for magnetic resonance imaging (MRI), enabling MRI-guided GdNCT of cancer (Figure 1) [2]. This can not only help optimize the GdNCT plan, but also enhance the accuracy and efficacy of GdNCT. In this context, developing efficient Gd-containing agents is crucial. We have recently developed Gd-containing inorganic nanoparticles grafted with poly(glycerol) (GdNP-PG), showing excellent dispersibility (> 10 mg Gd/mL in saline) and colloidal stability in physiological media. Upon intravenous administration, GdNP-PG nanoparticles accumulated in subcutaneous CT26 mouse colon tumor through enhanced permeability and retention (EPR) effect, reaching a high Gd concentration of about 150 μg/g in the tumor at 24 h postinjection.

Preliminary MRI measurements of the mice bearing CT26 tumor were carried out on a Bruker Biospec 47/40® system before and after intravenous injection with saline dispersion of GdNP-PG. A brightened T_1-weighted image (T_1WI) of the tumor was observed at 1 h postinjection as compared to that before injection, due to the T_1-shortening effect of GdNP-PG. The T_1WI of the tumor became brighter at 24 h postinjection, suggesting that GdNP-PG gradually penetrated into the tumor tissue with time.

Encouraged by the MRI results, we conducted preliminary GdNCT of cancer mediated by GdNP-PG. After intravenous injection with the saline dispersion of GdNP-PG for 24 h, the mice bearing CT26 tumor were irradiated with thermal neutrons at a reactor power of 5 MW for 12 min. The results show that GdNP-PG-mediated GdNCT significantly suppressed the growth of CT26 tumor as compared to the control groups. In particular, two out of the three mice subjected to the GdNCT displayed a shrinking tumor size after the neutron irradiation. In addition, no obvious difference was observed in body weight between the GdNCT and the control groups, suggesting the low in vivo toxicity of GdNP-PG.

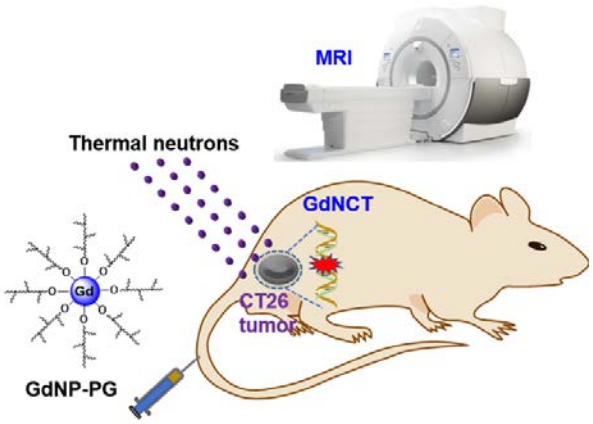

Figure 1. MRI-guided GdNCT using GdNP-PG as a theranostic agent.

To sum up, preliminary MRI and GdNCT experiments collectively indicate that GdNP-PG should be a promising theranostic agent for cancer treatment. However, more detailed MRI measurements are required to monitor the GdNP-PG's accumulation in the tumor tissue, according to which the neutron irradiation timing for GdNCT can be adjusted to achieve better efficacy. In addition, the therapeutic mechanism of GdNP-PG-mediated GdNCT will also be explored in the future.

Reference:

[1] D. Duan *et al.,* CCS Chemistry, (2023) (doi) 10.31635/ccschem.023.202202488.
[2] P. Mi *et al.,* ACS Nano, **9 (6)** (2015) 5913-5921.

R4161 Revised : July 18th, 2023

CO7-35 Development of theranostic agents for boron neutron capture therapy and its companion diagnostics

K. Ogawa[1], S. Imai and M. Suzuki[2]

Graduate School of Medical Sciences, Kanazawa University
[1]Institute for Frontier Science Initiative, Kanazawa University
[2]Institute for Integrated Radiation and Nuclear Science, Kyoto University

INTRODUCTION:

Boron neutron capture therapy (BNCT) using ^{10}B-labeled agents with companion diagnostics is promising for cancer theranostics. In current clinical practice, companion diagnostics using positron emission tomography (PET) with 4-borono-2-[^{18}F]fluoro-L-phenyl alanine ([^{18}F]FBPA) can be performed before BNCT with 4-[^{10}B]borono-L-phenylalanine ([^{10}B]BPA) [1]. If BNCT and companion PET imaging can be performed with compounds of the same structure, it will be possible to predict the therapeutic and side effects of compounds for BNCT with higher accuracy. For the establishment of a new BNCT system, we synthesized and evaluated a probe [^{67}Ga]**1** containing *closo*-dodecaborate ($[B_{12}H_{12}]^{2-}$) as a boron cluster, a [^{67}Ga]Ga-DOTA derivative for imaging, and an RGD (arginine-glycine-aspartic acid) peptide for tumor-targeting. Recently, we demonstrated that [^{67}Ga]**1** highly accumulated in U-87MG tumors with high expression of $\alpha_v\beta_3$ integrin. In this study, we evaluated the therapeutic effect of [^{10}B]**1** with neutron irradiation using U-87MG cells.

EXPERIMENTS:

WST assay

U-87MG human glioma cells were cultured in EMEM medium containing 10% FBS and 1% penicillin-streptomycin at 37°C under 5% CO_2. [^{10}B]BPA (192 μM, ^{10}B 40 ppm) and [^{10}B]**1** (16 μM, ^{10}B 192 ppm) were prepared in FBS-free EMEM medium. In a microtube, U-87MG cells (1×10^5 cells) were suspended in 1 mL of the prepared medium and shaken at room temperature at 550 rpm for 1 h. After removing the drug-containing medium, the cells were seeded on 96-well plates at 1×10^4 cells/well in FBS-free EMEM medium. Neutron irradiation (1 MW) was performed for 15 or 30 min. The irradiated cells were incubated at 37°C under 5% CO_2 for 24 h. After adding WST-8 and incubating for 90 min at 37°C under 5% CO_2, the absorbance at 450 nm was measured using a plate reader.

Colony formation assay

U-87MG cells were seeded on a 96-well plate at 1×10^4 cells/well in EMEM medium and pre-incubated at 37°C under 5% CO_2 for 24 h. FBS-free EMEM medium containing [^{10}B]BPA (192 μM, ^{10}B 40 ppm) and [^{10}B]**1** (1 μM, ^{10}B 12 ppm) were added and incubated for 3 h. Neutron irradiation (1 MW) was performed for 15 or 30 min. The drug-containing medium was removed, and the cells were harvested. The collected cells were seeded on a 6-well plate and incubated at 37°C under 5% CO_2 for 6 days. After staining and fixing with 0.1% crystal violet in 70% EtOH (1 mL/well), the cells were dissolved in 30% acetic acid (1 mL/well), and the absorbance at 570 nm was measured using a plate reader.

RESULTS:

In WST assay and colony formation assay using U-87MG cells, [^{10}B]**1** showed significantly lower cell viability than control group when irradiated for 15 and 30 min. In the colony formation assay, [^{10}B]**1** showed a higher therapeutic effect than [^{10}B]BPA. These results suggests that [^{10}B]**1** would be useful as a drug for BNCT.

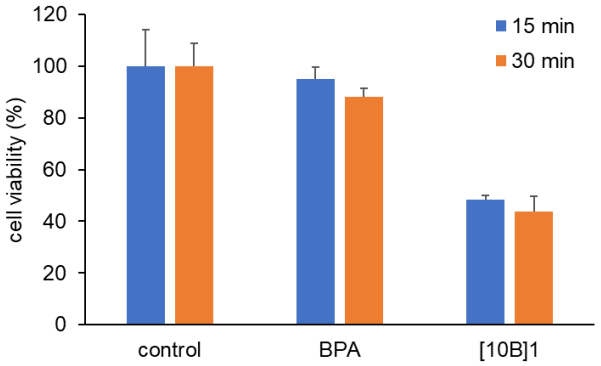

Fig. 1. BNCT effects on cell viability after thermal neu-tron irradiation by WST assay

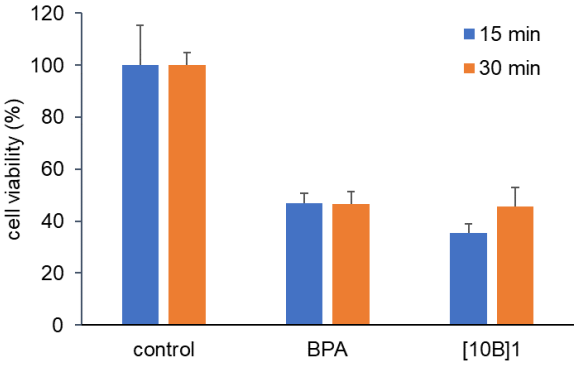

Fig. 2. BNCT effects on cell viability after thermal neutron irradiation by colony formation assay

REFERENCES:

[1] N. Fukumitsu and Y. Matsumoto, Cells, **10(8)** (2021) 2135.

CO7-36 Development of Novel Small-molecule Boron Neutron Capture Therapy Drugs Targeting Tumor-specific Enzymatic Activity

J. Tsunetomi[1], M. Suzuki[2], M. Kamiya[3], Y. Urano[1,4]

[1] *Graduate School of Pharmaceutical Sciences, The University of Tokyo*
[2] *Institute for Integrated Radiation and Nuclear Science, Kyoto University*
[3] *Departments of Life Science and Technology., Tokyo Institute of Technology*
[4] *Graduate School of Medicine, The University of Tokyo*

INTRODUCTION: In boron neutron capture therapy (BNCT), *p*-boronophenylalanine (BPA), the only approved BNCT agent, is selectively taken up by tumor cells through LAT1, which is a biomarker-transporter overexpressed in tumor cells. However, BPA faces the following challenges: 1) BPA accumulation is insufficient in some types of cancer because of poor LAT1 expression, and 2) BPA gradually leaks out of cells over time. Therefore, the development of new BNCT drugs that target another cancer biomarker and have a mechanism for prolonged intracellular retention is necessary to expand the indications for BNCT and improve therapeutic effect.

We have developed a library of fluorescence probes that can detect various enzymatic activities, and by applying these probes to living cells and clinical specimens, we have established a technique that enables comprehensive evaluation of tumor cell-specific enzymatic activities[1]. By utilizing the enzymatic activities found by the above mentioned screening as a biomarker of certain cancers, we considered that it would be possible to develop novel BNCT drugs that accumulate in tumor cells with high selectivity.

We focused on an aminopeptidase, dipeptidyl peptidase 4 (DPP-4), which is specifically highly expressed in esophageal cancer sites[2]. We designed and synthesized a novel small-molecule carborane-containing drug candidate targeting DPP-4 activity, EP-4OCB-FMA. This drug is designed to stay inside cells for a long time by generating *aza*-quinone methide species by being hydrolyzed by DPP-4, which is enough nucleophilic to form a covalent bond with intracellular nucleophiles such as proteins and glutathione.

EXPERIMENTS and RESULTS:

Cellular uptake assay

EP-4OCB-FMA was administered to live cells at a concentration of 10 μM and the intracellular boron concentration was measured by MP-AES after 3 hours of incubation. The results showed that the drug retained in DPP-4 highly expressing cells selectively and that sufficient intracellular boron concentration could be achieved.

Neutron capture therapy for H226 / Caco-2 cells

Based on the above results, we next performed BNCT on cultured cells to evaluate the therapeutic effect of EP-4OCB-FMA. After administering EP-4OCB-FMA (10 or 20 μM), which was not ^{10}B-enriched, with or without sitagliptin (DPP-4 inhibitor), or ^{10}BPA-fructose complex (3 mM and 7.7 mM each) to live cells, the cells were detached with trypsin after 2.5 or 3 hours-incubation. After thermal neutron irradiation, cells were seeded on 100 mm dish and cell viability was evaluated by colony formation assay after 2 weeks incubation. As a result, a high cell killing effect was observed in DPP-4 highly expressing cells, such as H226 cells and Caco-2 cells. This effect was cancelled by co-incubation of DPP-4 inhibitor sitagliptin, indicating that EP-4OCB-FMA has a selective effect depending on DPP-4 activity of cells. Furthermore, in Caco-2 cells, which express high levels of LAT1 as well as DPP-4, EP-4OCB-FMA showed a superior cell-killing effect compared to ^{10}BPA-fructose complex.

Biodistribution

Tumor-bearing BALB/c mice (female, 8-9 weeks old) were prepared by injecting subcutaneously (s.c.) a suspension of H226 cells (1.0×10^6 cells/ 100 μL/ mouse, 50 % Matrigel in PBS). The mice were injected intratumorally with EP-4OCB-FMA (0.1 mg/mouse, ~5 mg/kg), which was not ^{10}B-enriched, dissolved in saline containing < 5 % DMSO. The mice were euthanized 1, 6, or 24 hours after injection, and blood was obtained from heart, followed by collection of tumors and organs. The samples were put into Teflon tubes. The amount of boron in the samples was quantified by prompt gamma-ray analysis (PGA). The results suggested that high concentrations of boron remained in the tumor even after 24 hours post administration.

Neutron capture therapy to H226 tumor mouse models

Tumor-bearing BALB/c mice (female, 6-7 weeks old) were prepared by injecting subcutaneously (s.c.) a suspension of H226 cells (1.5×10^6 cells/ 100 μL/ mouse, 50 % Matrigel in PBS). EP-4OCB-FMA (0, 20 or 40 mg/kg), which was not ^{10}B-enriched, was intratumorally injected, with or without sitagliptin (40 mg/kg) in saline containing < 20 % DMSO. The mice were placed in acrylic holders, which were secured on a 5-mm-thick thermoplastic plate that contained 40 weight % (wt %) of ^{6}LiF (96% ^{6}Li) to block thermal neutrons and had a circular hole in the center. The thigh containing the tumor was stretched over the hole, and the tumor was irradiated with epi-/thermal neutrons for 15 min (fluence: 4.7×10^{11} to 2.6×10^{12} neutrons/ cm^2) 2.5 hours after injection. The results showed that tumor growth was suppressed in a drug-, enzyme-, and neutron-irradiation-dependent manner. These results indicate that EP-4OCB-FMA is a useful BNCT drug that targets tumor cell-selective enzymatic activity with an intracellular retention ability.

REFERENCES:

[1] Y. Kuriki *et al.*, Chem.Sci., **13**(2022) 4474-4481.
[2] H. Onoyama *et al.*, Sci Rep., **6** (2016) 26399.

R4167

CO7-37 Quantitative Evaluation Method of Elemental Contents Related to Activation in Radiation Shielding Concrete

T. Takata, K. Kimura[1], Y. Sakurai, H. Tanaka, and K. Takamiya

Institute for Integrated Radiation and Nuclear Science, Kyoto University
[1]*Fujita Corporation*

INTRODUCTION: Concrete is a very useful material for all aspects of construction, including infrastructure, office buildings, and facilities. In addition, concrete is widely used as radiation shield in nuclear reactors and irradiation facilities because of its flexibility, sufficient supply and low cost. On the other hand, once these facilities start operating, the concrete for shielding is affected by the radiation and becomes radioactive in facilities where neutrons are generated. For the above situation, low activation concrete is the one of the ways to solve the problem [1-3]. Especially, Boron Neutron Capture Therapy (BNCT) should be effective facilities to apply the low activation concrete.

To estimate the level of activation in shielding concrete, we have performed neutron activation analyses (NAA) on more than several hundred samples of shielding concrete and raw materials using KUR facilities. The results of the NAA are reported in detail in Ref. 4. We describe a summary of the method including sample preparation, irradiation, and post-irradiation process for gamma-ray spectroscopy.

MATERIALS ANDS METHODS: Three nuclides produced by reactions of $^{151}Eu(n,\gamma)^{152}Eu$, $^{59}Co(n,\gamma)^{60}Co$ and $^{133}Cs(n,\gamma)^{134}Cs$ in concrete and raw materials were subject to quantitative evaluation. Since FY2018 we have been exploring various experimental conditions; since FY2019 we have been conducting a series of analyses under almost constant conditions. The procedure is described below.

Samples were prepared as powder or small grain by Fujita Corporation. Each sample of about 0.7 to 1 g was sealed in double plastic bags to prevent radioactive contamination. Commercially available Rock reference materials and an in-house reference powder sample with known concentrations of Eu, Co and Cs were prepared in the same way as internal standards. Approximately 7 to 10 samples, including the two internal standards, were encapsulated in a polyethylene irradiation capsule.

Using Pn-2 system, each capsule was irradiated for 60 minutes, 8 capsules per session, 2 or 3 sessions per year for a total of 16 to 24 capsules. The irradiated capsules were opened sequentially for measurement after about two months or more of radioactive cooling. The samples were individually sealed in additional outer plastic bags to prevent radioactive contamination.

The gamma-ray spectrum of each sample was measured one by one with an HP-Ge detector with automatic measurement system equipped with sample changer. In the quantitative analysis of nuclide concentrations, we focused on the peaks at 1408 keV for ^{152}Eu, 1333 keV for ^{60}Co, and 795 keV for ^{134}Cs, respectively. The target uncertainty of the peak quantification analysis was set to less than 10%. Measurements of 18,000 to 20,000 s were performed for all samples, and longer measurements were performed for samples with large uncertainties.

RESULTS: The content of each nuclide was calculated by comparison with the measured values of internal standards. Figure 1 shows the frequency distribution of elemental concentrations for 568 samples measured in FY2019-2021. For ^{60}Co, the target uncertainty was achieved for almost all samples by measuring for about 20,000 seconds. For ^{152}Eu and ^{134}Cs, there were samples with low content, for which measurements were performed for up to about 160,000 seconds. The mean radioactivity immediately after irradiation, estimated from the content of nuclides, was 1.7 kBq/g for ^{152}Eu, 0.9 kBq/g for ^{60}Co, and 0.45 kBq/g for ^{134}Cs, respectively.

In FY2022, 236 new samples were irradiated. We will conduct a detailed analysis of the data acquired to date and continue to accumulate data to build a materials database.

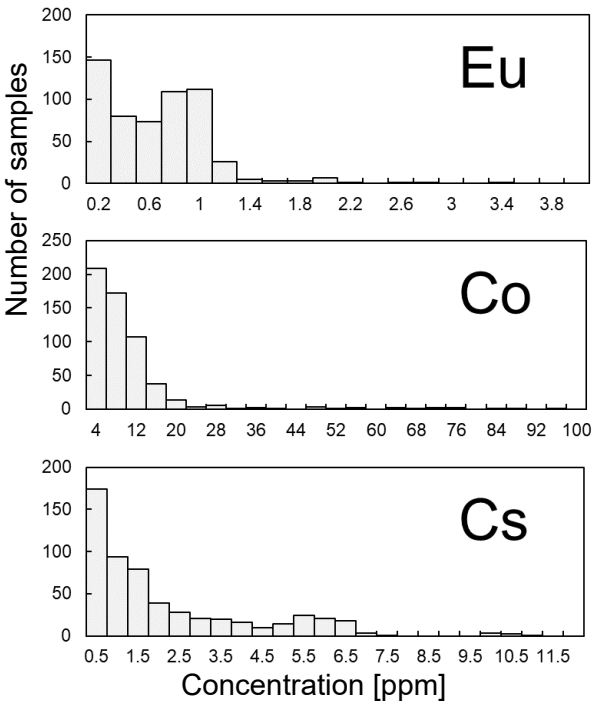

Fig. 1. Frequency distributions of elemental contents for samples analyzed in FY2019-2021.

REFERENCES:

[1] K. Kimura *et al.,* Proc. of 8th Int. Conf. on Radiation Shielding, ANS inc, Arlington, USA.,**1**(1994) 5-42.
[2] M. Kinno *et al.,* ANS Radiation Protection & Shielding Conference, Spokane, USA, (2022) 673-678.
[3] K. Kimura *et al.,* Proc. of Int. Conf. on Nuclear Engineering (ICONE16), Florida, USA, (2008) 4848.
[4] K. Kimura *et al.,* KURNS Progress Report 2018-2021.

CO7-38 Synthesis and evaluation of a novel boron neutron capture therapy agent

H. Kimura[1] and M. Suzuki[2]

[1] *Department of Analytical and Bioinorganic Chemistry, Division of Analytical and Physical Sciences, Kyoto Pharmaceutical University*

[2]*Institute for Integrated Radiation and Nuclear Science, Kyoto University*

INTRODUCTION:

Neuroendocrine Neoplasms (NEN) is a general term for tumors that arise from cells of the neuroendocrine system and have developed an abnormal growth. Because the neuroendocrine system is distributed throughout the body, neuroendocrine tumors can occur anywhere in the systemic organs. The incidence is particularly high in the pancreas, gastrointestinal tract, and lungs. It is a relatively rare disease with an incidence of approximately 5 per 100,000 people, and has been considered a "rare cancer." In recent years, however, its incidence has been increasing due to improvements in diagnostic techniques and other factors clinically, NEN is classified into functional NEN, which presents with specific symptoms depending on the hormone-producing capacity of the tumor, and nonfunctional NEN, which does not present with hormone-specific symptoms.[1)]

Pathologically, pancreatic NETs were classified into three categories in the 2010 WHO classification (digestive organs) based on the Ki-67 index and fission images: Grade 1 and 2 NETs with low mitotic activity were classified as Neuroendocrine Tumor (NET) and Grade 3 NETs with high mitotic activity as Neuroendocrine Carcinoma (NEC). For pancreatic NETs, the 2017 WHO Classification of Endocrine Organs subdivided the NEC part and incorporated a new definition, NET-G3, which classifies the disease into four categories: NET-G1, G2, G3, and NEC-G3. Furthermore, the WHO Classification (Gastrointestinal) was revised in 2019 and the definition of pancreatic NET G3 was incorporated directly in the gastrointestinal tract, unifying the same grading system for both pancreatic and gastrointestinal tract.

NETs are known to be characterized by high expression of somatostatin receptors (SSTRs) on the tumor cell membrane. Somatostatin is a cyclic peptide discovered as a hypothalamic factor that potently inhibits growth hormone secretion from the pituitary gland. There are five subtypes of somatostatin receptors (SSTR1-5), and SSTR2 is highly expressed in NETs. Therefore, somatostatin analogs with high binding to SSTR2 are used for treatment.[2) - 4)] Furthermore, Peptide Receptor-mediated Radionuclide Therapy (PRRT), which uses somatostatin analogs as nuclear medicine drugs for NET patients, has recently been implemented in Europe, and LUTATHERA ® was approved for manufacturing and marketing in Japan for the first time on June 23, 2021 as a drug for PRRT in Japan. However, there is a need for the development of new therapies with greater therapeutic efficacy. Therefore, in this study, we conducted a basic study on the potential of BNCT for NETs.

EXPERIMENTS:

Cell culture: AR42J cells, a cell type that highly expresses SSTR2, were cultured.The cells were cultured as in Ham's F-12K medium supplemented with 20% fetal bovine serum, glutamine, and antibiotics (penicillin/ streptomycin) in a humidified CO_2 incubator (37°C/5% CO_2).

Mouse Tumor-Bearing Models: Cell suspensions prepared by suspending AR42J cells in D-PBS (-) were injected subcutaneously into the legs of male BALB/c Slc-nu/nu mice (5 weeks old) at 100 μL (5.0×10^6 cells) per animal under isoflurane anesthesia.

Neutron irradiation: A newly developed boron drug was administered by tail vein and subcutaneously. Two hours after drug administration, tumor-bearing mice were neutron irradiated at 5 MW for 15 minutes.

RESULTS:

Tumor volume increased over time in mice that were exposed to neither drugs nor neutron radiation. On the other hand, the tumor volume of mice irradiated with both the drug and neutrons showed no increase in tumor volume up to 10 days after neutron irradiation. No significant differences were observed between subcutaneous and tail vein administration. In the future, we plan to conduct detailed studies including reproducibility, such as examining the time from drug administration to neutron irradiation and the amount of drug administered.

REFERENCES:

[1] T. Masui *et al.,* BMC Cancer, **20** (2020) 11-04.
[2] O. Keskin *et al.,* Onco Targets Ther., **6 (2013)** 471-483.
[3] T. Gunther *et al.,* Pharmacol Rev. **70** (2018) 763-835.
[4] E. Pauwels *et al.,* Am J Nucl Med Mol Imaging., **8(5)** (2018) 311-331.

CO7-39 Investigating Gd-EDTMP as a Neutron Capture Therapy Agent for Mammary Tumor Bone Metastasis in Mouse Models

T. Matsukawa[1], M. Suzuki[2], A. Kubota[1], A. Shinohara[1,3], K. Yokoyama[1,4]

[1] *Juntendo University Faculty of Medicine*
[2] *Institute for Integrated Radiation and Nuclear Science, Kyoto University*
[3] *Research Institute for Cultural Studies, Seisen University*
[4] *International University of Health and Welfare*

INTRODUCTION: In pursuit of advancing cancer radiation therapy, this study evaluated the tissue distribution and effects of Gd tetra (methylene phosphonic acid) chelate (Gd-EDTMP) as a potential neutron capture therapy agent. Prior experiments using Gd-EDTMP in young mice indicated a high dose distribution in femur regions, particularly in bones with an epiphyseal line. To further investigate the basis for neutron capture therapy, we developed a mouse model of carcinogenesis in elderly mice with closed epiphyseal lines. After neutron irradiation, the distribution of 157Gd in and around the bone was analyzed using laser ablation inductively coupled plasma mass spectrometry (LA-ICP-MS).

EXPERIMENTS: Gd-EDTMP solution was prepared from gadolinium chloride and EDTMP. Female BALB/cAJcl mice (12 weeks old) were acclimated for one week and then transplanted with the Luciferase expressing 4T1 mouse mammary tumor cell line JCRB1447 into their right tibia. After another week of acclimation and tumor formation confirmation, mice were divided into three groups (n=3 or 4): Gd-EDTMP treated and neutron irradiated (Gd+/Nu+), Gd-EDTMP treated and not neutron irradiated (Gd+/Nu-), and phosphate buffered saline treated and neutron irradiated (Gd-/Nu+). Gd+/Nu+ and Gd+/Nu- mice received a single intraperitoneal dose of 20 mg/kg body weight Gd-EDTMP (1 mg Gd/ml PBS) (n=3). Gd-/Nu+ mice (n=4) received an equivalent dose of PBS. Twenty four hours after Gd-EDTMP or PBS administration, Gd+/Nu+ and Gd-/Nu+ mice's lower limbs were irradiated with thermal neutrons for 15 minutes at the Kyoto University Research Reactor (KUR, 5MW), with an irradiation fluence of 3.6 x 10 12 cm 2 . Following irradiation, mice were monitored for 14 days with free access to food and water. After euthanasia, right thighs and shins were harvested, weighed for tumor weight, and prepared as non-decalcified frozen sections using the Kawamoto method. The distribution of 157 Gd was imaged by LA-ICP-MS (LA: NWR213, ICP-MS: Agilent 8800) according to previously established methods [1]. The tumor status was further assessed using micrographs of Hematoxylin Eosin (H.E.) stained sections of the lower limbs.

RESULTS and DISCUSSION: The ICP-MS analysis revealed that administering a 20 mg/kg intraperitoneal dose of Gd-EDTMP led to a concentration of 1000-2000 ppm of Gd in the bone after 24 hours. In a mouse model of bone metastasis originating from a 4T1 mammary tumor, a tumor shrinking effect was observed following neutron irradiation, although it was not statistically significant [2]. This finding suggests potential for future therapeutic applications. LA-ICP-MS imaging results showed that Gd accumulated in the bone. Interestingly, by muting the Gd signal in the bone distribution area, the distribution of Gd concentration outside the bone became observable. This image processing revealed that Gd was also present in the tumor cells themselves, which may contribute to the tumor shrinking effect.
To achieve a tumor suppressive effect suitable for therapy, it is necessary to further enrich Gd in the tumor area. Analyzing the accumulation mechanism of Gd in the 4T1 cells themselves, as observed in this study, is essential. Additionally, exploring more effective methods of administration could lead to improve therapeutic outcomes.

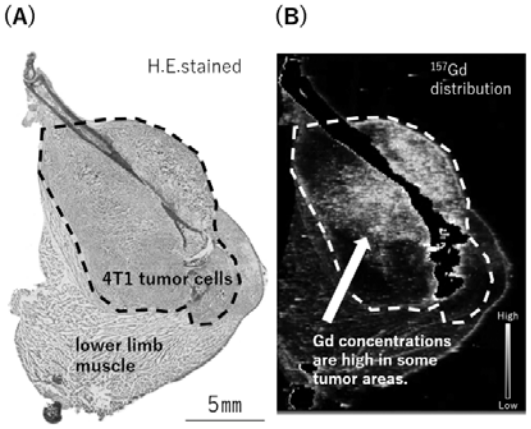

Fig.1 A leg section of a mouse with a 4T1 mammary tumor cell transplant after administering Gd tetra (methylene phosphonic acid) chelate (Gd-EDTMP) (20 mg/kg) for 14 days. Figure A shows the Hematoxylin and Eosin (H&E) stained image, and Figure B displays the 157 Gd distribution image obtained through Laser Ablation Inductively Coupled Plasma Mass Spectrometry (LA-ICP-MS), excluding the bone area. The area within the dotted line contains a high concentration of tumor cells. In Figure B, a concentration of Gd can be observed surrounding the 4T1 tumor cells that are in contact with the bone.

REFERENCES:

[1] A. Kubota *et al.*, Juntendo Medical Journal., **65** (2019) 461-467.
[2] T. Matsukawa *et al.,* 8th International symposium of Metallomics, Kanazawa, 7/11-14 (2022).

R4178

CO7-40 Tumour Growth Suppression by Intra-Tumoural Injection of Gadolinium-Polyplex with Bubble Liposome / Ultrasound Stimulation for Gadolinium-Neutron Capture Therapy to Pancreatic Cancer Model *inVivo*

H. Yanagie[1,2,3], X. Hou[4], S. Kageyama[5], K. Maruyama[5], T. Takata[6], M. Suzuki[6], T. Watanabe[6], Y. Sakurai[6], H. Tanaka[6], M. Nashimoto[3], J. Nakajima[2,7], M. Ono[2,8], T. Sugihara[3], and H. Takahashi[1,2,4]

[1]*Institute of Engineering Innovation, School of Engineering, The University of Tokyo,*
[2]*Cooperative Unit of Medicine & Engineering, The University of Tokyo Hos-pital,*
[3]*Niigata University of Pharmacy & Applied Life Sciences,*
[4]*Dept of Bioengineering, School of Engineering, The University of Tokyo,*
[5]*Faculty of Pharma-Science, Teikyo University,*
[6]*Kyoto University Institute for Integrated Radiation & Nuclear Science,*
[7]*Dept. of Pulmo-nary Surgery, The University of Tokyo Hospital,*
[8]*Dept. of Cardiac Surgery, The University of Tokyo* Hospital, JA-PAN

INTRODUCTION:

The cytotoxic effect by 1μm-range high LET Auger electron, and long-range gamma rays was estimated on Gadolinium-neutron capture therapy(GdNCT) [1, 2, 3]. For effective GdNCT, it is necessary to accumulate Gadolinium atoms into the tumor tissues selectively. We performed the experiments of Gadolinium delivery systems for GdNCT using meglumine gadoterate (Magnescope; $C_{16}H_{25}GdN_4O_8$ - $C_7H_{17}NO_5$; MW:753.86). The Magnescope is difficult to be kept in the cytoplasm and nucleus in the cancer cells, so we need to develop some functional delivery systems.

Recently, for effective gene transfectins, drug delivery using a combination of ultrasound and microbubbles has been reported [4, 5]. The interaction of microbubbles and US increases the local permeability of cancer cell membrane, allowing the injected plasmid DNA to move easily into the cells and increasing the concentration of plasmid DNA in the cancer cells.

In this study, we evaluated Magnescope / hyaluronic acid / protamine-mixed with cationic liposome (^{157}Gd-plex) as neutron capture therapy agent by in vivo experiment on AsPC-1 human pancreatic tumor-bearing mice. We also use perfluorocarbon microbubbles / Ultrasound external stimulation system combined catinic liposome as an method for selective delivery

of ^{157}Gd compound into the cells.

EXPERIMENTS:

^{157}Gd-plex were prepared mixed with 1.2mL of Magnescope (0.38 mg/mL), 0.24mL of a solution of 10mg/mL hyaluronic acid sodium, and 0.12mL of 10mg/mL of protamine incubating at room temperature for 30min, then, these mixing solutions were poured into 0.24mL of cationic Liposome; Lipofectamine3000. Human pancreatic cancer AsPC-1 cell was used for the *in vivo* anti-tumor effect evaluation. We prepared AsPC-1($5x10^5$) model by transplanting to right lower leg.

Ultrasound stimulation was performed after intra-tumoral injection of 0.1mL of ^{157}Gd-plex and 0.04mL of bubble liposomes, then, we performed thermal neutron irradiation at Institute for Integrated Radiation and Nuclear Science, Kyoto University (average neutron fluence of 3.0×10^{12} n/cm^2). The change in tumor growth and survival rate of the mice reflected the anti-tumor effect of ^{157}Gd-plex. While measuring the size of tumor, the weight change was also recorded for evaluation of the toxicity of these samples.

RESULTS:

The experimental results showed that tumor growth suppression in the treated group of ^{157}Gd-plex / Bubble Liposome / Ultrasound stimulation on NCT was 2 times superior compared with non-irradiated group. No significant weight loss were observed after treatment.

We attempted to enhance of retention of ^{157}Gd atoms by mixing ^{157}Gd-plex. It is thought that the Bubble Liposome / Ultrasound stimulation is effective to increase the ratio of transfection of the genes and compounds into the cytoplasms of cancer cells. We hope to apply these techniques including gene therapy and electrochemotherapy acutually using in clinical to GdNCT for local advanced cancers [6,7].

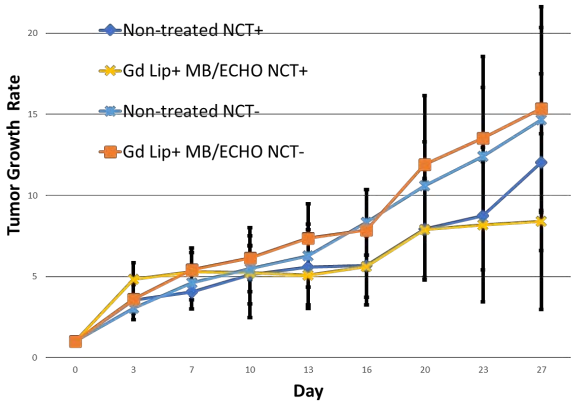

Figure 1. Tumor Growth Supression by NCT with Intra Tumoral Injection of ^{157}Gd-plex /Bubble Liposome and Ultrasound Stimulation

REFERENCES:

[1] N. Dewi *et al.,* Biomed & Pharmacother, **67** (2013) 451-7.
[2] N. Dewi *et al.,* J Can.Res.Clin.Oncol., **142**(4) (2016) 767-75.
[3] P. Mi *et al.,* J Cont. Release, **174** (2014) 63-71.
[4] I. Yokoe *et al.,* Drug Deliv., **28(1)** (2021) 530-541.
[5] I. Yokoe *et al.,* Cancers, **12(9)** (2020) 2423.
[6] L. Lambricht *et al.*, Expert Opin Drug Deliv., **13(2)** (2016) 295-310.
[7] B. Trotovšek *et al.,* World J Gastroenterol, **27(48)** (2021) 8216-8226.

R4179

CO7-41 Basic research on new BNCT strategies for melanoma

H. Michiue[1], T. Fujimoto[1,2], N. Kanehira[1,2], K. Igawa[1], Y. Sakurai[3], N. Kondo[4], T. Takata[3], and M. Suzuki[3]

[1]Neutron Therapy Research Center, Okayama University; 2-5-1, Shikata-cho, Kita-ku, Okayama City, Okayama, Japan.
[2]Department of Gastroenterological Surgery, Okayama University; 2-5-1, Shikata-cho, Kita-ku, Okayama City, Okayama, Japan.
[3]Institute for Integrated Radiation and Nuclear Science, Kyoto University, 2-1010, Asashiro-Nishi, Kumatori-cho, Sennan-gun, Osaka, Japan.

INTRODUCTION:

The starting point for melanin synthesis in vivo is aromatic amino acids such as phenylalanine and tyrosine, and melanin synthesis is enhanced in cutaneous malignancies such as malignant melanoma. Boron-phenylalanine (BPA), a boron atom bonded to these amino acids, was created as a melanoma-targeted boron drug, and the success of BPA-BNCT was demonstrated in the 1989 Lancet article by Dr Mishima et al: "Treatment of malignant melanoma by single Malignant melanoma by single thermal neutron capture therapy with melanoma-seeking 10B-compound", published by Dr Mishima et al in the Lancet in 1989 [1]. This clinical study paved the way for the effectiveness of BNCT with boron drugs with cell-specific uptake and neutron irradiation of the cancer tissue area.

Melanoma is a cutaneous malignancy with an incidence of 1-2 per 100 000 people and is considered a rare cancer. In Australia, it is a disease with regional and racial variation, with an incidence of around 35 per 100 000 people. Surgery is the standard treatment of first choice for localized melanoma, and the prognosis is very good for Stage I melanomas, which have a low likelihood of spreading to the regional lymph nodes. The prognosis, mainly surgery, for localized melanoma is very good with a 5-year survival rate of 95-100% and the disease is reported to be curable by surgery. The usefulness of BNCT for localized melanoma is that there is no pain or functional impairment associated with surgery, which makes BNCT highly useful for melanoma patients, many of whom are elderly.

Clinical trials with BPA-BNCT for cutaneous malignancies (melanoma, angiosarcoma) are currently underway at the National Cancer Centre, and the results of the efficacy in these trials are expected.

While the efficacy of mainly surgical therapies in localized melanoma has been established, the development of treatments in inoperable advanced-stage melanoma is setting a new direction for malignancies as a whole. In particular, the discovery of immune checkpoint inhibitors targeting PD-1 by Professor Honjo Tusk and colleagues, who were awarded the 2018 Nobel Prize in Physiology or Medicine, has led to new breakthroughs in cancer treatment. Immune cells in our bodies are quick to attack foreign invaders such as viruses. On the other hand, they are unable to attack cancer cells that originate from our own cells because they are our own cells, even if they multiply in the body. Dr Honjo and colleagues have shown that the reason for the immune cells' inability to recognize antigens on cancer cells is due to the binding of an immune checkpoint molecule called PD-1 on the surface of cytotoxic T cells.

EXPERIMENTS:

We purchased the B16-F10 mouse melanoma cell line to create a melanoma model, B16-F10 has high melanin synthesis capacity and has a large amount of black melanin pigment even in cultured cells. We used melanoma model mice transplanted with B16-F10 into C57BL/6 mice and Balb/c nu/nu mice. Animal experiments were performed after strict approval by the ethics committees for animal experiments at Okayama University and Kyoto University.

Experiments were conducted while giving due consideration to the intensity of neutron radiation at the neutron irradiation site and at the shielded site.

RESULTS:

We used BPA as an effective boron agent for melanoma and confirmed the anti-tumor effect of neutron irradiation. The results were favorable, and are useful for the development of BPA-BNCT for melanoma in the future. We would like to express our deepest gratitude to the many collaborators who assisted in this project.

REFERENCES:

[1] Y. Mishima *et al.*, Lancet, **334** (1989) 388–9.

CO7-42 New boron drug development research targeting pancreatic cancer

H. Michiue[1], T. Fujimoto[1,2], N. Kanehira[1,2], K. Igawa[1], Y. Sakurai[3], N. Kondo[4], T. Takata[3], and M. Suzuki[3]

[1]Neutron Therapy Research Center, Okayama University; 2-5-1, Shikata-cho, Kita-ku, Okayama City, Okayama, Japan.
[2]Department of Gastroenterological Surgery, Okayama University; 2-5-1, Shikata-cho, Kita-ku, Okayama City, Okayama, Japan.
[3]Institute for Integrated Radiation and Nuclear Science, Kyoto University, 2-1010, Asashiro-Nishi, Kumatori-cho, Sennan-gun, Osaka, Japan.

INTRODUCTION:

Pancreatic cancer refers to malignant tumors arising from the pancreas, but generally refers to pancreatic ductal carcinoma. Ductal carcinoma originates from the pancreatic duct epithelium and accounts for 80-90% of all neoplastic lesions in the pancreas. According to national statistics, it was the fifth leading cause of death after lung cancer, stomach cancer, colorectal cancer, and liver cancer. Pancreatic cancer in our country has been on the rise in recent years, with more than 30,000 people dying from pancreatic cancer each year.

The number of pancreatic cancer deaths has increased more than eightfold in the past 30 years, and the disease is more common in people in their 60s and slightly more common in men. It has been associated with smoking, family history of pancreatic cancer, diabetes, and chronic pancreatitis.

Ultrasonography, CT, MRI, endoscopic pancreatography, and angiography are used to diagnose pancreatic cancer. If pancreatic cancer is suspected, the pancreas cannot be seen from the surface of the body, so an ultrasound or CT scan is first performed to check for the presence of a mass in the pancreas. CT scan can also be used to check for metastasis of pancreatic cancer to other organs such as the lungs and liver.

One of the characteristic imaging findings of pancreatic cancer is that the normal pancreas is contrasted without contrasting the pancreatic cancerous area when contrast enhanced CT scan is performed.

Usually, malignant tumors have more pronounced tumor vascular growth than normal tissues due to the rapid development of tumor blood vessels to nourish the tumor. In addition, these tumor vessels maintain a very leaky structure to provide a high degree of oxygen and nutrition to the tumor and are easily detectable using contrast media. However, pancreatic cancer, despite being a malignant tumor, is characterized by the fact that tumor blood vessels are somewhat scarce compared to normal, and the stroma between tumor cells is hyperplastic, making it difficult to receive the contrast effect of contrast media.

DDS (Drug Delivery System) is a research field that delivers drugs such as anticancer agents to such malignant tumors. It has been reported that when a liposomal formulation containing a drug is administered to a tumor-bearing model, such a macromolecular drug accumulates specifically in the tumor by leaking from the tumor blood vessels. This effect is called the EPR effect (Enhanced Permeability and Retention effect) and has been proposed as a theory that minimizes drug damage to normal tissue and maximizes the effect on tumor tissue.

For pancreatic cancer that does not undergo contrast effect, we believe that it is difficult to use polymeric DDS formulations, which mainly have EPR effect, for future clinical applications. Therefore, we focused on PET (Positron Emission Tomography) using 18F-FDG, which is used in the diagnosis of pancreatic cancer. FDG is a test reagent of a glucose derivative called fluorodeoxyglucose F18. Glucose is labeled with 18F, a radionuclide, and is used as a test reagent for various types of cancer. In this study, we focused on glucose metabolism in cancer, and decided to develop a glucose-based boron drug [1].

EXPERIMENTS:

In the present study, we planned to develop a boron drug for pancreatic cancer, a small molecule compound that does not utilize the EPR effect and targets glucose transporters. We focused on the tumor marker carbohydrate antigen CA19-9, called carbohydrate antigen 19-9, in the classification of pancreatic cancer. It has a high positive predictive value for cancer and is known to be elevated in uterine, ovarian and lung cancers, etc. Pancreatic cancers with high CA19-9 levels are known to have a poor prognosis and a CA19-9 high human pancreatic cancer cell line and CA19-9 low pancreatic cancer cells were used in the present experiment. Experiments were conducted with three different boron agents: glucose boron, BPA and BSH.

RESULTS:

In this study we have successfully synthesized a glucose-binding boron drug and have filed a patent application. The glucose boron drug was found to be efficiently introduced into cells via glucose transporters (GLUTs), which are highly expressed in pancreatic cancer. The anti-tumor effect of a novel drug agent in a mouse model of pancreatic cancer was confirmed in vitro and in vivo by neutron irradiation in a nuclear reactor, CA19-9, at the Institute for Complex Nuclear Science, Kyoto University, where a high therapeutic effect was obtained in a pre-experiment. The results are further developed and reported as a novel boron drug for targeting pancreatic cancer with high CA19-9 levels. We thank the many collaborators for their cooperation.

REFERENCES:

[1] RD Leone *et al.*, Science. **366 (6468)** (2019)1013-1021.

CO7-43 Boron-compound diagnostics in the plant using a neutron capture reaction

T. Kinouchi

Institute for Integrated Radiation and Nuclear Science, Kyoto University

INTRODUCTION: Mutation breeding of plants is a method of expanding genetic variation by artificially inducing mutations into the target DNA. The process starts by exposing seeds to chemicals (e.g., ethyl methanesulfonate, dimethyl sulfate) or radiation (e.g., γ-ray, ion-beam, neutron) in order to improve the new crops with desirable characters or phenotypes. More than 3,000 mutagenic plant varieties have already been released around the world, and more than 450 of these varieties were produced in Japan. Approximately 80% of them are caused by γ-ray radiation. On the other hand, γ-rays have a low linear energy transfer (LET), suggesting that they cannot deliver high energy locally to the target DNA, resulting in low relative biological effectiveness (RBE) and low mutation rates. We therefore focused on the phenomenon that a stable isotope of boron (^{10}B) irradiated by low-energy neutrons undergo a nuclear reaction into a high-energy helium nucleus (α-particle) and a lithium nucleus. Since those heavily charged particles can efficiently generate DNA double-strand breaks in the target cells, they would mutate or induce cell death. In fact, this reaction has been applied in combination with ^{10}B-compounds, such as *p*-boronophenylalanine (BPA), in a therapy to selectively destroy cancer cells, known as the boron neutron capture therapy (BNCT). However, BPA has not been well characterized in terms of mutagen for the mutation breeding. Therefore, to determine how much BPA added externally is absorbed by the seeds and where absorbed BPA localizes in them, *in situ* high-resolution visualization technique capable of detecting BPA in the seeds was examined with a solid-state nuclear tracking detector, CR-39.

EXPERIMENTS: Plant materials and growth conditions> Seeds used in analysis were harvested from a dwarf tomato cultivar, 'Micro-Tom' (*Solanum lycopersicum* L). Micro-Tom was originally derived for home gardens as the dwarf cultivar, but is now used as a major material for various plant research. The original seeds were obtained from Inplanta Innovations Inc. and seeded on the moderately moisturized vermiculite and cultivated at 23°C under a 16-h light/8-h dark cycle in a 60%-humidified growth chamber. A week later, their seedlings were transferred to the hydroponic media containing major nutrients (1 mM $Ca(NO_3)_2$, 0.5 mM KH_2PO_4, 0.5 mM K_2SO_4, 1 mM $MgSO_4$, and 1.5 mM NH_4NO_3) and micronutrients (75 μM EDTA-Fe, 46 μM $H_3{}^{11}BO_3$, 9 μM $MnSO_4$, 0.8 μM $ZnSO_4$, 0.3 μM $CuSO_4$, and 0.8 μM Na_2MoO_4) under the same conditions.

In situ visualization of BPA in a Micro-Tom seed> Micro-Tom seeds were immersed in BPA solution (100 mM) for 24 hrs. A mounted slice (10-μm thickness) of the seeds onto a solid-state nuclear tracking detector, CR-39 (20 mm×30 mm) was irradiated with epithermal neutron for 20 min by applying the pneumatic tube in the graphite thermal column (Tc-Pn) of Kyoto University Research Reactor (KUR). The irradiated CR-39 plate was etched in 6 M NaOH solution for 60 min at 70°C, and the resulting etch-pits were observed under an optical microscope as small black spots.

RESULTS: Both Figs. 1(A) and (B) show a cross section prepared from the same Micro-Tom seed, which was harvested from a parental strain cultivated in the ^{10}B-free hydroponic media. Fig. 1(A) is an optical microscopic image of the cross section of the seed. Black and white arrows indicate albumen and embryo, respectively. On the other hand, Fig. 1(B) is *in situ* visualization of BPA-distribution in the cross section. A large number of etch-pits derived from ^{10}B contained in BPA were concentrated on the outer seed coat and were barely detectable inside the seed. This strongly suggests that it is very difficult for BPA alone to pass through the seed coat. Since prolonged immersion (over 24 hrs) of seeds in a BPA solution may turn on germination, in order to increase BPA penetration into the seed, BPA concentration and carriers such as surfactants would need to be considered.

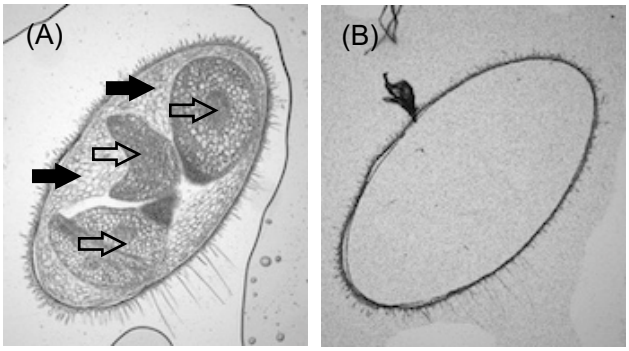

Fig.1 Detection of BPA in the Micro-Tom seed.
(A): Optical microscopic images of the cross section of the seed. Black and white arrows indicate albumen and embryo, respectively. (B): *In situ* visualization of BPA.

R4183

Revised : July 18th, 2023

CO8-1 Demonstration experiment of detecting the HEU sample using a low-cost inspection system

M. Komeda[1], K. Tanabe[2], Y. Toh[1], Y. Kitamura[3] and T. Misawa[3]

[1]Nuclear Science and Engineering Center, Japan Atomic Energy Agency
[2]National Research Institute of Police Science
[3]Institute for Integrated Radiation and Nuclear Science, Kyoto University

INTRODUCTION: A compact and low-cost non-destructive inspection system to detect hidden nuclear material is required in the fields of nuclear security. We developed a new nuclear material detection method, called the active rotation method, using a neutron source of Californium-252. In the method, a neutron source is rotated at a speed of thousands of rpm by the rotation machine nearby a measurement object. Meanwhile, it is possible to detect nuclear materials by confirming the deformation of the time-distribution spectrum obtained by a neutron detector near the object. The rotation machine is compact and low-cost. In addition to the rotation machine, we developed a water Cherenkov detector as a low-cost neutron detector. In previous studies, we accomplished detections of natural uranium of approximately 8,000 g by using a low-cost non-destructive nuclear material detection system composed of a rotation machine and a water Cherenkov neutron detector (WCND) in KUCA[1]. The purpose of this year is to detect smaller nuclear material, which is approximately 4 g of highly enriched uranium (HEU) using the developed system.

EXPERIMENTS: The experimental setup is shown in Fig.1. The dimensions of the neutron rotation machine are approximately 60cm in width, depth, and height. The rotation machine can rotate the disk (diameter 32cm), where a neutron source is installed at its outer periphery, at a rotation speed between 0 and 4000 rpm. A neutron source of Californium-252 is set in the disk, the radioactivity was 2.2 MBq. It is noted that the 2.2 MBq is smaller than the 3.7 MBq of the Japanese-approved devices with a certification label of Californium-252. In this experiment, we used approximately 4 g of HEU. The uranium sample was surrounded by polyethylene blocks. The WCND basically consists of an aquarium (30x25x30cm) and four PMTs (Photomultiplier tube). The PMT (2 inches diameter) is the Hamamatsu H11284-100. A transparent acrylic panel is attached to the top of the aquarium, installing the PMTs there. Since water filled up to the top surface, there was no air gap between the PMT and water. Measurements of the neutron time distribution were performed by a multi-channel scaler (MCS) that was synchronized with the disc rotation signal from the servomotor.

RESULTS: Figure 2 shows an example of experimental results of the HEU sample when the rotation speed is 4000 rpm. The measurement time for the experiment was 10 minutes. A comparison between the time-distribution spectra at 4000 rpm and 300 rpm reveals that the integrated value after the center (around 6000 micro-seconds at 4000 rpm) increased only for the HEU sample, but not for a blank sample (sample without nuclear material).
Thus, we have successfully detected approximately 4 g of HEU using low-cost non-destructive nuclear material detection system.

Fig. 1. The rotation machine (left), the water Cherenkov detector (right), and measurement object containing HEU (middle).

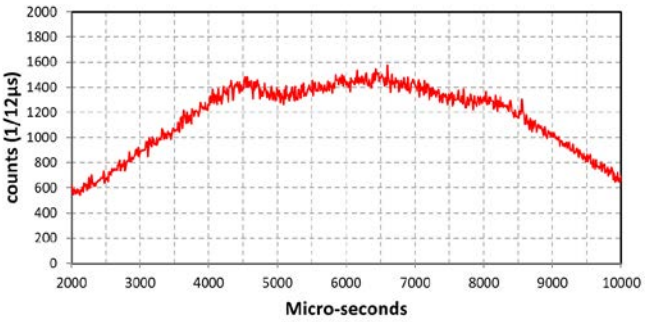

Fig. 2. Neutron events distribution of the HEU sample. The measurement time was 10 minutes with the rotation speed of 4000 rpm.

REFERENCES:

[1] K. Tanabe *et.al.,* J. nucl. sci. technol., (2022). (doi)10.1080/00223131.2022.2143449.

CO8-2 Establishment of a novel mutation breeding using Boron Neutron Capture Reaction (BNCR)

M. Kirihata, S. Segami[1], Y. Hattori, T. Kinouchi[2], Y. Kinashi[2]

Research Center of BNCT, Osaka Prefecture University

[1]Research Institute of Environment, Agriculture and Fisheries, Osaka Prefecture

[2]Institute for Integrated Radiation and Nuclear Science, Kyoto University

INTRODUCTION: Boron Neutron Capture Reaction (BNCR) is based on the nuclear reaction of ^{10}B atom with thermal/epithermal neutron already applied to cancer treatment (BNCT) [1, 2]. As a new utilization method of BNCR, this study aims to establish a novel mutation breeding using BNCR.

The method attempts mutagenesis by immersing plant seeds in a ^{10}B-enriched boron compound, re-drying, and then irradiating the seeds with thermal neutrons to induce BNCR. A similar method has been tried with barley and observed an effect in the M1 generation and a mutagenic effect in the M_2 generation [4, 5]. Its mutagenic effect depends on chemical and physical factors such as ^{10}B concentration, thermal neutron intensity, and irradiation time. In our previous experiments, they have tried immersing seeds in ^{10}B-enriched *p*-boronophenylalanine (BPA) [3] and ^{10}B-enriched boric acid ($H_3{}^{10}BO_3$) as ^{10}B-enriched boron compounds in rice. The germination rate of each treated seed was investigated after BNCR, and the results showed that there was no decrease in germination rate for BPA-treated seeds in the 1-100 mM concentration range, whereas $H_3{}^{10}BO_3$ treated seeds showed a concentration-dependent decrease in germination rate. It is assumed that these results are due to differences in the uptake of ^{10}B into plant seeds by different boric acid compounds. Currently, the effects of mutagenesis are being confirmed. This report selected disodium mercaptoundecahydrododecaborate (BSH), a boron cluster, as a new boron compound to be examined.

EXPERIMENTS: The experimental material used *Oryza sativa* L. cv. Nipponbare. The dry seeds were immersed into different boron concentrations (0, 10, 50, 100, 1000, 2000 ppm) of ^{10}B-enriched BSH for 24 h and 1000 and 2000 ppm BSH for 36 h. The solvent used was PBS buffer. The samples were washed with water and re-dried. The seeds in 6-mL tubes were irradiated with thermal neutron for 90 minutes in the Kyoto University Research Reactor (KUR). After the irradiation treatment, the seeds were cultured in petri-dishes with continual moistening of filter paper at 25°C under a photoperiod of 16 h light and 8 h dark, and the germination rate was examined 14 and 21 days after sowing. As a control experiment, seeds that were only treated with BSH soaking and not irradiated with thermal neutrons were sown in the same method, and germination rates were investigated.

RESULTS: BSH treatment did not decrease the germination rate with or without BNCR. This result is similar to BPA treatment. In $H_3{}^{10}BO_3$ treatment, seeds immersed for 24 or 36 h in solutions of 50 mM or higher concentration have been found to significantly decrease the germination rate of seeds with BNCR, in our results. These results indicate the selection of boron compounds to be used in this mutation breeding in BNCR. To determine these differential effects on germination rate, the uptake and localization of ^{10}B in seeds are currently being investigated using molecular biological techniques. In addition, the treated M1 and M2 generations are being grown sequentially in the field to investigate mutants.

REFERENCES:

[1] H. A. Soloway *et al.*, Chem. Rev., **98** (1998) 1515-1562.

[2] B. Farhood, *et al*., Rep. Pract. Oncol. Radiother., **23** (2018) 462-473.

[3] H. R. Snyder, *et al*., J. Am. Chem. Soc., **80** (1958) 835-838.

[4] Y. Ukai and A. Yamashita, Institute of Radiation Breeding Tech. News, **30** (1987).

[5] T. Morikawa, *et al*., KURRI Progress report 2012 (2013) 170.

CO9-1 Extraction chromatography and solvent extraction of Eu using TEHDGA

K. Otsu, M. Ikeno, C. Saiga, S. Takahashi, C. Kato, T. Matsumura[1], H. Suzuki[1], S. Fukutani[2] and T. Fujii

Graduate School of Engineering, Osaka University
[1]Nuclear Science and Engineering Center, Japan Atomic Energy Agency
[2]Institute for Integrated Radiation and Nuclear Science, Kyoto University

INTRODUCTION: The disposal of high level radioactive liquid waste produced from nuclear power plants is one of the main problems surrounding nuclear energy. To solve this problem, partitioning and transmutation technologies for high-level radioactive liquid waste generated from the reprocessing of spent nuclear fuel from nuclear power plants is being developed. The Japan Atomic Energy Agency (JAEA) has proposed the "SELECT Process" which involves the separation and transmutation of radioactive nuclides as a method of managing radioactive waste [e.g. 1]. The SELECT process consists of four steps, in which various extractants are used to separate minor actinides (MA) and rare earth elements (REE) from the spent nuclear fuel solution. In this study, we focused on europium (Eu), which is a REE that has two radioisotopes, ^{154}Eu and ^{155}Eu with a half-life of 8.6 years and 4.8 years respectively [2]. TEHDGA (Tetra-2-ethylhexyldiglycolamide), is a new extractant synthesized at JAEA that has both excellent extraction and separation performance for minor actinides and REE. In order to understand its chemical behavior and to compare is efficiency during different extraction methods, solvent extraction and extraction chromatography were carried out using TEHDGA on Eu.

EXPERIMENTS: The organic phase was prepared by diluting the extractant TEHDGA with a 4:1 mixed solution of n-dodecane and 1-octanol to adjust the concentration to 0.01, 0.02, 0.04 and 0.10 M. 1 ppm Eu was dissolved in 1.5 M HNO_3 for the aqueous phase. The phases were stirred for 30 mins to reach equilibrium and then separated by centrifugation. Back extraction was performed with a 0.1 M HNO_3 solution. To prepare the resin for extraction chromatography, 1 g of TEHDGA was dissolved in 50ml of ethanol (99.5% purity) to make a 0.001 M solution. 1 g of styrene divinylbenzene was added to the solution and the ethanol was evaporated. For the extraction chromatography experiment, 1.5 M HNO_3 was added to the resin and then transferred into a column. The column was attached under another column which introduced the feed solution to the resin filled column. A valve was attached between the columns to regulate the flow to ensure the resin filled column would not be saturated by the feed solution and to not disturb the resin. 10 ml of 1.5 M $Eu(NO_3)_2$ solution was introduced to the upper column and the eluted solution was collected in increments of 1 ml. For the batch experiment, a separate batch of resin was prepared with the same method and was shaken for 15 mins with 1.5 M $Eu(NO_3)_2$ and the liquid was collected. Europium concentration from all experiments were measured by Inductively Coupled Plasma Quadrupole Mass Spectrometry (ICP-QMS) at Kyoto University.

RESULTS AND DISCUSSIONS: A slope 2 correlation between the TEHDGA concentration and Eu concentration was observed (Fig. 1). This suggests that a TEHDGA : Eu = 2 : 1 complex forms in this acidity, and the following equation can be obtained.

$$Eu^{3+} + 3NO_3^- + 2TEHDGA \leftrightharpoons Eu(NO_3)_3 \cdot 2TEHDGA$$

A breakthrough curve was obtained with the extraction chromatography (Fig 2). After 5ml, the relative concentration of Eu maintains a flat peak, suggesting the resin became saturated with Eu. The number of theoretical plates was calculated as 12.2, and the height equivalent of one theoretical plane (HETP) as 2.5 mm. From the batch experiment, this value was proven to be reasonable.

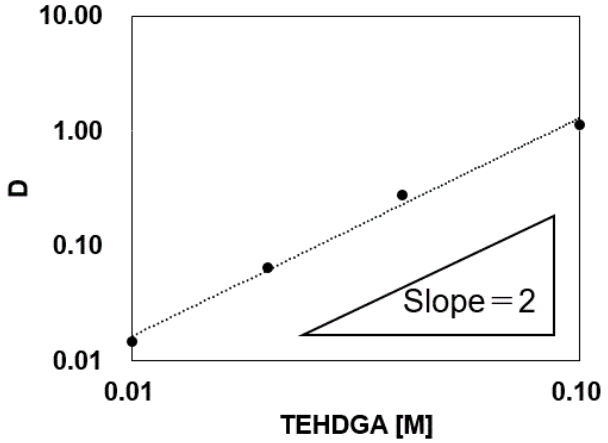

Fig. 1. Dependence of D on TEHDGA concentration for Eu.

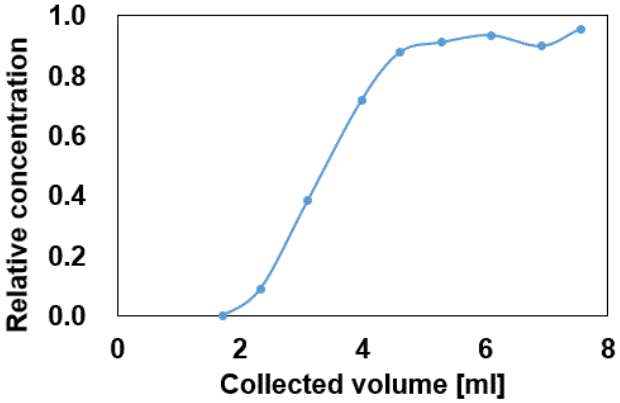

Fig. 2. Eu elution curve of extraction chromatography. Concentration is normalized to the starting Eu solution.

REFERENCES:

[1] T. Matsumura, Kino Zairyo, **40** (2020) 60-71.
[2] G. Audi. *et al.*, Nucl. Phys. A, **729** (2003) 3-128.

CO9-2 Electrochemical Behavior of U in NaCl-$CaCl_2$ Melt at 823 K

T. Murakami, Y. Sakamura and K. Takamiya[1]

Central Research Institute of Electric Power Industry
[1]Institute for Integrated Radiation and Nuclear Science, Kyoto University

INTRODUCTION: The mixture of NaCl and $CaCl_2$ is one of the promising candidates as the base salt for molten chloride salt fast reactor from the viewpoints of melting point, solubility of actinides, applicability to reprocessing, restraining of radioactive elements formation by irradiation and so on. Electrochemical properties of actinides in the melt are required for constructing a reprocessing process of the spent molten chloride fuel salt. However, reports on electrochemical measurements of actinides in NaCl-$CaCl_2$ melt [1, 2] are very limited. Thus, this study investigated electrochemical behavior of U to evaluate the redox potential of U in eutectic NaCl-$CaCl_2$ melt at 823 K.

EXPERIMENTS: All experiments were performed in a glove box filled with purified Ar gas. Eutectic NaCl-$CaCl_2$ melt containing UCl_3 was prepared as follows. NaCl (23.4 g), $CaCl_2$ (48.1 g) and $CdCl_2$ (0.587 g) were loaded in an alumina crucible and melted at 823 K. A U metal rod (36.0 g) was immersed in the melt for overnight to form UCl_3 in the melt,

$$2U + 3CdCl_2 \rightarrow 2UCl_3 + 3Cd \quad (1)$$

Gibbs energy of reaction 1 is -577 kJ at 823 K [3] suggesting that almost all of $CdCl_2$ was consumed to dissolve U. Thus, the resulting concentration of UCl_3 in the melt was calculated to be 0.255 mol% based on reaction 1. The remained U metal rod was recovered after the completion of the reaction.

Electrochemical measurements were performed in the prepared melt at 823 K. The working electrode was W wire (1 mmφ). The Ag/AgCl reference electrode was used, of which potential was -1.255 V (vs. Cl_2/Cl^-). Glassy carbon rod (3 mmφ) was used as the counter electrode.

RESULTS: Fig. 1 shows cyclic voltammogram of W wire electrode in the melt. A cathodic current, c1, increasing from around -2.5 V (vs. Cl_2/Cl^-) was ascribed to U metal deposition (reaction 2),

$$U^{3+} + 3e^- \rightarrow U \quad (2)$$

The corresponding anodic current, a1, was due to the dissolution of the deposited U (reverse reaction of reaction 2). A broad cathodic (c2) and anodic (a2) current couple at around -1.2 V was considered to correspond to the following reaction,

$$U^{4+} + e^- = U^{3+} \quad (3)$$

The additional cathodic (c3) and anodic (a3) currents might be due to U adsorption and desorption, respectively.

Based on the results of the cyclic voltammetry, galvanostatic electrolysis at -10 mA was performed for 10 seconds to deposit U metal on the W wire electrode. Then, the applied current was set at 0 mA to measure the redox potential of the U metal on the W in NaCl-$CaCl_2$-0.255mol%UCl_3 melt. By using the measured redox potential (E = -2.466 V), the formal standard redox potential ($E^{0\prime}$) was calculated to be -2.325 V according to the following Nernst equation of reaction 2,

$$E = E^{0\prime} + \frac{RT}{3F}\ln C_{UCl3} \quad (4)$$

R is gas constant, T is temperature in Kelvin, F is faraday constant, C_{UCl3} is the concentration of UCl_3 in the melt. The obtained formal standard redox potential in NaCl-$CaCl_2$ melt (-2.325 V) was higher than that in LiCl-KCl melt (-2.466 V [4]). The difference in the formal standard redox potential indicated the stability of U^{3+} could depend on the cations of the solvent.

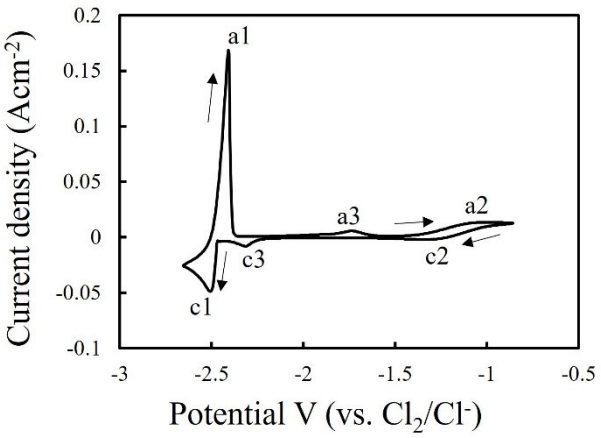

Fig. 1. Cyclic voltammogram of the W wire electrode in NaCl-$CaCl_2$ melt containing 0.255 mol% UCl_3 at 823 K. Scan rate was 50 mV・s^{-1}.

REFERENCES:

[1] H. Zhang *et al.*, J. Electrochem. Soc., **168** (2021) 056521.
[2] M. L. Newton *et al.*, ECS Trans., **98** (2020) 19-25.
[3] C. W. Bale *et al.,* FactSage Thermochemical Software and Databases, 2010-2016, Calphad, **54**, (2016) 35-53 <www.factsage.com>.
[4] P. Masset *et al*., J. Electrochem. Soc., **152** (2005) A1109-A1115.

CO9-3 Solid phase analysis of $(Zr,Ce)O_2$ solid solutions in aqueous systems

T. Kobayashi, Y. Sato, T. Sasaki, S. Sekimoto[1], K. Takamiya[2]

Graduate School of Engineering, Kyoto University
[1] Institute for Integrated Radiation and Nuclear Science, Kyoto University

INTRODUCTION: It is important to understand the solubility behavior of $(Zr,U)O_2$ solid solution in aqueous systems for the management of nuclear fuel debris generated in the Fukushima Daiichi Nuclear Power Plant accident since $(Zr,U)O_2$ solid solution is one of the possible major components of the debris. Many studies have been dedicated to establishing a robust thermodynamic model to quantitatively explain the solubility of ZrO_2 and UO_2, while less is known for the solubility of mixed systems. In the present study, we focused on $(Zr,Ce)O_2$ solid solution as an analog of $(Zr,U)O_2$ solid solution. In the phase diagram of $(Zr,Ce)O_2$ solid solution at 1000 ℃, for example, pure ZrO_2 exhibits a monoclinic phase, and tetragonal ZrO_2 and cubic CeO_2 phases appear with increasing Ce molar ratio [1]. This trend is similar to that observed in the phase diagram of $(Zr,U)O_2$ solid solution [2]. In this study, $(Zr,Ce)O_2$ solid solution was prepared with the molar ratio of Zr/Ce = 7/3 at 1000 ℃ and characterized using powder X-ray diffraction (XRD) . Then, the solid phase was placed into aqueous sample solutions under reducing conditions ranging from pH 0.8 to 8.0 for several months. After the immersion of given periods, the solid phase was separated, dried and investigated by powder XRD to elucidate the change in the state of solid phase and discuss their solubility behavior.

EXPERIMENTS: Acidic stock solutions of Zr(IV) nitrate and Ce(IV) nitrate were prepared and mixed with the molar ratio of Zr/Ce = 7/3. Portions of concentrated polyvinyl alcohol (PVA) were added to the mixed solution and heated to dryness at 200 ℃. The dried powder was then heated at 1000 ℃ for 4 hours in a muffle furnace to synthesize $(Zr,Ce)O_2$ solid solution. The preparation method is known as a polymeric steric entrapment method, which enables synthesizing of metal oxide solid solution at a lower temperature [3]. The powder XRD pattern of the synthesized solid phase is shown in Fig. 1. Diffraction peaks corresponding to tetragonal ZrO_2 and cubic CeO_2 were observed in the pattern, indicating that the solid phase is a mixture. This solid phase was put into polypropylene sample tubes and aqueous solutions ranging from pH 0.8 to 8.0 with the ionic strength (I) of I = 0.5 by $NaClO_4$ were added to the sample tubes. It is noted that to enhance the dissolution of Ce in the solid phase, 1 mM $Sn(II)Cl_2$ was added as a reducing chemical. After several months, the solid phase was separated, dried in a vacuum dedicator, and investigated using powder XRD.

RESULTS AND DISCUSSION: Figure 1 shows the powder XRD patterns of the solid phase after the immersion of the sample solution at pH 1.1 and after the immersion without Sn(II). It is noted that a peak corresponding to cubic CeO_2 at $2\theta = 29°$ in the diffraction patterns of pH 1.1 with Sn(II) became more clear compared to that in the patterns without Sn(II) and before immersion. This suggests the possible transformation of the solid phase by contacting the reducing aqueous solution. For more detailed analysis, the diffraction patterns were analyzed using Rietveld refinement. For the initial synthesized solid phase, the obtained lattice parameter as cubic CeO_2 was slightly smaller than that of pure cubic CeO_2, indicating a portion of Zr incorporated into the cubic phase to form a cubic CeO_2-based solid solution.
Similarly, ZrO_2 was considered a tetragonal ZrO_2-based solid solution, which agreed with the reported phase diagram [1]. The lattice parameters of the solid phase after the immersion without Sn(II) were the same as those of the solid phase before the immersion. In contrast, the lattice parameter of cubic CeO_2 was found to increase after the immersion at pH 1.1 with Sn(II). The composition of cubic CeO_2-based solid solution changed to decrease the Zr ratio in the solid solution. Since the change is only observed in the presence of Sn(II), the redox reaction of Ce(IV) in the solid phase may be involved. Further studies are needed to clarify the solubility behavior of $(Zr,Ce)O_2$ solid solution.

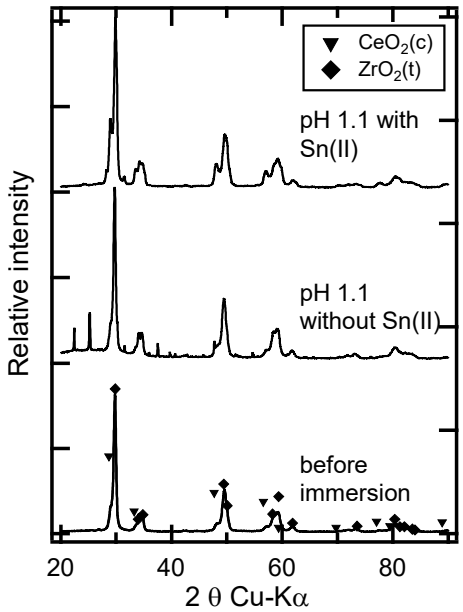

Fig. 1. Powder XRD patterns of $(Zr,Ce)O_2$ solid solution before and after the immersion in aqueous systems.

REFERENCES:

[1] M. Yashima *et al.*, J. Am. Cer. Soc., **77** (1994) 1869-1874.
[2] P.E. Evans, J. Am. Cer. Soc., **43** (1960) 443-447.
[3] M.H. Nguyen *et al.,* J. Mater. Res., 14 (1999) 3417-3426.

CO9-4 Solid-liquid extraction and precipitation experiments of ^{47}Ca for the chemical study of nobelium

Y. Kasamatsu,[1, 2] R. Wang, [1, 2] Y. Itakura, [1, 2]
E. Watanabe,[1, 2] R. Nakanishi,[1,2] S. Otaka,[1,2] K. Takamiya[3] and A. Shinohara[4, 5]

[1]*Graduate School of Science, Osaka University*
[2]*RIKEN Nishina Center for Accelerator-Based Science*
[3]*Institute for Integrated Radiation and Nuclear Science, Kyoto University*
[4]*Institute for Radiation Science, Osaka University*
[5]*Osaka Aoyama University*

INTRODUCTION: Element 102, nobelium (No) is a member of actinide elements. While other f-block elements stably exist at +3 or higher valence states in aqueous solutions, No is reportred to form +2 valence state stably because of its electronic configuration: [Rn]5f^{14} 7s^2. In previous ion-exchange experiments, No is reported to exhibit similar chemical behavior to that of Ca^{2+} and Sr^{2+} [1]. Our group has recently suggested that No^{2+} shows different behavior from alkaline earth metal ions, in the samarium hydroxide coprecipitation [2]. Further systematic studies are needed on the No^{2+} comparing with group 2 elements.

In this study, we investigated precipitation behaviors of Ca, Sr, and Ba maleate and acetylacetonate to find suitable conditions for coprecitation experiment of No.

In addition, we consider that the complexes of No having clear molecular structure in the solution should be selected to investigated the chemical properties of No because in the discussion on the data of No theoretical supports are of significant importance. We focus on solid-liquid extraction using crown ether, and have indeed performed extraction experiments with Sr resin which is commercially available crown-ether supported resin. The crown ether has extraction selectivity for alkaline earth ions, and this selectivity is sensitive to ligan ions in the aqueous solutions subh as Cl^- and NO_3^- [3,4]. In addition, we plan to use the other type of crown ether resins which have reaction groups. In this study, we performed extraction experiment of Ca using crown ether resin having nitro or carboxyl group for future No extraction experiment.

EXPERIMENTS: In precipitation experiment, first 20 mL of aqueous solutions containing Sr, Ba or Ca (5 mg) were mixed with 20 mL of 0.5 M potassium maleate or 1 M acetylacetone in ethanol, and shaken for 10–1440 min. Then, the precipitate was filtrated on a polypropylene memblane filter. For Ca sample, ^{47}Ca radiotracer was added. ^{47}Ca was produced by neutron irradiation to ^{nat}CaO powder at KURNS and chemically purified before the precipitation expeirments.

In solid-liquid extraction, 0.5 mL of 2 M HCl solutions containing ^{47}Ca tracer was contacted with 50 mg of nitro or calboxyl resins for 1-30 min. Afterthat, the resin and solution was separated through a filter unit. We synthesized the resins used in this experiment.

After the precipitation and extraction experiments, the samples were subjected to γ-ray measurement with a Ge semiconductor detector to measure the amount of ^{47}Ca. precipitation yields were estimated form the counts. In extraction, the distribution coefficients, K_d, were calculated by the equation

$$K_d = (A_{STD} - A_s)V / A_s w,$$

where A_s and A_{STD} are radioactivities of the aqueous phase of the extraction sample and the control sample which was obtained in the extraction without the resin. V is the volume of the aqueous phase (mL), and w is the mass of the dry resin (g).

RESULTS: In the precipitation experiment, almost 0% yields were obtained under all experimental conditions. When pH of the solution was higher, we were able to see the formation of precipitates for Sr and Ba; however, we cannot exclude the possibility of formation of hydroxide precipitates in high pH solutions. In conclusion, we did not find suitable experimental conditions to investigate the maleate and acetylacetone precipitation of No.

In extraction experiment, the K_d values of ^{47}Ca were almost constant for shaking time from 1 to 30 min. This result indicates that the chemical reactions involved in the present complexation and extraction are sufficiently fast for the investigation of extraction behavior of ^{255}No whose half-life is about 3 min. Though the K_d values for nitro resin were slightly lower than those for calboxyl resin, the all values were similar and indeed range in 3-9 g/mL. For detailed discussion, further experiments in various concentrations of HCl and other acids are needed. In addition, we plan to perform extraction experiments using radiotracers of other group 2 elements. Based on the obtained data, we want to find suitable experimental conditions for extraction of No.

REFERENCES:

[1] R. Silva *et al.*, Inorg. Chem., **13** (1974) 2233.
[2] H. Ninomiya, Master thesis, Osaka Univ. (2019).
[3] E. P. Horwitz *et al.,* Solv. Extr. Ion Exch., **10** (1992) 313.
[4] D. V. Filosofov *et al.,* Solv. Extr. Ion Exch., **33** (2015) 496.

CO9-5 Stability of Cyclic Monoamide Extractants for U(VI) with Longer Side Chains against γ-Ray Irradiation in HNO_3

H. Kita[1], R. Hamashiro[1], M. Nogami[2], and N. Sato[3]

[1]*Graduate School of Science and Engineering Research, Kindai University*
[2]*Faculty of Science and Engineering, Kindai University*
[3] *Institute for Integrated Radiation and Nuclear Science, Kyoto University*

INTRODUCTION: Uranium is the predominantly major component in spent fuels, and novel extractants with high selectivity and capacity for U(VI) and radiation stability in nitric acid media are desired in the world. Our attention as candidate extractants has been paid for 1,3-dialkyl-2-pyrrolidone (DRP) (Fig. 1), one of cyclic monoamide compounds, and previously stability against γ-ray irradiation for DRPs with straight and relatively shorter R and R', i.e., 1,3-dibutyl-2-pyrrolidone (DBP : R, R' = $-C_4H_9$) and 1,3-dihexyl-2-pyrrolidone (DHP : R, R' = $-C_6H_{13}$), was investigated[1]. In this study, DRPs with relatively longer R and R', *i.e.*, 1,3-dioctyl-2-pyrrolidone (DOP : R, R' = $-C_8H_{17}$), 1,3-didodecyl-2-pyrrolidone (DDP : R, R' = $-C_{12}H_{25}$), and 1,3-di(2-ethylhexyl)-2-pyrrolidone (DEhP : R, R' = $-C_8H_{17}$) was similarly studied.

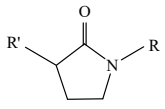

(R, R': hydrocarbon group)

Fig. 1. Chemical structure of DRP.

EXPERIMENTS: Among the above-mentioned five DRPs, only DDP is present as solid at room temperature and the other four are liquid. For the sample for γ-ray irradiation to DRPs, solutions consisting of 30 vol% DRP in *n*- dodecane as the organic phase and 3 or 6 mol/dm^3 (= M) HNO_3 as the aqueous phase were prepared in a Pyrex tube (O/A=1 (v/v)). Irradiation was carried out by the ^{60}Co source up to ca. 1.1 MGy at room temperature under ambient atmosphere similarly to the earlier study[1]. Organic phases of the irradiated samples were then analyzed by ^{1}H NMR using $CDCl_3$ and tetramethylsilane (TMS) as solvent and internal standard material, respectively. The residual ratios of DRPs were calculated by the area ratio of each signal in DRPs with that of TMS.

RESULTS: In a ^{1}H NMR spectrum, neat DRP shows several signals, e.g., (A)1.7, (B)2.2, (C)3.3 ppm for DEhP. The residual ratios for DEhP irradiated with 3 and 6 M HNO_3, respectively, were calculated from each signal and are shown in Fig. 3 together with the relationship between the position of hydrogen in the structure of DEhP and that of the signal. It can be seen for both HNO_3 concentrations that the residual ratios are decreased linearly and similarly with increasing dose up to ca. 1 MGy. Also, there is little difference in the residual ratio among the position (A) through (C).

In case of DHP[1], the residual ratios of ca. 50 % were obtained after irradiation with 6 M HNO_3 at ca. 0.75 MGy, which is similar to the result for DEhP. However, unlike the case for DEhP, the residual ratios at pyrrolidone ring (corresponding to the positions (B) and (C) in Fig. 2) were apparently lower than those at the side chains. On the contrary, for the sample irradiated with 3 M HNO_3, nearly no decomposition occurred after irradiation at ca. 0.8 MGy, which is a different trend compared with DEhP.

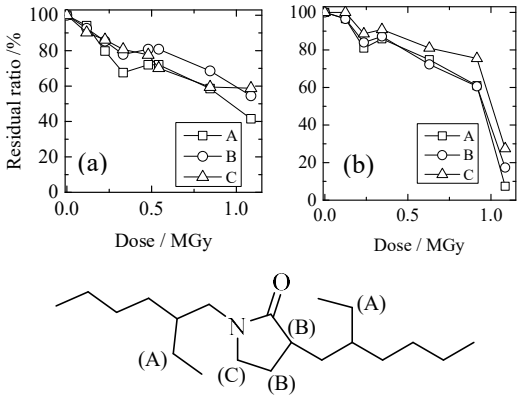

Fig.2. Dependence of residual ratio of DEhP on dose; (a) 3 M HNO_3, (b) 6 M HNO_3 and chemical structure of DEhP.

The results for DOP and DDP obtained in a similar manner to DEhP are shown in Table 1. Summarizing these results, in general, the samples irradiated with 3 M HNO_3 are more stable than those irradiated with 6 M HNO_3. This is in accordance with the results for water-soluble *N*-butylpyrrolidone (NBP) which has similar chemical structure to DRPs[2].

The relationship between the chemical structure of DRP and the stability remains unclear and further investigation would be necessary.

Table 1. Relationship between dose and residual ratio of DOP and DDP.

DRP	Dose / MGy	[HNO_3] / M	Residual ratio / %
DOP	0.79	3	65
DOP	0.83	6	40
DDP	0.71	6	60

REFERENCES:

[1] Y. Uemoto *et al.,* KURRI Progress Report 2015, (2016) CO9-1.
[2] M. Nogami *et al.,* Sci. China Chem., **55** (2012) 1739-1745.

CO10-1 Application of KURAMA-II to Radiation Monitoring of Soil Separation Facilities in Fukushima Prefecture

A. Maekawa, H.Hada[1], H. Inoue and M. Tanigaki[2]

Fukushima Prefectural Centre for Environmental Creation
[1]Interim Storage Facility and Decontamination Management Division, Fukushima Prefectural Government
[2]Institute for Integrated Radiation and Nuclear Science, Kyoto University

INTRODUCTION: KURAMA (Kyoto University RAdiation MApping system)-II is a radiation measurement system characterized by its compactness, autonomous operation, and acquisition of pulse-height spectrum data (Fig. 1) [1]. KURAMA-II measures ambient dose equivalent rate (hereafter referred to as air dose rate) and GPS position and automatically transmits them to a dedicated cloud server. We used a backpack-style KURAMA-II (Fig. 2) for the radiation monitoring of soil separation facilities in an interim storage facility to assess whether the radioactive material was scattered under demolition.

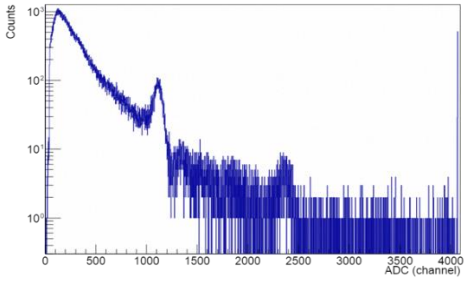

Fig. 1. A typical example of pulse-height spectrum obtained by KURAMA-II measurement.

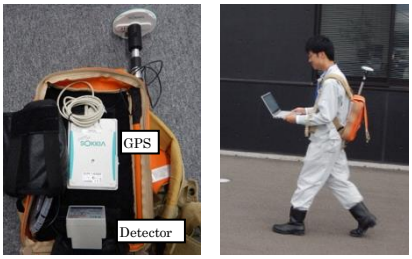

Fig. 2. KURAMA-II in a backpack.

EXPERIMENTS: The air dose rates of two soil separation facilities (facility A and facility B) were measured on foot with a KURAMA-II in a backpack. The date of the measurement and the demolition period are shown in Table 1.

Table 1. The date of the measurement and the demolition period.

	Facility A	Facility B
Demolition	Apr. 2022 - Nov. 2022	Jun. 2022 - Oct. 2022
1st measurement	13 Jul. 2022	13 Jul. 2022
2nd measurement	16 Dec. 2022	16 Dec. 2022

A CsI (Tl) scintillation detector (C12137-4034, Hamamatsu Photonics) was used for measurement. The air dose rate and GPS position were measured every second. For 1st measurement, the air dose rate was measured by walking along the facility's boundary under demolition. After the demolition, 2nd measurement was carried out in the whole area of the facility. The measurement data were averaged in a 15-meter mesh and visualized to the colored air dose rate maps using GIS software (QGIS 3.20.3). Several points of the boundaries of facilities were measured by a NaI (Tl) scintillation survey meter.

RESULTS: The air dose rate maps are shown in Fig.3-6, and the ranges of the air dose rate are summarized in Table 2. No apparent differences were found between 1st and 2nd measurements at both facilities. KURAMA-II results were comparable to those of the survey meter. As shown in Fig.5 and 6, no apparent contamination was found in the study area. In conclusion, no clear effect of the demolition of the soil separation facilities on the air dose rate was found in the present study.

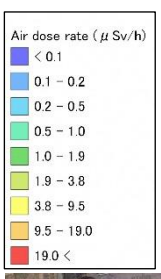

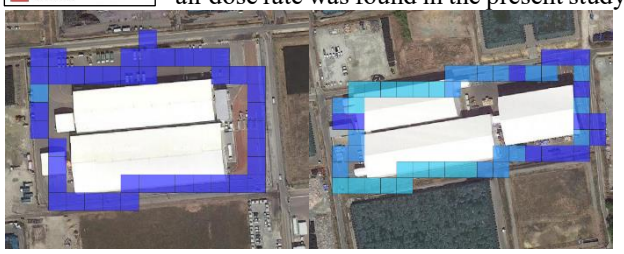

Fig. 3. 1st measurement at facility A.

Fig. 4. 1st measurement at facility B.

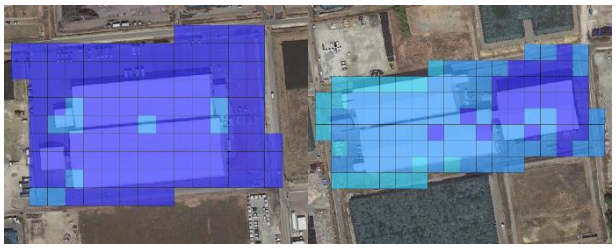

Fig. 5. 2nd measurement at facility A.

Fig. 6. 2nd measurement at facility B.

Table 2. The air dose rates measured by KURAMA-II and by survey meter (μSv/h). The range of KURAMA-II (1st) was calculated from the mesh measured in both measurements.

	Method	Facility A	Facility B
1st	KURAMA-II	0.06-0.11	0.07-0.40
	Survey meter	0.08-0.11	0.11-0.28
2nd	KURAMA-II	0.07-0.11	0.09-0.35
	Survey meter	0.08-0.12	0.10-0.33

REFERENCES:

[1] M. Tanigaki *et al.*, Nucl. Instrum. Meth. Phys. Res., **781** (2015) 57-64.

R4016

CO10-2 Effective Measures on Safety, Security, Hygiene and Disaster Prevention in Laboratories

T. Iimoto[1], M.M. Hasan[1], H. Koike[1], Y. Cai[1], T. Miyazaki[1], K. Takamiya[2]

[1] *The University of Tokyo*

[2] *Institute for Integrated Radiation and Nuclear Science, Kyoto University*

INTRODUCTION:

Important aspects of the study can be found in the following keywords, such as safety, security, hygiene and disaster prevention. Nuclear research reactor is one of representative facilities together with these keywords under their operation. It is effective to investigate the latest status on practical measures on these keywords in various facilities including nuclear research reactors, to compare each other among facilities, and to discuss more optimized ones for our positive safety management. Through this process, it is also essential to investigate the latest international and/or national regulations and the movement of revision of them. In addition, development of human resource and public literacy on nuclear science and technology is also within the scope of the research. The total discussion contents and their fruits are directly useful for all relating laboratories.

RESEARCH APPROACH:

General research approach is as follows.

- Measures of safety management during operation or standstill status of the real facilities would be investigated. This information would be used for our research discussion on the positive and more optimized safety management.
- It would not be a single year research, but maybe two to three years research for one theme.
- Information source of facilities would not be only KUR, KUCA or the other facilities in Kyoto University, but also the Kindai university research nuclear reactor or the facility of National Institute of Fusion Science, etc. This research is an active joint-research with these relating facilities and positive researchers on safety management.
- One of the distinctive features of this research is to involve office staffs as cooperators as well as researchers and technical staffs. In The University of Tokyo, most of the members in Division for Environment, Health and Safety are office staffs who knows real situation of safety management in laboratories very well.

Concrete discussion target in FY of 2022 was determined as the followings; “developing a set of educational videos for safety managers and researchers in universities using accelerators” and “analysis of effects on radiation education in secondary schools.

DEVELOPING EDUCATIONAL VIDEOS IN UNIV. FOR USERS OF ACCEARATORS:

A refresher training videos "Accelerator Safety Application for Radiation Workers in The University of Tokyo” were produced. With the cooperation of the managers and experts of the off-campus facilities (e.g. J-PARC and KEK), the contents were carefully examined and included features and safety points for each facility that should be communicated to radiation workers in advance, not only for radiation workers of the facilities at The University of Tokyo, but also for ones sent to the off-campus facilities.

The educational items were subdivided into the following six issues, which were presented as short videos of 5 to 8 minutes each, with a maximum overall duration of 45 minutes or less. These are (1) types and characteristics of accelerators, (2) safe handling of accelerators, (3) examples of accidents and troubles related to accelerators, (4) on-campus accelerator facility - MALT section, (5) domestic accelerator facilities - J -PARC, and (6) domestic accelerator facilities -KEK. Each facility section of (4) to (6) includes facility features, main research achievements, safety considerations and a message from the administrator.

ANALYSIS OF RADIATION EDUCATION EFFECTS IN SECONDARY SCHOOL

A questionnaire survey of secondary schools and their teachers in eight countries in the Asia-Pacific region, including Japan, was conducted from around the end of 2020 to the end of 2021. The survey asked about the teachers' values on radiation, an overview of the actual implementation of the lessons (e.g. the content of each item), and the students' impressions, knowledge and interest in radiation.

We analyzed the results of questionnaires on the effectiveness of radiation education in secondary schools. The degree to which students perceive radiation as ”Interesting” became stronger after the STEAM radiation lecture. Radiation education with the WOW factor is effective. In the analysis of changes in students’ impressions based on teacher characteristics, teachers who perceive radiation as ”Simple” or ”Easy to be understood” are more likely to teach radiation basics attractively. On the other hand, in the overall analysis, the degree to which students perceive radiation as ”Interesting” or ”Easy to understand” decreased when taught by the teacher who perceive it as “Good”. It is possible the students were influenced negatively by the teachers' strong impressions and messages.

R4085

CO10-3 Study of Penetration/Leaching Behavior from Concrete Contaminated with Cs -Analysis of changes in mortar structure accompanied by dry-wet cycles-

K. Kondo[1] and I. Sato[1]

[1]*Tokyo City University*

INTRODUCTION: Cesium (Cs) penetration/leaching experiments on concrete of reactor containment structural materials are contributed to understanding of contamination mechanism by radioactive materials, which is one of six important issues identified by the Nuclear Damage Compensation and Decommissioning Facilitation Corporation (NDF). The contaminated concretes are exposed to the environment changes, which means that Cs concentration behavior may changes.

EXPERIMENTS: Mortar specimens (without aggregates) were made with ordinary Portland cement (W/C=0.37, S/C=2.1) in a cubic of 15mm×15mm×15mm. They were embedded into acrylic resin, so that only one surface remains for penetration/leaching of Cs. The Cs penetration solution (15 ml) was CsOH solution adjusted to 10^{-2}M. Table 1 shows four dry and wet conditions given to mortars. For example, a penetration experiment using mortar given condition 1 was named P1 and a leaching experiment was named L1, and P1-P4 and L1-L4 were prepared. The mortars of P1-P4 were soaked in CsOH solution for 15 days for penetration. Mortars of L1-L4 were soaked in CsOH solution for 15 days for penetration and then in water for 15 days for leaching. After the experiments, the mortars were scraped with sandpaper (particle size: #60) to powder. The powders were analyzed by INAA to determine amounts of Cs remaining in them.

RESULTS&DISCUSSION: Fig.1 shows results of the penetration experiments. The number of times the mortar was dried is written after "d " in the figure, and the number of times it was wetted after "w". The penetration experiment results for P1-P4 showed the amount of Cs was greater at depth than at the surface. This is possibly due to the fact only the powder collected at a depth of 0.5 mm from the mortar surface had a higher percentage of acrylic resin, resulting in smaller amount of Cs. Fig.2 shows the results of the leaching experiments. In the leaching experiment CsOH solution in contact with the mortar surface would change from CsOH solution to water containing no Cs, resulting in a larger concentration gradient. If the migration of Cs was considered to proportional to the concentration gradient, it is assumed that Cs concentration decreases near the surface and is relatively higher inside, like a "mountain" distribution. Then, the Cs concentration distribution "flatten" by concentration gradient. The leaching experiments showed such a profile, but the position of the "mountain" differed depending on the number of dry/wet cycle. If the mortar given a dry/wet cycle is regarded to migrate Cs greater [1], leaching is more advanced in profiles L3 and L4 than in profiles L1 and L2. It suggests a change in the position of "mountain". As the cause of this penetration and leaching behavior, it is possible that the different number of dry/wet cycles may complicate the diffusion phenomenon by physically and chemically changing the mortar structure. Examples include capillary action and hydration reactions. It is thought Cs migration to be influenced not only by diffusion through water filled paths, but also by the dry/wet cycle and moisture conditions [2].

In the future, our team conduct the following to study the detailed concrete structure and Cs penetration/leaching behavior. (a) Simulation and calculation of Cs permeation/leaching behavior (FEM analysis).
(b) Estimation of Cs and major elements (Fe, Ca, Si, Al) of concrete by setting irradiation time and decay time in detail with INAA. (c) Investigate microstructure by pouring fluorescent paint into concrete.

Table.1. Four dry and wet conditions given to the mortar.

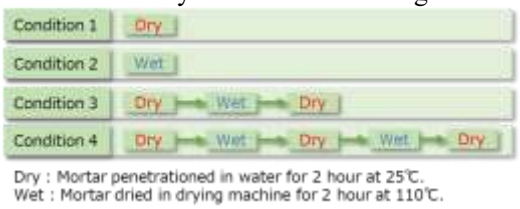

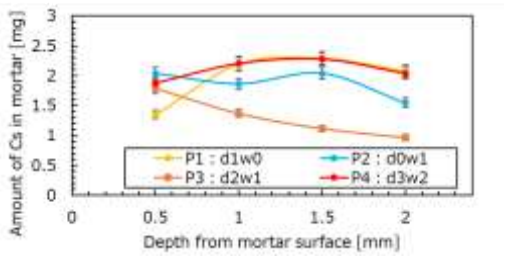

Fig.1. Amount of Cs present at each mortar depth in the penetration experiment.

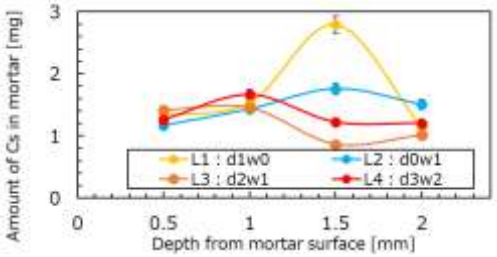

Fig.2. Amount of Cs present at each mortar depth in the leaching experiment.

REFERENCES:

[1] S. Bioubakhsh, Ph.D. Thesis, UCL (University College London) (2011).
[2] T. Kaneko *et al.*, J. Struct. Constr. Eng., AIJ, **79(70)** (2014)1073-1079.

CO10-4 Modeling of slope-directed migration of Cs in forest soils

Y. Motoie[1], H. Miyata[1], M. Yoneda[1], Y. Shimada[1], S. Fukutani[2], M. Ikegami[2]

[1]*Graduate School of Engineering, Kyoto University*
[2]*Institute for Integrated Radiation and Nuclear Science, Kyoto University*

INTRODUCTION: A previous study on quantitative evaluation of air dose rates in forest was conducted by Miyata et al.[1] for the evaluation of the effectiveness of decontamination in a forest using the point-decay nuclear integration method. In this calculation, the distribution of Cs concentration in soil in the forest was assumed to be the same in all locations, and the distribution in the direction of the slope was not considered. As a result, the calculated air dose rates underestimated the measured ones, especially at the monitoring points located at the bottom of the slope, and the error of air dose rate between the calculated and measured values was large. In this study, we developed a model to estimate the slope directional distribution of radioactive Cs in forest soils, and validated it by comparing it with the measured air dose rate.

MODEL FOR SLOPE MOVEMENT OF Cs: Advection of Cs-sorbed soil particles by subsoil flow was considered as a mechanism that causes the distribution of radioactive Cs concentrations in forest soils in the slope direction. In this study, the slope is divided into n compartments, and Cs in soil particles is considered to move from the top to the bottom of the slope due to the movement of soil particles from the solid phase to the liquid phase caused by rainfall and the movement of water from the top to the bottom of the slope. We then construct a simultaneous ordinary differential equation that shows the amount of change in radioactivity per unit time in each compartment due to advection. By solving the equations, the Cs concentration in the soil at the end of rainfall is calculated. Then, assuming that all soil particles in the water return to the solid phase after the end of rainfall, we calculate the distribution of Cs concentration in the soil at the desired date and time by repeating the simulation of multiple rainfall events. The amount of Cs transferred per unit time into the water in the i-th compartment due to the transfer of soil particles from the solid phase to the liquid phase, P_i, is calculated by the following equation:

$$P_i = \alpha (1-\phi) DL\cos\theta \cdot \rho S_i^{o} e^{-\alpha t} \quad (1)$$

where, S_i^{o}:Radioactivity concentration in unit soil mass in the i-th compartment at the start of rainfall; t:Time since the start of rainfall; D:Cross-sectional area of the x-sectional slope; L:Slope length of each compartment, ϕ:Porosity of soil, ρ :Density of soil solid phase; θ : Maximum slope angle; α :Coefficient of radioactive runoff. α is a coefficient that expresses how much of the amount of radioactivity in a unit volume is flown up into the flowing water in a unit time, and is calculated by the following formula.

$$\alpha = (E_s S_m)/((1-\phi)\rho S_x) \quad (2)$$

where, α :Coefficient of radioactive runoff (1/s); E_s: Amount of soil flow per unit volume and per unit time ($g/m^3/s$); S_m:Radioactivity concentration in unit mass of soil which flowed away (Bq/g); S_x:Radioactivity concentration in unit mass of soil before the flow (Bq/g); $(1-\phi)\rho$:Apparent density of soil (g/m^3).

The unit time transfer of Cs from the i-th compartment to the i+1-th compartment due to the movement of water from the top to the bottom of the slope, $A_{i,i+1}$, is calculated by the following formula:

$$A_{i,i+1} = \phi \gamma C_i q_i D \quad (3)$$

where, C_i:Cs concentration in water in the i-th compartment; q_i: Flow rate per unit area in the i-th compartment; D:Cross-sectional area of slope in x-section; Φ:Porosity of soil; γ :Coefficient of velocity of particle movement relative to water.

The flow rate q_i in the i-th compartment due to rainfall shown in equation (3) is assumed to be calculated by the following equation:

$$q_i = (p' x_i)/d \quad (4)$$

where, q_i:Flow rate per unit area in the i-th compartment; x_i:x-coordinate of the center of the i-th compartment; d:Slope depth at which soil particle movement occurs due to rainfall; p':(Daily precipitation during rainfall) - (average daily evaporation).

As shown in equation (4), the flow rate q_i is assumed to increase in proportion to the distance x from the top of the slope, but we assumed that the flow rate q_i reach maximum value at about 40m from the top of the slope. The slope depth d, at which soil particles move due to rainfall, is set to 10 cm in this study.

RESULTS AND DISCUSSION: The soil runoff E_s in equation (2) was measured in an actual forest. Other parameters and rainfall values were obtained from the model of Miyata et al. The calculated values were compared with the distribution of Cs concentration in soil obtained by fitting the measured values of air dose rate, assuming a linear change of Cs concentration in soil in the slope direction. As a result, the distribution of Cs concentration in soil was significantly different from the distribution of Cs concentration obtained by fitting to air dose rates. The value of α that produces a distribution similar to the Cs concentration distribution in soil obtained by fitting to the measured air dose rates was 1200 times larger than the value of α determined from the measured soil flux. One of the reason for the much larger value of α was thought that Cs was more abundant near the ground surface immediately after the nuclear power plant accident, and the amount of Cs migration due to slope movement of soil particles caused by rainfall may have been much larger than the average soil runoff velocity obtained in this study.

REFERENCES:

[1] H. Miyata *et al.*, The 11th Environmental Radiation Decontamination Research Conference, Koriyama City, Japan (2022) S3-5.

CO10-5 Geological Standard Samples for Elemental Analysis of Accelerator Concrete

G. Yoshida, K. Nishikawa[1], T. N. Bui[2], K. Tsugane, H. Yashima[3], M. Inagaki[3], T. Miura, A. Toyoda, H. Nakamura, H. Matsumura, and K. Masumoto

Radiation Science Center, KEK
[1] Quantum Life and Medical Science Directorate, QST
[2] The Graduate University for Advanced Studies, SOKENDAI
[3] Institute for Integrated Radiation and Nuclear Science, Kyoto University

INTRODUCTION: Concrete, which constitutes the building of accelerator facilities, accounts for the almost mass in the facility. Therefore, whether the concrete is activated or not will affect the amount of radioactive waste generated, which will become apparent as a cost when the facility is decommissioned. Especially, long-lived nuclides of ^{152}Eu and ^{60}Co would become problematic as waste. We have investigated the elemental concentrations of natural Eu and Co in concrete from various accelerator facilities in Japan, the origin of ^{152}Eu and ^{60}Co, by neutron activation analysis [1]. The elemental concentrations have been determined as relative values using two types of igneous rock standards, JA-1 and JG-3. Whereas concrete is a mixture of cement and some aggregates, and it might contain various materials other than igneous rock. To further discuss the elemental composition of accelerator concrete, we have irradiated various geological standard samples such as sedimentary rock, sand, and fly ash and compared the irradiation results with those of concrete.

EXPERIMENTS: The irradiated samples are as follows. Seven igneous rocks: JA-1, JB-1b, JG-1, JGb-1, JGb-2, JR-1, JR-2. Two sedimentary rocks: JSl-1, JSl-2. Three river and lake sediments: JLk-1, JSd-2, JSd-3. Three soil and other samples: JSO-1, JCFA-1, JMn-1. These are summarized in Table 1. All samples were weighed 100 mg of each after drying, then sealed with double-layered polyethylene films. Neutron irradiations to the samples were performed in February 2023 in the pneumatic transport tubes (Pn-2 and Pn-3) at KUR. After 10 seconds of irradiation with Pn-3 at a thermal power of 1 MW, γ-ray spectrometry was performed with a Ge detector within 5 minutes. The same samples were then irradiated with Pn-2 at a thermal power of 5 MW for 50 minutes. After 10 days of irradiation, all samples were measured with a Ge detector within 20 minutes.

RESULTS: The γ-ray spectrometry results for Pn-3 irradiated samples (1MW-10s) showed that the peaks of ^{24}Na, ^{28}Al, ^{42}K, ^{49}Ca, ^{51}Ti, ^{52}V, and ^{56}Mn were identified. Although the results of Pn-2 irradiated samples (5MW-50min) are still under analysis, we were able to identify ^{82}Br (half-life: 35.3h), ^{140}La (half-life: 40.3h), ^{153}Sm (half-life: 46.3h), and other nuclides with half-lives of less than 2 days. These rare earth and halogen elements could not be determined in our previous experiments due to their difficulty in γ-ray spectrometry. It is suggested that the determination of these elements is possible even in concrete samples.

Table. 1. Representative geological standard samples for reference of elemental concentration analysis of accelerator concrete materials [2-5].

Name	Kinds of rocks	Samping place
	Igneous rock	
JA-1	Andesite	Hakone volcano
JB-1b	Basalt	Kitamatsuura basalt
JG-1	Granodiorite	Sori granodiorite
JGb-1	Gabbro	Utsushigatake
JGb-2	Gabbro	Tsukuba-san leucogabbro
JR-1	Rhyolite	Wada Toge obsidian
JR-2	Rhyolite	Wada Toge obsidian
	Sedimentary rock	
JSl-1	Slate	Toyoma clay slate
JSl-2	Slate	Toyoma clay slate
	Sediments	
JLk-1	Lake sediment	Lake Biwa
JSd-2	Stream sediment	Eastern region, Ibaraki
JSd-3	Stream sediment	Central region, Ibaraki
	Soil	
JSO-1	Soil	Machida, Tokyo
	Coal fly ash	
JCFA-1	Coal fly ash	Isogo, Yokohama
	Ore	
JMn-1	Manganese Nodule	Southern Central Pacific Basin

REFERENCES:

[1] G. Yoshida *et al.*, J. Radioanal. Nucl.Chem., **325** (2020) 801-806.
[2] N. Imai *et al.*, Geostandards Newsletter, **19** (1995) 135-213.
[3] N. Imai *et al.*, Geostandards Newsletter, **20** (1996) 165-216.
[4] N. Imai *et al.*, Geostandards Newsletter, **23** (1999) 223-250.
[5] S. Terashima *et al.*, Geostandards Newsletter, **26** (2002) 165-216.

CO10-6 Particle Size Measurement for Aerosol Particles Generated from Molten Gold Using a High-Frequency Induction Furnace System

Y. Oki

Institute for Integrated Radiation and Nuclear Science, Kyoto University

INTRODUCTION:

Recently high intensity accelerators have been developed for medical application and isotope production. Target melting accidents, such as the J-PARC accident in 2013, could occur by mishandling of a high-intensity beam. Various radionuclides were released from a molten radioactive gold target in the J-PARC accident. The characteristics of the released radionuclides were very important to estimate both external and internal doses. The radioactive aerosol particles are formed by incorporation of radioactive nuclides into the aerosol particles formed through condensation process of evaporated target metal material. Particle size of the radioactive aerosol particles gives us useful information on the formation mechanism. To simulate the target accidents it is necessary to develop a high temperature furnace dedicated to aerosol sampling.

A high-frequency induction furnace system has been developed [1] for collection and size analysis of radioactive aerosol particles formed from molten radioactive metal samples. In this work, particle size was studied for gold aerosol particles formed from molten gold using the furnace system/

EXPERIMENTS:

Furnace system: Metal samples were heated using the high-frequency induction furnace system which was specially designed for aerosol collection. The furnace system consists of the induction quartz tube furnace and a low-pressure impactor for particle size analysis (Fig. 1). Highly pure carbon (graphite) crucibles were used for induction heating in the furnace. A disadvantage of induction heating in aerosol experiments is that high concentration fine particles are often produced from heated material. In this experiment, emission of the fine particles was successfully suppressed by long preheating of the crucibles under vacuum and in pure argon.

Heating of samples and collection of aerosols: Granular gold samples were heated in the preconditioned carbon crucible in the furnace up to 1,750 ºC in a flow of highly pure argon. The generated aerosols were introduced to the impactor by the argon flow. The impactor used was a so-called "jack-up" or "drawer" type low pressure impactor. It consists of 13 collection stages and a back-up filter. Teflon-binder glass fiber filter was used as the collection substrate.

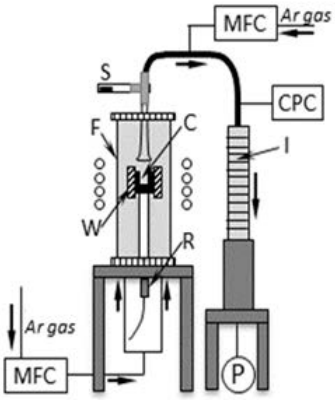

Fig.1 High Frequency Induction Furnace System

Particle size analysis: Weight of gold aerosol particles collected on each collection stage of the impactor was determined by activation analysis. Small piece of the collection substrate containing five spots of collected particles were cut from the substrate filter of each collection stage. The pieces were subjected to neutron irradiation in the Pn-1 pneumatic tube of the Kyoto University Research Reactor (KUR). The activity of ^{198}Au was measured with Ge semiconductor detectors.

RESULTS AND DISCUSSION:

Neutron activation analysis was adopted for determination of gold because the dispersion ratio from molten gold was estimated to be very small at 1,750 ºC. Weight of gold of each collection stage was determined with high accuracy. Mass medium aerodynamic diameter (MMAD) was found to be approximately 1 μm. The MMAD was almost the same as that of aluminum [2] although their vapor pressure is quite different.

REFERENCES:

[1] Y. Oki *et al.,* KEK Proceedings, 2020-4 (2020) 46-50.
[2] Y. Oki *et al.,* KEK Proceedings, 2021-2 (2021) 125-129.

CO12-1 Survey on Radioactive Cesium Migration between Environment and Body of Wild Boar (*Sus scrofa*) Living in Fukushima Prefecture

M. Fukushima[1], Y. Tsuji[1], Y. Iinuma[2], H. Komatsu[3], R. Kumada[3], K. Kanda[3]

Graduate School of Science, Kyoto University

[1]Faculty of Science and Engineering, Ishinomaki Senshu University

[2]Institute for Integrated Radiation and Nuclear Science, Kyoto University

[3]Fukushima Prefectual Centre for Environmental Creation

INTRODUCTION: Migration of radioactive cesium caused by Fukushima-Daiichi Reactor accident between environment and several species of wild animals in 2011 has been studied by several groups including Fukushima Prefecture Centre for Environmental Creation. In their results, radioactive cesium levels showed correation between wild boar muscle and stomach contents[1], and it suggested that radioactive cesuim migrate from diets to wild animal bodies. Wild boar diets show seasonal changes, and it is expected that trace elements levels in wild animals show seasonal changes. For these purposes, we have analyzed several elements in muscles and gastrointestinal contents including stomach, colon, and rectum of wild boars living in Fukushima Pref.

EXPERIMENTS: Wild boars were trapped in Nihonmatsu City, Fukushima Pref. under the permission of Fukushima Pref. from May 2018 to February 2022. After euthanasia by neck shot, musclus quadriceps, contents of the stomach, colon, rectum, and the liver were removed from body, freeze-dried, pulverized, and gamma-ray counting was done for Cs-134 and Cs-137 radioactivity. Also, before freeze-drying, some amount of stomach content was kept in 70% ethanol soln. and separated each materials unter optical microscope for estimating wild boar diet. One portion of dried power was supplied for short irradiation and another portion was used for long irradiation in KUR. Eight elements of Ca, Cl, Cu, K, Mg, Mn, Na, and V were analyzed by the condition of 1.5 min TcPn irradiation, 3 min cooling time, and 10 min gannma counting using germanium detector with Compton suppression system, also eight elements of Co, Cr, Cs, Fe, Rb, Sc, Se, and Zn were irradiated for 1 hour and gamma counting was done for 20 - 30 min after 1 month cooling time. For different standard reference materials were used: NIST SRM 1575 Pine Needles, NIST SRM 1577b Bovine Liver, NIST SRM 1573a Tomato Leaves, and NIST SRM 1515 Apple Leaves.

RESULTS: **<Wild boar diet>** Stomach contents were mainly consisted by leaves, stem, and fleshy fruits for whole study periods. Roots was main diet in autumn and winter, likely due to poor fruiting of acorns, which is known as main diet of the wild boar in these seasons. **<Radioactive Cs levels between muscle and stomach content>** Correation factor (R^2) of Cs-137 levels between muscles and stomach contents for 20 wild boars showed 0.05, and it meant there is no relationship between them caught in 2021 and 2022.

<Muscle > Long irradiation was done for 25 different muscle samples and obtained 5 levels of elements. Their averages and standard deviations are shown is shown in Table 1.

Table 1. Elemental levels in wild boar muscles. (unit: mg/kg, dry weight)

	Se	Cr	Rb	Fe	Zn
Avg	0.95	0.86	21.2	92.9	109
SD	0.39	0.73	16.4	22.0	38

<Gastrointestinal contents> Long irradiation was done for 3 different gastrointestinal contents and obtained 7 elemental levels, and their averages and standard deviations are shown in Table 2.

Table 2. Elemental levels in gastrointestinal contents. (unit: mg/kg, dry weight)

Element		Se	Cr	Sc	Rb	Fe	Zn	Co
Sc[*1]	Avg	1.97	6.23	1.34	4.23	4190	30.5	1.06
	SD	2.34	6.01	0.05	7.32	260	5.9	0.16
Cc[*2]	Avg	3.78	16.5	5.53	36.9	16300	67.6	4.94
	SD	4.55	5.1	0.49	8.1	800	29.3	0.56

Sc[*1]: stomach content, Cc[*2]: colon content.

When gamma spectra were measured, high levels of photopeaks caused from Sb-124 were found, and the highest peak energy of Sb-124 is 602.7 keV, which almost overlaps with photopeak of 604 keV caused from Cs-134. Sb and high levels of Fe are supposed to be the content of soil ingested with diets such as potatos, fallen acorns, insects, and so on. For investigating the migration of radioactive Cs, equilibrium of stable Cs and radioactive Cs in both environment and diet, it is important to analyze stable Cs both in the body of wild boars and in environment. Since stable Cs changes to Cs-134 by neutron irradiation, separation of soil and diet in stomach contents is needed.

REFERENCES:

[1] Y. Nemoto *et al*., Journal of Environmental Radioactivity, **225** (2020) 106342.

CO12-2 Synthesis of high-quality crystals for laser shock experiments: Implicartions for understanding the giant planet interiors

Y. Umeda[1], Y. Seto[2], T. Sekine[3], T. Duffy[4], F. Coppari[5], R. Smith[5], and T. Okuchi[1]

[1]*Institute for Integrated Radiation and Nuclear Science, Kyoto University*
[2]*Graduate School of Science, Osaka Metropolitan University*
[3]*Center for High Pressure Science & Technology Advanced Research*
[4]*Department of Geosciences, Princeton University*
[5]*Lawrence Livermore National Laboratory*

INTRODUCTION: The properties of ferropericlase, (Mg, Fe)O, especially its phase transition from the B1 (NaCl) to the B2 (CsCl) -type structure, may play a key role in controlling the deep dynamics of many rocky exoplanets, influencing properties such as mantle viscosity, heat flow, and magnetic field generation[1,2]. However, shock wave experiments to date have focused almost exclusively on the MgO or FeO endmembers. There are very limited shock compression data on planetary-relevant intermediate (Mg, Fe)O compositions.

In this study, we synthesized the single crystal of ferropericlase with high purity and chemical uniformity to understand the interiors of giant planets with a more reasonable chemical composition. This project will provide the first experimental data for directly testing recent theoretical predictions of metallization and phase stability of this material under conditions of super-Earth interiors and provide insights into the kinetics of polymorphic phase transitions under shock compression.

EXPERIMENTS: The (100) single crystal periclase MgO plate (5 x 5 x 0.05~0.15 mm), MgO powder, and FeO powder were prepared as starting materials. At first, mixed powder in fixed FeO and MgO ratios were grounded using an agate mortar and pestle. Mixing ratio was FeO:MgO=0.11: 0.89. Pellets were made of mixed powder using pelletizer at 2 MPa. The pellets of the mixed powder were baked for 18 h at 1400ºC and CO_2=340 cc/min, H_2=80 cc/min ($logfO_2$=-7.5) in a gas-mixing furnace at Kobe university using H_2/CO_2 gases, keeping O_2 fugacity between iron-wustite (IW) and quartz-fayalite-magnetite (QFM) buffer.

In next, the MgO plates were packed by pre-synthesized $(Fe_{0.11}, Mg_{0.89})O$ powder using pelletizer. Packed pellets were backed for 30 hours at 1450ºC and CO_2=340 cc/min, H_2=80 cc/min using H_2/CO_2 gases, keeping O_2 fugacity between IW and QFM buffer. After that, we excavated the crystal and polish it for X-ray diffraction (XRD) and Scanning electron microscopy (SEM) analyses to evaluate homogeneity and chemical compositions.

RESULTS: Single crystal ferropericlase has been synthesized via the interdiffusion of Mg-Fe between MgO plates and pre-synthesized (Mg, Fe)O powder in a gas-mixing furnace (Fig. 1).

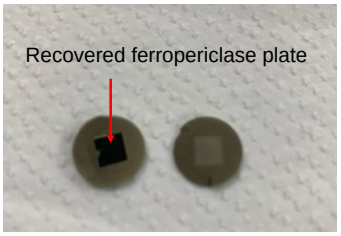

Fig. 1. Photo of single crystal ferropericlase synthesized for this study.

Scanning electron microscopy (SEM) imaging and energy dispersive X-ray (EDX) compositional analyses were performed across the short dimension of the single crystals and show that the samples are free of porosity and chemically homogenous Mg/(Mg+Fe) composition 92.9 ± 0.2 (Fig. 2).

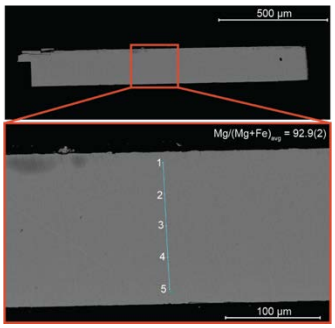

Fig. 2. SEM image of a ~100 µm thick (Mg,Fe)O single crystal synthesized in this study. Five EDX analyses were performed across the short dimension of the single crystal.

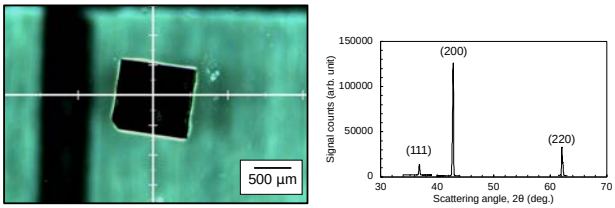

Fig. 3. Synthesized single crystal Ferropericlase, (Mg, Fe)O. X-ray diffraction profile of the synthesized crystal by micro focus XRD.

In summary, we succeeded in synthesizing the target composition $(Mg_{90}, Fe_{10})O$ of single crystal ferropericlase. The establishment of synthesis in this study is expected to enable us to obtain high-precision data for a wider range of compositions as laser shock targets.

REFERENCES:

[1] F. Coppari *et al.,* Nat. Geosci., **14** (2021) 121–126.
[2] S. Ritterbex *et al.,* Icarus, **305**, (2018) 350–357.

CO12-3 Neutron Activation Analysis of High Purity Material

T. Miura[1], S. Sekimoto[2], R. Okumura[2], H. Yoshinaga[2], Y. Iinuma[2]

[1]AIST, National Metrology Institute of Japan
[2]Institute for Integrated Radiation and Nuclear Science, Kyoto University

INTRODUCTION: National Metrology Institute of Japan (NMIJ) is responsible for developing certified reference materials and for establishing the traceability of SI (The International System of Units) on chemical metrology in Japan. To establish SI traceability, the primary method of measurements should be applied to the characterization of the certified reference materials. Neutron activation analysis using comparator standard is recognized as a potential primary ratio method [1]. Despite the potential of neutron activation analysis as primary ratio method, the evaluation the measurement capability and the measurement uncertainty are required in any analysis. In general, there are three main components of uncertainty in neutron activation analysis, that is, sample preparation uncertainty, neutron flux homogeneity, and gamma ray measurement uncertainty. Usually, flux monitor is used to correct the neutron flux heterogeneity. However, although the flux monitor can correct the neutron flux variation using the count rate of the known amount of the monitor nuclide, it does not reflect the neutron flux of the actual sample. The most practical method to eliminate neutron flux heterogeneity to improve gamma ray measurement uncertainty is an internal standard method [2, 3]. For the development of primary inorganic standard solution as national standard, the purity of starting material must be determined. The high purity yttrium oxide was candidate starting material for preparation of Y standard solution as national standard of Japan. The several trace analytical methods including neutron activation analysis, were used for purity determination of the high purity yttrium oxide. In this work, we presented that capability of instrumental neutron activation analysis for determination of Sc, La, Pr, Nd, Sm, Eu, Gd, Tb, Dy, Ho, Er, Yb, and Lu as impurity about rare earth elements in the high purity yttrium oxide.

EXPERIMENTS: The high purity yttrium oxide purchased from FUJIFILM Wako Pure Chemical Corporation. The informative purity value of the yttrium oxide and neodymium oxide were 99.99 %. NIST SRM single element standard solutions (3148a Sc, 3127a La, 3142a Pr, 3135a Nd, 3147a Sm, 3117a Eu, 3118a Gd, 3157a Tb, 3115a Dy, 3123a Ho, 3116a Er, 3160a Tm, 3166a Yb, 3130a Lu) were used for calibration standard in impurity analysis of the neodymium oxide, respectively. The standard solutions were added on filter paper to prepare the calibration standard in the analysis. The prepared calibration standards were heat sealed into polyethylene bags. Ten to 100 mg of the yttrium oxide samples were used for impurity analysis. The neutron irradiations for yttrium oxide performed by KUR Pn2 (thermal neutron flux: 5.5×10^{12} $cm^{-2}s^{-1}$) for 2 h, Pn3 (thermal neutron flux: 4.7×10^{12} $cm^{-2}s^{-1}$) for 5 min. The irradiated samples were cooled appropriately. The gamma rays form irradiated samples were measured using Canberra GC4070-7500 Ge detector with Laboratory Equipment Corporation MCA 600. The measure radioactive isotopes were ^{46}Sc, ^{140}La, ^{141}Ce, ^{142}Pr, ^{147}Nd, ^{153}Sm, ^{152}Eu, ^{159}Gd, ^{160}Tb, ^{165}Dy, ^{166}Ho, ^{171}Er, ^{170}Tm, ^{175}Yb and ^{177}Lu.

RESULTS: Analytical results of the high purity yttrium oxide were shown in Table 1. In this measurement, Sc, La, Ce, Pr, Nd, Sm, Eu, Gd, Tb, Dy, Ho, Er, Yb, and Lu in the yttrium oxide sample could not be detected by instrumental neutron activation analysis. Therefore, the detection limits for these elements were estimate from the count rate of energy region of gamma rays emitted by induced radioactive nuclides. The estimated detection limits were also presented on Table 1. The analytical results show the useful analytical capability of neutron activation analysis for the impurity analysis of the high purity yttrium oxide.

Table 1. Analytical results of the high purity yttrium oxide.

	Yttrium oxide
	Measured values, mg/kg
Sc	$< 3.6\times10^{-4}$
La	$< 1.6\times10^{-2}$
Ce	$< 8.8\times10^{-2}$
Pr	$< 7\times10^{-3}$
Nd	< 1.1
Sm	< 0.17
Eu	$< 2.3\times10^{-3}$
Gd	< 0.15
Tb	$< 1.9\times10^{-3}$
Dy	$< 3.6\times10^{-3}$
Ho	< 0.36
Er	< 0.48
Tm	$< 2.4\times10^{-2}$
Yb	< 0.5
Lu	$< 1.5\times10^{-2}$

REFERENCES:

[1] R. Greenberg, Spectrochim. Acta B, **66** (2011) 193-241.
[2] T. Miura *et al.,* Talanta, **82** (2010) 1143-1148.
[3] T. Miura *et al.,* J. Radioanal. Nucl. Chem., **303** (2015) 1417-1420.
[4] NuDat 2, National Nuclear Data Center in Brookhaven National Laboratory, https://www.nndc.bnl.gov/nudat2/index.jsp.

CO12-4 Development of Value assignment method of Uranium Solution

T. Miura[1] and K. Takamiya[2]

[1]*AIST, National Metrology Institute of Japan*
[2]*Institute for Integrated Radiation and Nuclear Science, Kyoto University*

INTRODUCTION:

National Metrology Institute of Japan (NMIJ) is responsible for developing certified reference materials and for establishing the traceability of SI (The International System of Units) on chemical metrology in Japan. To establish SI traceability, the primary method of measurements should be applied to the characterization of the certified reference materials[1)]. Gravimetric analysis[2)], titration method[1)], and coulometric analysis are recognized primary method for high purity inorganic material or inorganic standard solution. In this study, EDTA (ethylenediamine-*N*, *N*, *N*', *N*'-tetra-acetic acid) chelatometric titration method was applied for determination of U in solution sample. Uranyl ion is difficult to titrate with EDTA because of its small complexation constant with EDTA. On the other hand, the logarithm of the stability constant between U(IV) and EDTA (Log $K_{U(IV)Y}$) is about 25, which allows titration at low pH (pH 1 to 3) where there is little interference from coexisting metal ions.

REAGENTS and INSTRUMENTS:

The 100 g of U solution was prepared by dissolving the 0.2 g of Uranium oxide (Mitsuwa Chemical Co.Ltd., Osaka, Japan) using nitric acid. Dojindo Laboratories EDTA and Xylenol orange (XO) were purchased from FUJIFILM Wako Pure Chemicals Corporation. NMIJ CRM Bi standard solution was used for back titration. Other chemical reagents (nitric acid, acetic acid, ammonium acetate, ascorbic acid, etc.,) were analytical grade or JIS special grade. AT-510 automatic titrator (Kyoto Electronics Manufacturing Co., Ltd, Kyoto, Japan) was used for titration for U in the sample solution. ATX324 chemical balance (Shimadzu Corporation, Kyoto, Japan) was used to sample weighing. HM-30 pH meter (TOA-DKK, Tokyo, Japan) were used for pH measurement.

TITRATION METHOD:

The pH of the sample solution was adjusted from 3 to 4 by dropping ammonium acetate solution into the sample solution containing about 2 mg of uranyl ion. Excess amounts of EDTA standard solution (0.01 mol/kg) and ascorbic acid (100 mg) were added to the sample solution. The sample solution was then heated and boiled on a hot plate for approximately 10 minutes to form the U(IV)-EDTA complex. After the sample solution was cooled to room temperature, acetic acid was added to the sample solution to adjust the pH from 2 to 3. Finally, 0.01 % XO indicator solution was added to the sample solution and back titrated with 0.01 mol/kg Bi standard solution.

RESULTS:

Analytical results of the U in the sample solution by EDTA titration method were shown in Table 1. In this experiment, titration was performed by changing the pH of the sample solution in steps from 2 to 3. The experimental results showed that the effect of pH was small in this pH range. From this titration experiment, it was verified that the EDTA titration method can be determined a small amount of uranium (about 2 mg) with a repeatability of less than 0.2%.

Table 1. Analytical results of the U in the sample solution.

Run No.	pH	U mg/kg
1	3.00	1851
2	2.86	1850
3	2.73	1849
4	2.62	1854
5	2.55	1858
6	2.41	1852
7	2.32	1846
8	2.27	1853
9	2.22	1854
	Mean	1852
	RSD	0.185 %

REFERENCES:

[1] J. Vogl *et al*., Metrologia, **55** (2018) 211.
[2] T. Miura and A. Wada, Front. Chem., (2022) 88863.
[3] J. Kinnunen and B. Wennerstrand, Chem. Anal., **46** (1957) 92.

CO12-5 Experimental Study of Superposition of Coherent Transition Radiation Using a Ring-type Resonator

N. Sei and T. Takahashi[1]

Research Institute for Measurement and Analytical Instrumentation, National Institute of Advanced Industrial Science and Technology

[1]Institute for Integrated Radiation and Nuclear Science, Kyoto University

INTRODUCTION: Nonlinear optical phenomena such as hole burning [1], which were once popular in the infrared region, have been studied in the terahertz region, and terahertz light sources with high peak power are desired. To meet this requirement using high-energy electron beams, we have developed a technique of pulse superposition of coherent transition radiation (CTR) using a ring-type resonator. By orbiting the ring-type resonator, the electric field of the CTR micropulses is superimposed, and the peak power of the CTR increases nonlinearly. We installed a ring-type resonator in the electron beam orbit and inserted a cyclo-olefin polymer substrate into the resonator as an output coupler. By inserting a millimeter-wave absorber into the resonator, we confirmed that the CTR accumulated in the resonator. The power of the CTR micropulse increased approximately twice in spite of a large cavity loss, and the experimental results suggest that the electric field of the CTR micropulses were superimposed in positive phase.

EXPERIMENTS: An electron beam with the energy of 39 MeV and the average current of 1.8 μA was used for the experiments at L-band linac of Kyoto University. The reputation frequency of the electron-beam macropulse was 15 Hz. Because the macropulse duration was 100 ns, the number of electron-beam micropulse in a macropulse was 130. Schematic layout of the ring-type resonator used in the experiments is shown in Fig. 1. The electron beam generated CTR at two thin polyethylene films vapor-deposited with aluminum when it passed through them. The thickness of the polyethylene film was 6 μm. These polyethylene films were also used as mirrors constituting the resonator. The two CTR beams were confined in the resonator composed of four mirrors, which included two parabolic mirrors with the focal length of 508 mm. The cavity length of the resonator was 922 mm, which was four times the interval of the electron bunches. The downstream parabolic mirror was mounted on a linear stage and the cavity length could be adjusted. In order to extract the resonate CTR beam from the resonator, a cyclo-olefin polymer substrate with a thickness of 3 mm was inserted into the resonator at an angle of 45 degrees with respect to the optical axis. The cyclo-olefin polymer was almost transparent in a frequency range below 1 THz, and its refractive index was 1.53 [2]. The extraction efficiency for the CTR beam due to reflection on the front and back of the substrate was approximately 10%.

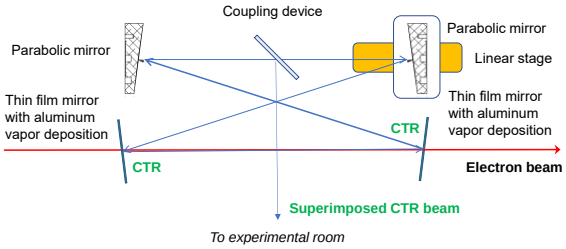

Fig. 1. Schematic layout of the ring-type resonator.

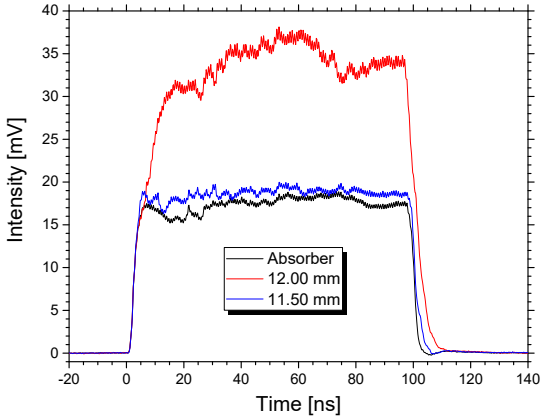

Fig. 2. Measured temporal evolution of the horizontal component of CTR micropulse power.

RESULTS: The CTR beam transported to the experimental room was measured by a D-band diode detector (Millitech Inc., DXP-06). Figure 2 shows temporal evolution of the horizontal component of the CTR micropulse. When a scale of the linear stage was 12.00 mm, the power of the resonated CTR micropulse was approximately twice that inserting a millimeter-wave absorber in the resonator. When the stage was moved by -0.5 mm, the CTR power decreased to almost the same power with the absorber. This variation of the power of the CTR micropulse suggests that the longitudinal mode appeared due to the change of the cavity length. Therefore, it was confirmed that the electric field of the CTR micropulses was superimposed by the resonator positively.

In these experiments, the amplification of the CTR micropulse power caused by the pulse superposition was insufficient due to the large cavity loss of the resonator. We are planning to remodel the resonator so that the superposition rate can be increased.

REFERENCES:

[1] J. Dong *et al.*, Opt. Rev., **15**, (2008) 57–74.
[2] E. Mavrona, Opt. Mat. Express, **11** (2021) 2495-2504.

CO12-6 The Third-year Trial to Analyze the Texture of Roof-tile: Toward Detailed Provenancial Studies of Excavated Ceramics by INAA

M. Tomii, K. Takamiya[1], H. Yoshii[2], M. Kidachi[3], Y. Chiba[2], and A. Ito[2]

Faculty of Literature, Taisho University
[1]Institute for Integrated Radiation and Nuclear Science, Kyoto University
[2] Graduate School of Letters, Kyoto University
[3] College of Letters, Ritsumeikan University

INTRODUCTION: Aiming to establish the procedures to archaeologically identify local groups for production of ceramics in Japan, 20 pieces of the roof-tiles with stamp impression from the same collection as the one in the first year are analyzed this year. They were excavated from the archaeological site in the Kyoto University campus in 1992, where the garrison from the *Tosa* domain had temporally occupied in 1860s. The roof-tiles in the collection is almost exclusively composed of the ones having the stamp impressions, each of which indicates the name of maker/atelier of the tile. There are 24 kinds of stamp impression of Chinese characters, and 23 stamp impression groups of them suggest the makers in *Tosa* region respectively [1], though there is no difference in size, production technique, and the appearance of texture. This study tries to check whether the stamp impression groups correspond with the groups of tile texture in detail, to consider whether all these roof-tiles were produced at local ateliers.

EXPERIMENTS: Conventional INAA was applied to determine the elemental composition of samples of the tiles, each of which had been drilled into a fine powder as a sample and then had been enclosed in a polyethylene bag [2]. 18 pieces of the roof-tile of normal (right-sloping) type, composed of two stamp impression groups, were chosen; ten were from the "AKANOGIN" group and the others from "KATATSUNE" group. Five tiles of each group are of normal type. Another five of AKANOGIN are of left-sloping type. Among the rest three of KATATSUNE, one is of left-sloping type, and the other two are of façade-placed tiles; the decoration of the façade side of such tiles had been made with mould, meaning that this part might require finer clay through elutriation. One of the two façade tiles for analysis is of right-sloping, and another is of left-sloping, both of which serve two samples, respectively, from façade side and from back side.

Each 20 samples was neutron-irradiated, firstly at Pn-3 (1 MW for 90 seconds) to detect short-lived nuclides, and then at Pn-2 (1MW for 2 hours) to determine long-lived nuclides. The comparative standards (JR-3, JB-1b) were irradiated with the same condition. 15 mg was used for Pn-3 and 45 mg for Pn-2, in each sample.

The gamma-ray spectrometry of the irradiated samples for long-lived nuclides was performed one time (after around 30 days), while that for short-lived nuclides was done four times: just after the irradiation, after 15 minutes, 40 minutes, and around 24 hours. The photo-peak analysis was performed by using FitzPeaks [3]. Concentrations of elements included in the samples were estimated by comparison of the intensity of gamma-rays between the comparative standard and tile samples.

RESULTS: Concentrations of ten elements (Al, V, Ti, Mg, Mn, K, Ga, Na, Sm and La) in every sample were determined with irradiation by Pn-3. With irradiation by Pn-2, concentrations of twelve elements (Yb, Lu, Nd, Rb, Ce, Hf, Fe, Tb, Sc, Ta, Cs and Eu) would be determined in every sample, though the determination has not been fully completed in all samples so far. Nevertheless, the following two results can be pointed out;

a) two elements (Na and Mn) show clear difference in concentration to divide 20 samples into two groups, respectively, and the two groups fully correspond with the stamp groups (Fig.1).

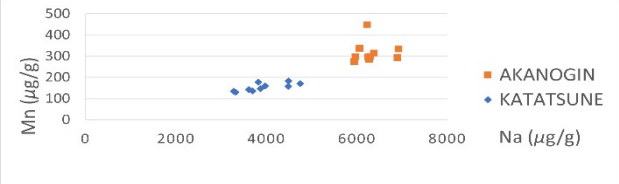

Fig. 1. Distribution of 20 samples on the concentrations combination of Na with Mn.

b) Fe does not show clear difference in concentration among the KATATSUNE groups. This might tell that elutriation for finer clay had not been operated. This atelier might use the same texture for all types (Fig.2).

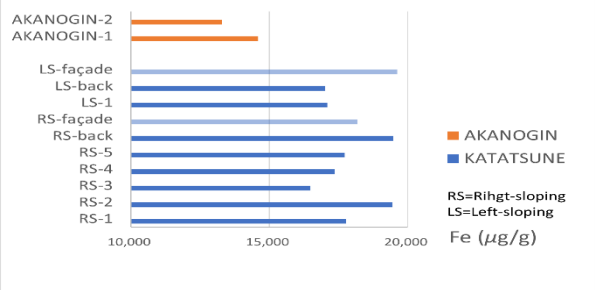

Fig. 2. Mean values of Fe of the KATATSUNE group (with the examples of the AKANOGIN group for comparison).

ACKNOWLEDGEMENT
We would like to thank Dr Johannes Sterba and Dr Maria Shinoto for advising the sampling procedures on the sherds according to the workflow established in Vienna.

REFERENCES:

[1] Y. Chiba et al., Annual Report of Archaeological Researches in KU sites for 1992., (1995) 65-125.
[2] J. Sterba, J. Radio. Nucl. Chem., 316 (2018) 753-759.
[3] J. Fitzgerald, Fitz Peaks Gamma Analysis and Calibration Software, https://www.jimfitz.co.uk/fitzpeak.htm.

CO12-7 Study for activity measurement techique of radioactive xenon gases using a plastic scintillator

T. Yamada[1,2], K. Mori[2], R. Furukawa[3] , H. Yashima[4]

Kindai University
[1]Atomic Energy Research Institute
[2]Graduate school of Science and Engineering
[3]National Metrology Institute of Japan
[4]Institute for Integrated Radiation and Nuclear Science, Kyoto University

INTRODUCTION: In order to calibrate monitors used for measuring radioactive xenon isotopes in nuclear facilities, use of activity reference measurement standard gases shall be required. A β-ray counting technique using a set of multiple ventilated proportional counters having different lengths is generally used to determine activity concentration of standard gases [1]. In this study, a method based on the 4πβ-γ spectroscopy method using a plastic scintillator (PS) as a β-detector was carried out to determine β-counting efficiency of ^{133}Xe absolutely as an alternative approach.

EXPERIMENTS: ^{133}Xe gas was produced via ^{132}Xe(n,γ)^{133}Xe reaction. Naturally occurring xenon gas consists of seven stable isotopes was filled into the small acryl container having 10 ml with atmospheric pressure and was irradiated for 60 s at the bottom of KUR-SLY under operating at 1 MW thermal output. Around 3 kBq of ^{133}Xe was produced with 7.84×10^{11} $n^{-1}s^{-1}cm^{-2}$ of the nominal flux of the thermal neutron.

A small acrylic gas container with internal dimensions of φ60 mm × 40 mm (113 ml) was used as the β-detection part of the measurement system. The entire inner wall of the container was lined with 1 mm thick of PS. The container was covered with aluminum tape on the sides and white tape on the top as a reflector, and a photomultiplier tube (PMT) was connected to the top of the container and stored in a light-shielded case. The β-detector was placed directly onto the Ge detector, and the signal outputs from the β- and γ-detectors were fed to the signal inputs of a list-mode multi-channel analyzer (MCA) capable of acquiring data in list mode to obtain list data consisting of the pulse height from each detector and a time stamp of the detection time.^{133}Xe emits γ-ray (E_γ=81 keV) following disintegration by beta minus decay to excited levels of ^{133}Cs with branching ratio of 0.9912 [2]. In order to obtain the β-γ coincidence spectrum from the time-stamped pulse height data, the γ- signals derived within 4.5 μs from the β-detection time stamps were considered as true coincidences. β-counting efficiency ε_β is determined as the ratio of net peak area in the coincidence spectrum n_c to the net peak area n_γ in the γ-spectrum. The use of naturally occurring xenon gas consists of seven stable isotopes could produce impurities of ^{129m}Xe, ^{131m}Xe, ^{133m}Xe, ^{135m}Xe, ^{135}Xe and ^{137}Xe. In the present study measurements were carried out 2 days after the end of irradiation, although there exist impurities (≈ 30 % or less) of ^{129m}Xe, ^{131m}Xe, ^{133m}Xe and ^{135}Xe.

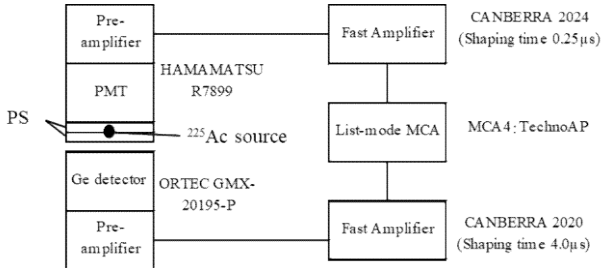

Fig. 1. Schematic diagram of the 4πβ-γ coincidence spectroscopy system used in the present study.

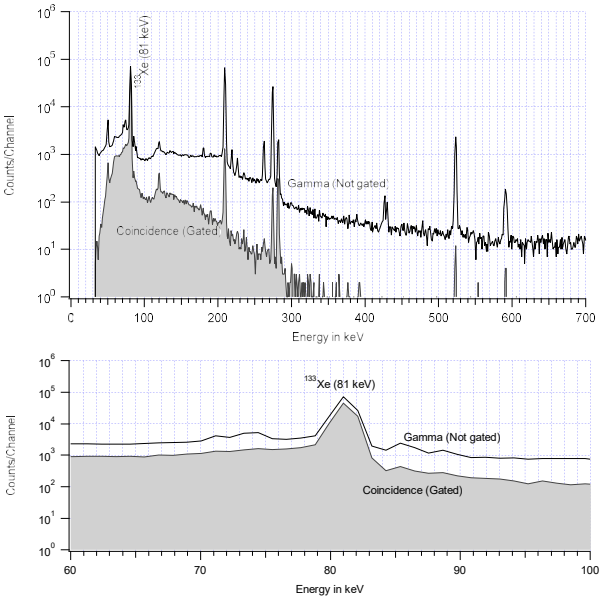

Fig. 1. Coincidence- and γ-spectra obtained from the present measurement.

RESULTS: Figure 1 shows the coincidence and γ-ray spectra obtained in the present experiment. β-counting efficiency determined as n_c / n_γ was 0.667±0.004. Even though around 0.9 of detection efficiency was obtainable for ^{41}Ar by use of the same β-counter in the previous study [3], significant loss of detection efficiency was found for ^{133}Xe. Further study should be needed to determine the cause of decrease in counting efficiency and to improve it.

REFERENCES:

[1] A. Yunoki *et al.*, KURNS Progress Report 2020 (2021) CO12-12 (R2116).
[2] Bé, M., 2011. Table of Radionuclides. http://www.nucleide.org/DDEP_WG/DDEPdata.htm.
[3] T. Yamada *et al.*, KURNS Progress Report 2021, (2022), CO12-9 (R3100).

CO12-8 Development of Compensation Method for Faster Measurement with SPND

C. H. Pyeon[1], R. Okumura[1], M. Sasano[2], R. Tanaka[3], T. Azuma[2] and M. Hayashi[2]

[1] *Institute for Integrated Radiation and Nuclear Science, Kyoto University*
[2] *Advanced Technology R&D Center, Mitsubishi Electric Corporation*
[3] *Energy Systems Center, Mitsubishi Electric Corporation*

INTRODUCTION: For safety monitoring and control of conventional pressurized water reactors, neuron signals are mainly measured from outside the reactor. For safer reactor control, constant neutron monitoring inside the reactor is required in the future. The self-powered neutron detector (SPND) is the detector that attains signals from β-decay associated with activation as a current, and outputs a current within 10 nA at 10^{12} nv. SPND is suitable for measurement in high-intensity neutron environments, but the delay in detector response due to the half-life of β-decay is one of the main technical issues in this study. We evaluated then techniques to compensate for the delay in the SPDN detector response.

EXPERIMENTS: Measurements were conducted on two days, 2023/01/12 and 2023/01/19. At the first one, we evaluated the detector power during the 0.1 MW operation. In addition, experimental data were acquired on the detector response during the start-up of the reactor and the increase in power up to 5 MW. On the second day, the detector output at 1 MW reactor power was acquired. From these data, we evaluated the compensated detector response and the linearity of the detector against the reactor power.

RESULTS: The results of plotting the SPND output, when the reactor was ramped up to 5 MW of power from the startup of the reactor, show that the detector output was raised with a delay of only 40 s and 4.4 min half-life of ^{104}Rh and ^{104m}Rh, respectively, and the time response of the SPND is 4.4 min. The gap between raw output and reactor power was over 100 s. To correct for this time response, calculations were based on the following ^{104}Rh and ^{104m}Rh β-decay. The correction can be made by deriving f in Eqs. (1) and (2).

$$N_{Rh^{104}} = -\lambda_{Rh^{104}} N_{Rh^{104}} + \lambda_{Rh^{104m}} N_{Rh^{104m}} + N_{Rh^{103}} \sigma f \quad , \quad (1)$$

$$N_{Rh^{104}} = -\lambda_{Rh^{104m}} N_{Rh^{104m}} + N_{Rh^{103}} \sigma f \quad . \quad (2)$$

Figure 1. shows the time variation of the raw detector output and the compensated one. The maximum rate of increase in reactor output is 0.045 MW/s. There was a slight delay in the maximum increase in reactor power. However, after reaching the maximum output, it was confirmed that the correction came with a delay of about 10 s or less. Also, when the increase rate of reactor output is 0.02 MW/s or less, the compensated output was observed to be followed within 5%. This is a significant improvement over the delay less than 100 s in the uncompensated data. In Fig. 2., the SPND current data obtained in the three reactor outputs were found, 0.1, 1.0 and 5.0 MW. The plots of current output versus 0.1, 1.0, and 5.0 MW are shown in Fig. 3. The results revealed that the outputs have a linearity tendency between 0.1 and 5.0 MW.

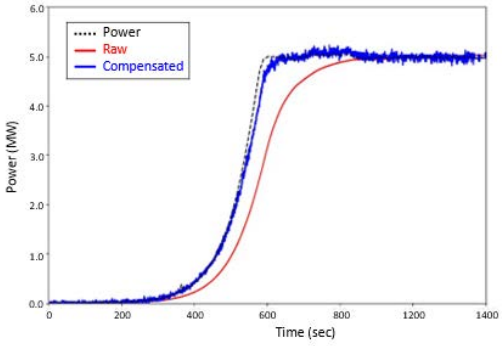

Fig. 1. The plot of normalized SPND measured current (red and blue lines mean raw and compensated, respectively) and the reactor power via time.

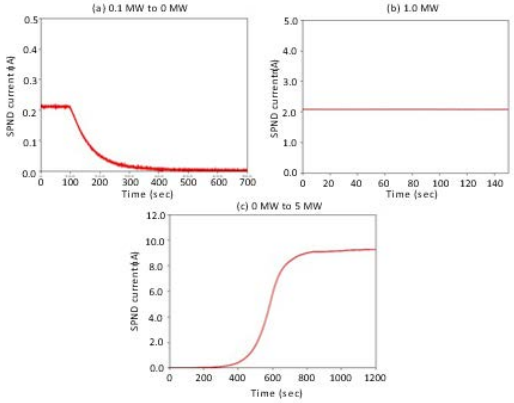

Fig. 2. The plot of SPND measured current with three conditions. (a): 0.1 MW to 0.0 MW, (b): 1.0 MW and (c): 0.0 to 5.0 MW

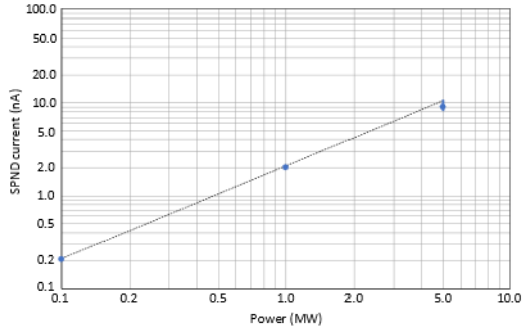

Fig. 3. The linearity of SPND output current. The plot of the current via KUR reactor power.

CO12-9 SEM-EDS analysis of sprayed and dried particles from fine particles of $(U,Zr)O_2$ for decommissioning of Fukushima Daiichi Nuclear Power Plant

A. Toyoshima, K. Takamiya[1], K. Nagata[2], and H. Furutani[3]

Institute for Radiation Sciences, Osaka University
[1]Institute for Integrated Radiation and Nuclear Science, Kyoto University
[2]Graduate School of Science, Osaka University
[3]Center for Scientific Instrument Renovation and Manufacturing Support, Osaka University

INTRODUCTION: First preliminary removal of the fuel debris remaining in the reactors of Fukushima Daiichi Nuclear Power Plant is planned to be started soon. In the removal, however, fine particles containing such as ^{235}U and ^{239}Pu are concerned to be yielded in the cutting process of the debris. We are therefore developing a novel real-time detection method of the dispersed fine particles using Aerosol Time-Of-Flight Mass Spectrometer (ATOFMS). At present, we are developing an enlargement and condensation apparatus to increase the detection sensitivity of ATOFMS by enlarging its non-detectable tiny particles to detectable-sized ones before the ATOFMS measurement. Previously, we performed SEM-EDS measurement of modeled fine particles containing ^{238}U without its enlargement. In the present study, we carried out SEM-EDS for enlarged ^{238}U particles using the developing apparatus.

EXPERIMENTS: Fine particles were prepared separately from $(U,Zr)O_2$ pellets as well as a ZrO_2 one by laser ablation. Laser power was approximately 30 mW. In a closed chamber, the pellet was irradiated by the laser. The yielded fine particles were swept out of the chamber by carrier gas of dried air and were continuously collected in water using PILS (Particle Into Liquid Sampler, Metrohm AG). The solution containing fine particles were sprayed using the developing enlargement and condensation apparatus. Polystyrene latex (PLS) standard particles were also sprayed as references. Sprayed droplets were then dried by dried air (carrier gas) and diffusion dryers. The resulting dried particles were then collected on a carbon tape set in a small impactor. SEM-EDS measurement of the collected samples was carried out after the transportation of those to KURNS. Energy of bombarded electrons was 10 kV or 15 kV. SEM images and X-ray spectra of the samples were taken for a thousand of fine particles found on the carbon tapes.

RESULTS: In Fig. 1, a SEM image of the standard fine particles with a diameter of 150 nm is shown. Many of PSL standard particles are observed. Some of these particles form aggregated clusters which are enlarged with the developed apparatus. As shown in Fig. 2, we also found similar aggregated clusters made from the U/Zr particles, element composition of which was obtained by the EDS analysis, although the amount of the enlarged particles is small. This is our first successful result on preparation of enlarged particles consisting of the tiny U/Zr particles. In the future, we will improve the enlargement and condensation apparatus for the increase of condensation efficiency.

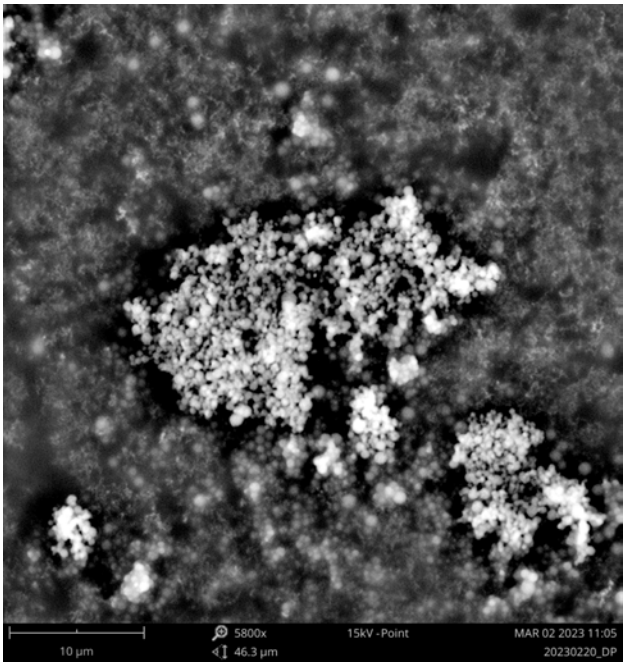

Fig. 1. SEM image of PSL particles.

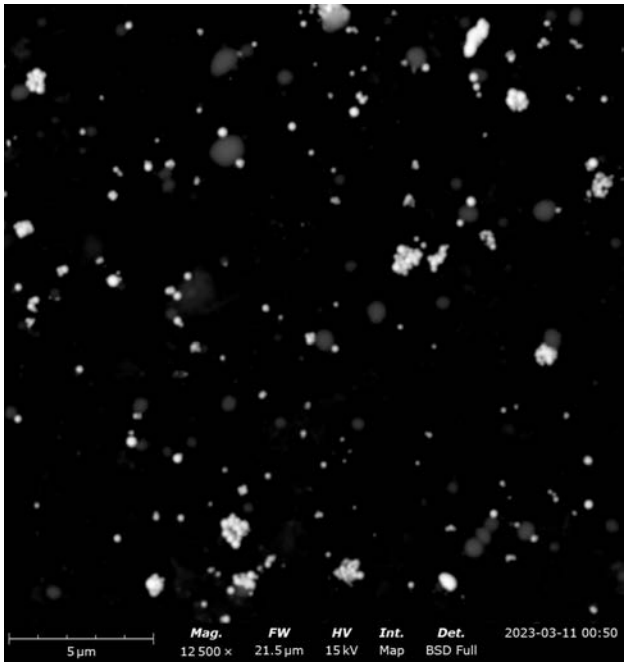

Fig. 2. SEM image of U/Zr particles.

CO12-10 Testing of a N_2-NBM readout setup at KUR CN-3

H. Ohshita, H. Endo, T. Seya, S. Matoba, M. Hino[1]

Institute of Materials Structure Science, KEK
[1]Institute of Integrated Radiation and Nuclear Science, Kyoto University

INTRODUCTION: With the advent of high-intensity pulsed neutron-source facilities, such as the Materials and Life Science Experimental Facility (MLF) at J-PARC, neutron detectors with high counting rate characteristics are required. Neutron beam monitors filled with nitrogen gas (N_2-NBMs) are known to operate in high-intensity neutron environments [1]. Neutrons were detected by measuring the rapidly charged particles emitted during the $^{14}N(n, p)^{14}C$ reaction. The *Q* value of the neutron reaction was 0.62 MeV, and the initial energies of the proton and ^{14}C were 0.58 MeV and 0.04 MeV, respectively. The cross section of the $^{14}N(n, p)^{14}C$ reaction for a thermal neutron of 1.8 Å is 1.91 b, which is $1/36000^{th}$ of the commonly used $^3He(n, p)^3H$ reaction cross section. Therefore, the application of neutron detectors based on the $^{14}N(n, p)^{14}C$ reaction is limited to neutron-beam monitoring in high-intensity neutron environments. However, in high-intensity pulsed neutron-source facilities such as the MLF, neutron-beam monitors with a thermal neutron efficiency lower than 10^{-5} are needed to suppress the counting rate, and N_2-NBM is the only realistic neutron detector. The N_2-NBM (E68953) produced by CANON Electron Tubes and Devices [2] was introduced at the MLF, and its active area of 65 mm × 65 mm was filled with a mixture of argon and nitrogen as the chamber gas. The filling pressures of argon and nitrogen were 786 Torr and 50 Torr, respectively. The expected thermal neutron efficiency was 3.9×10^{-6}. Figure 1 shows a typical readout setup of the N_2-NBM at the MLF, where the analog signal output from the N_2-NBM is pulse-shaped using a pre-amplifier 595H and a post-amplifier 4467A. A sufficiently long collection time was ensured in the first-stage preamplifier to collect the charges generated in the active area. The pulse-shaping time in the post-amplifier was 500 ns, which was designed for operation under a high-intensity pulsed neutron source. Finally, the analog signal was input to GateNET [3], where the time-of-flight (TOF) and pulse-height values were measured for the timing signal. GateNET is widely used at the MLF and can be easily integrated into existing neutron detector systems. This paper describes the testing of the N_2-NBM readout setup at KUR CN-3.

EXPERIMENTS: The A neutron detector was established downstream of the CN-3 beamline to measure the TOF during the testing of the N_2-NBM readout setup. The typical neutron intensity at the detector position was 694.5 neutrons/s·cm^2·MW. If an N_2-NBM is installed, an extremely long measurement time is required to obtain measurements with sufficient statistics. Therefore, in the test, a 3-helium proportional counter was used instead of an N_2-NBM (replacing the neutron detector in the setup shown in Figure 1). The other experimental conditions were the same as those used in previous neutron irradiation tests [4]. Figure 2 shows a comparison of the pulse height distributions for varying post-amplifier gains and shaping times. The distribution (black line) obtained using the settings shown in Figure 1 (gain 50; shaping time 500 ns) was used as the reference. In this distribution, the total absorption peak due to the $^3He(n, p)^3H$ reaction and the edges due to protons and tritons were visible, and good nγ discrimination was achieved. In general, a change in gain enlarges or shrinks the pulse height distribution, whereas a change in shaping time significantly distorts the distribution. The results shown in Figure 2, obtained at the same operating voltage, indicate that a good pulse height distribution can be obtained at a lower operating voltage by optimizing the readout setup parameters. By selecting a long shaping time, the operating voltage can be reduced by several hundred volts, which is expected to contribute to a longer detector life.

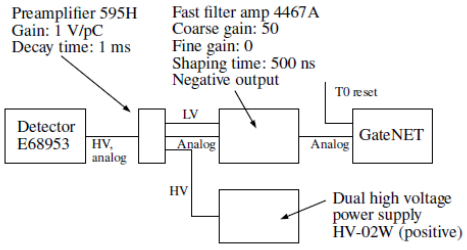

Figure 1. Typical readout setup of N_2-NBM at MLF.

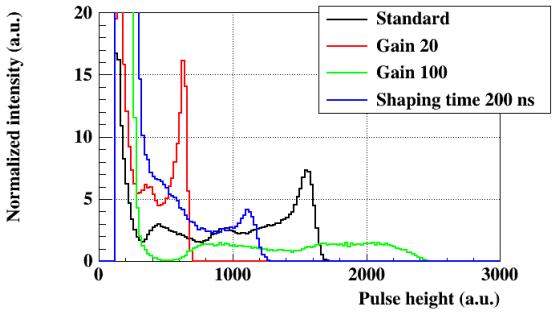

Figure 2. Comparison of pulse height distributions when the parameter settings such as gain and shaping time are varied.

REFERENCES:

[1] F. Issa, *et al.*, Phys. Rev. Accel. Beams **20** (2017) 092801.
[2] web page of CANON Electron Tubes & Devices Co., Ltd., https://etd.canon/en/index.html.
[3] S. Satoh, *et al.*, in proceedings of the ICANS XIX (2010) IP132.
[4] H. Ohshita, *et al.*, KURNS Proc. Rep. 2020 (2021) CO12-5.

CO12-11 Structural Analysis of Additives in Lubricants by Small-Angle X-ray Scattering

T. Hirayama, S. Nambo[1], W. Yagi[1], Y. Takashima[2], N. Sato[3] and M. Sugiyama[3]

Graduate School of Engineering, Kyoto University
[1]Graduate School of Engineering, Kyoto University
[2]Idemitsu Kosan Co., Ltd.
[3]Institute for Integrated Radiation and Nuclear Science, Kyoto University

INTRODUCTION: The use of low-viscosity lubricating oil is effective in reducing friction loss on sliding surfaces. However, when low-viscosity lubricating oil is used, the sliding surfaces tend to transition to a boundary lubrication state at high temperatures. Therefore, in the case of lubricating oils used over a wide temperature range, such as engine oil, it is desirable for the viscosity of the lubricating oil to change little as the temperature changes, and a polymer called a 'viscosity index improver' (VII) is added.

The structure of VII molecules in the base oil affects the viscosity characteristics of the lubricant, but it is difficult to analyze the structure of VII molecules one by one during lubricant development. Furthermore, few studies have actually analyzed the structure of VII molecules in base oils, and the relationship between the solubility of VII in base oils and its structure in base oils is unclear. In this study, we investigated the relationship between the structure of VII molecules in base oils and its solubility in base oils by dissolving VII in several base oils, analyzing the structure of VII in base oils, and evaluating the solubility of VII in base oils by the 'Hansen solubility parameter (HSP)'.

EXPERIMENT: In this study, we investigated the relationship between structure and solubility in base oils for a VII molecule called 'Comb PMA'. Five solvents were selected: tri-n-decylamine, tridodecylamine, squalane, toluene, and tetrahydrofuran. Comb PMA was dissolved in each solvent to a mass percent concentration of 2%, and SAXS measurements of Comb PMA in each solvent at 25°C were performed using a Cu small-angle X-ray scattering apparatus (NANOPIX, RIGAKU) at the Institute for Integrated Radiation and Nuclear Science, Kyoto University. The solubility of Comb PMA in solvents was evaluated using HSP, which are the solubility parameters (SP) divided into three parts: London dispersion force term, dipole inter-dipole force term, and hydrogen bonding force term, allowing for polarity that cannot be taken into account by SP values.

RESULTS: The scattering profiles obtained by SAXS measurements are shown in Fig. 1. The scattering profiles of Comb PMA in tri-n-decylamine, tridodecylamine, and squalane showed the same trend, which was different from that in toluene and tetrahydrofuran. PMA was contracted in tri-n-decylamine, tridodecylamine, and squalane, while Comb PMA was expanded in toluene and tetrahydrofuran.

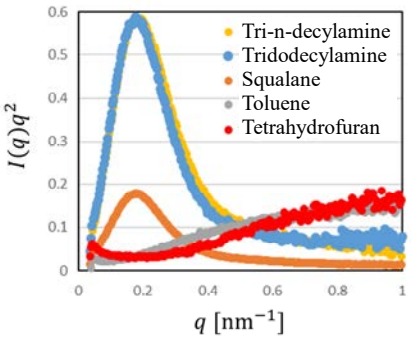

Fig.1. Kratky plots of Comb PMA in various oils.

DISCUSSION: The HSP distance between Comb PMA and each solvent was calculated, and the order of HSP distance from shortest to longest was toluene, tri-n-decylamine, tridodecylamine, squalane, and tetrahydrofuran. However, SAXS analysis showed that Comb PMA expanded in both toluene and tetrahydrofuran, and the general relationship of molecular expansion in solvents with high solubility and contraction in solvents with low solubility was not established. The HSP values of Comb PMA in 34 different solvents were determined using a solubility test, but it was not possible to determine whether the solubility of the main chain or the side chains of Comb PMA determines the solubility of Comb PMA itself. The Combs PMA used in this study has longer side chains than general-purpose PMA, but the main chain is 25 times longer than the side chains, so the structural analysis by SAXS is considered to reflect mainly the structure of the main chain.

Therefore, we divided Comb PMA into main chains and side chains and determined their HSP values. Polymethyl methacrylate was used as a model for the main chain and polyethylene as a model for the side chains, and the HSP values from the database were used. As a result, the structure of Comb PMA was found to be as follows, depending on the solubility in the base oil to which it is added. (1) In a base oil with low solubility of the main chain and high solubility of the side chains, the main chain of the Comb PMA molecule shrinks and the side chains expand. (2) In a base oil with high solubility of both the main chain and side chains, both the main chain and side chains expand. (3) In a base oil with low solubility of the main chain but even lower solubility of the side chains, the contraction of the side chains prevents the contraction of the main chain.

In addition, when the viscosity index of the solutions with each pure solvent and Comb PMA was examined, a remarkable viscosity index improvement effect was observed in the solvent in which the main chain of Comb PMA was shrunk at 25°C. The viscosity index of the solution with Comb PMA was higher in the solvent in which the main chain of Comb PMA was shrunk at 25°C than in the pure solvent in which the main chain was shrunk.

CO12-12 Nanostructural Analysis of Lubricant/Metal Interface by Neutron Reflectometry

T. Hirayama, N. Yamashita[1] and M. Hino[2]

Graduate School of Engineering, Kyoto University
[1]Graduate School of Engineering, Kyoto University
[2]Institute for Integrated Radiation and Nuclear Science, Kyoto University

INTRODUCTION: Our research group has focused on ester derivatives, which are ashless lubricant additives, and has evaluated their tribological properties. In high-speed reciprocating friction and wear tests, this additive has been found to have the same friction-reducing effect as glycerin monooleate at room temperature and the same wear-inhibiting effect as ZDDP and phosphate ester amine salts at high temperatures.

In this study, we focused on additives with enhanced adsorption performance by introducing an oxyalkylene (AO) group between the ester carbonyl and alkyl groups of the ester derivative. In general, it is known that the adsorption performance of additives decreases when the moisture content in lubricating oil is low. Therefore, in this study, the difference in adsorption performance between lubricants with and without AO groups was verified by using lubricants with low moisture content. Specifically, the structure of the adsorption layer and friction characteristics were evaluated by neutron reflectometry and AFM friction measurements.

SAMPLES: In this study, an oxyalkylene group (FM-1) was added to a certain ester derivative (FM-0) used in the previous study. For the neutron reflectometry, these additives were added to deuterated hexadecane at a concentration of 0.1 wt%, and for the AFM friction measurement, each additive was added to polyalpha olefin (50 cSt@40°C) at a concentration of 0.1 wt%.

NEUTRON REFLECTOMETRY: A substrate with a thickness of about 30 nm of iron deposited on the surface of a 50 × 50 × 10 mm silicon block using a sputtering system was used. BL16 SOFIA at MLF in J-PARC was used for the NR measurement. Table 1 shows the analysis results of the data measured at 25°C after 30 minutes in a drop of lubricating oil. In the neutron reflectometry, fitting analysis was performed assuming a simplified layer structure model. Therefore, although it is necessary to allow for some errors in the results when the actual film structure is complex, there were no significant differences in the adsorption layer structures formed by FM-0 and FM-1. Considering that oleic acid, which has the same alkyl chain length as the additive used in this study, generally forms an adsorption layer of about 2 nm, the thickness of the film formed by FM-0 and FM-1 is more than 3 nm, although the polar groups are different, suggesting that the adsorption layers may not be simple single-layer structures.

Table 1. Film structure formed by additives.

	Thickness, nm	Film density, %
FM-0	3.0	47
FM-1	3.1	44

FRICTION TEST: To evaluate the friction and wear properties of each additive, friction tests were conducted using an AFM (SPM-9700, Shimadzu). Cantilevers (AIOAL-TL-B, BudgetSensors) with 8 μm diameter silica spheres bonded to them were used for the measurements. The experimental procedure is described below.

(i) A drop of each lubricant was placed on a silicon chip on which iron had been deposited by a sputtering machine, and the chip was placed in the AFM.
(ii) The area was scanned at a surface pressure of approximately 400 MPa and a speed of 40 μm/s, and 100 images (128 lines/image) of a 2 × 2 μm area were acquired.

An example of the results obtained is shown in Fig. 2. In particular, the friction coefficient of FM-1 shows a small value immediately after the start of friction, indicating that the fluctuation is small. This indicates that the AO groups introduced into the material increase the adsorption strength on the iron surface, which may increase the stability against friction. Thus, the combination of the neutron reflectometry and the friction test is an example of how the neutron reflectometry can contribute to the advancement of tribological research.

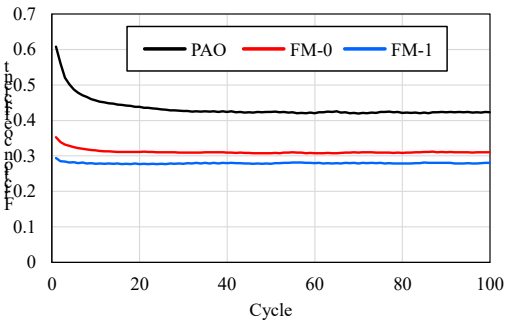

Fig. 2. Friction coefficients of interface with additives.

CO12-13 Study of Isotope Separation via Chemical Exchange Reaction

R. Hazama, P. Kumsut, T. Yoshimoto, A. Rittirong[1], C. Pitakchaianan, K. Kosinarkaranun, Y. Sakuma[2], T. Fujii[3], T. Fukutani[4], Y. Shibahara[4], T. Kishimoto[1]

Graduate School of Human Environment, Osaka Sangyo University,
[1]Research Center for Nuclear Physics, Osaka University,
[2]Laboratory for Advanced Nuclear Energy, Tokyo Institute of Technology,
[3]Graduate School of Engineering, Osaka University
[4]Institute for Integrated Radiation and Nuclear Science, Kyoto University

INTRODUCTION: Chemical isotope separation for calcium and lithium has been studied by liquid-liquid extraction (LLE) with DC18C6 crown-ether [1,2]. This report describes distribution coefficient (D) for chemical equilibrium (reaction time) of the two phase (aqueous and organic) reaction of LLE.

EXPERIMENTS: Chemical Isotopic exchange occurs according to the following chemical exchange reaction:
$^{40}Ca^{2+}_{(aq)} + {}^{48}CaL^{2+}_{(org)} \rightarrow {}^{48}Ca^{2+}_{(aq)} + {}^{40}CaL^{2+}_{(org)}$ (1)
, where L represents macrocyclic polyether(18-crown-6). Calcium chloride solution (30% w/w $CaCl_2$ (aq), and $CaCl_2$) was mixed in an Erlenmeyer flask with 0.07M DC18C6 in chloroform, by the volume ratio of 20/200 mL (aq/org), for 1 second, 1, 10, 30, and 60 minute. The mixture solution was put in the separating funnel for 10 minutes before separation. The water volume for back extraction is 1/10 of the volume ratio of water to organic phase after extraction.

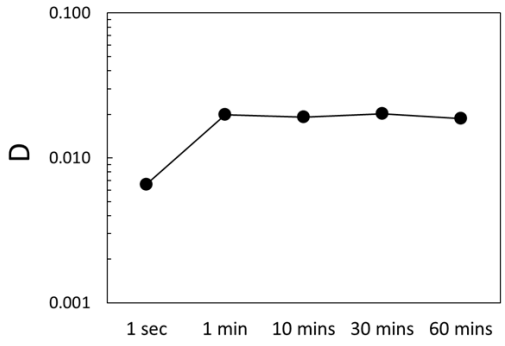

Fig. 1. Distribution coefficient (D) of Ca isotope on various extraction time using DC18C6 crown-ether: Preliminary.

In the case of lithium, K. Nishizawa et al. [3] reported the equilibria chemical exchange of lithium (LiCl) and in the organic solution contained B15C5 crown-ether to be 0.0029. The distribution coefficient was one order smaller than our finding (0.0292±0.0001). The reason was that the extraction system was different. K. Nishizawa used 20 mL of 0.186 M B15C5 and 20 mL of 8.0M LiCl (volume ratio (aq/org) = 1/1), while our experiment was 200 mL 0.07M DC18C6 and 20 mL 8.4M LiCl (volume ratio (aq/org) = 1/10).

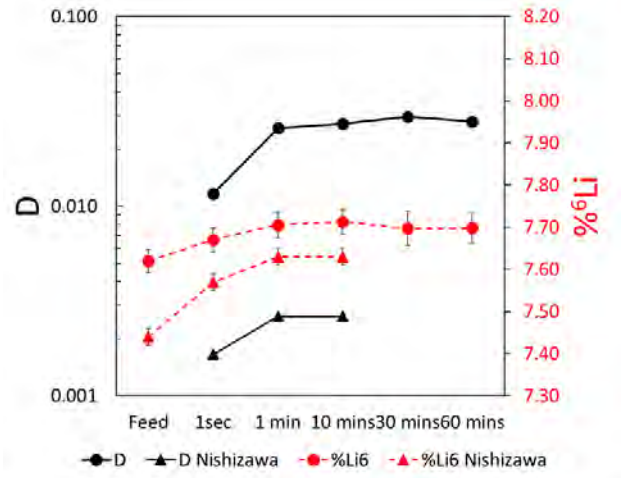

Fig. 2. Comparison between our result and K. Nishizawa et al. [3] on the isotope separation of lithium using B15C5 crown-ether: Preliminary.

RESULTS: The distribution coefficient (D) results indicate that the chemical exchange between ion and crown-ether becomes equilibrium on a magnetic stirrer's extraction time of at least 1 minute. This finding is in good agreement with K. Nishizawa et al. [3] on the study of the isotope separation via liquid-liquid extraction of lithium isotope. Their finding indicated that the chemical equilibria of 5 seconds and isotope equilibria at 30 seconds by mixing stirrer. Compared to our experiments, the extraction time was studied from 1 second and 1 minute, implying that the extraction at 1 minute using a magnetic stirrer is sufficient for equilibria the chemical and isotope exchange. The finding could benefit the shortened time required for micro-reactor extraction [4]. Fig 2 shows the comparison between this research and K. Nishizawa et al. in terms of D and $\%^6Li$ in the organic phase.

REFERENCES:

[1] A. Rittirong, Doctor Thesis, OSU (2022).
[2] A. Rittirong *et al.,* J. Phys.: Conf. Ser., **2147** (2022) 012015.
[3] K. Nishizawa *et al.,* J. Nucl. Sci. Technol., **218(9)** (1984) 694.
[4] R. Hazama *et al.,* KURRI Progress Report 2018 (2019) 252, KURRI Progress Report 2019, (2020) 282.

CO12-14 Development of neutron phase imaging system with Talbot-Lau interferometer for medium power reactor source

Y. Seki, T. Samoto, R. Nakamura[1], M. Hino[1]

Institute of Multidisciplinary Research for Advanced Materials, Tohoku university
[1]Institute for Integrated Radiation and Nuclear Science, Kyoto University

INTRODUCTION: The neutron phase imaging technique [1] offers high-sensitivity and microscopic information on samples that cannot be obtained using conventional absorption imaging techniques. Among various methods, the Talbot-Lau (TL) interferometry, a type of grating interferometry, is widely used worldwide. This method has advantages for use in medium reactor sources such as KUR. Compared to crystal-based methods, TL interferometry requires relatively mild spatial and temporal coherence conditions, which enables the use of white beams without the need to collimate incident beams narrowly. We have recently installed a neutron phase imaging system based on the TL interferometer at the CN-3 port.

EXPERIMENTS: In this experiment, we have specifically developed a new absorption grating (G2) with a large area of 64 × 64 mm^2 for the TL interferometer. The absorption lines were formed on a silicon mold using the oblique evaporation technique of gadolinium [1, 2]. By precisely adjusting the evaporation angle and repeating gradual deposition, we achieved a thick gadolinium line with a thickness of 20 μm. The performance of this new G2 was evaluated experimentally at the CN-3. Additionally, utilizing the TL interferometry, we observed a carbon steel (JIS S45C) disk subjected to high-pressure torsion (HPT) process, which introduces shear strains and refines the grain size of the material.

RESULTS: An observed neutron transmission of G2 is presented in Fig. 1. The average transmission in the grating region was 0.5, consistent with the design value. A visibility map of the interference pattern is depicted in Fig. 2 with an average value of 49%. This result is also in good agreement with the theoretical value obtained by assuming the wavelength spectrum at the CN-3.

Figure 3 displays resultant visibility images of the samples. For comparison, a disk without undergoing the HPT process was simultaneously observed. The visibility images indicate the degree of small angle scattering by microstructures in the sample, whose size is characterized by an auto-correlation length. At an auto-correlation length of 1.2 μm (Fig. 3(a)), the visibility of the unprocessed disk is higher than that of the processed one. Conversely, at an auto-correlation length of 3.8 μm (Fig. 3(b)), the visibility of the non-processed disk is lower than the other, whose visibility remains unchanged. These results suggest that the HPT process effectively reduces the grain size in the disk to less than about 1 μm.

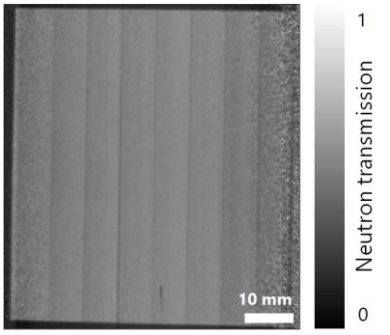

Fig. 1. Neutron transmission of the new G2.

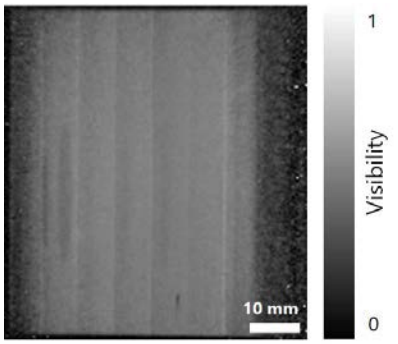

Fig. 2. Visibility map of interference pattern of the TL interferometer including the new G2.

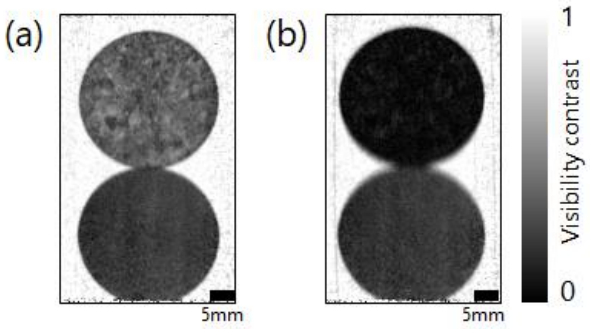

Fig. 3. Visibility images of carbon steel disks. The upper and lower disks are unprocessed and pressed by HPT, respectively. (a) auto-correlation length is 1.2 μm. (b) auto-correlation length is 3.8 μm.

REFERENCES:

[1] T. Samoto *et al.*, Jpn. J. Appl. Phys., **58** (2019) SDDF12.
[2] T. Samoto *et al.*, Mater. Sci. Semicond., **92** (2019) 91-95.

CO12-15 Fiber-reading Radiation Monitoring System with an Optical Fiber and Red-emitting Scintillator at the ^{60}Co Radiation Facility III

S. Kurosawa[1,2,3], C. Fujiwara[2,4], D. Matsukura[2,4], S. Ishizawa[2], A. Yamaji[1,2], T. Takata[5], H. Tanaka[5]

[1]*New Industry Creation Hatchery Center, Tohoku University*
[2] *Institute for Materials Research Tohoku University*
[3] *Institute of Laser Engineering, Osaka University*
[4] *Department of Materials Science, Graduate School of Engineering, Tohoku University*
[5] *Institute for Integrated Radiation and Nuclear Science, Kyoto University*

INTRODUCTION: Decommissioning reactors at nuclear power plant safety is an important issue, and a real-time dose-rate monitor in extremely high radiation dose conditions is required. We have proposed a dose-rate monitor system consisting of a scintillator, optical fiber and Charge Coupled Device (CCD) spectrometer, and scintillation photons through the fiber are read under the lower dose condition with the CCD. As we mentioned in the previous reports [1-2], the scintillator is required to have a long-emission wavelength (550 – 1,000 nm) and (ii) high light output (over 40,000 photons/ thermal neutron).

Cs_2HfI_6 (CHI) has a high light output (over 60,000 photons/MeV), high effective-atomic number (over 60), red and infrared emission (600 – 800 nm) and no afterglow (less than 1% within 1s), and this material is available for such dose monitors [1][3].

However, CHI has insufficient sensitivity to neutrons. Neutrons from ^{244}Cm and ^{242}Cm are assumed to exist inside the reactors, and we focused on Li_2HfBr_6 and other candidates [4].

EXPERIMENTS: Row materials powders were inserted in a quartz ampoule in Ar gas atmosphere. The ampoule was evacuated and sealed off by an oxyhydrogen burner, and the crystals were grown by the vertical Bridgman-Stockbarger method.

Using the scintillator, we operated the demonstration of the dose-rate monitoring system under high neutron and gamma-ray intensity at The Heavy Water Neutron Irradiation Facility (HWNIF) or research reactors (KUR) and the ^{60}Co facility, respectively. The scintillation spectra were measured for the sample with a neutron flux of around 6.0×10^{8}-4.0×10^{6} n cm^{-2}s^{-1} using a CCD through the optical fiber with a length and core diameter of 20 m and 0.6 mm, respectively.

RESULTS: We succeeded in growing the Li_2HfBr_6 crystal, and the single phase was confirmed by the result of the powder X-ray diffraction. Li_2HfBr_6 had an emission wavelength of around 600 nm excited by X-rays and light output of around 50,000 photons/ thermal neutron.

Li_2HfBr_6 had emission peaks at approximately 600 nm excited by gamma rays from the ^{60}Co source, the dose-rate dynamic range for the monitor system was up to a few kGy/h.

Scintillation spectra for the Li_2HfBr_6 sample irradiated with neutrons under the 6.0×10^{8}~4.0×10^{6} neutrons cm^{-2}s^{-1}. Figure 1 shows the emission spectrum for Li_2HfBr_6 under the 6.0×10^{8} neutrons cm-2s-1, and the emission band was observed at around 600 nm. In addition, we measured the emission spectrum without the scintillator as background evaluations, and no signal was observed as shown in Fig. 1.

To detect gamma rays, we also measured other scintillation materials, instead of Li_2HfBr_6, with a lower detection efficiency for neutrons. The result shows no significant signal excited by gamma rays was observed. The signal intensities, defined as the integration of the emission spectrum, as a function of neutron flux were fitted by the power law function.

Thus, the dose-rate monitor system with Li_2HfBr_6 can be applied to both gamma-ray and neutron monitors.

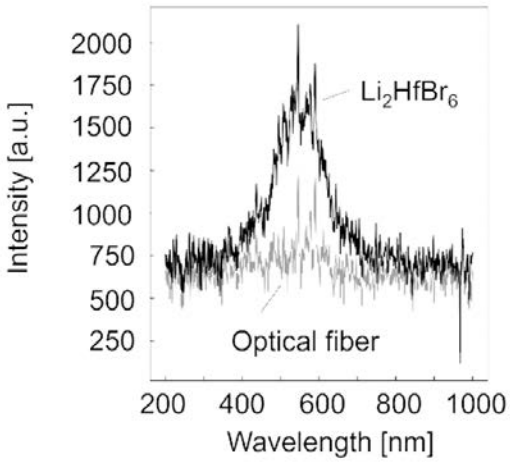

Fig. 1. Emission spectra of the dose-rate monitor system with Li_2HfBr_6 and without the crystal; the signal was generated from only optical fiber.

REFERENCES:

[1] S. Kurosawa *et al.*, KURNS PROGRESS REPORT 2020 (2021) 79.
[2] S. Kurosawa *et al.*, KURNS PROGRESS REPORT 2021 (2022) 248.
[3] S. Kodama *et al.*, Ra-diat. Meas., **124** (2019) 54-58.
[4] JAEA&IRID report (in Japanese). https://www.meti.go.jp/earthquake/nuclear/decommissioning/committee/osensuitaisakuteam/2016/11/3-04-03.pdf.

II. PUBLICATION LIST
(APRIL 2022 – MARCH 2023)

1. Slow Neutron Physics and Neutron Scattering

Papers

Local structure analysis of disordered materials via contrast variation in scanning transmission electron microscopy
Kimoto Koji, Shiga Motoki, Kohara Shinji, Kikkawa Jun, Cretu Ovidiu, Onodera Yohei, Ishizuka Kazuo
AIP Advances 12(9) (2022) 095219 (doi) 10.1063/5.0104798

A novel nuclear emulsion detector for measurement of quantum states of ultracold neutrons in the Earth's gravitational field
Muto N., Abele H., Ariga T., Bosina J., Hino M., Hirota K., Ichikawa G., Jenke T., Kawahara H., Kawasaki S., Kitaguchi M., Micko J., Mishima K., Naganawa N., Nakamura M., Roccia S., Sato O., Sedmik R.I.P., Seki Y., Shimizu H.M., Tada S., Umemoto A.
Journal of Instrumentation 17(7) (2022) P07014 (doi) 10.1088/1748-0221/17/07/P07014

Microscopic observation of the effects of elongation on the polymer chain dynamics of crosslinked polybutadiene using quasi-elastic γ-ray scattering
Mashita Ryo, Saito Makina, Yoda Yoshitaka, Kishimoto Hiroyuki, Seto Makoto, Kanaya Toshiji
Journal of Synchrotron Radiation 29(5) (2022) 1180- 1186 (doi) 10.1107/S1600577522007998

Time-resolved resonant soft X-ray scattering combined with MHz synchrotron X-ray and laser pulses at the Photon Factory
Fukaya Ryo, Adachi Jun-ichi, Nakao Hironori, Yamasaki Yuichi, Tabata Chihiro, Nozawa Shunsuke, Ichiyanagi Kouhei, Ishii Yuta, Kimura Hiroyuki, Adachi Shin-ichi
Journal of Synchrotron Radiation 29(6) (2022) 1414-1419 (doi) 10.1107/S1600577522008724

Rayleigh Scattering of Synchrotron Mössbauer Radiation Using a Variable Bandwidth Nuclear Bragg Monochromator
Mitsui Takaya, Masuda Ryo, Kitao Shinji, Kobayashi Yasuhiro, Seto Makoto
Journal of the Physical Society of Japan 91(6) (2022) 64001 (doi) 10.7566/JPSJ.91.064001

Characterization of Precipitated Phase in Cu–Ni–Si Alloy by Small-Angle X-ray Scattering, Small Angle Neutron Scattering and Atom Probe Tomography
Sasaki Hirokazu, Akiya Shunta, Oba Yojiro, Onuma Masato, Giddings A.D., Ohkubo Tadakatsu
MATERIALS TRANSACTIONS 63(10) (2022) 1384-1389 (doi) 10.2320/matertrans.MT-D2022003

Study on the reusability of fluorescent nuclear track detectors using optical bleaching
Muneem Abdul, Yoshida Junya, Ekawa Hiroyuki, Hino Masahiro, Hirota Katsuya, Ichikawa Go, Kasagi Ayumi, Kitaguchi Masaaki, Kodaira Satoshi, Mishima Kenji, Nabi Jameel-Un, Nakagawa Manami, Sakashita Michio, Saito Norihito, Saito Takehiko R., Wada Satoshi, Yasuda Nakahiro
Radiation Measurements 158 (2023) 106863 (doi) 10.1016/j.radmeas.2022.106863

Extracting time series matching a small-angle X-ray scattering profile from trajectories of molecular dynamics simulations
Shimizu Masahiro, Okuda Aya, Morishima Ken, Inoue Rintaro, Sato Nobuhiro, Yunoki Yasuhiro, Urade Reiko, Sugiyama Masaaki
Scientific Reports 12(1) (2022) 9970 (doi) 10.1038/s41598-022-13982-9

Proceedings

Development of a program for MRI by means of beta-NMR method
T. Sugisaki, Y. Kimura, G. Takayama, M. Tanaka, Y. Mizoi, M. Mihara, M. Fukuda, Y. Otani, M. Fukutome, R. Taguchi, T. Izumikawa, N. Noguchi, K. Takatsu, T. Ohtsubo, K. Matsuda, A. Kitagawa, S. Sato
Proceedings of the Specialists' Meeting on "Nuclear Spectroscopy and Condensed Matter Physics Using Short-Lived Nuclei Ⅷ" Online (Jan. 28, 2022) 45-49 (in Japanese)

Laser spectroscopy at KISS
Y. Hirayama, M. Mukai, Y.X. Watanabe, P. Schury, H. Choi, J.Y. Moon, T. Hashimoto, S. Iimura, M. Oyaizu, S.C. Jeong, T. Niwase, M. Tajima, A. Taniguchi, M. Wada, H. Miyatake
Proceedings of the Specialists' Meeting on "Nuclear Spectroscopy and Condensed Matter Physics Using Short-Lived Nuclei Ⅷ" Online (Jan. 28, 2022) 40-44 (in Japanese)

Structural Analysis of Additive in Lubricants by Means of Small Angle X-ray Scattering
Tomoko Hirayama, Sohei Nambo, Naoki Yamashita, Yoriyuki Takashima, Nobuhiro Sato, Masaaki Sugiyama
Proceedings of the 57th KURNS Scientific Meeting Online/Kumatori, Japan (Feb. 14-15, 2023) 17 (in Japanese)

2. Nuclear Physics and Nuclear Data

Papers

Reprint of The improvement of the energy resolution in epi-thermal neutron region of Bonner sphere using boric acid water solution moderator
Ueda H., Tanaka H., Sakurai Y.
Applied Radiation and Isotopes 106 (2022) 107-110 (doi) 10.1016/j.apradiso.2015.10.010

Multibeam Laser Plasma Interaction at Gekko XII laser facility in conditions relevant for Direct-Drive Inertial Confinement Fusion
Cristoforetti G., Koester P., Atzeni S., Batani D., Fujioka S., Hironaka Y., Hüller S., Idesaka T., Katagiri K., Kawasaki K., Kodama R., Mancelli D., Nicolai Ph., Ozaki N., Schiavi A., Shigemori K., Takizawa R., Tamagawa T., Tanaka D., Tentori A., Umeda Y., Yogo A., Gizzi L.A.
High Power Laser Science and Engineering 11 (2023) e24 (doi) 10.1017/hpl.2023.13

Development of a water Cherenkov neutron detector for the active rotation method and demonstration of nuclear material detection
Tanabe Kosuke, Komeda Masao, Toh Yosuke, Kitamura Yasunori, Misawa Tsuyoshi, Tsuchiya Ken'ichi, Akiba Norimitsu, Kakuda Hidetoshi, Shibasaki Kazunari, Sagara Hiroshi
Journal of Nuclear Science and Technology 61(7) (2022) 1-13 (doi) 10.1080/00223131.2022.2143449

Spectroscopic and electric properties of the TaO^+ molecule ion for the search of new physics: A platform for identification and state control
Sunaga Ayaki, Fleig Timo
Journal of Quantitative Spectroscopy and Radiative Transfer 288 (2022) 108229 (doi) 10.1016/j.jqsrt.2022.108229

Measurement of neutron flux parameters for implementation of k0-INAA at Kyoto University Research Reactor
Soliman Mohamed, Abdou Fatma S., Ho Van-Doanh, Sekimoto Shun, Takamiya Koichi, Mohamed Nader M. A., Ohtsuki Tsutomu
Journal of Radioanalytical and Nuclear Chemistry 331(9) (2022) 3949-3956 (doi) 10.1007/s10967-022-08391-1

In-gas-cell laser resonance ionization spectroscopy of Pt200, 201
Hirayama Y., Mukai M., Watanabe Y. X., Schury P., Nakada H., Moon J. Y., Hashimoto T., Iimura S., Jeong S. C., Rosenbusch M., Oyaizu M., Niwase T., Tajima M., Taniguchi A., Wada M., Miyatake H.
Physical Review C 106(3) (2022) 34326 (doi) 10.1103/PhysRevC.106.034326

Spin-charge coupling and decoupling in perovskite-type iron oxides $(Sr_{1-x}Bax)_{2/3}$ $La_{1/3}FeO_3$
Onose M., Takahashi H., Saito T., Kamiyama T., Takahashi R., Wadati H., Kitao S., Seto M., Sagayama H., Yamasaki Y., Sato T., Kagawa F., Ishiwata S.
Physical Review Materials 6(9) (2022) 94401 (doi) 10.1103/PhysRevMaterials.6.094401

Proceedings

[61]Mössbauer Spectroscopy for Supramolecular Bridging Cyanide Complexes
T. Kitazawa, K. Kitase, D. Ueda, D. Fujimoto, S. Arai, Y. Kobayashi, S. Kitao, T. Kubota, M. Seto
Proceedings of the Specialists' Meeting on "Nuclear Spectroscopy and Condensed Matter Physics Using Short-Lived Nuclei Ⅷ" Online (Jan. 28, 2022) 1-5 (in Japanese)

Discussion of spin bistability on Fe-Ag-type cyanobridged complex type using Mössbauer effect
K. Kitase, T. Kitazawa
Proceedings of the Specialists' Meeting on "Nuclear Spectroscopy and Condensed Matter Physics Using Short-Lived Nuclei Ⅷ" Online (Jan. 28, 2022) 22-26 (in Japanese)

Gamma Ray Spectrum Measurement from Capture Reactions of Uranium-238 for Thermal and Resonance Energy Neutrons
Y. Nauchi, J. Hori, K. Terada, T. Sano
International conference on nuclear data (ND2022) Online (Jul. 21-29, 2022)

Local Structure of Cadmium Doped $SrTiO_3$
S. Komatsuda, W. Sato, A. Taniguchi, M. Tanigaki, Y. Ohkubo
Proceedings of the Specialists' Meeting on "Nuclear Spectroscopy and Condensed Matter Physics Using Short-Lived Nuclei Ⅷ" Online (Jan. 28, 2022) 10-14 (in Japanese)

Present Status and Approach for Industrial Application of Various-Element Mossbauer Spectroscopy using KUR, LINAC and Synchrotron Radiation
Shinji Kitao, Yasuhiro Kobayashi, Masayuki Kurokuzu, Makoto Seto, Hiroyuki Tajima, Hiroyuki Yamashita, Hidetoshi Ota, Takumi Kubota, Ryo Masuda
Proceedings of the 57th KURNS Scientific Meeting Online/Kumatori, Japan (Feb. 14-15, 2023) 22 (in Japanese)

Present Status and Future Projects for Mössbauer Spectroscopy at Institute for Integrated Radiation and Nuclear Kyoto University
S. Kitao, Y. Kobayashi, M. Kurokozu, T. Kubota, H. Tajima, T. Fujiwara, R. Masuda, M. Seto
Proceedings of the Specialists' Meeting on "Nuclear Spectroscopy and Condensed Matter Physics Using Short-Lived Nuclei Ⅷ" Online (Jan. 28, 2022) 6-9 (in Japanese)

Research on the chemical state of nitrogen in H_2O byμ^-SR and β-NMR spectroscopy
Y. Kimura, M. Mihara, K. Matsuta, M. Fukuda, R. Wakabayashi, Y. Otani, M. Fukutome, G. Takayama, T. Minamisono, D. Nishimura, H. Takahashi, T. Izumikawa, T. Ohtsubo, N. Noguchi, M. Ogose, M. Sato, K. Takatsu, S. Momota, A. Ozawa, T. Nagamoto, A. Kitagawa, S. Sato, M.K. Kubo, K. Shimomura, A. Koda, S. Takeshita
Proceedings of the Specialists' Meeting on "Nuclear Spectroscopy and Condensed Matter Physics Using Short-Lived Nuclei Ⅷ" Online (Jan. 28, 2022) 50-55 (in Japanese)

β-decay spectroscopy of rare fisson products with 4πclover detector using an Isotope Separator On-Line KUR-ISOL-Search for γ-rays in the decay of ^{155}Pr
Y. Irie, S. Sakakibara, M. Shibata, A. Taniguchi
Proceedings of the Specialists' Meeting on "Nuclear Spectroscopy and Condensed Matter Physics Using Short-Lived Nuclei Ⅷ" Online (Jan. 28, 2022) 35-39 (in Japanese)

Reviews

Development and application of the neutron standards
Matsumoto Tetsuro, Masuda Akihiko, Harano Hideki
Journal of the Atomic Energy Society of Japan 63(6) (2022) 480-484 (in Japanese) (doi)10.3327/jaesjb.63.6_480

Others

Yield measurements for 86Kr + 198Pt at KISS
Y.X. Watanabe, Y. Hirayama, M. Mukai, T. Niwase, P. Schury, M. Rosenbusch, M. Wada, H. Miyatake, S.C. Jeong, S. Iimura, M. Oyaizu, A. Taniguchi
RIKEN Accelerator Progress Repport 2021 55 (2022) 25

In-gas-cell laser ionization spectroscopy of 200gPt using MRTOF-MS at KISS
Y. Hirayama, M. Mukai, Y.X. Watanabe, P. Schury, J.Y. Moon, T. Hashimoto, S. Iimura, S.C. Jeong, M. Rosenbusch, M. Oyaizu, T. Niwase, M. Tajima, A. Taniguchi, M. Wada, H. Miyatake
RIKEN Accelerator Progress Repport 2021 55 (2022) 26

β-decay spectroscopy of rare fission products with a 4π clover detector using an Isotope Separator On-Line KUR-ISOL
S. Sakakibara, Y. Irie, T. Yamaguchi, T. Miyazawa, M. Shibata, A. Taniguchi
KURNS Progress report 2021 (2022) 94

3. Reactor Physics and Reactor Engineering

Papers

Hybrid Organic–Inorganic Perovskite Semiconductor-Based High-Flux Neutron Detector with BN Converter
Okuno Yasuki, Matsui Taisuke, Kobayashi Tomohiro, Imaizumi Mitsuru, Jimba Yuki, Hao Yu, Kondo Sosuke, Kaneko Yukihiro, Kasada Ryuta
ACS Applied Electronic Materials 4(7) (2022) 3411-3420 (doi) 10.1021/acsaelm.2c00258

Dynamic mode decomposition application to dominance ratio assessment in Monte Carlo k-eigenvalue calculation
Yamamoto Toshihiro, Shen Xiuzhong, Sakamoto Hiroki
Annals of Nuclear Energy 175 (2022) 109205 (doi) 10.1016/j.anucene.2022.109205

Dynamic mode decomposition for subcriticality measurement using measured data at single location
Yamamoto Toshihiro, Sakamoto Hiroki
Annals of Nuclear Energy 180 (2023) 109480 (doi) 10.1016/j.anucene.2022.109480

Higher harmonic analyses of the Rossi-α method and application of dynamic mode decomposition for time decay constant determination in a 1D subcritical system
Yamamoto Toshihiro, Sakamoto Hiroki
Annals of Nuclear Energy 168 (2022) 108886 (doi) 10.1016/j.anucene.2021.108886

Monte Carlo sensitivity analyses of isothermal temperature coefficient in solid-moderated and solid-reflected cores at Kyoto University critical assembly
Song Kyoseong, Ho Pyeon Cheol, Jin Shim Hyung
Annals of Nuclear Energy 180 (2023) 109491 (doi) 10.1016/j.anucene.2022.109491

Fast-neutron capture cross section data measurement of minor actinides for development of nuclear transmutation systems
Katabuchi Tatsuya, Iwamoto Osamu, Hori Jun-ich, Kimura Atsushi, Iwamoto Nobuyuki, Nakamura Shoji, Rovira Gerard, Endo Shunsuke, Shibahara Yuji, Terada Kazushi, Kodama Yu, Nakano Hideto, Sato Yaoki, Matsuura Shota
EPJ Web of Conferences 281 (2023) 00014 (doi) 10.1051/epjconf/202328100014

Interfacial area concentration in gas-liquid metal two-phase flow
Shen Xiuzhong, Yamamoto Toshihiro, Han Xu, Hibiki Takashi
Experimental and Computational Multiphase Flow 5(1) (2023) 84-98 (doi) 10.1007/s42757-021-0110-x

Two-phase interfacial structure development in vertical narrow rectangular channels
Shen Xiuzhong, Hibiki Takashi
International Journal of Heat and Mass Transfer 191 (2022) 122832 (doi) 10.1016/j.ijheatmasstransfer.2022.122832

Visualization of Gas-Liquid Interfacial Behavior in a Narrow Channel Using High-Speed Neutron Imaging
Daisuke ITO, Naoya ODAIRA, Kei ITO, Yasushi SAITO, Keisuke KURITA, Hiroshi IIKURA
JAPANESE JOURNAL OF MULTIPHASE FLOW 37(1) (2023) 73-78 (in Japanese) (doi) 10.3811/jjmf.2023.007

X 線イメージングを用いた球充填層内のボイド率分布計測
YAMAMOTO Seishiro, ODAIRA Naoya, ITO Daisuke, ITO Kei, SAITO Yasushi, IMAIZUMI Yuya, MATSUBA Kenichi, KAMIYAMA KenjiKenichi, KAMIYAMA Kenji
JAPANESE JOURNAL OF MULTIPHASE FLOW 37(1) (2023) 79-85 (in Japanese) (doi) 10.3811/jjmf.2023.008

Monte Carlo sensitivity calculation in fixed source problems with the derivative source method
Yamamoto Toshihiro, Sakamoto Hiroki
Journal of Computational Physics 460 (2022) 111155 (doi) 10.1016/j.jcp.2022.111155

Spatial distribution and preferred orientation of crystalline microstructure of lead-bismuth eutectic
Ito Daisuke, Sato Hirotaka, Odaira Naoya, Saito Yasushi, Parker Joseph Don, Shinohara Takenao, Kai Tetsuya, Oikawa Kenichi
Journal of Nuclear Materials 569 (2022) 153921 (doi) 10.1016/j.jnucmat.2022.153921

Application of dynamic mode decomposition to Rossi-α method in a critical state using file-by-file moving block bootstrap method
Endo Tomohiro, Nishioka Fuga, Yamamoto Akio, Watanabe Kenichi, Pyeon Cheol Ho
Journal of Nuclear Science and Technology 59(9) (2022) 1117-1126 (doi) 10.1080/00223131.2022.2030260

Development of a critical heat flux correlation based on a mechanistic model under subcooled flow boiling conditions
Yodo Tadakatsu, Odaira Naoya, Ito Kei, Ito Daisuke, Saito Yasushi
Journal of Nuclear Science and Technology 60(3) (2022) 197-214 (doi) 10.1080/00223131.2022.2091054

Uncertainty Quantification of Light-Water-Moderated and Light-Water-Reflected Cores with Highly-Enriched Uranium Fuel at Kyoto University Critical Assembly
C. H. Pyeon and K. Morioka
Journal of Nuclear Science and Technology 59 (2022) 898-906 (doi) 10.1080/00223131.2021.2017371

Pressure drop evaluation based on two-phase flow observation in packed bed system
YASUGI Noriaki, ODAIRA Naoya, ITO Daisuke, ITO Kei, SAITO Yasushi
Mechanical Engineering Journal 9(4) (2022) 21-00437 (doi) 10.1299/mej.21-00437

Conceptual design of a target station using a 30-MeV cyclotron accelerator for the basic study of boron neutron capture therapy at KURNS
Nakamura R., Hino M., Tanaka H., Kuriyama Y., Iwashita Y.
Nuclear Instruments and Methods in Physics Research Section A: Accelerators, Spectrometers, Detectors and Associated Equipment 1042 (2022) 167425 (doi) 10.1016/j.nima.2022.167425

Nuclear Data-Induced Uncertainty of Criticality in Solid-Moderated and Solid-Reflected Cores with Highly-Enriched Uranium Fuel at Kyoto University Critical Assembly
C. H. Pyeon and K. Morioka
Nuclear Science and Engineering 196 (2022) 1147-1160 (doi) 10.1080/00295639.2022.2070385

Theoretical Derivation of a Unique Combination Number Hidden in the Higher-Order Neutron Correlation Factors Using the Pál-Bell Equation
Endo Tomohiro, Nishioka Fuga, Yamamoto Akio, Watanabe Kenichi, Pyeon Cheol Ho
Nuclear Science and Engineering 197Z(2) (2022) 176-188 (doi) 10.1080/00295639.2022.2049992

Proceedings

Double Heterogeneity Effect on Reactivity of U-Mo Research Reactor Fuel
H. Unesaki
European Research Reactor Conference-RRFM2022 Budapest, Hungary (Jun. 6-10 2022) 334-341

High-Radiation-Tolerant CIGS Solar Cell based Self-Power Driven Radiation Dosimeter for IF
奥野泰希, 今泉充, 上川由紀子, 岡本保, 小林知洋, 牧野裔紘, 笠田竜太
Proceedings of the 57th KURNS Scientific Meeting Online/Kumatori, Japan (Feb. 14-15, 2023) 1-3 (in Japanese)

Measurement of U-233 Sample Reactivity Worth in KUCA for Integral Validation of Nuclear Data
T. Sano, J. Hori, Y. Takahashi, K. Terada, T. Kanda, H. Unesaki
International Conference on Physics of Reactors (PHYSOR 2022) Pittsburgh, U.S.A. (May 15-20, 2022) 2822-2830

Preliminary Experiment in a Graphite-Moderated Core to Avoid Full Mock-up Experiment for the Future First Commercial HTGR
S. Okita, Y. Fukaya, A. Sakon, T. Sano, Y. Takahashi, H. Unesaki
International Conference on Physics of Reactors (PHYSOR 2022) Pittsburgh, U.S.A. (May 15-20, 2022) 2338-2346

Subcritical Experiment using U-7Mo LEU at KUCA facility
Y. Takahashi, K. Wakabayashi, Y. Kitamura, H. Unesaki, T. Misawa
RERTR 2022 - 42nd International Meeting on Reduced Enrichment for Research and Test Reactors Vienna, Austria (Oct. 3-5, 2022)

Void fraction prediction for gas-liquid two-phase flow in plate-type fuel assembly
Xiuzhong Shen, Toshihiro Yamamoto, Ken Nakajima, Takashi Hibiki
Proceedings of the 57th KURNS Scientific Meeting Online/Kumatori, Japan (Feb. 14-15, 2023) 21 (in Japanese)

Reviews

Channel size effect on drift-flux parameters for adiabatic and boiling two-phase flows
Hibiki Takashi, Ju Peng, Rassame Somboon, Miwa Shuichiro, Shen Xiuzhong, Ozaki Tetsuhiro
International Journal of Heat and Mass Transfer 185 (2022) 122410
(doi)10.1016/j.ijheatmasstransfer.2021.122410

Development of a reactor-based slow-positron beamline
Atsushi Kinomura, Atsushi Yabuuchi
Positron sciences 19 (2022) 3-12 (in Japanese)

Books

Introduction to Nuclear Reactor Experiments
Wakabayashi Genichiro, Yamada Takahiro, Endo Tomohiro, Pyeon Cheol Ho
Springer Nature Singapore 2022 (ISBN) 9789811965883 (doi) 10.1007/978-981-19-6589-0

Others

Development of accident tolerant control rod (3) Compatibility between novel neutron absorbing and core structural materials at high temperature
Kinya NAKAMURA, Hirokazu, OHTA
Atomic Energy Society of Japan 2021 Annual Meeting (2021) 2K02 (in Japanese)

Development of accident tolerant control rod (3) Reactivity measurement of candidate neutron absorbing materials
Hirokazu Ohta, Yasushi Nauchi, Kinya Nakamura and Tadafumi Sano
Atomic Energy Society of Japan 2018 Annual Meeting (2018) 2F16 (in Japanese)

4. Material Science and Radiation Effects

Papers

Improvement of laccase biosensor characteristics using sulfur-doped TiO_2 nanoparticles
Kavetskyy Taras, Smutok Oleh, Demkiv Olha, Kukhazh Yuliia, Stasyuk Nataliya, Leonenko Evhen, Kiv Arnold, Kobayashi Yoshinori, Kinomura Atsushi, Šauša Ondrej, Gonchar Mykhailo, Katz
Evgeny Bioelectrochemistry 147 (2022) 108215 (doi) 10.1016/j.bioelechem.2022.108215

Preparation of Li_2TiO_3-Li_4SiO_4-Pb tritium breeding ceramic and its mechanical properties
Wang Qiao, Zhou Qilai, Xiong Qingbi, Zhou Jianglin, Li Sicheng, Hirata Shiori, Oya Yasuhisa
Ceramics International 40(18) (2022) 26742-26749 (doi) 10.1016/j.ceramint.2022.05.369

High thermal conductivity of stishovite promotes rapid warming of a sinking slab in Earth's mantle
Hsieh Wen-Pin, Marzotto Enrico, Tsao Yi-Chi, Okuchi Takuo, Lin Jung-Fu
Earth and Planetary Science Letters 584 (2022) 117477 (doi) 10.1016/j.epsl.2022.117477

Acoustic Wave Velocities of Ferrous-Bearing $MgSiO_3$ Glass up to 158 GPa With Implications for Dense Silicate Melts at the Base of the Earth's Mantle
Mashino Izumi, Murakami Motohiko, Kitao Shinji, Mitsui Takaya, Masuda Ryo, Seto Makoto
Geophysical Research Letters 49(19) (2022) e2022GL098279 (doi) 10.1029/2022GL098279

Evaluation of Radiation Damage to LAN-Cable Sheaths in a Vacum Vessel for Neutron Scattering
Taiki Tominaga, Misaki Ueda, Kawakita Yukinobu, Toshiyuki Chatake, Tsuyoshi Saito, Nobuhiro Sato
Hamon 32(2) (2022) 91-95 (in Japanese)

^{161}Dy synchrotron-radiation-based Mössbauer absorption spectroscopy
Masuda Ryo, Kitao Shinji, Tajima Hiroyuki, Taniguchi Hiroki, Mitsui Takaya, Fujiwara Kosuke, Yoda Yoshitaka, Nagasawa Nobumoto, Ishikawa Daisuke, Baron Alfred. Q. R., Yoshida Takefumi, Sato Tetsu, Katoh Keiichi, Kobayashi Hisao, Seto Makoto
Hyperfine Interactions 243(1) (2022) 17-1- 17-8 (doi) 10.1007/s10751-022-01802-5

Energy domain synchrotron-radiation-based Mössbauer spectroscopy of EuH2 under a few GPa pressure
Masuda Ryo, Hirao Naohisa, Fujiwara Kosuke, Mitsui Takaya, Fujihara Taku, Yamashita Hiroyuki, Tajima Hiroyuki, Kurokuzu Masayuki, Kitao Shinji, Seto Makoto
Hyperfine Interactions 244(1) (2023) 5 (doi) 10.1007/s10751-022-01815-0

Mössbauer study of the material of the electric power transformers
Kobayashi Yasuhiro, Kitao Shinji, Yuasa Kosuke, Seto Makoto
Hyperfine Interactions 243 (2022) 26 (doi) 10.1007/s10751-022-01810-5

Hugoniot and released state of calcite above 200 GPa with implications for hypervelocity planetary impacts
Umeda Yuhei, Fukui Keiya, Sekine Toshimori, Guarguaglini Marco, Benuzzi-Mounaix Alessandra, Kamimura Nobuki, Katagiri Kento, Kodama Ryosuke, Matsuoka Takeshi, Miyanishi Kohei, Ravasio Alessandra, Sano Takayoshi, Ozaki Norimasa
Icarus 377 (2022) 114901 (doi) 10.1016/j.icarus.2022.114901

Repetitive Irradiation Tests at Cryogenic Temperature by Neutrons and Protons on Stabilizer Materials of Superconductor
Yoshida M., Nakamoto T., Ogitsu T., Xu Q., Yoshiie T., Meigo S., Iwamoto Y.
IEEE Transactions on Applied Superconductivity 32 (2022) 7100405 (doi) 10.1109/TASC.2022.3178944

Effect of neutron dose on the tritium release behavior of Li_2TiO_3–$0.5Li_4SiO_4$ biphasic ceramic
Zhou Qilai, Sun Fei, Hirata Shiori, Li Sicheng, Li Yuanyuan, Oya Yasuhisa
International Journal of Hydrogen Energy 48(11) (2023) 4363-4370 (doi) 10.1016/j.ijhydene.2022.11.009

Investigation of defect states in light-irradiated single-crystal ZnO by low-temperature positron annihilation lifetime spectroscopy
Nakajima Makoto, Kinomura Atsushi, Yabuuchi Atsushi, Kuriyama Kazuo
Japanese Journal of Applied Physics 10 (2022) 100905 (doi) 10.35848/1347-4065/ac9103

Rare-earth silicides: the promising candidates for thermoelectric applications at near room temperature
Tanusilp Sora-at, Kurosaki Ken
Japanese Journal of Applied Physics 62(SD) (2022) SD0802 (doi) 10.35848/1347-4065/aca0fc

Response of piezoelectric lead zirconate titanate to 20 MeV electron beam irradiation
Takechi Seiji, Morita Yudai, Niiya Shingo, Miyachi Takashi, Kobayashi Masanori, Okudaira Osamu, Okada Nagaya, Takahashi Toshiharu, Abe Naoya
Japanese Journal of Applied Physics 61(12) (2022) 128001 (doi) 10.35848/1347-4065/ac9e30

Comparative study of vacancy cluster formation in pure Ni, CoCrNi, and CoCrFeNi with a CoCrFeMnNi multicomponent system
Xu Q., Guan H.Q., Huang S.S., Zhong Z.H.
Journal of Alloys and Compounds 918 (2022) 165747 (doi) 10.1016/j.jallcom.2022.165747

Compositional stability in medium and high-entropy alloys of CoCrFeMnNi system under ion irradiation
Xu Q., Guan H.Q., Huang S.S., Zhong Z.H., Watanabe H., Tokitani M.
Journal of Alloys and Compounds 925 (2022) 166697 (doi) 10.1016/j.jallcom.2022.166697

Large thermopower in novel thermoelectric $Yb(Si_{1-x}Ge_x)_2$ induced by valence fluctuation
Nishide Akinori, Tanusilp Sora-at, Kowa Wataru, Yashima Mitsuharu, Nambu Akira, Hayakawa Jun, Ohishi Yuji, Muta Hiroaki, Mukuda Hidekazu, Kurosaki Ken
Journal of Applied Physics 132(6) (2022) 065106 (doi) 10.1063/5.0092002

Elasticity of Hydrated Al-Bearing Stishovite and Post-Stishovite: Implications for Understanding Regional Seismic V_S Anomalies Along Subducting Slabs in the Lower Mantle
Zhang Yanyao, Fu Suyu, Karato Shun-ichiro, Okuchi Takuo, Chariton Stella, Prakapenka Vitali B., Lin Jung-Fu
Journal of Geophysical Research: Solid Earth 127(4) (2022) e2021JB023170 (doi) 10.1029/2021JB023170

Sorption of Cs^+ and Eu^{3+} ions onto sedimentary rock in the presence of gamma-irradiated humic acid
Zhao Qi, Saito Takeshi, Miyakawa Kazuya, Sasamoto Hiroshi, Kobayashi Taishi, Sasaki Takayuki
Journal of Hazardous Materials 428 (2022) 128211 (doi) 10.1016/j.jhazmat.2021.128211

Influence of interatomic potential and simulation procedures on the structures and properties of sodium aluminosilicate glasses from molecular dynamics simulations
Kalahe Jayani, Onodera Yohei, Takimoto Yasuyuki, Hijiya Hiroyuki, Ono Madoka, Miyatani Katsuaki, Kohara Shinji, Urata Shingo, Du Jincheng
Journal of Non-Crystalline Solids 588 (2022) 121639 (doi) 10.1016/j.jnoncrysol.2022.121639

Tritium recovery behavior for tritium breeder Li_4SiO_4-Li_2TiO_3 biphasic material
Hirata Shiori, Ashizawa Kyosuke, Sun Fei, Feng Yongjin, Wang Xiaoyu, Wang Hailiang, Kobayashi Makoto, Taguchi Akira, Oya Yasuhisa
Journal of Nuclear Materials 567 (2022) 153838 (doi) 10.1016/j.jnucmat.2022.153838

Phase behavior of oxidized Ce and Gd-doped (U, Zr)O_2
Sun Yifan, Watanabe Shiho, Muta Hiroaki, Ohishi Yuji, Kurosaki Ken
Journal of Nuclear Science and Technology 60(4) (2022) 425-434 (doi) 10.1080/00223131.2022.2112782

Thermophysical and mechanical properties of LaB_6 and CeB_6 synthesized through spark plasma sintering
Sun Yifan, Ohishi Yuji, Higaki Junya, Muta Hiroaki, Kurosaki Ken
Journal of Nuclear Science and Technology (2023) 1-9 (doi) 10.1080/00223131.2023.2192728

Development of Time- and Energy-Resolved Synchrotron-Radiation-Based Mössbauer Spectroscopy
Kitao Shinji, Masuda Ryo, Fujihara Taku, Tajima Hiroyuki, Nagasawa Nobumoto, Yoda Yoshitaka, Masuda Takahiro, Yoshimura Koji and Seto Makoto
Journal of Physics: Conference Series 2380 (2022) 012136 (doi) 10.1088/1742-6596/2380/1/012136

Investigation of the Structure of Atomically Dispersed NiN_x Sites in Ni and N-Doped Carbon Electrocatalysts by ^{61}Ni Mössbauer Spectroscopy and Simulations
Koshy David M., Hossain Md Delowar, Masuda Ryo, Yoda Yoshitaka, Gee Leland B., Abiose Kabir, Gong Huaxin, Davis Ryan, Seto Makoto, Gallo Alessandro, Hahn Christopher, Bajdich Michal, Bao Zhenan, Jaramillo Thomas F.
Journal of the American Chemical Society 144(47) (2022) 21741-21750 (doi) 10.1021/jacs.2c09825

Effect of adding Ag_2O to vanadium-containing low-melting glass for low-temperature sealing
Aoyagi Takuya, Onodera Yohei, Kohara Shinji, Naito Takashi, Ina Toshiaki, Takamatsu Daiko, Onodera Taigo, Miyake Tatsuya, Tachizono Shinichi, Yoshimura Kei
Journal of the Ceramic Society of Japan 130(7) (2022) 504-508 (doi) 10.2109/jcersj2.22024

Topological analyses of structure of glassy materials toward extraction of order hidden in disordered structure Yohei Onodera
Journal of the Ceramic Society of Japan 130(8) (2022) 627-638 (doi) 10.2109/jcersj2.22033

Nucleation mechanisms in a SiO_2-Li_2O-P_2O_5-ZrO_2 biomedical glass-ceramic: Insights on crystallisation, residual glasses and Zr^{4+} structural environment
Cicconi M.R., Belli R., Brehl M., Lubauer J., Hayakawa T., Kimura K., Hirota T., Usui K., Kohara S., Onodera Y., Lohbauer U., Hayashi K., de Ligny D.
Journal of the European Ceramic Society 42(4) (2022) 1762-1775 (doi) 10.1016/j.jeurceramsoc.2021.12.009

Radiation-induced precipitates in ferritic-martensitic steels and their radiation resistance effects
Zhu Te, Jin Shuoxue, Yan Qingzhi, Wang Baoyi, Song Ligang, Hong Zhiyuan, Zhang Peng, Zhang Qiaoli, Fan Ping, Yuan Daqing, Cao Xingzhong, Ngan Alfonso H.W., Xu Qiu
Materials Today Communications 33 (2022) 104629 (doi) 10.1016/j.mtcomm.2022.104629

Micron-scale phenomena observed in a turbulent laser-produced plasma
Rigon G., Albertazzi B., Pikuz T., Mabey P., Bouffetier V., Ozaki N., Vinci T., Barbato F., Falize E., Inubushi Y., Kamimura N., Katagiri K., Makarov S., Manuel M. J.-E., Miyanishi K., Pikuz S., Poujade O., Sueda K., Togashi T., Umeda Y., Yabashi M., Yabuuchi T., Gregori G., Kodama R., Casner A., Koenig M.
Nature Communications 12 (2022) 2679 (doi) 10.1038/s41467-021-22891-w

Solid-state amorphization of gold and silicon bilayer films by annealing
Toshimasa Yoshiie
Philosophical Magazine 102(15) (2022) 1446-1460 (doi) 10.1080/14786435.2022.2078517

Atomic level control of association-dissociation behavior of In impurities in polycrystalline ZnO
Sato W., Takata M., Shimizu H., Komatsuda S., Yoshida Y., Moriyama A., Shimamura K., Ohkubo Y.
Physical Review Materials 6(6) (2022) 63801 (doi) 10.1103/PhysRevMaterials.6.063801

Observation of a critical charge mode in a strange metal
Kobayashi Hisao, Sakaguchi Yui, Kitagawa Hayato, Oura Momoko, Ikeda Shugo, Kuga Kentaro, Suzuki Shintaro, Nakatsuji Satoru, Masuda Ryo, Kobayashi Yasuhiro, Seto Makoto, Yoda Yoshitaka, Tamasaku Kenji, Komijani Yashar, Chandra Premala, Coleman Piers
Science 379(6635) (2023) 908-912 (doi) 10.1126/science.abc4787

Effects of hydrogen charging and deformation on tensile properties of a multi-component alloy for nuclear applications
Zhu Te, Zhong Zhi-Hong, Sato Koichi, Song Ya-Min, Ye Feng-Jiao, Wang Qian-Qian, Dong Ye, Zhang Peng, Yu Run-Sheng, Wang Bao-Yi, Ngan Alfonso H. W., Cao Xing-Zhong, Xu Qiu
Tungsten 4 (2022) 212-218 (doi) 10.1007/s42864-022-00148-3

Effects of Zr/Mo addition on He bubble formation in Y_2O_3-added W alloys
Xu Qiu, Miyamoto M., Luo Lai-Ma
Tungsten 4 (2022) 203-211 (doi) 10.1007/s42864-021-00131-4

Proceedings

Atomic Level Control of Association-Discussion Behavior of In Donors in ZnO
W. Sato, M. Takata, H. Shimizu, S. Komatsuda, Y. Ohkubo
Proceedings of the Specialists' Meeting on "Nuclear Spectroscopy and Condensed Matter Physics Using Short-Lived Nuclei Ⅷ" Online (Jan. 28, 2022) 15-17 (in Japanese)

Development of High-Dose Rate Real-Time Monitors with an Optical Fiber
Shunsuke Kurosawa, Hiroki Tanaka, Takushi Takada, Daisuke Matsukura, Chihaya Fujiwara, Satoshi Ishizawa, Akihiro Yamaji, Shohei Kodama
Proceedings of the 57th KURNS Scientific Meeting Online/Kumatori, Japan (Feb. 14-15, 2023) 28 (in Japanese)

Development of very small d-spacing multilayers and neutron focusing supermirror
Masahiro Hino, Tatsuro Oda, Riichiro Nakamura, Hisao Yoshinaga, Takuya Hosobata, Masahiro Takeda, Yutaka Yamagata, Hitoshi Endo
Proceedings of the 57th KURNS Scientific Meeting Online/Kumatori, Japan (Feb. 14-15, 2023) 19 (in Japanese)

Evaluation of nanovoids in Si irradiated with hydrogen ions and annealed at high temperature by positron beams
Masatoshi Hiroe, Atsushi Kinomura, Kinji Uda, Kohtaku Suzuki, Toshihiko Hori, KojiMichishio, Seiya Manabe, Tetsuro Matsumoto
Proceedings of the 57th KURNS Scientific Meeting Online/Kumatori, Japan (Feb. 14-15, 2023) 36 (in Japanese)

Evaluation of Oxide Ion Conduction Properties on solid Oxide Fuel Cell Material YSZ Using Short-Lived Nucleus ^{19}O
Y. Otani, M. Mihara, K. Matsuta, M. Fukuda, R. Wakabayashi, N. Okimoto, M. Fukutome, Y, Kimura, G. Takayama, T. Izumikawa, N. Noguchi, M. Ogose, M. Sato, K. Takatsu, T. Ohtsubo, D. Nishimura, H. Takahashi, S. Sugawara, A. Gladkov, H. Ishiyama, A. Kitagawa, S. Sato, S. Momota, H. Okumura. T. Moriguchi, A. Ozawa, K. Tomita, N. Nakase, A. Yano
Proceedings of the Specialists' Meeting on "Nuclear Spectroscopy and Condensed Matter Physics Using Short-Lived Nuclei Ⅷ" Online (Jan. 28, 2022) 56-60 (in Japanese)

Gamma dose evaluation method with BeO OSLD in BNCT
Nishiki Matsubayashi, Takushi Takata, Naonori Ko, Akihiro Sasaki, Tetsuya Mukawa, Keita Suga, Yoshinori Sakurai, Hiroki Tanaka
Proceedings of the 57th KURNS Scientific Meeting Online/Kumatori, Japan (Feb. 14-15, 2023) 20 (in Japanese)

Interaction between radiation induced defects and hydrogen in bulk metals by using Gamma beam induced Positron Spectroscopy
S. Araki, X. Qiu, Y. Taira and F. Hori
Proceedings of the 57th KURNS Scientific Meeting Online/Kumatori, Japan (Feb. 14-15, 2023) 17 (in Japanese)

Mössbauer spectra of YIG substituted with Bi
M. Yishida,Y. Watanabe, Y. Kobayashi
Proceedings of the Specialists' Meeting on "Nuclear Spectroscopy and Condensed Matter Physics Using Short-Lived Nuclei Ⅷ" Online (Jan. 28, 2022) 18-21 (in Japanese)

Solid State Physics Research via βNMR
K. Matsuta
Proceedings of the Specialists' Meeting on "Nuclear Spectroscopy and Condensed Matter Physics Using Short-Lived Nuclei Ⅷ" Online (Jan. 28, 2022) 61-66 (in Japanese)

Stability of novel neutron absorbing materials in coolant water and under low fluence irradiation
H. Ohta, K. Nakamura, T. Sano, Y. Takahashi
The Nuclear Materials Conference (NuMAT2022) Ghent, Belgium (Oct. 24-28, 2022) O1-O5

Study on Oxide Doped with Nb Mössbauer Spectroscopy
H. Rahman, S. Nakajima
Proceedings of the Specialists' Meeting on "Nuclear Spectroscopy and Condensed Matter Physics Using Short-Lived Nuclei Ⅷ" Online (Jan. 28, 2022) 27-29 (in Japanese)

Reviews

DX application to the field of nuclear materials and its issues (1)
Ken Kurosaki
Journal of the Atomic Energy Society of Japan 10 (2022) 569-571 (in Japanese) (doi)10.3327/jaesjb.64.10_569

Topological analyses of structure of glassy materials toward extraction of order hidden in disordered structure
Yohei Onodera
Journal of the Ceramic Society of Japan 130(8) (2022) 627-638 (doi)10.2109/jcersj2.22033

元素擬人化と動画コンテンツによる科学教育の可能性
Agedoridori, Masaya Kumagai, Ken Kurosaki
Journal of the Thermoelectrics Society of Japan 19(2) (2022) 75-77 (in Japanese)

量子ビーム回折によるガラス構造の研究―乱れた原子配列の理解から新規材料開発を目指す―
Yohei Onodera
Ceramics Japan 57(8) (2022) 517-520 (in Japanese)

Books

Development and Market of Renewable Energy
豊島安健、西脇文男、菊地隆司、黒﨑健、郷右近展之、飯野光政、海江田秀志、飯尾昭一郎、田丸浩、澤田陽樹、シーエムシー出版　編集部
CMC Publishing (2023) (ISBN) 978-4-7813-1723-6

Others

Development of accident tolerant control rod (5) Leaching test of novel neutron absorbing materials in PWR coolant water
Hirokazu OHTA, Kinya NAKAMURA
Atomic Energy Society of Japan 2022 Annual Meeting (2022) 3J10 (in Japanese)

Development of Accident Tolerant Control Rod for Light Water Reactors- Stability of novel neutron absorbing materials in coolant water and under low fluence irradiation -
Hirokazu Ohta, Kinya Nakamura, Tadafumi Sano and Yoshiyuki Takahashi
NuMat2022：The Nuclear Materials Conference (2022) O1.5

High-temperature behavior of accident-tolerant control rods clad with Zr alloy during BDBA and SA leading to reaction with molten fuel
Kinya Nakamura, Hirokazu Ohta and Masahide Takano
27th International QUENCH Workshop (2022)

CRIEPI Accident Tolerant Control Rod update
Kinya Nakamura and Hirokazu Ohta
12th Annual EPRI/DOE/INL Joint Combined Workshop on ATF and HBU (2023)

化合物合金における空孔型欠陥と注入水素原子挙動に関する研究
Fuminobu Hori
九州大学応用力学研究所共同利用研究成果報告書 25 (2022) 143 (in Japanese)

TDPAC Measurement of ^{111}Cd(←^{111}In) in Ultrafine Bubble Water
M. Tanigaki, D. Hayashi, Y. Ohkubo, A. taniguchi, Y. Ueda, Y. Tokuda
KURNS Progress report 2021 (2022) 124

TDPAC Spectra of the ^{111}Cd(←^{111}mCd) and ^{117}In(←^{117}Cd) Probes in $CdIn_2O_4$
W. Sato, S. Komatsuda, A. Taniguchi, M. Tanigaki, Y. Ohkubo
KURNS Progress report 2021 (2022) 112

Concentration Dependence of Local Structures at Cd Sites in $Cd_xSr_{1-x}TiO_3$ studied by TDPAC Method
S. Komatsuda, W. Sato, A. Taniguchi, M. tanigaki, Y. Ohkubo
KURNS Progress report 2021 (2022) 116

5. Geochemistry and Environmental Science

Papers

Development of Nondestructive Elemental Analysis System for Hayabusa2 Samples Using Muonic X-rays
Osawa Takahito, Nagasawa Shunsaku, Ninomiya Kazuhiko, Takahashi Tadayuki, Nakamura Tomoki, Wada Taiga, Taniguchi Akihiro, Umegaki Izumi, Kubo Kenya M., Terada Kentaro, Chiu I-Huan, Takeda Shinichiro, Katsuragawa Miho, Minami Takahiro, Watanabe Shin, Azuma Toshiyuki, Mizumoto Kazumi, Yoshida Go, Takeshita Soshi, Tampo Motonobu, Shimomura Koichiro, Miyake Yasuhiro
ACS Earth and Space Chemistry 7(4) (2023) 699-711 (doi) 10.1021/acsearthspacechem.2c00303

Vertical distribution of airborne microorganisms over forest environments: A potential source of ice-nucleating bioaerosols
Maki Teruya, Hosaka Kentaro, Lee Kevin C., Kawabata Yasuhiro, Kajino Mizuo, Uto Maoto, Kita Kazuyuki, Igarashi Yasuhito
Atmospheric Environment 302 (2023) 119726 (doi) 10.1016/j.atmosenv.2023.119726

Middle Miocene forearc alkaline magmatism in Amami-Oshima Island, central Ryukyu Arc: implications for paleoreconstruction of Shikoku Basin
Motohashi Ginta, Ishizuka Osamu, Oda Hirokuni, Sano Takashi, Sekimoto Shun, Ujiie Kohtaro
Earth Planets and Space 75(1) (2023) 9 (doi) 10.1186/s40623-022-01760-w

Origin and Age of Magmatism in the Northern Philippine Sea Basins
Ishizuka Osamu, Tani Kenichiro, Taylor Rex N., Umino Susumu, Sakamoto Izumi, Yokoyama Yuka, Shimoda Gen, Harigane Yumiko, Ohara Yasuhiko, Conway Chris E., Perez Americus, Sekimoto Shun
Geochemistry, Geophysics, Geosystems 23(4) (2022) e2021GC010242 (doi) 10.1029/2021GC010242

Stratigraphic reconstruction of the lower–middle Miocene Goto Group, Nagasaki Prefecture, Japan
Kiyokawa Shoichi, Yasunaga Masaru, Hasegawa Takanori, Yamamoto Ayako, Kaneko Daisaku, Ikebata Yuta, Hasebe Noriko, Tsutsumi Yukiyasu, Takehara Mami, Horie Kenji
Island Arc 31(1) (2022) e12456 (doi) 10.1111/iar.12456

History of Research and Developments, and Latest Trends in Decomposition Techniques for PFOS and PFOA in Water
FUJIKAWA Yoko, HASHIGUCHI Ayumi
Journal of Environmental Conservation Engineering 51(6) (2022) 316-326 (in Japanese) (doi) 10.5956/jriet.51.6_316

ADSORPTION OF HEAVY METALS AND DISSOLUTION OF STRUCTURAL ELEMENTS FROM CLAY MINERALS EFFECTED BY HEAT TREATMENT
Maiko IKEGAMI, Satoshi FUKUTANI
Journal of Japan Society of Civil Engineers, Ser. G (Environmental Research) 78(7) (2022) III_449- III_458 (in Japanese) (doi) 10.2208/jscejer.78.7_III_449

$^{87}Sr/^{86}Sr$ Isotopic Ratio of Ferromanganese Crusts as a Record of Detrital Influx to the Western North Pacific Ocean
Azami Keishiro, Hirano Naoto, Kimura Jun-Ichi, Chang Qing, Sumino Hirochika, Machida Shiki, Yasukawa Kazutaka, Kato Yasuhiro
Minerals 12(8) (2022) 943 (doi) 10.3390/min12080943

A pristine record of outer Solar System materials from asteroid Ryugu's returned sample
Ito Motoo *et al*.
Nature Astronomy 6(10) (2022) 1163-171 (doi) 10.1038/s41550-022-01745-5

Oxygen isotope evidence from Ryugu samples for early water delivery to Earth by CI chondrites
Greenwood Richard C. *et al*.
Nature Astronomy 7 (2022) 29-38 (doi) 10.1038/s41550-022-01824-7

Phase transition and melting in zircon by nanosecond shock loading
Takagi Sota, Ichiyanagi Kouhei, Kyono Atsushi, Kawai Nobuaki, Nozawa Shunsuke, Ozaki Norimasa, Seto Yusuke, Okuchi Takuo, Nitta Souma, Okada Satoru, Miyanishi Kohei, Sueda Keiichi, Togashi Tadashi, Yabuuchi Toshinori
Physics and Chemistry of Minerals 49(5) (2022) 8 (doi) 10.1007/s00269-022-01184-8

Impacts on air dose rates after the Fukushima accident over the North Pacific from 19 March 2011 to 2 September 2015
Wang Kuo-Ying, Nedelec Philippe, Clark Hannah, Harris Neil, Kajino Mizuo, Igarashi Yasuhito
PLOS ONE 17(8) (2022) e0272937 (doi) 10.1371/journal.pone.0272937

ACTIVITY CONCENTRATIONS OF RADIOCAESIUM, 90SR AND 129I IN AGRICULTURAL CROPS COLLECTED FROM FUKUSHIMA AND REFERENCE AREAS IN JAPAN, AND INTERNAL RADIATION DOSES
Tsukada H, Takahashi T, Fukutani S
Radiation Protection Dosimetry 198 (13-15) (2022) 1104-1108 (doi) 10.1093/rpd/ncac066

Formation and evolution of carbonaceous asteroid Ryugu: Direct evidence from returned samples
T. Nakamura *et al*.
Science 379 (6634) (2023) 787 (doi) 10.1126/science.abn8671

Noble gases and nitrogen in samples of asteroid Ryugu record its volatile sources and recent surface evolution
R. Okazaki *et al*.
Science 379 (6634) (2022) eabo0431 (doi) 10.1126/science.abo0431

First asteroid gas sample delivered by the Hayabusa2 mission: A treasure box from Ryugu
R. Okazaki *et al*.
Science Advances 8(46) (2022) eabo7239 (doi) 10.1126/sciadv.abo7239

Proceedings

Comparison of the Mass Balance Trends of Organobromine in Sediments from Osaka Bay, Beppu Bay, and Lake Biwa
Ito. K, Fujimori. T, Fukutani S, Anh. H. Q, Kuwae. M, Takaoka. M, Takahashi. S.
Dioxin 2022 New Orleans, USA (Oct. 10-14, 2022)

Comparison of the Temporal Trends of Extractable Organochlorine and Organobromine in Archive Samples 6th
Ito. K, Fujimori. T, Fukutani S, Mizukawa. H, Kunisue. T, Takaoka. M, Takahashi. S.
Chemical Hazard Symposium Hokkaido, Japan (Jan. 12-13, 2023)

Effect of Redox Condition on the Precipitation of Fe Oxide/Hydroxide in the Presence of Silicic Acid
H. HIRANO, K. YONEZU, T. YOKOYAMA
International Symposium on Earth Science and Technology 2022 Fukuoka, Japan (Dec. 1-2, 2022) 232-237

Generation of radiocesium-bearing microparticles originating from the Fukushima nuclear accident by laser heating
Makoto Inagaki, Shun Sekimoto, Koichi Takamiya, Yuichi Oki, Tsutomu Ohtsuki
Proceedings of the 23rd Workshop on Environmental Radioactivity Tsukuba, Japan (Mar. 8-10, 2022) 159-164 (in Japanese)

Size distribution of metal elements of the atmospheric aerosol
Norio lto, Akira Mizohata
Proceedings of the 57th KURNS Scientific Meeting Online/Kumatori, Japan (Feb. 14-15, 2023) 37 (in Japanese)

The Formation Factors of Silica Scale from Geothermal Water with Low Silica Concentration and Near Neutral pH
K. ARISATO, S. JUHRI, K. YONEZU, S. MIYABE, E. WATANABE, T. YOKOYAMA
International Symposium on Earth Science and Technology 2022 Fukuoka, Japan (Dec. 1-2, 2022) 63-66

大阪湾底質コアを用いた有機塩素マスバランスの時系列変化
Ito. K, Fujimori. T, Fukutani S, Kuwae. M, Takaoka. M, Takahashi. S.
第 30 回環境化学討論会 Toyama, Japan (Jun. 13-16 2022) 227-278 (in Japanese)

中性子放射化分析における揮発性液体試料中塩素・臭素の測定方法の検討
Ito. K, Fujimori. T, Shiota. S, Fukutani S, Oshita. K, Takaoka. M, Takahashi. S.
第 30 回環境化学討論会 Toyama, Japan (Jun. 13-16 2022) 430-431 (in Japanese)

Reviews

Progress of radiocesium studies and contributions from soil and plant sciences
3. Current status and problems of agricultural land after decontamination
Takashi Saito, Minoru Tanigaki
Japanese Journal of Soil Science and Plant Nutrition 94(1) (2023) 38-43 (in Japanese)

Ultrafast structure transformation of olivine to ringwoodite during laser-driven shock compression
Takuo Okuchi
SPring-8/SACLA Research Frontiers 2021 21 (2022) 94-95

特集のねらい〈有機フッ素化合物の分析と分解処理〉
Yoko Fujikawa
環境技術 51(5) (2022) 239 (in Japanese)

Others

石の年齢をはかる
Osamu Ishizuka
毎日小学生新聞 2022.8.16 号 (2022) (in Japanese)

6. Life Science and Medical Science

Papers

Rapid and Highly Stable Membrane Reconstitution by LAiR Enables the Study of Physiological Integral Membrane Protein Functions
Godoy-Hernandez Albert, Asseri Amer H., Purugganan Aiden J., Jiko Chimari, de Ram Carol, Lill Holger, Pabst Martin, Mitsuoka Kaoru, Gerle Christoph, Bald Dirk, McMillan Duncan G. G.
ACS Central Science 9(3) (2023) 494- 507 (doi) 10.1021/acscentsci.2c01170

Protonation states of hen egg-white lysozyme observed using D/H contrast neutron crystallography
Chatake Toshiyuki, Tanaka Ichiro, Kusaka Katsuhiro, Fujiwara Satoru
Acta Crystallographica Section D Structural Biology 78(6) (2022) 770-778
(doi) 10.1107/S2059798322004521

Efficient Multiple Domain Ligation for Proteins Using Asparaginyl Endopeptidase by Selection of Appropriate Ligation Sites Based on Steric Hindrance
Okuda Aya, Shimizu Masahiro, Inoue Rintaro, Urade Reiko, Sugiyama Masaaki
Angewandte Chemie International Edition 62(1) (2022) e202214412 (doi) 10.1002/anie.202214412

Induction of Paraptosis by Cyclometalated Iridium Complex-Peptide Hybrids and CGP37157 via a Mitochondrial Ca^{2+} Overload Triggered by Membrane Fusion between Mitochondria and the Endoplasmic Reticulum
Yokoi Kenta, Yamaguchi Kohei, Umezawa Masakazu, Tsuchiya Koji, Aoki Shin
Biochemistry 61(8) (2022) 639-655 (doi) 10.1021/acs.biochem.2c00061

Design, Synthesis, and Anticancer Activity of Triptycene–Peptide Hybrids that Induce Paraptotic Cell Death in Cancer Cells
Yamaguchi Kohei, Yokoi Kenta, Umezawa Masakazu, Tsuchiya Koji, Yamada Yasuyuki, Aoki Shin **Bioconjugate Chemistry 33(4) (2022) 691-717 (doi) 10.1021/acs.bioconjchem.2c00076**

Design, synthesis and biological evaluation of 2-pyrrolone derivatives as radioprotectors
Satoh Hidetoshi, Ochi Shintaro, Mizuno Kosuke, Saga Yutaka, Ujita Shohei, Toyoda Miyu, Nishiyama Yuichi, Tada Kasumi, Matsushita Yosuke, Deguchi Yuichi, Suzuki Keiji, Tanaka Yoshimasa, Ueda Hiroshi, Inaba Toshiya, Hosoi Yoshio, Morita Akinori, Aoki Shin
Bioorganic & Medicinal Chemistry 67 (2022) 116764 (doi) 10.1016/j.bmc.2022.116764

Identification of D-amino Acid Residues in Proteins Using Mass Spectrometry
Takumi Takata
BUNSEKI KAGAKU 71(6) (2022) 319- 324 (in Japanese) (doi) 10.2116/bunsekikagaku.71.319

Multi-Targeted Neutron Capture Therapy Combined with an 18 kDa Translocator Protein-Targeted Boron Compound Is an Effective Strategy in a Rat Brain Tumor Model
Kashiwagi Hideki, Hattori Yoshihide, Kawabata Shinji, Kayama Ryo, Yoshimura Kohei, Fukuo Yusuke, Kanemitsu Takuya, Shiba Hiroyuki, Hiramatsu Ryo, Takami Toshihiro, Takata Takushi, Tanaka Hiroki, Watanabe Tsubasa, Suzuki Minoru, Hu Naonori, Miyatake Shin-Ichi, Kirihata Mitsunori, Wanibuchi Masahiko
Cancers 15(4) (2023) 1034 (doi) 10.3390/cancers15041034

Design, Synthesis, and Biological Applications of Boron-Containing Polyamine and Sugar Derivatives
Aoki Shin, Ueda Hiroki, Tanaka Tomohiro, Itoh Taiki, Suzuki Minoru, Sakurai Yoshinori
Characteristics and Applications of Boron (2022) 82908 (doi) 10.5772/intechopen.105998

A Novel Amphotericin B Hydrogel Composed of Poly(Vinyl Alcohol)/Borate Complex for Ophthalmic Formulation
Banshoya Kengo, Shirakawa Makoto, Hieda Yuhzo, Ohnishi Masatoshi, Sato Yuhki, Inoue Atsuko, Tanaka Tetsuro, Kaneo Yoshiharu
Chemical and Pharmaceutical Bulletin 71(1) (2023) 70-73 (doi) 10.1248/cpb.c22-00534

$ZBTB_2$ links p53 deficiency to HIF-1-mediated hypoxia signaling to promote cancer aggressiveness
Koyasu Sho, Horita Shoichiro, Saito Keisuke, Kobayashi Minoru, Ishikita Hiroshi, Chow Christalle CT, Kambe Gouki, Nishikawa Shigeto, Menju Toshi, Morinibu Akiyo, Okochi Yasushi, Tabuchi Yoshiaki, Onodera Yasuhito, Takeda Norihiko, Date Hiroshi, Semenza Gregg L, Hammond Ester M, Harada Hiroshi
EMBO reports 11(24) (2022) e54042 (doi) 10.15252/embr.202154042

Relevance of Amorphous and Amyloid-Like Aggregates of the p53 Core Domain to Loss of its DNA-Binding Activity
Hibino Emi, Tenno Takeshi, Hiroaki Hidekazu
Frontiers in Molecular Biosciences 9 (2022) 869851 (doi) 10.3389/fmolb.2022.869851

Profiling Differential Effects of 5 Selective Serotonin Reuptake Inhibitors on TLRs-Dependent and -Independent IL-6 Production in Immune Cells Identifies Fluoxetine as Preferred Anti-Inflammatory Drug Candidate
Takenaka Yohei, Tanaka Ryu, Kitabatake Kazuki, Kuramochi Kouji, Aoki Shin, Tsukimoto Mitsutoshi
Frontiers in Pharmacology 13 (2022) 874375 (doi) 10.3389/fphar.2022.874375

The Advantage of Small-angle Neutron Scattering Revaled through analyzing the Overall Structure of a Fully Assembled comlpex in Circadian Clock
Yunoki Yasuhiro, Atsushi Matsumoto, Ken Morisima, Anne Martel, Lionel Porcar, Nobuhiro Sato, Rina Yogo, Taiki Tominaga, Maho Yagi-Utsumi, Rintaro Inoue, Hidetoshi Kono, Hirokazu Yagi, Koichi Kato, Masaaki Sugiyama
Hamon 32(4) (2022) 158-164 (in Japanese)

Effect of N-benzyl group in indole scaffold of thiosemicarbazones on the biological activity of their Pd(II) complexes: DFT, biomolecular interactions, in silico docking, ADME and cytotoxicity studies
Balakrishnan Nithya, Haribabu Jebiti, Eshaghi Malekshah Rahime, Swaminathan Srividya, Balachandran Chandrasekar, Bhuvanesh Nattamai, Aoki Shin, Karvembu Ramasamy
Inorganica Chimica Acta 534 (2022) 120805 (doi) 10.1016/j.ica.2022.120805

The mutual relationship between the host immune system and radiotherapy: stimulating the action of immune cells by irradiation
Watanabe Tsubasa, Sato Genki Edward, Yoshimura Michio, Suzuki Minoru, Mizowaki Takashi
International Journal of Clinical Oncology 28(2) (2023) 201-208 (doi) 10.1007/s10147-022-02172-2

Mutational and Environmental Effects on the Dynamic Conformational Distributions of Lys48-Linked Ubiquitin Chains
Hiranyakorn Methanee, Yagi-Utsumi Maho, Yanaka Saeko, Ohtsuka Naoya, Momiyama Norie, Satoh Tadashi, Kato Koichi
International Journal of Molecular Sciences 24(7) (2023) 6075 (doi) 10.3390/ijms24076075

Boron neutron capture therapy using dodecaborated albumin conjugates with maleimide is effective in a rat glioma model
Kashiwagi Hideki, Kawabata Shinji, Yoshimura Kohei, Fukuo Yusuke, Kanemitsu Takuya, Takeuchi Koji, Hiramatsu Ryo, Nishimura Kai, Kawai Kazuki, Takata Takushi, Tanaka Hiroki, Watanabe Tsubasa, Suzuki Minoru, Miyatake Shin-Ichi, Nakamura Hiroyuki, Wanibuchi Masahiko
Investigational New Drugs 40(2) (2022) 255-264 (doi) 10.1007/s10637-021-01201-7

Promising anticancer activity with high selectivity of DNA/plasma protein targeting new phthalazin-1(2H)-one heterocyclic scaffolds
Kesavan Mookkandi Palsamy, Ravi Lokesh, Balachandran Chandrasekar, Thangadurai T. Daniel, Aoki Shin, Webster Thomas J., Rajesh Jegathalaprathaban
Journal of Molecular Structure 1274(1) (2023) 134423 (doi) 10.1016/j.molstruc.2022.134423

Data Collection for Dilute Protein Solutions via a Neutron Backscattering Spectrometer
Tominaga Taiki, Nakagawa Hiroshi, Sahara Masae, Oda Takashi, Inoue Rintaro, Sugiyama Masaaki
Life 12(5) (2022) 675 (doi) 10.3390/life12050675

Hydrogen/Deuterium Exchange Behavior During Denaturing/Refolding Processes Determined in Tetragonal Hen Egg-White Lysozyme Crystals
Kita Akiko, Morimoto Yukio
Molecular Biotechnology 64(5) (2022) 590-597 (doi) 10.1007/s12033-022-00447-7

Development of Wireless Power-Transmission-Based Photodynamic Therapy for the Induction of Cell Death in Cancer Cells by Cyclometalated Iridium(III) Complexes
Yokoi Kenta, Yasuda Yoshitaka, Kanbe Azusa, Imura Takehiro, Aoki Shin
Molecules 28(3) (2023) 1433 (doi) 10.3390/molecules28031433

Pathway Dependence of the Formation and Development of Prefibrillar Aggregates in Insulin B Chain
Yoshikawa Yuki, Yuzu Keisuke, Yamamoto Naoki, Morishima Ken, Inoue Rintaro, Sugiyama Masaaki, Iwasaki Tetsushi, So Masatomo, Goto Yuji, Tamura Atsuo, Chatani Eri
Molecules 27(13) (2022) 3964 (doi) 10.3390/molecules27133964

Design and synthesis of spirooxindole–pyrrolidines embedded with indole and pyridine heterocycles by multicomponent reaction: anticancer and in silico studies
Mayakrishnan Sivakalai, Kathirvelan Devarajan, Arun Yuvaraj, Saranraj Krishnan, Balachandran Chandrasekaran, Aoki Shin, Yuvaraj Pannerselvam, Maheswarai Narayanan Uma
New Journal of Chemistry 21(13) (2022) 10089-10106 (doi) 10.1039/D1NJ05839H

Activation imaging: New concept of visualizing drug distribution with wide-band X-ray and gamma-ray imager
Koshikawa N., Omata A., Masubuchi M., Kataoka J., Kadonaga Y., Tokoi K., Nakagawa S., Imada A., Toyoshima A., Matsunaga K., Kato H., Wakabayashi Y., Kobayashi T., Takamiya K., Ueda M.
Nuclear Instruments and Methods in Physics Research Section A: Accelerators, Spectrometers, Detectors and Associated Equipment 1045 (2023) 167599 (doi) 10.1016/j.nima.2022.167599

Influence of Boron Neutron Capture Therapy on Normal Liver Tissue
Tamari Yuki, Takata Takushi, Takeno Satoshi, Tanaka Hiroki, Yamazaki Hideya, Yamada Kei, Suzuki Minoru
Radiation Research 198(4) (2022) 368-374 (doi) 10.1667/rade-22-00018.1

Potassium tert-Butoxide Promoted Intramolecular Mizoroki–Heck-Type Radical Cyclization: Photoluminescence Properties and Application in Live Cancer-Cell Imaging
Sivaraman Mahalingam, Maheswari Narayanan Uma, Perumal Paramasivan T., Mayakrishnan Sivakalai, Balachandran Chandrasekar, Aoki Shin
Synlett 33(08) (2022) 785-790 (doi) 10.1055/a-1782-7150

Inhibition ofATPsynthase reverse activity restores energy homeostasis in mitochondrial pathologies
Acin-Perez Rebeca, Benincá Cristiane, Fernandez del Rio Lucia, Shu Cynthia, Baghdasarian Siyouneh, Zanette Vanessa, Gerle Christoph, Jiko Chimari, Khairallah Ramzi, Khan Shaharyar, Rincon Fernandez Pacheco David, Shabane Byourak, Erion Karel, Masand Ruchi, Dugar Sundeep, Ghenoiu Cristina, Schreiner George, Stiles Linsey, Liesa Marc, Shirihai Orian S
The EMBO Journal (2023) e111699 (doi) 10.15252/embj.2022111699

Structural basis of the 24B3 antibody against the toxic conformer of amyloid β with a turn at positions 22 and 23.
Yumi Irie, Yuka Matsushima, Akiko Kita, Kunio Miki, Tatsuya Segawa, Masahiro Maeda, Ryo C. Yanagita, Kazuhiro Irie
Biochemical and Biophysical Research Communications 621 (2022) 162-167 (doi) 10.1016/j.bbrc.2022.07.010

Tracking the Structural Development of Amyloid Precursors in the Insulin B Chain and the Inhibition Effect by Fibrinogen
Yamamoto Naoki, Inoue Rintaro, Makino Yoshiteru, Sekiguchi Hiroshi, Shibayama Naoya, Naito Akira, Sugiyama Masaaki, Chatani Eri
The Journal of Physical Chemistry B 26(51) (2022) 10797-10812 (doi) 10.1021/acs.jpcb.2c05136

Proceedings

Altered gene expression levels of evolved radioresistant E. coli relative to wild-type E. coli
Takeshi Saito
Proceedings of the 57th KURNS Scientific Meeting Online/Kumatori, Japan (Feb. 14-15, 2023) 31 (in Japanese)

Gallium isotope ratio of samples of GSJ standard rocks
Rikuya Aso, Chizu Kato, Satoshi Fukutani, Ryoichi Nakada, Kazuya Nagaishi, Shigeyuki Wakaki, Toshiyuki Fujii
Proceedings of the 57th KURNS Scientific Meeting Online/Kumatori, Japan (Feb. 14-15, 2023) 32 (in Japanese)

lncreased Asp isomerization in abnormal β B 1-crystallin aggregates in human aged lens
Yuta Kagasawa, lngu Kim, Takumi Takata
Proceedings of the 57th KURNS Scientific Meeting Online/Kumatori, Japan (Feb. 14-15, 2023) 38 (in Japanese)

Neutron crystallographic approach to reveal hydration structure of protein
Toshiyuki Chatake, Ichiro Tanaka, Katsuhiro Kusaka, Tomoko Sunami, Satoru Fujiwara
Proceedings of the 57th KURNS Scientific Meeting Online/Kumatori, Japan (Feb. 14-15, 2023) 30 (in Japanese)

Production experiments for 225Ac using an electron linear accelerator and radiolabeling tests using the produced alpha emitter
M. Maeda, T. Tadokoro, Y. Ueno, K. Nishida, Y. Kani, T. Sasaki, T.Watanabe, H. Kikunaga, S. Kashiwagi, K. Shirasaki, S. Sekimoto, T. Ohtsuki, M. Inagaki, S. Fukutani, Y. Shibahara, H. Fujii, M.Yoshimoto, K. Ohnuki
Annual Congress of the European Association of Nuclear Medicine Barcelona, Spain (Oct. 15-19, 2022)

Rapid isomerization of Asp 151 in aA-crystallin in human lens and its effect for heat stability
Haruna Sugawa, Takumi Takata
Proceedings of the 57th KURNS Scientific Meeting Online/Kumatori, Japan (Feb. 14-15, 2023) 29 (in Japanese)

Reviews

Cataract: Lens Protein Misfolding Disease
Takumi Takata
日本白内障学会誌 34(1) (2022) 23-28 (in Japanese)

Identification of D-amino Acid Residues in Proteins Using Mass Spectrometry
Takumi Takata
BUNSEKI KAGAKU 71(6) (2022) 319-324 (in Japanese) (doi)10.2116/bunsekikagaku.71.319

Multistep growth of amyloid intermediates and its inhibition toward exploring therapeutic way: A case study using insulin B chain and fibrinogen
Yamamoto Naoki, Chatani Eri
Biophysics and Physicobiology 19 (2023) 3190017 (doi)10.2142/biophysico.bppb-v19.0017

Post-complexation Functionalization of Cyclometalated Iridium(III) Complexes and Applications to Biomedical and Material Sciences
Aoki Shin, Yokoi Kenta, Hisamatsu Yosuke, Balachandran Chandrasekar, Tamura Yuichi, Tanaka Tomohiro
Topics in Current Chemistry 380(5) (2022) 36 (doi) 10.1007/s41061-022-00401-w

Others

Structural Analysis of TxCo-1 Antibody Effective Against the Toxic Conformer of Amyloid β.
Kazuhiro Irie, Yumi Irie, Yuka Matsushima, Akiko Kita, Yusuke Kageyama, Ikuo Tooyama
Photon Factory Highlights (PF Highlights) (2021) 30-31

7. Neutron Capture Therapy

Papers

Improved Boron Neutron Capture Therapy Using Integrin αvβ3-Targeted Long-Retention-Type Boron Carrier in a F98 Rat Glioma Model
Tsujino Kohei, Kashiwagi Hideki, Nishimura Kai, Kayama Ryo, Yoshimura Kohei, Fukuo Yusuke, Shiba Hiroyuki, Hiramatsu Ryo, Nonoguchi Naosuke, Furuse Motomasa, Takami Toshihiro, Miyatake Shin-Ichi, Hu Naonori, Takata Takushi, Tanaka Hiroki, Suzuki Minoru, Kawabata Shinji, Nakamura Hiroyuki, Wanibuchi Masahiko
Biology 12(3) (2023) 377 (doi) 10.3390/biology12030377

Anti-tumor effect of boron neutron capture therapy in pelvic human colorectal cancer in a mouse model
Arima Jun, Taniguchi Kohei, Yamamoto Masashi, Watanabe Tsubasa, Suzuki Yusuke, Hamamoto Hiroki, Inomata Yosuke, Kashiwagi Hideki, Kawabata Shinji, Tanaka Keitaro, Uchiyama Kazuhisa, Suzuki Minoru, Lee Sang-Woong
Biomedicine & Pharmacotherapy 154 (2022) 113632 (doi) 10.1016/j.biopha.2022.113632

DNA damage and biological responses induced by Boron Neutron Capture Therapy (BNCT)
Natsuko Kondo
Enzymes 51 (2022) 65-78 (doi) 10.1016/bs.enz.2022.08.005

Measurements of γ-rays and neutrons in BNCT irradiation field using thermoluminescent phosphor
Shinsho Kiyomitsu, Oh Ryoken, Tanaka Masaya, Sugioka Natsumi, Tanaka Hiroki, Wakabayashi Genichiro, Takata Takushi, Chang Weishan, Matsumoto Shinnosuke, Okada Go, Sugawara Satoru, Sasaki Ema, Watanabe Kenichi, Koba Yusuke, Nagasaka Kosei, Yoshihashi Sachiko, Uritani Akira, Negishi Toru
Japanese Journal of Applied Physics 62(1) (2022) 010502 (doi) 10.35848/1347-4065/ac971e

Boron neutron capture therapy and add-on bevacizumab in patients with recurrent malignant glioma
Furuse Motomasa, Kawabata Shinji, Wanibuchi Masahiko, Shiba Hiroyuki, Takeuchi Koji, Kondo Natsuko, Tanaka Hiroki, Sakurai Yoshinori, Suzuki Minoru, Ono Koji, Miyatake Shin-Ichi
Japanese Journal of Clinical Oncology 52(5) (2022) 433-440 (doi) 10.1093/jjco/hyac004

γ-Ray measurements in boron neutron capture therapy using BeO ceramic thermoluminescence dosimeter
Tanaka Masaya, Oh Ryoken, Sugioka Natsumi, Tanaka Hiroki, Takata Takushi, Wakabayashi Genichiro, Sugawara Satoru, Watanabe Kenichi, Uritani Akira, Yoshihashi Sachiko, Nagasaka Kosei, Okada Go, Negishi Toru, Shinsho Kiyomitsu
Journal of Materials Science: Materials in Electronics 33 (2022) 20271-20279
(doi) 10.1007/s10854-022-08843-0

Accelerator based epithermal neutron source for clinical boron neutron capture therapy
Hu Naonori, Tanaka Hiroki, Akita Kazuhiko, Kakino Ryo, Aihara Teruhito, Nihei Keiji, Ono Koji
Journal of Neutron Research 24(3-4) (2023) 359-366 (doi) 10.3233/JNR-220037

Analysis of boron neutron capture reaction sensitivity using Monte Carlo simulation and proposal of a new dosimetry index in boron neutron capture therapy
Takeno Satoshi, Tanaka Hiroki, Ono Koji, Mizowaki Takashi, Suzuki Minoru
Journal of Radiation Research 63(5) (2022) 780-791 (doi) 10.1093/jrr/rrac038

Correlation between the expression of LAT1 in cancer cells and the potential efficacy of boron neutron capture therapy
Watanabe Tsubasa, Sanada Yu, Hattori Yoshihide, Suzuki Minoru
Journal of Radiation Research 64(1) (2023) 91-98 (doi) 10.1093/jrr/rrac077

Determining a methodology of dosimetric quality assurance for commercially available accelerator-based boron neutron capture therapy system
Hirose Katsumi, Kato Takahiro, Harada Takaomi, Motoyanagi Tomoaki, Tanaka Hiroki, Takeuchi Akihiko, Kato Ryohei, Komori Shinya, Yamazaki Yuhei, Arai Kazuhiro, Kadoya Noriyuki, Sato Mariko, Takai Yoshihiro
Journal of Radiation Research 63(4) (2022) 620-635 (doi) 10.1093/jrr/rrac030

Intensity-modulated irradiation for superficial tumors by overlapping irradiation fields using intensity modulators in accelerator-based BNCT
Sasaki Akinori, Hu Naonori, Takata Takushi, Matsubayashi Nishiki, Sakurai Yoshinori, Suzuki Minoru, Tanaka Hiroki
Journal of Radiation Research 63(6) (2022) 866-873 (doi) 10.1093/jrr/rrac052

The impact of TP53 status of tumor cells including the type and the concentration of administered ^{10}B delivery agents on compound biological effectiveness in boron neutron capture therapy
Masunaga Shin-ichiro, Sanada Yu, Takata Takushi, Tanaka Hiroki, Sakurai Yoshinori, Suzuki Minoru, Kirihata Mitsunori, Ono Koji
Journal of Radiation Research 64(2) (2023) 399-411 (doi) 10.1093/jrr/rrad001

Compassionate Treatment of Brainstem Tumors with Boron Neutron Capture Therapy: A Case Series
Chen Yi-Wei, Lee Yi-Yen, Lin Chun-Fu, Huang Ting-Yu, Ke Shih-Hung, Mu Pei-Fan, Pan Po-Shen, Chen Jen-Kun, Lan Tien-Li, Hsu Ping-Chuan, Liang Muh-Lii, Chen Hsin-Hung, Chang Feng-Chi, Wu Chih-Chun, Lin Shih-Chieh, Lee Jia-Cheng, Chen Shih-Kuan, Liu Hong-Ming, Peir Jinn-Jer, Tsai Hui-Yu, Lin Ko-Han, Peng Nan-Jing, Chen Kuan-Hsuan, Wu Yuan-Hung, Kang Yu-Mei, Yang Wan-Chin, Liou Shueh-Chun, Huang Wei-Hsuan, Tanaka Hiroki, Wong Tai-Tong, Chao Yee, Chou Fong-In
Life 12(4) (2022) 566 (doi) 10.3390/life12040566

Comprehensive evaluation of dosimetric impact against position errors in accelerator‐based BNCT under different treatment parameter settings
Kakino Ryo, Hu Naonori, Isohashi Kayako, Aihara Teruhito, Nihei Keiji, Ono Koji
Medical Physics 49(8) (2022) 4944-4954 (doi) 10.1002/mp.15823

Design of a filtration system to improve the dose distribution of an accelerator‐based neutron capture therapy system
Hu Naonori, Tanaka Hiroki, Ono Koji
Medical Physics 49(10) (2022) 6609-6621 (doi) 10.1002/mp.15864

Carborane bearing pullulan nanogel-boron oxide nanoparticle hybrid for boron neutron capture therapy
Kawasaki Riku, Hirano Hidetoshi, Yamana Keita, Isozaki Hinata, Kawamura Shogo, Sanada Yu, Bando Kaori, Tabata Anri, Yoshikawa Kouhei, Azuma Hideki, Takata Takushi, Tanaka Hiroki, Sakurai Yoshinori, Suzuki Minoru, Tarutani Naoki, Katagiri Kiyofumi, Sawada Shin-ichi, Sasaki Yoshihiro, Akiyoshi Kazunari, Nagasaki Takeshi, Ikeda Atsushi
Nanomedicine: Nanotechnology, Biology and Medicine 49 (2023) 102659 (doi) 10.1016/j.nano.2023.102659

Air ionization chamber combined with $LiCaAlF_6$ scintillator for γ-ray dose evaluation in boron neutron capture therapy
Matsubayashi Nishiki, Hu Naonori, Takata Takushi, Sasaki Akinori, Nojiri Mai, Mukawa Tetsuya, Sakurai Yoshinori, Tanaka Hiroki
Nuclear Instruments and Methods in Physics Research Section A: Accelerators, Spectrometers, Detectors and Associated Equipment 1047 (2023) 167883 (doi) 10.1016/j.nima.2022.167883

Characteristics of optically stimulated luminescent dosimeter of beryllium oxide in BNCT irradiation field
Matsubayashi Nishiki, Hu Naonori, Takata Takushi, Sasaki Akinori, Mukawa Tetsuya, Suga Keita, Sakurai Yoshinori, Tanaka Hiroki
Radiation Measurements 161 (2023) 106900 (doi) 10.1016/j.radmeas.2023.106900

Enhancement of Cancer Cell-Killing Effects of Boron Neutron Capture Therapy by Manipulating the Expression of L-Type Amino Acid Transporter 1
Ohnishi Ken, Misawa Masaki, Sikano Naoto, Nakai Kei, Suzuki Minoru
Radiation Research 196(1) (2022) 17-22 (doi) 10.1667/RADE-20-00214.1

Improvement in the neutron beam collimation for application in boron neutron capture therapy of the head and neck region
Hu Naonori, Tanaka Hiroki, Kakino Ryo, Yoshikawa Syuushi, Miyao Mamoru, Akita Kazuhiko, Aihara Teruhito, Nihei Keiji, Ono Koji
Scientific Reports 12(1) (2022) 13778 (doi) 10.1038/s41598-022-17974-7

Persistent elevation of lysophosphatidylcholine promotes radiation brain necrosis with microglial recruitment by P2RX4 activation
Kondo Natsuko, Sakurai Yoshinori, Takata Takushi, Kano Kuniyuki, Kume Kyo, Maeda Munetoshi, Takai Nobuhiko, Suzuki Shugo, Eto Fumihiro, Kikushima Kenji, Wanibuchi Hideki, Miyatake Shin-Ichi, Kajihara Takayuki, Oda Shoji, Setou Mitsutoshi, Aoki Junken, Suzuki Minoru
Scientific Reports 12(1) (2022) 8718 (doi) 10.1038/s41598-022-12293-3

Polyglycerol Functionalized ^{10}B Enriched Boron Carbide Nanoparticle as an Effective Bimodal Anticancer Nanosensitizer for Boron Neutron Capture and Photothermal Therapies
Wang Yuquan, Reina Giacomo, Kang Heon Gyu, Chen Xiaoxiao, Zou Yajuan, Ishikawa Yoshie, Suzuki Minoru, Komatsu Naoki
Small 18(37) (2022) 2204044 (doi) 10.1002/smll.202204044

類上皮肉腫に対するホウ素中性子捕捉療法(BNCT)を用いた新たな治療方法の開発
Takuya Fujimoto, Tooru Andoh, Toshiko Sakuma, Ikuo Fujita, Masayuki Morishita, Masahide Fujita, Teruya Kawamoto, Ryosuke Kuroda, Akisue Toshihiro, Takanori Hirose, Minoru Suzuki
The Journal of the Japanese Orthopaedic Association 96(6) (2022) S1300 (in Japanese)

Proceedings

Advancement of integrated system for dose estimation in BNCT
Yoshinori Sakurai, Kenichi Watanabe, Sachiko Yoshihashi, Akihiko Masuda, Masayori Ishikawa, Akihiro Nohtomi, Isao Murata, Satoru Endo, Kenichi Tanaka, Shoji Uno, Kiyomitsu Shinsho, Masataka Oita, Shinichiro Hayashi, Hiroki Tanaka, Shunsuke Kurosawa, Toru Tanimori, Atsushi Takada, Satoshi Nakamura, Tak:ushi Takata, Tak:eshi Kamomae, Hiroyuki Michiue, Hiroshi Yasuda, Shinichiro Kuroki, Kazuyo Igawa
Proceedings of the 57th KURNS Scientific Meeting Online/Kumatori, Japan (Feb. 14-15, 2023) 46-50 (in Japanese)

Attempts to enhance the anti-tumor effects ofBNCT by targeting the tumor microenvironment
Yu Sanada, Takushi Takata, Hiroki Tanaka, Yoshinori Sakurai, Tsubasa Watanabe
Proceedings of the 57th KURNS Scientific Meeting Online/Kumatori, Japan (Feb. 14-15, 2023) 26 (in Japanese)

Biology study for BNCT
Yuko Kinashi
Proceedings of the 57th KURNS Scientific Meeting Online/Kumatori, Japan (Feb. 14-15, 2023) 12-14 (in Japanese)

Commissioning of the world's first clinical BNCT treatment planning system and validation against an independent Monte Carlo dose calculation system
Naonori Hu
Proceedings of the 57th KURNS Scientific Meeting Online/Kumatori, Japan (Feb. 14-15, 2023) 6 (in Japanese)

Development of carborane-containing amino acid derivatives for boron neutron capture therapy (BNCT)
H. Nagasawa
2023 Taiwan-Japan Neutron Capture Therapy Academic Conference of Elite Hsinchu, Taiwan (Mar. 18, 2023) 34-35

Evaluation of thermal neutron flux using Imaging Plate for BNCT
Mai Nojiri, Takushi Takata, Yoshinori Sakurai, Minoru Suzuki, Hiroki Tanaka
Proceedings of the 57th KURNS Scientific Meeting Online/Kumatori, Japan (Feb. 14-15, 2023) 27 (in Japanese)

Investigation of the effects on the ambient environment by activation of animals' bodies for the adaptation of BNCT to companion animals
Yusuke Wada, Takushi Takata, Minoru Suzuki
Proceedings of the 57th KURNS Scientific Meeting Online/Kumatori, Japan (Feb. 14-15, 2023) 10-11 (in Japanese)

Structural Analysis of Solid-Liquid Interface by Neutron Reflectometry for Tribology Study
Naoki Yamashita, Tomoko Hirayama, Masahiro Hino
Proceedings of the 57th KURNS Scientific Meeting Online/Kumatori, Japan (Feb. 14-15 2023) 40 (in Japanese)

Study of dose distribution formation by neutron intensity-modulated irradiation method for accelerator-based BNCT
Akinori Sasaki, Naonori Hu,Takushi Takata, Nishiki Matsubayashi, Yoshinori Sakurai, Minoru Suzuki, Hiroki Tanaka
Proceedings of the 57th KURNS Scientific Meeting Online/Kumatori, Japan (Feb. 14-15, 2023) 39 (in Japanese)

ホウ素中性子捕捉療法 (BNCT) がマウス正常骨に与える生物学的影響
Ryota Iwasaki, Ryutaro Yoshikawa, Takashi Mori, Takehisa Matsukawa, Satoshi Takeno, Minoru Suzuki, Koji Ono**日本放射線腫瘍学会第 59 回生物部会学術大会, Sapporo, Japan (Jun. 24-25 2022) 27 (in Japanese)**

Reviews

BNCT/Neutrons in Clinical Practice: BNCT
Hiroki Tanaka
Japanese Journal of Medical Physics (Igakubutsuri) 42(3) (2022) 143-148 (in Japanese)

Measurements of γ-rays and neutrons in BNCT irradiation field using thermoluminescent phosphor
Shinsho Kiyomitsu, Oh Ryoken, Tanaka Masaya, Sugioka Natsumi, Tanaka Hiroki, Wakabayashi Genichiro, Takata Takushi, Chang Weishan, Matsumoto Shinnosuke, Okada Go, Sugawara Satoru, Sasaki Ema, Watanabe Kenichi, Koba Yusuke, Nagasaka Kosei, Yoshihashi Sachiko, Uritani Akira, Negishi Toru
Japanese Journal of Applied Physics 62 (2022) 010502 (doi)10.35848/1347-4065/ac971e

加速器中性子源を用いた BNCT の展開
Kazuyo Igawa, Hiroyuki Michiue, Atsushi Fujimura
Medical Science Digest (2023) (in Japanese)

Others

Computational investigation of polymer gel composition doped with 33S for epithermal neutron measurement for BNCT
K. Tanaka, T. Kajimoto, Y. Sakurai, S. Hayashi, H. Tanaka, T. Takata, G. Bengua, S. Endo
Bulletin of Kyoto Pharmaceutical University 3(2) (2023) 224-236

8. Neutron Radiography and Radiation Application

Papers

Evaluation of subcooled void fraction in downward flow under low mass flux condition by using neutron radiography
Ami Takeyuki, Umekawa Hisashi, Ito Daisuke, Saito Yasushi
Experimental Thermal and Fluid Science 141 (2023) 110799 (doi) 10.1016/j.expthermflusci.2022.110799

Investigation of neutron imaging applications using fine-grained nuclear emulsion
Muneem Abdul, Yoshida Junya, Ekawa Hiroyuki, Hino Masahiro, Hirota Katsuya, Ichikawa Go, Kasagi Ayumi, Kitaguchi Masaaki, Muto Naoto, Mishima Kenji, Nabi Jameel-Un, Nakagawa Manami, Naganawa Naotaka, Saito Takehiko R.
Journal of Applied Physics 133(5) (2023) 054902 (doi) 10.1063/5.0131098

Effects of the mixer shape in a flow-type supercritical hydrothermal reactor as evaluated by neutron radiography and CeO_2 nanoparticle synthesis
Sato Kosei, Sasaki Ryosuke, Xie Bo, Takami Seiichi, Kubo Masaki, Tsukada Takao, Sugimoto Katsumi, Odaira Naoya, Ito Daisuke, Saito Yasushi
Reaction Chemistry & Engineering (2023) (doi) 10.1039/D3RE00018D

Proceedings

Frost Formation on Automobile Heat Exchange
Rikuto Kuroda, Ryosuke Matsumoto, Yutaka Oda, Ao Fukai, Kenta Kida, Hiroshi Iikura, Keisuke Kurita
2022 JSRAE Annual Conference Okayama, Japan (Sep. 7-9, 2022) B124 (in Japanese)

Neutron imaging of thermal-hydraulic phenomena under severe conditions
Daisuke lto, Naoya Odaira, Kei lto, Yasushi Saito
Proceedings of the 57th KURNS Scientific Meeting Online/Kumatori, Japan (Feb. 14-15, 2023) 41-42 (in Japanese)

Neutron phase imaging of lNCONEL rods fabricated by additive manufacturing
Yoshichika Seki, Masahiro Hino, Riichiro Nakamura, Takenao Shinohara, Tomoko Hirayama
Proceedings of the 57th KURNS Scientific Meeting Online/Kumatori, Japan (Feb. 14-15, 2023) 25 (in Japanese)

Project for Neutron Imaging
Yasushi Saito, Daisuke Ito, Naoya Odaira
Proceedings of the 57th KURNS Scientific Meeting Online/Kumatori, Japan (Feb. 14-15, 2023) 43-45 (in Japanese)

Review

Frosting Phenomena on Heat Exchanger and Frost Micro Structure
―Novel Development on the Frost Research by Using Radiography Technique―
Ryosuke Matsumoto
Earozoru Kenkyu 37(4) (2022) 268-274 (in Japanese)

9. TRU and Nuclear Chemistry

Papers

Improvement of spatial resolution of elemental imaging using laser ablation-ICP-mass spectrometry
Tanaka Eisei, Matsukawa Takehisa, Kuroki Yasuo, Suzuki Minoru, Yokoyama Kazuhito, Hirata Takafumi
Analytical Sciences 38(4) (2022) 695-702 (doi) 10.1007/s44211-022-00085-8

Non-Destructive Composition Identification for Mixtures of Iron Compounds Using a Chemical Environmental Effect on a Muon Capture Process
Ninomiya Kazuhiko, Kajino Meito, Nambu Akihiro, Inagaki Makoto, Kudo Takuto, Sato Akira, Terada Kentaro, Shinohara Atsushi, Tomono Dai, Kawashima Yoshitaka, Sakai Yoichi, Takayama Tsutomu
Bulletin of the Chemical Society of Japan 95(12) (2022) 1769-1774 (doi) 10.1246/bcsj.20220289

Influence of additives on low-temperature hydrothermal synthesis of UO_{2+x} and ThO_2
Tabata Chihiro, Shirasaki Kenji, Sakai Hironori, Sunaga Ayaki, Li Dexin, Konaka Mariko, Yamamura Tomoo
CrystEngComm 2022 (2022) (doi) 10.1039/D2CE00278G

Diffuse Basis Functions for Relativistic s and d Block Gaussian Basis Sets Dyall
Kenneth G., Tecmer Paweł, Sunaga Ayaki
Journal of Chemical Theory and Computation 19(1) (2023) 198-210 (doi) 10.1021/acs.jctc.2c01050

Homogeneity of (U, M)O_2 (M = Th, Np) prepared by supercritical hydrothermal synthesis
Shirasaki Kenji, Tabata Chihiro, Sunaga Ayaki, Sakai Hironori, Li Dexin, Konaka Mariko, Yamamura Tomoo
Journal of Nuclear Materials 563 (2022) 153608 (doi) 10.1016/j.jnucmat.2022.153608

Thermal-Neutron capture cross-section measurements of Neptunium-237 with graphite thermal column in KUR
Nakamura Shoji, Shibahara Yuji, Endo Shunsuke, Kimura Atsushi
Journal of Nuclear Science and Technology 59(11) (2022) 1388-1398 (doi) 10.1080/00223131.2022.2058639

Structural Approach to Understanding the Formation of Amorphous Metal Hydroxides
Kobayashi Taishi, Fushimi Tomokazu, Mizukoshi Hirofumi, Motokawa Ryuhei, Sasaki Takayuki
Langmuir 38(48) (2022) 14656-14665 (doi) 10.1021/acs.langmuir.2c02081

Phase analysis of simulated nuclear fuel debris synthesized using UO_2, Zr, and stainless steel and leaching behavior of the fission products and matrix elements
Tonna Ryutaro, Sasaki Takayuki, Kodama Yuji, Kobayashi Taishi, Akiyama Daisuke, Kirishima Akira, Sato Nobuaki, Kumagai Yuta, Kusaka Ryoji, Watanabe Masayuki
Nuclear Engineering and Technology 4 (2022) 1300-1309 (doi) 10.1016/j.net.2022.12.017

Discovery of New Isotope U241 and Systematic High-Precision Atomic Mass Measurements of Neutron-Rich Pa-Pu Nuclei Produced via Multinucleon Transfer Reactions
Niwase T., Watanabe Y. X., Hirayama Y., Mukai M., Schury P., Andreyev A. N., Hashimoto T., Iimura S., Ishiyama H., Ito Y., Jeong S. C., Kaji D., Kimura S., Miyatake H., Morimoto K., Moon J.-Y., Oyaizu M., Rosenbusch M., Taniguchi A., Wada M.
Physical Review Letters 130 (2023) 132502 (doi) 10.1103/PhysRevLett.130.132502

A summary of environmental radioactivity research studies by members of the Japan Society of Nuclear and Radiochemical Sciences
Y. Igarashi, K. Tagami, K. Takamiya, A. Shinohara
Radiochimica Acta 110(6-9) (2022) 785-797 (doi) 10.1515/ract-2022-0019

Sr(ii) extraction by crown ether in HFC: entropy driven mechanism through H_2 PFTOUD
Shirasaki Kenji, Nagai Mitsuie, Nakase Masahiko, Tabata Chihiro, Sunaga Ayaki, Yaita Tsuyoshi, Yamamura Tomoo
RSC Advances 12(41) (2022) 26922-26933 (doi) 10.1039/d2ra04411k

Linearity and Chemical Bond of UO_2^{2+} Revisited: A Comparison Study with UN_2 and UE_2^{2+} (E = S, Se, and Te) Based on Relativistic Calculations
Sunaga Ayaki, Tabata Chihiro, Yamamura Tomoo
The Journal of Physical Chemistry A 126(46) (2022) 8606-8617 (doi) 10.1021/acs.jpca.2c05216

Proceedings

Characteristics of solvent extraction of antimony from nitric acid solutions using a new extractant
Chuya Saiga, Chizu Kato, Satoshi Fukutani, Tatsuro Matsumura, Toshiyuki Fujii
Proceedings of the 57th KURNS Scientific Meeting, Online/Kumatori, Japan (Feb. 14-15, 2023) 24（in Japanese)

Experiments on the formation of radionuclide endohedral fullerenes by laser
Makoto Inagaki
Proceedings of the 57th KURNS Scientific Meeting, Online/Kumatori, Japan (Feb. 14-15, 2023) 4-5（in Japanese)

Gallium concentrations in GSJ standard materials
Chizu Kato, Satoshi Fukutani, Toshiyuki Fuji,
Proceedings of the 57th KURNS Scientific Meeting, Online/Kumatori, Japan (Feb. 14-15, 2023) 16（in Japanese)

Redox behavior of vanadium ions in sodium orthovanadate solutions
Yuki Yokoyama, Akihiro Uehara, Naoya Wada, Renki, Sugiyama, Takuma Mototani, Chizu Kato, Toshiyuki Fuji
Proceedings of the 57th KURNS Scientific Meeting, Online/Kumatori, Japan (Feb. 14-15, 2023) 23（in Japanese)

Redox reaction of vanadium ions in the malonic acid system
Renki Sugiyama, Akihiro Uehara, Naoya Wada, Yuki Yokoyama, Takuma Mototani, Chizu Kato, Toshiyuki Fujii
Proceedings of the 57th KURNS Scientific Meeting, Online/Kumatori, Japan (Feb. 14-15, 2023) 33（in Japanese)

Solvent extraction characteristics of europium andt erbium from nitrica cid solutions usinga n ovelex tractant
Masaya lkeno, Chizu Kato, Satoshi Fukutani, Tatsuro Matsumura, Toshiyuki Fuji
Proceedings of the 57th KURNS Scientific Meeting, Online/Kumatori, Japan (Feb. 14-15, 2023) 15（in Japanese)

Study of lsotope Separation via Chemical Exchange Reaction
Ryuta Hazama, Takaaki Yoshimoto, Kumsut Pantiwa, Anawat Rttirong, Yoichi Sakuma, Toshiyuki Fujii, Satoshi Fukutani, Yuji Shibahara
Proceedings of the 57th KURNS Scientific Meeting, Online/Kumatori, Japan (Feb. 14-15, 2023) 34 (in Japanese)

Study on the solid phase and solubility of Zr, Ce oxide solid solutions
Yutaro Sato, Taishi Kobayashi, Takayuki Sasaki, Atsushi lkeda-Ohno, Daiju Matsumura, Ryuhei Motokawa
Proceedings of the 57th KURNS Scientific Meeting, Online/Kumatori, Japan (Feb. 14-15, 2023) 35（in Japanese)

Review

Discussion on Translational Research of Drug Product for Targeted Alpha Therapy-Part 8-Discussion on Targeted Alpha Therapy for Viral Infection
Yano Tsuneo, Takesi Fuchigami, Yutaka Takahasi, Yuichiro Kadonaga, Koki Hasegawa, Hiroki Kato, Tadashi Watabe, Tomoo Yamamura, Tatsuhiko Sato, Hirabayashi Yoko, Hirofumi Fujii, Yoshiharu Yonekura, Koichi Fukase
Pharmaceutical and medical device regulatory science 38(13) (2022) 2187-2200 (in Japanese)

10. Health Physics and Waste Management

Papers

Development of stabilization treatment technology for radioactive aluminum waste
SEKI Misaki, FUJITA Yoshitaka, FUJIHARA Yasuyuki, J. Zhang, YOSHINAGA Hisao, SANO Tadafumi, HORI Junichi, NAGATA Hiroshi, OTSUKA Kaoru, OMORI Takazumi, TAKEUCHI Tomoaki, IDE Hiroshi, TSUCHIYA Kunihiko
Journal of Nuclear Fuel Cycle and Environment 29(1) (2022) 2-9 (in Japanese) (doi) 10.3327/jnuce.29.1_2

Potential alpha particle detection with thin poly (ether sulfone) substrates
Nakamura Hidehito, Mori Kazuhiro, Shirakawa Yoshiyuki
Physica Scripta 97(8) (2022) 085303 (doi) 10.1088/1402-4896/ac807e

DEVELOPMENT OF A ROBOT FOR THE MEASUREMENT OF RADIOACTIVE CONTAMINATION AND FERTILITY OF THE SOIL IN FARMLAND
Tanigaki Minoru, Inoue Yoshio, Momota Sadao, Saito Takashi, Nemoto Tomoaki, Ono Tsukasa, Wada Akira, Ohashi Masaharu, Tsuno Koichi, Kano Masahiro, Matsuura Takahiro, Yasuoka Tadaaki, Hanai Hiroyuki, Arakawa Koichi
Radiation Protection Dosimetry 198(13-15) (2022) 964-970 (doi) 10.1093/rpd/ncac020

Reviews

Development of stabilization treatment technology for radioactive aluminum waste
SEKI Misaki, FUJITA Yoshitaka, FUJIHARA Yasuyuki, J. Zhang, YOSHINAGA Hisao, SANO Tadafumi, HORI Junichi, NAGATA Hiroshi, OTSUKA Kaoru, OMORI Takazumi, TAKEUCHI Tomoaki, IDE Hiroshi, TSUCHIYA Kunihiko
Journal of Nuclear Fuel Cycle and Environment 29(1) (2022) 2-9 (in Japanese) (doi) 10.3327/jnuce.29.1_2

Study on a relation between effective dose equivalents and risk weighted dose equivalents depending on age and sex.
Urabe Itsumasa
Japanese Journal of Health Physics 21(4) (2022) 251-256 (in Japanese) (doi) 10.5453/jhps.21.251

11. Accelerator Physics

Papers

Development of Combined-Function Multipole Permanent Magnet for High-Intensity Beam Transportation
Fuwa Y., Takayanagi T., Iwashita Y.
IEEE Transactions on Applied Superconductivity 32(6) (2022) 4006705 (doi) 10.1109/TASC.2022.3176251

Magnetic Field Shielding With Superconductors
Iwashita Y., Kuriyama Y., Tongu H., Fuwa Y.
IEEE Transactions on Applied Superconductivity 32(6) (2022) 3500404 (doi) 10.1109/tasc.2022.3167623

Performance of Bipolar Correction Magnet with Permanent Magnets
Kuriyama Yasutoshi, Iwashita Yoshihisa, Fuwa Yasuhiro, Terunuma Nobuhiro
IEEE Transactions on Applied Superconductivity 32(6) (2022) 1-4 (doi) 10.1109/TASC.2022.3180300

Properties of Praseodymium Permanent Magnet for Cryogenic Hybrid Magnet
Fuwa Yasuhiro, Iwashita Yoshihisa, Kondo Akihiro
IEEE Transactions on Applied Superconductivity 32(6) (2022) 4007304 (doi) 10.1109/TASC.2022.3179996

Measurement of 107-MeV proton-induced double-differential thick target neutron yields for Fe, Pb, and Bi using a fixed-field alternating gradient accelerator at Kyoto University
Iwamoto Hiroki, Nakano Keita, Meigo Shin-Ichiro, Satoh Daiki, Iwamoto Yosuke, Sugihara Kenta, Nishio Katsuhisa, Ishi Yoshihiro, Uesugi Tomonori, Kuriyama Yasutoshi, Yashima Hiroshi, Okabe Kota, Makii Hiroyuki, Hirose Kentaro, Orlandi Riccardo, Suzaki Fumi, Oizumi Akito, Tsukada Kazuaki, Maekawa Fujio, Mori Yoshiharu
Journal of Nuclear Science and Technology 60(4) (2022) 435-449 (doi) 10.1080/00223131.2022.2115423

Study on construction of an additional beamline for a compact neutron source using a 30 MeV proton cyclotron
Kuriyama Y., Hino M., Iwashita Y., Nakamura R., Tanaka H.
Journal of Physics: Conference Series 2420 (2022) 012110 (doi) 10.1088/1742-6596/2420/1/012110

Ionoacoustic application of an optical hydrophone to detect proton beam range in water
Sueyasu Shota, Takayanagi Taisuke, Miyazaki Koichi, Kuriyama Yasutoshi, Ishi Yoshihiro, Uesugi Tomonori, Unlu Mehmet Burcin, Kudo Nobuki, Chen Ye, Kasamatsu Koki, Fujii Masayuki, Kobayashi Masanori, Rohringer Wolfgang, Matsuura Taeko
Medical Physics 50(4) (2023) 2438- 2449 (doi) 10.1002/mp.16189

Proceedings

FABRICATION AND LOW-POWER TEST OF DISK-AND-WASHER CAVITY FOR MUON ACCELERATION
Y. Takeuchi, J. Tojo, Y. Nakazawa,Y. Kondo, R. Kitamura, T. Morishita, E. Cicek, H. Ego, K. Futatsukawa, N. Kawamura, M. Otani, T. Yamazaki, M. Yoshida, T. Mibe, N. Saito, Y. Iwashita, U. Sue, K. Sumi, M. Yotsuzuka, H. Yasuda
13th International Particle Accelerator Conference (IPAC22) Bangkok, Thailand (Jun. 12-17, 2022) 1534-1537

MAGNETIC FIELD SHIELD FOR SC-CAVITY WITH THIN Nb SHEET
Y. Iwashita, Y. Kuriyama, H. Tongu, Y. Fuwa
13th International Particle Accelerator Conference (IPAC22) Bangkok, Thailand (Jun. 12-17, 2022) 3090-3092

Spin-Polarrized Beam Production by Low-Energy Nuclear Reaction Using Inverse kinematics
M. Mihara, Y. Otani, Y. Kimura, T. Sugisaki, T. Moriguchi, A. Yano, K. Tomita, N. Kaname, A. Ozawa, H. Ishiyama, M. Fukutome, G. Takayama, R. Uda, H. Yuta, M. Fukuda
Proceedings of the Specialists' Meeting on "Nuclear Spectroscopy and Condensed Matter Physics Using Short-Lived Nuclei Ⅷ" Online (Jan. 28, 2022) 30-34 (in Japanese)

STUDY ON CONSTRUCTION OF AN ADDITIONAL BEAMLINE FOR A COMPACT NEUTRON SOURCE USING A 30 MeV PROTON CYCLOTRON
Y. Kuriyama, M. Hino, Y. Iwashita, R. Nakamura, H. Tanaka
13th International Particle Accelerator Conference (IPAC22) Bangkok, Thailand (Jun. 12-17, 2022) 3087- 3089

12. Other

Papers

Ultralow Thermal Conductivity of Highly Dense ZrW_2O_8 Ceramics with Negative Thermal Expansion
Tanusilp Sora-at, Kumagai Masaya, Ohishi Yuji, Furusawa Hideki, Suwabe Motoomi, Kurosaki Ken
Advanced Engineering Materials 24(9) (2022) 2101720 (doi) 10.1002/adem.202101720

Phase velocity of the Love wave estimated from the microtremor array records in the Wakayama plain, Japan, by using array-derived rotation
Kunikazu Yoshida, Hirotoshi Uebayashi, Michihiro Ohori
BUTSURI-TANSA(Geophysical Exploration) 75 (2022) 70-78 (in Japanese) (doi) 10.3124/segj.75.70

High-Pressure Diffusion Control: Na Extraction from $NaAlB_{14}$
Fujioka Masaya, Hoshino Mihiro, Iwasaki Suguru, Morito Haruhiko, Kumagai Masaya, Katsura Yukari, Zagarzusem Khurelbaatar, Ono Madoka, Nishii Junji
Chemistry of Materials 35(7) (2023) 3008-3014 (doi) 10.1021/acs.chemmater.3c00318

Compositional dependence of intensity and electric field gradient tensors for Fe^{2+} at the *M*1 site in Ca−rich pyroxene by single crystal Mössbauer spectroscopy
FUKUYAMA Daiki, SHINODA Keiji, TAKAGI Daigo, KOBAYASHI Yasuhiro
Journal of Mineralogical and Petrological Sciences 117(1) (2022) 220506 (doi) 10.2465/jmps.220506

Structured Approach for the Negotiation of the FM(C)T
Kumekawa Hirokazu, Tsuboi Hiroshi, Unesaki Hironobu
Journal of Nuclear Materials Management 50(3) (2022) 22-33

Deformation of an electron bunch caused by free-electron lasers
Sei Norihiro, Zen Heishun, Ohgaki Hideaki
Physica Scripta 98(2) (2023) 025510 (doi) 10.1088/1402-4896/acb253

X-ray diffraction study of phase transformation dynamics of Fe and Fe-Si alloys along the shock Hugoniot using an x-ray free electron laser
Krygier A., Harmand M., Albertazzi B., McBride E. E., Miyanishi K., Antonangeli D., Inubushi Y., Kodama R., Koenig M., Matsuoka T., Mogni G., Pietrucci F., Saitta A. M., Togashi T., Umeda Y., Vinci T., Yabashi M., Yabuuchi T., Fiquet G., Ozaki N.
Physical Review B 105(22) (2022) L220102 (doi) 10.1103/PhysRevB.105.L220102

Effects of data bias on machine-learning–based material discovery using experimental property data
Kumagai Masaya, Ando Yuki, Tanaka Atsumi, Tsuda Koji, Katsura Yukari, Kurosaki Ken
Science and Technology of Advanced Materials: Methods 2(1) (2022) 302-309
(doi) 10.1080/27660400.2022.2109447

Density Functional Study on the Photopolymerization of Styrene Using Dinuclear Ru–Pd and Ir–Pd Complexes with Naphthyl-Substituted Ligands
Salmahaminati, Inagaki Akiko, Hada Masahiko, Abe Minori
The Journal of Physical Chemistry A 127(12) (2023) 2810-2818 (doi) 10.1021/acs.jpca.3c01299

Studies on Networks for Monitoring Posts Based on Mesh-Type LPWA
TANIGAKI Minoru, TANAKA Atsunori, OKUMURA Ryo, YOSHINAGA Hisao, IINUMA Yuto, IKUTA Misao
Transactions of the Atomic Energy Society of Japan 22(1) (2023) 38-49 (in Japanese)
(doi) 10.3327/taesj.J21.025

Proceedings

Development of a method for controlling the physical properties of stored materials and a direct conversion process for the separation and temporary storage of MA
Tomoo Yamamura, Masahiko Nakase, Kenji Takeshita, Takashi Shimada, Koichi Kakinoki, Taisuke Tsukamoto, Hitomi Ishida, Ryo Takahashi
International Symposium on Zero Carbon Energy System Tokyo, Japan (Jan. 10-12, 2023) A23-3

Dissolution of Thorium Dioxide in Aqueous Solution by using Thermochemical Conversion
Feng Yin, ZuoRan Ma, Chihiro Tabata, Satoshi Fukutani, Tomoo Yamamura, Tatsuya Suzuki
International Symposium on Zero Carbon Energy System Tokyo, Japan (Jan. 10-12, 2023) A31-A33

Extraction behavior of the lightest Actinide, Actinium, for targeted alpha therapy
Masahiko Nakase, Kenji Shirasaki, Miki Harigai, Shingo Sugawara, Shinta Watanabe, Chihiro Tabata, Tomoo Yamamura
International Symposium on Zero Carbon Energy System Tokyo, Japan (Jan. 10-12, 2023) A23-1

Measurement of the Neutron Capture Cross Section of Am-243 with the ANNRI beam line, MLF/J-PARC
Yu Kodama, T. Katabuchi, G. Rovira, A. Kimura, S. Nakamura, S. Endo, N. Iwamoto, H. Nakano, Y. Sato, J. Hori, Y. Shibahara, K. Terada
15th International Conference on Nuclear Data for Science and Technology (ND2022) California, USA (Jul. 24-29, 2022)

Neutron beam filter system for neutron capture cross-section measurement at the ANNRI beamline of MLF/J-PARC
G. Rovira , A. Kimura , S. Nakamura , S. Endo, O. Iwamoto, N.Iwamoto, T. Katabuchi , Y. Kodama , H. Nakano, J. Hori, Y. Shibahara , K. Terada
15th International Conference on Nuclear Data for Science and Technology (ND2022) California, USA (Jul. 24-29, 2022)

Neutron capture cross-section measurement of lead-204 by mass spectrometry
Shoji NAKAMURA, Atsushi KIMURA, Syunsuke ENDO, Yuji SHIBAHARA, Toshiyuki SHIZUMA
2022 Fall Meeting of the Atomic Energy Society of Japan, Ibaraki, Japan (Sep. 7-9, 2022) 3N04 (in Japanese)

Scale up production of Ac-225 using an electron linear accelerator and drug labeling experiment
Mizuho Maeda, Takahiro Tadokoro, Yuichiro Ueno, Takahiro Watanabe, Hidetoshi Kikunaga, Kenji Shirasaki, Mitsuyoshi Yoshimoto, Hirofumi Fujii, Shun Sekimoto, Tsutomu Ohtsuki, Yuko Kani, Kento Nishida, Takahiro Sasaki, Shigeru Kashiwagi, Kazunobu Ohnuki, Makoto Inagaki, Satoshi Fukutani, Yuji Shibahara
2022 Fall Meeting of the Atomic Energy Society of Japan, Ibaraki, Japan (Sep. 7-9, 2022) S0818B (in Japanese)

Thed evelopment of ana cceleratorb asedt hermalne utronf ield and are actorb asedc old neutrons ource using P HlTS code.
Riichiro Nakamura, Masaliro Hino, Hiroki Tanaka, Yasutoshi Kuriyama, Yoshihisa Iwashita, Masakai Sugiyama, Nobuhiro Sato, Yutaka Abe, Masaji Arai, Yuji Kawabata, Ken Nakajima
Proceedings of the 57th KURNS Scientific Meeting, Online/Kumatori, Japan (Feb. 14-15, 2023) 7-9 (in Japanese)

Reviews

Basic Knowledge of Neutron: Generation of Neutrons Accompanied with the High-Energy Photon Therapy
Akihiro Nohtomi
Japanese Journal of Medical Physics (Igakubutsuri) 42(3) (2022) 149 (in Japanese)

Toward construction of cross-organizational education system for nuclear engineering
Kurosaki Ken, Kozaki Tamotsu, Nakashima Hiroshi, Obara Toru, Wakabayashi Genichiro, Pyeon Cheolho, Matsuyama Shigeo, Abe Hiroshi, Uno Masayoshi, Yamamoto Akio
Journal of the Atomic Energy Society of Japan 64(9) (2022) 520-524 (in Japanese) (doi)10.3327/jaesjb.64.9_520

Others

Evaluatation Test of Quantitative 3-D Measurement of Gamma Dose in the Reactor Bulding by ETCC
T. Tanimori, S. Sonoda, A. Takada, M. Tsuda, K. Tahara, K. Kobayasi, H. Nagai, T. Sato, H. Nakayama, M.Tanigaki, A. Taniguchi
KURNS Progress report 2021 (2022) 254

KURNS Progress Report 2022

Issued in July 2023

Issued by the Institute for Integrated Radiation and Nuclear Science,
Kyoto University
Kumatori-cho, Sennan-gun, Osaka 590-0494 Japan

Tel. +81-72-451-2300
Fax. +81-72-451-2600

In case that corrections are made, overwrite the modified version
in the following web page:
https://www.rri.kyoto-u.ac.jp/PUB/report/PR/ProgRep2022/ProgRep2022.html

Publication Team

INOUE, Rintaro (Chief)
ISHI, Yoshihiro
KOBAYASHI, Norika
NAKATANI, Maki
NAKAYAMA, Chiyoko
SAKURAI, Yoshinori (Subchief)
SHEN, Xiuzhong
TAKAGI, Masae
TAKATA, Takumi
TOMINAGA, Yuta
UMEDA, Yuhei
YOKOTA, Kaori